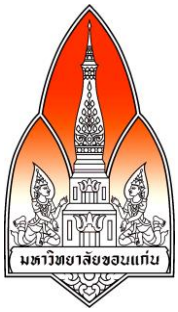

รายงานวิจัยฉบับสมบูรณ์

โครงการ
“การออกแบบเชิงผลึกและสมบัติฟังก์ชันของโครงข่ายโลหะอินทรีย์”

โดย ศ.ดร. สุจิตรา ยังมี และคณะ

กรกฎาคม 2559

สัญญาเลขที่ BRG5680009

รายงานวิจัยฉบับสมบูรณ์

โครงการ“การออกแบบเชิงผลึกและสมบัติฟังก์ชันของโครงข่ายโลหะอินทรีย์”

คณะผู้วิจัย

1. ศ.ดร.สุจิตรา ยังมี	มหาวิทยาลัยขอนแก่น
2. ผศ.ดร.เชวง ภควัตชัย	มหาวิทยาลัยสงขลานครินทร์
3. ผศ.ดร.กิตติพงษ์ ไชยนอก	มหาวิทยาลัยธรรมศาสตร์
4. ดร.เจ้าทรัพย์ บุญมาก	มหาวิทยาลัยขอนแก่น
5. Prof. Keith S. Murray	Monash University, Australia
6. Prof. Patrick Gamez	Universitat de Barcelona, Spain
7. Prof. Francesc Illas	Universitat de Barcelona, Spain

สนับสนุนโดยสำนักงานกองทุนสนับสนุนการวิจัยและมหาวิทยาลัยขอนแก่น

สัญญาเลขที่ BRG5680009

โครงการ “การออกแบบเชิงผลึกและสมบัติฟังก์ชันของโครงข่ายโลหะอินทรีย์”

(Crystal designs and functional properties of metal-organic frameworks)

Abstract

The field of metal-organic frameworks has been extensively investigated over the past few decades with a focus on functional material research and crystal engineering. One of the challenges in this field is to forecast the crystal structure from the building units. This research discusses the crystal structures and functional properties toward catalysis, spin-crossover, and the structural dynamic behaviors in a novel series of metal-organic frameworks and metal-supramolecular frameworks containing various carboxylates and *N*-donor organic ligands. In the first system, carboxylato zinc(II) metal-organic frameworks with 1,2-bis(4-pyridyl)ethane exhibit diverse structural frameworks and act as active heterogeneous catalysts for the high-yield cyanosilylation reactions and show highly size-selective properties for the substrate benzaldehyde. Next, the study of the magnetic properties of new spin-crossover iron(II) complexes with 2,2′-dipyridylamino/*s*-triazine-based ligands and triply-bridged dinuclear copper(II) complexes are reported. Interestingly, the spin-crossover properties of these complexes present distinct behaviors which are both ligand- and anion-dependent. The investigation carried out clearly shows the importance of supramolecular contacts in the cooperativity of the spin-transition process. Finally, a variety of novel cobalt(II) coordination polymers and supramolecular frameworks reveal solvent-induced reversible structural dynamic behaviors with chromotropism.

Keywords: crystal engineering, metal-organic framework, heterogeneous catalyst, spin-crossover, structural dynamic behaviors, magnetic properties

สัญญาเลขที่ BRG5680009

โครงการ “การออกแบบเชิงผลึกและสมบัติฟังก์ชันของโครงข่ายโลหะอินทรีย์”

(Crystal designs and functional properties of metal-organic frameworks)

บทคัดย่อ

งานวิจัยในเรื่องโครงข่ายโลหะอินทรีย์ได้รับความสนใจเป็นอย่างยิ่ง ทั้งในด้านสมบัติฟังก์ชันของวัสดุและด้านวิศวกรรมเชิงผลึก ในงานวิจัยฉบับนี้ได้อภิปรายการศึกษาโครงสร้างผลึกและสมบัติฟังก์ชันในด้านการเร่งปฏิกิริยา สปินครอส-โอเวอร์ และพฤติกรรมโครงสร้างเชิงพลวัติ ของซีรีย์โครงข่ายโลหะอินทรีย์และโครงข่ายโลหะซุปราโมเลกุลชนิดใหม่ที่ประกอบด้วยลิแกนด์คาร์บอกซิเลตและลิแกนด์อินทรีย์ชนิด N-ดอเนอร์ที่หลากหลาย ในระบบแรกเป็นโครงข่ายโลหะอินทรีย์คาร์บอกซิเลโต Zn(II) ที่ประกอบด้วยลิแกนด์ 1,2-bis(4-pyridyl)ethane แสดงความหลากหลายทางโครงสร้างและเป็นตัวเร่งปฏิกิริยาวิวิธพันธ์ที่มีประสิทธิภาพสำหรับปฏิกิริยา cyanosilylation และแสดงสมบัติความจำเพาะต่อขนาดของซับสเทรตชนิด benzaldehyde ในระบบถัดมาเป็นการศึกษาสมบัติทางแม่เหล็กของสารเชิงซ้อนสปินครอส-โอเวอร์ Fe(II) กับลิแกนด์ 2,2′-dipyridylamino/s-triazine และสมบัติทางแม่เหล็กของสารเชิงซ้อน triply-bridged dinuclear Cu(II) ชนิดใหม่ เป็นที่น่าสนใจว่า สมบัติสปินครอส-โอเวอร์ของสารเชิงซ้อนในกลุ่มนี้ แสดงพฤติกรรมที่ขึ้นกับชนิดของลิแกนด์และชนิดของไอออนลบที่เป็นองค์ประกอบและผลการศึกษานี้แสดงให้เห็นถึงบทบาทสำคัญของของอันตรกิริยาซุปราโมเลกุลในโครงสร้างผลึกต่อ cooperativity ในกระบวนการแทรนซิชันของสปิน และในระบบสุดท้าย โคออร์ดิเนชันพอลิเมอร์และโครงข่ายซุปราโมเลกุลชนิดใหม่ที่ประกอบด้วยไอออน Co(II) แสดงพฤติกรรมโครงสร้างเชิงพลวัติแบบผันกลับได้ พร้อมการเปลี่ยนแปลงสีเมื่อถูกเหนี่ยวนำด้วยตัวทำละลาย

คำสำคัญ: วิศวกรรมเชิงผลึก โครงข่ายโลหะอินทรีย์ ตัวเร่งปฏิกิริยาวิวิธพันธ์ สปินครอส-โอเวอร์ พฤติกรรมโครงสร้างเชิงพลวัติ สมบัติแม่เหล็ก

สัญญาเลขที่ BRG5680009

โครงการ "การออกแบบเชิงผลึกและสมบัติฟังก์ชันของโครงข่ายโลหะอินทรีย์"

(Crystal designs and functional properties of metal-organic frameworks)

Executive Summary

Metal-organic frameworks (MOFs) also known as coordination polymers, are crystalline compounds consisting of infinite lattices built up of the inorganic secondary building unit (metal ions or clusters) and organic linkers, connected by coordination bonds of moderate strength. Distinct from traditional inorganic materials, MOFs can be synthesized from well-defined molecular building blocks thanks to both the reliability of molecular synthesis and the hierarchical organization via crystal engineering. Crystal engineering may be regarded as the rational design and building of crystal structures from well-chosen constituent molecules. Although great progress has been achieved through several decades of intense investigation in this area of chemistry, there is still no general approach to predict precisely the arrangement of molecules in crystalline lattices. The obvious reason for this situation is the potential involvement of numerous factors during the crystallization process in addition to the specific nature of the molecular building blocks. Accordingly, external factors such as solvent, temperature, pH, pressure, super-saturation or the presence of impurities may play a crucial role in crystallization. The crystal engineering of MOFs has drawn great interest from the scientific community in the last 15 years. This enthusiasm for MOFs is due to their high structural versatility, porosity and their broad variety of properties, functions and potential applications, such as gas adsorption and storage, magnetism, luminescence, catalysis and ion exchange.

In this research, a novel series of transition metal complex-assemblies in inorganic-organic hybrid materials including MOFs and metal-supramolecular frameworks containing carboxylates and *N*-donor organic linkers have been synthesized by various techniques, and then spectroscopically and crystallographically characterized. Their functional properties *i.e.* catalysis, spin-crossover, and the structural dynamics will be studied. An emphasis is therefore given to the analyses of the crystal structures and functional properties of many product systems. Thus, this research can be separated into three parts:

Part I addresses the syntheses, structural characterization and catalytic properties of carboxylato metal-organic frameworks containing 1,2-bis(4-pyridyl)ethene. Two new MOFs, $\{[Zn(dpe)(\mu\text{-}OOCCH_3)_2](H_2O)\}_n$(**1**) and $\{[Zn_3(dpe)_4(\mu\text{-}OOCC_2H_5)_4](dpe)\text{-}(ClO_4)_2\}_n$(**2**) (dpe = 1,2-bis(4-pyridyl)ethene), have been prepared and investigated. Their structures were determined by X-ray crystallography. The different structures of both compounds indicate that the different steric constraints for a methyl group (acetato, compound **1**) and an ethyl group (propionato, compound **2**), as well as the counterion effects (ClO_4^- for **2**), play an important role in the formation and structure of these

coordination polymers. The 1D (**1**) and 2D (**2**) networks exhibit voids that contain guest water molecules for **1** and perchlorate/dpe for **2**. Interestingly, both Zn(II) compounds act as active heterogeneous catalysts for the high-yield cyanosilylation of acetaldehyde in dichloromethane and show highly size-selective properties for the substrate benzaldehyde. The metal sites in each compound have been studied in some more detail by using doped species with Mn(II) and Cu(II) and the EPR properties.

Part II deals with the study of the magnetic properties of new spin-crossover (SCO) iron(II) complexes and triply-bridged dinuclear copper(II) complexes. In the first instance, the investigation of the SCO properties of a series of six new iron(II) complexes of formula *trans*-[Fe(L)], where L = 2,2′-dipyridylamino/*s*-triazine-based ligands and X = S or Se, is reported. The SCO properties were investigated by means of single-crystal X-ray diffraction studies, magnetic susceptibility measurements, photomagnetic (LIESST) studies and differential-scanning calorimetry (DSC) experiments. Interestingly, the SCO properties of these iron(II) compounds present distinct behaviors which are both ligand- and anion-dependent. Secondly, new triply-bridged dinuclear copper(II) compounds are described, for which the magnetic properties have been examined, both experimentally and theoretically. These complementary studies have allowed to assess magneto-structural correlations, and to develop a computational procedure to predict accurately the magnetic coupling constant, *J*, for such molecules. All copper complexes have been characterized spectroscopically and structurally. Their magnetic properties have been investigated by means of magnetic susceptibility measurements and theoretical calculations, applying state of the art density functional theory (DFT) methods, where the effect of the type of functionals and of the basis sets used to represent the electron density has been explored.

Part III addresses the syntheses, structural characterization of cobalt(II)-supramolecular networks and their functional properties toward dynamic structural transformation with chromotropism, which are separated into four systems including solvent-induced reversible crystal-to-amorphous transformation properties of cobalt(II) 4-aminomethylpyridine-sulfate with chromotropism, flexible metal-supramolecular framework of 2D cobalt(II) coordination polymer with 3,5-pyridinedicarboxylate, next, water-induced reversible crystal-to-amorphous structural transformation of $[Co_2(2,4\text{-}pydc)_2(bpa)(H_2O)_6](H2O)_2$, and water-induced structural dynamics of cobalt(II) coordination and supramolecular frameworks containing benzene-1,2,4,5-tetracarboxylic acid and trans-1-(2-pyridyl)-2-(4-pyridyl)ethylene. All results verify that the solvent molecules play a key role by acting as an essential support to the structure of the host framework and it is important for expanding the field of crystal engineering by controlling the weak interaction of MOFs.

The research outcome includes 18 international publication papers.

TABLE OF CONTENTS

PART I

CARBOXYLATO METAL-ORGANIC FRAMEWORKS CONTAINING 1,2-BIS(4-PYRIDYL)ETHENE: TOPOLOGY AND CATALYTIC PROPERTIES

Introduction

The design and construction of coordination polymers, often called metal organic frameworks, have attracted great attention owing to their interesting topologies, their potential applications in catalysis, gas storage, molecular recognition, and their magnetic, electrical, and non-linear optical properties [1-10]. Generally, the preparation of such materials can be influenced by many factors, such as the nature of organic ligands, the coordination preference of central metal ion, the crystallization conditions, the metal/ligand ratio, and the reaction solvent system, etc. [11-16]. Numerous examples of metal organic frameworks were constructed making use of hydrogen bonding, π–π contacts, and/or other weak and non-covalent interactions [17 - 18]. In the vast amount of the reported work, a variety of 1D, 2D, and 3D metal organic frameworks have been successfully obtained via the use of coordinating functional groups, such as carboxylates, 4,4′-bpy-based ligands, and mixtures of both carboxylate and 4,4′-bpy ligands [19-22]. In coordination networks in general the 4,4′-bpy ligands may act in a bidentate bridging, or monodentate terminal modes, resulting in 1D linear, zigzag, ladder, molecular antenna railroads and chains, 2D bilayer, square and rectangular grid networks, or 3D non-interpenetrated and interpenetrated networks.

Therefore, the diversity and topologies on the molecular architecture have now been further extended by using a more flexible organic linker, i.e. 1,2-bis(4-pyridyl)ethene (dpe) (Scheme 1), during the synthesis of the coordination assembly and related to recent literature [23-27].

In the present study, the semi-flexible ligand dpe (see Scheme 1), the effect of the steric hindrance of different carboxylato ligands (acetato and propionato ligands) and the influence of the nature of the anion used, on the solid-state structure of the corresponding coordination materials have been investigated. Thus, multicomponent polymeric networks have been synthesized from zinc(II) ions, dpe and a carboxylato ligand. It appears that their single-crystal X-ray structures reveal a significant influence of a methyl (acetate) and an ethyl (propionate) group on the assembly of the coordination framework, as well as the effect of counteranion on the observed coordination topology. The compounds $\{[Zn(dpe)(\mu\text{-}OOCCH_3)_2](H_2O)\}_n$ (**1**) and $\{[Zn_3(dpe)_4(\mu\text{-}OOCC_2H_5)_4](dpe)(ClO_4)_2\}_n$ (**2**) have been synthesized and characterized using XRD and EPR of their doped Mn(II) and Cu(II) derivatives. The thermal stability and catalytic properties of both compounds in the cyanosilylation of aldehydes have been investigated. Furthermore, the potential use in cation-exchange for compound **2** has been explored.

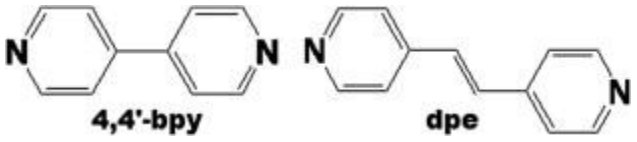

Scheme 1.1 The conformations of rigid ligand 4,4′-bpy and semi-flexible ligand dpe.

Experimental

Synthesis

1. Synthesis of $\{[Zn(dpe)(\mu\text{-}OOCCH_3)_2](H_2O)\}_n$ (**1**)

An aqueous solution (15 mL) of $Zn(NO_3)_2{\cdot}6H_2O$ (0.306 g, 1.0 mmol) was added to a solution of dpe (0.182 g, 1.0 mmol) in ethanol (10 mL). Next, an aqueous solution (20 mL) of NaO_2CCH_3 (0.138 g, 2.0 mmol) was added under continuous stirring. This solution was allowed to stand unperturbed for the slow evaporation of the solvent at room temperature, producing colorless needle crystals of 1 after a few days. Yield ca. 69%. Elemental *Anal.* Calc. for $C_{16}H_{18}N_2O_5Zn$ (383.71): C, 50.08; H, 4.73; N, 7.30. Found: C, 50.09; H, 4.84; N, 7.59%. IR (cm^{-1}): ν_{as}(COO) 1575, ν_s(COO) 1416, δ(O–C–O) 644.

2. Synthesis of $\{[Zn_3(dpe)_4(\mu\text{-}OOCC_2H_5)_4](dpe)(ClO_4)_2\}_n$ (**2**)

An aqueous solution (10 mL) of $Zn(NO_3)_2{\cdot}6H_2O$ (0.313 g, 1.0 mmol) was added to a solution of dpe (0.182 g, 1.0 mmol) in ethanol (10 mL). Subsequently, an aqueous solution (10 mL) of $NaCOOCH_2CH_3$ (0.201 g, 2.0 mmol) was added, followed by $KClO_4$(0.152 g, 1.0 mmol) under continuous stirring. Next, a few drops of 98% CH_3CH_2COOH were added, yielding a clear colorless solution, which was allowed to stand unperturbed for the slow evaporation of the solvent at room temperature. Colorless crystals of 2 were collected from the solution by filtration after several days. Yield ca. 70%. Elemental *Anal.*Calc. for $C_{72}H_{70}Cl_2N_{10}O_{16}Zn_3$ (1598.46): C, 54.10; H, 4.41; N, 8.76. Found: C, 53.72; H, 4.74; N, 9.07%. IR (cm^{-1}): ν_{as}(COO) 1569, ν_s(COO) 1417, δ(O–C–O) 643, $\nu(ClO_4)$ 1104–1045.

3. Synthesis of $\{[Zn_3(dpe)_4(\mu\text{-}OOCC_2H_5)_4](dpe)(ClO_4)_2\}_n$ (**2**) doped with Cu^{2+} (**2a**) and Mn^{2+} (**2b**)

An aqueous solution (10 mL) of $Zn(NO_3)_2{\cdot}6H_2O$ (0.313 g, 1.0 mmol) was added to a solution of dpe (0.184 g, 1.0 mmol) in ethanol (10 mL). Subsequently, an aqueous solution (10 mL) of $NaCOOCH_2CH_3$ (0.201 g, 2.0 mmol) was added, followed by $KClO_4$(0.152 g, 1.0 mmol) and 0.003 g (0.002 mmol) of $Cu(NO_3)_2{\cdot}3H_2O$ (or 0.003 g $Mn(NO_3)_2{\cdot}4H_2O$ (0.002 mmol)) under continuous stirring. Next, a few drops of CH_3CH_2COOH 98% were added, yielding a clear colorless solution, which was allowed to stand unperturbed for the slow evaporation of the solvent at room temperature. After several days, colorless crystals of **2a** (or **2b**) were obtained. The crystals were filtered, washed with the mother liquor and dried in air. Yield ca. 66% (ca. 58% for **2b**). The IR spectra of **2a** and **2b** are similar to that of **2**.

Crystal structure determination

The X-ray single-crystal data for compounds **1** and **2** were collected at 293(2) K on a 1 K Bruker SMART CCD area detector diffractometer using graphite monochromated Mo Kα radiation (λ = 0.71073 Å) at a detector distance of 4.5 cm and swing angle of −35°. A hemisphere of the reciprocal space was covered by combination of three sets of exposures; each set had a different ϕ angle (0°, 88°, and 180°) and each exposure of 40 s covered 0.3° in ω. Data reduction and cell refinements were performed using the program SAINT[28]. An empirical absorption correction by using the SADABS[29] program was applied, which resulted in transmission coefficients ranging from 0.642 to 0.823 and 0.600 to 0.680 for compounds **1** and **2**, respectively. The structures were solved by direct methods and refined by full matrix least-squares method on $(F_{obs})^2$ with anisotropic thermal parameters for all non-hydrogen atoms using the SHELXTL-PC V 6.12 software package [30]. The H atoms were introduced at calculated positions and refined with a fixed geometry with respect to their carrier atoms. One water oxygen atom of **1** and the perchlorate groups of **2** were found disordered and were refined with site occupancies of 0.5.

Catalytic reactions

A typical cyanosilylation reaction was performed as follows: 40 mg (0.006 mmol, 0.2 mmol of Zn) of MOF catalyst was suspended in 5 mL of dry dichloromethane (CH_2Cl_2) or tetrahydrofuran (THF), followed by the addition of the aldehyde (1.5 mmol) and trimethylsilyl cyanide (3 mmol). The reaction mixtures were stirred at room temperature under argon. The reaction conversions as a function of time were determined by gas chromatography (GC) analysis.

Results and discussion

Synthesis and structure

Crystalline materials were obtained for both compounds prepared from zinc(II) ions, dpe and carboxylato ligands in ethanol–H_2O solvent mixtures. Other solvent combinations were used, i.e. methanol–H_2O and acetone–H_2O, but the solvent pair ethanol–H_2O gave the best results in terms of yield and quality of crystals. Moreover, other counter anions (i.e. PF_6^-, BF_4^- and $CF_3SO_3^-$) were examined. Unfortunately, the quality of these crystals was not good enough for single-crystal X-ray analysis. Compounds **1** and **2**exhibit different topologies, induced by the different carboxylate ligands used, as well as the counteranion effects (ClO_4^- for **2**), play an important role in the formation and structure of these coordination polymers.

The combination Zn(II)/dpe/acetate generates a 1D zig–zag polymeric chain of **1**resulting from the secondary building units with tetrahedral geometry (Fig. 2(A)). The complete replacement of acetate by propionate for the case of the ClO_4^- ion results in the formation of a 2D network (compound **2**; Fig. 5). This simple framework is built from trinuclear propionato-bridged units that are linked to two adjacent ones, to form a triple-stranded chain.

Crystal structure of {[Zn(dpe)(μ-$OOCCH_3$)$_2$](H_2O)}$_n$ (1)

The 1D molecular structure of compound **1** exhibits only one type of zinc(II) ion, with a tetrahedral N_2O_2 coordination environment (Fig. 1). Each Zn(II) ion lies on an inversion centre and is surrounded by two oxygen atoms belonging to two acetato ligands and two nitrogen atoms occupying by two pyridine N-donors from two different (bridging) dpe moieties. Two acetato ligands [O1 and O1a] act as a monodentate terminal ligands. The Zn–O and Zn–N bond distances can be considered as normal for this type of ZnN_2O_2coordination environment [31]. The distance Zn–O2 of 2.982(1) Å is too long to be considered as coordination.

The metal organic framework is formed from mononuclear units which are connected through two dpe ligands to the other Zn(II) ions, generating 1D zig–zag infinite chains (Fig. 2A). These chains show π–π interactions along dpe units (with centroid-to-centroid distances ranging from 3.711(1) to 4.704(1) Å) and are connected to each other producing the closely packed 2D layers (Fig. 2B). Each layer is linked to one layer above and to one layer below through hydrogen bonded lattice water molecules forming “ABAB..” layers (Fig. 2C), and the corresponding schematic mode, illustrated top layer and bottom layer by blue and green, respectively (Fig. 2D). The corners of these layers, made up by the $Zn(OOCH_3)_2$ groups, are surrounded by the disordered water molecules and all of these are connected to the acetato ligands in corners via relatively strong O–H···H hydrogen bonding interactions (O5a···O2 = 2.690(1) Å and O5b···O2 = 2.865(1) Å). Through these hydrogen bonds the zig–zag layers are connected with each other via the guest water molecules (O5) to form a 3D supramolecular network with an empty cavity (Fig. 3).

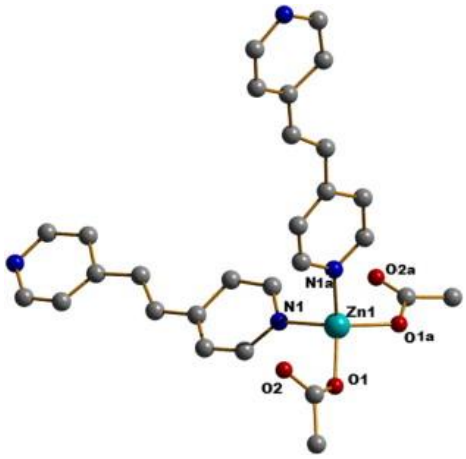

Fig. 1. Representation of part of the molecular structure of **1** showing the atom labeling scheme for the zinc(II) ion. The H atoms are not shown for clarity. Symmetry operations: (a) $1 - x, y, 0.5 - z$.

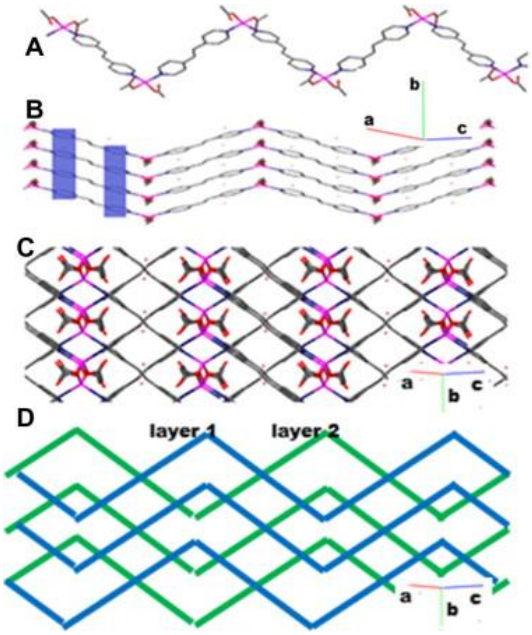

Fig. 2. (A) 1D zig–zag infinite chain of **1**, (B) the π–π interactions along dpe units form 2D layers, (C) and (D) each layer is stacked atop of each other to form a square grid structure in the top view and the corresponding schematic mode.

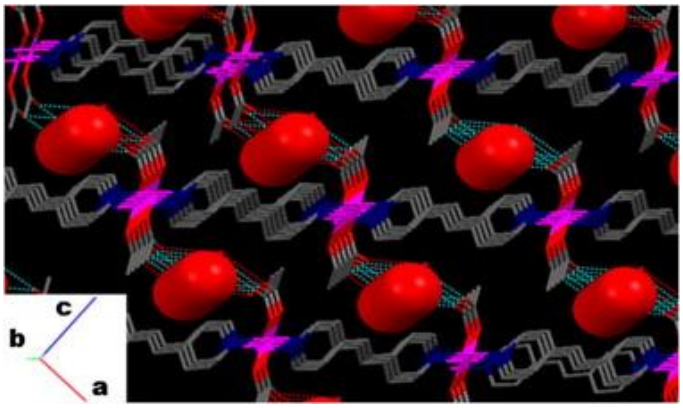

Fig. 3. 3D packing structure of **1** projected on the *bc* plane, and illustrating the intermolecular hydrogen bonding by the dotted lines.

Crystal structure of {[Zn_3(dpe)$_4$(μ-$OOCC_2H_5$)$_4$](dpe)(ClO_4)$_2$}$_n$ (2)

The influence of counteranion and steric effect on the molecular architecture has been investigated by using a propionato ligand during the synthesis of the coordination assembly from reaction of the $Zn(NO_3)_2 \cdot 6H_2O$, dpe and propionato ligand in an $EtOH/H_2O$ mixture with an incorporated ClO_4^- anion during synthesis procedure. Indeed, the solid-state structure of compound {[Zn_3(dpe)$_4$(μ-$OOCC_2H_5$)$_4$](dpe)(ClO_4)$_2$}$_n$ (**2**), bearing ethyl groups, shows significant differences compared to that of **1** (holding methyl groups).

The 2D molecular structure of compound **2** exhibits two different types of zinc(II) ions with octahedral-based N_3O_3 (Zn1) and N_2O_4 (Zn2) geometries (Fig. 4). Zn1 is characterized by a strongly distorted octahedral coordination environment, owing to the small bite angle of the μ-O,O′,O′ bridging mode of one of the two propionato ligands (the angle O3–Zn1–O4 is only 59.4(2) Å). The basal plane is constituted of three oxygen atoms belonging to two propionato ligands (O2, O3 and O4) and one dpe ligand (N3). The octahedron is completed by two dpe nitrogen atoms (N1 and N2), at the axial positions, linking Zn1 to two symmetry-related Zn1a ions, generating a polymeric chain exhibiting the sequence {Zn1, Zn1a, Zn1, Zn1a,…} along *c* axis (Fig. 5). The Zn–O and Zn–N bond distances are in normal ranges for this type of coordination moiety [32].

Zn2 lies on an inversion centre. The coordination environment around the Zn2 ion is an almost undistorted octahedron, since the basal angles, varying from 88.7(2)° to 91.3(2)°, are close to the ideal value of 90°. At the basal plane, Zn2 is coordinated by four oxygen atoms (O1, O3, O1a and O3a) from different propionato ligands. The axial positions are occupied by nitrogen atoms N4 and N4a, belonging to two dpe ligands (located on an inversion centre) at common distances. Zn2 is bridged to two symmetry-related Zn1 ions via two μ-O,O′- and two μ-O,O′,O′-propionato ligands, generating a linear trinuclear [Zn1a, Zn2, Zn1] cluster (Fig. 5).

The trinuclear [Zn1a, Zn2, Zn1] clusters are connected to each other, in a head-to-tail fashion, through the coordination of the zinc(II) ions by dpe ligands, producing a 1D chain exhibiting the sequence {Zn2, Zn2, Zn2,…} for the central metal ion and {Zn1, Zn1a, Zn1, Zn1a,…} for the external zinc(II) ions. This arrangement gives rise to triple-stranded chains, illustrated by the blue, green and yellow dpe ligands in Fig. 5. These coordination polymeric chains are compared to those observed for compound **1** (see Fig. 2 and Fig. 5). In contrast to the methyl groups in **1**, the ethyl groups of the propionato ligands in **2** do not allow a close packing of

the zig-zag polymeric chains, as the result of steric constraints (Fig. 6). This spatial organization allows the coordination of dpe ligands at the two external positions of the trizinc moieties (red-colored dpe ligands coordinated to Zn1 and Zn1a along *a* axis; Fig. 5), connecting the triple-stranded chains to each other to form a 2D network. Consequently, each layer in **2** exhibits two distinct types of channels, narrow channels (3.820 × 13.719 $Å^2$) within the triple-stranded chains and larger channels (13.578 × 13.719 $Å^2$) between the triple-stranded chains are found (see Fig. 7). Indeed, the shorter interlayer Zn···Zn separation distance is 7.054(3) Å for compound **2**, while that of **1** is 9.401(3) Å.

The herringbone-type architecture exhibits large cavities that can accommodate bulky guest molecules, namely non-coordinated dpe ligands and disordered perchlorate anions (Fig. 7) which are hydrogen-bonded to each other ($O(ClO_4)$···H–C = 2.527(6)–2.671(6) Å. In addition, these guest molecules do significantly interact with the metal organic framework. The non-coordinated dpe ligands are hydrogen bonded to pyridine rings of dpe ligands to adjacent layer (N5···H–C = 3.471(6)–3.662(6) Å) and the disordered perchlorate anions are also hydrogen bonded to the pyridine rings of the dpe ligands to adjacent layer (O5B···H–C = 2.459(6)–2.527(6) Å, O6A···H–C = 2.362(6)–2.617(6) Å, O6B···H–C = 2.598(6)–2.612(6) Å, and O8B···H–C = 2.558(6)–2.675(6) Å). This intricate network of supramolecular bonds produces a three-dimensional structure.

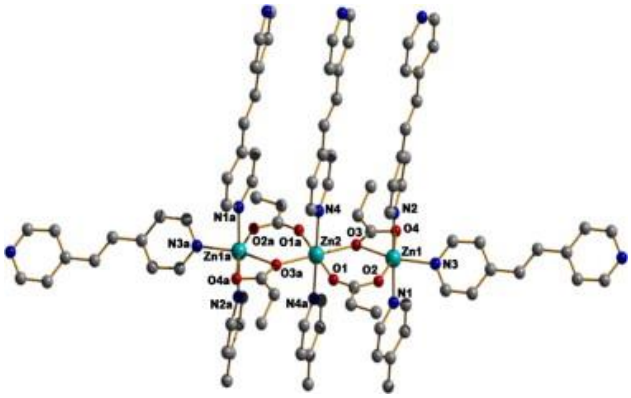

Fig. 4. Representation of the molecular structure of **2** showing the atom labeling scheme for the zinc(II) ions. The perchlorate anions, the lattice dpe molecules and the H atoms are not shown for clarity. Symmetry operations: (a) −*x*, 2 − *y*, 1 − *z*.

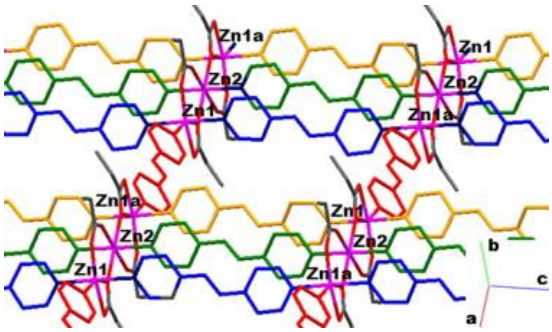

Fig. 5. 2D coordination network in **2**. The dpe ligands involved in the formation of trinuclear zinc(II) units are shown in blue, green and yellow-orange and those connecting the 1D triple-stranded chains are shown in red.

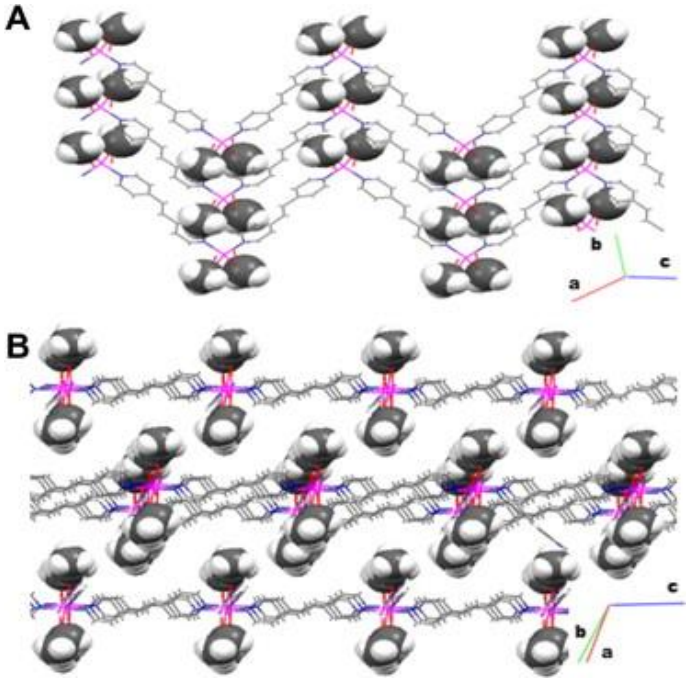

Fig. 6. Illustrations of the steric hindrance due to the acetato methyl groups (shown in the space-filling mode) in **1**(A) and propionato ethyl groups in **2** (B), which prevents close contacts between the 1D zig-zag chains.

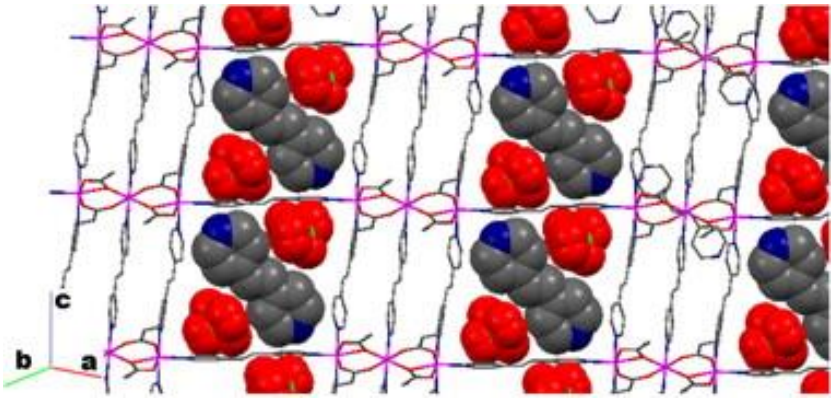

Fig. 7. Representation of the 2D network of compound **2**, illustrating the large cavities which contain non-coordinated dpe ligands and disordered perchlorate anions (space-filling mode).

Effect of the couteranion and carboxylato ligand on the topologies of compounds 1and 2

Single crystal X-ray analyses revealed that compounds **1** and **2** have different structural topologies. The use of slightly different carboxylato, namely the acetato and propionato moieties as secondary co-ligands of [Zn(II)/dpe] coordination units, applying the similar reaction conditions, but with additional ClO_4^- ions for **2**, indeed leads to the formation of drastically distinct networks (Scheme 2). The combination of Zn(II) ions, dpe ligands and acetato co-ligands

in **1** generates a 1D zig–zag polymeric chain (Scheme 2A) resulting from the assembly of mononuclear chain secondary building units with tetrahedral geometry. The sole replacement of acetate by propionate without additional ClO_4^- ion, did not result in a crystalline product. Hence the $KClO_4$ was added to the reaction during synthesis procedure, and these results in the formation of 2D network (Scheme 2B) confirming that ClO_4^- anions influence in the formation of the framework. This simple framework is built from trinuclear propionato-bridged units that are linked to two adjacent ones, to form a triple-stranded chain. These triple-stranded chains are connected to each other via dpe ligands (vertical red lines in Scheme 2B). This indicates that not only the steric hindrance between acetate and propionate ligands but also the nature of the counter ion is one of the factors that can affect the overall structure of coordination networks [33]. Therefore, the combination of effects between steric hindrance of carboxylate ligands and anions play an important role in the construction of metal organic frameworks.

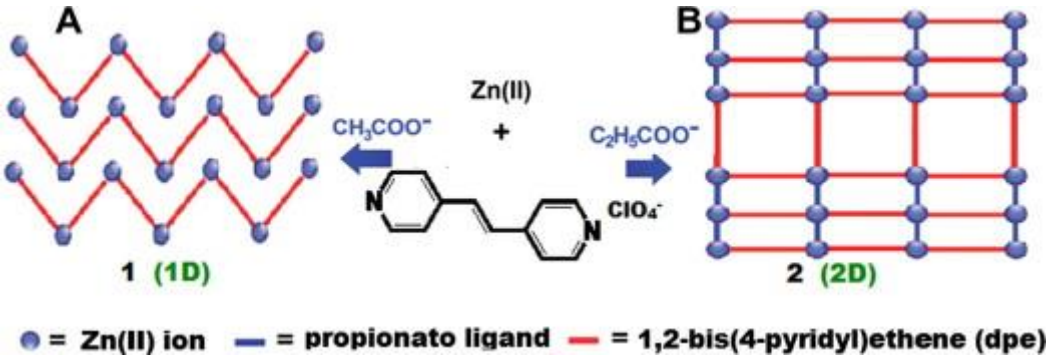

Scheme 2. Coordination networks of mononuclear 1D zig–zag chain of compound **1** and trinuclear 2D layers of compound **2**.

Thermogravimetric analysis

The thermal analysis of **1** (Fig. 8A) exhibits a two-stage decomposition of the material. A first weight loss of 4.49% is observed in the temperature range 52–95 °C, which corresponds to the release of one lattice water molecule (calculated 4.69%). The structure is stable up to about 230 °C, when it starts to decomposes gradually to produce a white residue of ZnO at ca. 300 °C. The thermogravimetric analysis of compound **2** (Fig. 8B) shows a first weight loss in the temperature range 100–300 °C, characterizing the loss of guest dpe ligand and two propionate ligands (experimental value, 21.09%; calculated, 20.54%). In the temperature range 300–400 °C, the decomposition of the coordination material is observed. As for compound **1**, a white residue (ZnO) of **2** is obtained when the sample is heated to 400 °C.

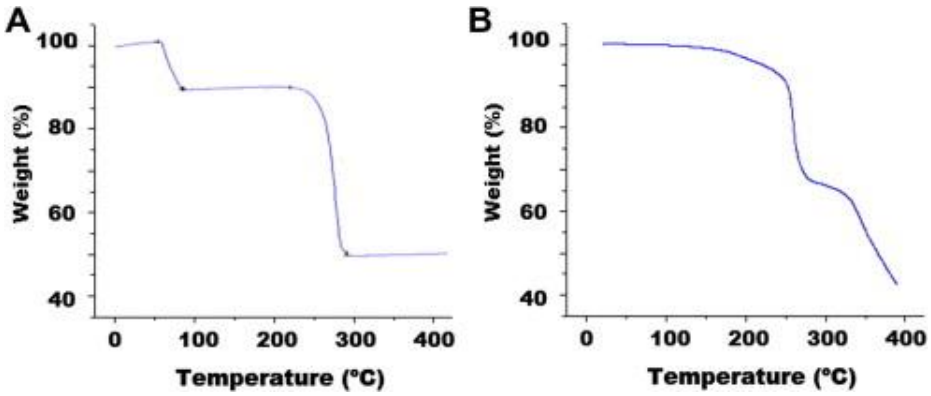

Fig. 8. Thermogravimetric analysis of compounds **1**(A) and **2**(B).

Zn(II) compounds doped with Cu(II) and Mn(II)

To learn more on the details of the coordination site, the influence of the nature of the doping metal ion, namely Cu(II) and Mn(II), has been investigated by EPR. This study illustrates the flexibility of the coordination geometry of Cu(II) compared to Mn(II). Such investigations are of great interest in the context of potential cation-exchange properties of metal organic frameworks with structure retention. All doped compounds have been characterized by IR spectroscopy and EPR at room temperature and 70 K (see Fig. 9 and Fig. 10). The IR spectra of the doped compounds are similar to that of the original Zn(II) compound, thus indicating that the structure and therefore the environment around the zinc(II) centers are essentially not altered.

The polycrystalline EPR spectrum of the trinuclear secondary building units of Zn(II) compound **2** doped with Cu(II) shows signals revealing the presence of only one type of Cu(II) species which is characterized by a four-lines hyperfine pattern with $g_{//} = 2.314$; (with $A_{//} = 124$, Fig. 9A) $g_{\perp} = 2.080$; this would be in agreement with a distorted-octahedral geometry [34]. No super-hyperfine splitting is resolved. These EPR data are could be indicative of the occurrence of only one predominant site for the Zn(II) ions in **2**, which has been replaced by Cu(II) ions. In fact only a small fraction of Zn ions in site I species are replaced by Cu or Mn, so in a very small amount (by far not every Zn in site I is replaced. In the molecular structure of **2** two distinct coordination geometries for the zinc(II) ions are present, i.e. a highly distorted octahedron (site I) and a rather perfect octahedron (site II in Fig. 9B) [35]. The simple EPR, i.e. one species, could suggest that the EPR spectrum of the Cu(II) ion is due to only one site, and hardly any in the other site. So it could be that the EPR parameters are due to the outer two ions, as a central Cu(II) would have a different EPR (compressed octahedron). However, given the low resolution no firm conclusion about a single species is allowed. Similarly, the doping with Mn(II) ions leads to a heteronuclear compound, whose EPR spectrum shows only a simple spectrum with one set of six lines, characterizing a Mn(II) species (Fig. 10A). These data would suggest that only one from the two potential coordination sites has experienced cation exchange. Probably the Mn(II) ions are occupying only site II (Fig. 10B), since Mn(II) has the tendency to form rather regular octahedral complexes.

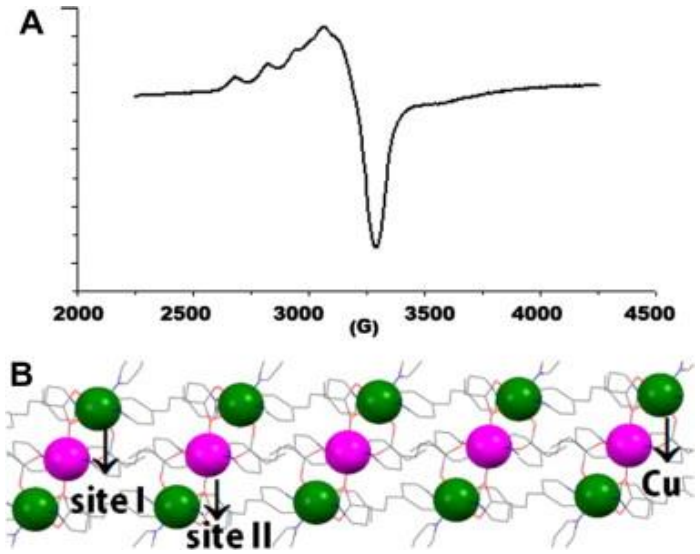

Fig. 9. (A) Polycrystalline EPR spectrum of **2** doped with Cu(II), recorded at 70 K and (B) Trinuclear Zn(II) units of **2** where zinc(II) ions (pink) have been replaced by Cu(II) ions (green) in only one site I.

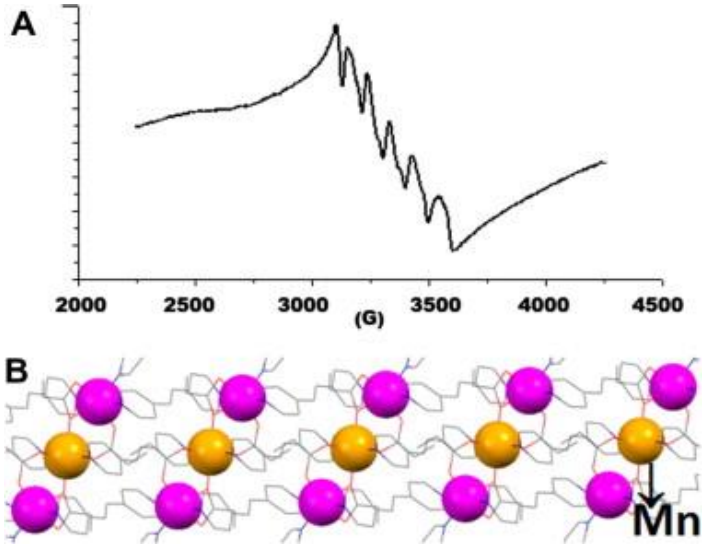

Fig. 10. (A) Polycrystalline EPR spectrum of **2** doped with Mn(II), recorded at 70 K and (B) Trinuclear Zn(II) unit of **2**, where only the central Zn(II) sites have been replaced by Mn(II) ions (orange).

Catalytic properties

Both MOFs **1** and **2** have been tested as heterogeneous catalysts for the cyanosilylation of acetaldehyde and benzaldehyde. Thus, the selectivity and activity of the 1D (**1**) and 2D (**2**) coordination polymers have been examined. Typically, the powdered catalyst is suspended in CH_2Cl_2 or THF. The aldehydic substrate and trimethylsilyl cyanide (1:2 molar ratio) are subsequently added at room temperature and the reaction is carried out for 24 h (Scheme 3) [36]. The course of the reactions has been monitored by gas chromatography.

Blank reactions have been performed by carrying the cyanosilylation of acetaldehyde and benzaldehyde without solid catalyst, at 25 °C. These test reactions give only conversions of 18% for acetaldehyde and 10% for benzaldehyde, after a reaction time of 24 h. When solid **1** is used as catalyst, a conversion of 74% (and even 82% when using **2**) of acetaldehyde is reached after 24 h reaction time in CH_2Cl_2 (Table 1 and Fig. 11). This high conversion suggests first of all that both catalysts act as a efficient catalyst for this reaction, and that both acetaldehyde and trimethylsilyl cyanide can diffuse through the pores to attain the Lewis metallic sites, to generate 2-(methylsiloxy)propionitrile with a yield of 74% (**1**) and 82% (**2**).

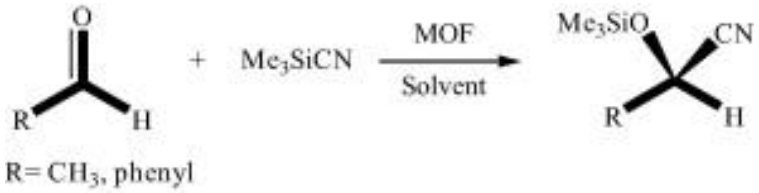

Scheme 3. Cyanosilylation reaction.

When benzaldehyde, a sterically more demanding substrate, is used under similar reaction conditions, a conversion of only 14% is observed (18% for **2**; Table 1). This significantly lower reactivity, hardly better than the blank, suggests that the dimension of the channels of the porous coordination polymer plays an important role and leads to size selectivity.

Next, the influence of another organic solvent, namely THF, on the conversion of acetaldehyde has been examined for each MOF catalyst. For instance, in THF, compound **1** promotes the conversion of only 57% acetaldehyde (59% for **2**; Table 1). So, the reaction is less efficient in THF, which may be explained by a competitive binding of the substrate and the solvent to the metal site. This competitive binding obviously does not occur with CH_2Cl_2 as the solvent.

For instance, the reactions performed of **2** are more efficient than for **1** (Table 1). These disparities regarding the distinct catalytic activities in CH_2Cl_2 and THF may be explained by structural features characterizing both compounds. As mentioned above, the crystal packing of the 2D framework of **2** generates huge cavities filled with perchlorate anions and non-coordinated 1,2-bis(4-pyridyl)ethene (dpe) molecules. Most likely, both solvents are capable of displacing the dpe guest molecules of **2**, therefore increasing the accessibility of the aldehydic substrate to the metal centers, as compared to the close contacts between the 1D zig–zag chains in **1**.

The catalytic activities of compounds **1** and **2** for the cyanosilylation of aldehydes have been compared with those of zinc(II) porous coordination frameworks, as well as with other porous coordination frameworks. As reported earlier by our group [37], $\{[Zn_3(4,4'\text{-bpy})_{3.5}(\mu\text{-}O_2CH)_4(H_2O)_2](ClO_4)_2(H_2O)_2\}_n$ (3D), $\{[Zn_3(4,4'\text{-bpy})_4(\mu\text{-}O_2CCH_2CH_3)_4](ClO_4)_2(4,4'\text{-bpy})_2(H_2O)_4\}_n$ (2D) and $\{[Zn_3(4,4'\text{-bpy})_3(\mu\text{-}O_2CCH_3)_4(H_2O)_2](PF_6)_2(H_2O)_2\}_n$(1D), have been tested as heterogeneous catalysts for the cyanosilylation of acetaldehyde and benzaldehyde. For example, the conversion of 3D framework (95%) is significantly higher than that of 2D and 1D frameworks (86% and 71%, respectively). This significant reactivity suggests that the dimension of the channels of the MOF plays an important role and leads to size selectivity. When, the catalytic properties of both Zn(II) compounds are compared with those of copper(II) coordination frameworks, i.e. the 2D networks $\{[Cu_3(4,4'\text{-bpy})_3(\mu\text{-OOCH})_4(H_2O)_2](ClO_4)_2(H_2O)_6\}_n$, $\{[Cu(4,4'\text{-bpy})(\mu\text{-OOCH})(NO_3)]\}_n$ and $\{[Cu_2(4,4'\text{-bpy})_2(\mu\text{-OOCCH}_3)_3](PF_6)(H_2O)\}_n$ a much lower activity

is observed [38]. The higher catalytic activities of **1** and **2** may suggest that the Lewis acidity of these zinc(II) compounds is higher than that of the tested copper(II) ones.

Table 1. Cyanosilylation of aldehydes catalyzed by compounds **1** and **2**.

Catalyst	Types	Substrate	Solvent	Time (h)	Conversion (%)
1	1D	acetaldehyde	CH_2Cl_2	24	74
		acetaldehyde	THF	24	57
		benzaldehyde	CH_2Cl_2	24	14
2	2D	acetaldehyde	CH_2Cl_2	24	82
		acetaldehyde	THF	24	59
		benzaldehyde	CH_2Cl_2	24	18

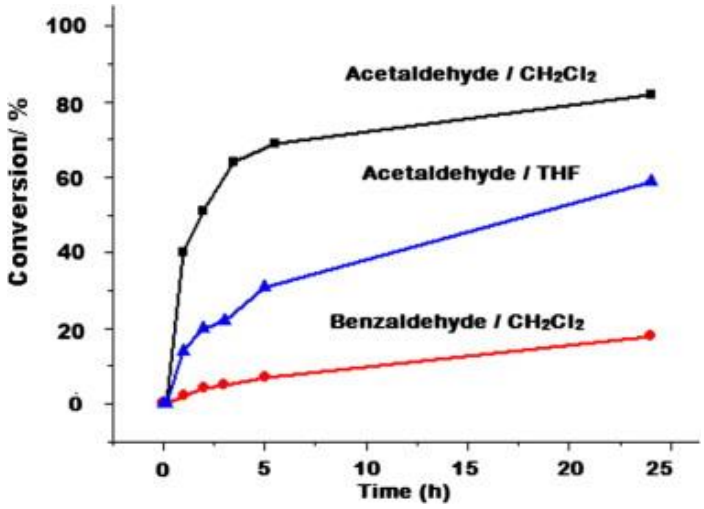

Fig. 11. Cyanosilylation of acetaldehyde and benzaldehyde with MOF **2** as catalyst.

Conclusions

In summary, two new metal organic frameworks, [Zn(II)/dpe/carboxylato] crystalline solids based on 1D and 2D coordination networks of different topology have been prepared and characterized crystallographically. The influence of small secondary ligands, namely common monocarboxylato ligands and the nature of the counter ion, on the overall solid state structure of both compounds have been investigated. This study suggests that the steric hindrance of the carboxylato co-ligand (acetato or propionato) and the effect of counteranion may have drastic effects on the resultant coordination networks. These results clearly indicate that *a priori* minor synthetic changes give rise to the formation of drastically distinct frameworks. Such studies are important in crystal engineering, as they contribute to increase knowledge about ligand steric effect on framework topologies. Furthermore, the catalytic activities of zinc(II)-dpe-carboxylato compounds in the cyanosilylation of aldehydes have been investigated. Both compounds display good heterogeneous catalytic properties and show a high conversion of acetaldehyde in dichloromethane and also showed highly size-selective for the substrate compound with benzaldehyde.

References

[1] S. Keskin, J. Liu, R.B. Rankin, J.K. Johnson, D.S. Sholl, Ind. Eng. Chem. Res., 48 (2009), 2355
[2] J. Crassous, Chem. Soc. Rev., 38 (2009), 830
[3] Z. Wang, G. Chen, K.L. Ding, Chem. Rev., 109 (2009), 322
[4] J.M. Yan, X.B. Zhang, S. Han, H. Shioyama, Q. Xu, Angew. Chem., Int. Ed., 47 (2008), 2287
[5] H.K. Liu, X.H. Huang, T. Lu, X. Wang, W.Y. Sun, B.S. Kang, Dalton Trans. (2008), 3178
[6] G. Ferey, C. Mellot-Draznieks, C. Serre, F. Millange, Acc. Chem. Res., 38 (2005), p. 217
[7] B.-B. Ding, Y.-Q. Weng, Z.-W. Mao, C.-K. Lam, X.-M. Chen, B.-H. Ye, Inorg. Chem., 44 (2005), 8836
[8] L. Pan, D.H. Olson, L.R. Ciemnolonski, R. Heddy, J. Li, Angew. Chem., Int. Ed., 45 (2006), 616
[9] Q. Fang, G. Zhu, M. Xue, J. Sun, F. Sun, S. Qiu, Inorg. Chem., 45 (2006), 3582
[10] G. Becht, S.-J. Hwu, Chem. Mater., 18 (2006), 4221
[11] Y.J. Song, H. Kwak, Y.M. Lee, S.H. Kim, S.H. Lee, B.K. Park, J.Y. Jun, S.M. Yu, C.l. Yu, S.-J. Kim, Y. Kim, Polyhedron, 28 (2009), 1241
[12] M. Du, X.-G. Wang, Z.-H. Zhang, L.-F. Tang, X.-J. Zhao, CrystEngComm, 8 (2006), 788
[13] A.-Q. Wu, Y. Li, F.-K. Zheng, G.-C. Guo, J.-S. Huang, Cryst. Growth Des., 6 (2006), 444
[14] P. Ren, N. Xu, C. Chen, H.-B. Song, W. Shi, P. Cheng, Inorg. Chem. Commun., 11 (2008), 730
[15] C.Y. Chen, P.Y. Cheng, H.H. Wu, H.M. Lee, Inorg. Chem., 46 (2007), 5691
[16] P. Phuengphai, S. Youngme, P. Kongsaeree, C. Pakawatchai, N. Chaichit, S.J. Teat, P. Gamez, J. Reedijk, CrystEngComm, 11 (2009), 1723
[17] K. Biradha, CrystEngComm, 5 (2003), 374
[18] D. Braga, Chem. Commun. (2003), 2751
[19] X.J. Li, C. Rong, D.F. Feng, W.H. Bi, Y. Wang, X. Li, M.C. Hong, Cryst. Growth Des., 4 (2004), 775
[20] J.C. Dai, X.-T. Wu, S.-M. Hu, Z.-Y. Fu, J.-J. Zhang, W.-X. Du, H.-H. Zhang, R.-Q. Sun,Eur. J. Inorg. Chem. (2004), 2096
[21] Q.-Y. Liu, L. Xu, CrystEngComm, 7 (2005), 87
[22] Y.-C. Liao, F.-L. Liao, W.-K. Chang, S.-L. Wang, J. Am. Chem. Soc., 126 (2004), 1320
[23] S.P. Jang, J.I. Poong, S.H. Kim, T.G. Lee, J.Y. Noh, C. Kim, Y. Kim, S.-J. Kim,Polyhedron, 33 (2012), 194
[24] C.R. Maldonado, M. Quiros, J.M. Salas, Inorg. Chim. Acta, 365 (2011), 371
[25] Aslani, A. Morsali, V.T. Yilmaz, O. Büyükgüngör, Inorg. Chim. Acta, 362 (2009), 1506
[26] Z.R. Ranjbar, A. Morsali, Inorg. Chim. Acta, 360 (2007), 2056
[27] H.W. Roesky, M. Andruh, Coord. Chem. Rev., 236 (2003), 91
[28] Saint, Version 4 Software Reference Manual, Siemens Analytical X-Ray Systems, Inc., Madison, WI, USA, 1996.
[29] G.M. Sheldrick, sadabs, Program for Empirical Absorption correction of Area Dectector, University of Göttingen, Göttingen, Germany, 1996.
[30] shelxtl, Version 6.12 Reference Manual, Siemens Analytical X-Ray Systems, Inc., Madison, WI, USA, 1997.
[31] B.F. Hoskins, R. Robson, J. Am. Chem. Soc., 112 (1990), 1546
[32] Y.M. Dai, E. Ma, E. Tang, J. Zhang, Z.J. Li, X.D. Huang, Y.G. Yao, Cryst. Growth Des., 5 (2005), 1313
[33] L. Carlucci, G. Ciani, D.M. Proserpio, S. Rizzato, CrystEngComm, 4 (2002), 121
[34] B.J. Hathaway, G. Wilkinson, R.D. Gill, J.A. McCleverty (Eds.), Comprehensive Coordination Chemistry, vol. 5, Pergamon Press, Oxford, 1987.

[35] J.M. Thomas, Angew. Chem., Int. Ed. Engl., 27 (1988), 1673
[36] S. Horike, M. Dinca, K. Tamaki, J.R. Long, J. Am. Chem. Soc., 130 (2008), 5854
[37] P. Phuengphai, S. Youngme, P. Gamez, J. Reedijk, Dalton Trans., 39 (2010), 7936
[38] P. Phuengphai, S. Youngme, I. Mutikainen, P. Gamez, J. Reedijk, Polyhedron, 42 (2012), 10

PART II

SYNTHESES, STRUCTURAL CHARACTERIZATION OF COORDINATION COMPOUNDS AND THEIR FUNCTIONS TOWARD MAGNETISM AND SPIN-CROSSOVER PHENOMENA

This part deals with the study of the magnetic properties of new spin-crossover (SCO) iron(II) coordination compounds and triply-bridged dinuclear copper(II) complexes. In the first instance, the investigation of the SCO properties of a series of six new mononuclear iron(II) compounds of formula *trans*-[Fe(L)], where L = 2,2′-dipyridylamino/*s*-triazine-based ligands and X = S or Se, is reported. The SCO properties were investigated by means of single-crystal X-ray diffraction studies, magnetic susceptibility measurements, photomagnetic (LIESST) studies and Differential-Scanning Calorimetry (DSC) experiments. Interestingly, the SCO properties of these iron(II) compounds present distinct behaviours which are both ligand- and anion-dependent. Secondly, twelve new triply-bridged dinuclear copper(II) compounds are described, for which the magnetic properties have been examined, both experimentally and theoretically. These complementary studies have allowed to assess magneto-structural correlations, and to develop a computational procedure to predict accurately the magnetic coupling constant, *J*, for such molecules. All copper complexes have been characterized spectroscopically and structurally, and their global topologies categorize them into two classes, namely class F for the antiferromagnetic compounds (three examples in the present work), and class B for the ferromagenetic ones (nine examples in the present work). Their magnetic properties have been investigated by means of magnetic susceptibility measurements and theoretical calculations, applying state of the art density functional theory (DFT) methods, where the effect of the type of functionals and of the basis sets used to represent the electron density has been explored.

II-1: Spin-crossover iron(II) compounds containing (2,2′-dipyridylamine/*s*-triazine)-based ligands

In the present investigation, the SCO properties of iron(II) compounds from those 2,2′-dipyridylamino-substituted-triazine ligands have been examined. Hence, six new mononuclear Fe(II) compounds of formula *trans*-[Fe**L**2(NCX)] (where X = S or Se) have been successfully synthesized and fully characterized. The effect of the substituents of the 2,2′-dipyridylamine/*s*-triazine-2(NCS)2 based ligands on the SCO properties of the corresponding iron(II) compounds has been appraised. These compounds are divided into three categories depending on the different substituents.

Category 1: Subtlety of the Spin-Crossover Phenomenon Observed with Dipyridylamino-Substituted Triazine Ligands

Introduction

The phenomenon of spin crossover (SCO) is a particular and very interesting illustration of the ligand-field theory.1,2 For octahedral coordination complexes of transition-metal ions, the d orbitals split into two sets, i.e. the t_{2g} and e_g sets, whose energy difference is given by the crystal-field splitting parameter Δ_{oct}.3 The size of Δ_{oct} determines the electronic structure of the d^4–d^7 metal ions. Thus, for iron(II) complexes, a small Δ_{oct} will favour the high-spin state (HS, $e_g^2t_{2g}^4$, $S = 2$) while a large Δ_{oct} will produce a low-spin (LS, t_{2g}^6, $S = 0$) compound. With an appropriate ligand-field strength (namely for an intermediate Δ_{oct} value), the transition-metal compound may exhibit LS ↔ HS bistability through the application of an external stimulus, like temperature, pressure or light.4–7 Hence, such SCO materials may find potential applications in molecular switches, data storage devices and optical displays,

especially in the case of Fe^{II} ions, for which the LS state is diamagnetic.8–11 Therefore, SCO species have received a great deal of attention from the scientific community for the past decade.12,13 A great number of SCO Fe^{II} complexes have been synthesized that were principally obtained from ligands based on nitrogen-containing aromatic donor groups (such as pyridine and azole rings).14–19

For the past seven years, we have been involved in the design and preparation of SCO iron(II) compounds with polypyridine ligands.20–22In particular, the use of a ligand derived from the *s*-triazine ring and 2,2′-dipyridylamine units, namely 2,4,6-tris(dipyridin-2-ylamino)-1,3,5-triazine (dpyatriz),23 has led to remarkable SCO systems.22,24,25 Subsequently, Murray and coworkers have developed a variety of dipyridylamino-substituted-triazine ligands,26–30 which were easily prepared from the highly versatile building block 2,4,6-trichloro-1,3,5-triazine.31–33 The utilization of these ligands has allowed the preparation of SCO coordination compounds, hence corroborating the great potential of (2,2′dipyridylamine/triazine)-based ligands to generate molecular switches.

In the present study, we have taken advantage of the straightforward and highly selective substitution of the chloride atoms of 2,4,6-trichloro-1,3,5-triazine to synthesize two related dipyridylamino-substituted-triazine ligands, namely 4,6-dichloro-*N*,*N*-di(pyridine-2-yl)-1,3,5-triazine-amine (Cldpat) and 6-chloro-*N*′-phenyl-*N*,*N*-di(pyridin-2-yl)-1,3,5-triazine-2,4-diamine (Cladpat) (Scheme 1), whose sole difference lies in the replacement of one of the two chloride atoms of Cldpat by an aniline unit, producing Cladpat. Actually, the use of these similar ligands to bind iron(II) ions leads to the formation of mononuclear coordination compounds with similar molecular structures, but dissimilar magnetic behaviours, thus revealing the drastic effect of tiny structural changes on the physical properties of related molecules.

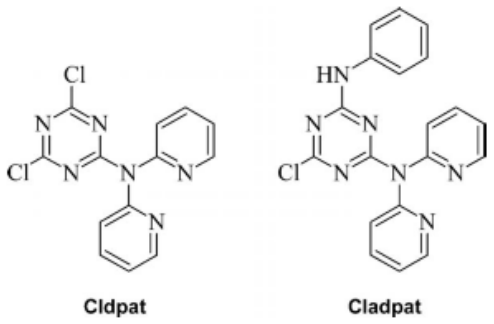

Scheme 1. Triazine-based ligands 4,6-dichloro-*N*,*N*-di(pyridine-2-yl)-1,3,5-triazine-amine (Cldpat) and 6-chloro-*N*′-phenyl-*N*,*N*-di(pyridin-2-yl)-1,3,5-triazine-2,4-diamine (Cladpat).

Results and Discussion

Synthesis

As evidenced by earlier studies by Murray26–29 and some of us,22,24,25 *s*-triazine-based ligands containing at least one 2,2′-dipyridylamine unit allow the preparation of SCO iron(II) compounds. Herein, it was decided to investigate the potential ability of the simplest member of this family of dipyridylamino-substituted-triazine ligands, namely 4,6-dichloro-*N*,*N*-di(pyridine-2-yl)-1,3,5-triazine-amine (Cldpat; Scheme 1), to generate SCO properties upon coordination to an iron(II) ion in the presence of thiocyanates or selenocyanates. Hence, Cldpat was prepared in THF by the reaction of 2,2′-dipyridylamine with 1 equiv. of 2,4,6-trichloro-1,3,5-triazine, in the presence of*N*,*N*-diisopropylethylamine (DIPEA).

Next, one of the chloride atoms of Cldpat was replaced by an aniline group with the aim of examining the influence of this slight modification of the ligand on the magnetic properties of the ensuing iron(II) complex. Thus, the ligand 6-chloro-*N*′-phenyl-*N*,*N*-di(pyridin-2-yl)-1,3,5-triazine-2,4-diamine (Cladpat; Scheme 1) was synthesized from Cldpat through substitution of one of its chloride atoms by aniline, using sodium carbonate as a base in acetone/water. The molecular structure of Cladpat could be determined by single-crystal X-ray diffraction. The solid-state structure of Cladpat shows that the molecules are strongly associated by strong hydrogen-bonding interactions [$N_{aniline}$–H···$N_{triazine}$ = 2.972(3) Å; [ang] $N_{aniline}$–H–$N_{triazine}$ = 176(3)°], giving rise to a 1D supramolecular chain along the crystallographic *c* axis. Such anticipated H bonds, for which the ligand Cladpat was actually designed, may be crucial to favour the occurrence of cooperative SCO, if maintained in complexes of Cladpat.

The coordination compounds **1**–**3** were synthesized by the direct addition of a freshly prepared methanolic solution of $Fe(NCX)_2$ (X = S or Se) to a methanolic solution containing 2 equiv. of the dipyridylamino-substituted-triazine ligand (Cldpat or Cladpat). The solution of $Fe(NCS)_2$ was obtained from iron(II) sulfate and potassium thiocyanate while $Fe(NCSe)_2$ was made from iron(II) perchlorate and potassium selenocyanate.

Description of the Crystal Structure of *trans*-[Fe(Cldpat)$_2$(NCS)$_2$](H$_2$O) (1)

Reaction of 1 equiv. of iron(II) thiocyanate with 2 equiv. of Cldpat generates compound **1** with a yield of 73 %. Structural information on **1** has been obtained from X-ray diffraction studies at 100 K. The high *R* value found is most likely due to unresolved crystal twinning. Nevertheless, the data collected are satisfactory for a reasonably accurate determination of the molecular structure of **1**. Actually, the iron(II) centre in **1** exhibits the anticipated octahedral coordination environment [typically observed for iron(II) thiocyanate complexes with this family of ligands 25,34], which is formed by two Cldpat ligands in the equatorial plane and two *trans* thiocyanate anions (Figure 1). Surprisingly, The Fe–N_{Py} bond lengths in the range 2.214(13)–2.264(15) Å and the Fe–N_{NCS} distances of 2.090(13) Å characterize a high-spin iron(II) compound. This fact is confirmed by temperature-dependent magnetic-susceptibility measurements revealing that the FeN_6 species in **1**, rather unexpectedly, does not present a SCO process.

The solid-state structure of **1** shows the occurrence of intramolecular lone pair···π interactions [Cg10···S2 = 3.337(8) Å]. In addition, the molecules are associated by means of intermolecular lone pair···π interactions [Cg10···S2s = 3.242(7) Å], which generate a supramolecular 1D chain. The chains interact with each other through $S_{lonepair}$···$triazine_{\pi}$ contacts, producing a 2D layer in the crystallographic *bc* plane (Figures 2). These 2D layers are further connected through hydrogen bonds between lattice water molecules and the chloride atoms of the triazine rings that give rise to a 3D network.

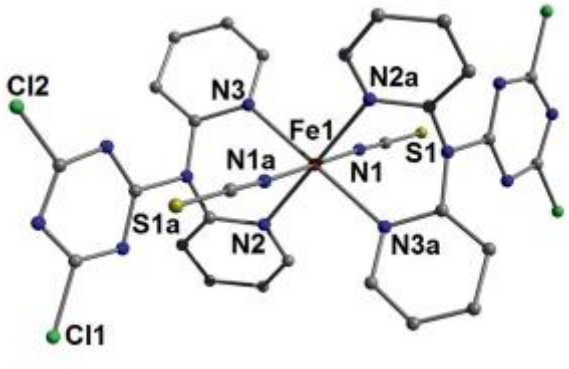

Fig. 1. Representation of the molecular structure of compound **1** with partial atom numbering scheme. The thermal ellipsoids are drawn at the 50 % probability level. The hydrogen atoms and the lattice water molecule are not shown for clarity. Symmetry operation: a, 1 – *x*, 1 – *y*, – *z*.

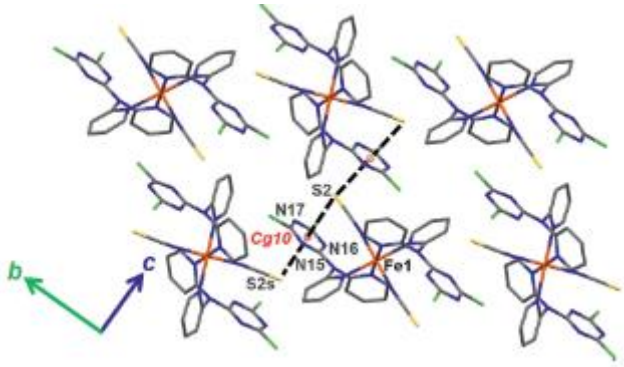

Fig. 2. View of the crystal packing of **1** showing the formation of a supramolecular 2D network in the *bc* plane by means of lone pair···π interactions (black dotted lines) between the triazine rings and neighbouring thiocyanate anions [Cg10···S2 = 3.337(8) Å and Cg10···S2s = 3.242(7) Å]. Symmetry operation: s – *x*, 1/2 + *y*, 1/2 – *z*.

Description of the Crystal Structure of *trans*-[Fe(Cladpat)$_2$(NCS)$_2$] (2)

Reaction of 1 equiv. of iron(II) thiocyanate with 2 equiv. of Cladpat produces compound **2** with a yield of 89 %. Compound **2**, which shows SCO properties (see magnetic studies), crystallizes in the monoclinic space group $P2_1/c$, both at 100 K and at 270 K.The molecular structure of low-spin **2** is depicted in Figure 3. Compound **2** consists of an octahedral iron(II) ion coordinated by four pyridine units from two Cladpat ligands and two *trans* N-bonded thiocyanate anions.

Such a FeN_6 coordination environment is known to potentially produce SCO iron(II) species.35 The Fe–N_{Py} distances ranging from 1.965(3) to 2.000(4) Å are typical of a LS iron(II) entity, as is the case for the Fe–N_{NCS} distances of 1.945(4) and 1.948(4) Å. These bond lengths increase by ca. 0.20 Å for Fe–N_{Py} and ca. 0.15 Å for Fe–N_{NCS} when the temperature is raised to 270 K, which is indicative of a full spin transition, as also observed during magnetic studies on **2** (see below).

The distortion parameters $\Sigma°$ and $\Phi°$ reflect the deviation from an ideal octahedral geometry.38 $\Sigma°$ directly measures the distortion from a perfect octahedron while $\Phi°$ defines the deformation of the octahedral coordination geometry towards a trigonal-prismatic

environment.12 For a perfect octahedron, $\Sigma^\circ = \Phi^\circ = 0$. For LS **2**, $\Sigma^\circ = 32$ and $\Phi^\circ = 43$, whereas the respective values for HS **2** are 43 and 70. The lower Σ° and Φ° values for the LS compound are typical since LS complexes are less deformed than HS ones.35,37 Hence, $\Delta\Sigma^\circ$ ($\Sigma^\circ_{HS} - \Sigma^\circ L_{HS}$) and $\Delta\Phi^\circ$ ($\Phi^\circ_{HS} - \Phi^\circ_{LS}$) quantify the magnitude of the structural changes occurring during the SCO. For **2**, $\Delta\Sigma^\circ = 15$ and $\Delta\Phi^\circ = 27$; the high $\Delta\Phi^\circ$ value observed for **2** is indicative of a significant alteration of the octahedral geometry upon the LS ⟶ HS transition. Such a large structural variation may be associated with cooperativity between the iron(II) centres, possibly through intermolecular interactions (actually, the magnetic measurements show a relatively cooperative SCO; see below). In fact, the crystal packing reveals that the iron(II) molecules are connected through double $N_{aniline}$–H⋯$N_{triazine}$ bonds, which generate a 1D supramolecular chain (Figure 4). These hydrogen bonds are affected by the spin transition (a variation of about 0.025 Å is observed); in particular, the N9–H9⋯N15a bond experiences a bending of ca. 7 %, the angle varying from 177(6)° to 165(6)° during the LS ⟶ HS transition. In addition, the molecules of **2**exhibit intramolecular lone pair⋯π interactions39,40 (Cg5⋯S2 and Cg8⋯S1 contacts; Figure 4), which are also altered by the SCO. A closer look at the solid-state structure of **2** reveals that the 1D supramolecular chains are linked into a 2D layer by parallel-displaced π–π interactions,41,42 involving neighbouring aniline rings [centroid-to-centroid distance Cg9⋯Cg10 = 3.976(3) Å in LS **2**]. The shortest arene–arene contact distances are C17⋯C39i = 3.257(7) Å and C18⋯C40i = 3.335(7) Å, and rise to 3.283(12) Å and 3.397(11) Å, respectively, upon LS ⟶ HS transition [corresponding to an increase of the centroid-to-centroid distance of ca. 7 %, from 3.976(3) to 4.236(5) Å]. All these supramolecular bonding interactions may favour cooperativity between the transiting iron(II) ions.

It has to be noted that the Σ° and Φ° values for HS **2** are comparable to those of **1**, therefore suggesting analogous octahedral distortions for the two high-spin molecules, and corroborating the metal coordination environment in **1**. Reaction of the ligand Cladpat with iron(II) selenocyanate [instead of iron(II) thiocyanate] yields the analogous compound $[Fe(Cladpat)_2(NCSe)_2]$ (**3**), as indicated by elemental analyses, which also exhibits SCO properties (see the section Magnetic Studies). Although the molecular structure of **3** could not be determined by X-ray diffraction studies, it is expected that the coordination environment of the iron(II) centres in **3** is equivalent to those of **1** and **2**, with two *trans* N-bonded selenocyanate ions. Actually, the IR absorption band observed at 2061 cm^{-1} for compound **3** is identical to that reported by Murray and coworkers for an iron(II) SCO complex from a dipyridylamino-substituted-triazine ligand with *trans*-coordinated NCSe ions.30

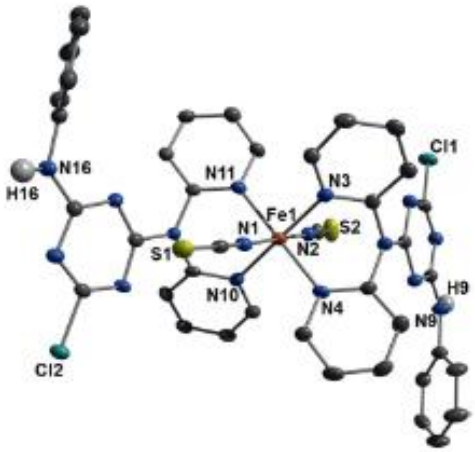

Fig. 3. Representation of the molecular structure of compound **2** (LS state, determined at 100 K) with partial atom numbering scheme. The thermal ellipsoids are drawn at the 50 % probability level, and only the hydrogen atoms involved in hydrogen-bonding interactions are shown for clarity.

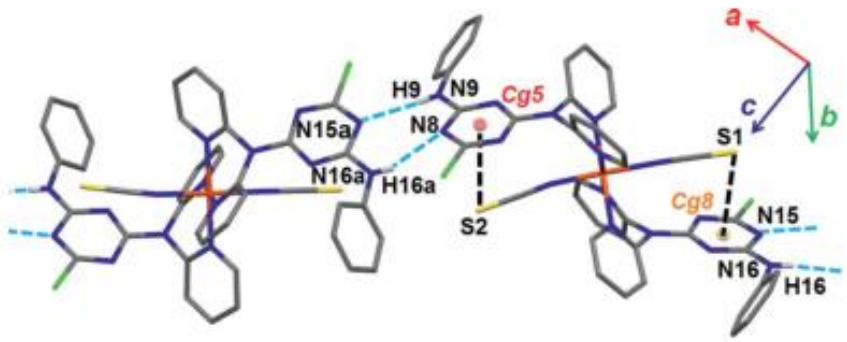

Fig. 4. View of the crystal packing of LS **2** showing $N_{aniline}$–H···$N_{triazine}$bonds [N9–H9···N15a = 3.010(5) Å and N16a–H16a···N8 = 2.995(5) Å; blue dotted lines] connecting the iron(II) molecules to generate a 1D supramolecular chain. Intramolecular lone pair···π interactions (black dotted lines) take place between the thiocyanate sulfur atoms and the triazine rings [Cg5···S2 = 3.459(2) Å and Cg8···S1 = 3.504(2) Å]. Symmetry operations: a $1 - x, -1/2 + y, 1/2 - z$.

Magnetic Studies

The effect of the substituent (ligands Cldpat and Cladpat) and the replacement of thiocyanate by selenocyanate anions have been investigated by magnetic measurements. Hence, the temperature dependence of the χT product of compounds **1**–**3**, χ being the molar paramagnetic susceptibility, were derived from magnetization measurements on bulk samples in an applied field of 0.5 T for **1** and **3**, and 1 T for **2** (see Experimental Section), and in the temperature range 2–300 K. The data for compounds **1** and **2**, shown in Figure 5, corroborate the structural observations, evidencing the occurrence of a complete thermal SCO for compound **2**, and the – surprising – absence of such a process in the case of compound **1**. Indeed, the χT product of **1** remains practically constant at 3.11–3.09 $cm^3\ mol^{-1}$ K from 300 K down to 50 K, the temperature below which a decrease of χT is observed down to 2.18 $cm^3\ mol^{-1}$ K. The magnetic properties of **1** are thus in agreement with an $S = 2$ HS ground

state for the Fe^{II} ion, with g close to 2, throughout the whole temperature range considered, the decrease at low temperatures being due to zero-field-splitting effects of the $S = 2$ spins. Magnetization vs. field measurements at 2 K indeed show saturation at ca. 4.05 $N_A\mu_B$ at 5 T, in agreement with an $S = 2$ spin ground state and a g value slightly above 2. On the other hand, the χT product of **2** decreases upon cooling, from similar values to those of **1**, i.e. 3.13 $cm^3\ mol^{-1}$ K at 280 K, reaching a plateau at 0.11 $cm^3\ mol^{-1}$ K below 100 K, and down to 0.08 $cm^3\ mol^{-1}$ K at 5 K. Compound **2** thus undergoes a complete SCO centred at ca. 178 K and with a limited cooperative character, as indicated by a ΔT_{80} of 50 K (80 % of the transition occurs within about 50 K). In agreement with the structural observations, the process of SCO is virtually completed at 100 K. These observations are perfectly reproducible upon warming, thus with no detectable hysteresis, and over various cycles.

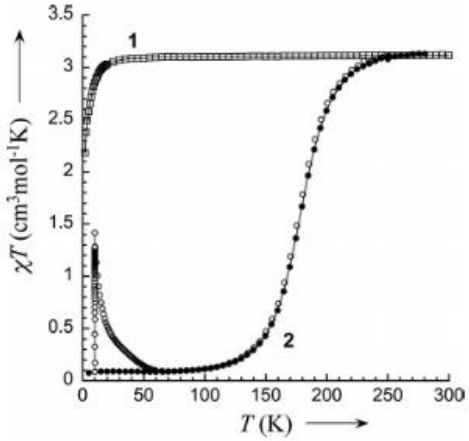

Fig. 5. χT vs. T plot for **1** (squares) and **2**, showing the process of SCO (full circles), the partial LS to HS photo-induced trapping at 10 K (LIESST effect) and the relaxation back to the LS ground state and normal behaviour upon warming (empty circles).

The possibility of trapping the HS metastable state at low temperature through irradiation, the so-called LIESST effect,43 was examined on a thin sample of **2**. At 10 K, a fast increase of χT is indeed observed when irradiating with green light, clearly demonstrating the efficiency of the LIESST effect in this compound (Figures 5 and 6 top). Nevertheless, the rate of increase rapidly drops and virtually stable values are reached after ca. 1 h (Figure 6 top). After turning the irradiation OFF and thermalization, the resulting χT value of 1.42 $cm^3\ mol^{-1}$ K corresponds to ca. 50 % of trapped HS centres, based on the χT value of **1** at the same temperature. An incomplete LIESST effect in thin samples with an apparent steady state similar to that observed herein may be due to an overlap of the $^5T_2 \rightarrow {}^5E$ (HS) and $^1A_1 \rightarrow {}^3T_1$ (LS) bands, resulting in competitive LIESST and reverse-LIESST processes.44 Another cause of such an incomplete light-induced trapping, even in thin samples, is the competition of the light-induced LS→HS trapping with the relaxation of the trapped HS species back to the LS ground state, at the origin of light-induced bistability in cooperative SCO systems.45,46 Measurements vs. time at 10 K after 1 h of irradiation for **2** indeed show that χT rapidly drops in an exponential manner, already reaching values of ca. 0.40 $cm^3\ mol^{-1}$ K after only 1 h. It is therefore clear that the HS→LS relaxation is fast, even at 10 K (Figure 6 bottom). An estimation of the characteristic relaxation time at 10 K of 765 s is

obtained by adjusting the experimental data to a stretched exponential with $\beta = 0.67$ (red line in Figure 6 bottom). Confirmation of the relative instability of the trapped HS state is obtained from the measurements upon warming after irradiation (Figure 5).χT rapidly decreases to reach values similar to those of a normal LS state at temperatures as low as 55 K, as could be expected from the thermal activation of a relaxation process that is already fast at 10 K.

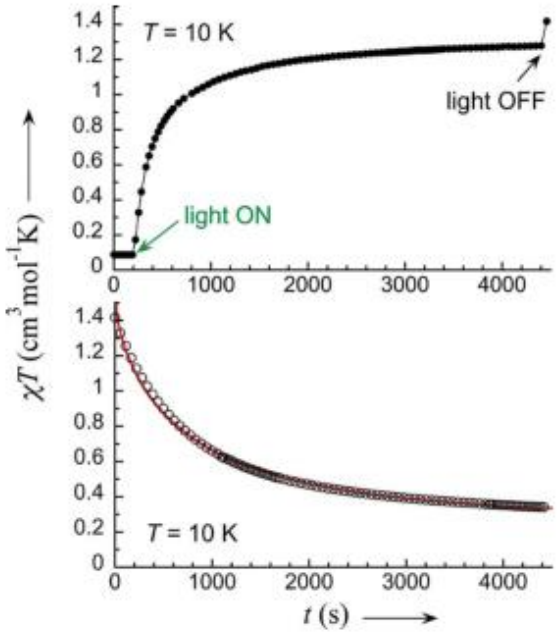

Fig. 6. Top: χT vs. time evolution for **2** at 10 K showing the increase due to LIESST during irradiation with a green light. Bottom: χT vs. time evolution for **2**at 10 K in obscurity after the irradiation with a green light, showing an exponential-like behaviour. The full red line is a fit to a stretched exponential with $\beta = 0.67$ and critical time of 765 s.

Magnetic properties of compound **3** are shown in Figure 7 as a χT vs. T plot. Similar to **2**, a decrease of χT is observed, from 3.43 $cm^3\,mol^{-1}\,K$ at 280 K, down to a plateau at ca. 0.15–0.11 $cm^3\,mol^{-1}\,K$ below 90 K and down to 0.11 $cm^3\,mol^{-1}\,K$ at 5 K, thus confirming a likely comparable molecular structure to that of **2**. Compound **3** thus also presents a complete SCO, although centred at a lower temperature, e.g. 166 K, and more gradual than that of **2**, with a ΔT_{80} of ca. 80 K. Such a low cooperativity in a selenocyanate compound with respect to its thiocyanate analogue is documented, and is possibly related to the participation of the more diffuse Se atom in intermolecular interactions.47,48 This is likely the case here since the S atoms in the structure of **2** do participate in the network of intermolecular interactions (see above). The lower SCO temperature in **3** with respect to **2** is more surprising since the replacement of S by Se in NCX^--based SCO compounds usually results in an increase in the SCO temperature.47–51

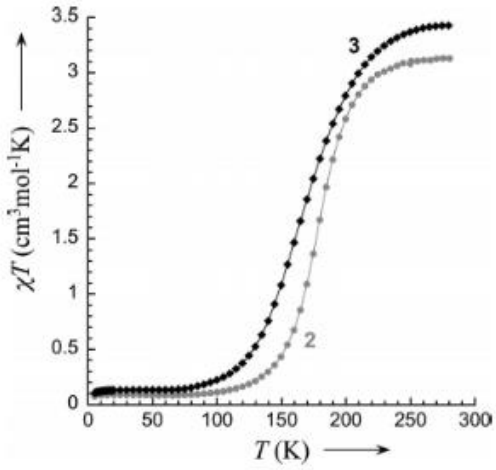

Fig. 7. χT vs. T plot for **3** (rhombus), showing a complete SCO centred at around 166 K. The data of compound **2** is recalled as light circles for comparison.

Thermal Properties

The molar heat capacity at constant pressure, C_p, of **2** was derived from differential scanning calorimetry (DSC) measurements over the temperature range 110–290 K. A strong heat capacity anomaly is detected between 135 and 245 K, culminating at ca. 180 K, which can be associated with the SCO phenomenon in **2**. Indeed, both the temperature range and maxima are in excellent agreement with the magnetic data. A lattice heat capacity was estimated from data below 135 K and above 245 K (dashed line in Figure 8), allowing the determination of the excess heat capacity associated with the SCO phenomenon in **2** (inset in Figure 8). The related excess enthalpy and entropy were derived by integration of the excess heat capacity and amount to 8.08 kJ mol^{-1} and 44.6 J mol^{-1} K^{-1}, respectively. Both figures are relatively large, which is usually taken as a consequence of a cooperative character of the SCO. In particular, the excess entropy is well above the purely electronic component, *R*Ln5, thus containing a significant content arising from the coupling of the electronic transition with lattice phonons. The so-called domain model (developed by Sorai and widely used in SCO studies when calorimetric data are available52) allows such a cooperative character to be quantified through the number n of like-spin SCO centres within an interacting domain; the larger the domains are, the more cooperative the transition is. Values of n close to 1 are typical of solution-like gradual SCO,53–55 while values of ca. 10 to 9547,56,57 have been derived for cooperative to very cooperative systems. Here, the excess heat capacity of **2** is very nicely reproduced by this model with n = 3.33 (red line in the inset of Figure 8), indicative of a relatively weakly cooperative SCO, and in agreement with the magnetic studies.

In summary, the present study has shown that an apparent minor modification of a ligand, namely the substitution of one of the chloride atoms of Cldpat by an aniline group (ligand Cladpat) gives rise to a drastic change of the magnetic properties of the corresponding iron(II) complexes. Indeed, the coordination compounds **1** and **2**, which exhibit identical coordination spheres for their metal centre, display distinct magnetic behaviours; **1** is a high-spin species whereas **2** is a SCO complex with a (weakly cooperative) transition. These opposite comportments are obviously due to the different ligands. Since the coordination bond lengths and angles are comparable for **1** and HS **2**, the distinct magnetic properties observed are most likely caused by different ligand-field strengths (i.e. Cldpat has a smaller Δ_{oct} value). Theoretical studies and the preparation of dipyridylamino-substituted triazine

ligands bearing electron-withdrawing and/or electron-donating substituents may help to understand these disparities. Therefore, these investigations will be carried out and the results will be reported in a future paper.

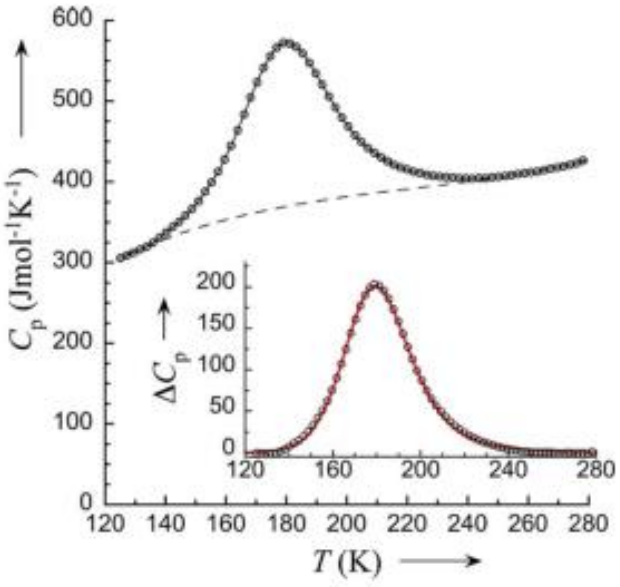

Fig. 8. Molar heat capacities of **2** showing a broad hump associated with the SCO. The dashed line is the estimated lattice component. Inset: excess heat capacities associated with the SCO in **2**. The full line is a fit to the domain model of Sorai with n = 3.3.

References

[1] B. N. Figgis , M. A. Hitchman , in *Ligand Field Theory and Its Applications*, Wiley-VCH, New York, 2000 .
[2] B. Koudriavtsev , W. Linert , *J. Struct. Chem.* 2010 , **51** , 335 –365 .
[3] B. P. Lever , in *Werner Centennial* (Ed.: G. B. Kauffman) , ACS Publications, Washington, USA, 1967 , pp. 430–451.
[4] P. Gütlich , A. Hauser , H. Spiering , *Angew. Chem.* 1994 , **106** , 2109 ; Angew. Chem. Int. Ed. Engl. 1994 , 33 , 2024 –2054 .
[5] P. Gütlich , H. A. Goodwin , in *Spin Crossover in Transition Metal Compounds I*, Springer-Verlag Berlin, Berlin, 2004 , vol. 233 , pp. 1–47.
[6] J. A. Real , A. B. Gaspar , M. C. Muñoz , *Dalton Trans.* 2005 , 2062 –2079 .
[7] Bousseksou , G. Molnar , J. A. Real , K. Tanaka , *Coord. Chem. Rev.* 2007 , **251** , 1822 –1833 .
[8] B. Gaspar , M. Seredyuk , R. Gütlich , *Coord. Chem. Rev.* 2009 , **253** , 2399 –2413 .
[9] P. Gamez , J. S. Costa , M. Quesada , G. Aromí , *Dalton Trans.* 2009 , 7845 –7853 .
[10] Bousseksou , G. Molnar , L. Salmon , W. Nicolazzi , *Chem. Soc. Rev.* 2011 , **40** , 3313 –3335 .
[11] P. Gütlich , Y. Garcia , H. A. Goodwin , *Chem. Soc. Rev.* 2000 , **29** , 419 –427 .
[12] M. A. Halcrow , *Chem. Soc. Rev.* 2011 , **40** , 4119 –4142 .
[13] J. Tao , R. J. Wei , R. B. Huang , L. S. Zheng , *Chem. Soc. Rev.* 2012 , **41** , 703 –737 .
[14] G. Aromí , L. A. Barrios , O. Roubeau , P. Gamez , *Coord. Chem. Rev.* 2011 , **255** , 485 –546 .
[15] J. Olguin , S. Brooker , *Coord. Chem. Rev.* 2011 , **255** , 203 –240 .
[16] M. Boca , R. F. Jameson , W. Linert , *Coord. Chem. Rev.* 2011 , **255** , 290 –317 .

[17] M. A. Halcrow , *Coord. Chem. Rev.* 2009 , **253** , 2493 –2514 .
[18] J. A. Kitchen , S. Brooker , *Coord. Chem. Rev.* 2008 , **252** , 2072 –2092 .
[19] K. S. Murray , *Eur. J. Inorg. Chem.* 2008 , 3101 –3121 .
[20] S. Bonnet , M. A. Siegler , J. S. Costa , G. Molnar , A. Bousseksou , A. L. Spek , P. Gamez , J. Reedijk , *Chem. Commun.* 2008 ,5619 –5621 .
[21] J. S. Costa , K. Lappalainen , G. de Ruiter , M. Quesada , J. K. Tang , I. Mutikainen , U. Turpeinen , C. M. Grunert , P. Gütlich , H. Z. Lazar , J. F. Létard , P. Gamez , J. Reedijk , *Inorg. Chem.* 2007 , **46** , 4079 –4089 .
[22] M. Quesada , V. A. de la Pena-O'Shea , G. Aromí , S. Geremia , C. Massera , O. Roubeau , P. Gamez , J. Reedijk , *Adv. Mater.* 2007 ,**19** , 1397 –1402 .
[23] P. Gamez , P. de Hoog , M. Lutz , W. L. Driessen , A. L. Spek , J. Reedijk , *Polyhedron* 2003 , **22** , 205 –210 .
[24] M. Quesada , P. de Hoog , P. Gamez , O. Roubeau , G. Aromí , B. Donnadieu , C. Massera , M. Lutz , A. L. Spek , J. Reedijk , *Eur. J. Inorg. Chem.* 2006 , 1353 –1361 .
[25] M. Quesada , M. Monrabal , G. Aromí , V. A. de la Pena-O'Shea , M. Gich , E. Molins , O. Roubeau , S. J. Teat , E. J. MacLean , P. Gamez , J. Reedijk , *J. Mater. Chem.* 2006 , **16** , 2669 –2676 .
[26] T. M. Ross , B. Moubaraki , S. R. Batten , K. S. Murray , *Dalton Trans.* 2012 , **41** , 2571 –2581 .
[27] T. M. Ross , B. Moubaraki , S. M. Neville , S. R. Batten , K. S. Murray , *Dalton Trans.* 2012 , **41** , 1512 –1523 .
[28] T. M. Ross , B. Moubaraki , D. R. Turner , G. J. Halder , G. Chastanet , S. M. Neville , J. D. Cashion , J. F. Létard , S. R. Batten , K. S. Murray , *Eur. J. Inorg. Chem.* 2011 , 1395 –1417 .
[29] T. M. Ross , B. Moubaraki , K. S. Wallwork , S. R. Batten , K. S. Murray , *Dalton Trans.* 2011 , **40** , 10147 –10155 .
[30] S. M. Neville , B. A. Leita , D. A. Offermann , M. B. Duriska , B. Moubaraki , K. W. Chapman , G. J. Halder , K. S. Murray , *Eur. J. Inorg. Chem.* 2007 , 1073 –1085 .
[31] T. J. Mooibroek , P. Gamez , *Inorg. Chim. Acta* 2007 , **360** , 381 –404 .
[32] P. Gamez , J. Reedijk , *Eur. J. Inorg. Chem.* 2006 , 29 –42 .
[33] P. de Hoog , P. Gamez , W. L. Driessen , J. Reedijk , *Tetrahedron Lett.* 2002 , **43** , 6783 –6786 .
[34] H. S. Scott , T. M. Ross , S. R. Batten , I. A. Gass , B. Moubaraki , S. M. Neville , K. S. Murray , *Aust. J. Chem.* 2012 , **65** , 874 –882 .
[35] P. Guionneau , M. Marchivie , G. Bravic , J. F. Létard , D. Chasseau , *Top. Curr. Chem.* 2004 , **234** , 97 –128 .
[36] M. Quesada , F. Prins , E. Bill , H. Kooijman , P. Gamez , O. Roubeau , A. L. Spek , J. G. Haasnoot , J. Reedijk , *Chem. Eur. J.* 2008 ,**14** , 8486 –8499 .
[37] M. Marchivie , P. Guionneau , J. F. Létard , D. Chasseau , *Acta Crystallogr., Sect. B-Struct. Sci.* 2005 , **61** , 25 –28 .
[38] J. K. McCusker , A. L. Rheingold , D. N. Hendrickson , *Inorg. Chem.* 1996 , **35** , 2100 –2112 .
[39] T. J. Mooibroek , P. Gamez , *CrystEngComm* 2012 , **14** , 1027 –1030 .
[40] T. J. Mooibroek , P. Gamez , *CrystEngComm* 2012 , **14** , 3902 –3906 .
[41] C. A. Hunter , J. K. M. Sanders , *J. Am. Chem. Soc.* 1990 , **112** , 5525 –5534 .
[42] S. A. Arnstein , C. D. Sherrill , *Phys. Chem. Chem. Phys.* 2008 , **10** , 2646 –2655 .
[43] Hauser , *Top. Curr. Chem.* 2004 , **234** , 155 –198 .
[44] Hauser , *J. Chem. Phys.* 1991 , **94** , 2741 –2748 .

[45] Desaix , O. Roubeau , J. Jeftic , J. G. Haasnoot , K. Boukheddaden , E. Codjovi , J. Linarès , M. Noguès , F. Varret , *Eur. Phys. J. B*1998 , **6** , 183 –193 .
[46] F. Varret , K. Boukheddaden , E. Codjovi , C. Enachescu , J. Linarès , *Top. Curr. Chem.* 2004 , **234** , 199 –229 .
[47] M. Sorai , S. Seki , *J. Phys. Chem. Solids* 1974 , **35** , 555 –570 .
[48] L. Capes , J.-F. Létard , O. Kahn , *Chem. Eur. J.* 2000 , **6** , 2246 –2255 .
[49] T. Buchen , H. Toftlund , P. Gütlich , *Chem. Eur. J.* 1996 , **2** , 1129 –1133 .
[50] J. A. Real , I. Castro , A. Bousseksou , M. Verdaguer , R. Burriel , M. Castro , J. Linarès , F. Varret , *Inorg. Chem.* 1997 , **36** , 455–464 .
[51] N. Moliner , M. C. Muñoz , J.-F. Létard , X. Solans , R. Burriel , M. Castro , O. Kahn , J. A. Real , *Inorg. Chim. Acta* 1999 , **291** , 279–288 .
[52] M. Sorai , *Chem. Rev.* 1996 , **106** , 976 –1031 .
[53] T. Nakamoto , Z. C. Tan , M. Sorai , *Inorg. Chem.* 2001 , **40** , 3805 –3809 .
[54] O. Roubeau , M. de Vos , A. F. Stassen , R. Burriel , J. G. Haasnoot , J. Reedijk , *J. Phys. Chem. Solids* 2003 , **64** , 1003 –1013 .
[55] O. Roubeau , M. Evangelisti , E. Natividad , *Chem. Commun.* 2012 , **48** , 7604 –7606 .
[56] M. Sorai , *Top. Curr. Chem.* 2004 , **235** , 153 –170 .
[57] Z. Arcis-Castíllo , S. Zheng , M. A. Siegler , O. Roubeau , S. Bedoui , S. Bonnet , *Chem. Eur. J.* 2011 , **17** , 14826 –14836 .
[58] G. M. Sheldrick , *Acta Crystallogr., Sect. A* 2008 , **64** , 112 –122 .

Category 2: Influence of supramolecular bonding contacts on the spin crossover behaviour of iron(II) complexes from 2,2′-dipyridylamino/*s*-triazine ligands

Introduction

The spin-crossover (SCO) phenomenon is a particularly interesting manifestation of the ligand-field theory.[1, 2] Hence, for octahedral d^4–d^7 transition-metal complexes that may be either low spin (LS) or high spin (HS), the occurrence of SCO is associated to intermediate ligand-field strength,[3] for which the transition-metal compound may present HS ↔LS bistability through the application of an external stimulus like temperature, pressure or light.[4-7] Such behaviour is obviously very attractive, especially with d^6 Fe(II) ions for which the LS state is diamagnetic and sharp differences in optical properties are often associated with the SCO; therefore, SCO compounds may find applications in molecular switches,[8] data-storage devices[9, 10] and optical displays.[11-13] Consequently, SCO has received a great deal of attention from the scientific community during decades, and this area of research is experiencing a tremendous development since the past 5 years.[14-18] Thus, many SCO iron(II) complexes have been reported, typically exhibiting an octahedral $[FeN_6]$ core obtained from ligands containing aromatic nitrogen-donor groups, such as pyridine or azole rings.[19-22]

Since 2006, we have been involved in the design and preparation of various types of pyridine-containing ligands for the generation of SCO compounds.[23-27] In particular, one of the families of ligands developed is based on the 1,3,5-triazine (or *s*-triazine) ring.[28] For instance, the ligand 2,4,6-tris(dipyridin-2-ylamino)-1,3,5-triazine (dpyatriz),[29] including three 2,2'-dipyridylamine units on a *s*-triazine ring, has allowed to synthesize iron(II) coordination compounds with interesting SCO properties.[23, 28, 30, 31] Then, Murray and co-workers have described various dipyridylamino-substituted-triazine ligands, which have produced a number of SCO compounds with distinct transition behaviours,[32-36] thus illustrating the potential of this category of ligands to create molecular switches.

In the present study, two new members of this family of 2,2'-dipyridylamino/*s*-triazine ligands have been prepared. The straightforward and selective substitutions of the three chloride atoms of 2,4,6-trichloro-1,3,5-triazine by phenolic reagents and 2,2'-dipyridylamine yield the related ligands 2-(*N*,*N*-bis(2-Pyridyl))-4,6-bis(phenoxy)-(1,3,5)triazine (**L1**, R = H; Scheme 1) and 2-(*N*,*N*-bis(2-Pyridyl))-4,6-bis(pentafluorophenoxy)-(1,3,5)triazine (**L1^{F}**, R = F; Scheme 1). These two ligands, which differ by the replacement of the hydrogen atoms of the phenoxyl groups of **L1** by fluorides (**L1^{F}**), have been designed to investigate the role played by supramolecular interactions (i.e. π···π interactions, halogen bonding) induced by the distinct aryl groups on the SCO properties of the corresponding *trans*-[Fe**L**$_2$(NCS)$_2$] complexes.

Results and discussion

Synthesis and crystal structures. The ligands 2-(*N*,*N*-bis(2-Pyridyl))-4,6-bis(phenoxy)-(1,3,5)triazine (**L1**) and 2-(*N*,*N*-bis(2-Pyridyl))-4,6-bis(pentafluorophenoxy)-(1,3,5)triazine (**L1^{F}**) are readily prepared *via* a two-step reaction in THF from 2,4,6-trichloro-1,3,5-triazine, following a straightforward synthetic procedure (Scheme 1)

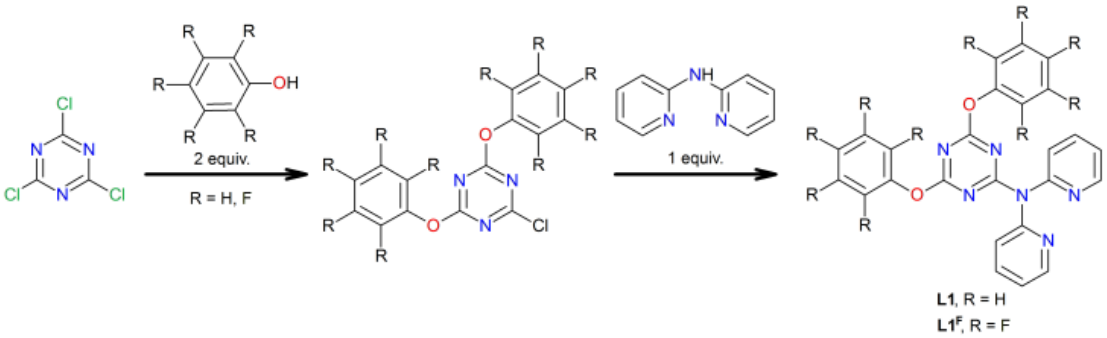

Scheme 1 Preparation of ligands 2-(*N*,*N*-bis(2-Pyridyl))-4,6-bis(phenoxy)-(1,3,5)triazine (**L1**) and 2-(*N*,*N*-bis(2-Pyridyl))-4,6-bis(pentafluorophenoxy)-(1,3,5)triazine (**L1^{F}**)

Compound **1,** *trans*-[Fe(**L1**)$_2$(NCS)$_2$]·2CH$_2$Cl$_2$, is obtained with a yield of 70% by direct addition of a freshly prepared water/methanol solution of iron(II) thiocyanate (1 equiv.) to a dichloromethane solution containing 2 equiv. of **L1**. **1**, which exhibits SCO properties, crystallizes in the triclinic space group *P*–1, at 100, 240 and 300 K. A representation of the molecular structure of **1** (low-spin state) is depicted in Figure 1. Selected bond lengths and angles are listed in Table 1.

The iron(II) centre in **1** displays the expected octahedral coordination environment, typically observed for iron(II) thiocyanate complexes with this family of dipyridylamino-substituted-triazine ligands.[23, 31-36] The metal ion is coordinated by two **L1** ligands in the equatorial plane of the octahedron, the apical positions being occupied by two *trans* thiocyanate anions (Figure 1). At 100 K, the Fe–N$_{pyridine}$ distances in the range 1.981(2)–1.992(2) Å are characteristic of a LS iron(II) ion. The Fe–N$_{NCS}$ bond lengths of 1.943(2) Å are also indicative of a LS state. These coordination bond lengths increase by ca. 0.22 Å for Fe–N$_{pyridine}$ and ca. 0.13 Å for Fe–N$_{NCS}$ when the temperature is raised to 300 K (Table 1), which describe a full spin transition that has been observed as well by variable-temperature magnetic susceptibility measurements (see below). At 240 K, the distances found, *i.e.* 2.149(2)–2.163(2) Å for Fe–N$_{pyridine}$ and 2.051(2) Å for Fe–N$_{NCS}$, correspond to a HS/LS mixture of about 78/22, in agreement with bulk magnetic studies.

The distortion parameters Σ° and Φ° gauge the magnitude of the deformation of the coordination geometry relative to a perfect octahedron (for which $\Sigma^{\circ} = \Phi^{\circ} = 0$).[15, 41, 42]

For LS **1**, Σ° = 31 and Φ° = 37 and these values increase to respectively 46 and 67 for the HS state (Table 1). $\Delta\Sigma^{\circ}$ ($\Sigma^{\circ}_{HS} - \Sigma^{\circ}_{LS}$) and $\Delta\Phi^{\circ}$ ($\Phi^{\circ}_{HS} - \Phi^{\circ}_{LS}$) thus illustrate the extent of the structural changes that take place during the spin transition. For **1**, $\Delta\Sigma^{\circ}$ = 15 and $\Delta\Phi^{\circ}$ = 30. The high $\Delta\Phi^{\circ}$ value indicates a severe distortion of the original octahedral geometry towards a trigonal prismatic structure, feature that is commonly noticed upon LS → HS transition.[15] Such a structural distortion may induce cooperativity between the switching centres, which is normally reflected by an abrupt LS ↔ HS crossover phenomenon. Actually, the magnetic studies (see below) reveal a weakly cooperative behaviour since a complete HS-to-LS conversion is realized within a temperature range of ca. 90 K.

Table 1 Coordination bond lengths (Å) and angles (°), and supramolecular interactions for compound **1** at three different temperatures

Bond	100 K (LS)	240 K	300 K (HS)
Fe1–N1	1.943(2)	2.051(2)	2.075(4)
Fe1–N2	1.992(2)	2.163(2)	2.216(3)
Fe1–N3	1.981(2)	2.149(2)	2.203(3)
Fe1···Fe1$_{inter}$[a]	10.138(2)	10.239(2)	10.301(4)
Angle	100 K	240 K	300 K
N2–Fe1–N3	86.8(6)	83.5(8)	82.4(1)
N2–Fe1–N3a	93.3(6)	96.5(8)	97.6(1)
N1–Fe1–N1a	180	180	180
ΣFe1°[c]	31	40	46
Φ°[d]	37	58	67
H-bonding contacts	100 K	240 K	300 K
C11–H11A···O2	3.559(3)	3.609(4)	3.642(8)
C27–H27A···C13	3.415(3)	3.508(4)	3.526(7)
Lone pair···π interactions	100 K	240 K	300 K
Cg5···S1	3.459(1)	3.561(1)	3.598(2)

[a] Closest inter-monomer Fe···Fe distance. [b] Symmetry operation: a, 1–*x*, 1–*y*, 1–*z*. [c] Σ° = the sum of $|90 - \theta|$ for the 12 N–Fe–N angles in the octahedron.[43, 44] [d] Φ° = sum of $|60 - \theta|$ for the 24 N–Fe–N angles describing the trigonal twist angle.[15, 41]

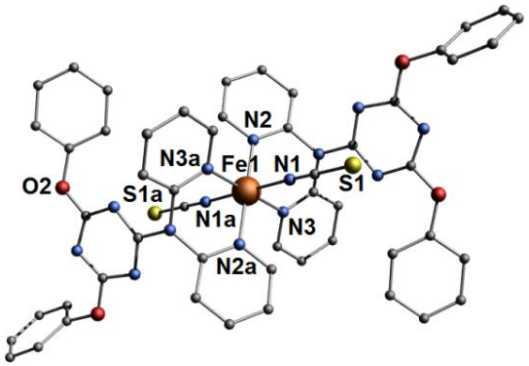

Fig. 1 Representation of the molecular structure of compound **1** (LS state, determined at 100 K) with partial atom-numbering scheme. The hydrogen atoms and the lattice dichloromethane molecules are not shown for clarity. Symmetry operation: a, 1–*x*, 1–*y*, 1–*z*.

The crystal packing of **1** shows that the iron(II) centres weakly interact along the crystallographic *c* axis through C–H···O and C–H···π contacts (which are affected by the

transition; see Table 1), producing a supramolecular 1D chain (Figure 2A). These chains do not significantly interact with each other (Figure 2B), which may explain the moderate cooperativity of the SCO behaviour observed by magnetic measurements (see below).

In addition, the molecules of **1** display intramolecular lone pair···π interactions[45] between the thiocyanate sulfur atoms and the triazine rings (Cg5···S1 = 3.459(1) Å).

Compound **2**, *trans*-[Fe(**L1**)$_2$(NCSe)$_2$]·4CH_2Cl_2·4CH_3OH, is obtained with a yield of 63%, applying the same synthetic procedure as that used to prepare **1**, replacing iron(II) thiocyanate by iron(II) selenocyanate. As anticipated, **2** is a SCO compound, which crystallizes in the monoclinic space group $P2_1/c$ in its LS state. A view of the molecular structure of **2** is shown in Figure 3.

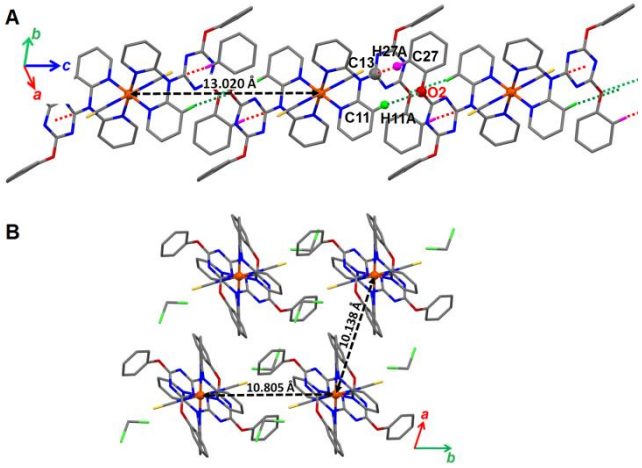

Fig. 2 Views of the crystal packing of LS **1** showing A) the formation of a supramolecular 1D chain along the crystallographic *c* axis by means of weak C–H···O and C–H···π contacts (respectively C11–H11A···O2 = 3.559(3) Å, green dotted lines and C27–H27A···C13 = 3.415(3) Å, red dotted lines); B) the arrangement of the chains in the *ab* plane illustrating the lack of significant interactions between them

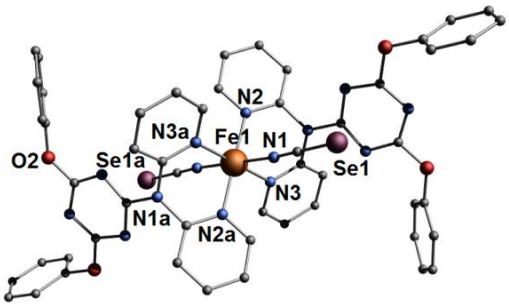

Fig. 3 Representation of the molecular structure of compound **2** (LS state, determined at 100 K) with partial atom-numbering scheme. The hydrogen atoms and the lattice dichloromethane molecules are not shown for clarity. Symmetry operation: a, 1–*x*, 1–*y*, 1–*z*

Unsurprisingly, the coordination environment of the iron(II) ion in **2** is similar to that of **1** (see Figures 1 and 3). The observed octahedral geometry is formed by four pyridine donors in the equatorial plane (belonging to two **L1** ligands) and two axial $NCSe^-$ anions. The Fe–$N_{pyridine}$ bond lengths ranging from 1.992(4) to 2.009(4) Å and the Fe–N_{NCSe} distances of 1.940(4) Å (Table 2) are typical for a LS iron(II) system, and are comparable to those found for **1** (Tables 1 and 2). Unfortunately, crystallographic data for HS **2** could not be obtained.

Actually, single crystals of **2** did not diffract enough at room temperature, most likely as the result of solvent evaporation (and particularly dichloromethane).

The crystal packing of LS **2** reveals the formation of a 1D chain of iron(II) complexes that are connected by parallel-displaced π···π interactions involving the phenyl ring [C21, C22, C23, C24, C25, C26), with a centroid-to-centroid distance of 3.717(4) Å (Cg7···Cg7j; see Table 2 and Figure 4A). These π stacks are characterized by short C···C contact distances of 3.208(8) Å (C22···C23j) and 3.234(9) Å (C22···C24j). It has to be noted that these π···π stacking interactions (which are not occurring in **1**) give rise to a different orientation of the corresponding phenyl rings in compounds **1** and **2** (see phenyl rings of the oxygen atom O2 in Figures 1 and 3). These chains are weakly interacting with each other *via* π···π (C8···C10d) and C–H···π (C4–H4A···C17g and C5–H5A···C18g) long contacts (see Table 2 and Figure 4B).

Surprisingly, although the iron(II) complexes appear to better interact with each other compared to those in **1**, the SCO behaviour of **2** is clearly much less cooperative; actually, the transition is very gradual as the HS state is fully converted into the LS state within a temperature range of over 150 K. This feature may be explained by the presence of numerous solvent molecules in the crystal lattice of **2**. Indeed, compound **2** is surrounded by 8 solvent molecules, *i.e.* 4 CH_3OH and 4 CH_2Cl_2, while only 2 CH_2Cl_2 are found for **1**. Therefore, all these solvent molecules in **2** (which are interacting with each other and with the complex; see hydrogen bonds in Table 2) most likely affect the propagation of the spin transition; hence, the behaviour of **2** resembles that of a diluted system, in which the metal centres within the solid are transiting independently, thus resulting in a non-cooperative conversion following Boltzmann population of states.

Finally, similarly to **1**, the molecules of **2** display intramolecular lone pair···π interactions between the selenocyanate selenium atoms and the triazine rings (Cg5···Se1 = 3.501(2) Å).

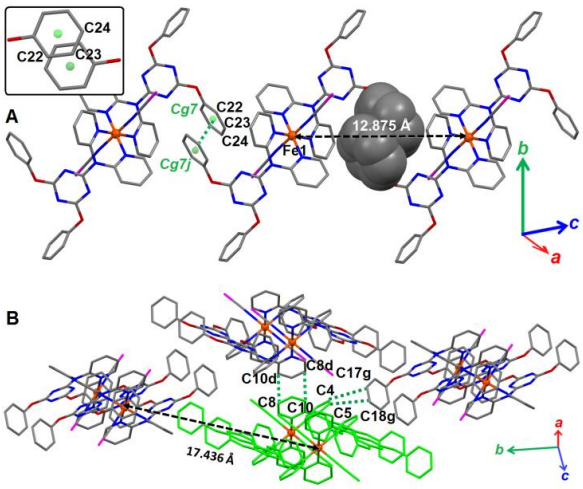

Fig. 4 Views of the crystal packing of LS **2** showing A) the formation of a supramolecular 1D chain *via* parallel-displaced π···π interactions (Cg7···Cg7j = 3.717(4) Å (the inset illustrates a parallel-displaced π···π stack); B) the feeble interactions of the chains (one chain is shown in green) by means of weak π···π (C8···C10d = 3.796(8) Å) and C–H···π (C4–H4A···C17g = 3.607(7) Å and C5–H5A···C18g = 3.552(7) Å) contacts. Symmetry operations: d, –x, 1–y, 1–z; g, x, 1/2–y, 1/2+z; j, –x, 1–y, –z

Compound **3,** *trans*-[Fe(**L1^{F}**)$_2$(NCS)$_2$]·2CH$_3$CN, is prepared with a yield of 65% by direct addition of a freshly prepared water/acetonitrile solution of iron(II) thiocyanate (1 equiv.) to an acetonitrile solution containing 2 equiv. of **L1^{F}**. As the previous two complexes, **3** exhibits spin-transition properties. **3** crystallizes in the triclinic *P*–1 space group at 100, 190 and 280 K. Selected coordination bond distances and angles are listed in Table 3. A view of the molecular structure of **3** is depicted in Figure 5.

Table 2 Coordination bond lengths (Å) and angles (°), and supramolecular interactions for compound **2** (low-spin and high-spin states)[a]

Bond	100 K (LS)
Fe1–N1	1.940(4)
Fe1–N2	1.992(4)
Fe1–N3	2.009(4)
Fe1···Fe1$_{inter}$[b]	8.642(4)
Angle	100 K (LS)
N2–Fe1–N3	86.5(2)
N2–Fe1–N3a	93.6(2)
N1–Fe1–N1a	180
ΣFe1°[c]	25
Φ°[d]	32
π···π interactions	100 K (LS)
Cg7···Cg7j	3.717(4)
C22···C24j	3.234(9)
C22···C23j	3.208(8)
C8···C10d	3.796(8)
C–H···π contacts	100 K (LS)
C4–H4A···C17g	3.607(7)
C5–H5A···C18g	3.552(7)
Lone pair···π interactions	
Cg5···Se1	3.501(2)
Hydrogen bond	
O1s–H1s···O2s	2.828(12)
O1s–H1s–O2s	150(8)
O2s–H2s···N5	3.074(9)
O2s–H2s–N5	155(7)

[a] Symmetry operation: a, 1–*x*, 1–*y*, 1–*z*; d, –x, 1–y, 1–z; g, x, 1/2–y, 1/2+z; j, –x, 1–y, –z. [b] Closest inter-monomer Fe···Fe distance. [c] Σ° = the sum of |90 – θ| for the 12 N–Fe–N angles in the octahedron.[43, 44] [d] Φ° = sum of |60 – θ| for the 24 N–Fe–N angles describing the trigonal twist angle.[15, 41]

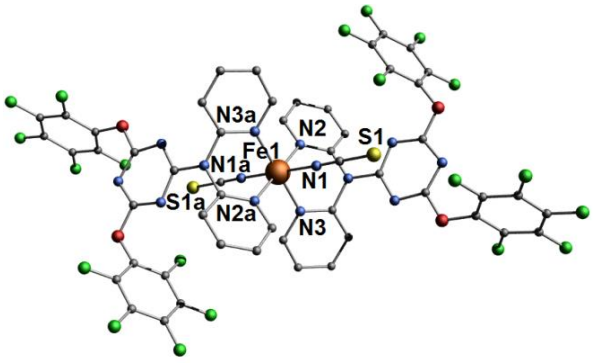

Fig. 5 Representation of the molecular structure of compound **3** (LS state, determined at 100 K) with partial atom-numbering scheme. The hydrogen atoms and the lattice dichloromethane molecules are not shown for clarity. Symmetry operation: a, 1–*x*, 1–*y*, 1–*z*.

The coordination environment of the iron(II) ion in **3** is analogous to those of compounds **1** and **2**. The equatorial plane of the octahedron contains four pyridine donors belonging to two **L1^{F}** ligands, and the axial positions are occupied by two thiocyanate anions. At 100 K, the Fe–$N_{pyridine}$ and Fe–N_{NCS} coordination bond lengths are typical for a LS FeN_6 (Table 3), and are comparable to those of **1** and **2**. For HS **3** at 280 K, these bond distances increase by respectively ca. 0.22 and 0.12 Å (Table 3), thus giving characteristic values for this spin state. This full LS→HS transition is corroborated by magnetic measurements (see below). At 190 K, the Fe–$N_{pyridine}$ and Fe–N_{NCS} distances are indicative of a LS/HS mixture of about 95/5, in agreement with the data obtained by magnetic-susceptibility measurements.

The distortion parameters Σ° and Φ° amount to respectively 30 and 36 for LS **3**, and to 41 and 72 for HS **3**. Hence, the corresponding $\Delta\Sigma^{\circ}$ and $\Delta\Phi^{\circ}$ values of respectively 11 and 36 again reflect a strong distortion of the octahedral geometry upon LS→HS transition. As mentioned above, such a distortion is often associated with cooperativity between the transiting centres. In the present case, $\Delta\Phi^{\circ}$ = 37 is higher than that found for the related complex **1** ($\Delta\Phi^{\circ}$ = 30). Therefore, a greater cooperative behaviour is expected for **3** in comparison to **1**; in fact, a clearly more abrupt transition (see the corresponding χT *vs.* T plots below) is observed for **3**, which may be rationalized by specific crystal-packing features induced (at least in part) by the fluorinated ligand **L1^{F}**.

Table 3 Coordination bond lengths (Å) and angles (°), and supramolecular interactions for compound **3** at three different temperatures

Bond	100 K (LS)	190 K	280 K (HS)
Fe1–N1	1.937(1)	1.943(1)	2.056(3)
Fe1–N2	1.979(1)	1.985(2)	2.194(2)
Fe1–N3	1.988(1)	1.989(1)	2.207(2)
Fe1···$Fe1_{inter}$[a]	8.350(1)	8.412(1)	8.643(2)
Angle	100 K	190 K	280 K
N2–Fe1–N3	86.16(5)	86.19(6)	81.83(9)
N2–Fe1–N3a	93.85(5)	93.81(6)	98.17(9)
N1–Fe1–N1a	180	180	180
ΣFe1°[c]	30	30	41
Φ°[d]	36	36	72
π···π interactions	100 K	190 K	280 K
O1···C16c	3.112(2)	3.118(3)	3.092(4)
O1···C17c	3.255(2)	3.247(3)	3.238(4)
C15···C16c	3.387(2)	3.378(3)	3.385(5)
Cg3···Cg3b	3.757(1)	3.747(1)	3.787(2)
halogen···halogen contacts	100 K	190 K	280 K
F8···F9l	2.781(2)	2.803(2)	2.815(4)
Lone pair···π interactions	100 K	190 K	280 K
Cg5···S1	3.457(1)	3.489(1)	3.579(2)

[a] Closest inter-monomer Fe···Fe distance. [b] Symmetry operation: a, 1–*x*, 1–*y*, 1–*z*; b, –1+*x*, *y*, *z*; c, 1–*x*, 1–*y*, 2–*z*; l, 2–*x*, 2–*y*, 1–*z*. [c] Σ° = the sum of $|90 - \theta|$ for the 12 N–Fe–N angles in the octahedron.[43, 44] [d] Φ° = sum of $|60 - \theta|$ for the 24 N–Fe–N angles describing the trigonal twist angle.[15, 41]

Actually, the crystal packing of LS **3** reveals an intricate network of strong supramolecular bonds (Figure 6). First, molecules of **3** are connected *via* strong lone pair···π (O1···C16c and O1···C17c; see Table 3 and Figure 6A) and π···π (C15···C16c; see Table 3 and Figure 6A) interactions. It has to be noted that the O1···C16c contact distance of 3.112(2) Å is below the sum of the van der Waals radii of O and C (i.e. 3.22 Å), thus indicating a very strong interaction between the fluorinated aromatic rings. These supramolecular bonds generate a 1D chain that runs along the crystallographic *c* axis. Next, the 1D chains are associated by means of nearly face-to-face π···π interactions between coordinated pyridine moieties characterized by a centroid-to-centroid distance of 3.757(1) Å (see Table 3 and Figure 6B). This spatial arrangement produces a 2D supramolecular sheet in the *ac* plane (Figure 6B). Finally, the 2D sheets are connected to each other by double strong F···F bonds (indeed, the F8···F9l distance of 2.781(2) Å is well below the sum of the van der Waals radii of two F atoms, namely 2.94 Å),[46] giving rise to a 3D framework (Figure 6C).

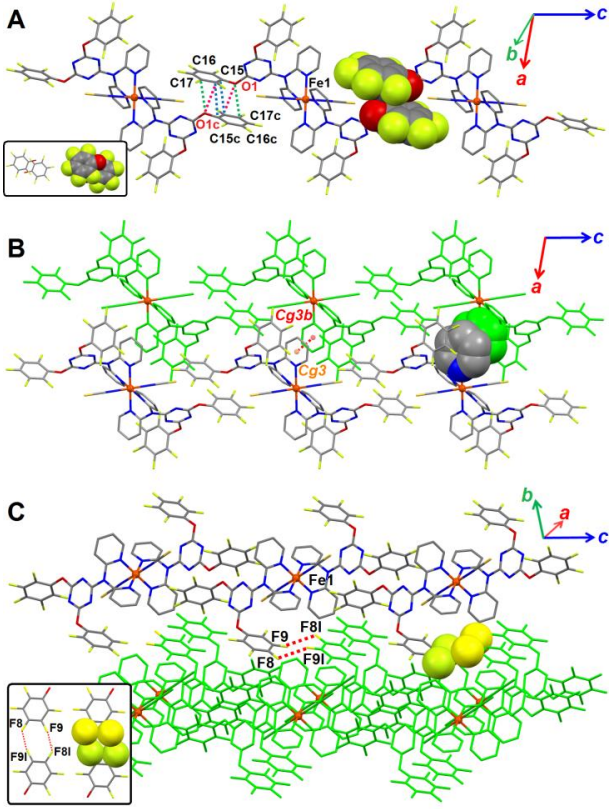

Fig. 6 Views of the crystal packing of LS **3** showing A) the formation of a supramolecular 1D chain *via* parallel-displaced pentafluorophenyl···pentafluorophenyl interactions (O1···C16c = 3.112(2) Å, O1···C17c = 3.255(2) Å and C15···C16c = 3.387(2) Å) (the inset illustrates the occurrence of a parallel-displaced stack between two pentafluorophenyl rings); B) the formation of 2D sheets by means of π···π interactions between coordinated pyridine rings (Cg3···Cg3b = 3.757(1) Å). one supramolecular chain is shown in green; C) the formation of a 3D supramolecular framework through the connection of the 2D sheets by strong F···F bonding contacts (F8···F9l = 2.781(2) Å) (the inset illustrates the bonding interaction of pentafluorophenyl rings *via* double halogen···halogen contacts) a 2D supramolecular sheet is shown in green. Symmetry operations: b, –1+*x*, *y*, *z*; c, 1–*x*, 1–*y*, 2–*z*; l, 2–*x*, 2–*y*, 1–*z*.

In summary, the transiting iron(II) centres are very well linked to each other (within all the crystal lattice, in contrast to **1** and **2**). Moreover, the solid-state structure of **3** includes

less lattice solvent molecules than **1** and **2** (which contains 8 molecules of solvent per iron(II) complex); hence **3** is clearly the most compact of the three systems. Therefore, an efficient cooperative behaviour has to be expected for **3**. As a matter of fact, the magnetic studies show the steepest HS ↔ LS transition for **3**, which is completed within a temperature range of ca. 60 K (while it is about 90 K for **1** and 150 K for **2**; see below).

As for **1** and **2**, lone pair···π interactions are realized between the thiocyanate sulfur atoms and the triazine rings (Cg5···S1 = 3.457(1) Å).

Magnetic, photomagnetic and thermal studies.

Confirmation of the process of thermal SCO indicated by the structural observations on single crystals of **1**–**3** was obtained through magnetization measurements on bulk samples in the temperature range 5–300 K. The resulting temperature dependencies of the χT product (Figure 7), χ being the molar paramagnetic susceptibility, evidence for all three compounds a complete and gradual thermal SCO. For compound **1**, the χT product is 3.19 cm^3 mol^{-1} K at 300 K, a value typical for an Fe(II) ion in a HS $S = 2$ state. χT starts to decrease already from 300 K to reach values of ca. 0.11–0.07 cm^3 mol^{-1} K below 160, which are now indicative of a fully populated LS $S = 0$ state. The corresponding transition is centred at $T½ = 233$ K. The selenocyanate derivative **2** exhibits a more gradual SCO centred at $T½ = 228$ K, with a χT value of only 2.95 cm^3 mol^{-1} K at 300 K (thus suggesting that the transition process has already started to take place at this temperature), and < 0.10 cm^3 mol^{-1} K below 130 K. In contrast, the SCO process, centred at $T½ = 238$ K, is more abrupt for **3** (as the result of a better cooperativity; see above), with a decrease of χT from 3.10 cm^3 mol^{-1} K at 280 K down to 0.2-0.1 below 200 K. This comparatively more cooperative character is illustrated by a smaller ΔT_{80} value of 50 K (80% of the transition occurs within about 50 K) for **3**, compared to those observed for **1** and **2**, respectively 90 and 130 K. These observations are reproduced upon warming, thus without detectable hysteresis, and over various cycles and batches, although only for fresh crystalline material in the case of **1**. Indeed, a more gradual, though complete, SCO centred at ca. 173 K is detected for the poorly crystalline powder **1'** obtained upon air exposure of **1**, which is ascribed to the loss of lattice solvent molecules (as indicated by Elemental Analysis; see Experimental section). The observation of a similar $T½$ for the thiocyanate and selenocyanate derivatives **1** and **3** agrees with our previous reports with the related complexes obtained with the ligand 6-chloro-*N*-phenyl-*N*,*N*-di(pyridin-2-yl)-1,3,5-triazine-2,4-diamine.[31] It thus seems that the replacement of S by Se in this family of *trans*-$[Fe^{II}\mathbf{L}_2(NCX)_2]$ compounds has only little influence on the SCO temperature, incontrast to other NCX-based SCO compounds.[47-51]

Confirmation of the relatively cooperative character of the SCO for **3** was obtained from Differencial-Scanning Calorimetry (DSC). Indeed, while only very broad poorly energetic humps are detected for **1'** and **2**, the molar heat capacity of **3** at constant pressure, C_p, exhibits a strong anomaly between 200 and 280 K, culminating at ca. 237 K (see Figure 8), which can be attributed to the SCO phenomenon in **3**. Both the associated excess enthalpy and entropy are relatively large, respectively at 11.70 kJ mol^{-1} and 49.6 J mol^{-1} K^{-1}, which is usually seen as a consequence of a cooperative character of the SCO.[52, 53] In particular, the excess entropy is well above the purely electronic component, RLn5; it thus encloses a significant content arising from the coupling of the electronic transition with lattice phonons. Fitting the excess heat capacity of **3** to Sorai's domain model[54] results in a number of interacting molecule per domain of $n = 6.2$ (red line in the inset of Figure 8), which is characteristic of a relatively cooperative SCO, in agreement with the magnetic studies.

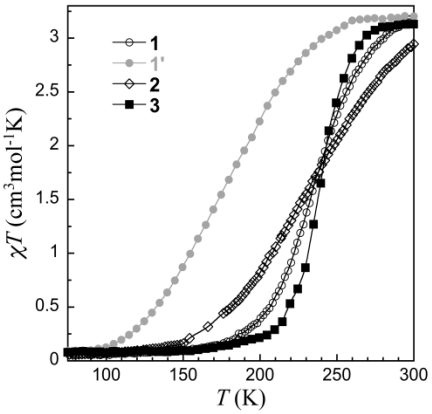

Fig. 7 χT vs. T plot for **1** (empty circles), **1'** (full circles), **2** (empty rhomboids) and **3** (full squares) showing the complete and gradual SCO. Lines are only guides to the eye.

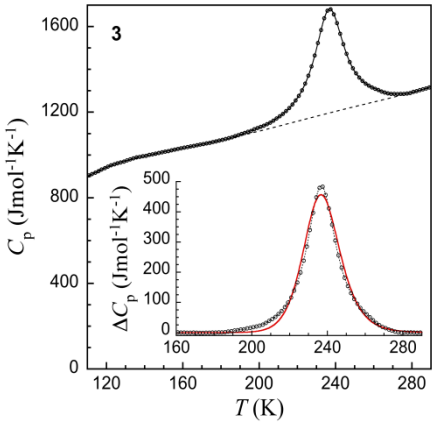

Fig. 8 Molar heat capacities of **3** showing a broad hump associated with the SCO. The dashed line is the estimated lattice component. Inset: excess heat capacities associated with the SCO in **3**. The full line is a fit to the domain model of Sorai (see text and ref. 44) with n = 6.2.

Preliminary photomagnetic studies on thin samples of **1'**, **2** and **3** indicate that a HS metastable state can be trapped for all three compounds at low temperatures through the so-called LIESST effect,[55] although with distinct efficacies. Indeed, while an increase of χT is detected upon irradiation in the 500–650 nm range at 10 K, the initial rate of increase is highest for **1'**, and smallest for **3**, for similar sample thickness. In addition, the rate of increase drops more rapidly for **2** and **3**, with stable values, corresponding to incomplete trapping of at most 40 and 20 % HS respectively, reached at longer irradiation times. On the other hand, a full HS state can be trapped in the case of **1'**. Upon warming, an increase of χT is first observed, which corresponds to the Zero-Field Splitting effect of trapped HS species. Subsequently, a decrease gradually sets in, which is due to the thermally-activated relaxation back to the LS state that is reached at ca. 85 K. A characteristic T_{LIESST} temperature of 58 K can be defined,[56] through the first derivative of χT. For the other two compounds, χT decreases already from 10 K to reach values similar to those of the normal LS state at ca. 70 K. Thus, even with a partial trapping, relaxation of the trapped HS species back to the LS ground state is not as fast at low temperatures as in the previously reported compound *trans*-$[Fe(Cladpat)_2(NCS)_2]$.[31] Therefore, considering that the three samples had similar thickness, the most likely origin of the lack of efficiency of the LIESST effect in **2** and **3** is an overlap of the $^5T_2 \rightarrow {}^5E$ (HS) band with a LS band (possibly $^1A_1 \rightarrow {}^3T_1$), giving rise to competitive LIESST and reverse-LIESST processes.[55, 57, 58]

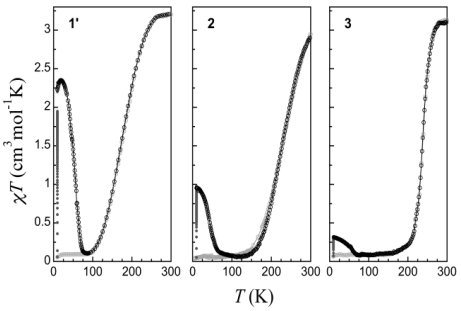

Fig. 9 χT vs. T plot for **1'** (left), **2** (middle) and **3** (right), showing the process of SCO (grey empty circles), the (partial) LS to HS photo-induced trapping at 10 K (full circles) and the relaxation back to the LS ground state and normal behaviour upon warming (black empty circles).

SCO systems based on 2,2'-dipyridylamino-substituted triazine ligands and Fe(NCS)$_2$. As mentioned earlier, iron(II) complexes of the type *trans*-[Fe^{II}**L**$_2$(NCS)$_2$], where **L** is a 2,2'-dipyridylamino-substituted triazine ligand (Scheme 2), usually display SCO properties, and the two new members of this family of compounds, namely **1** and **3**, verify this characteristic. Since the first report of such a SCO system by some of us,[23] we and Murray and co-workers have reported a number of 2,2'-dipyridylamino/triazine-based complexes.[31-33, 35, 36] Relevant structural features and SCO properties of these coordination compounds are described in Table 4. To date, 14 different *trans*[Fe^{II}**L**$_2$(NCS)$_2$] complexes have been obtained from 13 distinct ligands. Out of them, two do not show SCO properties; in fact, the simplest member of this family of ligands, namely when **R^1** = **R^2** = Cl, does not generate an iron(II) SCO compound.[31] Surprisingly, the *trans*-[Fe^{II}**L**$_2$(NCS)$_2$] complex whose ligand **L** contains two diphenylamine substituents is also a non-SCO material. All other compounds exhibit SCO properties (complete or incomplete transitions), with T½ values (T½ corresponds to the temperature at which half of the transiting iron(II) centres have changed their spin state) ranging from 110 up to 260 K, indicating that the transition can be fine-tuned through selection of the **R** groups (and the possibilities are limitless). All compounds display very gradual to gradual spin transitions, the more abrupt one (ΔT_{80} = 39 K) being obtained when **R^1** = dipyridylamine and **R^2** = phenol. It is actually a 1D polymeric chain[35] wherein the cooperativity between the iron(II) ions appears to be relativity efficient. By comparison, when dipyridylamine is replaced by a phenol, *i.e.* when **R^1** = **R^2** = phenol, a significantly more gradual behaviour (ΔT_{80} = 90 K) is observed for the corresponding monomeric species. No hysteretic behaviours have been observed for all these systems; however, it is assumed that careful design of a 2,2'-dipyridylamino-substituted triazine ligand(s) **L** with well-chosen **R** substituents will allow to enhance cooperativity between the iron(II) centres that may favour the occurrence of hysteresis.

It can be noted once again that lattice solvent molecules have a great effect on the SCO properties of a coordination compound. Indeed, for the *trans*-[Fe^{II}**L**$_2$(NCS)$_2$] complex with **R^1** = dipyridylamine and **R^2** = pyridine-4(1*H*)one, distinct SCO behaviours have been obtained in dichloromethane and in chloroform/methanol. In dichloromethane, the compound exhibits a very gradual transition (ΔT_{80} = 77 K) centred at T½ = 175 K, while a more abrupt transition (ΔT_{80} = 55 K) is observed in $CHCl_3$–CH_3OH, at a higher temperature (T½ = 200 K). This clearly illustrates the sensitivity of the SCO phenomenon, where not only the coordination sphere of the metal ion is important but also the interactions between the

complexes in the solid-state and the involvement of lattice solvent molecules (as observed for instance in the present study with compounds **1** and **1'**)

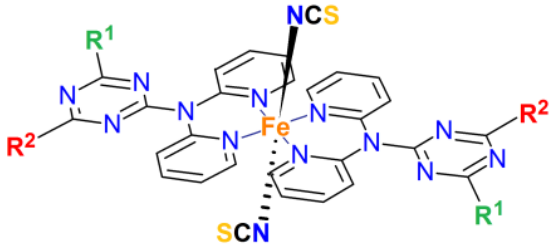

Scheme 2 Representation of the *trans*-[Fe^{II}**L**$_2$(NCS)$_2$] complexes whose structural and SCO properties are described in Table 4. **R^1** and **R^2** symbolize different substituents on the triazine ring (see Table 4)

Table 4 Structural and SCO properties of crystallographically characterized *trans*-[Fe^{II}**L**$_2$(NCS)$_2$] compounds with 2,2'-dipyridylamino-substituted triazine ligands **L** (Scheme 2)

R^1	**R^2**	Nuclearity	SCO character	SCO behaviour	hysteresis	$T_{½}$	$\Delta\Sigma^{\circ}$	$\Delta\Phi^{\circ}$	Lattice solvent(s)	Ref.
chlorine	chlorine	monomer	-	no	-	-	-	-	H_2O	[31]
chlorine	aniline	monomer	gradual; ΔT_{80}[a] = 50 K	complete	no	178 K	15	27	no	[31]
chlorine	dipyridylamine	polymer	very gradual; $\Delta T_{80} \approx 50$ K	incomplete (half SCO)[b]	no	~205 K	13/9[c]	26/0[c]	CH_3OH	[36]
dipyridylamine	dipyridylamine	monomer	gradual; $\Delta T_{80} = 40$ K	complete	no	200 K	12	31	no	[23]
dipyridylamine	pyridine-4(1*H*)one	polymer	very gradual; $\Delta T_{80} = 77$ K	complete	no	175 K	12/13[c]	22/24[c]	CH_2Cl_2	[35]
dipyridylamine	pyridine-4(1*H*)one	polymer	gradual; $\Delta T_{80} = 55$ K	complete	no	200 K	12/11[c]	21/6[c]	$CHCl_3$–CH_3OH	[35]
dipyridylamine	phenol	polymer	gradual; $\Delta T_{80} = 39$ K	incomplete	no	190 K	8/1[c]	20/6[c]	H_2O–CH_3OH	[35]
dipyridylamine	hydroquinone	polymer	gradual; $\Delta T_{80} = 50$ K	incomplete	no	260 K	4/3[c]	9/8[c]	CH_2Cl_2	[35]
dipyridylamine	aza-15-crown-5	polymer	very gradual; $\Delta T_{80} = 80$ K	complete	no	110 K	-[d]	-[d]	CH_3OH	[33]
dibenzylamine	dibenzylamine	monomer	gradual; $\Delta T_{80} = 50$ K	complete	no	~170 K[e]	13	27	no	[32]
diphenylamine	diphenylamine	monomer	-	no	-	-	-	-	CH_2Cl_2	[32]
aza-15-crown-5	aza-15-crown-5	monomer	very gradual; $\Delta T_{80} \approx 80$ K	complete	no	~240 K	14	31	*n*-C_3H_7OH	[33]
phenol	phenol	monomer	very gradual; $\Delta T_{80} = 90$ K	complete	no	233 K	15	30	CH_2Cl_2	this work
pentafluorophenol	pentafluorophenol	monomer	gradual; $\Delta T_{80} = 50$ K	complete	no	238 K	11	36	CH_3CN	this work

[a] ΔT_{80} is the temperature range within which 80% of the transition considered occurs. [b] The full LS state is not reached as only half of the iron(II) centres are transiting[36]. [c] The compound exhibits two crystallographically distinct iron(II) centres. [d] Only the X-ray structure of the LS compound has been reported.[33] [e] A different polymorphic form of this compound exhibits a very gradual spin transition ($\Delta T_{80} \approx 85$ K) centred at 300 K.

In summary, three new members of the still small (but increasing) family of SCO compounds based on the 2,2'-dipyridylamino/*s*-triazine moiety have been obtained and fully

characterized. The investigation carried out clearly shows the importance of supramolecular contacts in the cooperativity of the spin-transition process. Indeed, the triazine ligand containing the fluorinated phenolic groups generates a Fe(II)/NCS complex (*i.e.* **3**) whose SCO is significantly more abrupt (ΔT_{80} = 50 K) than that of the equivalent coordination compound (*i.e.* **1**) with the ligand bearing simple phenolic substituents (ΔT_{80} = 90 K). These distinct behaviours are obviously due to the fluoride atoms; actually, the F atoms give a π-acidic character to the phenyl rings, hence favouring the occurrence of strong intermolecular π···π interactions (which do not take place in the solid-state structure of compound **1**, which lacks the F atoms). In addition, the F atoms are involved in strong intermolecular halogen···halogen bonding contacts, improving further the cooperative character of the SCO.

References

[1] B.N. Figgis, M.A. Hitchman, Ligand Field Theory and Its Applications, Wiley-VCH, New York, 2000.
[2] A.B. Koudriavtsev, W. Linert, J. Struct. Chem. 51 (2010) 335-365.
[3] R. Boča, A Handbook of Magnetochemical Formulae, first ed., Elsevier, London, 2012, pp. 159-186.
[4] P. Gütlich, A. Hauser, H. Spiering, Angew. Chem.-Int. Ed. Engl. 33 (1994) 2024-2054.
[5] P. Gütlich, H.A. Goodwin, Spin Crossover in Transition Metal Compounds I 233 (2004) 1-47.
[6] J.A. Real, A.B. Gaspar, M.C. Muñoz, Dalton Trans. (2005) 2062-2079.
[7] A. Bousseksou, G. Molnár, J.A. Real, K. Tanaka, Coord. Chem. Rev. 251 (2007) 1822-1833.
[8] O. Sato, Proc. Jpn. Acad. Ser. B-Phys. Biol. Sci. 88 (2012) 213-225.
[9] M. Ruben, E. Breuning, J.M. Lehn, V. Ksenofontov, F. Renz, P. Gütlich, G.B.M. Vaughan, Chem.-Eur. J. 9 (2003) 4422-4429.
[10] A. Bousseksou, G. Molnár, P. Demont, J. Menegotto, J. Mater. Chem. 13 (2003) 2069-2071.
[11] P. Gütlich, Y. Garcia, H.A. Goodwin, Chem. Soc. Rev. 29 (2000) 419-427.
[12] C. Jay, F. Groliere, O. Kahn, J. Krober, Mol. Cryst. Liq. Cryst. Sci. Technol. Sect. A-Mol. Cryst. Liq. Cryst. 234 (1993) 255-262.
[13] O. Kahn, C.J. Martinez, Science 279 (1998) 44-48.
[14] A. Bousseksou, G. Molnár, L. Salmon, W. Nicolazzi, Chem. Soc. Rev. 40 (2011) 3313-3335.
[15] M.A. Halcrow, Chem. Soc. Rev. 40 (2011) 4119-4142.
[16] J. Tao, R.J. Wei, R.B. Huang, L.S. Zheng, Chem. Soc. Rev. 41 (2012) 703-737.
[17] D.J. Harding, D. Sertphon, P. Harding, K.S. Murray, B. Moubaraki, J.D. Cashion, H. Adams, Chem. Eur. J. (2013) DOI: 10.1002/chem.201202053.
[18] K. Bhar, S. Khan, J.S. Costa, J. Ribas, O. Roubeau, P. Mitra, B.K. Ghosh, Angew. Chem.-Int. Edit. 51 (2012) 2142-2145.
[19] G. Aromí, L.A. Barrios, O. Roubeau, P. Gamez, Coord. Chem. Rev. 255 (2011) 485-546.
[20] J. Olguin, S. Brooker, Coord. Chem. Rev. 255 (2011) 203-240.
[21] M. Boča, R.F. Jameson, W. Linert, Coord. Chem. Rev. 255 (2011) 290-317.
[22] K.S. Murray, European Journal of Inorganic Chemistry (2008) 3101-3121.
[23] M. Quesada, M. Monrabal, G. Aromí, V.A. de la Peña-O'Shea, M. Gich, E. Molins, O. Roubeau, S.J. Teat, E.J. MacLean, P. Gamez, J. Reedijk, J. Mater. Chem. 16 (2006) 2669-2676.
[24] J.S. Costa, K. Lappalainen, G. de Ruiter, M. Quesada, J.K. Tang, I. Mutikainen, U. Turpeinen, C.M. Grünert, P. Gütlich, H.Z. Lazar, J.F. Létard, P. Gamez, J. Reedijk, Inorg. Chem. 46 (2007) 4079-4089.
[25] S. Bonnet, M.A. Siegler, J.S. Costa, G. Molnár, A. Bousseksou, A.L. Spek, P. Gamez, J. Reedijk, Chem. Commun. (2008) 5619-5621.

[26] J.K. Tang, J.S. Costa, S. Smulders, G. Molnár, A. Bousseksou, S.J. Teat, Y.G. Li, G.A. van Albada, P. Gamez, J. Reedijk, Inorg. Chem. 48 (2009) 2128-2135.
[27] S. Bonnet, G. Molnár, J.S. Costa, M.A. Siegler, A.L. Spek, A. Bousseksou, W.T. Fu, P. Gamez, J. Reedijk, Chem. Mat. 21 (2009) 1123-1136.
[28] M. Quesada, V.A. de la Peña-O'Shea, G. Aromí, S. Geremia, C. Massera, O. Roubeau, P. Gamez, J. Reedijk, Adv. Mater. 19 (2007) 1397-1402.
[29] P. Gamez, P. de Hoog, M. Lutz, W.L. Driessen, A.L. Spek, J. Reedijk, Polyhedron 22 (2003) 205-210.
[30] M. Quesada, P. de Hoog, P. Gamez, O. Roubeau, G. Aromí, B. Donnadieu, C. Massera, M. Lutz, A.L. Spek, J. Reedijk, European Journal of Inorganic Chemistry (2006) 1353-1361.
[31] N. Wannarit, O. Roubeau, S. Youngme, P. Gamez, (2013) DOI: 10.1002/ejic.201201085.
[32] T.M. Ross, B. Moubaraki, S.M. Neville, S.R. Batten, K.S. Murray, Dalton Trans. 41 (2012) 1512-1523.
[33] T.M. Ross, B. Moubaraki, S.R. Batten, K.S. Murray, Dalton Trans. 41 (2012) 2571-2581.
[34] T.M. Ross, B. Moubaraki, K.S. Wallwork, S.R. Batten, K.S. Murray, Dalton Trans. 40 (2011) 10147-10155.
[35] T.M. Ross, B. Moubaraki, D.R. Turner, G.J. Halder, G. Chastanet, S.M. Neville, J.D. Cashion, J.F. Létard, S.R. Batten, K.S. Murray, Eur. J. Inorg. Chem. (2011) 1395-1417.
[36] S.M. Neville, B.A. Leita, D.A. Offermann, M.B. Duriska, B. Moubaraki, K.W. Chapman, G.J. Halder, K.S. Murray, Eur. J. Inorg. Chem. (2007) 1073-1085.
[37] P. de Hoog, P. Gamez, W.L. Driessen, J. Reedijk, Tetrahedron Lett. 43 (2002) 6783-6786.
[38] SAINT, version 6.02; SADABS, version 2.03 and SHELXTL. SAINT, SADABS and SHELXTL, Bruker AXS, Inc., Madison, WI , USA, 2002.
[39] A. Altomare, M.C. Burla, M. Camalli, G.L. Cascarano, C. Giacovazzo, A. Guagliardi, A.G.G. Moliterni, G. Polidori, R. Spagna, J. Appl. Crystallogr. 32 (1999) 115-119.
[40] G.M. Sheldrick, Acta Crystallogr. Sect. A 64 (2008) 112-122.
[41] M. Marchivie, P. Guionneau, J.F. Létard, D. Chasseau, Acta Crystallogr. Sect. B-Struct. Sci. 61 (2005) 25-28.
[42] J.K. McCusker, A.L. Rheingold, D.N. Hendrickson, Inorg. Chem. 35 (1996) 2100-2112.
[43] M. Quesada, F. Prins, E. Bill, H. Kooijman, P. Gamez, O. Roubeau, A.L. Spek, J.G. Haasnoot, J. Reedijk, Chem.-Eur. J. 14 (2008) 8486-8499.
[44] P. Guionneau, M. Marchivie, G. Bravic, J.F. Létard, D. Chasseau, Top. Curr. Chem. 234 (2004) 97-128.
[45] T.J. Mooibroek, P. Gamez, Crystengcomm 14 (2012) 1027-1030.
[46] T.J. Mooibroek, P. Gamez, Crystengcomm (2013) DOI:10.1039/C1032CE26853A.
[47] M. Sorai, S. Seki, J. Phys. Chem. Solids 35 (1974) 555-570.
[48] L. Capes, J.F. Létard, O. Kahn, Chem.-Eur. J. 6 (2000) 2246-2255.
[49] T. Buchen, H. Toftlund, P. Gütlich, Chem.-Eur. J. 2 (1996) 1129-1133.
[50] J.A. Real, I. Castro, A. Bousseksou, M. Verdaguer, R. Burriel, M. Castro, J. Linarès, F. Varret, Inorg. Chem. 36 (1997) 455-464.
[51] N. Moliner, M.C. Muñoz, S. Létard, J.F. Létard, X. Solans, R. Burriel, M. Castro, O. Kahn, J.A. Real, Inorg. Chim. Acta 291 (1999) 279-288.
[52] M. Sorai, Spin Crossover in Transition Metal Compounds Iii 235 (2004) 153-170.
[53] O. Roubeau, M. Castro, R. Burriel, J.G. Haasnoot, J. Reedijk, J. Phys. Chem. B 115 3003-3012.
[54] Note The phenomenological domain model proposed by Sorai, is widely used when accurate calorimetric data are available.[24] It is based on heterophase fluctuations and gives a measure of cooperativity through the number n of like-spin SCO centers per interacting domain, the larger the domains are, the more cooperative the transition is. See M. Sorai, *Chem. Rev.*, 1996, 1**106**, 1976-1031.

[55] A. Hauser, Spin Crossover in Transition Metal Compounds Ii 234 (2004) 155-198.
[56] J.F. Létard, J. Mater. Chem. 16 (2006) 2550-2559.
[57] A. Hauser, Spin Crossover in Transition Metal Compounds I 233 (2004) 49-58.
[58] A. Hauser, J. Chem. Phys. 94 (1991) 2741-2748.

Category 3: Drastic Effect of Lattice Propionitrile Molecules on the Spin-Transition Temperature of a 2,2′-Dipyridylamino/s-triazine-Based Iron(II) Complex

Introduction

The spin-crossover (SCO) phenomenon is a particular property of d^4–d^7 transition metal ions in which they may change their spin state from low spin (LS) to high spin (HS) and vice versa when appropriate donor atoms are coordinated to the metal centers, providing intermediate ligand-field strength.(1-3) This HS ↔ LS conversion may occur through the application of an external stimulus such as temperature, light, or pressure.(1, 4-6)

SCO was first observed in 1931 by Cambi and co-workers, who serendipitously discovered that the magnetic properties of iron(III) coordination compounds of the type [Fe(dithiocarbamate)$_3$] showed temperature-dependent reversibility of their magnetic moments, from $\mu_{eff} \approx 1.9\mu_B$ ($S = {}^1/_2$) at low temperatures to $\mu_{eff} \approx 5.9\mu_B$ ($S = 5/2$) at higher ones.(7) More than eight decades later, SCO represents an important research area of molecular magnetism, as illustrated by the continuously growing number of groups worldwide that are devoted to the design and investigation of new SCO materials.(8) The great potential of SCO compounds toward practical applications was recognized with 1D coordination polymers of the type $\{Fe^{II}$(4-R-1,2,4-triazole)$_3]X_2\}_n$ (for instance, with R = H or NH_2 and X = BF_4^- or NO_3^-), which show room-temperature spin transition associated with wide hysteresis loops.(9-12) Such materials have indeed been used to conceive a display device.(11, 13) Thus, the switching properties of these "bistable" molecules make them highly attractive because they may find a number of applications in molecular electronics.(11, 14-19) Most iron-based SCO compounds are iron(II) complexes with a [FeN_6] octahedral geometry that is typically formed by aromatic nitrogen donor groups, e.g., pyridine or azole rings.(20-25) For about 7 years, we have been developing a family of ligands based on 2,2′-dipyridylamine (dpa) unit(s) attached to a 1,3,5-triazine (or *s*-triazine) ring.(26) The first member of this family, namely, 2,4,6-tris(dipyridin-2-ylamino)-1,3,5-triazine (dpyatriz), was reported by some of us in 2003.(27) This ligand, containing three dpa groups on the *s*-triazine ring,(28) allowed for the preparation of iron(II) coordination compounds with attracting SCO properties.(26, 29, 30)Concurrently, Murray and co-workers have described a number of dipyridylamino-substituted-triazine ligands, which have engendered various SCO materials exhibiting diverse transition properties.(31-36) Recently, we have described the iron(II) complex *trans*-[Fe(**L1^F**)$_2$(NCS)$_2$]·2CH_3CN (**1^{NCS}·2MeCN**), with **L1^F** = 2-(*N*,*N*-bis(2-pyridyl)amino)-4,6-bis(pentafluorophenoxy)-(1,3,5)triazine, which exhibits a relatively cooperative SCO character.(37) In the present study, we report on the preparation and characterization of the comparable selenocyanate analogue complex [Fe(**L1^F**)$_2$(NCSe)$_2$]·2CH_3CH_2CN (**1^{NCSe}·2PrCN**), which shows solvent-dependent SCO properties.(38-41). These particular features are unraveled through thermal, magnetic, and variable-temperature structural studies, which are analyzed and compared with the properties of related compounds.

Results and Discussion

Synthesis and Crystal Structure of Compound $\mathbf{1}^{\mathbf{NCSe}}$

The ligand 2-(*N*,*N*-bis(2-pyridyl)amino)-4,6-bis(pentafluorophenoxy)-(1,3,5)triazine ($\mathbf{L1}^{\mathbf{F}}$) was prepared as described earlier for the preparation of $\mathbf{1}^{\mathbf{NCS}}\cdot\mathbf{2MeCN}$.(37) Compound $\mathbf{1}^{\mathbf{NCSe}}\cdot\mathbf{2PrCN}$, i.e., $[Fe(\mathbf{L1}^{\mathbf{F}})_2(NCSe)_2]\cdot 2CH_3CH_2CN$, was obtained with a yield of 60% by reaction of iron(II) perchlorate hexahydrate (1 equiv), potassium selenocyanate (1 equiv), and ligand $\mathbf{L1}^{\mathbf{F}}$ (2 equiv). $\mathbf{1}^{\mathbf{NCSe}}\cdot\mathbf{2PrCN}$ is triclinic, space group $P\bar{1}$, in the whole 100–300 K range (single-crystal data collections performed at 100, 200, 260, and 300 K). A representation of the molecular structure of $\mathbf{1}^{\mathbf{NCSe}}$ at 100 K (low-spin state) is depicted in Figure 1.

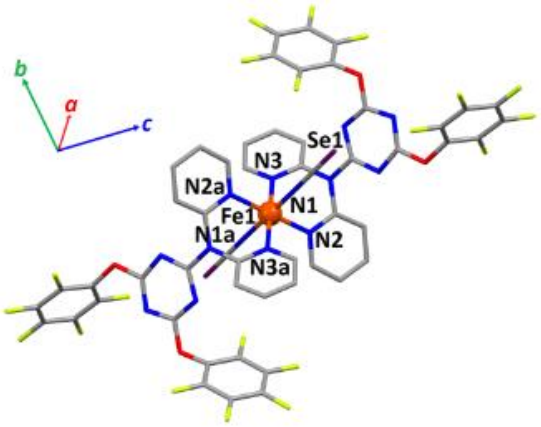

Fig. 1. Representation of the molecular structure of the iron(II) complex$\mathbf{1}^{\mathbf{NCSe}}\cdot\mathbf{2PrCN}$ (LS state, determined at 100 K) with partial atom-numbering scheme. Hydrogen atoms and lattice propionitrile molecules are not shown for clarity. Symmetry operation: $a = 1 - x, 1 - y, 1 - z$.

The coordination environment of the iron(II) ion in $\mathbf{1}^{\mathbf{NCSe}}$ is analogous to that of the previously reported compound $\mathbf{1}^{\mathbf{NCS}}$.(37) The octahedral geometry is formed by two $\mathbf{L1}^{\mathbf{F}}$ ligands in the equatorial plane and two *trans*, N-coordinated selenocyanate anions (Figure 1). The Fe–$N_{pyridine}$bond lengths of 1.981(1) (Fe–N2) and 1.979(1) Å (Fe–N3) are representative of an LS iron(II) ion (Table 1). Consistently, the Fe–N_{NCSe} distances of 1.930(1) Å are also indicative of an LS state. Actually, all Fe–N coordination distances observed in $\mathbf{1}^{\mathbf{NCSe}}$ are very similar to those of the related thiocyanate compound $\mathbf{1}^{\mathbf{NCS}}$ (measured at 100 K).(37) At 300 K, these bond lengths increase by ca. 0.17 Å (Fe–$N_{pyridine}$) and 0.11 Å (Fe–N_{NCSe}), hence illustrating the occurrence of a full (i.e., 100%) spin transition that is corroborated by variable-temperature magnetic susceptibility measurements. Such bond distance variations are typical for this type of SCO FeN_6 system.(42) Finally, the distances observed for $\mathbf{1}^{\mathbf{NCSe}}\cdot\mathbf{2PrCN}$ at 260 K, i.e., 2.007(4)–2.011(3) Å for Fe–$N_{pyridine}$ and 1.948(3) Å for Fe–N_{NCSe}, suggest the occurrence of a 1:7 HS/LS mixture, as estimated by properly weighing the bond length values found for the pure LS and HS states, shown in Table 1. In fact, the χT value of about 0.42 $cm^3\ mol^{-1}$ obtained at 260 K by bulk magnetic studies indicates the presence of ca. 15% HS centers, in fair agreement with the structural results.

The octahedral distortion parameters Σ and Φ estimate the magnitude of the deformation of the coordination geometry with respect to a perfect octahedron (for which the Σ and Φ values are 0).(43-45) Upon LS → HS transition, the coordination angles vary from 86.25(6) and 93.75(6)° to 82.85(13) and 97.15(13)°, respectively; as the angles move away from the ideal value of 90°, the increased distortion of the octahedron can be interpreted by the entropy-driven SCO

phenomenon.(46) Accordingly, for LS **1**$^{\mathbf{NCSe}}$, Σ = 31 and Φ = 25, and these values are increased for HS **1**$^{\mathbf{NCSe}}$ to 44 and 64, respectively. The ΔΣ ($\Sigma_{HS} - \Sigma_{LS}$) and ΔΦ ($\Phi_{HS} - \Phi_{LS}$) parameters characterize the extent of the structural changes induced by the spin transition. For**1**$^{\mathbf{NCSe}}$, ΔΣ and ΔΦ amount to 13 and 39, respectively; the rather high ΔΦ value is indicative of an alteration of the octahedral geometry when the iron(II) centers transit from the LS to the HS state. Such strong structural deformation may affect the mutual interaction, in the crystal, of the transition metal ions spins, hence potentially enhancing the cooperativity between the switching sites that would lead to an abrupt LS ↔ HS crossover event.(43) Because the ΔΦ value of the related thiocyanate compound **1**$^{\mathbf{NCS}}$**·2MeCN** is also high (namely, 36(37)), cooperative behavior may be expected as well for solid **1**$^{\mathbf{NCSe}}$**·2PrCN**.

The crystal packing of LS **1**$^{\mathbf{NCSe}}$**·2PrCN** reveals an intricate network of supramolecular interactions that strongly connect the iron(II) molecules. The metal complexes form a 1D supramolecular chain along the crystallographic *c* axis by means of parallel-displaced π···π interactions involving pentafluorophenoxy rings (Figure 2A). Actually, a very strong lone pair···π contact(47, 48) is observed between the oxygen atom O1 and a neighboring pentafluorophenoxy unit; for instance, the contact distance O1···C20g of 3.076(2) Å is significantly below the sum of the van der Waals radii of O and C (i.e., 3.22 Å). Moreover, the C15···C20g contact distance of 3.323(2) Å also reflects a strong arene···arene stacking interaction (the sum of the van der Waals radii of two C atoms is 3.40 Å). In fact, the $C_6F_5O\cdots C_6F_5O$ contacts are shorter in LS **1**$^{\mathbf{NCSe}}$**·2PrCN** compared to LS **1**$^{\mathbf{NCS}}$**·2MeCN** (for which the shortest O···C contact distance amounts to 3.112(2) Å(37)). Similar to that of**1**$^{\mathbf{NCS}}$**·2MeCN**, the iron(II) complexes are associated through nearly face-to-face π···π interactions between coordinated pyridine to generate another 1D chain that runs along the crystallographic *a* axis (Figure 2B). These supramolecular bonds are characterized by a centroid-to-centroid distance Cg4···Cg4p of 3.682(1) Å, which again is smaller than that of**1**$^{\mathbf{NCS}}$**·2MeCN** (3.757(1) Å(37)). Along the *a* direction, the 1D supramolecular chains are further stabilized via lone pair···π contacts involving the selenocyanate anions (Figure 3). Thus, the selenium atom Se1 interacts with an adjacent pentafluorophenoxy ring (Se1···Cg7 distance of 4.320(1) Å), with the shortest contact distances being Se1···C22b = 3.531(2) Å and Se1···C23b = 3.772(2) Å (Figure 3), which are close to the sum of the van der Waals radii of Se and C, namely, 3.60 Å. In addition, a very short close contact is observed between Se1 and F6b; indeed, the corresponding separation value of 3.192(1) Å is well below the sum of the van der Waals radii of Se and F, i.e., 3.37 Å. Se1 is also involved in an intramolecular lone pair···π interaction with a triazine ring (Se1···Cg5 = 3.585(1) Å; Figure 3).

Along the *c* direction, the formation of another type of 1D chain is observed, which is formed through double lone pair $(C_6F_5)\cdots\pi$(triazine) interactions (Figure 4), with centroid-to-fluorine distances Cg5···F1c and Cg5···F2c of 3.238(2) and 3.443(2) Å, respectively. These 1D chains are connected to the chains formed by the parallel-displaced $\pi_{C6F5O}\cdots\pi_{C6F5O}$interactions (see above and Figure 2A), in a parallel fashion. Furthermore, the chains interact with the lattice propionitrile molecules via lone pair···π contacts with pentafluorophenoxy rings (Figure 4). These noncovalent bonding interactions are characterized by distances of N1S···C21 = 3.202(3) Å and N1S···C26 = 3.278(3) Å (Figure 4 ; N1S···Cg7 = 3.413(2) Å), which are within the sum of the van der Waals radii of N and C, i.e., 3.25 Å.

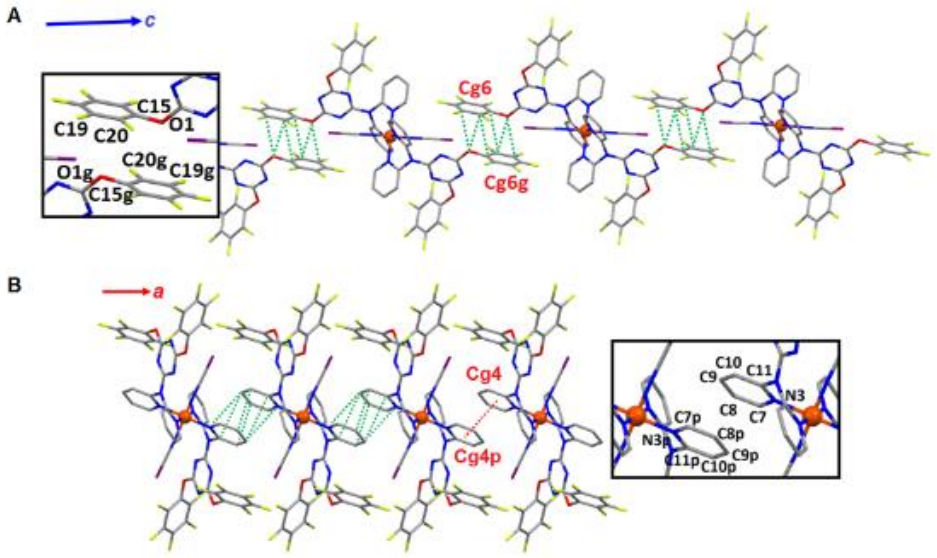

Fig. 2. Views of the crystal packing of LS **1**^{NCSe}**·2PrCN** showing (A) the formation of a supramolecular 1D chain along the crystallographic *c* axis by means of parallel-displaced π···π interactions between pentafluorophenoxy rings, with Cg6···Cg6g = 4.589(1) Å (the inset shows the labeling of the atoms involved in short supramolecular contacts (see Table 1), which are displayed as green dotted lines), and (B) the formation of a supramolecular 1D chain along the crystallographic *a* axis by means of π···π interactions between coordinated pyridine moieties, with Cg4···Cg4p = 3.682(1) Å (red dotted line) (the inset shows the labeling of the atoms involved in short supramolecular contacts (see Table 1), which are displayed as green dotted lines). Symmetry operations: *g*= 1 – *x*, 1 – *y*, 2 – *z*; *p* = 2 – *x*, 1 – *y*, 1 – *z*.

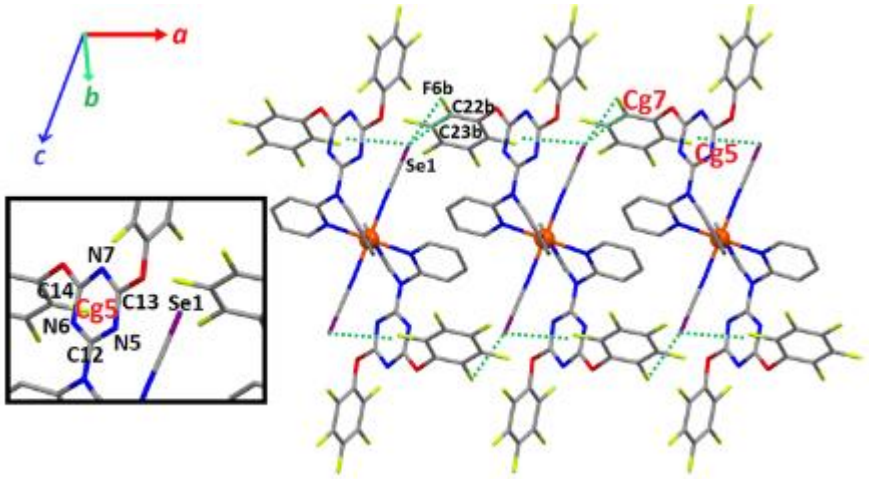

Fig. 3. View of the crystal packing of LS **1**^{NCSe}**·2PrCN** illustrating the occurrence of intermolecular lone pair···π interactions (green dotted lines) between the selenocyanate anions and adjacent pentafluorophenoxy moieties (Se1···C22b = 3.531(2) Å, Se1···C23b = 3.772(2) Å, and Se1···F6b = 3.192(1) Å) and intramolecular lone pair···π interactions between the selenocyanate anions and triazine rings (Se1···Cg5 = 3.585(1) Å). The inset shows the labeling of the atoms involved in lone pair···π interactions. Symmetry operation: *b* = −1 + *x*, *y*, *z*.

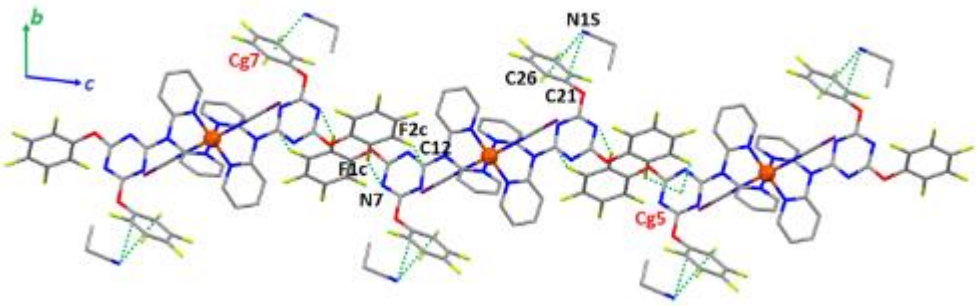

Fig.4. View of the crystal packing of LS **1**^{NCSe}**·2PrCN** showing the formation of a supramolecular 1D chain along the crystallographic *c* axis through double lone pair(C_6F_5)···π(triazine) interactions characterized by the short contact distances N7···F1c = 3.104(2) Å and C12···F2c = 3.014(2) Å. Symmetry operation:*c* = 2 – *x*, 1 – *y*, 2 – *z*.

The 2D supramolecular sheets in the *ac* plane are connected to each other by triple strong F···F bonds (*bc* plane; Figure 5); indeed, the contact distances F8···F9k and F8k···F9 of 2.780(2) Å and F4···F7e of 2.885(2) Å are all below the sum of the van der Waals radii of two F atoms, namely, 2.94 Å.(49) All of these supramolecular bonding interactions generate a 3D framework of tightly packed iron(II) complexes, indicating the likely cooperative character of the SCO, as indeed corroborated by magnetic and thermal studies (see below).

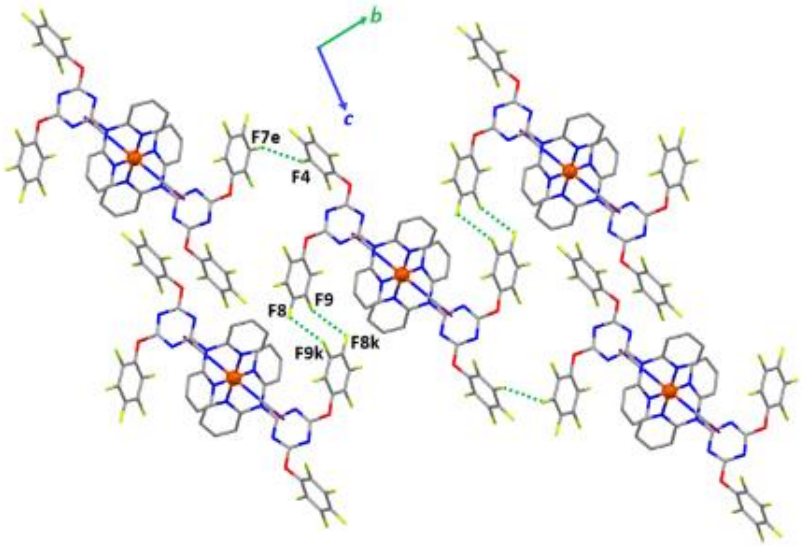

Fig. 5. View of the crystal packing of LS **1**^{NCSe}**·2PrCN** showing the formation of 2D sheets in the *bc* plane by means of strong F···F bonding contacts (green dotted lines; F8···F9k = 2.780(2) Å and F4···F7e = 2.885(2) Å). Symmetry operations: *e* = 2 – *x*, 2 – *y*, 2 – *z*; *k* = 2 – *x*, 2 – *y*, 1 – *z*.

Furthermore, the magnetic and thermal studies disclose an interesting behavior of **1**^{NCSe}**·2PrCN**upon aging or annealing. Indeed, a displacement of the transition temperature toward a lower value is observed upon progressive loss of lattice propionitrile molecules. To understand this phenomenon, we have attempted several crystallographic studies on single crystals of **1**^{NCSe}**·2PrCN**. First, measurements at temperatures above 300 K typically resulted in rapid crystal degradation, impeding the determination of the structure. Actually, **1**^{NCSe}**·2PrCN** also degrades within a few days, when left in air, at room temperature. Following the strategy adopted for the magnetic studies (see below), i.e., warming to 300 or 320

K for short periods of time and subsequent cooling to 100 K, we have collected seven single-crystal X-ray diffraction data sets of **1^{NCSe}·2PrCN** (. No changes are observed around the iron(II) ion or in the crystal lattice, where the propionitrile molecules are found. However, as manifested by a slight worsening of the agreement indices, these temperature-dependent studies have led to a progressive deterioration of the single crystal. Further thermal annealing above 320 K results in the complete loss of crystallinity; accordingly, the structural modifications associated with the elimination of propionitrile molecules from the crystal lattice could not be assessed by single-crystal diffraction studies.

Magnetic and Thermal Studies

Differential scanning calorimetry measurements on freshly prepared polycrystalline powders showed an endothermic/exothermic event upon warming/cooling, as expected for the SCO transition occurring in **1^{NCSe}·2PrCN**. However, upon repeating the measurements on powders left in contact with air, a second anomaly appeared at lower temperatures, whereas the original one was significantly lowered. After 1 week in contact with air, only this second anomaly at lower temperatures remained. In a similar manner, variable-temperature magnetic measurements showed a behavior highly dependent on the thermal history of the sample within the magnetometer. The first heating scan, performed up to 350 K, evidenced a complete thermal SCO centered at ca. 283 K, whereas the first cooling (to 5 K) and second heating (to 330 K) scans showed a conversion occurring in two similar steps centered at ca. 280 and 215 K. After this second warming scan, the conversion occurred again as a single step centered at ca. 217 K. No further variation of the behavior was then detected in further temperature scans. The similarity between the observations made with these two techniques points to a modification of**1^{NCSe}·2PrCN** occurring upon prolonged air exposure at RT or shorter periods of time at temperatures in the 330–350 K range in a He depression (the sample is subjected to vacuum at room temperature prior to insertion in the magnetometer sample space, so the modification seems to require slightly higher temperatures than 300 K), in agreement with the rapid loss of crystallinity of single crystals observed above 320 K. The two-step magnetic transition (evidenced also by the two DSC anomalies) corresponds to a situation in which two distinct phases are present in the material, i.e., with partial modification of pristine **1^{NCSe}·2PrCN**. Thermogravimetric measurements were thus carried out to ascertain a possible loss of the lattice propionitrile molecules. The data shows a 6.6% weight loss centered at 382 K, with an onset at around 330 K. These data agree perfectly with the loss of all propionitrile molecules from the crystal lattice (theoretical value, 6.86%). Under the dynamic conditions used here, the loss of propionitrile is completed at ca. 390 K, slightly above its conventional boiling temperature at ambient pressure. Clearly, upon moderate heating, **1^{NCSe}·2PrCN** tends to lose its lattice propionitrile, which, in the solid state, is only weekly bound by van der Waals interactions. Powder diffraction methods reveal that the resulting material is polycrystalline, with an infrared spectrum almost identical to that of **1^{NCSe}·2PrCN**; notably, the $NCSe^-$ vibrations at 2055 and 2098 cm^{-1} slightly broaden, the former being shifted by ca. 6 cm^{-1} toward lower wavenumbers. Not unexpectedly, the modified phase can thus be ascribed to desolvated **1^{NCSe}**.

The temperature dependence of the χT product of **1^{NCSe}·2PrCN** and **1^{NCSe}**, obtained reproducibly by thermal annealing of fresh **1^{NCSe}·2PrCN** for 2 h at 80 °C, is depicted in Figure 6, evidencing LS ↔ HS transitions centered on 283 and 220 K for **1^{NCSe}·2PrCN** and **1^{NCSe}**, respectively. The conversions are complete, with χT increasing from ca. 0.02–0.04 $cm^3\ mol^{-1}$ K below 220 K and above 120 K, respectively, a typical value for an Fe(II) ion in a LS $S = 0$ state, to ca. 2.97 $cm^3\ mol^{-1}$ K at 350 K and ca. 3.04–3.08 $cm^3\ mol^{-1}$ K above 300 K, respectively; both values are indicative of a mostly HS $S = 2$ state.

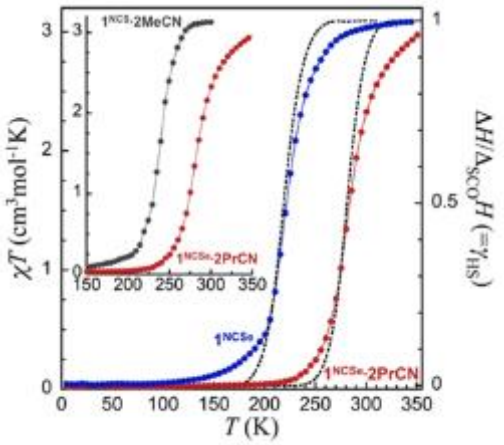

Fig. 6. χT vs T plot for **1^{NCSe}·2PrCN** (red dots) and **1^{NCSe}** (blue dots) depicting their full SCO process and corresponding temperature dependence of their excess enthalpies normalized to that involved in the process of SCO (black dashed lines). Note that the latter is equivalent to the temperature dependence of the HS fraction $\gamma_{HS}(T)$. The inset χT vs T plot compares the SCO of **1^{NCSe}·2PrCN** with that of the analogue compound **1^{NCS}·2MeCN** (gray dots). Full lines are guides to the eye.

The SCO curves of both materials are indeed very similar in shape, with that of **1^{NCSe}** simply being shifted to lower temperatures by ca. 63 K. The value of ΔT_{80}, the temperature range over which 80% of the LS ↔ HS conversion takes place, is indeed the same at about 65 K, slightly higher than that observed for **1^{NCS}·2MeCN**, namely, $\Delta T_{80} \approx 50$ K (see inset of Figure 6).(37)This less efficient cooperative character shown by **1^{NCSe}·2PrCN** (compared to that of**1^{NCS}·2MeCN**) might be interpreted by two concurrent effects: the presence of bulkier propionitrile molecules, compared to acetonitrile, and that of the more diffuse Se atom, resulting in weaker supramolecular interactions (with respect to those involving an S atom) and molecules and Fe(II) ions being kept (on average) further apart than when S atoms are present. This latter contribution seems to be particularly relevant, as the desolvated **1^{NCSe}** material has a similar (larger) ΔT_{80} (of ca. 70 K).

The temperature dependence of the molar heat capacity of **1^{NCSe}·2PrCN** and **1^{NCSe}** exhibit a marked anomaly, in the 240–320 and 180–260 K ranges, respectively, and culminating at 280 and 218 K (Figure 7, top). These features are in perfect agreement with the magnetic data and are thus due to the SCO process in **1^{NCSe}·2PrCN** and **1^{NCSe}**. The corresponding excess heat capacities allow the associated excess enthalpy and entropy to be determined as 9.71 kJ mol^{-1}and 34.6 J mol^{-1} K^{-1}, respectively, for **1^{NCSe}·2PrCN** and 8.27 kJ mol^{-1} and 37.9 J mol^{-1} K^{-1} for**1^{NCSe}**. Normalizing $\Delta H(T)$ to the corresponding ΔH_{SCO} also provides the temperature variation of the HS fraction, $\gamma_{HS}(T)$, depicted as dashed lines in Figure 6, which is again in excellent agreement with the magnetic data. To provide a comparable estimation of the cooperative character of the SCO in **1^{NCSe}·2PrCN** and **1^{NCSe}**, their excess heat capacities were fitted to Sorai's domain model,(50) often used in SCO systems, cooperative or not, for which accurate calorimetric data are available.(51-54) The model gives a measure of the cooperativity through the number, *n*, of like-spin SCO centers per interacting domain. Here, the derived best fits (red lines in Figure 7, bottom) provide moderate numbers of interacting molecules per domain at n = 8.1 and 5.2 for **1^{NCSe}·2PrCN** and **1^{NCSe}**, respectively. These values are in the same range as that of the **1^{NCS}·2MeCN** analogue (n = 6.2) and indicate a similar cooperative character of the SCO in these materials, significantly inferior to the value of 14.2 we recently reported for the

related $[Fe(\mathbf{L1})_2(NCS)_2]\cdot 2CH_3OH$ (**L1** = 2-chloro-4-(*N*,*N*-(2-pyridyl)amino)-6-(pentafluorophenoxy)-(1,3,5)triazine).(42) Although it gives rise to a decrease in the SCO temperature by nearly 60 K, the loss of the lattice propionitrile molecule does not seem to affect significantly the way the electronic transition couples to the lattice phonons, the major component of the SCO cooperativeness.

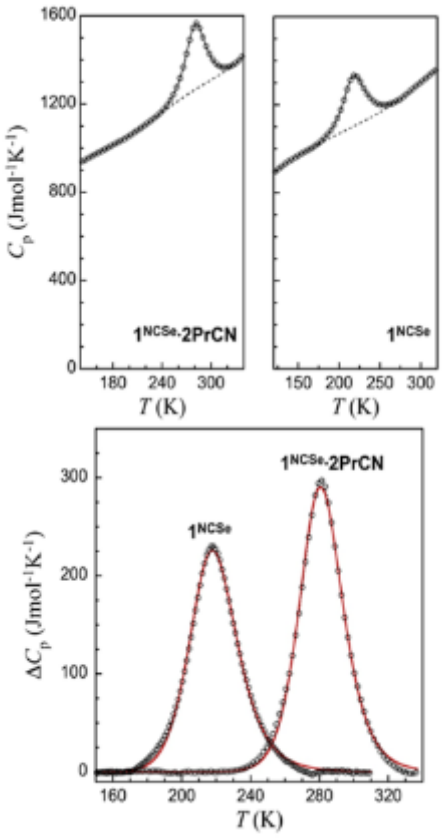

Fig. 7. (Top) Molar heat capacities of 1NCSe·2PrCN and 1NCSe showing a significant endothermic anomaly arising from the process of SCO. The dashed lines are the respective estimated lattice components. (Bottom) Excess molar heat capacities associated with the SCO of 1NCSe·2PrCN and 1NCSe. The full red lines are fits to Sorai's domain model (see text and ref 50), with n = 8.1 and TSCO = 281.7 K and n = 5.2 and TSCO = 219.4 K for 1NCSe·2PrCN and 1NCSe, respectively.

X-ray Powder Diffraction Studies

As mentioned above, the temperature effect on the solid-state structure of $\mathbf{1^{NCSe}\cdot 2PrCN}$ (with possible structural changes) could not be investigated by single-crystal X-ray diffraction as a result of the degradation of the material when $T > 320$ K. Therefore, X-ray powder-diffraction studies were carried out to explore potential temperature-dependent structural changes in $\mathbf{1^{NCSe}\cdot 2PrCN}$. Powder diffraction data, collected in the 300–370 K range (shown in Figure 8) and analyzed by the structureless Le Bail whole pattern profile method, allowed the relative changes of the lattice parameters to be retrieved (cell volume and the size and shape of the thermal strain tensor). These results are numerically reported in Table 1 and are graphically depicted in Figure 9. The shape and orientation of the thermal strain tensor, elongated in the $[1\bar{1}0]$ direction, was then compared with the known crystal structure, which evidenced the presence of

weakly bound slabs parallel to the $(1\bar{1}0)$ plane and is thus prone to more significant thermally induced dilatation.

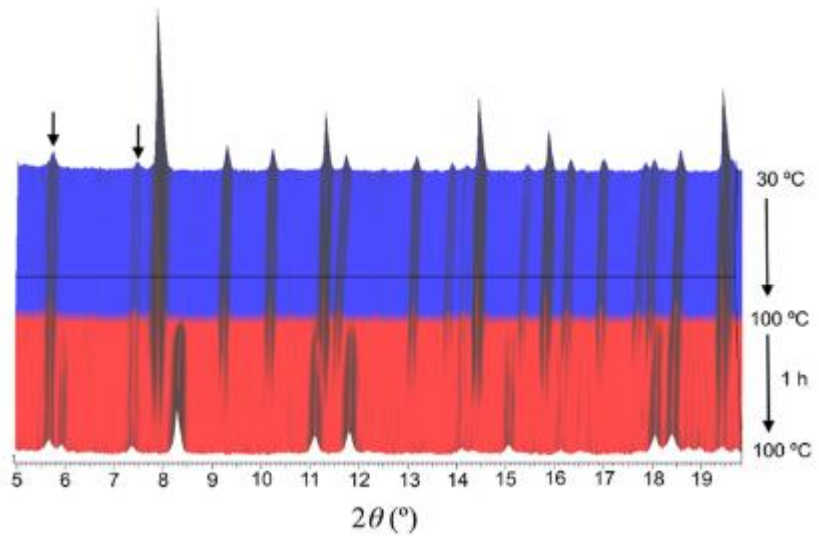

Fig. 8. Variable-temperature X-ray powder diffraction data, collected between 30 and 100 °C. Vertical axis (back to front: temperature increase). The blue portion refers to the pristine **1^{NCSe}·2PrCN** species, transforming into the (still triclinic and contracted, see text) unsolvated phase (the two weak low-angle peaks at 5.6 and 7.3°, highlighted by the black arrows, belong to an unknown contaminant generated by partial degradation). The red portion contains 12 XRPD traces collected under isothermal conditions (in air) at 100 °C (5 min each).

Table 1. Linear and Volumetric Thermal Expansion Coefficients of 1^{NCSe}·2PrCNin the Form of $\partial \ln x/\partial T$ (x = a, b, c, α, β, γ and V)[a]

$\partial \ln a/\partial T$	$\partial \ln b/\partial T$	$\partial \ln c/\partial T$	$\partial \ln \alpha/\partial T$	$\partial \ln \beta/\partial T$	$\partial \ln \gamma/\partial T$	$\partial \ln V/\partial T$
+160	+74	+78	+9	–18	+78	+227

[a] Units in M K^{-1}. Values were computed by fitting the TXRPD-derived data in the 30–95°C range, where a nearly linear trend was observed.

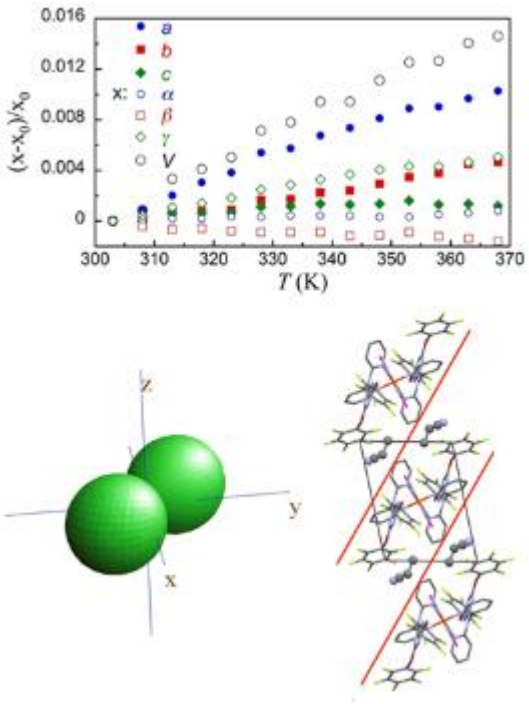

Fig. 9. (Top) Relative lattice parameter changes (including cell volume), measured by TXRPD data. Horizontal axis, temperature (T, K); vertical axis, $(x_T - x_{30})/x_{30}$ (x = a,b, c, α, β, γ, and V). (Bottom left) Thermal strain tensor for the 30–95 °C range, computed by Ohashi's method(63) and drawn with Wintensor.(64) (Bottom right) Crystal packing of **1**$^{\mathbf{NCSe}}$**·2PrCN** viewed approximately down [110], highlighting the $(1\bar{1}0)$ plane, separating slabs of weakly bound molecules, which conform to the longest axis of the thermal strain tensor shown on the left.

Prolonged heating at 370 K showed a progressive change of the diffraction trace, which was completed after ca. 1 h. After eliminating a few peaks (attributed to an unknown contaminant), a reliable unit cell for the HT phase was obtained (using TOPAS-R):(55) a = 8.87, b = 11.21, c = 15.40 Å, α = 102.3, β = 84.3, and γ = 103.4°, V = 1454 Å^3; GOF(20) = 21.(56) The crystal symmetry and the lattice parameters herein proposed match those found for the pristine solvated phase (V = 1557 Å^3 at 300 K). The difference in the molar volume (ΔV = −103 Å^3) is well-matched with that expected for the loss of two PrCN molecules (64 Å^3, as estimated by SMILE(57)). After cooling to room temperature, diffraction data were collected with an overnight measurement. Unfortunately, the powder pattern, due to partial degradation, contained too many peaks, making the crystal structure determination of the desolvated phase impossible.

The loss of the lattice propionitrile molecules will irremediably affect the solid-state packing of the iron(II) complexes. Actually, the propionitrile molecules connect the [Fe(**L1**$^{\mathbf{F}}$)$_2$(NCSe)$_2$] complexes, through lone pair···π interactions (Figure 10), generating a 1D supramolecular chain, and are therefore involved in the observed SCO properties of **1**$^{\mathbf{NCSe}}$**·2PrCN**. Consequently, their removal will have an effect on the magnetic properties of the material. In fact, the spin-transition properties of the propionitrile-free compound **1**$^{\mathbf{NCSe}}$ are modified compared to those of **1**$^{\mathbf{NCSe}}$**·2PrCN** (see above), as reflected by the lower $T_{1/2}$ (220 K instead of 283 K) and slightly lower cooperativity ($n/\Delta T_{80}$ value of ca. 5.2/70 K instead of 8.1/65 K).

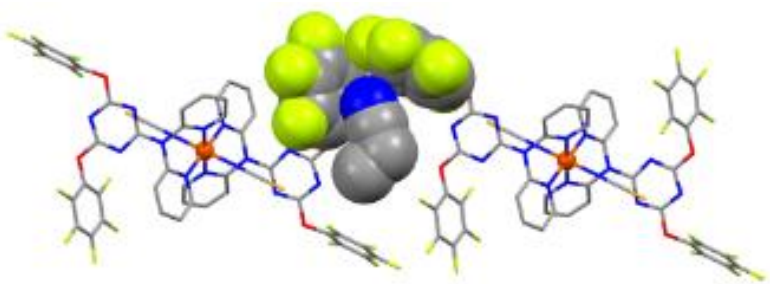

Fig. 10. View of the solid-state structure of **1**^{NCSe}**·2PrCN** showing the interaction of a propionitrile molecule with two pentafluorophenyl rings (in space-filling mode) belonging to two neighboring iron(II) complexes, through lone pair···π interactions.

In summary, for about 8 years, our group and that of Murray(31) have been investigating the SCO properties of a particular family of iron(II) systems obtained from 2,2′-dipyridylamino-substituted triazine ligands. Through ligand design, it has been possible to obtain members of this group of SCO complexes with interesting properties.(42) In the present study, a new compound belonging to this family was prepared that exhibits solvent-dependent SCO properties. Indeed, the loss of propionitrile molecules present in the crystal lattice of **1**^{NCSe}**·2PrCN** results in a strong alteration of its SCO behavior, which is reflected by an important shift of the transition temperature, from$T_{1/2}$ = 283 K to 220 K (for the desolvated compound **1**^{NCSe}). This variation of the magnetic properties is most likely due to a modification of the crystal packing of the transiting molecules, hence exemplifying the great sensitivity of the SCO phenomenon. In addition, the results reported herein illustrate the potential of (2,2′-dipyridylamine/triazine)-based iron(II) complexes to generate SCO materials with singular properties.

References

1. Gütlich, P.; Goodwin, H. A. *Top. Curr. Chem.* **2004**, 233, 1– 47
2. *Spin-Crossover Materials: Properties and Applications*; Halcrow, M. A., Ed.; John Wiley and Sons:Chichester, UK, **2013**.
3. Boča, R. *A Handbook of Magnetochemical Formulae*; Elsevier: London, **2012**; pp 159– 186.
4. Real, J. A.; Gaspar, A. B.; Munoz, M. C. *Dalton Trans.* **2005**, 2062– 2079
5. Bousseksou, A.; Molnár, G.; Real, J. A.; Tanaka, K. *Coord. Chem. Rev.* **2007**, 251, 1822– 1833
6. Gütlich, P.; Hauser, A.; Spiering, H. *Angew. Chem., Int. Ed. Engl.* **1994**, 33, 2024– 2054
7. Cambi, L.; Szego, L. *Ber. Dtsch. Chem. Ges.* **1931**, 64, 2591– 2598
8. Cluster Issue: Spin-Crossover Complexes *Eur. J. Inorg. Chem.* **2013**, 573– 1070.
9. Krober, J.; Codjovi, E.; Kahn, O.; Grolière, F.; Jay, C. *J. Am. Chem. Soc.* **1993**, 115, 9810– 9811
10. Cantin, C.; Daubric, H.; Kliava, J.; Servant, Y.; Sommier, L.; Kahn, O. *J. Phys.: Condens. Matter* **1998**, 10,7057– 7064
11. Kahn, O.; Martinez, C. J. *Science* **1998**, 279, 44– 48
12. Roubeau, O. *Chem.—Eur. J.* **2012**, 18, 15230– 15244
13. Létard, J. F.; Guionneau, P.; Goux-Capes, L. *Top. Curr. Chem.* **2004**, 235, 221– 249
14. Gaspar, A. B.; Seredyuk, M.; Gütlich, P. *Coord. Chem. Rev.* **2009**, 253, 2399– 2413
15. Gamez, P.; Costa, J. S.; Quesada, M.; Aromí, G. *Dalton Trans.* **2009**, 7845– 7853

16. Bousseksou, A.; Molnár, G.; Salmon, L.; Nicolazzi, W. *Chem. Soc. Rev.* **2011**, 40, 3313– 3335
17. Gütlich, P.; Garcia, Y.; Goodwin, H. A. *Chem. Soc. Rev.* **2000**, 29, 419– 427
18. Sato, O. *Proc. Jpn. Acad., Ser. B* **2012**, 88, 213– 225
19. Ruben, M.; Breuning, E.; Lehn, J. M.; Ksenofontov, V.; Renz, F.; Gütlich, P.; Vaughan, G. B. M. *Chem.—Eur. J.* **2003**, 9, 4422– 4429
20. Aromí, G.; Barrios, L. A.; Roubeau, O.; Gamez, P. *Coord. Chem. Rev.* **2011**, 255, 485– 546
21. Olguin, J.; Brooker, S. *Coord. Chem. Rev.* **2011**, 255, 203– 240
22. Boča, M.; Jameson, R. F.; Linert, W. *Coord. Chem. Rev.* **2011**, 255, 290– 317
23. Murray, K. S. *Eur. J. Inorg. Chem.* **2008**, 3101– 3121
24. Halcrow, M. A. *Coord. Chem. Rev.* **2009**, 253, 2493– 2514
25. Kitchen, J. A.; Brooker, S. *Coord. Chem. Rev.* **2008**, 252, 2072– 2092
26. Quesada, M.; de la Peña-O'Shea, V. A.; Aromí, G.; Geremia, S.; Massera, C.; Roubeau, O.; Gamez, P.;Reedijk, J. *Adv. Mater.* **2007**, 19, 1397– 1402
27. Gamez, P.; de Hoog, P.; Lutz, M.; Driessen, W. L.; Spek, A. L.; Reedijk, J. *Polyhedron* **2003**, 22, 205–210
28. Gamez, P.; de Hoog, P.; Lutz, M.; Spek, A. L.; Reedijk, J. *Inorg. Chim. Acta* **2003**, 351, 319–325
29. Quesada, M.; Monrabal, M.; Aromí, G.; de la Peña-O'Shea, V. A.; Gich, M.; Molins, E.; Roubeau, O.; Teat,S. J.; MacLean, E. J.; Gamez, P.; Reedijk, J. *J. Mater. Chem.* **2006**, 16, 2669– 2676
30. Quesada, M.; de Hoog, P.; Gamez, P.; Roubeau, O.; Aromí, G.; Donnadieu, B.; Massera, C.; Lutz, M.;Spek, A. L.; Reedijk, J. *Eur. J. Inorg. Chem.* **2006**, 1353– 1361
31. Scott, H. S.; Ross, T. M.; Chilton, N. F.; Gass, I. A.; Moubaraki, B.; Chastanet, G.; Paradis, N.; Létard, J. F.; Vignesh, K. R.; Rajaraman, G.; Battena, S. R.; Murray, K. S. *Dalton Trans.* **2013**, 42, 16494–16509
32. Scott, H. S.; Ross, T. M.; Batten, S. R.; Gass, I. A.; Moubaraki, B.; Neville, S. M.; Murray, K. S. *Aust. J. Chem.* **2012**, 65, 874– 882
33. Ross, T. M.; Moubaraki, B.; Batten, S. R.; Murray, K. S. *Dalton Trans.* **2012**, 41, 2571– 2581
34. Ross, T. M.; Moubaraki, B.; Neville, S. M.; Batten, S. R.; Murray, K. S. *Dalton Trans.* **2012**, 41, 1512–1523
35. Ross, T. M.; Moubaraki, B.; Turner, D. R.; Halder, G. J.; Chastanet, G.; Neville, S. M.; Cashion, J. D.;Létard, J. F.; Batten, S. R.; Murray, K. S. *Eur. J. Inorg. Chem.* **2011**, 1395– 1417
36. Neville, S. M.; Leita, B. A.; Offermann, D. A.; Duriska, M. B.; Moubaraki, B.; Chapman, K. W.; Halder, G. J.; Murray, K. S. *Eur. J. Inorg. Chem.* **2007**, 1073– 1085
37. Wannarit, N.; Roubeau, O.; Youngme, S.; Teat, S. J.; Gamez, P. *Dalton Trans.* **2013**, 42, 7120–7130
38. Gomez, V.; Benet-Buchholz, J.; Martin, E.; Galán-Mascarós, J. R. *Chem.—Eur. J.* **2014**, 20, 5369–5379
39. Costa, J. S.; Rodriguez-Jimenez, S.; Craig, G. A.; Barth, B.; Beavers, C. M.; Teat, S. J.; Aromí, G. *J. Am. Chem. Soc.* **2014**, 136, 3869– 3874

40. Wei, R. J.; Tao, J.; Huang, R. B.; Zheng, L. S. *Inorg. Chem.* **2011**, 50, 8553– 8564
41. Amoore, J. L. M.; Kepert, C. J.; Cashion, J. D.; Moubaraki, B.; Neville, S. M.; Murray, K. S. *Chem.—Eur. J.***2006**, 12, 8220– 8227
42. Nassirinia, N.; Amani, S.; Teat, S. J.; Roubeau, O.; Gamez, P. *Chem. Commun.* **2014**, 50, 1003–1005
43. Halcrow, M. A. *Chem. Soc. Rev.* **2011**, 40, 4119– 4142
44. Marchivie, M.; Guionneau, P.; Létard, J. F.; Chasseau, D. *Acta Crystallogr., Sect. B: Struct. Sci.* **2005**, 61,25– 28
45. McCusker, J. K.; Rheingold, A. L.; Hendrickson, D. N. *Inorg. Chem.* **1996**, 35, 2100– 2112
46. König, E. *Struct. Bonding (Berlin, Ger.)* **1991**, 76, 51– 152
47. Mooibroek, T. J.; Gamez, P. *CrystEngComm* **2012**, 14, 1027– 1030
48. Mooibroek, T. J.; Gamez, P. *CrystEngComm* **2012**, 14, 3902– 3906
49. Mooibroek, T. J.; Gamez, P. *CrystEngComm* **2013**, 15, 1802– 1805
50. Sorai, M.; Nakazawa, Y.; Nakano, M.; Miyazaki, Y. *Chem. Rev.* **2013**, 113, PR41– 122
51. Nakamoto, T.; Tan, Z. C.; Sorai, M. *Inorg. Chem.* **2001**, 40, 3805– 3809
52. Roubeau, O.; deVos, M.; Stassen, A. F.; Burriel, R.; Haasnoot, J. G.; Reedijk, J. *J. Phys. Chem. Solids***2003**, 64, 1003– 1013
53. Arcis-Castillo, Z.; Zheng, S.; Siegler, M. A.; Roubeau, O.; Bedoui, S.; Bonnet, S. *Chem.—Eur. J.* **2011**, 17,14826– 14836
54. Roubeau, O.; Castro, M.; Burriel, R.; Haasnoot, J. G.; Reedijk, J. *J. Phys. Chem. B* **2011**, 115, 3003–3012
55. TOPAS, 3.0; Bruker AXS: Karlsruhe, Germany, **2005**.
56. de Wolff, P. M. *J. Appl. Crystallogr.* **1968**, 1, 108– 113
57. Eufri, D.; Sironi, A. *J. Mol. Graphics* **1989**, 7, 165– 169
58. SAINT, SADABS, and SHELXTL; Bruker AXS Inc.: Madison, WI.
59. Altomare, A.; Burla, M. C.; Camalli, M.; Cascarano, G. L.; Giacovazzo, C.; Guagliardi, A.; Moliterni, A. G. G.; Polidori, G.; Spagna, R. *J. Appl. Crystallogr.* **1999**, 32, 115– 119
60. Burla, M. C.; Camalli, M.; Carrozzini, B.; Cascarano, G. L.; Giacovazzo, C.; Polidori, G.; Spagna, R. *Acta Crystallogr., Sect. A* **1999**, 55, 991– 999
61. Sheldrick, G. M. *Acta Crystallogr., Sect. A* **2008**, 64, 112– 122
62. Le Bail, A.; Duroy, H.; Fourquet, J. L. *Mater. Res. Bull.* **1988**, 23, 447– 452
63. Ohashi, Y. In *Comparative Crystal Chemistry*; Hazen, R. M.; Finger, L. W., Eds.; Wiley: New York, **1982**; pp 92– 102.
64. Kaminsli, W. WINTENSOR, V.1.4; University of Washington: Seattle, WA, **2011**.
65. Guionneau, P.; Marchivie, M.; Bravic, G.; Létard, J. F.; Chasseau, D. *Top. Curr. Chem.* **2004**, 234, 97–128
66. Quesada, M.; Prins, F.; Bill, E.; Kooijman, H.; Gamez, P.; Roubeau, O.; Spek, A. L.; Haasnoot, J. G.;Reedijk, J. *Chem.—Eur. J.* **2008**, 14, 8486– 8499

II-2: Crystal structures, magnetic properties and theoretical studies of triply-bridged dinuclear copper(II) compounds

Introduction

The magnetochemistry of Cu(II) systems have received much attention because of their interesting structural and magnetic properties, as well as their application as molecular based materials [1,,3]. In these materials, the Cu(II) ions exhibit a d^9 electronic configuration and, hence, can be considered as suitable candidates representative of basic models of magnetic coordination compounds, especially in di- and polynuclear Cu(II) systems [4,5]. A deep understanding of magneto-structural correlations is highly desirable to be able to predict the magnitude of the coupling constant, its character and the corresponding physical mechanism, thus allowing one to design and synthesize new molecular based materials with improved magnetic properties. Hence, magneto-structural correlations for a series of compounds with different structural and magnetic properties are usually derived either from experimental measurements or theoretical calculations. Clearly, compounds with strong ferromagnetic coupling are of great interest for potential technological applications [4-5,,,,,,12].

Among the different Cu(II) families with ferromagnetic properties, previous work has focused on the design, magnetic properties and magneto-structural correlations of the hetero triply-bridged dinuclear Cu(II) systems because this particular type of compounds exhibit moderate to strong ferromagnetic interactions [6,7,8,9,10]. In this type of systems, the magnetic interaction occurs via bridging ligands, although various pathways are possible [10], which depend on the coordination geometry of the Cu(II) ion, the Cu···Cu separation, the bond angles involving the bridging atoms, the dihedral angle between the planes containing the Cu(II) ions and the distance from the Cu(II) to the bridging ligands. Structurally, the Cu(II) ions are in a five-fold coordination which, however, corresponds to a rather broad range of geometries, from regular trigonal bipyramidal (TBP) to regular square-based pyramidal (SP). In a previous work [10], the possible topological arrangements of the dinuclear unit have been organized in six different classes: Class **A** corresponds to co-planar bases with a square pyramidal geometry for both Cu(II) environments and the two bridges (aquo or hydroxo) lying in the equatorial positions; Class **B** contains compounds with non-coplanar bases with a square pyramidal geometry for both Cu(II) ions with carboxylato and hydroxo bridges in the equatorial positions; Class **C** includes compounds with non-coplanar bases with a square pyramidal geometry for both Cu(II) ions and two carboxylato bridges lying in the equatorial positions; Class **D** stands for non-coplanar bases with a square pyramidal geometry for both Cu(II) ions, one single-atom or triatomic bridge in an equatorial-equatorial configuration and two carboxylato bridges in an axial-equatorial configuration; Class **E** stands for non-coplanar bases with a trigonal bipyramidal geometry for both Cu(II) ions and one hydroxo bridge in an axial-axial configuration; and, finally, Class **F** refers to non-coplanar bases with square pyramidal and trigonal bipyramidal geometries, two bridges occupying the axial-equatorial positions, with the third one in an equatorial-equatorial configuration. The knowledge of these topologies is useful to unravel the relationships between structural features and the value of the intramolecular magnetic exchange interaction in the triply-bridged dinuclear unit.

In previous studies, the magneto-structural correlations have been investigated for some of these compounds by the simple Extended Hückel (EH) method and a linear correlation has been found for class **B** compounds allowing a first step towards a proper understanding [10]. However, to obtain more quantitative relationships it is necessary to go beyond the semi-empirical EH method and to make use of more reliable electronic structure methods as demonstrated by

recent studies on other triply bridged dinuclear Cu(II) compounds which employed state of art density functional theory (DFT) based methods [11,12]. Six different exchange-correlation functionals have been used in order to fully understand the magneto-structural correlation and also to accurately predict the broad range of magnetic coupling constant (*J*) values exhibited by class **B** and class **F** compounds with ferro- and antiferromagnetic behavior, respectively. The DFT calculations have revealed that, for ferromagnetic class **B** compounds, the calculated *J* values almost quantitatively correlate with the sum of Addison's τ parameter [13] of each Cu(II) ion. The calculated and experimental *J* values of all compounds are in agreement [12], especially for the long-range separated hybrid LC-ωPBE method [14]. In particular, the DFT calculations properly reproduce the magnitude of the magnetic coupling constants in the whole range of topologies studied. However, the calculated *J* values of class **B** compounds exhibit a rather large dependence with the type of hybrid exchange-correlation functional and may even show noticeable deviations from the experimental values, especially in the ferromagnetic compounds. Therefore, the precise interpretation of the magnetic interactions in class **B** compounds with ferromagnetic interactions still require further attention and either accurate wave function based calculations or a more systematic study aimed precisely to better understand the performance of current DFT approaches in describing this type of systems is needed. There is little doubt that wave function based calculations using for instance the Difference Dedicated Configuration Interaction (DDCI) method will properly describe these systems as highlighted in the review paper by Moreira and Illas [15] although it is also clear that without a modeling of the external ligands, these calculations are likely to be computationally unfeasible. Therefore, in the present work we focus on the second possibility and, to this end, we extend the investigation of the magneto-structural correlations and accurate prediction of intramolecular magnetic interaction of this series of compounds by adding seven newly synthesized compounds of class **B** and analyzing simultaneously the effect of the type of DFT method and of the basis set used to represent the electron density. We will show that the current exchange-correlation functionals, which properly describe magnetostructural correlations involving antiferromagnetic interactions, face difficulties in properly reproducing the *J* values and trends along the series of ferromagnetic compounds which, therefore, constitute a challenge for state of the art exchange-correlation functionals.

Experimental

The new compounds can be generally described as members of the $[Cu_2(L)_2(\mu\text{-}OH)(\mu\text{-}OH_2)(\mu\text{-}O_2CR)]X_2$ series where L = bpy = 2,2′-bipyridine, 4,4′-dmbpy = 4,4′-dimethyl-2,2′-bipyridine and 5,5′-dmbpy = 5,5′-dimethyl-2,2′-bipyridine; R = H for formate, CH_3 for acetate, CH_2CH_3 for propionate and $C(CH_3)_3$ for trimethylacetate and X = $CF_3SO_3^-$ and ClO_4^-. In particular, the following compounds are considered: $[Cu_2(bpy)_2(\mu\text{-}OH)(\mu\text{-}OH_2)(\mu\text{-}O_2CCH_3)](CF_3SO_3)_2$ (**1**), $[Cu_2(4,4'\text{-}dmbpy)_2(\mu\text{-}OH)(\mu\text{-}OH_2)(\mu\text{-}O_2CH)]\text{-}(ClO_4)_2$ (**2**), $[Cu_2(4,4'\text{-}dmbpy)_2(\mu\text{-}OH)(\mu\text{-}OH_2)(\mu\text{-}O_2CCH_3)](ClO_4)_2$ (**3**), $[Cu_2(5,5'\text{-}dmbpy)_2(\mu\text{-}OH)(\mu\text{-}OH_2)(\mu\text{-}O_2CCH_3)](ClO_4)_2$ (**4**), $[Cu_2(5,5'\text{-}dmbpy)_2(\mu\text{-}OH)(\mu\text{-}OH_2)(\mu\text{-}O_2CC(CH_3)_3)](ClO_4)_2$ (**5**), $[Cu_2(5,5'\text{-}dmbpy)_2(\mu\text{-}OH)(\mu\text{-}OH_2)(\mu\text{-}O_2CCH_3)](CF_3SO_3)_2$ (**6**) and $[Cu_2(5,5'\text{-}dmbpy)_2(\mu\text{-}OH)(\mu\text{-}OH_2)(\mu\text{-}O_2CCH_2CH_3)](CF_3SO_3)_2$ (**7**) which structure can be easily understood by inspection of Scheme 1. The crystal structures, magnetic properties and a systematic theoretical study are described in the forthcoming sections.

Materials and measurements

2,2′-bipyridyl, 4,4′-dimethyl-2,2′-bipyridine and 5,5′-dimethyl-2,2′-bipyridine were purchased as commercial chemicals from Aldrich. All reagents are commercial grade materials and were used without further purification. Elemental analyses (C, H, N) were determined on a Perkin–Elmer PE 2400 CHNS/O Analyzer. IR spectra were recorded on Spectrum One FT-IR spectrophotometer as KBr disc in the 4000–450 cm^{-1} spectral range. Solid-state (diffuse reflectance) electronic spectra were measured as polycrystalline samples on a Perkin–Elmer Lambda2S spectrophotometer, over the range 8000–18000 cm^{-1}.

Magnetic susceptibility measurements for compounds **1-7** were carried out with a Quantum Design SQUID MPMS-XL magnetometer working in the temperature range 2-300 K at magnetic fields of 500 G (2-30 K) and 10 kG (2-300 K). Diamagnetic corrections for the measured susceptibilities were estimated from the Pascal tables. The EPR spectra of microcrystalline samples of **1-7** were recorded at X-band frequency ($\nu \sim 9.4214$ GHz) with a Brucker ES-200 spectrometer in the temperature range 300-4 K.

Synthesis

Here we describe in some detail the synthesis procedure and experimental conditions for *$[Cu_2(bpy)_2(\mu\text{-}OH)(\mu\text{-}OH_2)(\mu\text{-}O_2CCH_3)](CF_3SO_3)_2$ (**1**).*

A warmed methanol solution (10 ml) of bpy (0.156 g, 1.0 mmol) was added to a warmed aqueous solution (20 ml) of $Cu(CF_3SO_3)_2$ (0.361 g, 1.0 mmol). Then, an aqueous solution (5 ml) of NaO_2CCH_3 (0.204 g, 3.0 mmol) was slowly added. The mixture was warmed with adding DMF (2 ml), yielding a clear dark blue solution. On slow evaporation at room temperature for 6 days, the product **1** was isolated as violet-blue block-shaped crystals. The crystals were filtered off, washed with the mother liquid and air-dried. Yield: ca. 75%. Anal. Calc. for $C_{24}H_{22}Cu_2F_6N_4O_{10}S_2$: C, 34.62; H, 2.78; N, 6.73. Found: C, 34.60; H, 2.80; N, 6.69%.

Crystallography

X-ray data for single-crystal samples of compounds **1**, **2**, **4**, **6** and **7** were collected at 100 K, whereas those of compound **3** and compound **5** were collected at 150 and 173 K, respectively. Reflection data were collected on a 1K Bruker SMART APEX CCD area-detector diffractometer using rotating mode, graphite-monochromated Mo Kα radiation, (λ = 0.71073 Å) at a detector distance of 4.5 cm and swing angle of -30°. A hemisphere of the reciprocal space was covered by combination of three sets of exposures; each set had a different ϕ angle (0°, 88°, 180°) and each exposure of 40 s covered 0.3° in ω. Raw data frame integration was performed with the SAINT code [16], which also applied correction for Lorentz and Polarization effects. An empirical absorption correction by using the SADABS [17] program was applied, which resulted in transmission coefficients ranging from 1.000 to 0.678, 0.746 to 0.603, 1.000 to 0.818, 1.000 to 0.850, 0.891 to 0.665, 0.945 to 0.614 and 0.746 to 0.614 for **1**-**7**. The structures were solved by direct methods and refined by full-matrix least-squares method on $(F_{obs})^2$ using the SHELXTL-PC Version 6.12 software package [18].

All hydrogen atoms of compound **1**-**4**, were determined at the difference map and refined isotropically riding with the heavy atoms. For compound **5**, all hydrogen on carbon atoms were fixed except O-H hydrogen atoms whose positions were refined. One hydrogen atom of an aqua bridging molecule could be not located and the position was fixed according to geometry optimization from theoretical calculations. In addition, three methyl groups of trimethylacetate appear to be disordered. All hydrogen atoms on carbon atoms of compound **6** were fixed except O-H hydrogen atoms whose the positions were refined. One triflate group was also found to be

disordered. For compound **7,** all H atoms were determined at the difference map and refined isotropically and bonded to the heavy atoms except hydrogen atoms on C(6) and C(8) which were fixed.

Computational details

A series of DFT calculations with state of the art exchange-correlation functionals has been carried out considering the isolated dinuclear Cu(II) cations in vacuo. The electron density was described either explicitly considering all electrons or using small core (LANL2) effective core potential (ECP) for the Cu atoms which allows one to take scalar relativistic effects into account. For the all electron calculations we used a rather large standard basis sets of Gaussian Type Orbitals (GTO) which is the same as in previous works [11,12] and is defined as follows: 6-3111+G extended with an f-function (exponent(f) = 0.528) for Cu and 6-31G(d) for the remaining atoms. For the calculations where the Cu innermost 10 electrons are described through a relativistic ECP, two different basis have been used which are either the standard LANL2DZ or the more extended standard LANL2TZ [19] the rest of atoms are described at the all electrons level with the 6-31G(d) basis set. We will refer to the three sets of calculations as AE, ECP-DZ and ECP-TZ, respectively.

The DFT calculations have been carried out using a variety of exchange-correlation functionals including hybrid schemes such as the well-known B3LYP and BHHLYP [20,21], the M06 and M06-2X meta-GGA functionals developed by Zhao and Truhlar [22-24] and the short- (HSE) [25] and long-range (LC-ωPBE) functionals [14] proposed by Scuseria et al. In all cases the calculations were carried out within the unrestricted (spin-polarized) formalism. Clearly, in this type of formalism, the spin symmetry is not guaranteed. [26-2728] Nevertheless, in the unrestricted Kohn-Sham formalism one can approximate triplet (T) state using a single Slater determinant with two unpaired electrons (i.e., $S_z = 1$). However, to estimate the energy of the open shell singlet state it is possible to make use of the broken-symmetry (BS) approach imposing $S_z = 0$. In this way, the singlet-triplet gap energy has been obtained on the basis of the expectation value of the Heisenberg Hamiltonian as in Eq. (1)

$$\hat{H} = -J\,\hat{\mathbf{S}}_1 \cdot \hat{\mathbf{S}}_2 \qquad (1)$$

that using the appropriate mapping [15] leads to the approximate relation:

$$J = 2\,[\mathrm{E(BS)} - \mathrm{E(T)}] \qquad (2)$$

where E(BS) is the energy of the broken-symmetry state and E(T) is the energy of the spin unrestricted approximation to the triplet state [29]. Here, it is important to stress that Eq. (2) takes into account the so-called spin projection to approximately recover the spin symmetry lost in the BS approach and which is inherent to the use of a single Kohn-Sham determinant [30-32]. Here one must advert that alternative methods for calculating J couplings without the use of spin symmetry [33] lead to results that are not always accurate [34] when high quality range separated functionals like those employed in this work are used. Nevertheless, one must admit that magnetostructural correlation involving mainly antiferromagnetic compounds do not suffer from this limitation. Moreover, it has been recently shown that, for a given functional, results obtained using the mapping procedure in Eq. (2) are in agreement with those obtained using the spin flip Time Dependent DFT approach which properly accounts for spin symmetry in this type of systems [35].All calculations were carried out using the Gaussian09 suite of programs [36].

Results and discussions

Description of the crystal structures

The crystal structures of compounds **1**-**7** consist of a hetero triply-bridged dinuclear Cu(II) cationic unit and two counteranions ($CF_3SO_3^-$ for compounds **1**, **6** and **7**; ClO_4^- for compounds **2**-**5**). For each of the cationic units, two [Cu(L)] groups are linked together by three different bridging ligands namely aquo, hydroxo and carboxylato. Each Cu(II) geometry is described as distorted square pyramidal geometry of the CuN_2O_2O' chromophore, with τ values of 0.10 and 0.38 for the two Cu(II) centers. Let us recall that the Addison parameter is defined as $\tau = (\alpha-\beta)/60$, where α and β are the largest coordination angles. Hence, one has $\tau = 0$ for square pyramidal (SP) and $\tau = 1$ for trigonal bipyramidal (TBP) geometry [13]. The coordination environment around each Cu(II) ion contains two N atoms of the chelate ligand (Cu–N 1.978(1)-2.012(6) Å), an oxygen atom of the carboxylato bridging ligand (Cu–O 1.941(1)-1.983(1) Å) and an oxygen atom of hydroxo ligand (Cu–O 1.908(1)-1.938(5) Å) to form the square bases. The apical site of each Cu(II) atom is occupied by an oxygen atom of an aquo ligand at distances in range of 2.310(4)-2.442(1) Å. The *syn*,*syn*-coordinated carboxylato ligand bridges two equatorial planes of each Cu(II) chromophore, giving the Cu···Cu distances in the range of 2.979(1)-3.077(1) Å. The CuN_2O_2O' chromophores are non-planar with dihedral angles (γ in Table 1) between the CuN_2 and CuO_2 planes in the range of 10.10(2)-28.62(1)º. The dihedral angle between the equatorial planes (ϕ in Table 1) are in the range of 112.07(1)-122.08(1)º. The bridging angles of Cu–OH–Cu are in the range of 100.80(7)-107.26(5)º. According to these structural features, compounds **1**-**7** are classified as class B (Scheme 1).

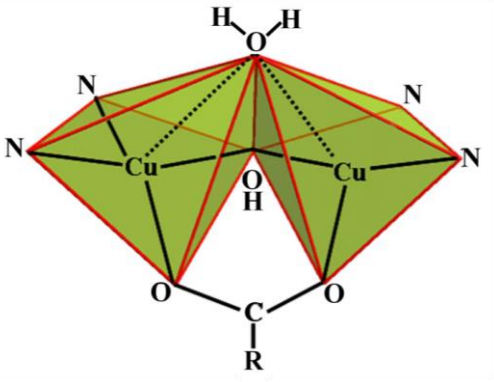

Scheme 1

The lattices of all compounds are stabilized by intermolecular π-π interactions between aromatic pyridine rings on chelate ligands of adjacent dinuclear cations and hydrogen bonding between the aquo and hydroxo bridges and triflate or perchlorate anions. The molecular structure of compound **1** is shown in Figure 1. For comparison purposes, the structural data of compounds **1**-**7** and of some other relevant hetero triply-bridged dinuclear Cu(II) compounds previously studied [10,12] are summarized in Table 1.

Table 1. Structural and magnetic data for Class B triply-bridged dinuclear copper(II) compounds.[c]

Compound[a]	Geom[b]	τ	ϕ	γ	Cu···Cu	Cu–X Axial	Cu–X Equatorial	Cu–OH–Cu	J_{exp}	Ref.[a]
$[Cu_2(dpyam)_2(\mu\text{-}OH)(\mu\text{-}OH_2)(\mu\text{-}O_2CCH_3)](S_2O_8)$ (I)	SP, SP	0.43	164.4	40.4	3.124	2.414	1.911–2.023	109.6	n.d.	10
$[Cu_2(bpy)_2(\mu\text{-}OH)(\mu\text{-}OH_2)(\mu\text{-}O_2CCH_3)](NO_3)_2$ (II)	SP, SP	0.21, 0.19	120.5	14.5, 11.6	3.049	2.347, 2.460	1.938–2.017	104.0	n.d.	10
$[Cu_2(phen)_2(\mu\text{-}OH)(\mu\text{-}OH_2)(\mu\text{-}O_2CCH_3)](BF_4)_2\cdot(H_2O)_{0.5}$ (III)	SP, SP	0.21, 0.16	114.6	17.0, 8.6	3.002	2.374, 2.390	1.925–2.008	102.1	120.8	10
$[Cu_2(bpy)_2(\mu\text{-}OH)(\mu\text{-}OH_2)(\mu\text{-}O_2CCH_3)](ClO_4)_2$ (IV)	SP, SP	0.14, 0.25	118.1	—	3.035	2.379, 2.405	2.006–2.010	103.8	19.3	10
$[Cu_2(phen)_2(\mu\text{-}OH)(\mu\text{-}OH_2)(\mu\text{-}O_2CCH_3)](ClO_4)_2$ (V)	SP, SP	0.02, 0.14	113.8	16.4, 8.2	2.989	2.360, 2.375	1.933–2.020	101.3	120.0	10
$[Cu_2(bpy)_2(\mu\text{-}OH)(\mu\text{-}OH_2)(\mu\text{-}O_2CCH_2CH_3)](ClO_4)_2$ (VI)	SP, SP	0.20, 0.16	120.1	15.0, 10.9	3.037	2.382, 2.415	1.920–2.005	104.5	148.9	10
$[Cu_2(bpy)_2(\mu\text{-}OH)(\mu\text{-}O_2CCH_3)(\mu\text{-}Cl)]Cl\cdot(H_2O)_{0.5}$ (VII)	SP, SP	0.41, 0.28	123.0	27.4, 18.9	3.040	2.632, 2.657	1.936–2.029	103.3	145.3	10
$[Cu_2(phen)_2(\mu\text{-}OH)(\mu\text{-}OH_2)(\mu\text{-}O_2CCH_2CH_3)](NO_3)_2$ (VIII)	SP, SP	0.19, 0.21	122.3	14.6, 12.2	3.026	2.344, 2.368	1.925–2.029	103.6	98.4	12
$[Cu_2(phen)_2(\mu\text{-}OH)(\mu\text{-}OH_2)(\mu\text{-}O_2CC(CH_3)_3)](ClO_4)_2(CH_3CH_2OH)$ (IX)	SP, SP	0.10, 0.22 0.08, 0.26	117.7, 120.4	9.9, 16.2 8.8, 21.2	3.010 3.034	2.419, 2.379 2.425, 2.369	1.911–2.015 1.893–2.012	103.8, 105.3	151.2	12
$[Cu_2(bpy)_2(\mu\text{-}OH)(\mu\text{-}O_2CCH_2CH_3)(\mu\text{-}O_2SOCF_3)](CF_3SO_3)(DMF)_{0.5}$ (X)	SP, SP	0.14, 0.15	154.8	11.2, 11.8	3.341	2.351, 2.354	1.906–2.019	122.3	104.5	12
$[Cu_2(bpy)_2(\mu\text{-}OH)(\mu\text{-}OH_2)(\mu\text{-}O_2CCH_3)](CF_3SO_3)_2$ (**1**)	SP, SP	0.24, 0.25	118.95	15.67, 18.73	3.024	2.394, 2.323	1.921–2.009	103.39	102.1	pw
$[Cu_2(4,4'\text{-}dmbpy)_2(\mu\text{-}OH)(\mu\text{-}OH_2)(\mu\text{-}OCH)](ClO_4)_2$ (**2**)	SP, SP	0.10, 0.38	122.08	10.10, 28.62	3.077	2.324, 2.409	1.908–1.999	107.26	72.6	pw
$[Cu_2(4,4'\text{-}dmbpy)_2(\mu\text{-}OH)(\mu\text{-}OH_2)(\mu\text{-}OCCH_3)](ClO_4)_2$ (**3**)	SP, SP	0.11, 0.30	120.19	11.37, 25.20	3.055	2.323, 2.442	1.918–1.999	105.55	90.2	pw
$[Cu_2(5,5'\text{-}dmbpy)_2(\mu\text{-}OH)(\mu\text{-}OH_2)(\mu\text{-}OCCH_3)](ClO_4)_2$ (**4**)	SP, SP	0.21, 0.22	112.07	14.81, 15.64	2.984	2.329, 2.346	1.929–2.003	101.07	104.3	pw
$[Cu_2(5,5'\text{-}dmbpy)_2(\mu\text{-}OH)(\mu\text{-}OH_2)(\mu\text{-}OCC(CH_3)_3)](ClO_4)_2$ (**5**)	SP, SP	0.17, 0.19	114.56	11.49, 13.99	3.008	2.320, 2.333	1.921–2.012	102.40	98.7	pw
$[Cu_2(5,5'\text{-}dmbpy)_2(\mu\text{-}OH)(\mu\text{-}OH_2)(\mu\text{-}OCCH_3)](CF_3SO_3)_2$ (**6**)	SP, SP	0.34, 0.31	118.72	22.29, 20.60	3.007	2.310, 2.323	1.923–2.003	102.57	92.1	pw
$[Cu_2(5,5'\text{-}dmbpy)_2(\mu\text{-}OH)(\mu\text{-}OH_2)(\mu\text{-}OCCH_2CH_3)](CF_3SO_3)_2$ (**7**)	SP, SP	0.23, 0.27	112.25	15.61, 18.04	2.979	2.321, 2.339	1.931–1.996	100.80	103.1	pw

[a] Abbreviations: bpy = 2,2′-bipyridine; dpyam = di-2-pyridylamine; phen = 1,10-phenanthroline, n.d. = not determined, pw = present work; [b] SP = distorted square pyramid; [c] Geom stands for the coordination of Cu(1) and Cu(2), τ is the Addison structural parameter for Cu(II) center for Cu(1)/Cu(2) and Cu(3)/Cu(4) pairs, ϕ is the angle between basal planes and γ is the tetrahedral twist angle, both in degrees. Cu···Cu and Cu-X distances are in Å and Cu-OH-Cu angles in degrees. J_{exp} is the experimentally derived magnetic coupling constant in cm^{-1}.

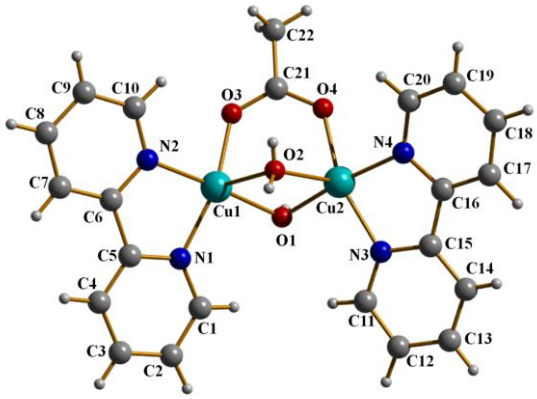

Fig. 1. Molecular structure and atomic numbering scheme for compound **1**. Triflate counteranions are omitted for clarity.

Spectral Characterizations

The infrared spectra display a broad band at 3510 cm^{-1} for **1,** 3519 cm^{-1} for **2,** 3524 cm^{-1} for **3,** 3434 cm^{-1} for **4,** 3401 cm^{-1} for **5,** 3475 cm^{-1} for **6** and 3479 cm^{-1} for **7**, which can be assigned to the bridging OH vibration of the hydroxo ligands and/or lattice water. The spectra also exhibit the intense bands at 1557 and 1445 cm^{-1} for **1**, 1577 and 1413 cm^{-1} for **2**, 1554 and 1443 cm^{-1} for **3**, 1557 and 1479 cm^{-1} for **4**, 1540 and 1480 cm^{-1} for **5**, 1564 and 1481 cm^{-1} for **6** and

1556 and 1479 cm^{-1} for **7**, corresponding to the $\nu_{as}(COO^-)$ and $\nu_s(COO^-)$ vibrations of carboxylato bridging ligands namely acetato for **1**, **3**, **4** and **6**, formato for **2**, trimethylacetato for **5** and propionato for **7**, respectively. The spectra of compounds **1**, **6** and **7** show the broad and intense bands of the stretching of $CF_3SO_3^-$ at 1277 ν_{as}(S–O), 1153 ν_{as}(C–F), and 1029 ν_s(S–O) cm^{-1} for **2**; 1279 ν_{as}(S–O), 1161 ν_{as}(C–F) and 1031 ν_s(S–O) cm^{-1} for **6** and 1281 ν_{as}(S–O), 1158 ν_{as}(C–F) and 1031 ν_s(S–O) cm^{-1} for **7**. The IR spectra of compounds **2-5** present the broad and intense bands of the stretching for ionic ClO_4^- anion (1103 cm^{-1} for **2**, 1106 cm^{-1} for **3,** 1111 cm^{-1} for **4** and 1120 cm^{-1} for **5**).

The diffuse reflectance spectra of compounds **1-7** display a broad band (16 530 cm^{-1} for **1**, 16 030 cm^{-1} for **2,** 16 340 cm^{-1} for **3**, 16 590 cm^{-1} for **4,** 16 490 cm^{-1} for **5**, 16 240 cm^{-1} for **6** and 16 320 cm^{-1} for **7**) and a lower energy shoulder (13 880 cm^{-1} for **1**, 13 060 cm^{-1} for **2,** 13 620 cm^{-1} for **3**, 13 960 cm^{-1} for **4,** 13 600 cm^{-1} for **5**, 13 540 cm^{-1} for **6** and 13 940 cm^{-1} for **7**). These features are typical and can be assigned to the d_{xy}, d_{yz}, $d_{xz} \rightarrow d_{x^2-y^2}$ and $d_{z^2} \rightarrow d_{x^2-y^2}$ transitions for the square pyramidal geometry of the class B triply-bridged dinuclear Cu(II) compounds. Notice that according to strict symmetry considerations for the distorted square pyramidal geometry of compounds 1-7, the d_{xy}, d_{yz}, d_{xz} orbitals are not triply degenerated which is the origin of the broad band mentioned above.

Electron Paramagnetic Resonance Spectra and magnetic properties

The Electron Paramagnetic Resonance Spectra (EPR) spectra of compounds **1-4** (X-band, $\nu \sim 9.4214$ GHz) have been recorded at different temperatures between 4 and 300 K for polycrystalline solid samples. The general shape of the spectra is similar for all compounds; we show the EPR spectra of compound **4** in Figure 2 as a representative example. A summary of data obtained from EPR measurements is reported Table 2.

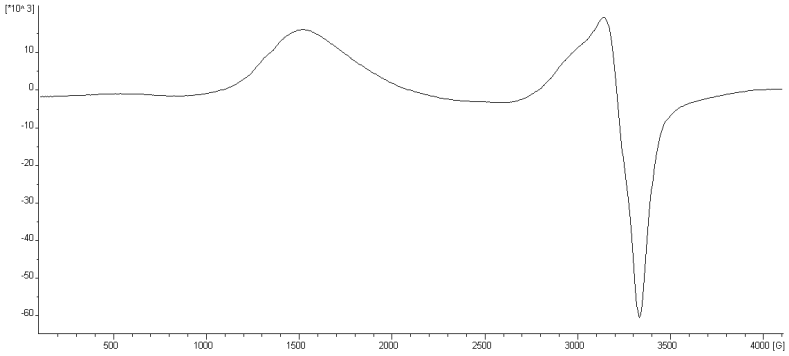

Fig. 2. EPR spectrum of compound **4** at 4 K.

Table 2. Experimental normal and half-field (at 4 K) EPR signals and best-fit susceptibility data to Eq.3 (g_{iso}, J_{exp} and θ) for compounds **1-7**. TIP parameter below 1.2·10-4 emu Kmol^{-1}.

Compound	g	$g_{1/2}$	g_{iso}	J_{exp} (cm^{-1})	θ(K)	$N\alpha(\times10^{-6})$	R ($\times10^{-4}$)
1	2.082	4.498	2.194	102	−0.39	30	2.4
2	2.095	4.350	2.163	73	−0.73	90	3.6
3	2.066	4.438	2.177	90	−0.58	60	3.3
4	2.092	4.429	2.167	104	−0.33	110	1.4
5	2.097	4.427	2.178	99	−0.31	50	2.1
6	2.074	4.426	2.196	92	−0.55	60	3.1
7	2.063	4.376	2.162	103	−0.38	40	2.3

As expected for ferromagnetic systems,[37] the principal transition band near g ~ 2.1 (corresponding to $\Delta m_s = 1$) shows some asymmetry but maintains the center of the band as T goes from 300 to 4 K. No significant fine structure is observed. A broad band near $g_{1/2} \sim 4.4$ is also observed and assigned to the half field transition (corresponding to $\Delta m_s = 2$). Both bands slightly increase their intensity as temperature increases and the $\Delta m_s = 2$ half field transition band shows important intensity with respect to the $\Delta m_s = 1$ transition. This observation confirms the ferromagnetic character of these compounds.

Molar magnetic susceptibility (χ_M) measurements were carried out using microcrystalline samples of compounds **1-7**. The as measured $\chi_M T$ vs T plots for all compounds are quite similar and display clear ferromagnetic behavior as shown in Figure 2. To account for the magnetic behaviour of the dinuclear Cu(II) complexes and to evaluate the corresponding coupling constant J, defined as the singlet-triplet splitting, we fitted the raw experimental susceptibility data using the Bleaney-Bowers equation[38] with an additional temperature independent paramagnetism (TIP) term. In addition, we corrected the Bleaney-Bowers expression with a mean-field Weiss θ parameter to account for the small antiferromagnetic intermolecular interactions detected in the low temperature region for these ferromagnetic dinuclear complexes:

$$\chi_M(T-\theta) = \frac{N\beta^2 g^2}{k_B}\frac{2e^{J/k_BT}}{1+3e^{J/k_BT}} + TIP \qquad (3)$$

Best-fit parameters were obtained by minimization of the error function $R = \Sigma\{[(\chi_M T)_{calc} - (\chi_M T)_{exp}]^2 / (\chi_M T)_{exp}^2\}$, and results are also shown in Table 2. Likewise, one must also consider the intrinsic low accuracy and overparametrization problems involving the fitting of ferromagnetically coupled Cu(II)-Cu(II) systems with rather large molecular weights. Therefore, the fitting was consistently carried out for all compounds using the minimum possible number of parameters. Note that for these ferromagnetic compounds, $\chi_M T$ ranges from 0.9 to 1.2. Because of this small $\chi_M T$ range, small instrumental inaccuracies appear magnified and evidences as small discontinuities near 50K although one must note that the J values are extracted from the high temperature part of the $\chi_M T$ versus T curve and, hence, the part below 50K is not as well described. The need for a small number of parameters in describing the $\chi_M T$ versus T curve of these ferromagnetic compounds also leads to a more difficult fitting to the magnetic model which affects especially the low T part of the $\chi_M T$ versus T curve. Nevertheless, the g values obtained from the fitting are consistent with those determined by EPR and also reported in Table 2. This

provides further support of the accuracy of the *J* values thus obtained which are discussed below. Here, we will mention on the selected magnetic plot of compound **4** (Figure 3) and the results of the rest compounds are summarized in supplementary. The $\chi_M T$ vs *T* plot of compound **4** shows a room temperature $\chi_M T$ product value of 1.02 cm^3Kmol^{-1}, slightly higher than that expected for two uncoupled Cu(II) ions. Lowering the temperature causes the $\chi_M T$ product to continuously increase until reaching a plateau value of 1.15 cm^3Kmol^{-1} at 50 K. On further cooling, $\chi_M T$ shows an abrupt descent for all compounds, which clearly suggests that this quantity tends to zero when temperature tends to 0 K. This behavior can be explained by the existence of ferromagnetically coupled Cu(II) pairs responsible of the high temperature regime, where the low-lying triplet state was increasingly populated in detriment of the singlet state. Below liquid nitrogen temperature, small antiferromagnetic intermolecular interactions manifest and tend to couple the triplet states in such a way that the *S*=1 spin moments of the different molecules cancel each other and, as a result, a zero global magnetization is approached near the liquid helium temperature.

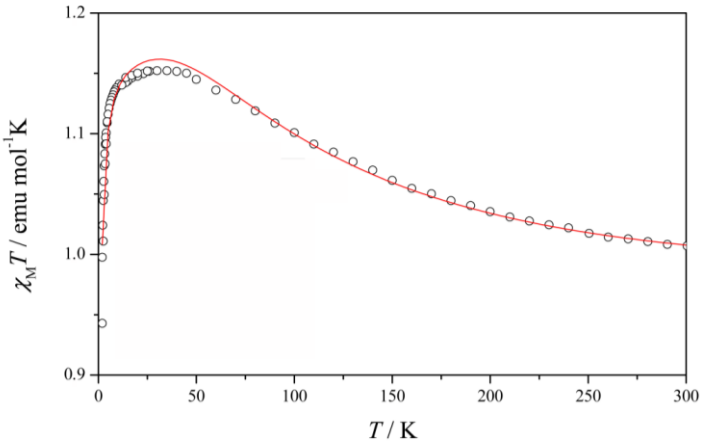

Fig. 3. Plot of magnetic susceptibility-temperature product ($\chi_M T$) versus temperature (*T*) for compound **4**.

Magneto-structural correlations

Here we analyze the common magnetostructural correlations involving the experimental value of the magnetic coupling constant (J_{exp}) and key feature of the molecular structure [4,5]. Figure 4 plots J_{exp} versus the distance between the two Cu centers and Figure 5 plots J_{exp} versus the angle formed by the Cu-OH-Cu structural moiety where the OH corresponds to a monoatomic bridge that links two Cu centers at equatorial position. Both plots exhibit a clear trend which is slightly more quantitative in the second case. These plots are important since they reveal a clear trend along the series indicating that the magnitude of the ferromagnetic coupling increases with decreasing Cu···Cu distance, as expected from simple arguments, and also increases with decreasing the Cu-OH-Cu bond angle which can also be explained in terms of qualitative rules. Hence, these empirical correlations provide a very useful testing ground for theoretical methods.

In previous work it has been suggested that the aggregate Addison τ parameter also provides useful information about the relationship between structure and magnetic coupling. In fact, the Addison parameter allows one to properly define compounds **1-7** as belonging to class **B**. However, it does not provide a suitable magnetostructural correlation, which is at variance of previous work [11]. This is likely to be due to the fact that values of the magnetic coupling

constant studied exhibited a broader range but also to their ferromagnetic character. This will be confirmed by the DFT calculations described in the next subsection.

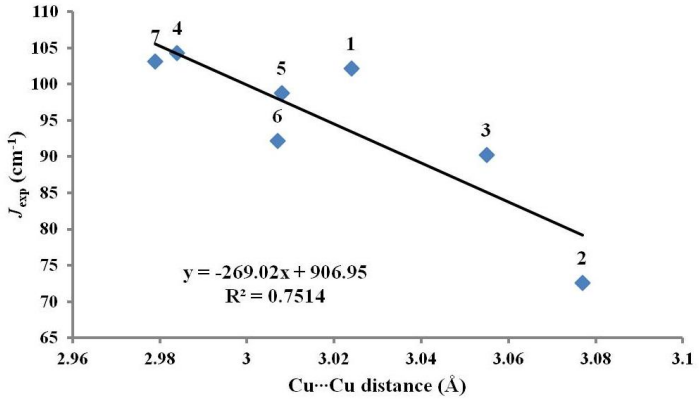

Figure 4. Plot of the experimental J (cm^{-1}) vs. Cu···Cu (Å) of compounds **1-7**.

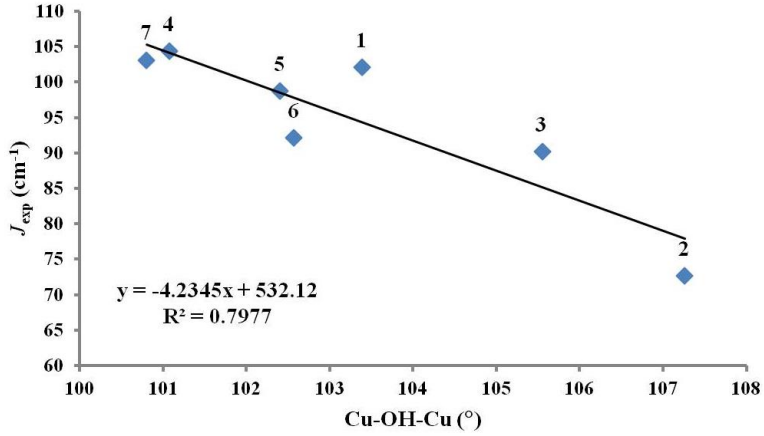

Figure 5. Plot of the experimental J (cm^{-1}) vs. Cu–OH–Cu (°) of compounds **1-7**.

Density functional theory based calculations

The calculated and experimental values of the magnetic coupling constants are summarized in Table 3 where the aggregate Addison τ parameter is also shown for comparison. All methods, including UHF which neglects electron correlation except for the part included by spin polarization, consistently predict these compounds to be ferromagnetic, in agreement with experiment and all methods regularly predict that all compounds have a similar value of the magnetic coupling constant, again in agreement with experiment. However, the fine details are more subtle, difficult to describe and do not always go in the expected direction. The calculated values of the magnetic coupling constant strongly depend on the type of exchange-correlation functional and, more precisely, in the amount of Fock exchange included in the exchange potential. This is not surprising and has been reported for quite a large number of systems although most of them exhibiting strong antiferromagnetic character [15,30]. The novelty here is that none of the studied methods is able to describe **2** as the compound with smallest J and **4** as the one with the largest. One can suggest that the experimental measurements and fitting procedures for these two compounds are intrinsically not enough accurate, although the

magnetostructural correlations in Figures 4 and 5 will not support such a claim. Even accepting that these two compounds represent exceptions and excluding them from the statistical analysis, one will face the same problem since none of the methods will now predict that **3** is the compound with the smallest *J* and **7** the one with the largest.

In order to define in a more precise way the failure of all theoretical methods it is convenient to make some considerations. Let us start with the UHF results; here the calculated values for a given compound arising from the AE and ECP calculations are almost the same and even the effect of the basis set is almost negligible since going from the LANL2DZ to the LANL2TZ changes the calculated values by less than 2 cm^{-1}. This is consistent with the fact that UHF neglects correlation and that the main effect of increasing the basis set would be precisely in the description of the correlation effects. This is obvious in the case electron correlation is accounted for in a configuration interaction type wave function. In fact, DFT calculations with these two basis sets exhibit significant differences and, in the case of the LANL2DZ, deviates too much from the AE values. This is clearly an artifact of the limited basis set and will no longer be commented here. Let us now discuss the results obtained with the popular B3LYP functional which contains a 20% of Fock exchange and which is known to overestimate the magnetic coupling constant of antiferromagnetic Cu(II) dinuclear compounds by a factor of ~2, provided the proper mapping (cf. Eq. 2) is used [15,30]. Results in Table 3 indicate that B3LYP calculated *J* values obtained at the AE level with the small core ECP and a triple-ζ valence basis set for the Cu atoms — hereafter referred to as ECP — are almost the same differing by at most 4 cm^{-1} or 2%. However, the calculated values are significantly larger than the experimental values although, at variance of antiferromagnetic dinuclear Cu(II) compounds the deviation factor varies from 2.2 to 1.5. Interestingly, the M06 predicted values are much larger and, surprisingly, AE and ECP predicted values differ by a larger amount of ~ 60 cm^{-1}. There is no clear explanation for these trends since M06 and B3LYP contain a similar amount of Fock exchange (27% and 20%, respectively) and one could perhaps conclude that these differences are a result of the parametrization of the M06 functional. This hypothesis seems to be confirmed by analysis of the results obtained by the BHHLYP and M06-2X functionals, containing 50% and 54% Fock exchange respectively. The BHHLYP calculated magnetic coupling constant values at the AE and ECP levels, as in the case of B3LYP, almost coincide with differences of at most ~ 2 cm^{-1}. In addition, these calculated values are those closest to the experimental ones which, again, is at variance of existing experience with the family antiferromagnetic dinuclear Cu(II) complexes. Interestingly, the values predicted by the M06-2X functional are almost on the experimental range but only when considering the results from ECP calculations which, as in the case of the M06 discussed above, deviate from the AE by ~ 30-40 cm^{-1}. The difference between AE and ECP calculated values in the M06 and M06-2X functionals remains difficult to understand. Finally, we discuss the HSE and LC-ωPBE short- and long-range separated functionals which, for the dinuclear Cu(II) complexes database investigated up to now, provide the most accurate results in terms of agreement with experiment [31,32]. Results in Table 3 show that also here results obtained at the AE and ECP levels deviate although by ~ 10-15 cm^{-1}, this is no doubt less than in the case of the M06 and M06-2X but still noticeable. Here, one will be tempted to attribute this difference to the range separation parameter which, as shown by Phillips and Peralta [32], has a significant influence in the calculated results. In the best scenario, the range separated functionals deviate from experiment by 30%.

The fact that exchange-correlation functionals that provide an almost quantitative description of antiferromagnetic compounds fail to describe the differences exhibited along a series of ferromagnetic dinuclear Cu(II) complexes is likely to be due to the different type of

electronic correlation effects governing the magnetic coupling. In the case of antiferromagnetic compounds, the largest contributions correspond to metal to metal and metal to ligand excitations. The first ones correspond to the well-known superexchange mechanism [39,40] which appear already at the CASSCF level and are essentially the result of non-dynamical correlation. The second ones involve double excitations from the reference CASSCF wave function to the virtual orbitals [42] and are described reasonably well by second order perturbation theory based methods [43], although one must also be aware of possible artifacts due to the slow convergence of the perturbation series [44]. In the case of ferromagnetic compounds, the main contribution comes from direct exchange [41,42] and it is necessary to go well beyond double excitation from the reference space to improve the description. It is likely that this is the origin of the difficulties of the present exchange-correlation functionals in describing ferromagnetic interactions.

Table 3. Calculated values of the coupling constant J (in cm-1) for compounds 1-7, using hybrid and screened functionals compared to experimental magnetic values. AE and ECP stand for calculations with all electrons and effective core potentials respectively. For the ECP only results with the more extended TZ basis are shown.

a	τ_{agg}	J_{calc}														J_{exp}
		UHF		M06-2X		BHHLYP		LC-*w*PBE		HSE		B3LYP		M06		
		AE	ECP	AE	ECP	AE	ECP	AE	ECP	AE	ECP	AE	ECP	AE	ECP	
1	0.49	37.12	38.09	67.11	95.83	83.50	85.62	135.33	143.09	147.66	155.50	169.50	170.47	238.91	301.91	102.1
2	0.48	37.59	39.37	66.47	96.70	82.11	85.28	133.12	143.02	146.02	155.72	165.82	168.56	231.01	299.14	72.6
3	0.41	38.29	39.44	67.92	96.88	84.10	86.34	134.22	141.76	148.13	155.72	170.01	170.69	240.29	303.95	90.2
4	0.43	36.02	37.22	65.75	94.48	81.88	84.59	132.29	141.35	145.24	154.41	167.04	169.73	236.77	300.51	104.3
5	0.36	34.84	35.48	64.78	93.46	80.01	81.90	133.04	141.85	145.85	155.03	168.72	171.21	240.25	308.67	98.7
6	0.65	37.07	38.49	68.01	100.00	84.02	87.20	138.3	148.75	150.7	161.50	173.40	177.00	249.20	326.13	92.1
7	0.50	36.34	38.03	66.14	96.67	82.42	86.20	133.17	143.69	146.04	157.08	168.00	172.49	237.62	305.68	103.1

In summary, a new series of seven dinuclear Cu(II) compounds with a common triple bridge consisting of hydroxo, aquo and carboxylato ligands has been synthesized, the crystal structures solved and the magnetic properties studied by EPR and magnetic susceptibility measurements as a function of temperature. The seven compounds thus obtained exhibit ferromagnetic coupling which is a consequence of the topology introduced by the type of bridging ligands as previously shown. [10-12]. Nevertheless, the magnetic coupling constant *J* between the Cu centers spans a rather broad range from 73 to 104 cm^{-1} which is clearly governed by the different external ligands. These affect the Cu---Cu distance and the Cu-OH-Cu bonding angle which indeed appear to be reasonable structural parameters defining magnetostructural correlations. Nevertheless, these trends are far from being quantitative.

The magnetic coupling in these triple bridged dinuclear compounds has been examined by a series of density functional methods going from simple hybrids such as B3LYP and BHHLYP to the M06 and M06-2X meta-hybrid and including also the HSE and LC-ωPBE range separated functionals. Interestingly, all these methods consistently predict the compounds to be ferromagnetic but all fail to reproduce the variation from compound to compound. In fact, for a given functional, the calculated *J* values along the series are almost constant and, in some cases very far away from experiment. The best results are provided by the BHHLYP functional where

results obtained and the AE and ECP levels are also close to each other. The M06-2X functional, which contains a similar amount of Fock exchange, also predicts values in the experimental range although here the AE and ECP calculated values differ by a noticeable amount. The popular B3LYP functional largely overestimates *J* and this is also the behavior of M06 which contains a similar amount of Fock exchange. In addition, M06-2X calculated values depend on whether the Cu core electrons are treated AE or with a small core ECP. This is similar to the behavior described above for the M06-2X and the origin remains unclear. Finally, the HSE and LC-ωPBE range separated functionals which have found to perform the best in previous work dealing with a family of compounds spanning a broad range of values, from moderately ferromagnetic to strong antiferromagnetic, fail to reproduce the order of magnitude of *J* for the present new compounds. Furthermore, AE and ECP values obtained with the range separated functionals differ, which may be due to the inadequacy of the standard parameter governing range separation.

Therefore, the most important conclusion of the present work is that while the different exchange-correlation functionals explored in this work to explore the magnetic coupling constant of the new ferromagnetic Cu(II) dinuclear compounds properly predict the qualitative nature of the experimental coupling, none of them is able to reproduce the trend in ferromagnetism along the series, and only BHHLYP predicts values in the experimental range. It is likely that the origin of the difficulties of the present exchange-correlation functionals in describing ferromagnetic interactions is due to the fact that a proper description in terms of wave function based methods requires including higher order terms in the perturbation treatment or, equivalently, to go beyond double excitations out of the CASSCF reference wave function defined by the magnetic orbitals only [45]. Clearly, the current density functional need to be further improved to be able to properly describe ferromagnetism. The present series of compounds provides an excellent playground to tests new and improved functional.

References

[1] J.R. Friedman, M.P. Sarachik, J. Tejada, R. Ziolo, *Phys. Rev. Lett.* 1996, **76**, 3830.

[2] G. L. J. A. Rikken, E. Raupach, *Nature* 2000, **405**, 932.

[3] S. Tanase, J. Reedijk, *Coord. Chem. Rev.* 2006, **250**, 2501.

[4] O. Kahn, Molecular Magnetism, VCH Publishers, New York, 1993.

[5] O. Kahn, *Adv. Inorg. Chem.* 1996, **43**, 179.

[6] G. Christou, S.P. Perlepes, E. Libby, K. Folting, J.C. Huffman, R.J. Webb, D.N. Hendrickson, *Inorg. Chem.* 1990, **29**, 3657.

[7] S. Youngme, C. Chailuecha, G.A. van Albada, C. Pakawatchai, N. Chaichit, J. Reedijk, *Inorg. Chim. Acta* 2004, **357**, 2532

[8] S. Youngme, C. Chailuecha, G.A. van Albada, C. Pakawatchai, N. Chaichit, J. Reedijk, *Inorg. Chim. Acta* 2005, **358**, 1068.

[9] C. Chailuecha, S. Youngme, C. Pakawatchai, N. Chaichit, G.A. van Albada, J. Reedijk, *Inorg. Chim. Acta* 2006, **359**, 4168.

[10] S. Youngme, J. Phatchimkun, N. Wannarit, N. Chaichit, S. Meejoo, G.A. van Albada, J. Reedijk, *Polyhedron* 2008, **27**, 304.

[11] R. Costa, I. de P. R. Moreira, S. Youngme, K. Siriwong, N. Wannarit, F. Illas, *Inorg. Chem.* 2010, **49**, 285.

[12] N. Wannarit, K. Siriwong, N. Chaichit, S. Youngme, R. Costa, I. de P. R. Moreira, F. Illas, *Inorg. Chem.* 2011, **50**, 10648.

[13] A. W. Addison, T. N. Rao, J. Reedijk, J. van Rijn, G.C. Verschoor, *J. Chem. Soc. Dalton Trans.* 1984, 1349.
[14] O. A. Vydrov, G. E. Scuseria, *J. Chem. Phys.* 2006, **125**, 234109.
[15] I. de P. R. Moreira, F. Illas, *Phys. Chem. Chem. Phys.* 2006, **8**, 1645 and references therein.
[16] Siemens SAINT, Version 4 Software Reference Manual, Siemens Analytical X-ray Systems, Inc., Madison, WI, USA, 1996.
[17] G.M. Sheldrick, SADABS: Program for Empirical Absorption correction of Area Detector Data, University of Göttingen, Göttingen, Germany, 1996.
[18] Bruker, XSHELL, Version 6.12 Reference Manual, Bruker AXS, Inc., Madison, WI, USA, 1999.
[19] Basis set parameters have been extracted from the Basis Set Exchange web page at https://bse.pnl.gov/bse/portal
[20] A. D. Becke, *J. Chem. Phys.* 1993, **98**, 5648.
[21] P.J. Stephens, F. J. Devlin, C.F. Chabalowski, M. J. Frisch, *J. Phys. Chem.* 1994, **98**, 11623.
[22] Y. Zhao, D. G. Truhlar, *J. Chem. Phys.* 2006, **125**, 194101.
[23] Y. Zhao, D. G. Truhlar, *J. Phys. Chem. A* 2006, **110**, 13126.
[24] Y. Zhao, D. G. Truhlar, *Theor. Chem. Acc.* 2008, **120**, 215.
[25] J. Heyd, G. E. Scuseria, M. Ernzernhof, *J. Chem. Phys.* 2003, **518**, 8207; ibid. 2006, **124**, 219906(E).
[26] F. Illas, I. de P. R. Moreira, J. M. Bofill, M. Filatov, *Phys. Rev. B* 2004, **70**, 132414.
[27] F. Illas, I. de P. R. Moreira, J. M. Bofill, M. Filatov, *Theor. Chem. Acc.* 2006, **115**, 587.
[28] I. de P. R. Moreira, R. Costa, M. Filatov, F. Illas, *J. Chem. Theory Comput.* 2007, **3**, 764.
[29] R. Caballol, O. Castell, F. Illas, J. P. Malrieu, I. de P. R. Moreira, *J. Phys. Chem. A* 1997, **101**, 7860.
[30] R. Valero, R. Costa, I. de P. R. Moreira, D. G. Truhlar, F. Illas, *J. Chem. Phys.* 2008, **128**, 114103.
[31] P. Rivero, I. de P. R. Moreira, F. Illas, G. E. Scuseria, *J. Chem. Phys.* 2008, **129**, 184110.
[32] J. J. Phillips, J. E. Peralta, *J. Chem. Phys.* 2011, **134**, 034108.
[33] E. Ruiz, P. Alemany, S. Alvarez, J. Cano, *J. Am. Chem. Soc.* 1997, **119**, 1297.
[34] E. Ruiz, *J. Comput. Chem.* 2011, **32**, 1998.
[35] R. Valero, F. Illas and D. G. Truhlar, *J. Chem. Theory and Comput.* 2011, **7**, 3523.
[36] M. J. Frisch, et al. Gaussian 09, Revision A.1; Gaussian, Inc.:Wallingford CT, 2009.
[37] A. Bencini, D. Gatteschi, Electron Paramagnetic Resonance of Exchange Coupled Systems, Springer-Verlag, Berlin and Heidelberg, 1990
[38] B. Bleaney, K. D. Bowers, *Proc.R.Soc.London, Ser. A* 1952, **97**, 451.
[39] P. W. Anderson, *Phys. Rev.* 1950, **79**, 350.
[40] P. W. Anderson in Theory of the Magnetic Interaction: Exchange in Insulators and Superconductors, Turnbull, F.; Seitz, F. Eds.; 1963, Academic Press, New York, Vol. 14, p. 99.
[41] C. J. Calzado, J. Cabrero, J. P. Malrieu, R. Caballol, J. Chem. Phys. 2002, **116**, 2728.
[42] C. J. Calzado, J. Cabrero, J. P. Malrieu, R. Caballol, J. Chem. Phys. 2002, **116**, 3985.
[43] C. de Graaf, C. Sousa, I. de P.R. Moreira, F. Illas, J. Phys. Chem. A 2001, **105**, 11371.
[44] C. J. Calzado, C. Angeli, D. Taratiel, R. Caballol, J. P. Malrieu, *J. Chem. Phys.* 2009, **131**, 044327.
[45] Ph. de Loth, P. Karafiloglou, J.P. Daudey, O. Kahn,. *J. Am. Chem. Soc.* 1988, **110**, 76.

PART III

FLEXIBLE COORDINATION AND NON-COORDINATION SUPRAMOLECULAR FRAMEWORK: DYNAMIC STRUCTURAL TRANSFORMATION WITH CHROMOTROPISM

A great interest of transition metal complex-assemblies in inorganic-organic hybrid framework materials has recently been devoted to the development of rational synthetic routes to novel one-, two- and three-dimensional crystal frameworks, due to their potential applications in many areas. The molecule-based crystal is a characteristic of the assemblage which is dissimilar to inorganic assemblage. This is ascribed to a variety of coordination geometries of building blocks and the coordination numbers. Furthermore, the functionality of organic and inorganic ligands as a connector is essential for the formation of coordination network structures and the intermolecular interactions involving hydrogen bonding and π-π stacking which all are necessary to rational design of crystal frameworks together with the fine tuning their functional properties.

This part deals with the structural dynamics with chromotropism in flexible coordination and non-coordination supramolecular framework. Recently, flexible and dynamic coordination compounds, which can change their structures in response to external stimuli, have attracted growing interest since they are important for the development of certain devices and sensors. Structural transformations involving coordination polymers and networks are more studied recently. These kinds of solid-state structural transformation not only directly reflect the relationship between the structures involved but also provide the effects on the properties of coordination polymers with small structural changes. Several types of structural transformations are primarily influenced by the following pathways, including the expansions of the metal coordination numbers, thermal dissociation/association, condensation, rearrangement of bonds or the removal or exchange of solvents. The guest-induced crystalline-to-amorphous transformation and the guest-induced backward transformation are typically found in the dynamic and flexible coordination frameworks supported by weak intermolecular interactions, such as hydrogen bonds, π-π stacking, van der Waals forces and others [1-20]. Therefore, the guest molecules may also play a key role by acting as an essential support to the cavity of the host framework. This part can be separated into four topics:

III-1 Solvent induced reversible crystal-to-amorphous transformation properties of cobalt(II) 4-aminomethylpyridine-sulfate with chromotropism

Introduction

From our previous work, we reported the reversible thermal dehydration and rehydration of the supramolecular frameworks $[M(H_2O)_4(ampyz)_2][M(H_2O)_6](SO_4)_2(H_2O)_2$ (M = Co^{II}, Fe^{II} and mixed Co^{II}/Fe^{II}, ampyz = 2-aminopyrazine) [21] and Co(II)-3,5-pyridinedicarboxylate compounds [22]. These compounds exhibit water-induced reversible crystal-to-amorphous transformations with chromotropism. The reversibility is driven by very strong hydrogen bonding between lattice and coordinated water molecules and sulfate anions. In this contribution, it is clearly known that sulfate is found as a framework former which has diverse coordination chemistry to transition metal ions, sometimes displaying more than one coordination mode in a single framework. Sulfate is also a very suitable anion for the construction of hydrogen bonded networks because it readily forms strong hydrogen bonds [23]. In our study, we sought to synthesize the coordination compounds with the strong (classical) hydrogen bonding properties of the sulfate anion to produce solids which featured both coordination polymers and

hydrogen-bonding motifs in the extended structures. During achieving this aim, we successfully synthesized a new 3D supramolecular framework $[Co(Hampy)_2(H_2O)_4](SO_4)_2(H_2O)_3$ which contains the strong intermolecular hydrogen bonding generated from coordinated and uncoordinated water molecules, amino and sulfate groups. This compound shows a reversible crystal-to-amorphous transformation up on desorption and resorption processes, which is verified by elemental analysis, TG measurement, X-ray powder diffraction, as well as spectroscopic identification.

Results and discussion

Spectroscopic characterizations

The IR spectra of compound **1** show strong band in the region 3400–3000 cm^{-1} which can be assigned to the stretching ν(N–H) of the primary amine in the Hampy ligand overlapping with ν(O–H) of water molecules. The NH_3 scissoring mode [24] shows medium band at 1625 cm^{-1} and the strongest bands due to SO_4^{2-} stretching vibrations are observed around 1100 cm^{-1} [25]. Those of the dehydrated materials show similar spectra to that of the original crystalline compound **1**, but the broad band of ν(O–H) of water molecules disappeared. The solid-state UV-vis diffuse reflectance spectrum of **1** agrees with the typical d–d transition of high-spin Co(II) in octahedral geometry with two observed bands at 20 408 cm^{-1} (490 nm) and slightly less than 9 000 cm^{-1} (1100 nm), which are assigned to the $^4T_{1g} \rightarrow {}^4T_{1g}(P)$ and $^4T_{1g} \rightarrow {}^4T_{2g}$ transitions, respectively, the $^4T_{1g} \rightarrow {}^4A_{2g}$ transition expected at around 600 nm was not observed. The band around 28 571 cm^{-1} (350 nm) appear due to charge transfer transition and internal transition within Hampy.

*Crystal structure of $[Co(Hampy)_2(H_2O)_4](SO_4)_2(H_2O)_3$ (**1**)*

Compound **1** crystallizes in the monoclinic crystal system with the P $2_1/c$ space group. The crystal structure of **1** consists of a compound cation, two sulfate anions and three water molecules as shown in Fig.1 together with the numbering scheme. The Co(II) ion exhibits distorted octahedral coordination through four aqua ligands with the average Co–O distance of 2.0825(1) Å composing the basal plane and two trans nitrogen atoms from the monodentate Hampy ligand with Co–N distances of 2.156(3) and 2.168(3) Å occupying the axial sites. Both Hampy ligands are protonated at NH_2, leading to a mononuclear cation unit $[Co(Hampy)_2(H_2O)_4]^{4+}$. The $Co–N_{Hampy}$ lengths in the title compound are in good agreement with the corresponding distances reported for other mononuclear Co(II) compounds such as $[Co(na)_2(H_2O)_4](sac)_2$ [Co–N: 2.153(1) Å] [29], $[Co(ina)_2(H_2O)_4](sac)_2$ [Co–N: 2.169(1) Å] [30] but slightly different from those found in $[Co(dmpy)_2](sac)_2(H_2O)_2$ [Co–N: 2.034(2) Å] [31]. The $Co–O_{aqua}$ distances are in good agreement with those found in $[Co(4\text{-}acpy)_2(H_2O)_4](sac)_2$ [Co–O: 2.068(1)–2.099(1) Å] [32] and $[Co(mein)_2(H_2O)_4](sac)_2$ [Co–O: 2.085(2)–2.099(1) Å] [33]. The basal plane is planar with a slight tetrahedral twist of 1.05˚ and the Co atom lies 0.136 Å above the basal plane toward the axial site. The bond angles around octahedron are in the ranges of 85.47(13)–93.69(14)˚ and 177.27(12)–179.33(15)˚, which are close to the ideal octahedral geometry. In the extended molecular structure each mononuclear cation units are linked by π-π stacking via pyridine rings of Hampy moieties to build 1D chain (Fig. 2). Moreover, these chains are supported by electrostatic forces and the intermolecular hydrogen bonds involving oxygen atoms of sulfate anions, amine moieties on Hampy (N3 and N4), coordination waters in $[Co(Hampy)_2(H_2O)_4]^{4+}$ unit (O1–O4), and lattice water molecules, to provide an entire 3D supramolecular structure of **1** as shown in Fig. 3.

Thermogravimetric Analysis

The thermal gravimetric analysis (TGA) was recorded for the crystalline samples in the temperature range 30–800 ˚C. TGA curve of compound **1** is shown in Fig. 4. The first step of weight loss in the temperature range 30-180 ˚C (found, 22.05% and calcd, 21.17%) corresponds to the loss of all seven water molecules per formula unit, resulting to the dehydrated form of $[Co(Hampy)_2(SO_4)_2]$ (**1A**). This dehydrated form of **1A** is stable up to ≈200 ˚C and then rapidly decomposes to unidentified products.

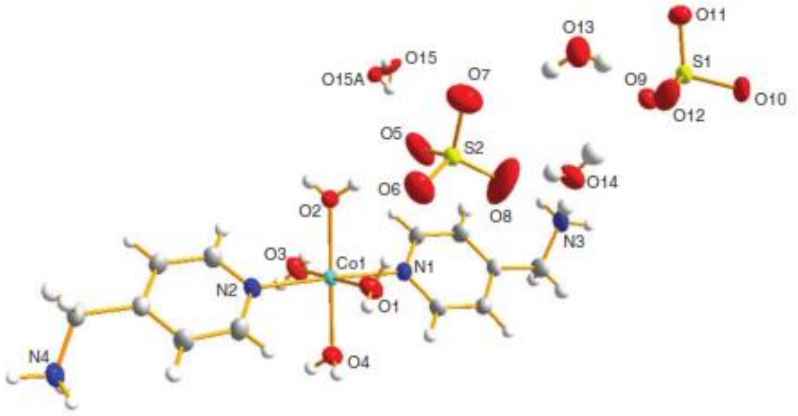

Fig. 1. Crystal structure and atomic labeling scheme of $[Co(Hampy)_2(H_2O)_4](SO_4)_2(H_2O)_3$ (**1**). The ellipsoid are shown at 50% probability level.

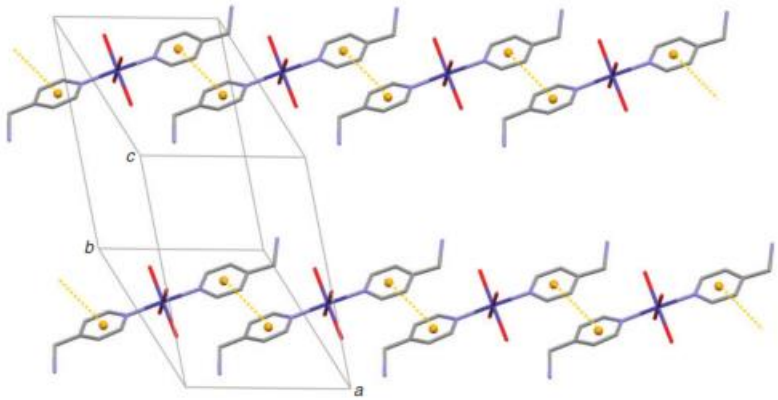

Fig. 2. 1D structure of compound **1** connected by face-to-face π-π interaction between pyridine rings of Hampy ligand. Hydrogen atoms, sulfate anions and lattice water molecules are omitted for clarity.

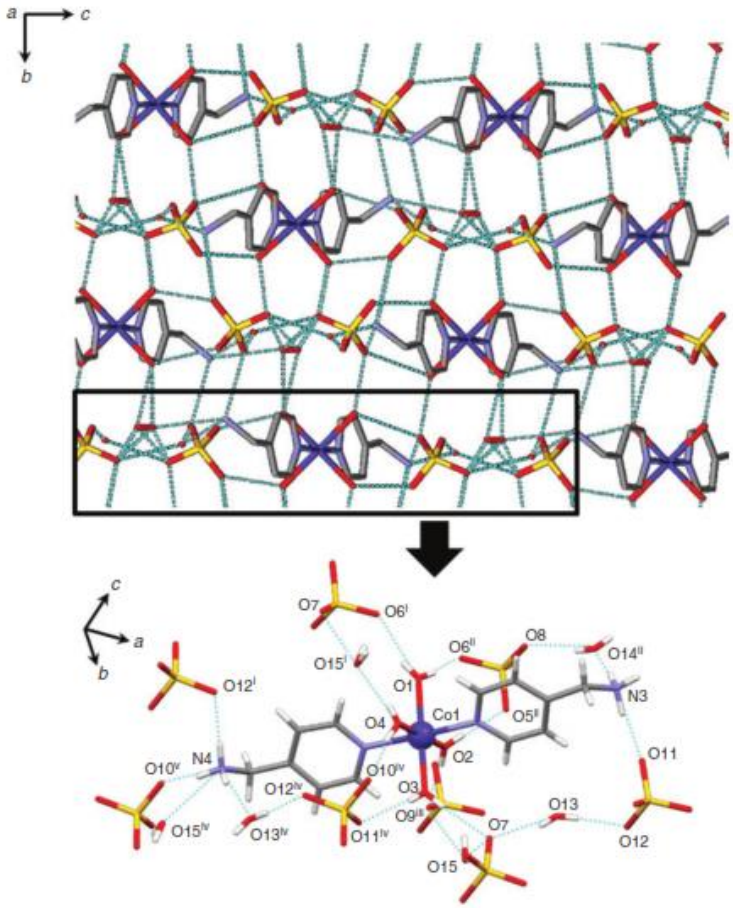

Fig. 3. 3D packing structure of compound **1** in *bc* plane formed by intermolecular hydrogen bonding (blue dot lines) among layers through Hampy, sulfate anions, lattice and coordinated water molecules.

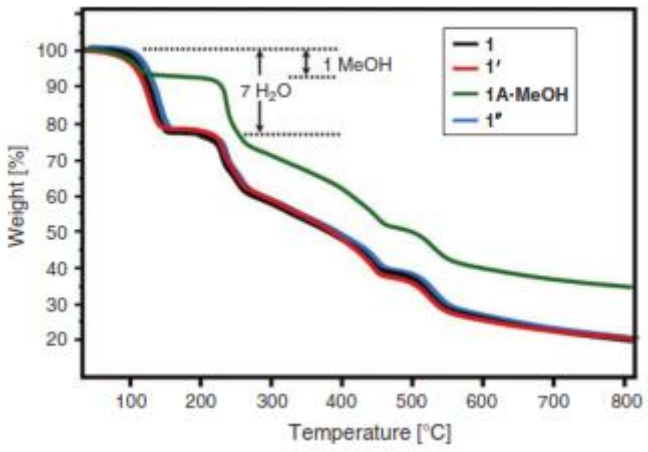

Fig. 4. TGA curves of as-synthesized **1**, the rehydrated form **1**′, the methanolic form **1A·MeOH** and the rehydrated form **1**″after exposed **1A·MeOH** in air for 3 h.

Solvent induced reversible crystal-to-amorphous transformation properties

Compound **1** contains both guest water and coordinated water. In order to get more insight into the dynamic properties relative to these water molecules, the dehydration and

rehydration processes were performed and verified by elemental analyses, TGA, XRPD and spectroscopic techniques. Interestingly, the water molecules can be readsorbed fully by exposing the evacuated samples to water vapor at room temperatures, evidenced by elemental analysis. The heating and exposing procedures were repeated for several times to demonstrate the reversibility of the de- and rehydration processes.

The most distinguished feature of the crystals of **1** is that it undergoes the water induced reversible crystal-to-amorphous transformation with chromotropism driven by thermal dehydration and rehydration. When the single crystals of **1** was heated to 200 ˚C in air and maintained at this temperature for 2 h, these crystals suddenly lose crystallinity and the color changes from orange (**1**) to purple (**1A**). The elemental analysis (Anal. Calcd: C, 30.71; H, 3.87; N, 11.94%. Found: C, 30.48; H, 3.70; N, 12.29%) and powder X-ray diffraction results (Fig. 5c) indicate that the chemical composition of the non-crystalline solid is $[Co(Hampy)_2(SO_4)_2]$ (**1A**) in an amorphous powder which is formed by the collapse of supramolecular structure of **1** accompanied with the destruction of hydrogen bonding network when all water molecules are removed. Interestingly, the amorphous form **1A** can be restored to the crystalline form $[Co(Hampy)_2(H_2O)_4](SO_4)_2(H_2O)_3$ (**1´**) in which the color returns to the original crystalline one after being exposed in air for 24 h, as confirmed by the elemental analysis (Anal. Calcd: C, 24.20; H, 5.42; N, 9.41%. Found: C, 24.10; H, 5.27; N, 9.30%) and the XRPD measurement results. The restored solid has the same XRPD pattern as the simulated one from single crystal X-ray diffraction data of **1** (see Figs. 5a and 5d). These results suggest the crystalline-to-amorphous and reversible amorphous-to-crystalline transformations in the supramolecular framework of **1** induced by the hydration control.

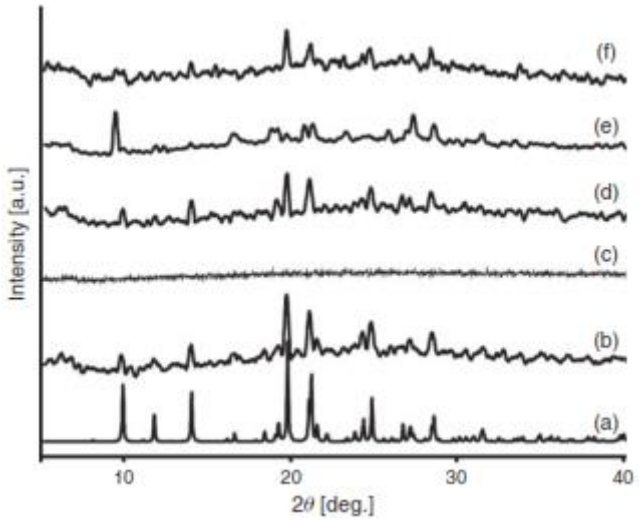

Fig. 5. The XRPD patterns for compound **1**; (a) simulated pattern based on the single-crystal X-ray raw data of **1**, (b) as-synthesized **1**, (c) dehydrated form **1A** that was prepared by drying at 200 ˚C under vacuum for 2 h. (d) rehydrated form **1´** after exposed in air for 24 h, (e) the methanolic form **1A·MeOH** after exposed to methanol vapor for 1 day at room temperature and (f) the rehydrated form **1˝** after exposing **1A·MeOH** in airfor 3 h.

Furthermore, to verify the solvent-induced reversible structural transformation properties, the dehydrated $[Co(Hampy)_2(SO_4)_2]$ (**1A**) was further study with various solvents (methanol, ethanol, acetone, acetonitrile, dichloromethane and hexane) by exposing **1A** to

solvents vapor for 1 day at room temperature. The results show that the purple color of solid **1A** in all solvents vapor still remain, excluding that one in methanol vapor with the color change from purple (**1A**) to pink (**1A·MeOH**). Then, the pink solid **1A·MeOH** loses methanol molecule after exposed in air for 3 h and the color returned from pink to the original orange crystalline sample (**1**˝). Moreover, after heating **1A·MeOH** at 200 ˚C for 20 min the color changes from pink (**1A·MeOH**) to purple (**1A**) which manifests the reversible process with chromotropism. Therefore, the rehydrated form **1A** was heated and cooled for many times to repeat the reversibility of the de- and re-adsorption processes. The results exhibit the color shuttle change from purple to orange (exposed in air) and from purple to pink (exposed in MeOH vapor), suggesting the solvent-induced reversible structural transformation phenomenon.

These dynamic structural behaviors with chromotropism are summarized as the schematic representation in Fig. 6 and these were proved by TGA, XRPD and spectroscopic techniques. The TGA curve of **1A·MeOH** (see Fig 4, green line) indicates the release of one methanol molecule from $Co(Hampy)_2(SO_4)_2(MeOH)$ (**1A·MeOH**). While the TG curve of **1**˝ is found to be identical weight loss to that of **1** and **1**´, indicating the same compositions. The XRPD pattern of **1A·MeOH** and **1**˝ are shown in Figs. 5e and 5f. When the amorphous phase **1A** exposed to methanol vapor, the XRPD pattern is readily converted into the second crystalline form of **1A·MeOH** in which the color changes to pink and then returned to the original orange crystalline form **1**˝after evaporation of methanol in air for 3 h.

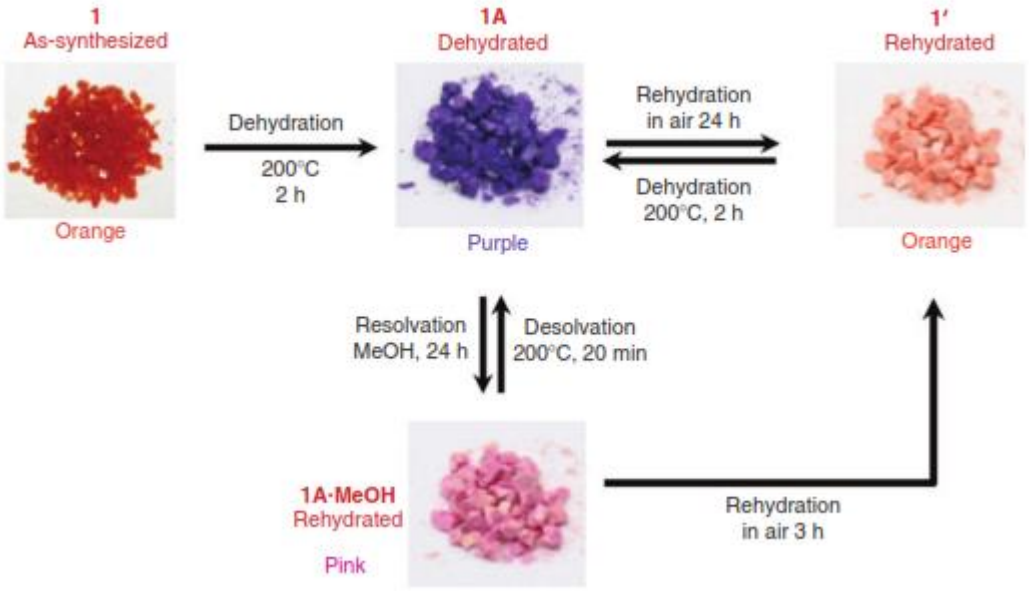

Fig. 6. Changes in color during de- and re-adsorption of water and methanol molecules in crystalline sample **1**.

In addition, the reversibility of the water or methanol adsorption and the change in the coordination environment can be visualized by the change in color of the compound [34-35]. This change of color can be attributed to the change of the crystal field splitting of the central Co^{2+} ions during the adsorption and removal of solvent molecules. The change in color of the Co compound prompted us to study the change in electronic transitions in the samples. For this, the solid-state UV-Vis diffuse reflectance spectra as shown in Fig. 7 clearly show that the bands observed in **1**, **1**´ and **1**˝correspond very well to the identical transitions causing the same color of products, and evidence that **1**, **1**´ and **1**˝have the same Co^{2+} environments. Whereas the amorphous form **1A** shows the different d-d transitions with two broad bands at 575 and around 1100 nm, and two

shoulders at around 660 and 417 nm, giving the distinctive purple color. The higher energy shoulder at 417 nm is due to charge transfer transition and internal transition within Hampy. That of the crystalline form **1A·MeOH** agrees with the typical d-d transitions of high spin Co^{2+} in distorted octahedral geometry with two broad bands at 540 and 1050 nm, with a shoulder around 640 nm, which are assigned to the $^4T_{1g} \rightarrow {}^4T_{1g}(P)$ and $^4T_{1g} \rightarrow {}^4T_{2g}$ and $^4T_{1g} \rightarrow {}^4A_{2g}$ transitions, respectively. The first broad band at 540 nm shows similar characteristic to that of the original crystalline form but slightly shifted around 50 nm to lower energy, resulting the distinctive pink color. The chromotropic behavior of this compound is principally ascribed to the changes of the d-orbital energy level, induced by the drastic change in the coordination environments around metal center during de- and re-adsorption processes [36]. As found in nature, cobalts-containing MOFs can have a wide range of colors which make it easy, in many cases, to identify different phases. The most common colors are a very light pink for octahedral coordinated ones and an intense blue for tetrahedral coordination. For distorted octahedra, the pink color can intensify to orange, dark red, purple and violet depending on the ligand and the type of distortions [37]. All of the results confirm the solvent-induced reversible transformation with chromotropism in supramolecular network of **1** and these are indication of high selective recognition of **1A** to water molecules. The selective methanol accommodation with chromotropism in dehydrated **1A** when comparing with many solvents excluding water could be attributed to the proper size of methanol molecules and weak host-guest interactions.

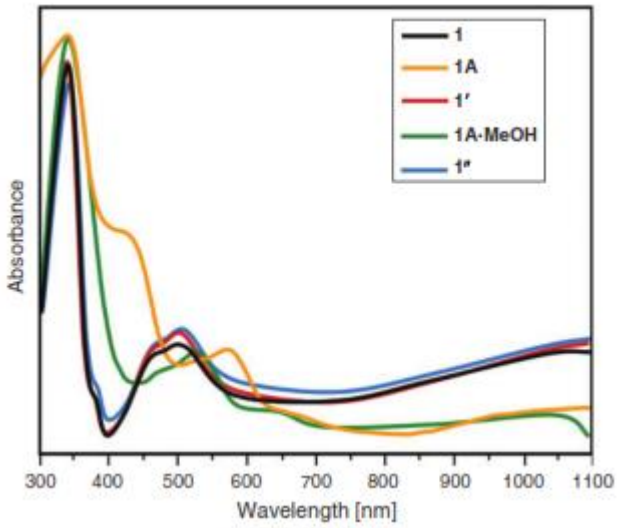

Fig. 7. The UV-vis diffuse reflectance spectra of as-synthesized **1**, the dehydrated form **1A**, the rehydrated form **1′**, the methanolic form **1A·MeOH** and the rehydrated form **1″**.

Interestingly, the conspicuous dynamic behavior of **1** is similar with that found in our previously published data of the mononuclear compounds $[M(H_2O)_4(ampyz)_2][M(H_2O)_6](SO_4)_2(H_2O)_2$, (M = Co^{II}, Fe^{II} and mixed Co^{II}/Fe^{II}) which exhibit crystal-to-amorphous transformation with chromotrophism [21]. Both **1** and those previous compounds contain abundant hydrogen donors and hydrogen acceptors from coordinated and uncoordinated water molecules, amino and sulfate groups to generate the intermolecular hydrogen bond interactions as well as π-π stacking. Thus, they have more accessible intermolecular hydrogen bonding that able to trigger the reversible crystal-to-amorphous transformation after de- and re-adsorption processes. In contrast, the reversible process are not found for the 2D framework $[Co(pydc)(H_2O)_2]_n$ [22]. This structure was not recovered but change to another

crystalline form of polymeric chain $[Co(pydc)(H_2O)_4]_n(H_2O)_n$ after the water re-adsorption process and the reversibility takes place between this resulting 1D compound and the dehydrated amorphous form after de- and re-hydration processes. This may be due to the less intermolecular interactions in the original structure which are not enough to trigger the structural transformation to the original 2D framework as compared to that of the title compound **1**.

The process of reversibility between the amorphous and crystalline materials only take place in the present of the water and methanol, and this could be a dissolution/recrystallization process rather than a solvent induced solid-state reaction as this involves the structural reorganization in supramolecular framework or rearrangements of the molecules interacting via intermolecular hydrogen bonds and non-covalent contacts [38].

In summary, $[Co(Hampy)_2(H_2O)_4](SO_4)_2(H_2O)_3$ with a three-dimensional supramolecular framework has been successfully prepared and structurally characterized. The crystal structure shows network of mononuclear units which contain intermolecular π-π stacking and hydrogen bonding interactions stabilizing the whole structure. Thermal decomposition, elemental analysis, XRPD and spectroscopic results indicate that the transformation from the crystal form of $[Co(Hampy)_2(H_2O)_4](SO_4)_2(H_2O)_3$ to the amorphous powder of $[Co(Hampy)_2(SO_4)_2]$ is reversible with the color changes. The original crystalline form is recovered from the collapsed amorphous sample by the restoration of water molecules. Moreover, the dried amorphous powder also transforms to the second crystalline form $Co(Hampy)_2(SO_4)_2(MeOH)$ after exposed in methanol vapor and then recovered to the original one in air. Thus the desorption/resorption processes involving the weak intermolecular interactions can trigger the reversible crystal-to-amorphous transformation with chromotropism for compounds **1** and the dried amorphous powder of $[Co(Hampy)_2(SO_4)_2]$ may be applied as an indicator for humidity and methanol vapor.

References

[1] E. Y. Lee, M. P. Suh, Angew. Chem., *Int. Ed.* **43** (2004) 2798.
[2] E. Y. Lee, S. Y. Jang, M. P. Suh, J. Am. Chem. Soc. **127** (2005) 6374.
[3] K. Biradha, M. Fujita, Angew. Chem., Int. Ed. **41**(2002) 3392.
[4] K. Biradha, Y. Hongo, M. Fujita, Angew. Chem., Int. Ed. **41** (2002) 3395.
[5] C. J. Kepert, M. J. Rosseinsky, Chem. Commun. (1999) 375.
[6] K. Takaoka, M. Kawano, M. Tominaga, M. Fujita, Angew. Chem., *Int. Ed.* **44** (2005) 2151.
[7] C.-D. Wu, W. Lin, Angew. Chem., *Int. Ed.* **44** (2005) 1958.
[8] D. N. Dybtsev, H. Chun, K. Kim, Angew. Chem., *Int. Ed.* **43** (2004) 5033.
[9] N. L. Toh, M. Nagarathinam, J. J. Vittal, Angew. Chem., *Int. Ed.* **44** (2005) 2237.
[10] T. H. Kim, Y. W. Shin, J. S. Kim, J. Kim, Angew. Chem., *Int. Ed.* **47** (2008) 685.
[11] J. Y. Lee, S. Y. Lee, W. Sim, K.M. Park, J. Kim, S. S. Lee, J. Am. Chem. Soc. **130** (2008) 6902.
[12] C. Hu, U. Englert, Angew. Chem., *Int. Ed.* **44** (2005) 2281.
[13] B. Rather, B. Moulton, R. D. B. Walsh, M. J. Zaworotko, Chem. Commun. (2002) 694.
[14] S. Oliver, A. Kuperman, A. Lough, G.A. Ozin, Chem. Mater. **8** (1996) 2391.
[15] W. Lin, O. R. Evans, R. G. Xiong, Z. Y. Wang, J. Am. Chem. Soc. **120** (1998) 13272.
[16] J.H. Kim, S.M. Hubig, S. V. Lindeman, J. K. Kochi, J. Am. Chem. Soc. **123** (2001) 87.
[17] J. J. Vittal, Coord. Chem. Rev. **251** (2007) 17.
[18] H. K. Chae, D. Y. Siberio-Perez, J. Kim, Y. Go, M. Eddaoudi,A. J. Matzger, M. O'Keeffe, O. M. Yaghi, Nature, **427** (2004) 523.
[19] P. Sozzani, S. Bracco, A. Comotti, L. Ferretti, R. Simonutti, Angew. Chem., *Int. Ed.* **44** (2005) 1816.

[20] T. K. Prasad, M. V. Rajasekharan, Cryst. Growth Des. **6** (2006) 488.
[21] J. Boonmak, M. Nakano, N. Chaichit, C. Pakawatchai, S. Youngme, Dalton Trans., **39** (2010) 8161.
[22] A. Cheansirisomboon, C. Pakawatchai, S. Youngme, Dalton Trans., **41** (2012) 10698.
[23] (a) T. J. Prior, B. Yotnoi, A. Rujiwatra, Polyhedron, **30** (2011) 259. (b) S.D. Huang, R.G. Xiong, P.H. Sotero, J. Solid State Chem. **138** (1998) 361.; (c) G.A. Jeffrey, An Introduction to Hydrogen Bonding, OUP, 1997.;
[24] J. R. Allan, A. D. Paton, K. Turvey, H. J. Bowley and D. L. Gerrad, Inorg. Chim. Acta, **134** (1987) 259.
[25] K. Nakamoto, in *Infrared and Raman Spectra of Inorganic and Coordination Compounds, 5th ed*, Wiley, New York, 1997.
[26] SAINT 4.0 Software Reference Manual; Siemens Analytical X-Ray Systems, Inc.: Madison, WI, 2000.
[27] Sheldrick, G. M. SADABS, Program for Empirical Absorption correction of Area Detector Data; University of Göttingen: Göttingen, Germany, 2000.
[28] Sheldrick, G. M. Acta Crystallogr. **A64** (2008) 112.
[29] E.E. Castellano, O.E. Piro, B.S. Parajon-Costa, E.J. Baran, Z. Naturforsch **57** (2002) 657.
[30] B. I. Uçar, H. Karabulut, O. Pasaõglu, A. Büuyükgüngör, Bulut, J. Mol. Struct. **787** (2006) 38.
[31] O. Andac, S. Guney, Y. Topcu, V. T. Yilmaz, W. T. A. Harrison, Acta Crystallogr. **C58** (2002) m17.
[32] Y. Çelik, E. Bozkurt, I. Uçar, B.Karabulut. Journal of Physics and Chemistry of Solids **73** (2012) 1010.
[33] E. Bozkurt, H. Ayaz, I. Uçar, B. Karabulut. Inorg. Chim. Acta **390** (2012) 1.
[34] K. Takaoka, M. Kawano, T. Hozumi, S. Ohkoshi, M. Fujita, Inorg. Chem. **45** (2006) 3976.
[35] M.-L. Sun, L. Zhang, Q.-P. Lin, J. Zhang, Y. -G. Yao, Cryst. Growth Des., **10** (2010) 1464.
[36] (a) D. Bradshaw, J. E. Warren, M. J. Rosseinsky, Science, 2007, **315**, 977.; (b) S. -J. Fu, C.-Y. Cheng, K.-J. Lin, Cryst. Growth Des. **7** (2007) 1381.; (c) C.- L. Chen, A. M. Goforth, M. D. Smith, C. -Y. Su, H.-C. zur Loye, Angew. Chem., *Int. Ed.*, **44** (2005) 6673.; (d) L.G. Beauvais, M. P. Shores, J. R. Long, J. Am. Chem. Soc., **122** (2000) 2673.
[37] M. Kurmoo, Chem. Soc. Rev., **38** (2009) 1353.
[38] A. N. Khlobystov, N. R. Champness, C. J. Roberts, S. J. B. Tendler, C. Thompson, M. Schroder, CrystEngComm., **4**(7), (2002) 426-431

III-2 Flexible metal supramolecular framework of 2D cobalt(II) coordination polymer with water-induced reversible crystal-to-amorphous transformation

The construction of metal-organic frameworks (MOFs) is currently attracting considerable attention because of their intriguing molecular topologies and crystal packing motifs, along with their potential applications such as adsorption, separation, ion exchange, catalysis, magnetism, optics, and electrical conductivity [1] and [2]. One of the important properties of MOFs is the framework flexibility which exhibits solid-state structural transformations with breaking, making, or rearrangement of bonds driven by chemical stimuli [3], [4] and [5]. The structural transformations are generally accompanied by removal or exchange of guest, changes in coordination number of metal containing nodes, and conformational changes in flexible parts of organic ligands [3]. The water-induced structural reversible transformation is typically found in the dynamic and flexible coordination frameworks supported by weak intermolecular interactions, such as hydrogen bonds, π–π stacking, van der Waals forces, and others. Therefore, the solvent molecules may also play a key role by acting as an essential support to the structure of the host framework and it is important for expanding the field of crystal engineering by controlling the weak interaction of MOFs [3], [4] and [5].

From our previous work, the reversible thermal dehydration and rehydration of 1D coordination framework $[Co(3,5\text{-pydc})(H_2O)_4]_n(H_2O)_n$; 3,5-pydc = 3,5-pyridinedicarboxylate have been reported [6]. The reversibility is driven by strong hydrogen bonding between guest water and coordinated water molecules and other components. Without guest water like a 2D coordination network $[Co(3,5\text{-pydc})(H_2O)_2]_n$, the irreversibility is observed. Herein, we report the contradictory case, the highly stable 3D supramolecular framework $[Co(4,4'\text{-bipy})(pro)_2(H_2O)]$ (**1**). Its 2D coordination layers are assembled by hydrogen bonding interactions, leading to a 3D supramolecular framework. This compound shows a reversible crystal-to-amorphous transformation upon desorption and resorption processes.

Single-crystal X-ray structural analysis shows that compound **1** is a 2D coordination network. The asymmetric unit consists of one cobalt atom, one 4,4′-bipy ligand, two pro ligands, and one coordinated water molecule (Fig. 1a) [7] and [7]. Each Co(II) ion exhibits a distorted octahedral geometry; the coordinate environment comprises of two O atoms from two different pro bridges, one O atom from water molecule and one O atom from a monodentate, terminal pro ligand, forming a square base (Fig. 1b), while two axial positions of octahedron are completed by two N atoms from different 4,4′-bipy ligands. These Co(II) ions are linked by the bridging 4,4′-bipy ligand (N(1) and N(2)) in *a* axis and the bridging pro ligand (O(3) and O(4)) along *c* axis, leading to an infinite 2D layer network (Fig. 1c) leaving a water molecule and a remaining monodentate propionate as the terminal ligands in which both coordinated water and the uncoordinated O(2) of non-bridging propionate ligand are hydrogen-bonded (O(5)—H(6w)···O(2)) to one another. These 2D layers of compound **1** are linked to one another by strong interlayer hydrogen bonding among the uncoordinated O atom of the monodentate, terminal propionate ligands and H atoms of 4,4′-bipy ligand (C(2)—H(2)···O(2) and C(9)—H(7)···O(2)) with H···O distances of 2.481(19) and 2.364(19) Å, leading to a 3D supramolecular framework.

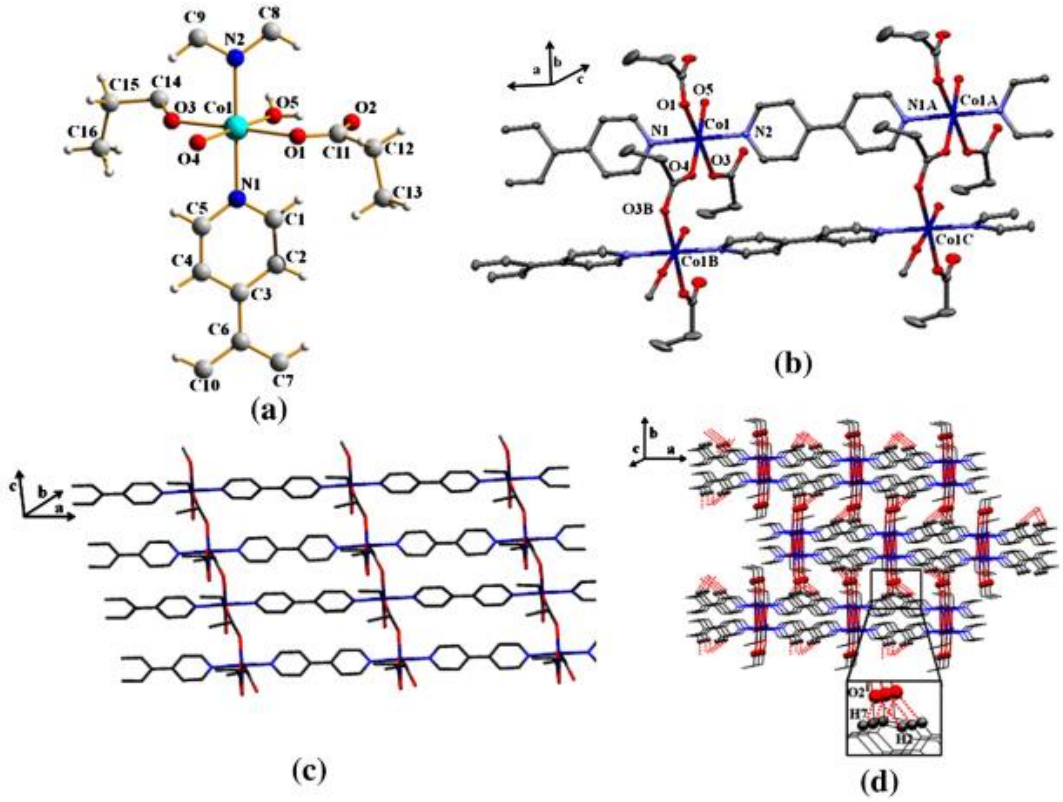

Fig. 1. Perspective view of **1** showing, (a) asymmetric unit and (b) coordination environment of the cobalt atom. (c) Crystal packing diagram of 2D layer structure in *ac* plane. (d) Crystal packing diagram of 3D supramolecular network, assembled by hydrogen bonding interactions. [Symmetry codes: A = −*x*, −*y*, −*z*; B = −*x*, 1/2-+*y*, 1/2-*z*; C = *x*, 1/2-*y*, 1/2 + *z*, i = 2 − *x*, 1 − *y*, 1 − *z*].

To assess the thermal stability, TGA was recorded for the single-phase polycrystalline samples in the temperature range of 30–800 °C. During the heating process, the TGA profile of **1** indicates the release of one coordinated water molecule at the first step of weight loss which is in the temperature range of 100–134 °C (found, 3.81%; anal. calcd, 4.21%), resulting to the dehydrated form of Co(4,4′-bipy)(pro)$_2$ (**1A**), which is stable up to ≈ 215 °C and then the structure rapidly decomposes at higher temperature.

The dynamic structural behaviors of **1** relating to their dehydration and rehydration processes are studied by elemental analyses, XRPD, and spectroscopic techniques. When the single crystals of **1** were heated to 150 °C in air for 20 min, these crystals suddenly lose their crystallinity and the color changes from orange (**1**) to pink (**1A**). Then this non-crystalline solid was exposed to water vapor for 12 h and the color of the solid **1A**was returned to that of the original crystals **1**′, as shown in Fig. 2 . For this, the solid-state UV–vis diffuse reflectance spectra, clearly show that the bands observed in **1** and **1**′ correspond very well to the identical transitions causing the same color of products, and evidence that **1** and **1**′ have the same Co(II) environments. This spectral feature agrees with the typical d–d transitions of high spin Co(II) in distorted octahedral geometry with two broad bands at 471 and 1180 nm, assigned to the ν_3:$^4T_{1g} \rightarrow {}^4T_{1g}(P)$ and ν_1: $^4T_{1g} \rightarrow {}^4T_{2g}$, transitions, respectively [9]. Whereas the amorphous form **1A** shows different d–d transitions with three broad bands, ν_3: $^4T_{1g} \rightarrow {}^4T_{1g}(P)$ which is splitted into two shoulders at around 484 nm and 518 nm (^4E_g and $^4A_{2g}$), ν_2:$^4T_{1g} \rightarrow {}^4A_{2g}$ at 656 nm and then ν_1: $^4T_{1g} \rightarrow {}^4T_{2g}$ which is splitted into two shoulders at around 934 nm and 1337 nm

($^4B_{2g}$ and ^4E_g), giving the distinctive pink color and corresponding to the tetragonally distorted octahedral geometry [9]. Furthermore, the IR spectra also confirm the structural transformation behavior in **1**, as shown in Fig S7. In**1A**, the broad and strong peaks of O—H stretching around 3300 cm^{-1} and H—O—H bending around 1500–1600 cm^{-1} of coordinated water molecule disappear, resulting to the sharper IR spectrum with different splitting feature and a shift in some peak positions. In contrast, these features are removed in the IR spectrum of the rehydrated form **1′**, which are identical to that of the as-synthesized **1**. The XRPD pattern of the as-synthesized product closely match the simulated one from the single-crystal data. However, the XRPD pattern of dehydrated **1A** shows peak disappearance, indicating that the dehydrated Co(4,4′-bipy)(pro)$_2$ (**1A**) is in an amorphous phase (anal. calcd: C, 53.19; H, 5.02; N, 7.75%. Found: C, 52.26; H, 5.04; N, 7.61%) which is formed by the collapse of supramolecular structure of **1** accompanied with the destruction of hydrogen bonding networks when all water molecules are removed. Interestingly, this amorphous phase **1A** can be restored to the original crystalline phase of **1′** in which the color returns to that of the original color after being exposed in water vapor for 24 h, as indicated by elemental analysis with the chemical composition of [Co(4,4′-bipy)(pro)$_2$(H_2O)] (**1′**) (anal. calcd: C, 50.67; H, 5.32; N, 7.39%. Found: C, 50.34; H, 5.28; N, 7.42%) and the XRPD measurement results. The restored solid has the same XRPD pattern as the simulated one from the single-crystal X-ray diffraction data of **1**. This behavior was also investigated for other solvents vapor such as methanol, ethanol, acetone, acetonitrile, dichloromethane, DMF and DMSO, but sensitive only with water vapor.

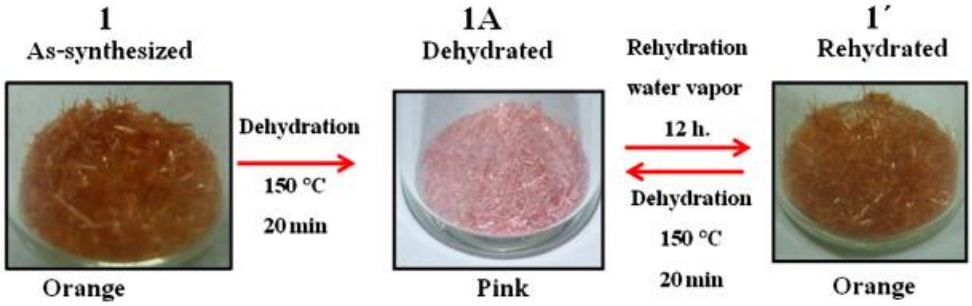

Fig. 2. Change in color during de- and rehydration in crystalline sample.

In the present case, although water molecule does not directly involve in the reversible crystal-to-amorphous transformation but induces the strong interlayer hydrogen bonding, after heating, water molecule is removed with the breaking of O(5)—H(6w)···O(2) hydrogen bonds in the layer. This consequently breaks the strong interlayer hydrogen bonds (C(2)—H(2)···O(2) and C(9)—H(7)···O(2)) as the uncoordinated O(2) atom of terminal propionate group may move toward metal center for weak coordination, thus immediately destroying such hydrogen bonds between layers.

In summary, a new 2D coordination framework **1** has been successfully prepared and structurally characterized. The layer networks are linked to one another by hydrogen bonds, leading to a 3D supramolecular framework. Compound **1** exhibits reversible structural transformation from the crystal form (**1**) to the amorphous powder (**1A**) with the color changes, triggered by the weak intermolecular interactions during the removal and restoration of water molecule. This work may have potential application as adsorbent material for moisture.

References

[1] Z.-Y. Liu, E.-C. Y, L.-L. Li, X.-J. Z, Dalton Trans., 41 (2012), pp. 6827–6832
[2] T.R. Cook, Y.-R. Zheng, P.J. Stang, Chem. Rev., 113 (2013), pp. 734–777

[3] A. Kondo, H. Kajiro, H. Noguchi, L. Carlucci, D.M. Proserpio, G. Ciani, K. Kato, M. Takata, H. Seki, M. Sakamoto, Y. Hattori, F. Okino, K. Maeda, T. Ohba, K. Kaneko, H. Kanoh, J. Am. Chem. Soc., 133 (2011), pp. 10512–10522
[4] J. Boonmak, M. Nakano, N. Chaichit, C. Pakawatchai, S. Youngme, Dalton Trans., 39 (2010), pp. 8161–8167
[5] A. Cheansirisomboon, C. Pakawatchai, S. Youngme, Aust. J. Chem., 66 (2013), pp. 477–484
[6] A. Cheansirisomboon, C. Pakawatchai, S. Youngme, Dalton Trans., 41 (2012), pp. 10698–10706
[7] Crystal data for **1**: formula: $CoC_{16}H_{20}N_2O_5$, M_r = 379.27, Monoclinic, space group $P2_1/c$,a = 11.4322(5), b = 17.8277(7), c = 8.5398(3) Å, α = 90.00° β = 103.9910(10)° λ = 90.00°V = 1688.86(12) Å^3, Z = 4; D_c = 1.492 g cm^{-3}, F(000) = 788.0, T = 150(2) K, R_1 = 0.0318,wR_2 = 0.0723, for 4197(0.0300) unique reflections and 259 parameters, S = 1.081. Structural data for **1** was collected on a Bruker Smart Apex CCD with graphite monochromated Mo Kα radiation. The struture was solved by direct methods and refined with the full matrix least-squares technique using the SHELXS-97 and SHELXL-97 programs [8]. CCDC: **1**, 977060.
[8] G.M. Sheldrick, University of Göttingen, Göttingen, Germany (1997)
[9] S.-J. Fu, C.-Y. Cheng, K.-J. Lin, Cryst. Growth Des., 7 (2007), pp. 1381–1384

III-3 Water-induced reversible crystal-to-amorphous transformation property of $[Co_2(2,4\text{-}pydc)_2(bpa)(H_2O)_6](H2O)_2$

The design and synthesis of extended frameworks via supramolecular interactions represent a new area of considerable interest [1] and [2]. In particular, hydrogen bonding has been exploited for molecular recognition associated with biological activity, and for engineering of molecular solids [1] and [2]. Much progress has been made in the construction of organic building blocks into 1D, 2D and 3D hydrogen-bonding architectures, and the use of metal complexes as building blocks to assemble multidimensional frameworks by hydrogen bonding has also attracted much recent attention [3]. Recently, flexible and dynamic coordination compounds, which can change their structures in response to external stimuli, have attracted growing interest since they are important for the development of certain devices and sensors [4],[5],[6],[7],[8], [9],[10]and[11].

The guest-induced crystalline-to-amorphous transformation and the guest-induced reverse transformation are typically found in the dynamic and flexible coordination frameworks supported by weak intermolecular interactions, such as hydrogen bonds, π–π stacking, van der Waals forces, and others. Therefore, the guest molecules may also play a key role by acting as an essential support to the structure of the host framework [12], [13] and [14]. From our previous works, we reported the reversible thermal dehydration and rehydration of the supramolecular frameworks, $[M(H_2O)_4(ampyz)_2][M(H_2O)_6](SO_4)_2(H_2O)_2$ (M = Co^{II}, Fe^{II} and mixed Co^{II}/Fe^{II}, ampyz = 2-aminopyrazine) [15] and $[Co(3,5\text{-}pydc)(H_2O)_2]_n$, $[Co(3,5\text{-}pydc)(H_2O)_4]_n(H_2O)_n$; 3,5-pydc = 3,5-pyridinedicarboxylate [16] and then $[Co(Hampy)_2(H_2O)_4](SO_4)_2(H_2O)_3$; ampy = 4-aminomethylpyridine [17]. The reversibility is driven by strong hydrogen bonding between lattice and coordinated water molecules and other components.

Herein, we report highly stable 3D supramolecular framework $[Co_2(2,4\text{-}pydc)_2(bpa)(H_2O)_6]$ $(H_2O)_2$ (**1**) which contains strong intermolecular hydrogen bonding generated from coordinated and uncoordinated water molecules (Fig. 1). This compound shows a reversible crystal-to-amorphous transformation upon desorption and resorption processes, which is verified

by elemental analysis, thermogravimetric analysis (TGA), X-ray powder diffraction (XRPD), as well as spectroscopic identification.

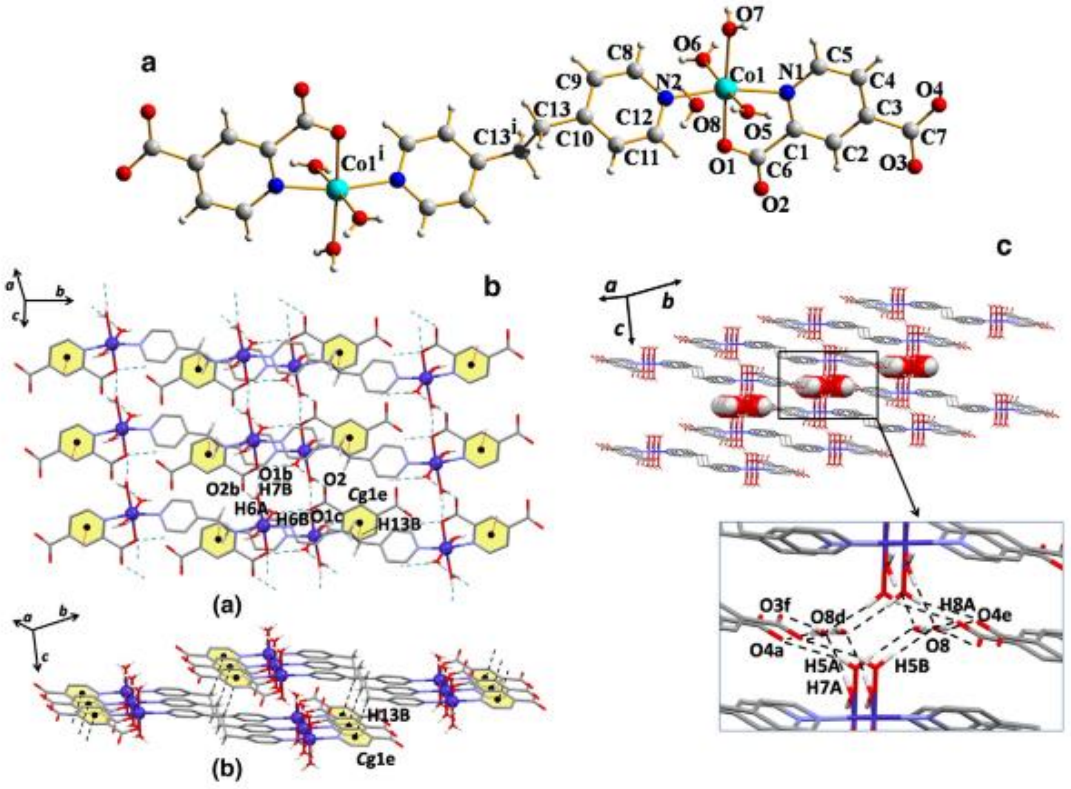

Fig. 1. (a) Perspective view of the coordination environment of the cobalt atom in compound **1**. (b) Crystal packing diagram of two-dimensional supramolecular structure of compound **1**, via hydrogen bonding and C–H···π interactions b(a) top view and b(b) side view. Hydrogen atoms on aromatic rings are omitted for clarity. (c) Crystal packing diagram of 3D supramolecular network of compound **1**, assembled by hydrogen bonding interactions. Hydrogen atoms on carbon atoms are omitted for clarity. [Symmetry codes: (i) = 1-x, -y, -z; (a) = 2-x, 2-y, 1-z; (b) =− 1 + x, y, z; (c) = 1-x, 1-y, -z; (d) = 1-x, 1-y, 1-z; (e) = x, -1 + y, z and (f) = 1 + x, 1 + y, z].

Single-crystal X-ray structural analysis shows that complex **1** is a 3D supramolecular network structure crystallized in the triclinic *P*-1 space group [18]. The symmetry-related dinuclear compound consisting of two six coordinated cobalt atoms, one bpa ligand, two 2,4-pydc ligands and two lattice water molecules. Each Co^{II} ion is coordinated by one oxygen atom and one nitrogen atom from 2,4-pydc bidentate chelate ligand, one nitrogen atom of bpa ligand and three water molecules, this feature give a distorted octahedral geometry with CoN_2O_4 chromophore (Fig. 1a). The bpa bidentate bridging ligand links between both chromophores in the axial positions. The Co1–N and Co1–O distances are in the range of 2.1081(14)–2.1466(14) Å and 2.0696(15)–2.1116(16) Å, respectively. The selected bond distances and angles are shown in Supplementary Material. These dimeric units are connected to each other via hydrogen bonds with distances of 2.724(2), 2.974(2) and 2.970 (2) Å for O6–H6A···O2b, O7–H7B···O1b and O6–H6B···O1c, respectively and C–H···π interactions with distances of 2.78 Å for C13–H13B···*C*g1e, generating two-dimensional network as shown in Fig. 1b. These 2D layers are assembled into a three-dimensional supramolecular framework as by hydrogen-bonding interactions through lattice water molecules with distances of 2.803(2) Å, 2.682(2), 2.764(3) and 2.680(2) for O5–H5B···O8,

O7–H7A···O8d, O8–H8A···O4e and O8–H8B···O3f and between coordinated water and caboxylate group of 2,4-pydc ligand with distance of 2.644(2) Å for O5–H5A···O4a (Fig. 1c).

Compound **1** contains both guest and coordinated water molecules. The stability and dynamic structural behavior of **1** relating to their dehydration and rehydration processes are studied by TGA, elemental analyses, powder X-ray diffraction UV–vis and IR spectra, and XRPD. TGA reveals a weight loss of six water molecules in a range of 100–170 °C (calcd 11.6%, obsd 11.3%). When the single-crystals of **1** were heated at 200 °C in air for 40 min, these crystals suddenly lose their crystallinity and the color changed from orange to purple. Then these non-crystalline solids **1A** were exposed to the laboratory air for 24 h and the color of solids **1A** returned to that of original crystals. Consequently, the bulk sample of **1** was used to study in detail. The dehydrated **1A** was obtained by heating the bulk samples at 200 °C in air for 24 h and the rehydrated **1′** was obtained by exposing the dehydrated sample to water vapor for 24 h at room temperature without condensation (Fig. 2). The elemental analysis, TGA and XRPD pattern results indicate that the chemical composition of the powder is Co_2(2,4-pydc)$_2$(bpe)(H_2O)$_2$ (**1A**) in an amorphous phase (Anal. Calcd: C, 46.58; H, 3.61; N, 8.36%. Found: C, 45.91; H, 3.92; N, 7.95%). Interestingly, this amorphous phase **1A** can be restored to the original crystalline phase of **1′** in which the color returns to that of the original after being exposed in water vapor for 24 h, as indicated by elemental analysis with the chemical composition of [Co_2(2,4-pydc)$_2$(bpe)(H_2O)$_6$](H_2O)$_2$ (**1**) (Anal. Calcd: C, 40.22; H, 4.41; N, 7.22%. Found: C, 39.54; H, 4.43; N, 7.06%) and the XRPD measurement results. The restored solid has the same XRPD pattern as the simulated one from the single-crystal X-ray diffraction data of **1**, indicating that**1′** and **1** are the same compound. These results suggest the crystalline-to-amorphous and amorphous-to-crystalline transformations in supramolecular network of **1** triggered by the hydration control. The heating and exposing procedures were repeated several times to demonstrate the reversibility of the de- and rehydration processes. Furthermore, this structural change of bulk sample is accompanied with a remarkable color change (Fig. 2) as confirmed by the solid-state UV–vis diffuse reflectance spectra. The electronic spectra clearly show that the bands observed in **1** and **1′** correspond very well to the identical transitions causing the same color of products, and evidence that **1** and **1′** have the same Co^{II} environments. That of the crystalline form **1** and **1′** agrees with the typical d–d transitions of high spin Co^{II} in distorted octahedral geometry with two broad bands at 498 and 1146 nm, which are assigned to the $^4T_{1g} \rightarrow {}^4T_{1g}$(P), and $^4T_{1g} \rightarrow {}^4T_{2g}$transitions, respectively. The amorphous form **1A** also shows the same d–d transitions with two broad bands, but remarkably shifted to 560 ($\Delta \sim 62$) and 1190 ($\Delta \sim 44$) nm, resulting in distinctive purple color and corresponding to the high-spin Co^{II} in distorted octahedral geometry with different type of distortion [19]. The chromotropic behavior of this compound is principally ascribed to the changes of the d-orbital energy level, induced by the drastic change in the coordination environments around the metal center during water de- and resorption processes. In addition, these results agree with the reversible change of the vibrational band in IR spectra where the broader bands are observed for the amorphous phase. In contrast, this feature is removed for the IR spectra of the rehydrated form, which are identical to those of the as-synthesized **1**.

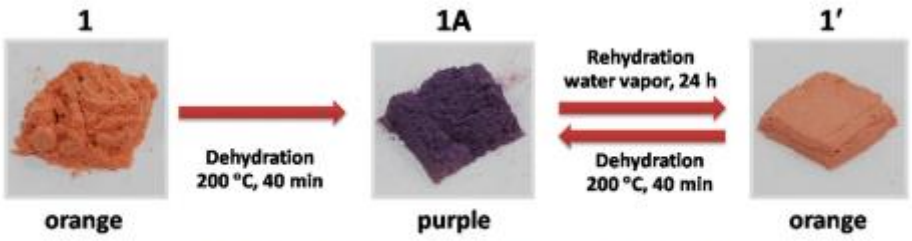

Fig. 2. Change in color during de- and rehydration processes in bulk samples.

Fig. 2. Change in color during de- and rehydration processes in bulk samples.

All of these results confirm the water-induced crystalline-to-amorphous phase transformation in the supramolecular network of **1** with reversible processes. Remarkably, the reversibility of the water adsorption and the change in the coordination environment can be visualized by the change in color of the compound. This behavior takes place in water which could be a dissolution/recrystallization process rather than a solvent-induced solid-state reaction as this involves structural reorganization of the supramolecular framework or rearrangements of the molecules interacting by inter-molecular hydrogen bonds and non-covalent contacts [20].

In summary, a novel 3D supramolecular network formed by hydrogen-bonding and C–H···π interaction, has been synthesized and structurally characterized. The successful synthesis of **1** shows that strong intermolecular interactions (C–H···π and hydrogen-bonding interactions) contribute to the formation of higher-dimensional network. Thermal decomposition, elemental analysis, XRPD, and spectroscopic results indicate that the transformation from the crystal form of $[Co_2(2,4\text{-pydc})_2(bpa)(H_2O)_6](H_2O)_2$ (**1**) to the amorphous powder of $Co_2(2,4\text{-pydc})_2(bpa)(H_2O)_2$ (**1A**) is reversible with the color changes. The original crystalline form is recovered from the collapsed amorphous sample by the restoration of water molecules. Thus, the desorption/resorption processes involving the weak intermolecular interactions can trigger the reversible crystal-to-amorphous transformation.

References

[1] G.A. Hogan, N.P. Rath, A.M. Beatty, Cryst. Growth Des., 11 (2011), pp. 3740–3743
[2] T.R. Cook, Y.-R. Zheng, P.J. Stang, Chem. Rev., 113 (2013), pp. 734–777
[3] S.-S. Yu, H. Zhou, H.-B. Duan**,** Synth. React. Inorg. Met. Org. Nano Met. Chem., 43 (2013), pp. 1521–1524
[4] E.Y. Lee, M.P. Suh**,** Angew. Chem. Int. Ed., 43 (2004), pp. 2798–2801
[5] E.Y. Lee, S.Y. Jang, M.P. Suh, J. Am. Chem. Soc., 127 (2005), pp. 6374–6381
[6] K. Biradha, M. Fujita, Angew. Chem. Int. Ed., 41 (2002), pp. 3392–3395
[7] K. Biradha, Y. Hongo, M. Fujita, Angew. Chem. Int. Ed., 41 (2002), pp. 3395–3398
[8] D.-X. Xue, W.-X. Zhang, X.-M. Chen, H.-Z. Wang, Chem. Commun. (2008), pp. 1551–1553
[9] K. Takaoka, M. Kawano, M. Tominaga, M. Fujita, Angew. Chem. Int. Ed., 44 (2005), pp. 2151–2154
[10] C.-D. Wu, W. Lin, Angew. Chem. Int. Ed., 44 (2005), pp. 1958–1961
[11] D.N. Dybtsev, H. Chun, K. Kim, Angew. Chem. Int. Ed., 43 (2004), pp. 5033–5036

[12] H.K. Chae, D.Y. Siberio-Pérez, J. Kim, Y.B. Go, M. Eddaoudi, A.J. Matzger, M. O'Keeffe, O.M. Yaghi, Nature, 427 (2004), pp. 523–527
[13] P. Sozzani, S. Bracco, A. Comotti, L. Ferretti, R. Simonutti, Angew. Chem. Int. Ed., 44 (2005), pp. 1816–1820

[14] T.K. Prasad, M.V. Rajasekharan, Cryst. Growth Des., 6 (2006), pp. 488–491
[15] J. Boonmak, M. Nakano, N. Chaichit, C. Pakawatchai, S. Youngme **,** Dalton Trans., 39 (2010), pp. 8161–8167
[16] A. Cheansirisomboon, C. Pakawatchai, S. Youngme, Dalton Trans., 41 (2012), pp. 10698–10706
[17] A. Cheansirisomboon, C. Pakawatchai, S. Youngme, Aust. J. Chem., 66 (2013), pp. 477–484
[18] Crystal data for **1**: formula: $C_{26}H_{34}N_4O_{16}Co_2$, M_r = 776.43, Triclinic, space group *P*-1, a = 6.0640(5),b = 11.365(9), c = 11.857(9) Å, α = 98.65(2)° β = 101.33(2)° λ = 102.75(2), V = 765.31(11) Å^3, Z = 1;D_c = 1.685 g cm^{-3}, F(000) = 400, T = 293(2) K, R_1 = 0.0330, wR_2 = 0.0782, for 3685 unique reflections and 249 parameters, S = 1.064. Structural data for **1** was collected on a Bruker Smart Apex CCD with graphite monochromated Mo Kα radiation. Their structures were solved by direct methods and refined with the full matrix least-squares technique using the SHELXS-97 and SHELXL-97 programs[21]. CCDC: **1**, 961055.
[19] M. Kurmoo, Chem. Soc. Rev., 38 (2009), pp. 1353–1379
[20] A.N. Khlobystov, N.R. Champness, C.J. Roberts, S.J.B. Tendler, C. Thompson, M. Schroder, CrystEngComm, 4 (2002), pp. 426–431
[21] G.M. Sheldrick, University of Göttingen, Göttingen, Germany (1997)

III-4 Water-induced dynamic crystal-to-amorphous transformation of cobalt(II) coordination and supramolecular frameworks containing benzene-1,2,4,5-tetracarboxylic acid and trans-1-(2-pyridyl)-2-(4-pyridyl)ethylene ligands

Introduction

Solid-state reversible structural transformations and functional studies of bistable dynamic coordination polymers (CPs) or metal organic frameworks (MOFs) and supramolecular frameworks have recently attracted great attention to obtain smart functional materials.[1-2] The dynamic frameworks have a blend of both rigidity and flexibility. Rigidity makes material efficient in storage and flexibility in selective sorption. Kitawaga et al. classified these dynamic frameworks as “third generation coordination polymers”, also called “soft porous crystals”.[3-5] Dynamic structural transformation based on flexible frameworks is one of the most interesting and presumably characteristic phenomena of coordination polymers.[6-7]

The bistable dynamic frameworks exhibit solid-state structural transformations with breaking, making, or rearrangement of bonds driven by external stimuli like heat, light, pressure, etc.[8] Structural transformations are generally accompanied by removal or exchange of guest, changes in coordination number of metal containing nodes, and conformational changes in flexible parts of organic ligands.[9] However, reports of such bistable dynamic MOFs are limited, especially in the supramolecular frameworks generated from discrete molecules. Generally, such structural changes in response to external stimuli are facilitated by weak bonding interactions like hydrogen-bonding and π–π and C−H···π interactions.[10-11] These structural transformations induced by chemical and/or physical processes are much more complicated than encountered in the rigid frameworks. Thus, investigation of solid-state structural transformations between bistable phases and their correlations with the properties is very crucial to design smart functional materials.

From our previous works, we reported the reversible thermal dehydration and rehydration of the supramolecular and 2D coordination frameworks, [Co_2(2,4-

pydc)$_2$(bpa)(H$_2$O)$_6$](H$_2$O)$_2$[8] (2,4-pydc = 2,4-pyridinedicarboxylate anion, bpa = 1,2-bis(2,4-pyridyl)ethane) and [Co(4,4′-bipy)(pro)$_2$(H$_2$O)][9] (4,4′-bipy = 4,4′-bipyridine, pro = propionate). The reversibility is driven by strong hydrogen bonding between lattice and coordinated water molecules and other components. Herein, we report the synthesis of the 3D coordination and supramolecular frameworks **1** and **2**, respectively and their dynamic behaviors. The reversible solid-state structural transformations were accompanied by distinct color change on de/rehydration. The selective sorption properties were observed for adsorbates like H$_2$O over methanol, ethanol, acetone, acetonitrile, dichloromethane, and hexane. The dynamic of the de/rehydrated forms of compounds **1** and **2** were performed to investigate the possible reversible structural transformations with chromotropism.

Results and discussion

Syntheses

Description of {Co$_2$(bpe)(btec)(H$_2$O)$_5$}$_n$ (1)

Single-crystal X-ray diffraction reveals that **1** crystallizes in the triclinic space group P-1, showing a 3D coordination network. The asymmetric unit contains two Co(II) atoms, one btec, one bpe and five coordinated H$_2$O molecules. The Co1 atom is coordinated by three carboxylato oxygen atoms from two btec ligands (Co(1)-O(3) 2.059(4), Co(1)-O(4) 2.430(5) and Co(1)-O(1A) 2.070(4) Å), one nitrogen atom from bpe (Co(1)-N(1) 2.104(5) Å) and two oxygen atoms from water molecules (Co(1)-O(9) 2.060(5) and Co(1)-O(10) 2.090(5) Å), showing distorted octahedral coordination geometry. The Co2 atom also adopts distorted octahedral coordination geometry, but it is coordinated by two carboxylato oxygen atoms of two different btec ligands (Co(2)-O(5) 2.082(5) and Co(2)-O(7) 2.063(4) Å), one nitrogen atom from bpe (Co(2)-N(2) 2.111(5) Å) and three oxygen atoms from water molecules ((Co(2)-O(11) 2.115(5), Co(2)-O(12) 2.215(8), Co(2)-O(13A) 2.23(2) and Co(2)-O(13B) 2.21(2) Å) (Fig. 1).

These Co(II) ions are linked by the bridging bpe ligand (N(1) and N(2)) with the Co1–Co2 distance of 9.1484(14) Å in *c*-axis and the bridging and twisting btec ligand in *a*- and *b*-axis, leading to an infinite flexible 3D framework (Figs. 2 and 3). In addition, the free carboxylate oxygens of btec and the coordinated waters are involved in an extensive hydrogen bonding (O9-H9A···O8^{i} 2.20(6), O10-H10A···O6^{ii} 1.86(6), O6 ···O11 2.8079(83) and O12···O2 3.2782(104) Å) (Fig. 4).

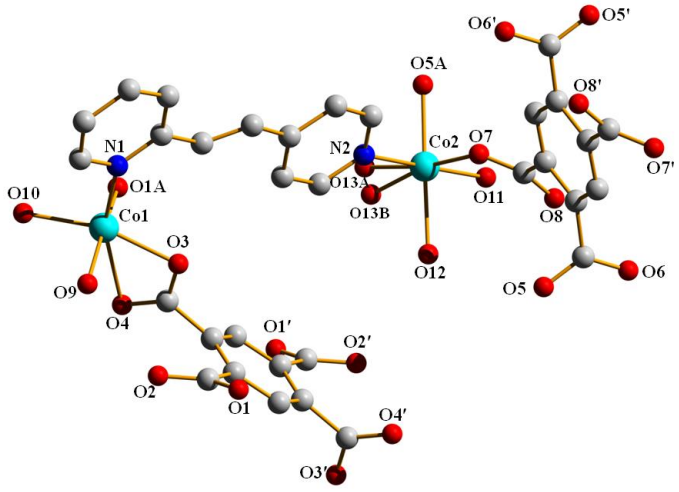

Fig. 1 Perspective view of the coordination environment of cobalt atoms in **1**. H atoms were omitted for clarity

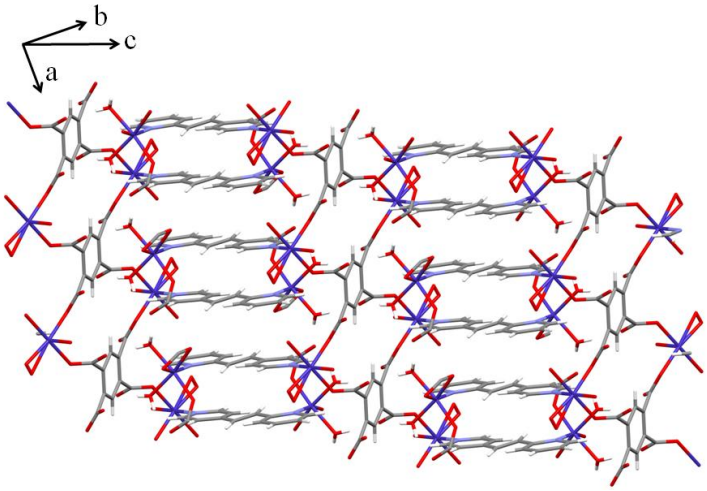

Fig. 2 A partial packing diagram in two-dimensional network of **1** in *ac* plane

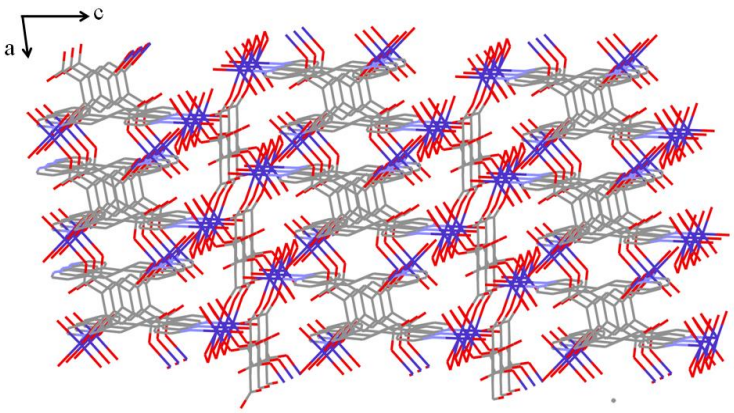

Fig. 3 3D framework of **1**, showing along the *b*-axis

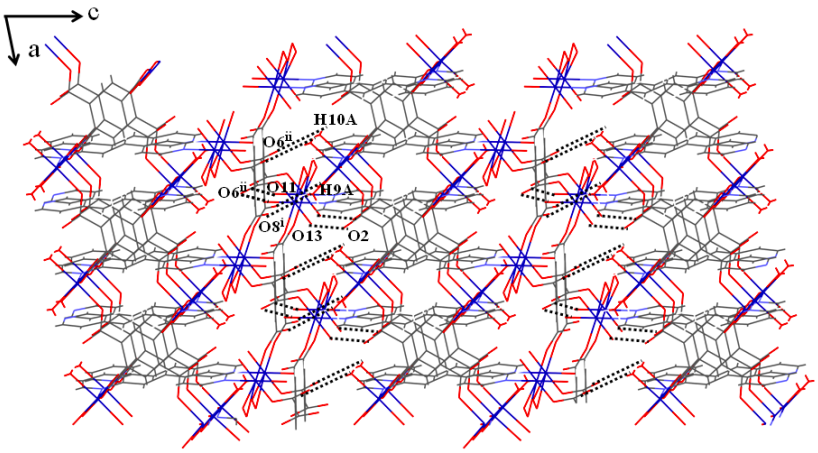

Fig. 4 3D framework of **1**, showing extensive hydrogen bonding interactions by free carboxylate oxygens of btec and the coordinated waters along the *b*- axis [Symmetry codes: i =1+*x*, *y*, -1+*z*; ii = *x*, *y*, -1+*z*]

Description of $[Co_2(bpe)_4(btec)(H_2O)_6]\cdot 4.5H_2O$ (2)

Single-crystal X-ray structural analysis shows that **2** is a dinuclear compound crystallized in the monoclinic P21/c space group. The symmetry-related dinuclear unit consists of two cobalts, four bpe ligands, one btec, six coordinated waters and eight lattice water molecules.

Each Co(II) ion is coordinated by two nitrogen atoms from two bpe terminal ligands (Co(1)-N(1) 2.159(4) and Co(1)-N(3) 2.128(4) Å), one oxygen atom of the bridging btec ligand (Co(1)-O(1) 2.032(3) Å) and three coordinated water molecules (Co(1)-O(5) 2.196(4), Co(1)-O(6) 2.045(3) and Co(1)-O(7) 2.134(4) Å), this feature gives a slightly distorted octahedral geometry with CoN_2O_4 chromophore (Fig. 5). The btec ligand links between both chromophores in monodentate fashion to each Co atom. These dimeric units are connected to each other in ABAB… arrangement via hydrogen bonds with distance of 1.82(5) Å for O6-H6B···O2 and 3.20(5) Å for O5-H5A···O7, generating 2D layer network in *bc* plane as shown in Fig. 6. All lattice water molecules (O8-O16) form a cluster via hydrogen bonds and occupy the channels between these layers along *c* axis, some of them bonded with free carboxylate oxygens (O4···O10 2.727 Å), nitrogen atom (N4···O9 2.799 Å) and coordinated waters (O6-H6A···O8 2.047 Å) as well as aromatic carbon atoms (C6-H6···O16 3.104, C9-H9···O16 2.542, C12-H12···O11 3.339, C13-H13···O12 2.987, C14-H14···O14 2.663, C18-H18···O13 3.905, C19-H19···O14 3.082 and C22-H22···O15 2.806 Å) on the surface of the tube, generating 3D supramolecular framework (Fig. 7). Interestingly water molecules filling in each nano tube are further extended to 1D water chain via hydrogen bond interactions along *c* axis, the bond distances O···O (D···A) are in the range of 2.362 – 3.524 Å which are typically expected for hydrogen bonding interaction[14] (Fig. 8).

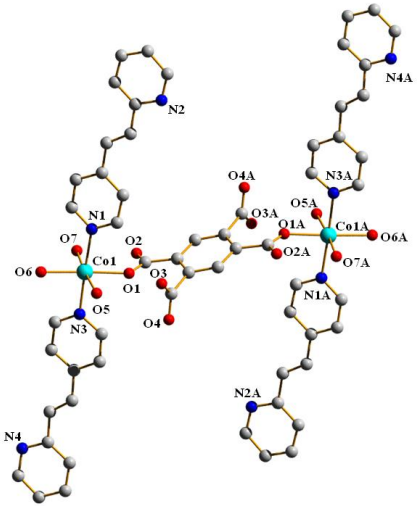

Fig. 5 Perspective view of the coordination environment of cobalt atom in **2.** H atoms were omitted for clarity

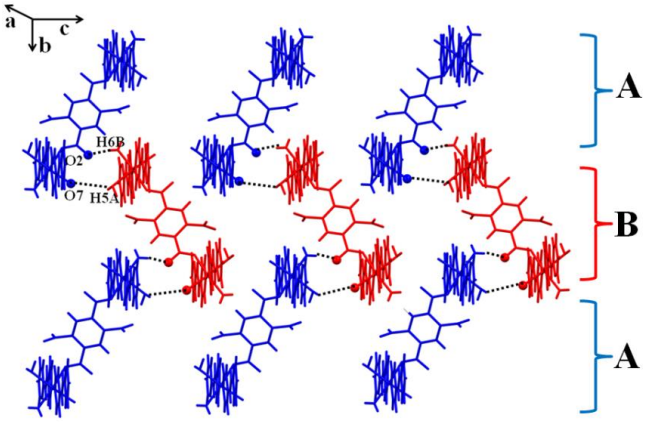

Fig. 6 Crystal packing of dimeric units in ABAB… arrangement of compound **2** via hydrogen bonding in *bc* plane, generating two-dimensional supramolecular structure.

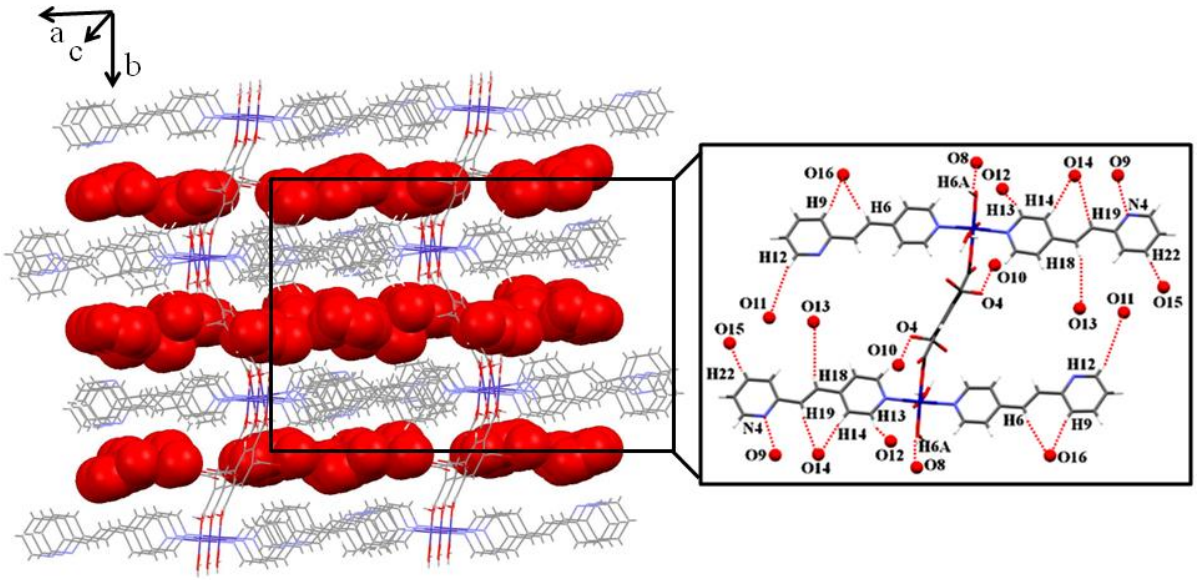

Fig.7 The channels along *c* axis are occupied by free water molecules represented by red balls in view of **2** in *ab* plane, in set shows some of these water molecules interacted with coordinated waters and free carboxylate oxygens on the surface of the tube through hydrogen bonding, generating 3D supramolecular network

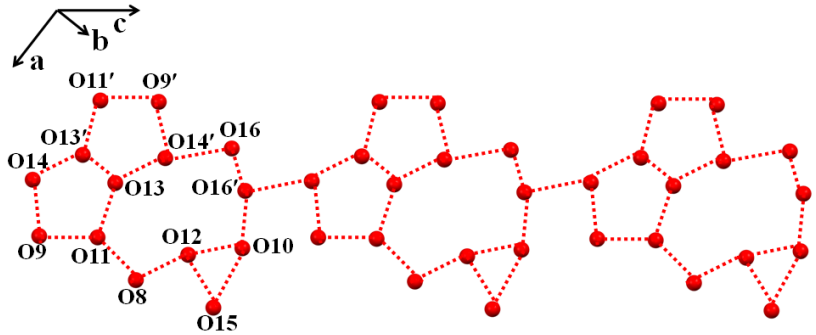

Fig. 8 View of 1D water chain of lattice water molecules via hydrogen bond in one nanotube along *c* axis of **2**

Thermogravimetric analyses

To assess the thermal stability, thermal gravimetric analysis (TGA) was recorded for the single-phase polycrystalline samples in the temperature range 30−700 °C. During the heating process, the TGA profile of **1** (Fig. 9) indicates that the release of five coordinated water molecules occurs at the first step of weight loss in the temperature range 100-250 °C (found, 14.85%; anal. calcd, 14.19 %), resulting to the dehydrated form of Co_2(bpe)(btec) (**1A**), which is stable up to ≈300 °C and then the structure rapidly decomposes at higher temperatures. For compound **2** (Fig. 10), the TGA profile indicates that the releases of all fourteen water molecules (coordinated and lattice water molecules) occur at the first step of weight loss in the temperature range 55–100 °C (found, 17.50%; Anal. Calcd, 17.30%) resulting in the dehydrated form of $Co_2(bpe)_4(btec)$ (**2A**). This dehydrated form **2A** is stable up to ≈150 °C and then rapidly decomposes to unidentified products.

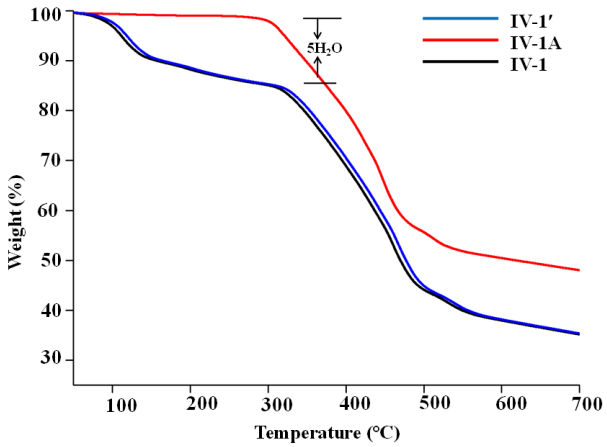

Fig. 9 TGA curves of compound **1**

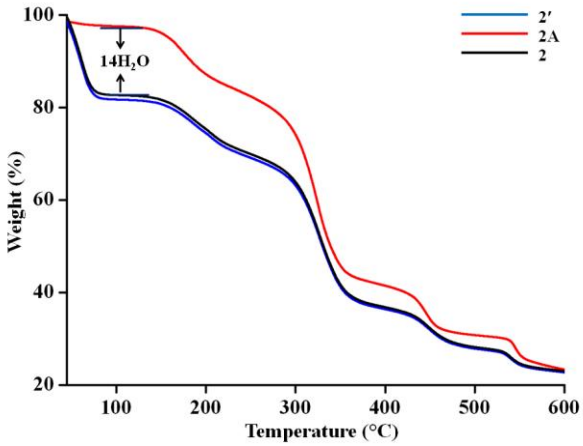

Fig. 10 TGA curves of compounds **2**, **2A** and **2′**

Structural phase transformation by thermal de/rehydration processes

The compound **1** contains only coordinated water molecules while **2** contains both lattice and coordinated water molecules. The stable dehydrated forms of **1A** and **2A** were clarified by TGA profiles. The dynamic structural behaviors of **1** and **2** relating to their dehydration and rehydration processes are studied by elemental analyses, XRPD, and spectroscopic techniques. Interestingly, the water molecules can be adsorbed fully by exposing the evacuated samples to water vapor over organic solvents at room temperature. The heating and exposing procedures were repeated five times to demonstrate the reversibility of the de- and rehydration processes.

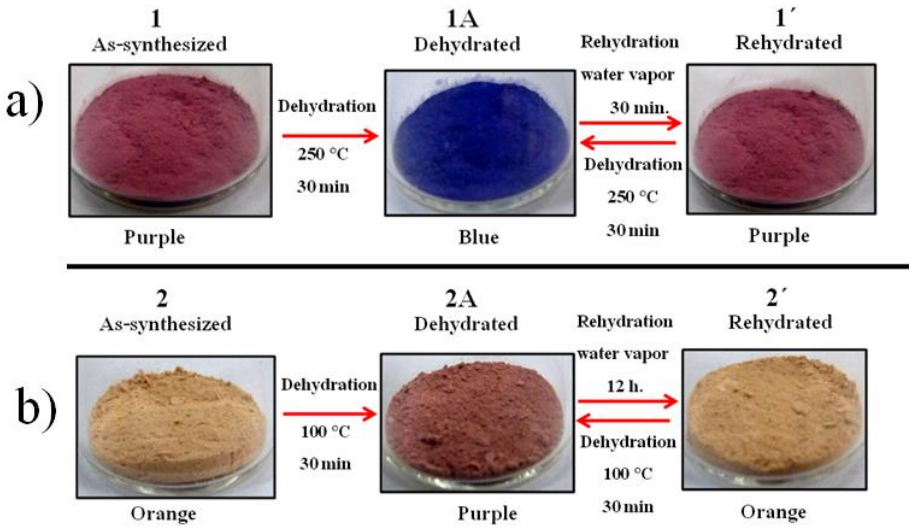

Fig. 11 Changes in color during de- and rehydration processes in bulk samples of a) compound **1** b) compoud **2**

When the crystalline samples were heated to 250 °C for **1** and 100 C° for **2** in air for 10 min, these crystals suddenly lose their crystallinity and the color changes from purple to blue for **1** and orange to purple for **2**. Then these noncrystalline solids were exposed to the laboratory air for 10 min for **1** and 8 h for **2**, and the color of both noncrystalline samples were returned to that of the original samples. Consequently, the bulk samples of **1** and **2** were used to study in detail. The dehydrated form **1A** was obtained by heating the bulk sample at 250 °C in air for 30 min and the re-hydrated form **1′** was obtained by exposing the dehydrated sample to water vapor for 3 min. In case of **2** the dehydrated form **2A** was obtained by heating the bulk sample at 100 °C in air for 30 min and the re-hydrated form **2′** was obtained by exposing the dehydrated sample to water vapor for 12 h at room temperature without condensation, as shown in Fig. 11. For this, the solid-state UV–vis diffuse reflectance spectra, clearly show that the bands observed in **1** and **1′** and also in **2** and **2′**, correspond very well to the identical transitions causing the same color of products, and evidence that **1** and **1′**, and also **2** and **2′** have the same Co^{II} environments. For **1** this spectral feature agrees with the typical d–d transitions of high spin Co^{II} in distorted octahedral geometry with two broad bands at 527 and 1254 nm, assigned to the ν_3: $^4T_{1g} \rightarrow {}^4T_{1g}(P)$ and ν_1: $^4T_{1g} \rightarrow {}^4T_{2g}$, transitions, respectively and a shoulder at around 700 nm arised from the ν_2: $^4T_{1g} \rightarrow {}^4A_{2g}$ transition.[15] Whereas the amorphous phase **1A** shows the different d−d transition with a lower-energy broad band centered around 587 nm and a very broad band centered around 1140 nm, giving distinctive blue color which correspond to the four-coordinate tetrahedral geometry in majority of **1A** (Fig. 12). In case of the **2,** the spectral feature and orange color agrees with the typical d–d transitions of high spin Co^{II} in a slightly distorted octahedral geometry with two higher-energy broad bands centred at 512 and 1120 nm as compared to that of **1**, which are assigned to the $^4T_{1g} \rightarrow {}^4T_{1g}(P)$, and $^4T_{1g} \rightarrow {}^4T_{2g}$ transitions, respectively. The amorphous form **2A** also shows the same d–d transitions with two broad bands, but remarkably shifted to lower energy at 541 and 1281 nm, resulting in distinctive purple color and corresponding to the majority of high-spin Co^{II} in a more distorted octahedral geometry with different degree and type of distortion in an amorphous phase[15] (Fig. 13). The chromotropic behaviors of **1** and **2** are principally ascribed to the changes of the d-orbital energy level, induced by the drastic change in the coordination environment around metal center during dehydration and rehydration

processes.[16] Furthermore, these results agree with the reversible change of the vibrational bands in IR spectra where the shifted bands are observed for the amorphous phase (**1A**). In **2A**, the broad and strong peaks of O–H stretching around 3300 cm^{-1} and H–O–H bending around 1500–1600 cm^{-1} of coordinated and lattice water molecules disappear, resulting to the sharper IR spectrum with different splitting feature and a shift in some peak positions. In contrast, these features are removed for the IR spectra of the rehydrated forms **1′** and **2′**, which are identical to those of the as-synthesized **1** and **2**. The XRPD patterns of the as-synthesized products **1** and **2** closely match the simulated ones from the single-crystal data (Fig. 14). However, the XRPD patterns of dehydrated **1A** and **2A** show peak disappearance, indicating that the dehydrated $Co_2(bpe)(btec)_2$ (**1A**) (anal. calcd: C, 55.75; H, 3.03; N, 7.65%. Found: C, 55.82; H, 3.15; N, 7.93%) and $Co_2(bpe)_4(btec)$ (**2A**) (Anal. Calcd: C, 63.28; H, 4.21; N, 10.18%. Found: C, 63.32; H, 4.35; N, 10.31%) are in an amorphous phase which are formed by the collapse of the frameworks of **1** and **2** accompanied with the destruction of the frameworks when same or all water molecules are removed. Interestingly, these amorphous phases, **1A** and **2A** can be restored to the original crystalline phases of **1′** and **2′** in which the color returns to that of the original color after being exposed in water vapor for 30 min for **1′** and 12 h for **2′**, as indicated by elemental analyses with the chemical composition of $[Co_2(bpe)(btec)_2(H_2O)_5]_n$ (**1′**) (anal. calcd: C, 41.01; H, 4.07; N, 4.35%. Found: C, 41.25; H, 4.18; N, 4.59%) and $[Co_2(bpe)_4(btec)(H_2O)_6]\cdot 8H_2O$ (**2′**) (Anal. Calcd: C, 52.42; H, 3.79; N, 8.43%. Found: C, 52.23; H, 3.78; N, 8.39%), and the XRPD measurement results. The restored solids have the same XRPD patterns as the simulated ones from the single-crystal X-ray diffraction data of **1** and **2**.

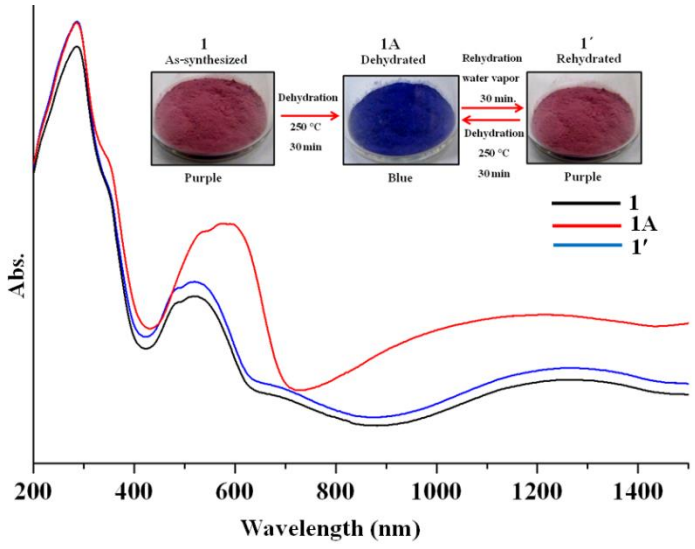

Fig. 12 The UV-vis diffuse reflectance spectra of as-synthesize **1** (black line), the dehydrated form **1A** (red line), and the rehydrated form **1′** (blue line), representing together with the chromatic changes in bulk samples

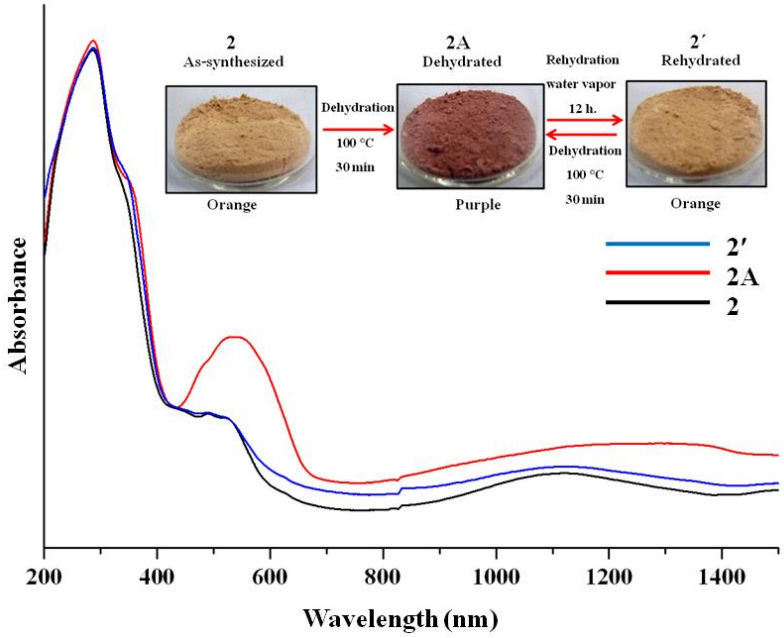

Fig. 13 The UV-vis diffuse reflectance spectra of as-synthesize **2** (black line), the dehydrated form **2A** (red line), and the rehydrated form **2´** (blue line), representing together with the chromatic changes in bulk samples

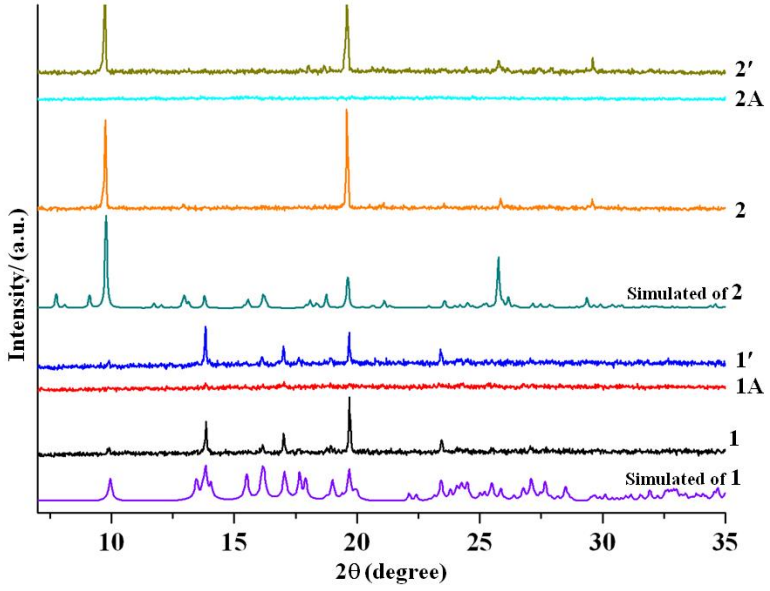

Fig. 14 XRPD patterns for **1** and **2** at different conditions: a) simulated of **1**, b) as-synthesized of **1 (1)**, c) dehydrated of **1A** (**1A**), d) rehydrated of **1'** (**1′**), e) simulated of **2**, f) as-synthesized of **2 (2)**, g) dehydrated of **2A** (**2A**) and h) rehydrated of **2'** (**2′**) respectively

These results of compounds **1** and **2** confirm the water-induced reversible crystalline-to-amorphous phase transformation with chromotropism. This behavior of both compounds was also investigated for other solvents vapor such as methanol, ethanol, acetone, acetonitrile, dichloromethane, DMF and DMSO, but sensitive only with water vapor, indicative of the high

selective recognition of **1A** and **2A** to water molecules. The selective water accommodation with chromotropism in dehydrated **1A** and **2A** when compared with many solvents could be attributed to the proper size of water molecules and weak host–guest interactions. Remarkably, the reversibility of the water adsorption and the change in the coordination environment can be visualized by the change in color of the compounds. This behavior takes place in water which could be a dissolution/recrystallization process rather than a water-induced solid-state reaction as this involves structural reorganization of the coordination and supramolecular frameworks or rearrangements of the molecules interacting by inter-molecular hydrogen bonds and non-covalent contacts.[17]

In summary, two novel 3D Co^{II} coordination and supramolecular frameworks containing carboxylate and N-donor ligands, $[Co_2(bpe)(btec)_2(H_2O)_5]_n$ **(1)** and $[Co_2(btec)\ (bpe)_4(H_2O)_6]\cdot 8H_2O$ **(2)** have been successfully synthesized by hydrothermal and direct methods, respectively. We have demonstrated that the water molecules in both compounds can be reversibly exchanged along with the changes in color of the samples. The dehydrated form **1A** is found to be very sensitive to water with the color change as compared to that of **2A.** However, the dehydrated form **2A** has much more water-adsorption efficiency. The reversibility of the solid transformation has been supported by spectroscopic techniques, elemental analysis, TGA and XRPD and shows that **1** and **2** exhibit water induced crystal-to-amorphous transformation with the selective water adsorption and the change in the coordination environments can be visualized by the change in color of the compounds. The crystalline-to-amorphous transformations between original crystalline phase (**1**, **2**) → dehydration (amorphous powder (**1A**, **2A**)) → rehydration (crystalline phase (**1′**, **2′**)) involve dynamic motions altering the coordination geometry of Co^{II}. These are triggered by the weak intermolecular interactions during the removal and restoration of water molecules. This work may contribute to potential application as sensing adsorbent material for moisture.

References

[1] (a) R. Kitaura, S. Noro and S. Kitagawa, *Angew. Chem., Int. Ed.* 2004, **43**, 2334; (b) S. Horike, S. Shimomura and S. Kitagawa, *Nat.Chem.* 2009, **1**, 695.

[2] (a) M. Dinca and J. R. Long, *Angew. Chem., Int. Ed*. 2008, **47**, 2. (b) J. J. Vittal, *Coord. Chem. Rev.* 2007, **251**, 1781. (b) S. Dalai. *Journal of Physical Sciences*, 2011**, 15**, 223.

[3] (a) K. Uemura, S. Kitagawa, M. Kondo, K. Fukui, R. Kitaura, H.-C. Chang and T. Mizutani. *Chem. Eur. J.* 2002**, 8,** 3586. (b) K.S. Min and M. P. Suh. *J. Am. Chem. Soc.* 2000, **122**, 6834. (c) B. Gomez-Lor, E. GutiYrrez-Puebla, M. Iglesias, and A. Ruiz Valero. *Inorg. Chem.* 2002, **41**, 2429.

[4] (a) S. Kitagawa, M. Kondo, *Bull. Chem. Soc. Jpn*. 1998, **71**, 1739. (b) S. Kitagawa, R. Kitaura and S. Noro, *Angew. Chem. Int. Ed.* 2004, **43**, 2334.

[5] (a) T. Pretsch, K. W. Chapman, G. J. Halder, and C. Kepert, *J. Chem. Commun*. 2006, 1857; (b) M. C. Bernini, F. Gandara, M. Iglesias, N. Snejko, E. Gutierrez-Puebla, E. V Brusau,G. E. Narda, and M. A. Monge, *Chem.Eur. J.* 2009, **15**, 4896.

[6] (a) S. K. Ghosh, S. Bureekaew and S. Kitagawa, Angew. *Chem., Int. Ed*. 2008, **47**, 3403; (b) X. Bao, P. Guo, J. Liu, J. Leng, and M. Tong, *Chem.Eur. J.* 2011, **17**, 2335.

[7] (a) S. Kitagawa, R. Kitaura and S. Noro. *Angew. Chem. Int. Ed.* 2004, **43**, 2334. (b) P.D. Beer, P.A Gale, and D.K. Smith, (1999). Supramolecular Chemistry. New York; Oxford University Press. (c) J.-M. Lehn. *Pure Appl*. 1978, **50**, 871.

[8] J. Piromchom, W. Nanthawat, B. Jaursup, C. Pakawatchai and S. Youngme, *Inorg. Chem Commu.* 2014, **40**, 59.

[9] J. Piromchom, W. Nanthawat, B. Jaursup, C. Pakawatchai, K. Chainok and S. Youngme,

Inorg. Chem.Commu. 2014, **44**, 111.
[10] SMART 5.6, Bruker AXS Inc., Madison, WI, 2000.
[11] SAINT 4.0 Software Reference Manual, Siemens Analytical X-Ray Systems, Inc., Madison, WI, 2000.
[12] G. M. Sheldrick, SADABS, Program for Empirical Absorption correction of Area Detector Data, University of Göttingen, Göttingen, Germany, 2000.
[13] G. M. Sheldrick, Acta Crystallogr., Sect. A: Fundam. Crystallogr., 2008, **A64**, 112.
[14] G.A. Jeffery, (1997). An Introduction to Hydrogen Bonding. Oxford; Oxford University Press.
[15] A. B. P. Lever, (1984). Inorganic electronic spectroscopy; 2 ed.; Elsevier: The Netherlands,
[16] M. Kurmoo, Magnetic metal–organic frameworks, *Chem. Soc. Rev*. 2009, **38**, 1353.
[17] A.N. Khlobystov, N.R. Champness, C.J. Roberts, S.J.B. Tendler, C. Thompson, and M.Schroder, *CrystEngComm*. 2002, **4**, 426.

OUTPUT OF THE RESEARCH

Ph.D Students:

1) Dr. Nanthawat Wannarit (2013): "Magnetic studies of spin-crossover iron(II) and triply-bridged dinuclear copper(II) compounds" Doctor of Philosophy Thesis in Chemistry, Graduate School, Khon Kaen University.
2) Dr. Achareeya Cheansirisomboon (2014): "Design of metal organic frameworks and their functions toward structural dynamics with chromotropism, sorption and optical properties" Doctor of Philosophy Thesis in Chemistry, Graduate School, Khon Kaen University.

MSc. Students:

1) Jureepan Piromchom (2014): "Water-induced dynamic structural transformation of cobalt(II) coordination and supramolecular frameworks containing carboxylate and N-donor ligands" Master of Science Thesis in Chemistry, Graduate School, Khon Kaen University.
2) Porntiva Suvanvapee (2015): "Series of cyanoacetato coordination polymers with various N,N'-organic bridges: syntheses, crystal structures, luminescent and magnetic properties" Master of Science Thesis in Chemistry, Graduate School, Khon Kaen University.

Publication papers:

1. N. Wannarit, C. Pakawatchai, I. Mutikainen, R. Costa, I. de P. R. Moreira, F. Illas, and S. Youngme, New Hetero Triply-bridged Dinuclear Copper(II) Compounds with Ferromagnetic Coupling: A challenge for current density functional, ***Phys. Chem. Chem. Phys.***, 2013, **15**, 1966.
2. N. Wannarit, O. Roubeau, S. Youngme, and P. Gamez, Subtlety of the spin-crossover phenomenon observed with dipyridylamino-substituted triazine ligands, ***Eur. J. Inorg. Chem.***, 2013, 730-737.
3. A. Cheansirisomboon, C. Pakawatchai, and S. Youngme, Solvent-Induced Reversible Crystal-to-Amorphous Transformation Properties of Cobalt(II) 4-Aminomethylpyridine-Sulfate with Chromotropism, ***Aust. J. Chem.*** 2013, **66**, 477-484.
4. N. Wannarit, O. Roubeau, S. Youngme, S. J. Teat and P. Gamez. Influence of supramolecular bonding contacts on the spin crossover behaviour of iron(II) complexes from 2,2′-dipyridylamino/*s*-triazine ligands, ***Dalton. Trans.***, 2013, **42**, 7120-7130.
5. P. Phuengphai, S. Youngme, N. Chaichit, J. Reedijk, New 3D supramolecular networks built from 1D and 2D frameworks via π–π and H-bonding interactions: Topology and catalytic properties, ***Inorg. Chim. Acta*** 2013, **403**, 35–42.
6. Wannarit, N., Pakawatchai, C., Youngme, S., Di-μ-acetato-κ4O:O′-bis[(1,10-phenanthroline-κ2 N,N′)(trifluoromethanesulfonato-κO)copper(II)], ***Acta Cryst. E***, 2013, **E69** (11), m591 - m592
7. Piromchom, J., Wannarit, N., Pakawatchai, C., Youngme, S., The heterometallic cadmium-silver complex cis-bis[dicyanidoargentato(I)- κN]bis(5,5′-dimethyl-2,2′-bipyridyl-κ2 N,N′)cadmium(II) monohydrate, ***Acta Cryst. C***, 2013, **C69** (10), 1136 – 1139.
8. J. Piromchom, N. Wannarit, J. Boonmak, K. Chainok, C. Pakawatchai, S. Youngme, Flexible metal supramolecular framework of 2D cobalt(II) coordination polymer with water-induced reversible crystal-to-amorphous transformation, ***Inorg. Chem. Commun.***, 2014, **44**, 111–113.

9. J. Piromchom, N. Wannarit, J. Boonmak, C. Pakawatchai, S. Youngme, Synthesis, crystal structure and water-induced reversible crystal-to-amorphous transformation property of $[Co_2(2,4\text{-pydc})_2(bpa)(H_2O)_6](H2O)_2$, ***Inorg. Chem. Commun.***, 2014, **40**, 59–61.
10. S. Kaenket, P. Phuengphai, C. Pakawatchaic, S. Youngme, Poly[tris(μ-4,4'-bipyridine-κ^2N:N')bis(dimethyl-sulfoxide-κO)tetrakis(thiocyanato-κN) dicobalt(II)], ***Acta Cryst. E***, 2014, **E70**, m265–m266.
11. Wannarit, N., Nassirinia, N., Amani, S., Masciocchi, N., Youngme, S., Roubeau, O., Teat, S.J., Gamez, P. Drastic effect of lattice propionitrile molecules on the spin-transition temperature of a 2,2'-dipyridylamino/s-triazine-based iron(II) complex ***Inorganic Chemistry***, 2014, **53** (18), 9827-9836.
12. Cheansirisomboon, A., Salinas-Uber, J., Massera, C., Roubeau, O., Youngme, S., Gamez, P. One-pot multiple metal-organic framework formation: Concomitant generation of structural isomers or of drastically distinct materials, ***Eur. J. Inorg. Chem.***, 2014, 4385-4393.
13. Othong, J., Wannarit, N., Pakawatchai, C., Youngme, S. Crystal structure of a two-dimensional grid-type iron(II) coordination polymer: Poly[[diaquatetra-μ-cyanido-diargentate(I)iron(II)] trans-1,2-bis(pyridin-2-yl)ethylene disolvate], ***Acta Cryst. E***, 2014, **E70**(8), 107-110.
14. J. Piromchom, J. Boonmak, K. Chainok, S. Youngme, Water-induced dynamic crystal-to-amorphous transformation of cobalt(II) coordination and supramolecular frameworks containing benzene-1,2,4,5-tetracarboxylic acid and trans-1-(2-pyridyl)-2-(4-pyridyl)ethylene ligands, ***Polyhedron***, 2015, **102**, 593-599.
15. J. Piromchom, J. Othong, J. Boonmak, I. Mutikainen, S. Youngme, A novel one-dimensional metal-organic framework with a μ-cyanido-argentate group: catena-poly[[(5,5'-dimethyl-2,2'-bipyridyl-κ^2N,N')silver(I)]-μ-cyanido-κ^2N:C], ***Acta Cryst.*** 2015, **C71**, 1057-1061.
16. P. Suvanvapee, J. Boonmak, F. Klongdee, C. Pakawatchai, B. Moubaraki, K.S. Murray, S. Youngme, A Series of cyanoacetato copper(II) coordination polymers with various *N*,*N*'-ditopic spacers: Structural diversity, supramolecular robustness and magnetic properties. ***Cryst. Growth & Des.,*** 2015, **15**(8), 3804.
17. P. Suvanvapee, J. Boonmak, S. Youngme, Structural diversity and luminescent properties of cyanoacetato zinc/cadmium coordination polymers with *N*,*N*'-ditopic auxiliary ligands**.** ***Polyhedron,*** 2015, **102**, 693.
18. P. Suvanvapee, J. Boonmak, S. Youngme, Synthesis, crystal structure and luminescent properties of three new zinc/cadmium coordination polymers containing cyanoacetate and 1,2-di(4-pyridyl)ethylene. ***Inorg. Chim. Acta,*** 2015, **437**, 11.

Presentations:

1. S. Youngme, J. Boonmak, A. Cheansirisomboon, N. Wannarit, C. Pakawatchai, P. Gamez "Influence of Supramolecular Contacts on Structural Transformation and Spin-crossover Behavior of Supramolecular Frameworks" *invited as an invited speaker a RGJ Seminar Series XCVIII*, at Department of Chemistry, Faculty of Science, Khon Kaen university, Thailand. 13 September, 2013
2. S. Youngme, A. Cheansirisomboon, N. Wannarit, C. Pakawatchai, P. Gamez "Influence of Supramolecular Contacts on Structural Transformation and Spin-crossover Behavior of Supramolecular Frameworks" *invited as an invited speaker at 4th Asian Conference on*

Coordination Chemistry (4th ACCC), at International Convention Center Jeju (ICCJEJU), Jeju, South Korea, 4-7 November, 2013

3. P. Suvanvapee, J. Boonmak, C. Pakawatchai, K. S. Murray, S.Youngme, Syntheses, Crystal Structures and Magnetic Properties of Copper(II) Coordination Networks Containing 1,2-Di(4-pyridyl)ethylene and Cyanoacetic Acid, *Poster presented at* Pure and Applied Chemistry International Conference 2014 (PACCON 2014), Centara Hotel and Convention Centre Khon Kaen, Thailand. January 8-10, 2014
4. J. Piromchom, N. Wannarit, J. Boonmak, C. Pakawatchai, S.Youngme, Synthesis, Crystal Structure and Water-induced Reversible Crystal-to-Amorphous Transformation Property of $[Co_2(2,4\text{-pydc})_2(bpa)\ (H_2O)_6](H_2O)_2$, *Poster presented at* Pure and Applied Chemistry International Conference 2014 (PACCON 2014), Centara Hotel and Convention Centre Khon Kaen, Thailand. January 8-10, 2014
5. N. Wannarit, C. Pakawatchai, S. Youngme, I. Mutikainen, R. Costa, I. de P. R. Moreira, and F. Illas, "Hetero Triply-bridged Dinuclear Copper(II) Compounds with Ferromagnetic Coupling: A challenge for current density functional" *poster presentation at RGJ Seminar Series XCVIII*, at Department of Chemistry, Faculty of Science, Khon Kaen university, Thailand. 13 September, 2013
6. N. Wannarit, S. Youngme, O. Roubeau, S.J. Teat and P. Gamez "SCO Fe(II) Compound Containing S-triazine/2,2'-Dipyridylamine" *poster presentation at RGJ Seminar Series XCVIII*, at Department of Chemistry, Faculty of Science, Khon Kaen university, Thailand. 13 September, 2013
7. A. Cheansirisomboon, J.S. Uber, O. Roubeau, P. Gamez, and S. Youngme, "Single-Crystal-to-Single-Crystal Transformations of a 3D Zinc(II) Metal-Organic Framework Triggered by Guest Exchange" *poster presentation at RGJ Seminar Series XCVIII*, at Department of Chemistry, Faculty of Science, Khon Kaen university, Thailand. 13 September, 2013
8. A. Cheansirisomboon, C. Pakawatchai, and S. Youngme, "Guest-Induced Phase Transformation with Chromotropism in Cobalt(II) Supramolecular Frameworks" *poster presentation at 4th Asian Conference on Coordination Chemistry (4th ACCC)*, at International Convention Center Jeju (ICCJEJU), Jeju, South Korea, 4-7 November, 2013
9. N. Wannarit, S. Youngme, O. Roubeau, and P. Gamez "Spin Crossover of Mononuclear Iron(II) Compound with 2,2'-dipyridylamino-Substituted Triazine Ligands" *poster presentation at 4th Asian Conference on Coordination Chemistry (4th ACCC)*, at International Convention Center Jeju (ICCJEJU), Jeju, South Korea, 4-7 November, 2013
10. J. Boonmak, F. Clongdee, P. Suvanvapee, C. Pakawatchai, and S. Youngme, "Robust Metal Supramolecular Frameworks Construced from Interlaced Chain Coordination Polymer Containing 4,4'-bipyridyl and Cyano acetate" *poster presentation at 4th Asian Conference on Coordination Chemistry (4th ACCC)*, at International Convention Center Jeju (ICCJEJU), Jeju, South Korea, 4-7 November, 2013
11. A. Cheansirisomboon, P. Gamez, D. Volkmer, and S. Youngme, "Flexible Metal−Organic Frameworks Based on 4,4´-oxybis(benzoicacid) ligand with Stepwise and Hysteretic Adsorption Properties" *poster presentation at RGJ-Ph.D. Congress XV*, 28-30 May 2014, Jomtien Palm Beach Hotel, Pattaya, Chonburi. Poster presented distinguished achievement award.
12. J. Boonmak, F. Klongdee, P. Suvanvapee, C. Pakawatchai and S. Youngme, Robust metal supramolecular frameworks constructed from interlaced chain coordination polymers containing

4,4′- bipyridyl and cyanoacetate, *Poster presented at 4th Asian Conference on Coordination Chemistry (ACCC 4)*, the International Convention Center, Jeju, Korea. November 4-7, 2013.

13. A. Cheansirisomboon, J. Salinase-Uber, O. Roubeau, S. J. Teat, P. Gamez and S. Youngme, "Single-crystal-to-single-crystal transformations of a 3D zinc(II) metal-organic framework triggered by guest exchange" *Poster presented* at 5th International Symposium Advanced Micro- and Mesoporous Materials, Golden Sands, Bulgaria. September 6-9, 2013.
14. J. Othong, J. Boonmak, S. Youngme, Hydrothermal syntheses of metal-organic framework constructed from imidazole-4,5-dicarboxylate and derivative carboxylate ligands, ***Poster*** *presented at* Pure and Applied Chemistry International Conference 2015 (PACCON 2015), Amari Watergate Hotel, Bangkok, Thailand. January 21-23, 2015
15. J. Othong, J. Boonmak, S. Youngme, Hydrothermal syntheses of metal-organic frameworks constructed from imidazole-4,5-dicarboxylate and 1,3,5-benzenetricarboxylate, ***Poster*** *presentated at 40th Congress on Science and Technology of Thailand*, Hotel Pullman Khon Kaen Raja Orchid, Khon Kaen, Thailand. December 2-4, 2014.
16. F. Klongdee, J. Boonmak, S. Youngme, Syntheses and crystal structures of trinuclear copper(II) complexes containing pyrazole-3,5-dicarboxlic acid with various N-donor ligands, ***Poster*** *presentated at 40th Congress on Science and Technology of Thailand*, Hotel Pullman Khon Kaen Raja Orchid, Khon Kaen, Thailand. December 2-4, 2014.
17. P. Suvanvapee, J. Boonmak, C. Pakawatchai, K. Chainok, K.S. Murray, S. Youngme, A series of cyanoacetato copper(II) coordination polymers with various *N,N'*-ditopic spacers: structural diversity, supramolecular robustness and magnetic properties, ***Poster*** *presentated at 40th Congress on Science and Technology of Thailand*, Hotel Pullman Khon Kaen Raja Orchid, Khon Kaen, Thailand. December 2-4, 2014.
18. J. Piromchom, J. Boonmak, K. Chainok, S. Youngme, Water-induced dynamic structural transformation of cobalt(II) coordination and supramolecular frameworks containing benzene-1,2,4,5-tetracarboxylic acid and trans-1-(2-pyridyl)-2-(4-pyridyl)ethylene ligands, ***Poster*** *presentated at 40th Congress on Science and Technology of Thailand*, Hotel Pullman Khon Kaen Raja Orchid, Khon Kaen, Thailand. December 2-4, 2014.
19. S. Phengthaisong, J. Boonmak, , S. Youngme, Solvent-induced syntheses and single-crystal-to-single-crystal transformation of 4,4'-bipyridine/3-sulfobenzoate-based metal organic frameworks, ***Poster*** *presentated at 40th Congress on Science and Technology of Thailand*, Hotel Pullman Khon Kaen Raja Orchid, Khon Kaen, Thailand. December 2-4, 2014.
20. A. Cheansirisomboon, P. Gamez, S. Youngme, Single-crystal-to-single-crystaltransformation of 3D zinc(II) metal organic framework triggered by guest exchange, , ***Poster*** *presentated at 40th Congress on Science and Technology of Thailand*, Hotel Pullman Khon Kaen Raja Orchid, Khon Kaen, Thailand. December 2-4, 2014.

Connections with other experts within and outside Thailand:

1. Assist. Prof. Chaveng Pakawatchai, Department of Chemistry, Faculty of Science, Prince of Songkla University, Hat Yai, Songkla 90112, Thailand.
2. Assist. Prof. Kittipong Chainok, Department of Physics, Thammasat University, Rangsit Campus, Klong Luang, Pathumthani 12121, Thailand.

3. Prof. Jan Reedijk, Leiden Institute of Chemistry, Gorlaeus Laboratories, Leiden University, P.O. Box 9502, 2300 RA Leiden, The Netherlands.
4. Prof. Patrick Gamez, *ICREA*, Universitat de Barcelona, Departament de Química Inorgànica, Martí i Franquès 1-11, 08028 Barcelona, Spain.
5. Prof. Francesc Illas, Departament de Química Física & Institut de Química Teòrica i Computacional (IQTCUB), Universitat de Barcelona, C/ Martí i Franquès 1, E-08028 Barcelona, Spain.
6. Dr. Ilpo Mutikainen, Laboratory of Inorganic Chemistry, Department of Chemistry, University of Helsinki, 00014 Helsinki, Finland.
7. Prof. Keith S. Murray, School of Chemistry, Building 23, 17 Rainforest Walk, Monash University, Melbourne, Victoria, 3800, Australia.

APPENDICES

PUBLICATION PAPERS OF PART I

1. P. Phuengphai, S. Youngme, N. Chaichit, J. Reedijk, New 3D supramolecular networks built from 1D and 2D frameworks via π–π and H-bonding interactions: Topology and catalytic properties, ***Inorg. Chim. Acta*** 2013, **403**, 35–42.

PUBLICATION PAPERS OF PART II

2. N. Wannarit, O. Roubeau, S. Youngme, and P. Gamez, Subtlety of the spin-crossover phenomenon observed with dipyridylamino-substituted triazine ligands, ***Eur. J. Inorg. Chem.***, 2013, 730-737.
3. N. Wannarit, O. Roubeau, S. Youngme, S. J. Teat and P. Gamez. Influence of supramolecular bonding contacts on the spin crossover behaviour of iron(II) complexes from 2,2′-dipyridylamino/*s*-triazine ligands, ***Dalton. Trans.***, 2013, **42**, 7120-7130.
4. Wannarit, N., Nassirinia, N., Amani, S., Masciocchi, N., Youngme, S., Roubeau, O., Teat, S.J., Gamez, P. Drastic effect of lattice propionitrile molecules on the spin-transition temperature of a 2,2'-dipyridylamino/s-triazine-based iron(II) complex ***Inorganic Chemistry***, 2014, **53** (18), 9827-9836.
5. N. Wannarit, C. Pakawatchai, I. Mutikainen, R. Costa, I. de P. R. Moreira, F. Illas, and S. Youngme, New Hetero Triply-bridged Dinuclear Copper(II) Compounds with Ferromagnetic Coupling: A challenge for current density functional, ***Phys. Chem. Chem. Phys.***, 2013, **15**, 1966.

PUBLICATION PAPERS OF PART III

6. A. Cheansirisomboon, C. Pakawatchai, and S. Youngme, Solvent-Induced Reversible Crystal-to-Amorphous Transformation Properties of Cobalt(II) 4-Aminomethylpyridine-Sulfate with Chromotropism, ***Aust. J. Chem.*** 2013, **66**, 477-484.
7. J. Piromchom, N. Wannarit, J. Boonmak, K. Chainok, C. Pakawatchai, S. Youngme, Flexible metal supramolecular framework of 2D cobalt(II) coordination polymer with water-induced reversible crystal-to-amorphous transformation, ***Inorg. Chem. Commun.***, 2014, **44**, 111–113.
8. J. Piromchom, N. Wannarit, J. Boonmak, C. Pakawatchai, S. Youngme, Synthesis, crystal structure and water-induced reversible crystal-to-amorphous transformation property of $[Co_2(2,4\text{-pydc})_2(bpa)(H_2O)_6](H2O)_2$, ***Inorg. Chem. Commun.***, 2014, **40**, 59–61.
9. J. Piromchom, J. Boonmak, K. Chainok, S. Youngme, Water-induced dynamic crystal-to-amorphous transformation of cobalt(II) coordination and supramolecular frameworks containing benzene-1,2,4,5-tetracarboxylic acid and trans-1-(2-pyridyl)-2-(4-pyridyl)ethylene ligands, ***Polyhedron***, 2015, **102**, 593-599.

PUBLICATION PAPERS OF MISCELLANEOUS RESULT

10. Cheansirisomboon, A., Salinas-Uber, J., Massera, C., Roubeau, O., Youngme, S., Gamez, P. One-pot multiple metal-organic framework formation: Concomitant generation of structural isomers or of drastically distinct materials, ***Eur. J. Inorg. Chem.***, 2014, 4385-4393.
11. Wannarit, N., Pakawatchai, C., Youngme, S., Di-μ-acetato-κ4O:O′-bis[(1,10-phenanthroline- κ2 N,N′)(trifluoromethanesulfonato-κO)copper(II)], ***Acta Cryst. E***, 2013, **E69** (11), m591 - m592
12. Piromchom, J., Wannarit, N., Pakawatchai, C., Youngme, S., The heterometallic cadmium-silver complex cis-bis[dicyanidoargentato(I)- κN]bis(5,5′-dimethyl-2,2′-bipyridyl-κ2 N,N′)cadmium(II) monohydrate, ***Acta Cryst. C***, 2013, **C69** (10), 1136 – 1139.
13. S. Kaenket, P. Phuengphai, C. Pakawatchaic, S. Youngme, Poly[tris(μ-4,4'-bipyridine-κ^2N:N')bis(dimethyl-sulfoxide-κO)tetrakis(thiocyanato-κN) dicobalt(II)], ***Acta Cryst. E***, 2014, **E70**, m265–m266.
14. Othong, J., Wannarit, N., Pakawatchai, C., Youngme, S. Crystal structure of a two-dimensional grid-type iron(II) coordination polymer: Poly[[diaquatetra-μ-cyanido-diargentate(I)iron(II)] trans-1,2-bis(pyridin-2-yl)ethylene disolvate], ***Acta Cryst. E***, 2014, **E70**(8), 107-110.
15. J. Piromchom, J. Othong, J. Boonmak, I. Mutikainen, S. Youngme, A novel one-dimensional metal-organic framework with a μ-cyanido-argentate group: catena-poly[[(5,5'-dimethyl-2,2'-bipyridyl-κ^2N,N')silver(I)]-μ-cyanido-κ^2N:C], ***Acta Cryst.*** 2015, **C71**, 1057-1061.
16. P. Suvanvapee, J. Boonmak, F. Klongdee, C. Pakawatchai, B. Moubaraki, K.S. Murray, S. Youngme, A Series of cyanoacetato copper(II) coordination polymers with various *N*,*N*'-ditopic spacers: Structural diversity, supramolecular robustness and magnetic properties. ***Cryst. Growth & Des.,*** 2015, **15**(8), 3804.
17. P. Suvanvapee, J. Boonmak, S. Youngme, Structural diversity and luminescent properties of cyanoacetato zinc/cadmium coordination polymers with *N*,*N*'-ditopic auxiliary ligands**.** ***Polyhedron,*** 2015, **102**, 693.
18. P. Suvanvapee, J. Boonmak, S. Youngme, Synthesis, crystal structure and luminescent properties of three new zinc/cadmium coordination polymers containing cyanoacetate and 1,2-di(4-pyridyl)ethylene. ***Inorg. Chim. Acta,*** 2015, **437**, 11.

Dalton Transactions

RSC Publishing

PAPER

View Article Online
View Journal | View Issue

Cite this: *Dalton Trans.*, 2013, **42**, 7120

Influence of supramolecular bonding contacts on the spin crossover behaviour of iron(II) complexes from 2,2′-dipyridylamino/*s*-triazine ligands†

Nanthawat Wannarit,[a,c] Olivier Roubeau,*[b] Sujittra Youngme,*[c] Simon J. Teat[d] and Patrick Gamez*[a,e]

Received 31st January 2013,
Accepted 27th February 2013

DOI: 10.1039/c3dt50326g

www.rsc.org/dalton

Reactions of the related ligands 2-(*N*,*N*-bis(2-pyridyl)amino)-4,6-bis(phenoxy)-(1,3,5)triazine (**L1**) and 2-(*N*,*N*-bis(2-pyridyl)amino)-4,6-bis(pentafluorophenoxy)-(1,3,5)triazine (**L1^F**) with iron(II) thiocyanate produced two spin-crossover coordination compounds with distinct cooperative behaviours. *trans*-[Fe(**L1**)$_2$(NCS)$_2$]·2CH$_2$Cl$_2$ (**1**) displays a very gradual transition centred at $T_{\frac{1}{2}}$ = 233 K, characterized by a ΔT_{80} (namely the temperature range within which 80% of the transition considered occurs) of 90 K, while that of fluorinated *trans*-[Fe(**L1^F**)$_2$(NCS)$_2$]·2CH$_3$CN (**3**) is significantly more abrupt (and centred at $T_{\frac{1}{2}}$ = 238 K), with a ΔT_{80} of 50 K, resulting from supramolecular contacts induced by the fluorinated phenol groups. The coordination compound equivalent to **1** with selenocyanate anions, namely *trans*-[Fe(**L1**)$_2$(NCSe)$_2$]·4CH$_2$Cl$_2$·4CH$_3$OH (**2**), also exhibits SCO properties centred at $T_{\frac{1}{2}}$ = 238 K, but the transition is very gradual (ΔT_{80} = 150 K). Light-induced excited spin-state trapping (LIESST) is effective although incomplete for **2** and **3**, while it is complete with a T_{LIESST} of 58 K for **1**.

Introduction

The spin-crossover (SCO) phenomenon is a particularly interesting manifestation of the ligand-field theory.[1,2] Hence, for octahedral d^4–d^7 transition-metal complexes that may be either low spin (LS) or high spin (HS), the occurrence of SCO is associated with intermediate ligand-field strength,[3] for which the transition-metal compound may present HS ↔ LS bistability through the application of an external stimulus like temperature, pressure or light.[4–7] Such behaviour is obviously very attractive, especially with d^6 Fe(II) ions for which the LS state is diamagnetic and sharp differences in optical properties are often associated with the SCO; therefore, SCO compounds may find applications in molecular switches,[8] data-storage devices[9,10] and optical displays.[11–13] Consequently, SCO has attracted a great deal of attention from the scientific community during decades, and this area of research has been experiencing a tremendous development since the past 5 years.[14–20] Thus, many SCO iron(II) complexes have been reported, typically exhibiting an octahedral [FeN$_6$] core obtained from ligands containing aromatic nitrogen-donor groups, such as pyridine or azole rings.[21–24]

Since 2006, we have been involved in the design and preparation of various types of pyridine-containing ligands for the generation of SCO compounds.[25–29] In particular, one of the families of ligands developed is based on the 1,3,5-triazine (or *s*-triazine) ring.[30] For instance, the ligand 2,4,6-tris(dipyridin-2-ylamino)-1,3,5-triazine (dpyatriz),[31] including three 2,2′-dipyridylamine units on a *s*-triazine ring, has allowed us to synthesize iron(II) coordination compounds with interesting SCO properties.[25,30,32,33] Then, Murray and co-workers have described various dipyridylamino-substituted-triazine ligands, which have produced a number of SCO compounds with distinct transition behaviours,[34–38] thus illustrating the potential of this category of ligands to create molecular switches.

[a]*Departament de Química Inorgànica, QBI, Universitat de Barcelona, Martí i Franquès 1-11, 08028, Barcelona, Spain. E-mail: patrick.gamez@qi.ub.es; http://www.bio-inorganic-chemistry-icrea-ub.com; Fax: +34 934907725*
[b]*Instituto de Ciencia de Materiales de Aragón (ICMA), CSIC and Universidad de Zaragoza, Plaza San Francisco s/n, 50009 Zaragoza, Spain*
[c]*Materials Chemistry Research Unit, Department of Chemistry and Centre of Excellence for Innovation in Chemistry, Faculty of Science, Khon Kaen University, Khon Kaen 40002, Thailand*
[d]*Advanced Light Source, Lawrence Berkeley National Laboratory, 1 Cyclotron Road, Berkeley, CA 94720, USA*
[e]*Institució Catalana de Recerca i Estudis Avançats (ICREA), Passeig Lluís Companys 23, 08010 Barcelona, Spain*

†Electronic supplementary information (ESI) available: Tables S1–S3 summarizing crystallographic and refinement parameters for **1–3**; Fig. S1–S4 illustrating particular features of the solid-state structures of **1–3**; ΔH and ΔS for **3** (Fig. S5); a d(χT)/dT *vs.* T plot for **3** (Fig. S6); Fig. S7 depicting the single-crystal X-ray structure of **L1**; Table S4 summarizing crystallographic and refinement parameters for **L1**. CCDC 921061–921067 and 922570. For ESI and crystallographic data in CIF or other electronic format see DOI: 10.1039/c3dt50326g

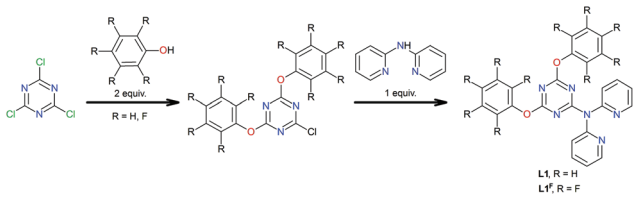

Scheme 1 Preparation of ligands 2-(*N*,*N*-bis(2-pyridyl)amino)-4,6-bis(phenoxy)-(1,3,5)triazine (**L1**) and 2-(*N*,*N*-bis(2-pyridyl)amino)-4,6-bis(pentafluorophenoxy)-(1,3,5)triazine (**L1^{F}**).

In the present study, two new members of this family of 2,2′-dipyridylamino/*s*-triazine ligands have been prepared. The straightforward and selective substitutions of the three chloride atoms of 2,4,6-trichloro-1,3,5-triazine by phenolic reagents and 2,2′-dipyridylamine yield the related ligands 2-(*N*,*N*-bis(2-pyridyl)amino)-4,6-bis(phenoxy)-(1,3,5)triazine (**L1**, R = H; Scheme 1) and 2-(*N*,*N*-bis(2-pyridyl)amino)-4,6-bis(pentafluorophenoxy)-(1,3,5)triazine (**L1^{F}**, R = F; Scheme 1). These two ligands, which differ by the replacement of the hydrogen atoms of the phenoxyl groups of **L1** by fluorides (**L1^{F}**), have been designed to investigate the role played by supramolecular interactions (*i.e.* π···π interactions, halogen bonding) induced by the distinct aryl groups in the SCO properties of the corresponding *trans*-[Fe**L**$_2$(NCS)$_2$] complexes.

Results and discussion

Synthesis and crystal structures

The ligands 2-(*N*,*N*-bis(2-pyridyl)amino)-4,6-bis(phenoxy)-(1,3,5)triazine (**L1**) and 2-(*N*,*N*-bis(2-pyridyl)amino)-4,6-bis-(pentafluorophenoxy)-(1,3,5)triazine (**L1^{F}**) are readily prepared *via* a two-step reaction in THF from 2,4,6-trichloro-1,3,5-triazine, following a straightforward synthetic procedure (Scheme 1 and the Experimental section).[39,40]

Compound **1**, *trans*-[Fe(**L1**)$_2$(NCS)$_2$]·2CH$_2$Cl$_2$, is obtained with a yield of 70% by direct addition of a freshly prepared water/methanol solution of iron(II) thiocyanate (1 equiv.) to a dichloromethane solution containing 2 equiv. of **L1**. **1**, which exhibits SCO properties (see section Magnetic studies), crystallizes in the triclinic space group $P\bar{1}$, at 100, 240 and 300 K (Table S1†). A representation of the molecular structure of **1** at 100 K (low-spin state) is depicted in Fig. 1. Selected bond lengths and angles are listed in Table 1.

The iron(II) centre in **1** displays the expected octahedral coordination environment, typically observed for iron(II) thiocyanate complexes with this family of dipyridylamino-substituted-triazine ligands.[25,33–38] The metal ion is coordinated by two **L1** ligands in the equatorial plane of the octahedron, the apical positions being occupied by two *trans* thiocyanate anions (Fig. 1). At 100 K, the Fe–N$_{pyridine}$ distances in the range 1.981(2)–1.992(2) Å are characteristic of an LS iron(II) ion. The Fe–N$_{NCS}$ bond lengths of 1.943(2) Å are also indicative of an LS state. These coordination bond lengths increase by *ca.* 0.22 Å for Fe–N$_{pyridine}$ and *ca.* 0.13 Å for Fe–N$_{NCS}$ when the temperature is raised to 300 K (Table 1), which describe a full spin transition that has been observed as well by variable-temperature magnetic susceptibility measurements (see below). At 240 K, the distances found, *i.e.* 2.149(2)–2.163(2) Å for Fe–N$_{pyridine}$ and 2.051(2) Å for Fe–N$_{NCS}$, correspond to an HS–LS mixture of about 78/22, in agreement with bulk magnetic studies.

The distortion parameters Σ and Φ gauge the magnitude of the deformation of the coordination geometry relative to a perfect octahedron (for which $\Sigma = \Phi = 0$).[15,41,42] For LS **1**, Σ = 31 and Φ = 37 and these values increase to respectively 46 and 67 for the HS state (Table 1). $\Delta\Sigma$ ($\Sigma_{HS} - \Sigma_{LS}$) and $\Delta\Phi$ ($\Phi_{HS} - \Phi_{LS}$) thus illustrate the extent of the structural changes that take place during the spin transition. For **1**, $\Delta\Sigma$ = 15 and $\Delta\Phi$ = 30. The high $\Delta\Phi$ value indicates a severe distortion of the

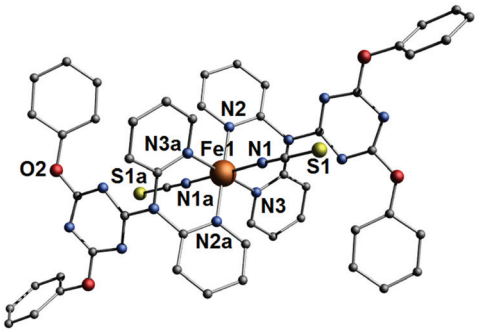

Fig. 1 Representation of the molecular structure of compound **1** (LS state, determined at 100 K) with a partial atom-numbering scheme. The hydrogen atoms and the lattice dichloromethane molecules are not shown for clarity. Symmetry operation: a, 1 − *x*, 1 − *y*, 1 − *z*.

Table 1 Coordination bond lengths (Å) and angles (°), and supramolecular interactions for compound **1** at three different temperatures

Bond	100 K (LS)	240 K	300 K (HS)
Fe1–N1	1.943(2)	2.051(2)	2.075(4)
Fe1–N2	1.992(2)	2.163(2)	2.216(3)
Fe1–N3	1.981(2)	2.149(2)	2.203(3)
Fe1···Fe1$_{inter}$ [a]	10.138(2)	10.239(2)	10.301(4)
Angle[b]	100 K	240 K	300 K
N2–Fe1–N3	86.8(6)	83.5(8)	82.4(1)
N2–Fe1–N3a	93.3(6)	96.5(8)	97.6(1)
N1–Fe1–N1a	180	180	180
ΣFe[c]	31	40	46
Φ[d]	37	58	67
H-bonding contacts	100 K	240 K	300 K
C11–H11A···O2	3.559(3)	3.609(4)	3.642(8)
C27–H27A···C13	3.415(3)	3.508(4)	3.526(7)
Lone pair···π interactions	100 K	240 K	300 K
Cg5···S1	3.459(1)	3.561(1)	3.598(2)

[a] Closest inter-monomer Fe···Fe distance. [b] Symmetry operation: a, 1 − *x*, 1 − *y*, 1 − *z*. [c] Σ = the sum of $|90 - \theta|$ for the 12 N–Fe–N angles in the octahedron.[43,44] [d] Φ = the sum of $|60 - \theta|$ for the 24 N–Fe–N angles describing the trigonal twist angle.[15,41]

original octahedral geometry towards a trigonal prismatic structure, a feature that is commonly noticed upon LS → HS transition.[15] Such a structural distortion may affect the degree of interaction between the spin active species, resulting in cooperativity between the switching centres that is normally reflected by an abrupt LS ↔ HS crossover phenomenon. Actually, the magnetic studies (see below) reveal a weakly cooperative behaviour since a complete HS-to-LS conversion is realized within a temperature range of *ca.* 90 K (see section Magnetic studies).

The crystal packing of **1** shows that the iron(II) centres weakly interact along the crystallographic *c* axis through C–H···O and C–H···π contacts (which are affected by the transition; see Table 1), producing a supramolecular 1D chain (Fig. 2A). These chains do not significantly interact with each other (Fig. 2B), which may explain the moderate cooperativity of the SCO behaviour observed by magnetic measurements (see below).

In addition, the molecules of **1** display intramolecular lone pair···π interactions[45] between the thiocyanate sulfur atoms and the triazine rings (Cg5···S1 = 3.459(1) Å; Fig. S1†).

Compound **2**, *trans*-$[Fe(\mathbf{L1})_2(NCSe)_2]\cdot 4CH_2Cl_2\cdot 4CH_3OH$, is obtained with a yield of 63%, applying the same synthetic procedure as that used to prepare **1**, replacing iron(II) thiocyanate by iron(II) selenocyanate. As anticipated, **2** is an SCO compound (see section Magnetic studies), which crystallizes in the monoclinic space group $P2_1/c$ in its LS state (Table S2†). A view of the molecular structure of **2** is shown in Fig. 3.

Unsurprisingly, the coordination environment of the iron(II) ion in **2** is similar to that of **1** (see Fig. 1 and 3). The observed octahedral geometry is formed by four pyridine donors in the equatorial plane (belonging to two **L1** ligands) and two axial $NCSe^-$ anions. The Fe–$N_{pyridine}$ bond lengths ranging from 1.992(4) to 2.009(4) Å and the Fe–N_{NCSe} distances of 1.940(4) Å

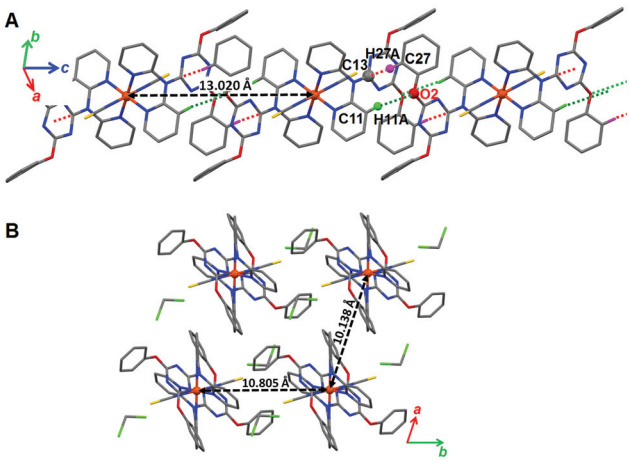

Fig. 2 Views of the crystal packing of LS **1** showing (A) the formation of a supramolecular 1D chain along the crystallographic *c* axis by means of weak C–H···O and C–H···π contacts (respectively C11–H11A···O2 = 3.559(3) Å, green dotted lines and C27–H27A···C13 = 3.415(3) Å, red dotted lines); (B) the arrangement of the chains in the *ab* plane illustrating the lack of significant interactions between them.

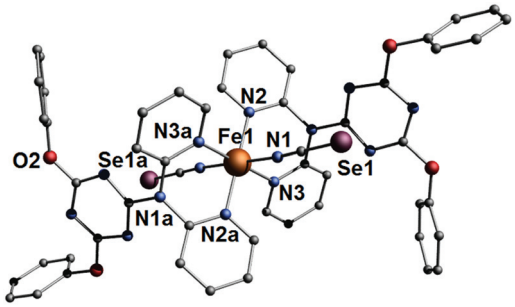

Fig. 3 Representation of the molecular structure of compound **2** (LS state, determined at 100 K) with a partial atom-numbering scheme. The hydrogen atoms and the lattice dichloromethane molecules are not shown for clarity. Symmetry operation: a, 1 − *x*, 1 − *y*, 1 − *z*.

Table 2 Coordination bond lengths (Å) and angles (°), and supramolecular interactions for compound **2** (low-spin state)[a]

Bond	100 K (LS)
Fe1–N1	1.940(4)
Fe1–N2	1.992(4)
Fe1–N3	2.009(4)
$Fe1\cdots Fe1_{inter}$ [b]	8.642(4)
Angle	**100 K (LS)**
N2–Fe1–N3	86.5(2)
N2–Fe1–N3a	93.6(2)
N1–Fe1–N1a	180
ΣFe[c]	25
Φ[d]	32
π···π interactions	**100 K (LS)**
Cg7···Cg7j	3.717(4)
C22···C24j	3.234(9)
C22···C23j	3.208(8)
C8···C10d	3.796(8)
C–H···π contacts	**100 K (LS)**
C4–H4A···C17g	3.607(7)
C5–H5A···C18g	3.552(7)
Lone pair···π interactions	
Cg5···Se1	3.501(2)
Hydrogen bond	
O1s–H1s···O2s	2.828(12)
O1s–H1s–O2s	150(8)
O2s–H2s···N5	3.074(9)
O2s–H2s–N5	155(7)

[a] Symmetry operation: a, 1 − *x*, 1 − *y*, 1 − *z*; d, −*x*, 1 − *y*, 1 − *z*; g, *x*, 1/2 − *y*, 1/2 + *z*; j, −*x*, 1 − *y*, −*z*. [b] Closest inter-monomer Fe···Fe distance. [c] Σ = the sum of $|90 - \theta|$ for the 12 N–Fe–N angles in the octahedron.[43,44] [d] Φ = the sum of $|60 - \theta|$ for the 24 N–Fe–N angles describing the trigonal twist angle.[15,41]

(Table 2) are typical for an LS iron(II) system, and are comparable to those found for **1** (Tables 1 and 2). Unfortunately, crystallographic data for HS **2** could not be obtained. Actually, single crystals of **2** did not diffract enough at room temperature, most likely as a result of solvent evaporation (and particularly dichloromethane).

The crystal packing of LS **2** reveals the formation of a 1D chain of iron(II) complexes that are connected by parallel-

displaced π···π interactions involving the phenyl ring (C21, C22, C23, C24, C25, C26), with a centroid-to-centroid distance of 3.717(4) Å (Cg7···Cg7j; see Table 2 and Fig. 4A). These π stacks are characterized by short C···C contact distances of 3.208(8) Å (C22···C23j) and 3.234(9) Å (C22···C24j). It has to be noted that these π···π stacking interactions (which are not occurring in **1**) give rise to a different orientation of the corresponding phenyl rings in compounds **1** and **2** (see phenyl rings of the oxygen atom O2 in Fig. 1 and 3). These chains are weakly interacting with each other *via* π···π (C8···C10d) and C–H···π (C4–H4A···C17g and C5–H5A···C18g) long contacts (see Table 2 and Fig. 4B).

Surprisingly, although the iron(II) complexes appear to better interact with each other compared to those in **1**, the SCO behaviour of **2** is clearly much less cooperative; actually, the transition is very gradual as the HS state is fully converted into the LS state within a temperature range of over 150 K (see section Magnetic studies). This feature may be explained by the presence of numerous solvent molecules in the crystal lattice of **2**. Indeed, compound **2** is surrounded by 8 solvent molecules, *i.e.* $4CH_3OH$ and $4CH_2Cl_2$, while only $2CH_2Cl_2$ are found for **1**. Therefore, all these solvent molecules in **2** (which are interacting with each other and with the complex; see hydrogen bonds in Table 2) most likely affect the propagation of the spin transition; hence, the behaviour of **2** resembles that of a diluted system (see Fig. S2†), in which the metal centres within the solid are transiting independently, thus resulting in a non-cooperative conversion following Boltzmann population of states.

Finally, similarly to **1**, the molecules of **2** display intramolecular lone pair···π interactions between the selenocyanate selenium atoms and the triazine rings (Cg5···Se1 = 3.501(2) Å; Fig. S3†).

Compound **3**, *trans*-$[Fe(\mathbf{L1^F})_2(NCS)_2]\cdot 2CH_3CN$, is prepared with a yield of 65% by direct addition of a freshly prepared water–acetonitrile solution of iron(II) thiocyanate (1 equiv.) to an acetonitrile solution containing 2 equiv. of $\mathbf{L1^F}$. As the previous two complexes, **3** exhibits spin-transition properties (see section Magnetic studies). **3** crystallizes in the triclinic $P\bar{1}$ space group at 100, 190 and 280 K (Table S3†). Selected coordination bond distances and angles are listed in Table 3. A view of the molecular structure of **3** is depicted in Fig. 5.

Table 3 Coordination bond lengths (Å) and angles (°), and supramolecular interactions for compound **3** at three different temperatures

Bond	100 K (LS)	190 K	280 K (HS)
Fe1–N1	1.937(1)	1.943(1)	2.056(3)
Fe1–N2	1.979(1)	1.985(2)	2.194(2)
Fe1–N3	1.988(1)	1.989(1)	2.207(2)
$Fe1\cdots Fe1_{inter}$ [a]	8.350(1)	8.412(1)	8.643(2)
Angle[b]	**100 K**	**190 K**	**280 K**
N2–Fe1–N3	86.16(5)	86.19(6)	81.83(9)
N2–Fe1–N3a	93.85(5)	93.81(6)	98.17(9)
N1–Fe1–N1a	180	180	180
ΣFe[c]	30	30	41
Φ[d]	36	36	72
π···π interactions[b]	**100 K**	**190 K**	**280 K**
O1···C16c	3.112(2)	3.118(3)	3.092(4)
O1···C17c	3.255(2)	3.247(3)	3.238(4)
C15···C16c	3.387(2)	3.378(3)	3.385(5)
Cg3···Cg3b	3.757(1)	3.747(1)	3.787(2)
Halogen···halogen contacts[b]	**100 K**	**190 K**	**280 K**
F8···F9l	2.781(2)	2.803(2)	2.815(4)
Lone pair···π interactions	**100 K**	**190 K**	**280 K**
Cg5···S1	3.457(1)	3.489(1)	3.579(2)

[a] Closest inter-monomer Fe···Fe distance. [b] Symmetry operation: a, 1 – *x*, 1 – *y*, 1 – *z*; b, –1 + *x*, *y*, *z*; c, 1 – *x*, 1 – *y*, 2 – *z*; l, 2 – *x*, 2 – *y*, 1 – *z*. [c] Σ = the sum of $|90 - \theta|$ for the 12 N–Fe–N angles in the octahedron.[43,44] [d] Φ = the sum of $|60 - \theta|$ for the 24 N–Fe–N angles describing the trigonal twist angle.[15,41]

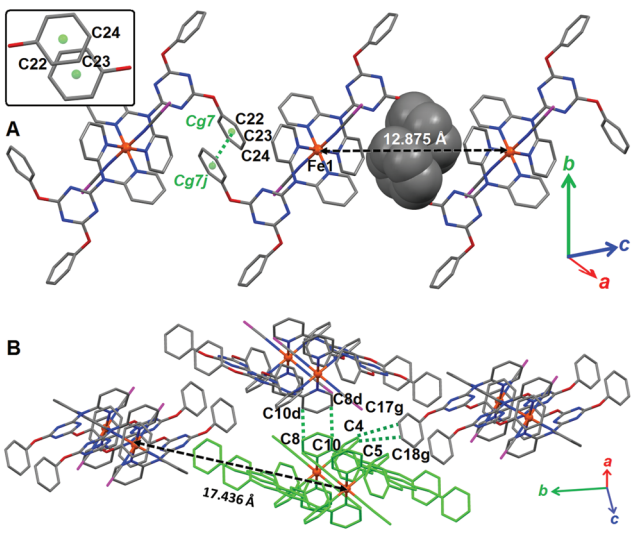

Fig. 4 Views of the crystal packing of LS **2** showing (A) the formation of a supramolecular 1D chain *via* parallel-displaced π···π interactions (Cg7···Cg7j = 3.717(4) Å (the inset illustrates a parallel-displaced π···π stack); (B) the feeble interactions of the chains (one chain is shown in green) by means of weak π···π (C8···C10d = 3.796(8) Å) and C–H···π (C4–H4A···C17g = 3.607(7) Å and C5–H5A···C18g = 3.552(7) Å) contacts. Symmetry operations: d, –*x*, 1 – *y*, 1 – *z*; g, *x*, 1/2 – *y*, 1/2 + *z*; j, –*x*, 1 – *y*, –*z*.

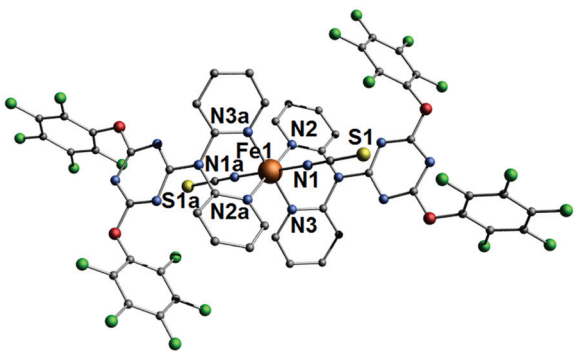

Fig. 5 Representation of the molecular structure of compound **3** (LS state, determined at 100 K) with a partial atom-numbering scheme. The hydrogen atoms and the lattice acetonitrile molecules are not shown for clarity. Symmetry operation: a, 1 – *x*, 1 – *y*, 1 – *z*.

The coordination environment of the iron(II) ion in **3** is analogous to those of compounds **1** and **2**. The equatorial plane of the octahedron contains four pyridine donors belonging to two $\mathbf{L1^F}$ ligands, and the axial positions are occupied by two thiocyanate anions. At 100 K, the Fe–$N_{pyridine}$ and Fe–N_{NCS} coordination bond lengths are typical for an LS FeN_6 (Table 3), and are comparable to those of **1** and **2**. For HS **3** at 280 K, these bond distances increase by respectively *ca.* 0.22 and 0.12 Å (Table 3), thus giving characteristic values for this spin state. This full LS → HS transition is corroborated by magnetic measurements (see below). At 190 K, the Fe–$N_{pyridine}$ and Fe–N_{NCS} distances are indicative of an LS–HS mixture of about 95/5, in agreement with the data obtained by magnetic-susceptibility measurements (see below).

The distortion parameters Σ and Φ amount to respectively 30 and 36 for LS **3**, and to 41 and 72 for HS **3**. Hence, the corresponding $\Delta\Sigma$ and $\Delta\Phi$ values of respectively 11 and 36 again reflect a strong distortion of the octahedral geometry upon LS → HS transition. As mentioned above, such a distortion is often associated with cooperativity between the transiting centres. In the present case, $\Delta\Phi = 36$ is higher than that found for the related complex **1** ($\Delta\Phi = 30$). Therefore, a greater cooperative behaviour is expected for **3** in comparison to **1**; in fact, a clearly more abrupt transition (see the corresponding χT *vs.* T plots below) is observed for **3**, which may be rationalized by specific crystal-packing features induced (at least in part) by the fluorinated ligand $\mathbf{L1^F}$.

Actually, the crystal packing of LS **3** reveals an intricate network of strong supramolecular bonds (Fig. 6). First, molecules of **3** are connected *via* strong lone pair···π (O1···C16c and O1···C17c; see Table 3 and Fig. 6A) and π···π (C15···C16c; see Table 3 and Fig. 6A) interactions. It has to be noted that the O1···C16c contact distance of 3.112(2) Å is below the sum of the van der Waals radii of O and C (*i.e.* 3.22 Å), thus indicating a very strong interaction between the fluorinated aromatic rings (through lone pair···π interactions[46–48]). These supramolecular bonds generate a 1D chain that runs along the crystallographic *c* axis. Next, the 1D chains are associated by means of nearly face-to-face π···π interactions between coordinated pyridine moieties characterized by a centroid-to-centroid distance of 3.757(1) Å (see Table 3 and Fig. 6B). This spatial arrangement produces a 2D supramolecular sheet in the *ac* plane (Fig. 6B). Finally, the 2D sheets are connected to each other by double strong F···F bonds (indeed, the F8···F9I distance of 2.781(2) Å is well below the sum of the van der Waals radii of two F atoms, namely 2.94 Å),[49] giving rise to a 3D framework (Fig. 6C).

In summary, the transiting iron(II) centres are very well linked to each other (within all the crystal lattice, in contrast to **1** and **2**). Moreover, the solid-state structure of **3** includes less lattice solvent molecules than **2** (which contains 8 molecules of the solvent per iron(II) complex); hence **3** is clearly the most compact of the three systems. Therefore, an efficient cooperative behaviour may be expected for **3**. As a matter of fact, the magnetic studies show the steepest HS ↔ LS transition for **3**, which is completed within a temperature range of

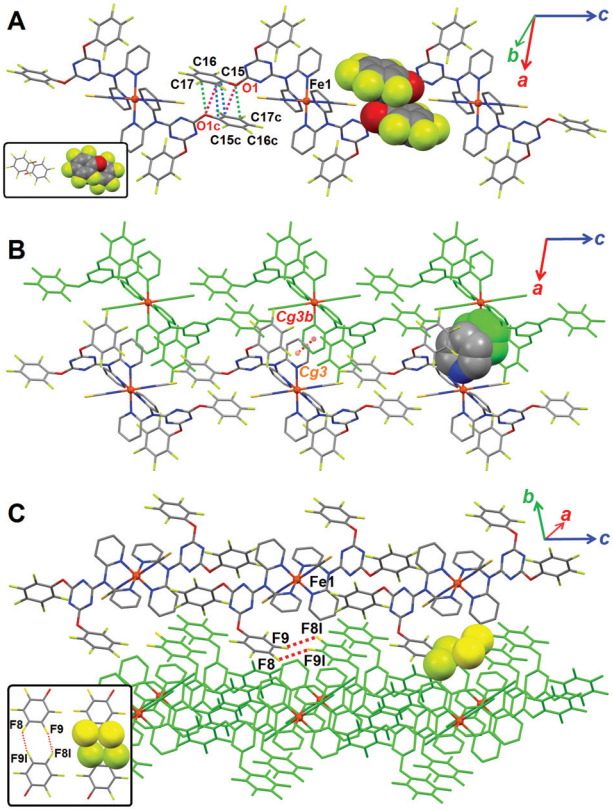

Fig. 6 Views of the crystal packing of LS **3** showing (A) the formation of a supramolecular 1D chain *via* parallel-displaced pentafluorophenyl···pentafluorophenyl interactions (O1···C16c = 3.112(2) Å, O1···C17c = 3.255(2) Å and C15···C16c = 3.387(2) Å) (the inset illustrates the occurrence of a parallel-displaced stack between two pentafluorophenyl rings); (B) the formation of 2D sheets by means of π···π interactions between coordinated pyridine rings (Cg3···Cg3b = 3.757(1) Å). One supramolecular chain is shown in green; (C) the formation of a 3D supramolecular framework through the connection of the 2D sheets by strong F···F bonding contacts (F8···F9I = 2.781(2) Å) (the inset illustrates the bonding interaction of pentafluorophenyl rings *via* double halogen··· halogen contacts), a 2D supramolecular sheet is shown in green. Symmetry operations: b, −1 + *x*, *y*, *z*; c, 1 − *x*, 1 − *y*, 2 − *z*; I, 2 − *x*, 2 − *y*, 1 − *z*.

ca. 50 K (while it is about 90 K for **1** and 150 K for **2**; see below).

As for **1** and **2**, lone pair···π interactions are realized between the thiocyanate sulfur atoms and the triazine rings (Cg5···S1 = 3.457(1) Å; Fig. S4†).

Magnetic, photomagnetic and thermal studies

Confirmation of the process of thermal SCO indicated by the structural observations on single crystals of **1–3** was obtained through magnetization measurements on bulk samples in the temperature range 5–300 K. The resulting temperature dependencies of the χT product (Fig. 7), χ being the molar paramagnetic susceptibility, evidence for all three compounds a complete and gradual thermal SCO. For compound **1**, the χT product is 3.19 $cm^3\ mol^{-1}$ K at 300 K, a value typical for an Fe(II) ion in an HS $S = 2$ state. χT starts to decrease already from 300 K to reach values of *ca.* 0.11–0.07 $cm^3\ mol^{-1}$ K below 160, which are now indicative of a fully populated LS $S = 0$

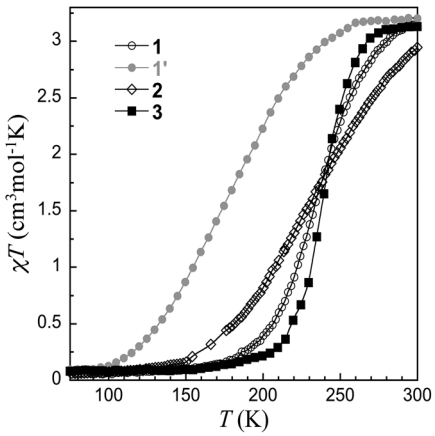

Fig. 7 χT *vs. T* plot for **1** (empty circles), **1′** (full circles), **2** (empty rhomboids) and **3** (full squares) showing the complete and gradual SCO. Lines are only guides to the eye.

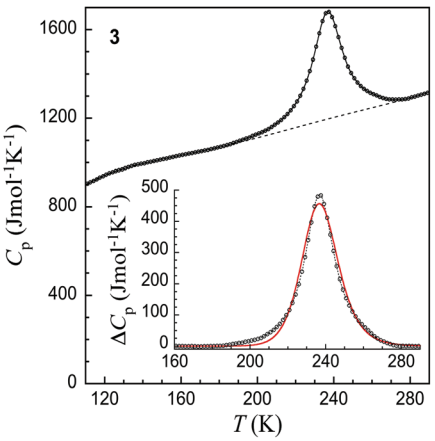

Fig. 8 Molar heat capacities of **3** showing a broad hump associated with the SCO. The dashed line is the estimated lattice component. Inset: excess heat capacities associated with the SCO in **3**. The full line is a fit to the domain model of Sorai (see the text and ref. 57) with n = 6.2.

state. The corresponding transition is centred at $T_{\frac{1}{2}}$ = 233 K. The selenocyanate derivative **2** exhibits a more gradual SCO centred at $T_{\frac{1}{2}}$ = 228 K, with a χT value of only 2.95 cm^3 mol^{-1} K at 300 K (thus suggesting that the transition process has already started to take place at this temperature), and <0.10 cm^3 mol^{-1} K below 130 K. In contrast, the SCO process, centred at $T_{\frac{1}{2}}$ = 238 K, is more abrupt for **3** (as a result of a better cooperativity; see above), with a decrease of χT from 3.10 cm^3 mol^{-1} K at 280 K down to 0.2–0.1 below 200 K. This comparatively more cooperative character is illustrated by a smaller ΔT_{80} value of 50 K (80% of the transition occurs within about 50 K) for **3**, compared to those observed for **1** and **2**, respectively, at 90 and 150 K. These observations are reproduced upon warming, thus without detectable hysteresis, and over various cycles and batches, although only for fresh crystalline material in the case of **1**. Indeed, a more gradual, though complete, SCO centred at *ca.* 173 K is detected for the poorly crystalline powder **1′** obtained upon air exposure of **1**, which is ascribed to the loss of lattice solvent molecules (as indicated by Elemental Analysis; see the Experimental section). The observation of a similar $T_{\frac{1}{2}}$ for the thiocyanate and selenocyanate derivatives **1** and **3** agrees with our previous report with the related complexes obtained with the ligand 6-chloro-*N*-phenyl-*N*,*N*-di(pyridin-2-yl)-1,3,5-triazine-2,4-diamine.[33] It thus seems that the replacement of S by Se in this family of *trans*-[Fe^{II}**L**$_2$(NCX)$_2$] compounds has only little influence on the SCO temperature, in contrast to other NCX-based SCO compounds.[50–54]

Confirmation of the relatively cooperative character of the SCO for **3** was obtained from Differential-Scanning Calorimetry (DSC). Indeed, while only very broad poorly energetic humps are detected for **1′** and **2**, the molar heat capacity of **3** at constant pressure, C_p, exhibits a strong anomaly between 200 and 280 K, culminating at *ca.* 237 K (see Fig. 8), which can be attributed to the SCO phenomenon in **3**. Both the associated excess enthalpy and entropy are relatively large, respectively, at 11.70 kJ mol^{-1} and 49.6 J mol^{-1} K^{-1} (see the Experimental section and Fig. S5†), which is usually seen as a consequence

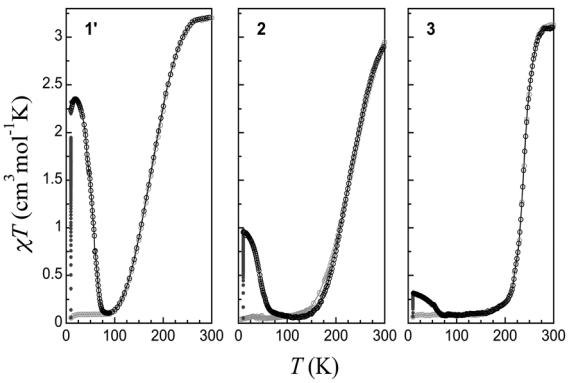

Fig. 9 χT *vs. T* plot for **1′** (left), **2** (middle) and **3** (right), showing the process of SCO (grey empty circles), the (partial) LS to HS photo-induced trapping at 10 K (full circles) and the relaxation back to the LS ground state and normal behaviour upon warming (black empty circles).

of a cooperative character of the SCO.[55,56] In particular, the excess entropy is well above the purely electronic component, *R*Ln5; it thus encloses a significant content arising from the coupling of the electronic transition with lattice phonons. Fitting the excess heat capacity of **3** to Sorai's domain model[57] results in a number of interacting molecules per domain of n = 6.2 (red line in the inset of Fig. 8), which is characteristic of a relatively cooperative SCO, in agreement with the magnetic studies (Fig. 9).

Preliminary photomagnetic studies on thin samples of **1′**, **2** and **3** indicate that an HS metastable state can be trapped for all three compounds at low temperatures through the so-called LIESST effect,[58] although with distinct efficacies. Indeed, while an increase of χT is detected upon irradiation in the 500–650 nm range at 10 K, the initial rate of increase is highest for **1′**, and smallest for **3**, for a similar sample thickness. In addition, the rate of increase drops more rapidly for **2** and **3**, with stable values, corresponding to incomplete trapping of at most 40 and 20% HS respectively, reached at longer

irradiation times. On the other hand, a full HS state can be trapped in the case of **1′**. Upon warming, an increase of χT is first observed, which corresponds to the Zero-Field Splitting effect of trapped HS species. Subsequently, a decrease gradually sets in, which is due to the thermally-activated relaxation back to the LS state that is reached at *ca.* 85 K. A characteristic T_{LIESST} temperature of 58 K can be defined,[59] through the first derivative of χT (Fig. S6†). For the other two compounds, χT decreases already from 10 K to reach values similar to those of the normal LS state at *ca.* 70 K. Thus, even with a partial trapping, relaxation of the trapped HS species back to the LS ground state is not as fast at low temperatures as in the previously reported compound *trans*-[Fe(Cladpat)$_2$(NCS)$_2$].[33] Therefore, considering that the three samples had a similar thickness, the most likely origin of the lack of efficiency of the LIESST effect in **2** and **3** is an overlap of the $^5T_2 \rightarrow {}^5E$ (HS) band with an LS band (possibly $^1A_1 \rightarrow {}^3T_1$), giving rise to competitive LIESST and reverse-LIESST processes.[58,60,61]

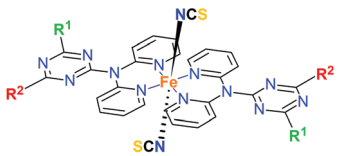

Scheme 2 Representation of the *trans*-[Fe^{II}**L**$_2$(NCS)$_2$] complexes whose structural and SCO properties are described in Table 4. **R^1** and **R^2** symbolize different substituents on the triazine ring (see Table 4).

SCO systems based on 2,2′-dipyridylamino-substituted triazine ligands and Fe(NCS)$_2$

As mentioned earlier, iron(II) complexes of the type *trans*-[Fe^{II}**L**$_2$(NCS)$_2$], where **L** is a 2,2′-dipyridylamino-substituted triazine ligand (Scheme 2), usually display SCO properties, and the two new members of this family of compounds, namely **1** and **3**, verify this characteristic. Since the first report of such an SCO system by some of us,[25] we and Murray and co-workers have reported a number of 2,2′-dipyridylamino/triazine-based complexes.[33–35,37,38] Relevant structural features and SCO properties of these coordination compounds are described in Table 4. To date, 14 different *trans*[Fe^{II}**L**$_2$(NCS)$_2$] complexes have been obtained from 13 distinct ligands. Out of them, two do not show SCO properties; in fact, the simplest member of this family of ligands, namely when **R^1** = **R^2** = Cl, does not generate an iron(II) SCO compound.[33] Surprisingly, the *trans*-[Fe^{II}**L**$_2$(NCS)$_2$] complex whose ligand **L** contains two diphenylamine substituents is also a non-SCO material. All other compounds exhibit SCO properties (complete or incomplete transitions), with $T_{\frac{1}{2}}$ values ($T_{\frac{1}{2}}$ corresponds to the temperature at which half of the transiting iron(II) centres have changed their spin state) ranging from 110 up to 260 K, indicating that the transition can be fine-tuned through selection of the R

Table 4 Structural and SCO properties of crystallographically characterized *trans*-[Fe^{II}**L**$_2$(NCS)$_2$] compounds with 2,2′-dipyridylamino-substituted triazine ligands **L** (Scheme 2)

R^1	**R^2**	Nuclearity	SCO character	SCO behaviour	Hysteresis	$T_{\frac{1}{2}}$	$\Delta\Sigma$	$\Delta\Phi$	Lattice solvent(s)	Ref.
Chlorine	Chlorine	Monomer	—	No	—	—	—	—	H_2O	33
Chlorine	Aniline	Monomer	Gradual; ΔT_{80} [a] = 50 K	Complete	No	178 K	15	27	No	33
Chlorine	Dipyridylamine	Polymer	Very gradual; $\Delta T_{80} \approx 50$ K	Incomplete (half SCO)[b]	No	~205 K	13/9[c]	26/0[c]	CH_3OH	38
Dipyridylamine	Dipyridylamine	Monomer	Gradual; $\Delta T_{80} = 40$ K	Complete	No	200 K	12	31	No	25
Dipyridylamine	Pyridine-4(1*H*)one	Polymer	Very gradual; $\Delta T_{80} = 77$ K	Complete	No	175 K	12/13[c]	22/24[c]	CH_2Cl_2	37
Dipyridylamine	Pyridine-4(1*H*)one	Polymer	Gradual; $\Delta T_{80} = 55$ K	Complete	No	200 K	12/11[c]	21/6[c]	$CHCl_3$–CH_3OH	37
Dipyridylamine	Phenol	Polymer	Gradual; $\Delta T_{80} = 39$ K	Incomplete	No	190 K	8/1[c]	20/6[c]	H_2O–CH_3OH	37
Dipyridylamine	Hydroquinone	Polymer	Gradual; $\Delta T_{80} = 50$ K	Incomplete	No	260 K	4/3[c]	9/8[c]	CH_2Cl_2	37
Dipyridylamine	Aza-15-crown-5	Polymer	Very gradual; $\Delta T_{80} = 80$ K	Complete	No	110 K	—[d]	—[d]	CH_3OH	35
Dibenzylamine	Dibenzylamine	Monomer	Gradual; $\Delta T_{80} = 50$ K	Complete	No	~170 K[e]	13	27	No	34
Diphenylamine	Diphenylamine	Monomer	—	No	—	—	—	—	CH_2Cl_2	34
Aza-15-crown-5	Aza-15-crown-5	Monomer	Very gradual; $\Delta T_{80} \approx 80$ K	Complete	No	~240 K	14	31	*n*-C_3H_7OH	35
Phenol	Phenol	Monomer	Very gradual; $\Delta T_{80} = 90$ K	Complete	No	233 K	15	30	CH_2Cl_2	This work
Pentafluorophenol	Pentafluorophenol	Monomer	Gradual; $\Delta T_{80} = 50$ K	Complete	No	238 K	11	36	CH_3CN	This work

[a] ΔT_{80} is the temperature range within which 80% of the transition considered occurs. [b] The full LS state is not reached as only half of the iron(II) centres are transiting.[38] [c] The compound exhibits two crystallographically distinct iron(II) centres. [d] Only the X-ray structure of the LS compound has been reported.[35] [e] A different polymorphic form of this compound exhibits a very gradual spin transition ($\Delta T_{80} \approx 85$ K) centred at 300 K.[34]

groups (and the possibilities are limitless). All compounds display very gradual to gradual spin transitions, the more abrupt one (ΔT_{80} = 39 K) being obtained when R^1 = dipyridylamine and R^2 = phenol. It is actually a 1D polymeric chain[37] wherein the cooperativity between the iron(II) ions appears to be relatively efficient. By comparison, when dipyridylamine is replaced by a phenol, *i.e.* when R^1 = R^2 = phenol, a significantly more gradual behaviour (ΔT_{80} = 90 K) is observed for the corresponding monomeric species. No hysteretic behaviours have been observed for all these systems; however, it is assumed that careful design of a 2,2′-dipyridylamino-substituted triazine ligand(s) **L** with well-chosen R substituents will allow us to enhance cooperativity between the iron(II) centres that may favour the occurrence of hysteresis.

It can be noted once again that lattice solvent molecules have a great effect on the SCO properties of a coordination compound. Indeed, for the *trans*-[$Fe^{II}L_2(NCS)_2$] complex with R^1 = dipyridylamine and R^2 = pyridine-4(1*H*)one, distinct SCO behaviours have been obtained in dichloromethane and in chloroform/methanol. In dichloromethane, the compound exhibits a very gradual transition (ΔT_{80} = 77 K) centred at $T_{\frac{1}{2}}$ = 175 K, while a more abrupt transition (ΔT_{80} = 55 K) is observed in $CHCl_3$–CH_3OH, at a higher temperature ($T_{\frac{1}{2}}$ = 200 K). This clearly illustrates the sensitivity of the SCO phenomenon, where not only the coordination sphere of the metal ion is important but also the interactions between the complexes in the solid-state and the involvement of lattice solvent molecules (as observed for instance in the present study with compounds **1** and **1′**).

Conclusions

In the present study, three new members of the still small (but increasing) family of SCO compounds based on the 2,2′-dipyridylamino/*s*-triazine moiety have been obtained and fully characterized. The investigation carried out clearly shows the importance of supramolecular contacts in the cooperativity of the spin-transition process. Indeed, the triazine ligand containing the fluorinated phenolic groups generates a Fe(II)–NCS complex (*i.e.* **3**) whose SCO is significantly more abrupt (ΔT_{80} = 50 K) than that of the equivalent coordination compound (*i.e.* **1**) with the ligand bearing simple phenolic substituents (ΔT_{80} = 90 K). These distinct behaviours are obviously due to the fluoride atoms; actually, the F atoms give a π-acidic character to the phenyl rings, hence favouring the occurrence of strong intermolecular π···π interactions (which do not take place in the solid-state structure of compound **1**, which lacks the F atoms). In addition, the F atoms are involved in strong intermolecular halogen···halogen bonding contacts (with F···F contact distances well below the sum of the vdW radii), improving further the cooperative character of the SCO.

The exploration of the physical properties of the iron(II) complexes (with NCS or NCSe anions) obtained from the mixed ligand, namely the 2,2′-dipyridylamino/*s*-triazine ligand containing both phenol and pentafluorophenol groups, represents the next logical step of investigation. Actually, these studies have been initiated by our group and the outcome will be reported in a future paper.

Experimental section

Physical measurements

Infra-red spectra (as KBr pellets) were recorded with a Nicolet 5700 FT-IR spectrometer. Elemental analyses were performed by the Servei de Microanalisi, Consejo Superior de Investigaciones Cientifícas (CSIC) of Barcelona. ^{1}H NMR spectra were recorded at room temperature with a Varian Unity 300 MHz spectrometer; chemical shifts are reported in ppm relative to the residual solvent signal of $CDCl_3$ (δ = 7.26 ppm).

Variable-temperature magnetic-susceptibility data were collected on microcrystalline samples of **1–3** with Quantum Design SQUID magnetometers housed at either the SAI Physical Measurements of the University of Zaragoza or the Serveis Cientificotècnics of the Universitat de Barcelona. Pascal's constants were used to estimate diamagnetic corrections to the molar paramagnetic susceptibility, and a correction was applied for the sample holder. Warming and cooling rates were of the order of 0.3 K min^{-1}. Irradiation experiments were performed using the Quantum Design fibre optics setup (FOSH) on thin pellets (<0.5 mm). The applied field was 1 T throughout the whole study. The light source was a Xenon arc lamp equipped with sets of short-pass and long-pass filters (SPF or LPF). Specifically for the present study, an SPF 650 nm and an LPF at 500 nm were used. Data were corrected for the empty FOSH signal, determined beforehand.

Differential Scanning Calorimetry (DSC) experiments were performed with a Q1000 calorimeter with the LNCS accessory from TA Instruments. The temperature and enthalpy scales were calibrated with a standard sample of indium, using its melting transition (156.6 °C, 3296 J mol^{-1}). Measurements were carried out using aluminium pans with a mechanical crimp, with an empty pan as a reference. The zero-heat flow procedure described by TA Instruments was followed to derive heat capacities, using a synthetic sapphire as a reference compound. An overall accuracy of *ca.* 0.2 K for the temperature and up to 5 to 10% for the heat capacity was estimated over the whole temperature range, by comparison with the synthetic sapphire. A lattice heat capacity was estimated from the data below and above the anomaly associated with the SCO process (dashed line in Fig. 8). Excess enthalpy and entropy were derived by integration of the excess heat capacity with respect to *T* and Ln*T*, respectively.

Materials and syntheses

All reactions were performed under aerobic conditions and all reagents and solvents were used as purchased. TLC was performed on Alugram® SIL G/UV/254 silica gel precoated sheets (Macherey–Nagel, Germany). Purification of the organic ligands was carried out by column chromatography using silica gel SDS 60 ACC (0.035–0.070 mm).

2-(*N*,*N*-Bis(2-pyridyl)amino)-4,6-bis(phenoxy)-(1,3,5)triazine (L1)

The synthesis of ligand **L1** was performed in two straightforward steps.

Preparation of 2-chloro-4,6-bis(phenoxy)-(1,3,5)triazine. 5.0 g (27.11 mmol) of 2,4,6-trichloro-(1,3,5)triazine were dissolved in 100 mL of dry THF. Two equivalents (7.01 g, 54.22 mmol) of *N*,*N*-diisopropylethylamine (DIPEA) were added subsequently under stirring. The resulting yellow solution was cooled down to 0 °C, and two equivalents (5.10 g, 54.22 mmol) of phenol were added portionwise. After completion of the addition, the ice bath was removed and the reaction mixture was stirred for 15 min. The white precipitate obtained (identified as a first crop of the chlorhydrate salt of DIPEA) was removed by filtration. The remaining solid was dissolved in diethyl ether and the undissolved white powder corresponding to a second crop of DIPEA·HCl was separated by filtration. Removal of the solvent under reduced pressure produced pure 2-chloro-4,6-bis(phenoxy)-(1,3,5)triazine as a white powder with a yield of 45% (6.08 g, 12.16 mmol). IR (KBr): ν = 3420(w), 3058(w), 1578(m), 1531(s), 1485(m), 1455(m), 1421(m), 1383(s), 1293(s), 1253(m), 1193(m), 1162(w), 1068(w), 985(w), 948(s), 867(w), 842(w), 802(w), 767(m), 693(m), 657(w), 485(5) cm^{-1}.

Preparation of 2-(*N*,*N*-bis(2-pyridyl)amino)-4,6-bis(phenoxy)-(1,3,5)triazine (L1). One equivalent (1.10 g, 8.80 mmol) of DIPEA was added to a solution of 4.20 g (8.80 mmol) of 2-chloro-4,6-bis(phenoxyl)-(1,3,5)triazine in 50 mL of dry THF. Next, one equivalent (1.50 g, 8.80 mmol) of 2-dipyridylamine was added and the reaction mixture was refluxed for two hours. Subsequently, the solution was cooled down to room temperature, and the solvent was evaporated under reduced pressure. The solid obtained was dissolved in diethyl ether and the remaining DIPEA·HCl salt was removed by filtration. The resulting crude compound was purified by column chromatography using the solvent mixture CH_2Cl_2–MeOH (99 : 1) as an eluent. Pure ligand **L1** (R_f = 0.42) was obtained as a white crystalline powder with a yield of 55% (2.86 g, 6.58 mmol). Elemental analyses calculated (found) (%) for $C_{25}H_{18}N_6O_2$: C: 69.11 (69.01), H: 4.18 (4.24), N: 19.34 (19.47). ^{1}H NMR (300 MHz, $CDCl_3$, room temp.): δ = 8.38–8.33 (m, 2H), 7.62 (ddd, J = 8.1, 7.5, 2.0 Hz, 2H), 7.47 (d, J = 8.1 Hz, 2H), 7.33–7.23 (m, 4H), 7.19–7.05 (m, 8H) ppm. IR (KBr): ν = 3427 (w), 3056(w), 2974(w), 2857(w), 1565(m), 1488(m), 1432(m), 1374(s), 1303(m), 1238(m), 1200(m), 1080(w), 995(w), 807(w), 770(m), 690(m) cm^{-1}. The molecular structure of **L1** was determined by single-crystal X-ray diffraction. A representation of the crystal structure of **L1** is depicted in Fig. S7.† The corresponding crystallographic and refinement parameters are summarized in Table S4.†

2-(*N*,*N*-Bis(2-pyridyl)amino)-4,6-bis(pentafluorophenoxy)-(1,3,5)triazine ($L1^F$)

Ligand $L1^F$ was synthesized in a similar manner using pentafluorophenol instead of phenol.

Preparation of 2-chloro-4,6-bis(pentafluorophenoxy)-(1,3,5)-triazine. 5.0 g (27.11 mmol) of 2,4,6-trichloro-1,3,5-triazine were dissolved in 100 mL of dry THF. Two equivalents (7.01 g, 54.22 mmol) of DIPEA were then added under stirring. The resulting yellow solution was cooled down to 0 °C and two equivalents (9.98 g, 54.22 mmol) of pentafluorophenol were added portionwise. After 15 minutes, the white crystalline precipitate of DIPEA·HCl was separated by filtration and the filtrate was evaporated under reduced pressure. The consequent solid material was dissolved in diethyl ether and the second crop of insoluble DIPEA·HCl was removed by filtration. After evaporation under reduced pressure, pure 2-chloro-4,6-bis(pentafluorophenoxy)-(1,3,5)triazine was obtained as a white powder with a yield of 45% (5.83 g, 11.22 mmol). IR (KBr): ν = 3431(w), 2991(w), 2674(w), 2465(w), 1655(m), 1609(s), 1577(s), 1522(br,s), 1475(s), 1437(m), 1372(s), 1306(s), 1224(w), 1169(m), 1155(m), 1078(s), 998(s), 805(m), 640(w) cm^{-1}.

Preparation of 2-(*N*,*N*-bis(2-pyridyl)amino)-4,6-bis(pentafluorophenoxy)-(1,3,5)triazine ($L1^F$). One equivalent of (1.10 g, 8.80 mmol) of DIPEA was added to a solution of 2-chloro-4,6-bis(pentafluorophenoxy)-(1,3,5)triazine (4.20 g, 8.80 mmol) in 50 mL of dry THF. Next, one equivalent (1.50 g, 8.80 mmol) of 2-dipyridylamine was added and the resulting reaction mixture was refluxed for two hours. The solution was then cooled down to room temperature, and the solvent was evaporated under reduced pressure. The remaining solid material was dissolved in diethyl ether and the insoluble white powder, *i.e.* DIPEA·HCl, was removed by filtration. The solvent was evaporated under reduced pressure and the crude compound was purified by column chromatography, using the solvent mixture EtOAc–*n*-hexane (50 : 50) as an eluent. Pure ligand $L1^F$ (R_f = 0.63) was obtained with a yield of 55% (2.96 g, 4.82 mmol). Elemental analyses calculated (found) (%) for $C_{25}H_8F_{10}N_6O_2$: C: 48.88 (50.16), H: 1.31 (1.10), N: 13.68 (13.64). It has to be noted that higher experimental values for C may be obtained with triazine-based compounds.[40] ^{1}H NMR (300 MHz, $CDCl_3$, room temp.): δ = 8.40 (ddd, J = 4.9, 1.9, 0.8 Hz, 2H), 7.73 (ddd, J = 8.0, 7.5, 2.0 Hz, 2H), 7.47 (dt, J = 8.1, 0.9 Hz, 2H), 7.20 (ddd, J = 7.5, 4.9, 1.0 Hz, 2H) ppm. IR (KBr): ν = 3428(w), 1596(s), 1562(s), 1519(s), 1417(s), 1435(m), 1375(s), 1309(m), 1305(m), 1254(m), 1234(m), 1166(m), 1076(s), 997(s), 812(w), 774(w), 697(w), 662(w) cm^{-1}.

trans-[Fe(L1)$_2$(NCS)$_2$]·2CH$_2$Cl$_2$ (1)

A methanolic solution (5 mL) of KNCS (0.019 g, 0.2 mmol) was added to an aqueous solution (2 mL) of $FeSO_4$·7H_2O (0.028 g, 0.1 mmol). After 15 minutes of stirring, the precipitate of K_2SO_4 was removed by filtration. Ascorbic acid (in small quantities) was added to the filtrate to prevent oxidation to iron(III). Subsequently, a solution of **L1** (0.086 g, 0.2 mmol) in dichloromethane was added to the iron(II) solution. The resulting yellow reaction mixture was filtered and the filtrate was left unperturbed for the slow evaporation of the solvent. After three days, small yellow single crystals of **1**, suitable for X-ray diffraction studies, were obtained with a yield of 70% (85 mg, 0.07 mmol, based on iron). Elemental analyses calculated

(found) (%) for $C_{53}H_{38}FeN_{14}O_4S_2Cl_2$ (**1** – CH_2Cl_2): C: 56.54 (55.71), H: 3.40 (3.30), N: 17.42 (17.59). IR (KBr): ν = 3435(w), 2067(m), 1604(m), 1556(m), 1488(m), 1376(s), 1309(m), 1245(m), 1201(m), 1016(w), 809(w), 772(w), 688(w) cm^{-1}.

trans-[Fe(L1)$_2$(NCSe)$_2$]·4CH$_2$Cl$_2$·4MeOH (2)

Compound **2** was obtained using the synthetic procedure applied to prepare **1**, but using KNCSe (0.029 g, 0.2 mmol) instead of KNCS. Single crystals of **2**, suitable for X-ray diffraction studies, were obtained after three days with a yield of 63% (101 mg, 0.063 mmol, based on iron). Elemental analyses calculated (found) (%) for $C_{55}H_{46}FeN_{14}O_6Se_2Cl_2$ (**2** – $4CH_2Cl_2$–4MeOH + $3H_2O$): C: 52.54 (52.03), H: 3.56 (3.08), N: 16.50 (17.04). IR (KBr): ν = 3425(w), 3066(w), 2074(s), 1602(m), 1559(m), 1487(m), 1435(m), 1373(s), 1311(m), 1249(m), 1194(m), 1077(w), 1018(w), 906(w), 808(w), 767(w), 687(w) cm^{-1}.

trans-[Fe(L1^F)$_2$(NCS)$_2$]·2CH$_3$CN (3)

Compound **3** was obtained applying the synthetic procedure used to prepare **1**, but the ligand **L1^F** (0.122 g, 0.2 mmol) was dissolved in acetonitrile instead of dichloromethane. Single crystals of **3**, suitable for X-ray diffraction studies, were obtained after three days with a yield of 65% (96 mg, 0.063 mmol, based on iron). Elemental analyses calculated (found) (%) for $C_{56}H_{22}F_{20}FeN_{16}O_4S_2$: C: 45.36 (46.19), H: 1.50 (1.74), N: 15.11 (15.10). IR (KBr): ν = 3464(w), 2056(s), 1610(m), 1557(w), 1519(s), 1475(m), 1372(s), 1309(m), 1241(m), 1078(m), 1000(m), 806(w), 781(w), 753(w), 642(m) cm^{-1}.

X-ray crystallography

X-ray diffraction data for **L1** at 250 K, for **1** at 100, 240 and 300 K and for **3** at 100, 190 and 280 K, were collected with a Bruker APEX II CCD diffractometer on the Advanced Light Source beamline 11.3.1 at Lawrence Berkeley National Laboratory, from a silicon 111 monochromator (λ = 0.7749 Å). Data for **2** at 100 K were obtained using Mo K_α radiation (λ = 0.7107 Å) on a Bruker APEX II QUAZAR diffractometer equipped with a microfocus multilayer monochromator. Data reduction and absorption corrections were performed with SAINT and SADABS.[62] The structure of **2** was solved with SIR97,[63] while those of **L1**, **1** and **3** were solved with SHELXS.[64] All structures were refined on F^2 using the SHELXTL suite.[64] Crystallographic and refinement parameters are summarized in Tables S1–S4. Selected bond distances and angles are given in Tables 1–3. All details can be found in the supplementary crystallographic data for this paper in cif format with CCDC numbers 921061–921067 (coordination compounds **1**–**3**) and 922570 (ligand **L1**).

Acknowledgements

PG acknowledges ICREA (Institució Catalana de Recerca i Estudis Avançats) and the Ministerio de Economía y Competitividad of Spain (Project CTQ2011-27929-C02-01). NW thanks the Royal Golden Jubilee Program (RGJ, Grant no. PHD/0234/2550) and Khon Kaen University for a research grant. SY acknowledges The Thailand Research Fund, the National Research University Project of Thailand, Office of the Higher Education Commission, through the Advanced Functional Materials Cluster of Khon Kaen University and the Center of Excellence for Innovation in Chemistry (PERCH-CIC), Office of the Higher Education Commission, Ministry of Education. The Advanced Light Source is supported by the Director, Office of Science, Office of Basic Energy Sciences of the U. S. Department of Energy under contract no. DE-AC02-05CH11231. OR acknowledges funding from the Ministerio de Economía y Competitividad of Spain (Project MAT2011-24284).

Notes and references

1 B. N. Figgis and M. A. Hitchman, *Ligand Field Theory and Its Applications*, Wiley-VCH, New York, 2000.
2 A. B. Koudriavtsev and W. Linert, *J. Struct. Chem.*, 2010, **51**, 335–365.
3 R. Boča, *in A Handbook of Magnetochemical Formulae*, Elsevier, London, 2012, pp. 159–186.
4 P. Gütlich, A. Hauser and H. Spiering, *Angew. Chem., Int. Ed. Engl.*, 1994, **33**, 2024–2054.
5 P. Gütlich and H. A. Goodwin, *Top. Curr. Chem.*, 2004, **233**, 1–47.
6 J. A. Real, A. B. Gaspar and M. C. Muñoz, *Dalton Trans.*, 2005, 2062–2079.
7 A. Bousseksou, G. Molnár, J. A. Real and K. Tanaka, *Coord. Chem. Rev.*, 2007, **251**, 1822–1833.
8 O. Sato, *Proc. Jpn. Acad. Ser. B-Phys. Biol. Sci.*, 2012, **88**, 213–225.
9 M. Ruben, E. Breuning, J. M. Lehn, V. Ksenofontov, F. Renz, P. Gütlich and G. B. M. Vaughan, *Chem.–Eur. J.*, 2003, **9**, 4422–4429.
10 A. Bousseksou, G. Molnár, P. Demont and J. Menegotto, *J. Mater. Chem.*, 2003, **13**, 2069–2071.
11 P. Gütlich, Y. Garcia and H. A. Goodwin, *Chem. Soc. Rev.*, 2000, **29**, 419–427.
12 C. Jay, F. Grolière, O. Kahn and J. Kröber, *Mol. Cryst. Liq. Cryst. Sci. Technol., Sect. A*, 1993, **234**, 255–262.
13 O. Kahn and C. J. Martinez, *Science*, 1998, **279**, 44–48.
14 A. Bousseksou, G. Molnár, L. Salmon and W. Nicolazzi, *Chem. Soc. Rev.*, 2011, **40**, 3313–3335.
15 M. A. Halcrow, *Chem. Soc. Rev.*, 2011, **40**, 4119–4142.
16 J. Tao, R. J. Wei, R. B. Huang and L. S. Zheng, *Chem. Soc. Rev.*, 2012, **41**, 703–737.
17 D. J. Harding, D. Sertphon, P. Harding, K. S. Murray, B. Moubaraki, J. D. Cashion and H. Adams, *Chem.–Eur. J.*, 2013, **19**, 1082–1090.
18 K. Bhar, S. Khan, J. S. Costa, J. Ribas, O. Roubeau, P. Mitra and B. K. Ghosh, *Angew. Chem., Int. Ed.*, 2012, **51**, 2142–2145.
19 P. Gamez, J. S. Costa, M. Quesada and G. Aromí, *Dalton Trans.*, 2009, 7845–7853.

20 G. A. Craig, J. S. Costa, O. Roubeau, S. J. Teat and G. Aromí, *Chem.–Eur. J.*, 2012, **18**, 11703–11715.
21 G. Aromí, L. A. Barrios, O. Roubeau and P. Gamez, *Coord. Chem. Rev.*, 2011, **255**, 485–546.
22 J. Olguin and S. Brooker, *Coord. Chem. Rev.*, 2011, **255**, 203–240.
23 M. Boča, R. F. Jameson and W. Linert, *Coord. Chem. Rev.*, 2011, **255**, 290–317.
24 K. S. Murray, *Eur. J. Inorg. Chem.*, 2008, 3101–3121.
25 M. Quesada, M. Monrabal, G. Aromí, V. A. de la Peña-O'Shea, M. Gich, E. Molins, O. Roubeau, S. J. Teat, E. J. MacLean, P. Gamez and J. Reedijk, *J. Mater. Chem.*, 2006, **16**, 2669–2676.
26 J. S. Costa, K. Lappalainen, G. de Ruiter, M. Quesada, J. K. Tang, I. Mutikainen, U. Turpeinen, C. M. Grünert, P. Gütlich, H. Z. Lazar, J. F. Létard, P. Gamez and J. Reedijk, *Inorg. Chem.*, 2007, **46**, 4079–4089.
27 S. Bonnet, M. A. Siegler, J. S. Costa, G. Molnár, A. Bousseksou, A. L. Spek, P. Gamez and J. Reedijk, *Chem. Commun.*, 2008, 5619–5621.
28 J. K. Tang, J. S. Costa, S. Smulders, G. Molnár, A. Bousseksou, S. J. Teat, Y. G. Li, G. A. van Albada, P. Gamez and J. Reedijk, *Inorg. Chem.*, 2009, **48**, 2128–2135.
29 S. Bonnet, G. Molnár, J. S. Costa, M. A. Siegler, A. L. Spek, A. Bousseksou, W. T. Fu, P. Gamez and J. Reedijk, *Chem. Mater.*, 2009, **21**, 1123–1136.
30 M. Quesada, V. A. de la Peña-O'Shea, G. Aromí, S. Geremia, C. Massera, O. Roubeau, P. Gamez and J. Reedijk, *Adv. Mater.*, 2007, **19**, 1397–1402.
31 P. Gamez, P. de Hoog, M. Lutz, W. L. Driessen, A. L. Spek and J. Reedijk, *Polyhedron*, 2003, **22**, 205–210.
32 M. Quesada, P. de Hoog, P. Gamez, O. Roubeau, G. Aromí, B. Donnadieu, C. Massera, M. Lutz, A. L. Spek and J. Reedijk, *Eur. J. Inorg. Chem.*, 2006, 1353–1361.
33 N. Wannarit, O. Roubeau, S. Youngme and P. Gamez, *Eur. J. Inorg. Chem.*, 2013, 730–737.
34 T. M. Ross, B. Moubaraki, S. M. Neville, S. R. Batten and K. S. Murray, *Dalton Trans.*, 2012, **41**, 1512–1523.
35 T. M. Ross, B. Moubaraki, S. R. Batten and K. S. Murray, *Dalton Trans.*, 2012, **41**, 2571–2581.
36 T. M. Ross, B. Moubaraki, K. S. Wallwork, S. R. Batten and K. S. Murray, *Dalton Trans.*, 2011, **40**, 10147–10155.
37 T. M. Ross, B. Moubaraki, D. R. Turner, G. J. Halder, G. Chastanet, S. M. Neville, J. D. Cashion, J. F. Létard, S. R. Batten and K. S. Murray, *Eur. J. Inorg. Chem.*, 2011, 1395–1417.
38 S. M. Neville, B. A. Leita, D. A. Offermann, M. B. Duriska, B. Moubaraki, K. W. Chapman, G. J. Halder and K. S. Murray, *Eur. J. Inorg. Chem.*, 2007, 1073–1085.
39 R. J. Götz, A. Robertazzi, I. Mutikainen, U. Turpeinen, P. Gamez and J. Reedijk, *Chem. Commun.*, 2008, 3384–3386.
40 P. de Hoog, P. Gamez, W. L. Driessen and J. Reedijk, *Tetrahedron Lett.*, 2002, **43**, 6783–6786.
41 M. Marchivie, P. Guionneau, J. F. Létard and D. Chasseau, *Acta Crystallogr., Sect. B: Struct. Sci.*, 2005, **61**, 25–28.
42 J. K. McCusker, A. L. Rheingold and D. N. Hendrickson, *Inorg. Chem.*, 1996, **35**, 2100–2112.
43 M. Quesada, F. Prins, E. Bill, H. Kooijman, P. Gamez, O. Roubeau, A. L. Spek, J. G. Haasnoot and J. Reedijk, *Chem.–Eur. J.*, 2008, **14**, 8486–8499.
44 P. Guionneau, M. Marchivie, G. Bravic, J. F. Létard and D. Chasseau, *Top. Curr. Chem.*, 2004, **234**, 97–128.
45 T. J. Mooibroek and P. Gamez, *CrystEngComm*, 2012, **14**, 1027–1030.
46 A. Das, S. R. Choudhury, C. Estarellas, B. Dey, A. Frontera, J. Hemming, M. Helliwell, P. Gamez and S. Mukhopadhyay, *CrystEngComm*, 2011, **13**, 4519–4527.
47 S. R. Choudhury, P. Gamez, A. Robertazzi, C. Y. Chen, H. M. Lee and S. Mukhopadhyay, *Cryst. Growth Des.*, 2008, **8**, 3773–3784.
48 T. J. Mooibroek and P. Gamez, *CrystEngComm*, 2012, **14**, 3902–3906.
49 T. J. Mooibroek and P. Gamez, *CrystEngComm*, 2013, **15**, 1802–1805.
50 M. Sorai and S. Seki, *J. Phys. Chem. Solids*, 1974, **35**, 555–570.
51 L. Capes, J. F. Létard and O. Kahn, *Chem.–Eur. J.*, 2000, **6**, 2246–2255.
52 T. Buchen, H. Toftlund and P. Gütlich, *Chem.–Eur. J.*, 1996, **2**, 1129–1133.
53 J. A. Real, I. Castro, A. Bousseksou, M. Verdaguer, R. Burriel, M. Castro, J. Linarès and F. Varret, *Inorg. Chem.*, 1997, **36**, 455–464.
54 N. Moliner, M. C. Muñoz, S. Létard, J. F. Létard, X. Solans, R. Burriel, M. Castro, O. Kahn and J. A. Real, *Inorg. Chim. Acta*, 1999, **291**, 279–288.
55 M. Sorai, *Top. Curr. Chem.*, 2004, **235**, 153–170.
56 O. Roubeau, M. Castro, R. Burriel, J. G. Haasnoot and J. Reedijk, *J. Phys. Chem. B*, 2011, **115**, 3003–3012.
57 The phenomenological domain model proposed by Sorai is widely used when accurate calorimetric data are available. It is based on heterophase fluctuations and gives a measure of cooperativity through the number *n* of like-spin SCO centers per interacting domain, the larger the domains are, the more cooperative the transition is. See: M. Sorai, *Chem. Rev.*, 1996, **1106**, 1976–1031.
58 A. Hauser, *Top. Curr. Chem.*, 2004, **234**, 155–198.
59 J. F. Létard, *J. Mater. Chem.*, 2006, **16**, 2550–2559.
60 A. Hauser, *Top. Curr. Chem.*, 2004, **233**, 49–58.
61 A. Hauser, *J. Chem. Phys.*, 1991, **94**, 2741–2748.
62 *SAINT, SADABS and SHELXTL*, Bruker AXS, Inc., Madison, WI, USA, 2002.
63 A. Altomare, M. C. Burla, M. Camalli, G. L. Cascarano, C. Giacovazzo, A. Guagliardi, A. G. G. Moliterni, G. Polidori and R. Spagna, *J. Appl. Crystallogr.*, 1999, **32**, 115–119.
64 G. M. Sheldrick, *Acta Crystallogr., Sect. A: Fundam. Crystallogr.*, 2008, **64**, 112–122.

Inorganic Chemistry

Article

pubs.acs.org/IC

Drastic Effect of Lattice Propionitrile Molecules on the Spin-Transition Temperature of a 2,2′-Dipyridylamino/s-triazine-Based Iron(II) Complex

Nanthawat Wannarit,[†,‡,○] Nassim Nassirinia,[†,§] Saeid Amani,[§] Norberto Masciocchi,*[,∥] Sujittra Youngme,[‡] Olivier Roubeau,*[,⊥] Simon J. Teat,[#] and Patrick Gamez*[,†,▽]

[†]Departament de Química Inorgànica, Universitat de Barcelona, Martí i Franquès 1-11, 08028 Barcelona, Spain

[‡]Materials Chemistry Research Unit, Department of Chemistry and Center of Excellence for Innovation in Chemistry, Faculty of Science, Khon Kaen University, Khon Kaen 40002, Thailand

[§]Faculty of Sciences, Department of Chemistry, Arak University, Arak 38156-8-8349, Iran

[∥]Dipartimento di Scienza e Alta Tecnologia and To.Sca.Lab, Università dell'Insubria, Via Valleggio 11, 22100 Como, Italy

[⊥]Instituto de Ciencia de Materiales de Aragón (ICMA), CSIC and Universidad de Zaragoza, Plaza San Francisco s/n, 50009 Zaragoza, Spain

[#]Advanced Light Source (ALS), Lawrence Berkeley National Laboratory, 1 Cyclotron Road, Berkeley, California 94720, United States

[▽]Institució Catalana de Recerca i Estudis Avançats (ICREA), Passeig Lluís Companys 23, 08010 Barcelona, Spain

Supporting Information

ABSTRACT: Reaction of iron(II) selenocyanate (obtained from $Fe(ClO_4)_2$ and KNCSe) with 2-(*N*,*N*-bis(2-pyridyl)amino)-4,6-bis(pentafluorophenoxy)-(1,3,5)triazine (**L1**^{F}) in propionitrile produces the compound $[Fe(\mathbf{L1}^{F})_2(NCSe)_2]\cdot 2CH_3CH_2CN$ (**1**^{NCSe}**·2PrCN**), which shows spin-crossover (SCO) properties characterized by a $T_{1/2}$ of 283 K and a ΔT_{80} (i.e., temperature range within which 80% of the transition considered occurs) of about 65 K. Upon air exposure, **1**^{NCSe}**·2PrCN** gradually converts to a new SCO species that exhibits different properties, as reflected by $T_{1/2}$ = 220 K and ΔT_{80} = 70 K. Various characterization techniques, namely, IR spectroscopy, thermogravimetric analysis, and thermodiffractometric studies, reveal that the new phase is obtained through the loss of the lattice propionitrile molecules within several days upon air exposure or several hours upon heating above 390 K.

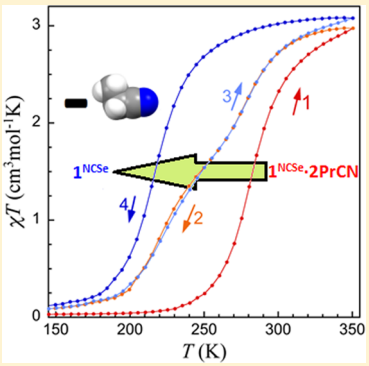

INTRODUCTION

The spin-crossover (SCO) phenomenon is a particular property of d^4−d^7 transition metal ions in which they may change their spin state from low spin (LS) to high spin (HS) and vice versa when appropriate donor atoms are coordinated to the metal centers, providing intermediate ligand-field strength.[1−3] This HS ↔ LS conversion may occur through the application of an external stimulus such as temperature, light, or pressure.[1,4−6]

SCO was first observed in 1931 by Cambi and co-workers, who serendipitously discovered that the magnetic properties of iron(III) coordination compounds of the type [Fe(dithiocarbamate)$_3$] showed temperature-dependent reversibility of their magnetic moments, from $\mu_{eff} \approx 1.9\mu_B$ ($S = {}^1/_2$) at low temperatures to $\mu_{eff} \approx 5.9\mu_B$ ($S = 5/2$) at higher ones.[7] More than eight decades later, SCO represents an important research area of molecular magnetism, as illustrated by the continuously growing number of groups worldwide that are devoted to the design and investigation of new SCO materials.[8] The great potential of SCO compounds toward practical applications was recognized with 1D coordination polymers of the type $\{Fe^{II}(4\text{-R-}1,2,4\text{-triazole})_3]X_2\}_n$ (for instance, with R = H or NH_2 and X = BF_4^- or NO_3^-), which show room-temperature spin transition associated with wide hysteresis loops.[9−12] Such materials have indeed been used to conceive a display device.[11,13] Thus, the switching properties of these "bistable" molecules make them highly attractive because they may find a number of applications in molecular electronics.[11,14−19]

Most iron-based SCO compounds are iron(II) complexes with a [FeN$_6$] octahedral geometry that is typically formed by aromatic nitrogen donor groups, e.g., pyridine or azole rings.[20−25] For about 7 years, we have been developing a family of ligands based on 2,2′-dipyridylamine (dpa) unit(s) attached to a 1,3,5-triazine (or *s*-triazine) ring.[26] The first member of this family, namely, 2,4,6-tris(dipyridin-2-ylamino)-1,3,5-triazine (dpyatriz), was reported by some of us in 2003.[27]

Received: June 17, 2014
Published: August 26, 2014

   dx.doi.org/10.1021/ic501389s | *Inorg. Chem.* 2014, 53, 9827−9836

This ligand, containing three dpa groups on the *s*-triazine ring,[28] allowed for the preparation of iron(II) coordination compounds with attracting SCO properties.[26,29,30] Concurrently, Murray and co-workers have described a number of dipyridylamino-substituted-triazine ligands, which have engendered various SCO materials exhibiting diverse transition properties.[31−36] Recently, we have described the iron(II) complex *trans*-$[Fe(\mathbf{L1^F})_2(NCS)_2]\cdot 2CH_3CN$ ($\mathbf{1^{NCS}\cdot 2MeCN}$), with $\mathbf{L1^F}$ = 2-(*N*,*N*-bis(2-pyridyl)amino)-4,6-bis(pentafluorophenoxy)-(1,3,5)triazine, which exhibits a relatively cooperative SCO character.[37] In the present study, we report on the preparation and characterization of the comparable selenocyanate analogue complex $[Fe(\mathbf{L1^F})_2(NCSe)_2]\cdot 2CH_3CH_2CN$ ($\mathbf{1^{NCSe}\cdot 2PrCN}$), which shows solvent-dependent SCO properties.[38−41] These particular features are unraveled through thermal, magnetic, and variable-temperature structural studies, which are analyzed and compared with the properties of related compounds.

RESULTS AND DISCUSSION

Synthesis and Crystal Structure of Compound $\mathbf{1^{NCSe}}$. The ligand 2-(*N*,*N*-bis(2-pyridyl)amino)-4,6-bis(pentafluorophenoxy)-(1,3,5)triazine ($\mathbf{L1^F}$) was prepared as described earlier for the preparation of $\mathbf{1^{NCS}\cdot 2MeCN}$.[37] Compound $\mathbf{1^{NCSe}\cdot 2PrCN}$, i.e., $[Fe(\mathbf{L1^F})_2(NCSe)_2]\cdot 2CH_3CH_2CN$, was obtained with a yield of 60% by reaction of iron(II) perchlorate hexahydrate (1 equiv), potassium selenocyanate (1 equiv), and ligand $\mathbf{L1^F}$ (2 equiv), as explained in the Experimental Section. $\mathbf{1^{NCSe}\cdot 2PrCN}$ is triclinic, space group $P\bar{1}$, in the whole 100−300 K range (single-crystal data collections performed at 100, 200, 260, and 300 K, Table S1). A representation of the molecular structure of $\mathbf{1^{NCSe}}$ at 100 K (low-spin state) is depicted in Figure 1. Selected bond lengths and angles are listed in Table 1.

The coordination environment of the iron(II) ion in $\mathbf{1^{NCSe}}$ is analogous to that of the previously reported compound $\mathbf{1^{NCS}}$.[37] The octahedral geometry is formed by two $\mathbf{L1^F}$ ligands in the equatorial plane and two *trans*, N-coordinated selenocyanate anions (Figure 1). The $Fe-N_{pyridine}$ bond lengths of 1.981(1) (Fe−N2) and 1.979(1) Å (Fe−N3) are representative of an LS iron(II) ion (Table 1). Consistently, the $Fe-N_{NCSe}$ distances of 1.930(1) Å are also indicative of an LS state. Actually, all Fe−N coordination distances observed in $\mathbf{1^{NCSe}}$ are very similar to those of the related thiocyanate compound $\mathbf{1^{NCS}}$ (measured at 100 K).[37] At 300 K, these bond lengths increase by ca. 0.17 Å ($Fe-N_{pyridine}$) and 0.11 Å ($Fe-N_{NCSe}$) (Table 1), hence illustrating the occurrence of a full (i.e., 100%) spin transition that is corroborated by variable-temperature magnetic susceptibility measurements (see Magnetic and Thermal Studies section). Such bond distance variations are typical for this type of SCO FeN_6 system.[42] Finally, the distances observed for $\mathbf{1^{NCSe}\cdot 2PrCN}$ at 260 K, i.e., 2.007(4)−2.011(3) Å for Fe−

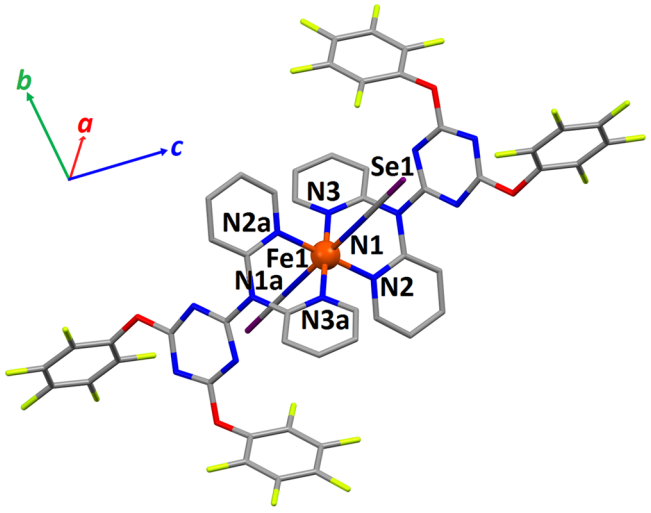

Figure 1. Representation of the molecular structure of the iron(II) complex $\mathbf{1^{NCSe}\cdot 2PrCN}$ (LS state, determined at 100 K) with partial atom-numbering scheme. Hydrogen atoms and lattice propionitrile molecules are not shown for clarity. Symmetry operation: $a = 1 - x, 1 - y, 1 - z$.

Table 1. Coordination Bond Lengths (Å) and Angles (Deg) and Supramolecular Interactions for Compound $\mathbf{1^{NCSe}}$·2PrCN at Three Different Temperatures[a]

bond	100 K (LS)	260 K	300 K (HS)
Fe1−N1	1.930(1)	1.948(3)	2.037(5)
Fe1−N2	1.981(1)	2.011(3)	2.161(3)
Fe1−N3	1.979(1)	2.007(4)	2.150(4)
$Fe1\cdots Fe1_{inter}$[b]	8.468(1)	8.638(3)	8.807(4)
angle	100 K (LS)	260 K	300 K (HS)
N2−Fe1−N3	86.25(6)	85.75(14)	82.85(13)
N3−Fe1−N2a	93.75(6)	94.25(14)	97.15(13)
N1−Fe1−N1a	180	180	180
ΣFe[c]	31	34	44
Φ[d]	25	40	64
$\pi\cdots\pi$ interactions[a]	100 K (LS)	260 K	300 K (HS)
O1···C19g	3.199(3)	3.205(6)	3.221(8)
O1···C20g	3.076(2)	3.119(6)	3.138(7)
C15···C20g	3.323(2)	3.350(6)	3.348(7)
Cg6···Cg6g	4.589(1)	4.603(3)	4.623(4)
C8···C10p	3.555(2)	3.589(6)	3.605(3)
C7···C10p	3.654(2)	3.736(5)	3.762(3)
C9···N3p	3.700(2)	3.783(6)	3.806(2)
Cg4···Cg4p	3.682(1)	3.764(3)	3.786(3)
halogen···halogen contacts[a]	100 K (LS)	260 K	300 K (HS)
F4···F7e	2.885(2)	2.933(5)	2.937(7)
F8···F9k	2.780(2)	2.852(5)	2.872(7)
lone pair···π interactions[a]	100 K (LS)	260 K	300 K (HS)
N7···F1c	3.104(2)	3.305(2)	3.268(7)
C12···F2c	3.014(2)	3.024(5)	3.047(7)
F1c···Cg5	3.238(2)	3.360(4)	3.478(5)
F2c···Cg5	3.443(2)	3.401(4)	3.398(5)
N1S···C21	3.202(3)	3.312(7)	3.332(10)
N1S···C26	3.278(3)	3.261(8)	3.320(11)
N1S···Cg7	3.413(2)	3.399(7)	3.466(10)
Se1···C22b	3.531(2)	3.663(5)	3.720(6)
Se1···C23b	3.772(2)	3.906(5)	3.935(5)
Se1···F6b	3.192(1)	3.239(3)	3.269(4)
Se1···Cg7	4.320(1)	4.486(3)	4.552(4)
Se1···C13	3.697(2)	3.755(4)	3.789(5)
Se1···Cg5	3.585(1)	3.654(2)	3.722(2)

[a]Symmetry operations: $a = 1 - x, 1 - y, 1 - z$; $b = -1 + x, y, z$; $c = 2 - x, 1 - y, 2 - z$; $e = 2 - x, 2 - y, 2 - z$; $g = 1 - x, 1 - y, 2 - z$; $k = 2 - x, 2 - y, 1 - z$; $p = 2 - x, 1 - y, 1 - z$. [b]Closest intermonomer Fe···Fe distance (observed along the crystallographic *a* axis). [c]$\sum$ = the sum of $|90 - \theta|$ for the 12 N−Fe−N angles in the octahedron.[65,66] [d]Φ = sum of $|60 - \theta|$ for the 24 N−Fe−N angles describing the trigonal twist angle.[43,44]

dx.doi.org/10.1021/ic501389s | Inorg. Chem. 2014, 53, 9827−9836

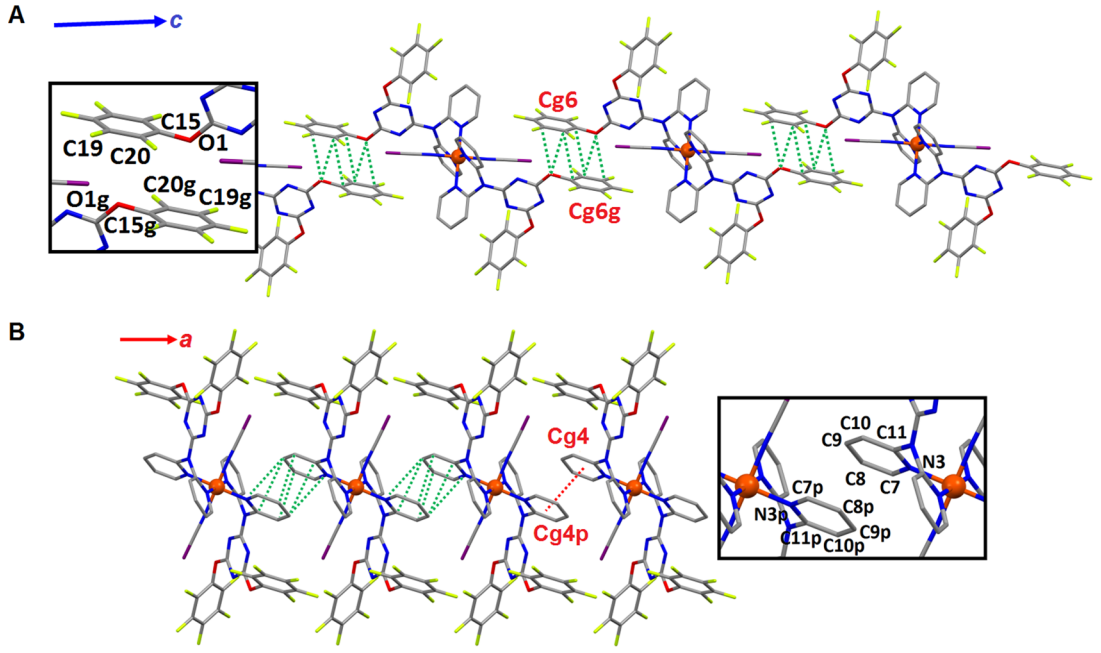

Figure 2. Views of the crystal packing of LS $\mathbf{1}^{NCSe}$**·2PrCN** showing (A) the formation of a supramolecular 1D chain along the crystallographic *c* axis by means of parallel-displaced $\pi\cdots\pi$ interactions between pentafluorophenoxy rings, with Cg6···Cg6g = 4.589(1) Å (the inset shows the labeling of the atoms involved in short supramolecular contacts (see Table 1), which are displayed as green dotted lines), and (B) the formation of a supramolecular 1D chain along the crystallographic *a* axis by means of $\pi\cdots\pi$ interactions between coordinated pyridine moieties, with Cg4···Cg4p = 3.682(1) Å (red dotted line) (the inset shows the labeling of the atoms involved in short supramolecular contacts (see Table 1), which are displayed as green dotted lines). Symmetry operations: $g = 1 - x, 1 - y, 2 - z$; $p = 2 - x, 1 - y, 1 - z$.

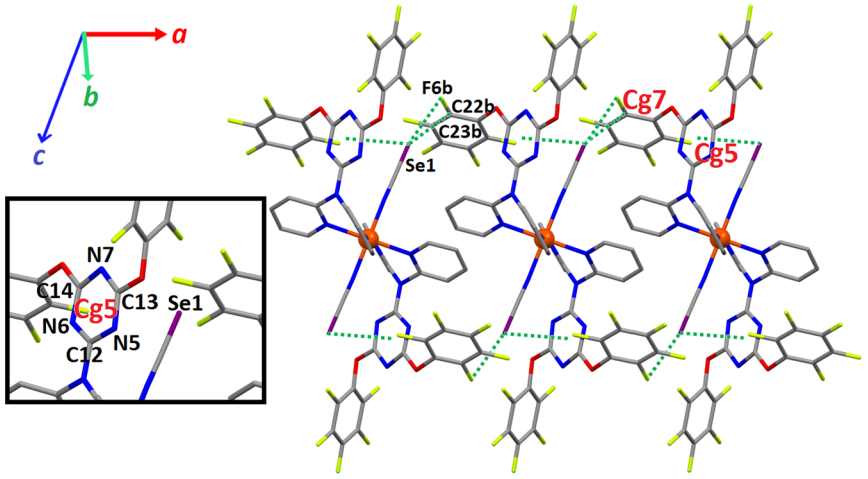

Figure 3. View of the crystal packing of LS $\mathbf{1}^{NCSe}$**·2PrCN** illustrating the occurrence of intermolecular lone pair$\cdots\pi$ interactions (green dotted lines) between the selenocyanate anions and adjacent pentafluorophenoxy moieties (Se1···C22b = 3.531(2) Å, Se1···C23b = 3.772(2) Å, and Se1···F6b = 3.192(1) Å) and intramolecular lone pair$\cdots\pi$ interactions between the selenocyanate anions and triazine rings (Se1···Cg5 = 3.585(1) Å). The inset shows the labeling of the atoms involved in lone pair$\cdots\pi$ interactions. Symmetry operation: $b = -1 + x, y, z$.

$N_{pyridine}$ and 1.948(3) Å for Fe−N_{NCSe} (Table 1), suggest the occurrence of a 1:7 HS/LS mixture, as estimated by properly weighing the bond length values found for the pure LS and HS states, shown in Table 1. In fact, the χT value of about 0.42 cm^3 mol^{-1} obtained at 260 K by bulk magnetic studies (see Magnetic and Thermal Studies section) indicates the presence of ca. 15% HS centers, in fair agreement with the structural results.

The octahedral distortion parameters Σ and Φ estimate the magnitude of the deformation of the coordination geometry with respect to a perfect octahedron (for which the Σ and Φ values are 0).[43−45] Upon LS → HS transition, the coordination angles vary from 86.25(6) and 93.75(6)° to 82.85(13) and 97.15(13)°, respectively; as the angles move away from the ideal value of 90°, the increased distortion of the octahedron can be interpreted by the entropy-driven SCO phenomenon.[46] Accordingly, for LS $\mathbf{1}^{NCSe}$, Σ = 31 and Φ = 25, and these values are increased for HS $\mathbf{1}^{NCSe}$ to 44 and 64, respectively (Table 1). The ΔΣ ($\Sigma_{HS} - \Sigma_{LS}$) and ΔΦ ($\Phi_{HS} - \Phi_{LS}$) parameters characterize the extent of the structural changes induced by the spin transition. For $\mathbf{1}^{NCSe}$, ΔΣ and ΔΦ amount to 13 and 39, respectively; the rather high ΔΦ value is indicative of an alteration of the octahedral geometry when the iron(II) centers transit from the LS to the HS state. Such strong structural

dx.doi.org/10.1021/ic501389s | *Inorg. Chem.* 2014, 53, 9827−9836

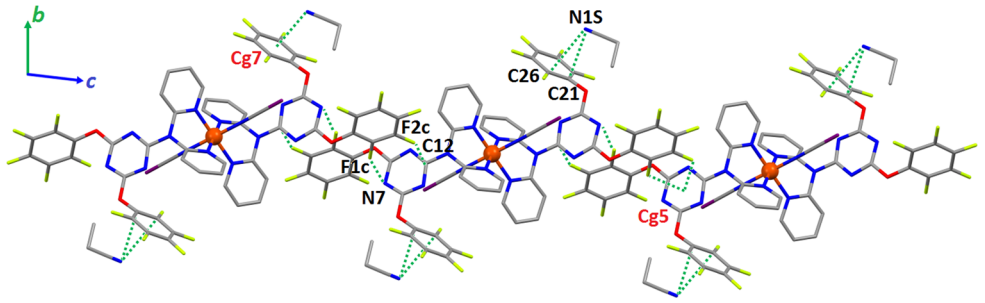

Figure 4. View of the crystal packing of LS $\mathbf{1}^{NCSe}$**·2PrCN** showing the formation of a supramolecular 1D chain along the crystallographic *c* axis through double lone pair(C_6F_5)···π(triazine) interactions characterized by the short contact distances N7···F1c = 3.104(2) Å and C12···F2c = 3.014(2) Å. Symmetry operation: $c = 2 - x, 1 - y, 2 - z$.

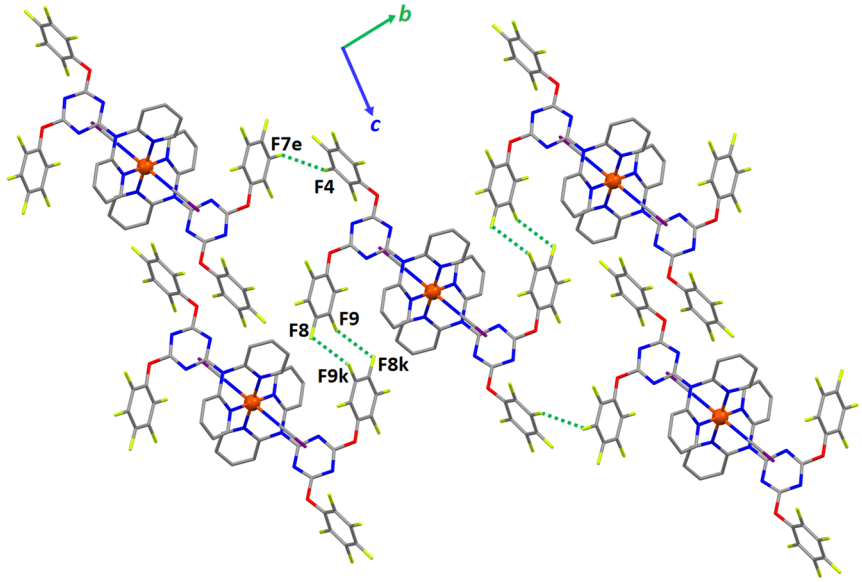

Figure 5. View of the crystal packing of LS $\mathbf{1}^{NCSe}$**·2PrCN** showing the formation of 2D sheets in the *bc* plane by means of strong F···F bonding contacts (green dotted lines; F8···F9k = 2.780(2) Å and F4···F7e = 2.885(2) Å). Symmetry operations: $e = 2 - x, 2 - y, 2 - z$; $k = 2 - x, 2 - y, 1 - z$.

deformation may affect the mutual interaction, in the crystal, of the transition metal ions spins, hence potentially enhancing the cooperativity between the switching sites that would lead to an abrupt LS ↔ HS crossover event.[43] Because the ΔΦ value of the related thiocyanate compound $\mathbf{1}^{NCS}$**·2MeCN** is also high (namely, 36[37]), cooperative behavior may be expected as well for solid $\mathbf{1}^{NCSe}$**·2PrCN**.

The crystal packing of LS $\mathbf{1}^{NCSe}$**·2PrCN** reveals an intricate network of supramolecular interactions that strongly connect the iron(II) molecules. The metal complexes form a 1D supramolecular chain along the crystallographic *c* axis by means of parallel-displaced π···π interactions involving pentafluorophenoxy rings (Figure 2A). Actually, a very strong lone pair···π contact[47,48] is observed between the oxygen atom O1 and a neighboring pentafluorophenoxy unit; for instance, the contact distance O1···C20g of 3.076(2) Å is significantly below the sum of the van der Waals radii of O and C (i.e., 3.22 Å). Moreover, the C15···C20g contact distance of 3.323(2) Å also reflects a strong arene···arene stacking interaction (the sum of the van der Waals radii of two C atoms is 3.40 Å). In fact, the C_6F_5O···C_6F_5O contacts are shorter in LS $\mathbf{1}^{NCSe}$**·2PrCN** compared to LS $\mathbf{1}^{NCS}$**·2MeCN** (for which the shortest O···C contact distance amounts to 3.112(2) Å[37]). Similar to that of $\mathbf{1}^{NCS}$**·2MeCN**, the iron(II) complexes are associated through nearly face-to-face π···π interactions between coordinated pyridine to generate another 1D chain that runs along the crystallographic *a* axis (Figure 2B). These supramolecular bonds are characterized by a centroid-to-centroid distance Cg4···Cg4p of 3.682(1) Å, which again is smaller than that of $\mathbf{1}^{NCS}$**·2MeCN** (3.757(1) Å[37]). Along the *a* direction, the 1D supramolecular chains are further stabilized via lone pair···π contacts involving the selenocyanate anions (Figure 3). Thus, the selenium atom Se1 interacts with an adjacent pentafluorophenoxy ring (Se1···Cg7 distance of 4.320(1) Å; Table 1), with the shortest contact distances being Se1···C22b = 3.531(2) Å and Se1···C23b = 3.772(2) Å (Figure 3), which are close to the sum of the van der Waals radii of Se and C, namely, 3.60 Å. In addition, a very short close contact is observed between Se1 and F6b; indeed, the corresponding separation value of 3.192(1) Å is well below the sum of the van der Waals radii of Se and F, i.e., 3.37 Å. Se1 is also involved in an intramolecular lone pair···π interaction with a triazine ring (Se1···Cg5 = 3.585(1) Å; Figure 3 and Table 1).

Along the *c* direction, the formation of another type of 1D chain is observed, which is formed through double lone pair (C_6F_5)···π(triazine) interactions (Figure 4), with centroid-to-fluorine distances Cg5···F1c and Cg5···F2c of 3.238(2) and 3.443(2) Å, respectively (Table 1). These 1D chains are

dx.doi.org/10.1021/ic501389s | *Inorg. Chem.* 2014, 53, 9827−9836

connected to the chains formed by the parallel-displaced $\pi_{C6F5O}\cdots\pi_{C6F5O}$ interactions (see above and Figure 2A), in a parallel fashion. Furthermore, the chains interact with the lattice propionitrile molecules via lone pair$\cdots\pi$ contacts with pentafluorophenoxy rings (Figure 4). These noncovalent bonding interactions are characterized by distances of N1S$\cdots$C21 = 3.202(3) Å and N1S$\cdots$C26 = 3.278(3) Å (Figure 4 and Table 1; N1S$\cdots$Cg7 = 3.413(2) Å), which are within the sum of the van der Waals radii of N and C, i.e., 3.25 Å.

The 2D supramolecular sheets in the *ac* plane are connected to each other by triple strong F$\cdots$F bonds (*bc* plane; Figure 5); indeed, the contact distances F8$\cdots$F9k and F8k$\cdots$F9 of 2.780(2) Å and F4$\cdots$F7e of 2.885(2) Å (Table 1) are all below the sum of the van der Waals radii of two F atoms, namely, 2.94 Å.[49] All of these supramolecular bonding interactions generate a 3D framework of tightly packed iron(II) complexes, indicating the likely cooperative character of the SCO, as indeed corroborated by magnetic and thermal studies (see below).

Furthermore, the magnetic and thermal studies disclose an interesting behavior of **1^{NCSe}·2PrCN** upon aging or annealing (see Magnetic and Thermal Studies section). Indeed, a displacement of the transition temperature toward a lower value is observed upon progressive loss of lattice propionitrile molecules. To understand this phenomenon, we have attempted several crystallographic studies on single crystals of **1^{NCSe}·2PrCN**. First, measurements at temperatures above 300 K typically resulted in rapid crystal degradation, impeding the determination of the structure. Actually, **1^{NCSe}·2PrCN** also degrades within a few days, when left in air, at room temperature.

Following the strategy adopted for the magnetic studies (see below), i.e., warming to 300 or 320 K for short periods of time and subsequent cooling to 100 K (see Scheme S1), we have collected seven single-crystal X-ray diffraction data sets of **1^{NCSe}·2PrCN** (see details in Table S1). No changes are observed around the iron(II) ion (see Table S2 for pertinent metric data) or in the crystal lattice, where the propionitrile molecules are found. However, as manifested by a slight worsening of the agreement indices, these temperature-dependent studies have led to a progressive deterioration of the single crystal. Further thermal annealing above 320 K results in the complete loss of crystallinity; accordingly, the structural modifications associated with the elimination of propionitrile molecules from the crystal lattice could not be assessed by single-crystal diffraction studies.

Magnetic and Thermal Studies. Differential scanning calorimetry measurements on freshly prepared polycrystalline powders showed an endothermic/exothermic event upon warming/cooling, as expected for the SCO transition occurring in **1^{NCSe}·2PrCN**. However, upon repeating the measurements on powders left in contact with air, a second anomaly appeared at lower temperatures, whereas the original one was significantly lowered. After 1 week in contact with air, only this second anomaly at lower temperatures remained (Figure S1). In a similar manner, variable-temperature magnetic measurements showed a behavior highly dependent on the thermal history of the sample within the magnetometer (see Figure S2 for a χT vs T plot, where χ is the molar paramagnetic susceptibility). The first heating scan, performed up to 350 K, evidenced a complete thermal SCO centered at ca. 283 K, whereas the first cooling (to 5 K) and second heating (to 330 K) scans showed a conversion occurring in two similar steps centered at ca. 280 and 215 K. After this second warming scan, the conversion occurred again as a single step centered at ca. 217 K. No further variation of the behavior was then detected in further temperature scans. The similarity between the observations made with these two techniques points to a modification of **1^{NCSe}·2PrCN** occurring upon prolonged air exposure at RT or shorter periods of time at temperatures in the 330−350 K range in a He depression (the sample is subjected to vacuum at room temperature prior to insertion in the magnetometer sample space, so the modification seems to require slightly higher temperatures than 300 K), in agreement with the rapid loss of crystallinity of single crystals observed above 320 K. The two-step magnetic transition (evidenced also by the two DSC anomalies) corresponds to a situation in which two distinct phases are present in the material, i.e., with partial modification of pristine **1^{NCSe}·2PrCN**. Thermogravimetric measurements were thus carried out to ascertain a possible loss of the lattice propionitrile molecules. The data shows a 6.6% weight loss centered at 382 K, with an onset at around 330 K (Figure S3). These data agree perfectly with the loss of all propionitrile molecules from the crystal lattice (theoretical value, 6.86%). Under the dynamic conditions used here, the loss of propionitrile is completed at ca. 390 K, slightly above its conventional boiling temperature at ambient pressure. Clearly, upon moderate heating, **1^{NCSe}·2PrCN** tends to lose its lattice propionitrile, which, in the solid state, is only weekly bound by van der Waals interactions. Powder diffraction methods reveal that the resulting material is polycrystalline, with an infrared spectrum almost identical to that of **1^{NCSe}·2PrCN**; notably, the $NCSe^-$ vibrations at 2055 and 2098 cm^{-1} slightly broaden, the former being shifted by ca. 6 cm^{-1} toward lower wavenumbers (Figure S4). Not unexpectedly, the modified phase can thus be ascribed to desolvated **1^{NCSe}**.

The temperature dependence of the χT product of **1^{NCSe}·2PrCN** and **1^{NCSe}**, obtained reproducibly by thermal annealing of fresh **1^{NCSe}·2PrCN** for 2 h at 80 °C, is depicted in Figure 6, evidencing LS ↔ HS transitions centered on 283 and 220 K for **1^{NCSe}·2PrCN** and **1^{NCSe}**, respectively. The conversions are complete, with χT increasing from ca. 0.02−0.04 $cm^3\ mol^{-1}\ K$

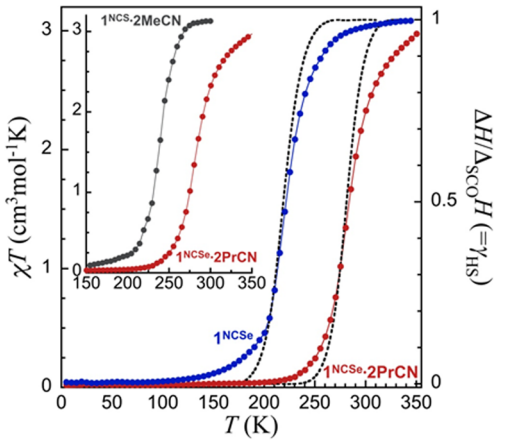

Figure 6. χT vs T plot for **1^{NCSe}·2PrCN** (red dots) and **1^{NCSe}** (blue dots) depicting their full SCO process and corresponding temperature dependence of their excess enthalpies normalized to that involved in the process of SCO (black dashed lines). Note that the latter is equivalent to the temperature dependence of the HS fraction $\gamma_{HS}(T)$. The inset χT vs T plot compares the SCO of **1^{NCSe}·2PrCN** with that of the analogue compound **1^{NCS}·2MeCN** (gray dots). Full lines are guides to the eye.

dx.doi.org/10.1021/ic501389s | *Inorg. Chem.* 2014, 53, 9827−9836

below 220 K and above 120 K, respectively, a typical value for an Fe(II) ion in a LS $S = 0$ state, to ca. 2.97 $cm^3\ mol^{-1}\ K$ at 350 K and ca. 3.04−3.08 $cm^3\ mol^{-1}\ K$ above 300 K, respectively; both values are indicative of a mostly HS $S = 2$ state.

The SCO curves of both materials are indeed very similar in shape, with that of $\mathbf{1}^{\mathbf{NCSe}}$ simply being shifted to lower temperatures by ca. 63 K. The value of ΔT_{80}, the temperature range over which 80% of the LS ↔ HS conversion takes place, is indeed the same at about 65 K, slightly higher than that observed for $\mathbf{1}^{\mathbf{NCS}}$**·2MeCN**, namely, $\Delta T_{80} \approx 50$ K (see inset of Figure 6).[37] This less efficient cooperative character shown by $\mathbf{1}^{\mathbf{NCSe}}$**·2PrCN** (compared to that of $\mathbf{1}^{\mathbf{NCS}}$**·2MeCN**) might be interpreted by two concurrent effects: the presence of bulkier propionitrile molecules, compared to acetonitrile, and that of the more diffuse Se atom, resulting in weaker supramolecular interactions (with respect to those involving an S atom) and molecules and Fe(II) ions being kept (on average) further apart than when S atoms are present. This latter contribution seems to be particularly relevant, as the desolvated $\mathbf{1}^{\mathbf{NCSe}}$ material has a similar (larger) ΔT_{80} (of ca. 70 K).

The temperature dependence of the molar heat capacity of $\mathbf{1}^{\mathbf{NCSe}}$**·2PrCN** and $\mathbf{1}^{\mathbf{NCSe}}$ exhibit a marked anomaly, in the 240−320 and 180−260 K ranges, respectively, and culminating at 280 and 218 K (Figure 7, top). These features are in perfect agreement with the magnetic data and are thus due to the SCO process in $\mathbf{1}^{\mathbf{NCSe}}$**·2PrCN** and $\mathbf{1}^{\mathbf{NCSe}}$. The corresponding excess heat capacities allow the associated excess enthalpy and entropy to be determined as 9.71 kJ mol^{-1} and 34.6 J $mol^{-1}\ K^{-1}$, respectively, for $\mathbf{1}^{\mathbf{NCSe}}$**·2PrCN** and 8.27 kJ mol^{-1} and 37.9 J $mol^{-1}\ K^{-1}$ for $\mathbf{1}^{\mathbf{NCSe}}$. Normalizing $\Delta H(T)$ to the corresponding ΔH_{SCO} also provides the temperature variation of the HS fraction, $\gamma_{HS}(T)$, depicted as dashed lines in Figure 6, which is again in excellent agreement with the magnetic data. To provide a comparable estimation of the cooperative character of the SCO in $\mathbf{1}^{\mathbf{NCSe}}$**·2PrCN** and $\mathbf{1}^{\mathbf{NCSe}}$, their excess heat capacities were fitted to Sorai's domain model (see the Supporting Information for details),[50] often used in SCO systems, cooperative or not, for which accurate calorimetric data are available.[51−54] The model gives a measure of the cooperativity through the number, n, of like-spin SCO centers per interacting domain. Here, the derived best fits (red lines in Figure 7, bottom) provide moderate numbers of interacting molecules per domain at $n = 8.1$ and 5.2 for $\mathbf{1}^{\mathbf{NCSe}}$**·2PrCN** and $\mathbf{1}^{\mathbf{NCSe}}$, respectively. These values are in the same range as that of the $\mathbf{1}^{\mathbf{NCS}}$**·2MeCN** analogue ($n = 6.2$) and indicate a similar cooperative character of the SCO in these materials, significantly inferior to the value of 14.2 we recently reported for the related $[Fe(\mathbf{L1})_2(NCS)_2]\cdot 2CH_3OH$ (**L1** = 2-chloro-4-(*N*,*N*-(2-pyridyl)amino)-6-(pentafluorophenoxy)-(1,3,5)-triazine).[42] Although it gives rise to a decrease in the SCO temperature by nearly 60 K, the loss of the lattice propionitrile molecule does not seem to affect significantly the way the electronic transition couples to the lattice phonons, the major component of the SCO cooperativeness.

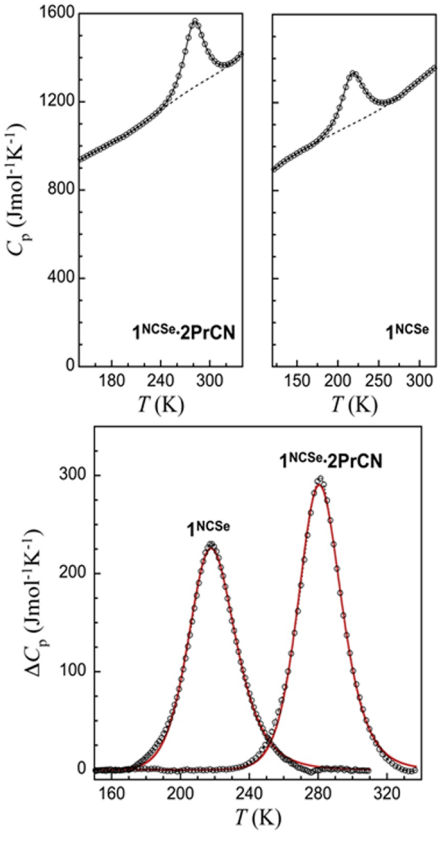

Figure 7. (Top) Molar heat capacities of $\mathbf{1}^{\mathbf{NCSe}}$**·2PrCN** and $\mathbf{1}^{\mathbf{NCSe}}$ showing a significant endothermic anomaly arising from the process of SCO. The dashed lines are the respective estimated lattice components. (Bottom) Excess molar heat capacities associated with the SCO of $\mathbf{1}^{\mathbf{NCSe}}$**·2PrCN** and $\mathbf{1}^{\mathbf{NCSe}}$. The full red lines are fits to Sorai's domain model (see text and ref 50), with $n = 8.1$ and $T_{SCO} = 281.7$ K and $n = 5.2$ and $T_{SCO} = 219.4$ K for $\mathbf{1}^{\mathbf{NCSe}}$**·2PrCN** and $\mathbf{1}^{\mathbf{NCSe}}$, respectively.

X-ray Powder Diffraction Studies. As mentioned above, the temperature effect on the solid-state structure of $\mathbf{1}^{\mathbf{NCSe}}$**·2PrCN** (with possible structural changes) could not be investigated by single-crystal X-ray diffraction as a result of the degradation of the material when $T > 320$ K. Therefore, X-ray powder-diffraction studies were carried out to explore potential temperature-dependent structural changes in $\mathbf{1}^{\mathbf{NCSe}}$**·2PrCN**. Powder diffraction data, collected in the 300−370 K range (shown in Figure 8) and analyzed by the structureless Le Bail whole pattern profile method, allowed the relative changes of the lattice parameters to be retrieved (cell volume and the size and shape of the thermal strain tensor). These results are numerically reported in Table 2 and are graphically depicted in Figure 9. The shape and orientation of the thermal strain tensor, elongated in the $[1\bar{1}0]$ direction, was then compared with the known crystal structure, which evidenced the presence of weakly bound slabs parallel to the $(1\bar{1}0)$ plane and is thus prone to more significant thermally induced dilatation.

Prolonged heating at 370 K showed a progressive change of the diffraction trace, which was completed after ca. 1 h. After eliminating a few peaks (attributed to an unknown contaminant), a reliable unit cell for the HT phase was obtained (using TOPAS-R):[55] $a = 8.87$, $b = 11.21$, $c = 15.40$ Å, $\alpha = 102.3$, $\beta = 84.3$, and $\gamma = 103.4°$, $V = 1454$ Å^3; GOF(20) = 21.[56] The crystal symmetry and the lattice parameters herein proposed match those found for the pristine solvated phase (see Table S1, $V = 1557$ Å^3 at 300 K). The difference in the molar volume ($\Delta V = -103$ Å^3) is well-matched with that expected for the loss of two PrCN molecules (64 Å^3, as estimated by SMILE[57]). After cooling to room temperature, diffraction data were collected with an overnight measurement (shown in Figure S5). Unfortunately, the powder pattern, due to partial degradation, contained too many peaks, making the crystal structure determination of the desolvated phase impossible.

dx.doi.org/10.1021/ic501389s | Inorg. Chem. 2014, 53, 9827−9836

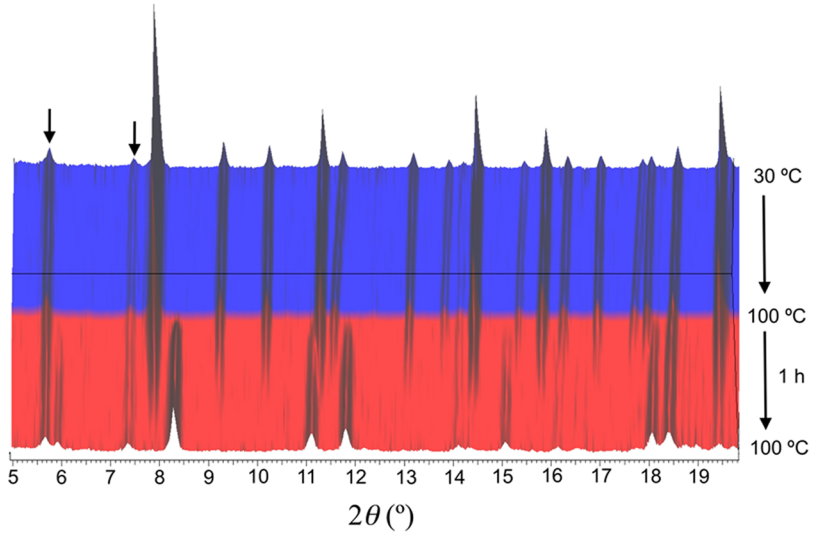

Figure 8. Variable-temperature X-ray powder diffraction data, collected between 30 and 100 °C. Vertical axis (back to front: temperature increase). The blue portion refers to the pristine **1**^{NCSe}**·2PrCN** species, transforming into the (still triclinic and contracted, see text) unsolvated phase (the two weak low-angle peaks at 5.6 and 7.3°, highlighted by the black arrows, belong to an unknown contaminant generated by partial degradation). The red portion contains 12 XRPD traces collected under isothermal conditions (in air) at 100 °C (5 min each).

Table 2. Linear and Volumetric Thermal Expansion Coefficients of 1^{NCSe}.2PrCN in the Form of $\partial \ln x/\partial T$ (x = a, b, c, α, β, γ and V)[a]

$\partial \ln a/\partial T$	$\partial \ln b/\partial T$	$\partial \ln c/\partial T$	$\partial \ln \alpha/\partial T$	$\partial \ln \beta/\partial T$	$\partial \ln \gamma/\partial T$	$\partial \ln V/\partial T$
+160	+74	+78	+9	−18	+78	+227

[a]Units in M K^{-1}. Values were computed by fitting the TXRPD-derived data in the 30−95°C range, where a nearly linear trend was observed.

The loss of the lattice propionitrile molecules will irremediably affect the solid-state packing of the iron(II) complexes. Actually, the propionitrile molecules connect the [Fe(**L1**^{F})$_2$(NCSe)$_2$] complexes, through lone pair···π interactions (Figure 10), generating a 1D supramolecular chain, and are therefore involved in the observed SCO properties of **1**^{NCSe}**·2PrCN**. Consequently, their removal will have an effect on the magnetic properties of the material (Figure S6). In fact, the spin-transition properties of the propionitrile-free compound **1**^{NCSe} are modified compared to those of **1**^{NCSe}**·2PrCN** (see above), as reflected by the lower $T_{1/2}$ (220 K instead of 283 K) and slightly lower cooperativity ($n/\Delta T_{80}$ value of ca. 5.2/70 K instead of 8.1/65 K).

EXPERIMENTAL SECTION

Physical Measurements. Infrared spectra were recorded with a Nicolet 5700 FT-IR spectrometer (as KBr pellets) or with a PerkinElmer Spectrum 100 apparatus equipped with an ATR device (neat samples). ^{1}H NMR spectra were recorded at room temperature with a Varian Unity 300 MHz spectrometer; chemical shifts are reported in ppm relative to the residual solvent signal of $CDCl_3$ (δ = 7.26 ppm). Elemental analyses were performed by the Servei de Microanalisi, Consejo Superior de Investigaciones Científicas (CSIC) of Barcelona. Thermogravimetric measurements were performed with a SDT2960 thermobalance from TA Instruments under synthetic air at 10 °C min^{-1}.

Magnetic measurements were performed on bulk microcrystalline powders using a commercial SQUID magnetometer of the Physical Measurements unit of the Servicio General de Apoyo a la Investigación−SAI, Universidad de Zaragoza. Correction for the experimentally measured contribution of the sample holder and the sample diamagnetism, estimated from Pascal's tables, were applied. In this setup, the sample space is maintained under a low-pressure He atmosphere, with the sample being held within a gelatin capsule and thus subjected to dry depression.

Differential scanning calorimetry (DSC) experiments were performed with a Q1000 calorimeter from TA Instruments equipped with the LNCS accessory. The temperature and enthalpy scales were calibrated with a standard sample of indium, using its melting transition (156.6 °C, 3296 J mol^{-1}). The measurements were carried out using aluminum pans with a mechanical crimp, with an empty pan as reference. The zero-heat flow procedure described by TA Instruments was followed to derive heat capacities, using synthetic sapphire as reference compound. An overall accuracy of ca. 0.2 K for the temperature and up to 5−10% for the heat capacity was estimated over the whole temperature range by comparison with the synthetic sapphire. A lattice heat capacity was estimated from data below and above the anomaly associated with the SCO process (dashed lines in Figure 7, top). Excess enthalpy and entropy were derived by integration of the excess heat capacity with respect to T and ln T, respectively.

Materials. The ligand 2-(*N*,*N*-bis(2-pyridyl)amino)-4,6-bis-(pentafluorophenoxy)-(1,3,5)triazine (**L1**^{F}) was prepared according to the literature.[37] $Fe(ClO_4)_2{\cdot}6H_2O$, ascorbic acid, KNCSe, and propionitrile were purchased from Sigma-Aldrich and used as supplied.

Synthesis of [Fe(L1^F)$_2$(NCSe)$_2$]·2CH$_3$CH$_2$CN (1^{NCSe}·2PrCN). A solution of ligand **L1**^{F} (0.122 g, 0.20 mmol) in propionitrile (5 mL) was added to a solution of $Fe(ClO_4)_2{\cdot}6H_2O$ (0.026 g, 0.10 mmol) in propionitrile (2 mL) containing ca. 5 mg of ascorbic acid (to prevent oxidation to iron(III)). Next, a solution of KNCSe (0.029 g, 0.20 mmol) in propionitrile (3 mL) was added, and the resulting light-yellow reaction mixture was filtered. The filtrate was left unperturbed for the slow evaporation of the solvent; after 4 days, single crystals of **1**^{NCSe}**·2PrCN**, suitable for X-ray diffraction analysis, were obtained with a yield of 60% (0.096 g, 0.06 mmol, based on iron). Elemental analyses calculated (found) (%) for $C_{58}H_{26}F_{20}FeN_{16}O_4Se_2$: C, 43.41 (43.59); H, 1.63 (1.67); N, 13.97 (13.81). IR (KBr): ν = 2096(w), 2061(m), 1607(m), 1558(m), 1521(s), 1471(m), 1437(w), 1371(s),

dx.doi.org/10.1021/ic501389s | Inorg. Chem. 2014, 53, 9827−9836

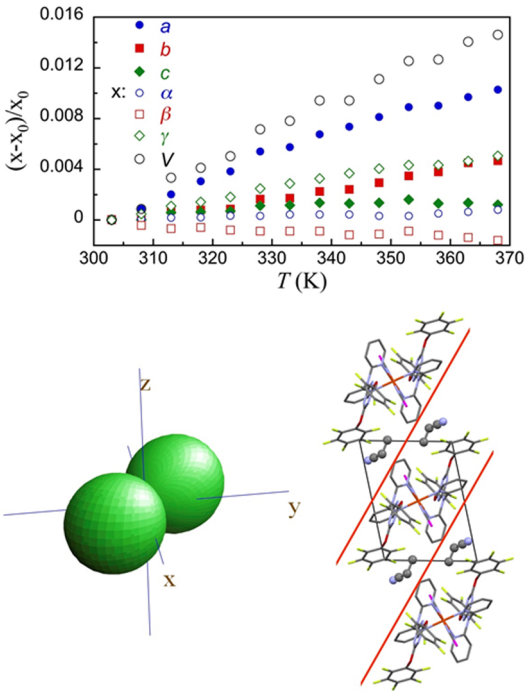

Figure 9. (Top) Relative lattice parameter changes (including cell volume), measured by TXRPD data. Horizontal axis, temperature (T, K); vertical axis, $(x_T - x_{30})/x_{30}$ (x = a, b, c, α, β, γ, and V). (Bottom left) Thermal strain tensor for the 30−95 °C range, computed by Ohashi's method[63] and drawn with Wintensor.[64] (Bottom right) Crystal packing of **1**^{NCSe}**·2PrCN** viewed approximately down [110], highlighting the $(1\bar{1}0)$ plane, separating slabs of weakly bound molecules, which conform to the longest axis of the thermal strain tensor shown on the left.

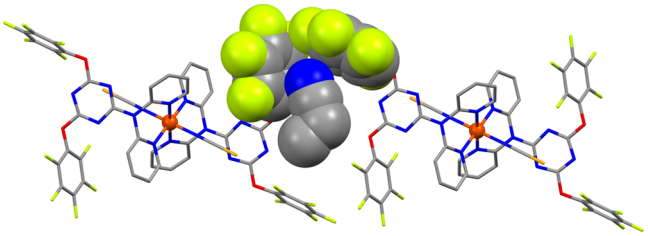

Figure 10. View of the solid-state structure of **1**^{NCSe}**·2PrCN** showing the interaction of a propionitrile molecule with two pentafluorophenyl rings (in space-filling mode) belonging to two neighboring iron(II) complexes, through lone pair···π interactions.

1307(m), 1244(m), 1158(m), 1079(m), 1001(m), 978(m), 806(w), 778(w), 644(w) cm^{-1}.

Single-Crystal X-ray Crystallography. X-ray diffraction data for **1**^{NCSe}**·2PrCN** were collected on a yellow (purple at 100 K) needle with a Bruker APEX II CCD diffractometer on the Advanced Light Source beamline 11.3.1 at Lawrence Berkeley National Laboratory from a silicon 111 monochromator (λ = 0.7749 Å). Seven data sets were acquired successively on the same crystal following the temperature sequence depicted in Scheme S1. Attempts at measuring at temperatures above 300 K or bringing crystals above 320 K for a longer period of time systematically resulted in loss of crystallinity. Data reduction and absorption corrections were performed with SAINT and SADABS, respectively.[58] The structures were solved using SIR97[59,60] and refined over F^2 using the SHELXTL suite.[58,61] Crystallographic and refinement parameters are summarized in Table S1. Selected bond distances and angles are given in Tables 1 and S2. All details can be found in the supplementary crystallographic data for this article in cif format with CCDC numbers 1007424−1007430. These data can be obtained free of charge from The Cambridge Crystallographic Data Centre via www.ccdc.cam.ac.uk/data_request/cif.

X-ray Powder Diffraction. Gently ground powders of **1**^{NCSe}**·2PrCN** were deposited in the hollow of a zero-background plate, 0.2 mm deep (a silicon monocrystal supplied by Assing SrL, Monterotondo, Italy). Diffraction experiments were performed on a vertical-scan Bruker AXS D8 Advance diffractometer in 2θ mode, equipped with a linear position-sensitive Lynxeye detector, primary beam Soller slits, and Ni-filtered Cu Kα radiation (λ = 1.5418 Å). Generator settings: 40 kV, 40 mA.

Thermodiffractometric (TXRPD) experiments were performed on a powdered batch of **1**^{NCSe}**·2PrCN**, deposited in the hollow of an aluminum-framed silicon monocrystal, mounted on a Peltier-driven sample heating stage, assembled by Officina Elettrotecnica di Tenno, Ponte Arche, Italy; diffractograms were acquired in air from 30 to 100 °C, with steps of 10 °C, in a significant low-angle 2θ range (5−20°) and, under isothermal conditions, at 100 °C for ca. 1 h. Lattice parameters at each T, for each phase, were refined by the structureless Le Bail procedure,[62] and linear thermal expansion coefficients were derived from data collected in the 30−100 °C range. Thermal strain tensors were computed using the STRAIN module available on the Bilbao Crystallographic Server following Ohashi's method.[63]

CONCLUSIONS

For about 8 years, our group and that of Murray[31] have been investigating the SCO properties of a particular family of iron(II) systems obtained from 2,2′-dipyridylamino-substituted triazine ligands. Through ligand design, it has been possible to obtain members of this group of SCO complexes with interesting properties.[42] In the present study, a new compound belonging to this family was prepared that exhibits solvent-dependent SCO properties. Indeed, the loss of propionitrile molecules present in the crystal lattice of **1**^{NCSe}**·2PrCN** results in a strong alteration of its SCO behavior, which is reflected by an important shift of the transition temperature, from $T_{1/2}$ = 283 K to 220 K (for the desolvated compound **1**^{NCSe}). This variation of the magnetic properties is most likely due to a modification of the crystal packing of the transiting molecules, hence exemplifying the great sensitivity of the SCO phenomenon. In addition, the results reported herein illustrate the potential of (2,2′-dipyridylamine/triazine)-based iron(II) complexes to generate SCO materials with singular properties.

ASSOCIATED CONTENT

Supporting Information

Crystallographic data for **1**^{NCSe}**·2PrCN** at different temperatures with the corresponding coordination bond distances and angles, DSC traces for fresh and aged **1**^{NCSe}**·2PrCN**, χT vs T plots, TGA of fresh **1**^{NCSe}**·2PrCN**, IR spectra of **1**^{NCSe}**·2PrCN** and **1**^{NCSe}, XRPD data for **1**^{NCSe}, and crystal packing views of **1**^{NCSe}**·2PrCN** showing the location of the lattice solvent molecules. This material is available free of charge via the Internet at http://pubs.acs.org.

AUTHOR INFORMATION

Corresponding Authors

*(N.M.) E-mail: norberto.masciocchi@uninsubria.it.
*(O.R.) E-mail: roubeau@unizar.es.
*(P.G.) E-mail: patrick.gamez@qi.ub.es.

Present Address

○Department of Chemistry, Faculty of Science and Technology, Thammasat University, Rangsit Campus, Klong 1, Klong Luang, Pathumthani 12121, Thailand.

Notes

The authors declare no competing financial interest.

■ ACKNOWLEDGMENTS

P.G. acknowledges ICREA (Institució Catalana de Recerca i Estudis Avançats) and the Ministerio de Economía y Competitividad of Spain (project CTQ2011-27929-C02-01). N.W. thanks the Royal Golden Jubilee Ph.D. Program (RGJ, grant no. PHD/0234/2550) and Khon Kaen University for a research grant. S.Y. acknowledges The Thailand Research Fund, the National Research University Project of Thailand, Office of the Higher Education Commission, through the Advanced Functional Materials Cluster of Khon Kaen University and the Center of Excellence for Innovation in Chemistry (PERCH-CIC), Office of the Higher Education Commission, Ministry of Education. The Advanced Light Source is supported by the Director, Office of Science, Office of Basic Energy Sciences of the U.S. Department of Energy under contract no. DE-AC02-05CH11231. O.R. acknowledges funding from the Ministerio de Economía y Competitividad of Spain (project MAT2011-24284).

■ REFERENCES

(1) Gütlich, P.; Goodwin, H. A. *Top. Curr. Chem.* **2004**, *233*, 1−47.
(2) *Spin-Crossover Materials: Properties and Applications*; Halcrow, M. A., Ed.; John Wiley and Sons: Chichester, UK, 2013.
(3) Boča, R. *A Handbook of Magnetochemical Formulae*; Elsevier: London, 2012; pp 159−186.
(4) Real, J. A.; Gaspar, A. B.; Munoz, M. C. *Dalton Trans.* **2005**, 2062−2079.
(5) Bousseksou, A.; Molnár, G.; Real, J. A.; Tanaka, K. *Coord. Chem. Rev.* **2007**, *251*, 1822−1833.
(6) Gütlich, P.; Hauser, A.; Spiering, H. *Angew. Chem., Int. Ed. Engl.* **1994**, *33*, 2024−2054.
(7) Cambi, L.; Szego, L. *Ber. Dtsch. Chem. Ges.* **1931**, *64*, 2591−2598.
(8) Cluster Issue: Spin-Crossover Complexes *Eur. J. Inorg. Chem.* **2013**, 573−1070.
(9) Krober, J.; Codjovi, E.; Kahn, O.; Grolière, F.; Jay, C. *J. Am. Chem. Soc.* **1993**, *115*, 9810−9811.
(10) Cantin, C.; Daubric, H.; Kliava, J.; Servant, Y.; Sommier, L.; Kahn, O. *J. Phys.: Condens. Matter* **1998**, *10*, 7057−7064.
(11) Kahn, O.; Martinez, C. J. *Science* **1998**, *279*, 44−48.
(12) Roubeau, O. *Chem.—Eur. J.* **2012**, *18*, 15230−15244.
(13) Létard, J. F.; Guionneau, P.; Goux-Capes, L. *Top. Curr. Chem.* **2004**, *235*, 221−249.
(14) Gaspar, A. B.; Seredyuk, M.; Gütlich, P. *Coord. Chem. Rev.* **2009**, *253*, 2399−2413.
(15) Gamez, P.; Costa, J. S.; Quesada, M.; Aromí, G. *Dalton Trans.* **2009**, 7845−7853.
(16) Bousseksou, A.; Molnár, G.; Salmon, L.; Nicolazzi, W. *Chem. Soc. Rev.* **2011**, *40*, 3313−3335.
(17) Gütlich, P.; Garcia, Y.; Goodwin, H. A. *Chem. Soc. Rev.* **2000**, *29*, 419−427.
(18) Sato, O. *Proc. Jpn. Acad., Ser. B* **2012**, *88*, 213−225.
(19) Ruben, M.; Breuning, E.; Lehn, J. M.; Ksenofontov, V.; Renz, F.; Gütlich, P.; Vaughan, G. B. M. *Chem.—Eur. J.* **2003**, *9*, 4422−4429.
(20) Aromí, G.; Barrios, L. A.; Roubeau, O.; Gamez, P. *Coord. Chem. Rev.* **2011**, *255*, 485−546.
(21) Olguin, J.; Brooker, S. *Coord. Chem. Rev.* **2011**, *255*, 203−240.
(22) Boča, M.; Jameson, R. F.; Linert, W. *Coord. Chem. Rev.* **2011**, *255*, 290−317.
(23) Murray, K. S. *Eur. J. Inorg. Chem.* **2008**, 3101−3121.
(24) Halcrow, M. A. *Coord. Chem. Rev.* **2009**, *253*, 2493−2514.
(25) Kitchen, J. A.; Brooker, S. *Coord. Chem. Rev.* **2008**, *252*, 2072−2092.
(26) Quesada, M.; de la Peña-O'Shea, V. A.; Aromí, G.; Geremia, S.; Massera, C.; Roubeau, O.; Gamez, P.; Reedijk, J. *Adv. Mater.* **2007**, *19*, 1397−1402.
(27) Gamez, P.; de Hoog, P.; Lutz, M.; Driessen, W. L.; Spek, A. L.; Reedijk, J. *Polyhedron* **2003**, *22*, 205−210.
(28) Gamez, P.; de Hoog, P.; Lutz, M.; Spek, A. L.; Reedijk, J. *Inorg. Chim. Acta* **2003**, *351*, 319−325.
(29) Quesada, M.; Monrabal, M.; Aromí, G.; de la Peña-O'Shea, V. A.; Gich, M.; Molins, E.; Roubeau, O.; Teat, S. J.; MacLean, E. J.; Gamez, P.; Reedijk, J. *J. Mater. Chem.* **2006**, *16*, 2669−2676.
(30) Quesada, M.; de Hoog, P.; Gamez, P.; Roubeau, O.; Aromí, G.; Donnadieu, B.; Massera, C.; Lutz, M.; Spek, A. L.; Reedijk, J. *Eur. J. Inorg. Chem.* **2006**, 1353−1361.
(31) Scott, H. S.; Ross, T. M.; Chilton, N. F.; Gass, I. A.; Moubaraki, B.; Chastanet, G.; Paradis, N.; Létard, J. F.; Vignesh, K. R.; Rajaraman, G.; Battena, S. R.; Murray, K. S. *Dalton Trans.* **2013**, *42*, 16494−16509.
(32) Scott, H. S.; Ross, T. M.; Batten, S. R.; Gass, I. A.; Moubaraki, B.; Neville, S. M.; Murray, K. S. *Aust. J. Chem.* **2012**, *65*, 874−882.
(33) Ross, T. M.; Moubaraki, B.; Batten, S. R.; Murray, K. S. *Dalton Trans.* **2012**, *41*, 2571−2581.
(34) Ross, T. M.; Moubaraki, B.; Neville, S. M.; Batten, S. R.; Murray, K. S. *Dalton Trans.* **2012**, *41*, 1512−1523.
(35) Ross, T. M.; Moubaraki, B.; Turner, D. R.; Halder, G. J.; Chastanet, G.; Neville, S. M.; Cashion, J. D.; Létard, J. F.; Batten, S. R.; Murray, K. S. *Eur. J. Inorg. Chem.* **2011**, 1395−1417.
(36) Neville, S. M.; Leita, B. A.; Offermann, D. A.; Duriska, M. B.; Moubaraki, B.; Chapman, K. W.; Halder, G. J.; Murray, K. S. *Eur. J. Inorg. Chem.* **2007**, 1073−1085.
(37) Wannarit, N.; Roubeau, O.; Youngme, S.; Teat, S. J.; Gamez, P. *Dalton Trans.* **2013**, *42*, 7120−7130.
(38) Gomez, V.; Benet-Buchholz, J.; Martin, E.; Galán-Mascarós, J. R. *Chem.—Eur. J.* **2014**, *20*, 5369−5379.
(39) Costa, J. S.; Rodriguez-Jimenez, S.; Craig, G. A.; Barth, B.; Beavers, C. M.; Teat, S. J.; Aromí, G. *J. Am. Chem. Soc.* **2014**, *136*, 3869−3874.
(40) Wei, R. J.; Tao, J.; Huang, R. B.; Zheng, L. S. *Inorg. Chem.* **2011**, *50*, 8553−8564.
(41) Amoore, J. L. M.; Kepert, C. J.; Cashion, J. D.; Moubaraki, B.; Neville, S. M.; Murray, K. S. *Chem.—Eur. J.* **2006**, *12*, 8220−8227.
(42) Nassirinia, N.; Amani, S.; Teat, S. J.; Roubeau, O.; Gamez, P. *Chem. Commun.* **2014**, *50*, 1003−1005.
(43) Halcrow, M. A. *Chem. Soc. Rev.* **2011**, *40*, 4119−4142.
(44) Marchivie, M.; Guionneau, P.; Létard, J. F.; Chasseau, D. *Acta Crystallogr., Sect. B: Struct. Sci.* **2005**, *61*, 25−28.
(45) McCusker, J. K.; Rheingold, A. L.; Hendrickson, D. N. *Inorg. Chem.* **1996**, *35*, 2100−2112.
(46) König, E. *Struct. Bonding (Berlin, Ger.)* **1991**, *76*, 51−152.
(47) Mooibroek, T. J.; Gamez, P. *CrystEngComm* **2012**, *14*, 1027−1030.
(48) Mooibroek, T. J.; Gamez, P. *CrystEngComm* **2012**, *14*, 3902−3906.
(49) Mooibroek, T. J.; Gamez, P. *CrystEngComm* **2013**, *15*, 1802−1805.
(50) Sorai, M.; Nakazawa, Y.; Nakano, M.; Miyazaki, Y. *Chem. Rev.* **2013**, *113*, PR41−122.
(51) Nakamoto, T.; Tan, Z. C.; Sorai, M. *Inorg. Chem.* **2001**, *40*, 3805−3809.
(52) Roubeau, O.; deVos, M.; Stassen, A. F.; Burriel, R.; Haasnoot, J. G.; Reedijk, J. *J. Phys. Chem. Solids* **2003**, *64*, 1003−1013.
(53) Arcis-Castillo, Z.; Zheng, S.; Siegler, M. A.; Roubeau, O.; Bedoui, S.; Bonnet, S. *Chem.—Eur. J.* **2011**, *17*, 14826−14836.
(54) Roubeau, O.; Castro, M.; Burriel, R.; Haasnoot, J. G.; Reedijk, J. *J. Phys. Chem. B* **2011**, *115*, 3003−3012.
(55) *TOPAS*, 3.0; Bruker AXS: Karlsruhe, Germany, 2005.
(56) de Wolff, P. M. *J. Appl. Crystallogr.* **1968**, *1*, 108−113.
(57) Eufri, D.; Sironi, A. *J. Mol. Graphics* **1989**, *7*, 165−169.
(58) *SAINT, SADABS, and SHELXTL*; Bruker AXS Inc.: Madison, WI.

(59) Altomare, A.; Burla, M. C.; Camalli, M.; Cascarano, G. L.; Giacovazzo, C.; Guagliardi, A.; Moliterni, A. G. G.; Polidori, G.; Spagna, R. *J. Appl. Crystallogr.* **1999**, *32*, 115−119.
(60) Burla, M. C.; Camalli, M.; Carrozzini, B.; Cascarano, G. L.; Giacovazzo, C.; Polidori, G.; Spagna, R. *Acta Crystallogr., Sect. A* **1999**, *55*, 991−999.
(61) Sheldrick, G. M. *Acta Crystallogr., Sect. A* **2008**, *64*, 112−122.
(62) Le Bail, A.; Duroy, H.; Fourquet, J. L. *Mater. Res. Bull.* **1988**, *23*, 447−452.
(63) Ohashi, Y. In *Comparative Crystal Chemistry*; Hazen, R. M., Finger, L. W., Eds.; Wiley: New York, 1982; pp 92−102.
(64) Kaminsli, W. *WINTENSOR*, V.1.4; University of Washington: Seattle, WA, 2011.
(65) Guionneau, P.; Marchivie, M.; Bravic, G.; Létard, J. F.; Chasseau, D. *Top. Curr. Chem.* **2004**, *234*, 97−128.
(66) Quesada, M.; Prins, F.; Bill, E.; Kooijman, H.; Gamez, P.; Roubeau, O.; Spek, A. L.; Haasnoot, J. G.; Reedijk, J. *Chem.—Eur. J.* **2008**, *14*, 8486−8499.

PCCP

RSC Publishing

PAPER

View Article Online
View Journal | View Issue

Hetero triply-bridged dinuclear copper(II) compounds with ferromagnetic coupling: a challenge for current density functionals†

Cite this: *Phys. Chem. Chem. Phys.*, 2013, **15**, 1966

Nanthawat Wannarit,[ab] Chaveng Pakawatchai,[c] Ilpo Mutikainen,[d] Ramon Costa,*[b] Ibério de P. R. Moreira,[e] Sujittra Youngme*[a] and Francesc Illas*[e]

Received 30th October 2012,
Accepted 4th December 2012

DOI: 10.1039/c2cp43839a

www.rsc.org/pccp

Seven new hetero triply-bridged dinuclear Cu(II) compounds have been synthesized and characterized corresponding to a series with general formula $[Cu_2(L)_2(\mu\text{-}OH)(\mu\text{-}OH_2)(\mu\text{-}O_2CR)]X_2$ (where L = bpy = 2,2′-bipyridine, 4,4′-dmbpy = 4,4′-dimethyl-2,2′-bipyridine and 5,5′-dmbpy = 5,5′-dimethyl-2,2′-bipyridine; R = H for formate, CH_3 for acetate, CH_2CH_3 for propionate and $C(CH_3)_3$ for trimethylacetate and X = $CF_3SO_3^-$ and ClO_4^-). All compounds exhibit ferromagnetic behavior with the experimental *J* values derived from magnetic susceptibility measurements being in the 73–104 cm^{-1} range. The overall qualitative behavior is reproduced by state of the art density functional theory based methods. However, none of the functionals is able to reproduce the fine details along the series which constitutes an excellent benchmark for future developments.

1. Introduction

The magnetochemistry of Cu(II) systems has received much attention because of their interesting structural and magnetic properties, as well as their application as molecular based materials.[1–3] In these materials, the Cu(II) ions exhibit a d^9 electronic configuration and, hence, can be considered as suitable candidates representative of basic models of magnetic coordination compounds, especially in di- and polynuclear Cu(II) systems.[4,5] A deep understanding of magneto-structural correlations is highly desirable to be able to predict the magnitude of the coupling constant, its character and the corresponding physical mechanism, thus allowing one to design and synthesize new molecular based materials with improved magnetic properties. Hence, magneto-structural correlations for a series of compounds with different structural and magnetic properties are usually derived either from experimental measurements or theoretical calculations. Clearly, compounds with strong ferromagnetic coupling are of great interest for potential technological applications.[4–12]

Among the different Cu(II) families with ferromagnetic properties, previous work has focused on the design, magnetic properties and magneto-structural correlations of the hetero triply-bridged dinuclear Cu(II) systems because this particular type of compound exhibits moderate to strong ferromagnetic interactions.[6–10] In this type of system, the magnetic interaction occurs *via* bridging ligands, although various pathways are possible,[10] which depend on the coordination geometry of the Cu(II) ion, the Cu···Cu separation, the bond angles involving the bridging atoms, the dihedral angle between the planes containing the Cu(II) ions and the distance from the Cu(II) to the bridging ligands. Structurally, the Cu(II) ions are in a five-fold coordination which, however, corresponds to a rather broad range of geometries, from regular trigonal bipyramidal (TBP) to regular square-based pyramidal (SP). In a previous work,[10] the possible topological arrangements of the dinuclear unit have been organized in six different classes: class A corresponds to co-planar bases with a square pyramidal geometry for both

[a] *Materials Chemistry Research Unit, Department of Chemistry and Center of Excellence for Innovation in Chemistry, Faculty of Science, Khon Kaen University, Khon Kaen 40002, Thailand. E-mail: sujittra@kku.ac.th; Fax: +66-43202373; Tel: +66-43202222 ext. 12243*
[b] *Departament de Química Inorgànica & Institut de Química Teòrica i Computacional (IQTCUB), Universitat de Barcelona, C/ Martí i Franquès 1, E-08028 Barcelona, Spain. E-mail: rcosta@ub.edu; Tel: +34-934039130*
[c] *Department of Chemistry, Faculty of Science, Prince of Songkla University, Hat Yai, Songkhla 90112, Thailand*
[d] *Laboratory of Inorganic Chemistry, Department of Chemistry, University of Helsinki, FIN-00014 Helsinki, Finland*
[e] *Departament de Química Física & Institut de Química Teòrica i Computacional (IQTCUB), Universitat de Barcelona, C/ Martí i Franquès 1, E-08028 Barcelona, Spain. E-mail: francesc.illas@ub.edu; Fax: +34-934021231; Tel: +34-934021229*

† Electronic supplementary information (ESI) available. Synthesis conditions, structural and magnetic data for compounds **2–7** are provided. In addition CCDC numbers 907230–907236 contain the supplementary crystallographic data for compounds **1–7**. For ESI and crystallographic data in CIF or other electronic format see DOI: 10.1039/c2cp43839a

Cu(II) environments and the two bridges (aquo or hydroxo) lying in the equatorial positions; class B contains compounds with non-coplanar bases with a square pyramidal geometry for both Cu(II) ions with carboxylato and hydroxo bridges in the equatorial positions; class C includes compounds with non-coplanar bases with a square pyramidal geometry for both Cu(II) ions and two carboxylato bridges lying in the equatorial positions; class D stands for non-coplanar bases with a square pyramidal geometry for both Cu(II) ions, one single-atom or triatomic bridge in an equatorial–equatorial configuration and two carboxylato bridges in an axial–equatorial configuration; class E stands for non-coplanar bases with a trigonal bipyramidal geometry for both Cu(II) ions and one hydroxo bridge in an axial–axial configuration; and, finally, class F refers to non-coplanar bases with square pyramidal and trigonal bipyramidal geometries, two bridges occupying the axial–equatorial positions, with the third one in an equatorial–equatorial configuration. The knowledge of these topologies is useful to unravel the relationships between structural features and the value of the intramolecular magnetic exchange interaction in the triply-bridged dinuclear unit.

In previous studies, the magneto-structural correlations have been investigated for some of these compounds by the simple Extended Hückel (EH) method and a linear correlation has been found for class B compounds allowing a first step towards a proper understanding.[10] However, to obtain more quantitative relationships it is necessary to go beyond the semi-empirical EH method and to make use of more reliable electronic structure methods as demonstrated by recent studies on other triply bridged dinuclear Cu(II) compounds which employed state of art density functional theory (DFT) based methods.[11,12] Six different exchange–correlation functionals have been used in order to fully understand the magneto-structural correlation and also to accurately predict the broad range of magnetic coupling constant (J) values exhibited by class B and class F compounds with ferro- and antiferromagnetic behavior, respectively. The DFT calculations have revealed that, for ferromagnetic class B compounds, the calculated J values almost quantitatively correlate with the sum of Addison's τ parameter[13] of each Cu(II) ion. The calculated and experimental J values of all compounds are in agreement,[12] especially for the long-range separated hybrid LC-ωPBE method.[14] In particular, the DFT calculations properly reproduce the magnitude of the magnetic coupling constants in the whole range of topologies studied. However, the calculated J values of class B compounds exhibit a rather large dependence on the type of hybrid exchange–correlation functional used and may even show noticeable deviations from the experimental values, especially in this type of ferromagnetic compound. Therefore, the precise interpretation of the magnetic interactions in class B compounds with ferromagnetic interactions still requires further attention and either accurate wave function based calculations or a more systematic study aimed precisely to better understand the performance of current DFT approaches in describing this type of system is needed. There is little doubt that wave function based calculations, using for instance the Difference Dedicated Configuration Interaction (DDCI) method, will properly describe these systems as highlighted in the review paper by Moreira and Illas.[15] It is also clear that without a modeling of the external ligands, these calculations are likely to be computationally unfeasible. Therefore, in the present paper we focus on the second possibility and, to this end, we extend the investigation of the magneto-structural correlations and accurate prediction of intramolecular magnetic interactions of this series of compounds by adding seven newly synthesized compounds of class B and analyzing simultaneously the effect of the type of DFT method and of the basis set used to represent the electron density. We will show that the current exchange–correlation functionals, which properly describe magnetostructural correlations involving antiferromagnetic interactions,[15] face difficulties in properly reproducing the J values and trends along the series of ferromagnetic compounds which, therefore, constitute a challenge for state of the art exchange–correlation functionals.

2. Experimental

The new compounds can be generally described as members of the $[Cu_2(L)_2(\mu\text{-}OH)(\mu\text{-}OH_2)(\mu\text{-}O_2CR)]X_2$ series where L = bpy = 2,2′-bipyridine, 4,4′-dmbpy = 4,4′-dimethyl-2,2′-bipyridine and 5,5′-dmbpy = 5,5′-dimethyl-2,2′-bipyridine; R = H for formate, CH_3 for acetate, CH_2CH_3 for propionate and $C(CH_3)_3$ for trimethylacetate and X = $CF_3SO_3^-$ and ClO_4^-. In particular, the following compounds are considered: $[Cu_2(bpy)_2(\mu\text{-}OH)(\mu\text{-}OH_2)(\mu\text{-}O_2CCH_3)](CF_3SO_3)_2$ (**1**), $[Cu_2(4,4'\text{-}dmbpy)_2(\mu\text{-}OH)(\mu\text{-}OH_2)(\mu\text{-}O_2CH)](ClO_4)_2$ (**2**), $[Cu_2(4,4'\text{-}dmbpy)_2(\mu\text{-}OH)(\mu\text{-}OH_2)(\mu\text{-}O_2CCH_3)](ClO_4)_2$ (**3**), $[Cu_2(5,5'\text{-}dmbpy)_2(\mu\text{-}OH)(\mu\text{-}OH_2)(\mu\text{-}O_2CCH_3)](ClO_4)_2$ (**4**), $[Cu_2(5,5'\text{-}dmbpy)_2(\mu\text{-}OH)(\mu\text{-}OH_2)(\mu\text{-}O_2CC(CH_3)_3)](ClO_4)_2$ (**5**), $[Cu_2(5,5'\text{-}dmbpy)_2(\mu\text{-}OH)(\mu\text{-}OH_2)(\mu\text{-}O_2CCH_3)](CF_3SO_3)_2$ (**6**) and $[Cu_2(5,5'\text{-}dmbpy)_2(\mu\text{-}OH)(\mu\text{-}OH_2)(\mu\text{-}O_2CCH_2CH_3)](CF_3SO_3)_2$ (**7**), for which structure can be easily understood by inspection of Scheme 1. The synthesis, crystal structures, magnetic properties and a systematic theoretical study are described in the forthcoming sections.

2.1. Materials and measurements

2,2′-Bipyridyl, 4,4′-dimethyl-2,2′-bipyridine and 5,5′-dimethyl-2,2′-bipyridine were purchased as commercial chemicals from Aldrich. All reagents are commercial grade materials and were used without further purification. Elemental analyses (C, H, N) were performed on a Perkin–Elmer PE 2400 CHNS/O Analyzer.

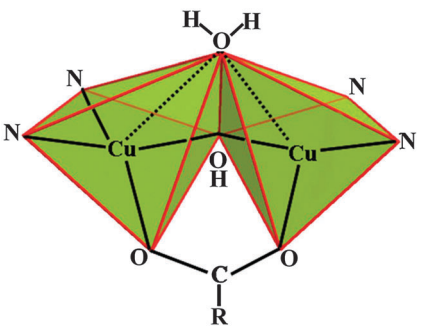

Scheme 1

IR spectra were recorded on Spectrum One FT-IR spectrophotometer as KBr disc in the 4000–450 cm^{-1} spectral range. Solid-state (diffuse reflectance) electronic spectra were measured as polycrystalline samples on a Perkin–Elmer Lambda2S spectrophotometer, over the range 8000–18 000 cm^{-1}.

Magnetic susceptibility measurements for compounds **1–7** were carried out with a Quantum Design SQUID MPMS-XL magnetometer working in the temperature range 2–300 K at magnetic fields of 500 G (2–30 K) and 10 kG (2–300 K). The EPR spectra of microcrystalline samples of **1–7** were recorded at X-band frequency ($\nu \sim 9.4214$ GHz) with a Brucker ES-200 spectrometer in the temperature range 300–4 K.

2.2. Synthesis

Here we describe in some detail the synthesis procedure and experimental conditions for $[Cu_2(bpy)_2(\mu\text{-}OH)(\mu\text{-}OH_2)(\mu\text{-}O_2CCH_3)](CF_3SO_3)_2$ (**1**); the corresponding description for the rest of compounds (**2** to **7**) has similar routes and are described in more detail in the ESI† file.

A warmed methanol solution (10 ml) of bpy (0.156 g, 1.0 mmol) was added to a warmed aqueous solution (20 ml) of $Cu(CF_3SO_3)_2$ (0.361 g, 1.0 mmol). Then, an aqueous solution (5 ml) of NaO_2CCH_3 (0.204 g, 3.0 mmol) was slowly added. The mixture was warmed, with the addition of DMF (2 ml), yielding a clear dark blue solution. Upon slow evaporation at room temperature for 6 days, the product **1** was isolated as violet-blue block-shaped crystals. The crystals were filtered off, washed with the mother liquid and air-dried. Yield: *ca.* 75%. Anal. calc. for $C_{24}H_{22}Cu_2F_6N_4O_{10}S_2$: C, 34.62; H, 2.78; N, 6.73%. Found: C, 34.60; H, 2.80; N, 6.69%.

Caution. Perchlorate salts are potentially dangerous, only small quantities should be prepared.

2.3 Crystallography

X-ray data for single-crystal samples of compounds **1**, **2**, **4**, **6** and **7** were collected at 100 K, whereas those of compound **3** and compound **5** were collected at 150 and 173 K, respectively. Reflection data were collected on a 1K Bruker SMART APEX CCD area-detector diffractometer using rotating mode, graphite-monochromated Mo Kα radiation ($\lambda = 0.71073$ Å) at a detector distance of 4.5 cm and a swing angle of -30°. A hemisphere of the reciprocal space was covered by combination of three sets of exposures; each set had a different ϕ angle (0°, 88°, 180°) and each exposure of 40 s covered 0.3° in ω. Raw data frame integration was performed with the SAINT code,[16] which also applied correction for Lorentz and Polarization effects. An empirical absorption correction by using the SADABS[17] program was applied, which resulted in transmission coefficients ranging from 1.000 to 0.678, 0.746 to 0.603, 1.000 to 0.818, 1.000 to 0.850, 0.891 to 0.665, 0.945 to 0.614 and 0.746 to 0.614 for **1–7**, respectively. The structures were solved by direct methods and refined by a full-matrix least-squares method on $(F_{obs})^2$ using the SHELXTL-PC Version 6.12 software package.[18]

All hydrogen atoms of compound **1–4** were determined at the difference map and refined isotropically by riding with the heavy atoms. For compound **5**, all hydrogen atoms on carbon atoms were fixed except O–H hydrogen atoms whose positions were refined. Also, one hydrogen atom of an aqua bridging molecule could not be located and the position was fixed according to geometry optimization from theoretical calculations. In addition, three methyl groups of trimethylacetate appear to be disordered. All hydrogen atoms on carbon atoms of compound **6** were fixed except O–H hydrogen atoms whose positions were refined. One triflate group was also found to be disordered. For compound **7**, all H atoms were determined at the difference map and refined isotropically and bonded to the heavy atoms except hydrogen atoms on C(6) and C(8) which were fixed.

The crystal and refinement details for compounds **1–7** are listed in Table S1 (ESI†). Selected bond lengths and angles are given in Tables S2–S8 (ESI†).

3. Computational details

A series of DFT calculations with state of the art exchange–correlation functionals has been carried out considering the isolated dinuclear Cu(II) cationic complexes *in vacuo*. The electron density was described either explicitly considering all electrons or using small core (LANL2) effective core potential (ECP) for the Cu atoms which allows one to take scalar relativistic effects into account. For the all electron calculations we used a rather large standard basis set of Gaussian Type Orbitals (GTO) which is the same as in previous works[11,12] and is defined as follows: 6-3111+G extended with an *f*-function (exponent(*f*) = 0.528) for Cu and 6-31G(d) for the remaining atoms. For the calculations where the Cu innermost 10 electrons are described through a relativistic ECP, two different bases have been used which are either the standard LANL2DZ or the more extended standard LANL2TZ.[19] The rest of atoms are described at the all electrons level with the 6-31G(d) basis set. We will refer to the three sets of calculations as AE, ECP-DZ and ECP-TZ, respectively.

The DFT calculations have been carried out using a variety of exchange–correlation functionals including hybrid schemes such as the well-known B3LYP and BHHLYP,[20,21] the M06 and M06-2X meta-GGA functionals developed by Zhao and Truhlar[22–24] and the short- (HSE)[25] and long-range (LC-ωPBE) functionals[14] proposed by Scuseria and collaborators. In all cases the calculations were carried out within the unrestricted (spin-polarized) formalism. Clearly, in this type of formalism, the spin symmetry is not guaranteed.[26–28] Nevertheless, in the unrestricted Kohn–Sham formalism one can approximate the triplet (T) state using a single Slater determinant with two unpaired electrons (*i.e.*, $S_z = 1$). However, to estimate the energy of the open shell singlet state it is possible to make use of the broken-symmetry (BS) approach imposing $S_z = 0$. In this way, the singlet–triplet gap energy has been obtained on the basis of the expectation value of the Heisenberg Hamiltonian as in eqn (1)

$$\hat{H} = -J\hat{\mathbf{S}}_1\cdot\hat{\mathbf{S}}_2 \quad (1)$$

that using the appropriate mapping[15] leads to the approximate relation:

$$J = 2[E(\mathrm{BS}) - E(\mathrm{T})] \quad (2)$$

where E(BS) is the energy of the broken-symmetry state and E(T) is the energy of the spin unrestricted approximation to the triplet state.[29] Here, it is important to stress that eqn (2) takes into account the so-called spin projection to approximately recover the spin symmetry lost in the BS approach and which is inherent to the use of a single Kohn–Sham determinant.[30–32] Here one must advert that alternative methods for calculating J couplings without the use of spin symmetry[33] lead to results that are not always accurate[34] when high quality range separated functionals like those employed in this paper are used. Nevertheless, one must admit that magnetostructural correlations involving mainly antiferromagnetic compounds do not suffer from this limitation. It has also been recently shown that, for a given functional, results obtained using the mapping procedure in eqn (2) are in agreement with those obtained using the spin flip Time Dependent DFT approach which properly accounts for spin symmetry in this type of system.[35]

All calculations were carried out using the Gaussian09 suite of programs.[36]

4. Results and discussions

4.1 Description of the crystal structures

The crystal structures of compounds **1–7** consist of a hetero triply-bridged dinuclear Cu(II) cationic unit and two counter-anions ($CF_3SO_3^-$ for compounds **1**, **6** and **7**; ClO_4^- for compounds **2–5**). For each of the cationic units, two [Cu(L)] groups are linked together by three different bridging ligands: aquo, hydroxo and carboxylato. The environment of each Cu(II) center corresponds to a distorted square pyramidal geometry of the CuN_2O_2O' chromophore, with τ values of 0.10 and 0.38 for the two Cu(II) centers. Let us recall that the Addison parameter is defined as $\tau = (\alpha - \beta)/60$, where α and β are the largest coordination angles. Hence, one has $\tau = 0$ for square pyramidal (SP) and $\tau = 1$ for trigonal bipyramidal (TBP) geometry.[13] The coordination environment around each Cu(II) ion contains two N atoms of the chelate ligand (Cu–N 1.978(1)–2.012(6) Å), an oxygen atom of the carboxylato bridging ligand (Cu–O 1.941(1)–1.983(1) Å) and an oxygen atom of the hydroxo ligand (Cu–O 1.908(1)–1.938(5) Å) to form the square bases. The apical site of each Cu(II) atom is occupied by an oxygen atom of an aquo ligand at distances in range of 2.310(4)–2.442(1) Å. The *syn,syn*-coordinated carboxylato ligand bridges two equatorial planes of each Cu(II) chromophore, giving the Cu···Cu distances in the range of 2.979(1)–3.077(1) Å. The CuN_2O_2O' chromophores are non-planar with dihedral angles (γ in Table 1) between the CuN_2 and CuO_2 planes in the range of 10.10(2)–28.62(1)°. The dihedral angles between the equatorial planes (ϕ in Table 1) are in the range of 112.07(1)–122.08(1)°. The bridging angles of Cu–OH–Cu are in the range of 100.80(7)–107.26(5)°. According to these structural features, compounds **1–7** are classified as class B (Scheme 1).

The lattices of all compounds are stabilized by intermolecular π–π interactions between aromatic pyridine rings on chelate ligands of adjacent dinuclear cations and hydrogen bonding between the aquo and hydroxo bridges and triflate or perchlorate anions. The molecular structure of compound **1** is shown in Fig. 1 whereas the rest of structures are shown in Fig. S1–S6 (ESI†). For comparison purposes, the structural data of compounds **1–7** and of some other relevant hetero triply-bridged dinuclear Cu(II) compounds previously studied[10,12] are summarized in Table 1.

4.2 Spectral characterizations

The infrared spectra display a broad band at 3510 cm^{-1} for **1**, 3519 cm^{-1} for **2**, 3524 cm^{-1} for **3**, 3434 cm^{-1} for **4**, 3401 cm^{-1} for **5**, 3475 cm^{-1} for **6** and 3479 cm^{-1} for **7**, which can be assigned to the bridging OH vibration of the hydroxo ligands and/or lattice water. The spectra also exhibit the intense bands at 1557 and 1445 cm^{-1} for **1**, 1577 and 1413 cm^{-1} for **2**, 1554 and 1443 cm^{-1} for **3**, 1557 and 1479 cm^{-1} for **4**, 1540 and 1480 cm^{-1} for **5**, 1564 and 1481 cm^{-1} for **6** and 1556 and 1479 cm^{-1} for **7**, corresponding to the $\nu_{as}(COO^-)$ and $\nu_s(COO^-)$ vibrations of carboxylato bridging ligands namely acetato for **1**, **3**, **4** and **6**, formato for **2**, trimethylacetato for **5** and propionato for **7**, respectively. The spectra of compounds **1**, **6** and **7** show the broad and intense bands of the stretching of $CF_3SO_3^-$ at 1277 ν_{as}(S–O), 1153 ν_{as}(C–F), and 1029 ν_s(S–O) cm^{-1} for **2**; 1279 ν_{as}(S–O), 1161 ν_{as}(C–F) and 1031 ν_s(S–O) cm^{-1} for **6** and 1281 ν_{as}(S–O), 1158 ν_{as}(C–F) and 1031 ν_s(S–O) cm^{-1} for **7**. The IR spectra of compounds **2–5** present the broad and intense bands of the stretching for the ionic ClO_4^- anion (1103 cm^{-1} for **2**, 1106 cm^{-1} for **3**, 1111 cm^{-1} for **4** and 1120 cm^{-1} for **5**).

The diffuse reflectance spectra of compounds **1–7** display a broad band (16 530 cm^{-1} for **1**, 16 030 cm^{-1} for **2**, 16 340 cm^{-1} for **3**, 16 590 cm^{-1} for **4**, 16 490 cm^{-1} for **5**, 16 240 cm^{-1} for **6** and 16 320 cm^{-1} for **7**) and a lower energy shoulder (13 880 cm^{-1} for **1**, 13 060 cm^{-1} for **2**, 13 620 cm^{-1} for **3**, 13 960 cm^{-1} for **4**, 13 600 cm^{-1} for **5**, 13 540 cm^{-1} for **6** and 13 940 cm^{-1} for **7**). These features are typical and can be assigned to the d_{xy}, d_{yz}, $d_{xz} \rightarrow d_{x^2-y^2}$ and $d_{z^2} \rightarrow d_{x^2-y^2}$ transitions for the square pyramidal geometry of the class B triply-bridged dinuclear Cu(II) compounds. Notice that according to strict symmetry considerations for the distorted square pyramidal geometry of compounds **1–7**, the d_{xy}, d_{yz}, d_{xz} orbitals are not triply degenerated which is the origin of the broad band mentioned above.

4.3 Electron paramagnetic resonance spectra and magnetic properties

The Electron Paramagnetic Resonance Spectra (EPR) of compounds **1–7** (X-band, $\nu \sim 9.4214$ GHz) have been recorded at different temperatures between 4 and 300 K for polycrystalline solid samples. The general shape of the spectra is similar for all compounds; we show the EPR spectra of compound **4** in Fig. 2 as a representative example. A summary of data obtained from EPR measurements is reported in Table 2.

As expected for ferromagnetic systems,[37] the principal transition band near $g \sim 2.1$ (corresponding to $\Delta m_s = 1$) shows some asymmetry but maintains the center of the band as T goes from 300 to 4 K. No significant fine structure is observed. A broad band near $g_{1/2} \sim 4.4$ is also observed and assigned to the half field transition (corresponding to $\Delta m_s = 2$). Both bands slightly increase their intensity as temperature increases

Table 1 Structural and magnetic data for Class B triply-bridged dinuclear copper(II) compounds[c]

Compound[a]	Geom [b]	τ	ϕ	γ	Cu···Cu	Cu–X Axial	Cu–X Equatorial	Cu–OH–Cu	J_{exp}	Ref.[a]
$[Cu_2(dpyam)_2(\mu\text{-}OH)(\mu\text{-}OH_2)(\mu\text{-}O_2CCH_3)](S_2O_8)$ (I)	SP, SP	0.43	164.4	40.4	3.124	2.414	1.911–2.023	109.6	n.d.	10
$[Cu_2(bpy)_2(\mu\text{-}OH)(\mu\text{-}OH_2)(\mu\text{-}O_2CCH_3)](NO_3)_2$ (II)	SP, SP	0.21, 0.19	120.5	14.5, 11.6	3.049	2.347, 2.460	1.938–2.017	104.0	n.d.	10
$[Cu_2(phen)_2(\mu\text{-}OH)(\mu\text{-}OH_2)(\mu\text{-}O_2CCH_3)](BF_4)_2\cdot(H_2O)_{0.5}$ (III)	SP, SP	0.21, 0.16	114.6	17.0, 8.6	3.002	2.374, 2.390	1.925–2.008	102.1	120.8	10
$[Cu_2(bpy)_2(\mu\text{-}OH)(\mu\text{-}OH_2)(\mu\text{-}O_2CCH_3)](ClO_4)_2$ (IV)	SP, SP	0.14, 0.25	118.1	—	3.035	2.379, 2.405	2.006–2.010	103.8	19.3	10
$[Cu_2(phen)_2(\mu\text{-}OH)(\mu\text{-}OH_2)(\mu\text{-}O_2CCH_3)](ClO_4)_2$ (V)	SP, SP	0.02, 0.14	113.8	16.4, 8.2	2.989	2.360, 2.375	1.933–2.020	101.3	120.0	10
$[Cu_2(bpy)_2(\mu\text{-}OH)(\mu\text{-}OH_2)(\mu\text{-}O_2CCH_2CH_3)](ClO_4)_2$ (VI)	SP, SP	0.20, 0.16	120.1	15.0, 10.9	3.037	2.382, 2.415	1.920–2.005	104.5	148.9	10
$[Cu_2(bpy)_2(\mu\text{-}OH)(\mu\text{-}O_2CCH_3)(\mu\text{-}Cl)]Cl\cdot(H_2O)_{0.5}$ (VII)	SP, SP	0.41, 0.28	123.0	27.4, 18.9	3.040	2.632, 2.657	1.936–2.029	103.3	145.3	10
$[Cu_2(phen)_2(\mu\text{-}OH)(\mu\text{-}OH_2)(\mu\text{-}O_2CCH_2CH_3)](NO_3)_2$ (VIII)	SP, SP	0.19, 0.21	122.3	14.6, 12.2	3.026	2.344, 2.368	1.925–2.029	103.6	98.4	12
$[Cu_2(phen)_2(\mu\text{-}OH)(\mu\text{-}OH_2)(\mu\text{-}O_2CC(CH_3)_3)](ClO_4)_2(CH_3CH_2OH)$ (IX)	SP, SP	0.10, 0.22 0.08, 0.26	117.7, 120.4	9.9, 16.2 8.8, 21.2	3.010 3.034	2.419, 2.379 2.425, 2.369	1.911–2.015 1.893–2.012	103.8, 105.3	151.2	12
$[Cu_2(bpy)_2(\mu\text{-}OH)(\mu\text{-}O_2CCH_2CH_3)(\mu\text{-}O_2SOCF_3)](CF_3SO_3)(DMF)_{0.5}$ (X)	SP, SP	0.14, 0.15	154.8	11.2, 11.8	3.341	2.351, 2.354	1.906–2.019	122.3	104.5	12
$[Cu_2(bpy)_2(\mu\text{-}OH)(\mu\text{-}OH_2)(\mu\text{-}O_2CCH_3)](CF_3SO_3)_2$ (**1**)	SP, SP	0.24, 0.25	118.95	15.67, 18.73	3.024	2.394, 2.323	1.921–2.009	103.39	102.1	pw
$[Cu_2(4,4'\text{-}dmbpy)_2(\mu\text{-}OH)(\mu\text{-}OH_2)(\mu\text{-}OCH)](ClO_4)_2$ (**2**)	SP, SP	0.10, 0.38	122.08	10.10, 28.62	3.077	2.324, 2.409	1.908–1.999	107.26	72.6	pw
$[Cu_2(4,4'\text{-}dmbpy)_2(\mu\text{-}OH)(\mu\text{-}OH_2)(\mu\text{-}OCCH_3)](ClO_4)_2$ (**3**)	SP, SP	0.11, 0.30	120.19	11.37, 25.20	3.055	2.323, 2.442	1.918–1.999	105.55	90.2	pw
$[Cu_2(5,5'\text{-}dmbpy)_2(\mu\text{-}OH)(\mu\text{-}OH_2)(\mu\text{-}OCCH_3)](ClO_4)_2$ (**4**)	SP, SP	0.21, 0.22	112.07	14.81, 15.64	2.984	2.329, 2.346	1.929–2.003	101.07	104.3	pw
$[Cu_2(5,5'\text{-}dmbpy)_2(\mu\text{-}OH)(\mu\text{-}OH_2)(\mu\text{-}OCC(CH_3)_3)](ClO_4)_2$ (**5**)	SP, SP	0.17, 0.19	114.56	11.49, 13.99	3.008	2.320, 2.333	1.921–2.012	102.40	98.7	pw
$[Cu_2(5,5'\text{-}dmbpy)_2(\mu\text{-}OH)(\mu\text{-}OH_2)(\mu\text{-}OCCH_3)](CF_3SO_3)_2$ (**6**)	SP, SP	0.34, 0.31	118.72	22.29, 20.60	3.007	2.310, 2.323	1.923–2.003	102.57	92.1	pw
$[Cu_2(5,5'\text{-}dmbpy)_2(\mu\text{-}OH)(\mu\text{-}OH_2)(\mu\text{-}OCCH_2CH_3)](CF_3SO_3)_2$ (**7**)	SP, SP	0.23, 0.27	112.25	15.61, 18.04	2.979	2.321, 2.339	1.931–1.996	100.80	103.1	pw

[a] Abbreviations: bpy = 2,2′-bipyridine, 4,4′-dmbpy = 4,4′-dimethyl-2,2′-bipyridine, 5,5′-dmbpy = 5,5′-dimethyl-2,2′-bipyridine, n.d. = not determined, pw = present work. [b] SP = distorted square pyramid. [c] Geom stands for the coordination of Cu(1) and Cu(2), τ is the Addison structural parameter for Cu(II) center, ϕ is the angle between basal planes and γ is the tetrahedral twist angle, both in degrees. Cu···Cu and Cu–X distances are in Å and Cu–OH–Cu angles in degrees. J_{exp} is the experimentally derived magnetic coupling constant in cm^{-1}.

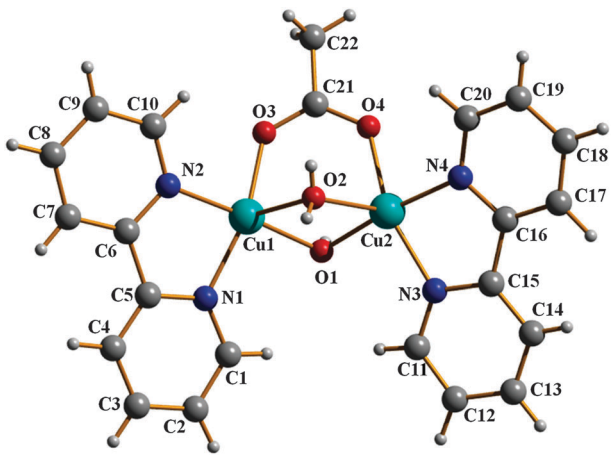

Fig. 1 Molecular structure and atomic numbering scheme for compound **1**. Triflate counteranions are omitted for clarity.

and the $\Delta m_s = 2$ half field transition band shows important intensity with respect to the $\Delta m_s = 1$ transition. This observation confirms the ferromagnetic character of these compounds.

Molar magnetic susceptibility (χ_M) measurements were carried out using microcrystalline samples of compounds **1–7** and diamagnetic corrections were calculated from the Pascal tables. The as measured $\chi_M T$ *vs.* T plots for all compounds are quite similar and display clear ferromagnetic behavior as shown in Fig. 3. At room temperature, the $\chi_M T$ values are in the 0.965–1.007 $cm^3\ Kmol^{-1}$ range, close to the value expected for two uncoupled Cu(II) ions. To account for the magnetic behavior of the dinuclear Cu(II) complexes and to evaluate the corresponding coupling constant J, defined as the singlet–triplet splitting, we fitted the raw experimental susceptibility data using the Bleaney–Bowers equation[38] with an additional temperature independent paramagnetism term, usually denoted as $N\alpha$. In addition, we corrected the Bleaney–Bowers expression with a mean-field Weiss θ parameter to account for the small antiferromagnetic intermolecular interactions detected in the low temperature region for these ferromagnetic dinuclear complexes:

$$\chi_M(T-\theta) = \frac{N\beta^2 g^2}{k_B}\frac{2e^{J/k_BT}}{1+3e^{J/k_BT}} + N\alpha T \qquad (3)$$

Best-fit parameters were obtained by minimization of the error function $R = \Sigma\{[(\chi_M T)_{calc} - (\chi_M T)_{exp}]^2/(\chi_M T)_{exp}^2\}$, and results

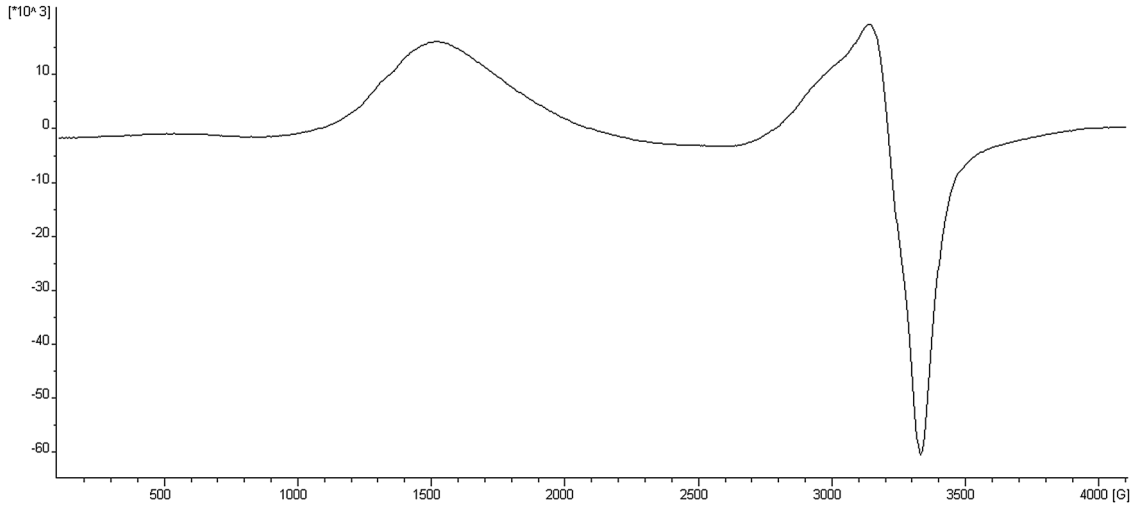

Fig. 2 EPR spectrum of compound **4** at 4 K.

Table 2 Experimental normal and half-field (at 4 K) EPR signals and best-fit susceptibility data to eqn (3) (g_{iso}, J_{exp} and θ) for compounds **1–7**. Additional details corresponding to the fitting are reported in Table S9, ESI

Compound	g	$g_{1/2}$	g_{iso}	J_{exp} (cm^{-1})	θ(K)	$N\alpha(\times10^{-6})$	R ($\times10^{-4}$)
1	2.082	4.498	2.194	102	−0.39	30	2.4
2	2.095	4.350	2.163	73	−0.73	90	3.6
3	2.066	4.438	2.177	90	−0.58	60	3.3
4	2.092	4.429	2.167	104	−0.33	110	1.4
5	2.097	4.427	2.178	99	−0.31	50	2.1
6	2.074	4.426	2.196	92	−0.55	60	3.1
7	2.063	4.376	2.162	103	−0.38	40	2.3

are also shown in Table 2. In the view of the intrinsic low accuracy involving the fitting of ferromagnetically coupled Cu(II)–Cu(II) systems with rather large molecular weights one should avoid overparametrization. Therefore, the fitting was here consistently carried out for all compounds using the minimum possible number of parameters. Note that for these ferromagnetic compounds, $\chi_M T$ ranges from 0.9 to 1.2. Because of this small $\chi_M T$ range, small instrumental inaccuracies appear magnified and evidences as small discontinuities near 50K—attributable to the technical use of two different temperature probes for the high and low T ranges—although one must note that the J values are extracted from the high temperature part of the $\chi_M T$ *versus* T curve. The need for a small number of parameters in describing the $\chi_M T$ *versus* T curve of these ferromagnetic compounds also leads to a more difficult fitting to the magnetic model which affects especially the low T part of the $\chi_M T$ *versus* T curve. The g_{iso} values obtained from the fitting are consistent with those corresponding to Cu(II) systems and to the g values measured at 4 K which essentially correspond to the triplet state (Table 2). Here, we will mention the selected magnetic plot of compound **4** (Fig. 3) and the results of the remaining compounds are summarized in ESI† (Fig. S7–S12). The $\chi_M T$ *vs.* T plot of compound **4** shows a room temperature $\chi_M T$ product value of 1.01 cm^3 $Kmol^{-1}$, slightly higher than that expected for two uncoupled Cu(II) ions. Lowering the temperature

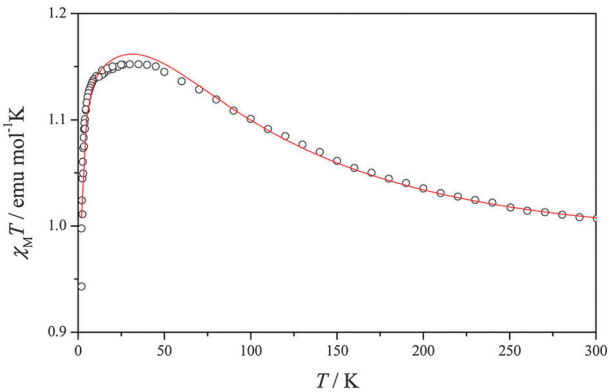

Fig. 3 Plot of magnetic susceptibility-temperature product ($\chi_M T$) *versus* temperature (T) for compound **4**.

causes the $\chi_M T$ product to continuously increase until reaching a plateau value of 1.15 cm^3 $Kmol^{-1}$ at 50 K. Upon further cooling, $\chi_M T$ shows an abrupt descent for all compounds, which clearly suggests that this quantity tends to zero when temperature tends to 0 K. This behavior can be explained by the existence of ferromagnetically coupled Cu(II) pairs responsible for the high temperature regime, where the low-lying triplet state was increasingly populated in detriment of the singlet state. Below liquid nitrogen temperature, small antiferromagnetic intermolecular interactions manifest and tend to couple the triplet states in such a way that the $S = 1$ spin moments of the different molecules cancel out each other and, as a result, a zero global magnetization is approached near the liquid helium temperature.

4.4 Magneto-structural correlations

Here we analyze the common magnetostructural correlations involving the experimental value of the magnetic coupling constant (J_{exp}) and the key feature of the molecular structure.[4,5] Fig. 4 plots J_{exp} *versus* the distance between the two Cu centers and Fig. 5 plots J_{exp} *versus* the angle formed by the Cu–OH–Cu structural moiety where the OH corresponds to a monoatomic

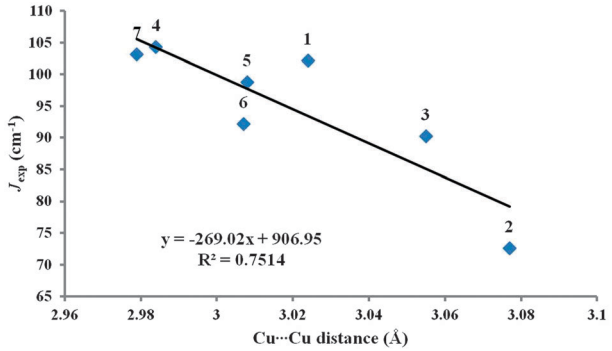

Fig. 4 Plot of the experimental J (cm^{-1}) *vs.* Cu···Cu (Å) of compounds **1–7**.

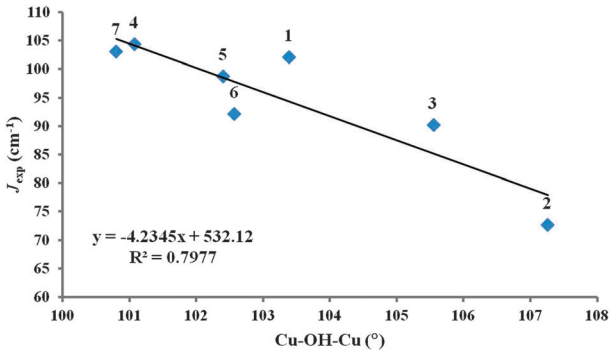

Fig. 5 Plot of the experimental J (cm^{-1}) *vs.* Cu–OH–Cu (deg.) of compounds **1–7**.

bridge that links two Cu centers at an equatorial position. Both plots exhibit a clear trend which is slightly more quantitative in the second case. These plots are important since they reveal a clear trend along the series indicating that the magnitude of the ferromagnetic coupling increases with decreasing Cu···Cu distance, as expected from simple arguments, and also increases with decreasing Cu–OH–Cu bond angle which can also be explained in terms of qualitative rules. Hence, these empirical correlations provide a very useful testing ground for theoretical methods.

In previous work it has been suggested that the aggregate Addison τ parameter also provides useful information about the relationship between structure and magnetic coupling. In fact, the Addison parameter allows one to properly define compounds **1–7** as belonging to class B. However, it does not provide a suitable magnetostructural correlation, which is at variance of previous work.[11] This is likely to be due to the fact that values of the magnetic coupling constant studied exhibited a broader range but also to their ferromagnetic character. This will be confirmed by the DFT calculations described in the next subsection.

4.5 Density functional theory based calculations

The calculated and experimental values of the magnetic coupling constants are summarized in Table 3 where the aggregate Addison τ parameter is also shown for comparison. All methods, including UHF which neglects electron correlation except for the part included by spin polarization, consistently predict these compounds to be ferromagnetic, in agreement with experiment and all methods regularly predict that all compounds have a similar value of the magnetic coupling constant, again in agreement with experiment. However, the fine details are more subtle, difficult to describe and do not always go in the expected direction. The calculated values of the magnetic coupling constant strongly depend on the type of exchange–correlation functional and, more precisely, on the amount of Fock exchange included in the exchange potential. This is not surprising and has been reported for quite a large number of systems although most of them exhibiting strong antiferromagnetic character.[15,30] The novelty here is that none of the studied methods is able to describe **2** as the compound with smallest J and **4** as the one with the largest. One can suggest that the experimental measurements and fitting procedures for these two compounds are intrinsically not enough and accurate, although the magnetostructural correlations in Fig. 4 and 5 will not support such a claim. Even accepting that these two compounds represent exceptions and excluding them from the statistical analysis, one will face the same problem since none of the methods will now predict that **3** is the compound with the smallest J and **7** the one with the largest.

In order to define in a more precise way the failure of all theoretical methods it is convenient to make some considerations. Let us start with the UHF results; here the calculated values for a given compound arising from the AE and ECP calculations are almost the same and even the effect of the basis set is almost negligible since going from the LANL2DZ to the LANL2TZ changes the calculated values by less than 2 cm^{-1}. This is consistent with the fact that UHF neglects correlation and that the main effect of increasing the basis set would be precisely in the description of the correlation effects. This is obvious in the case in which electron correlation is accounted for in a configuration interaction type wave function. In fact, DFT calculations with these two basis sets exhibit significant differences and, in the case of the LANL2DZ, deviates too much from the AE values. This is clearly an artifact of the limited basis set and will no longer be commented here. Let us now discuss the results obtained with the popular B3LYP functional which contains a 20% of Fock exchange and which is known to overestimate the magnetic coupling constant of antiferromagnetic Cu(II) dinuclear compounds by a factor of $\sim$2, provided the proper mapping (*cf.* eqn (2)) is used.[15,30] Results in Table 3 indicate that B3LYP calculated J values obtained at the AE level with the small core ECP and a triple-ζ valence basis set for the Cu atoms—hereafter referred to as ECP—are almost the same differing by at most 4 cm^{-1} or 2%. However, the calculated values are significantly larger than the experimental values although, at variance of antiferromagnetic dinuclear Cu(II) compounds the deviation factor varies from 2.2 to 1.5. Interestingly, the M06 predicted values are much larger and, surprisingly, AE and ECP predicted values differ by a larger amount of $\sim$60 cm^{-1}. There is no clear explanation for these trends since M06 and B3LYP contain a similar amount of Fock exchange (27% and 20%, respectively) and one could perhaps conclude that these differences are a result of the parametrization of the M06 functional.

Table 3 Calculated values of the coupling constant J (in cm^{-1}) for compounds **1–7**, using hybrid and screened functionals compared to experimental magnetic values. AE and ECP stand for calculations with all electrons and effective core potentials respectively. For the ECP only results with the more extended TZ basis are shown

		J_{calc}														
		UHF		M06-2X		BHHLYP		LC-ωPBE		HSE		B3LYP		M06		
[a]	τ_{agg}	AE	ECP	AE	ECP	AE	ECP	AE	ECP	AE	ECP	AE	ECP	AE	ECP	J_{exp}
1	0.49	37.1	38.1	67.1	95.8	83.5	85.6	135.3	143.1	147.7	155.5	169.5	170.5	238.9	301.9	102
2	0.48	37.6	39.4	66.5	96.7	82.1	85.3	133.1	143.0	146.0	155.7	165.8	168.6	231.0	299.1	73
3	0.41	38.3	39.4	67.9	96.9	84.1	86.3	134.2	141.8	148.1	155.7	170.0	170.7	240.3	304.0	90
4	0.43	36.0	37.2	65.8	94.5	81.9	84.6	132.3	141.4	145.2	154.4	167.0	169.7	236.8	300.5	104
5	0.36	34.8	35.5	64.8	93.5	80.0	81.9	133.0	141.9	145.9	155.0	168.7	171.2	240.3	308.7	99
6	0.65	37.1	38.5	68.0	100.0	84.0	87.2	138.3	148.8	150.7	161.5	173.4	177.0	249.0	326.1	92
7	0.50	36.3	38.0	66.1	96.7	82.4	86.2	133.2	143.7	146.0	157.1	168.0	172.5	237.6	305.7	103

This hypothesis seems to be confirmed by analysis of the results obtained by the BHHLYP and M06-2X functionals, containing 50% and 54% Fock exchange respectively. The BHHLYP calculated magnetic coupling constant values at the AE and ECP levels, as in the case of B3LYP, almost coincide with differences of at most $\sim$2 cm^{-1}. In addition, these calculated values are those closest to the experimental ones which, again, is at variance of existing experience with the family of antiferromagnetic dinuclear Cu(II) complexes. Interestingly, the values predicted by the M06-2X functional are almost in the experimental range but only when considering the results from ECP calculations which, as in the case of the M06 discussed above, deviate from the AE by $\sim$30–40 cm^{-1}. The difference between AE and ECP calculated values in the M06 and M06-2X functionals remains difficult to understand. Finally, we discuss the HSE and LC-ωPBE short- and long-range separated functionals which, for the dinuclear Cu(II) complexes database investigated up to now, provide the most accurate results in terms of agreement with experiment.[31,32] Results in Table 3 show that also here results obtained at the AE and ECP levels deviate although by $\sim$10–15 cm^{-1}, this is no doubt less than in the case of the M06 and M06-2X but still noticeable. Here, one will be tempted to attribute this difference to the range separation parameter which, as shown by Phillips and Peralta,[32] has a significant influence on the calculated results. In the best scenario, the range separated functionals deviate from experiment by 30%.

The fact that exchange–correlation functionals that provide an almost quantitative description of antiferromagnetic compounds fail to describe the differences exhibited along a series of ferromagnetic dinuclear Cu(II) complexes is likely to be due to the different types of electronic correlation effects governing the magnetic coupling. In the case of antiferromagnetic compounds, the largest contributions correspond to metal to metal and metal to ligand excitations. The first ones correspond to the well-known superexchange mechanism[39,40] which appear already at the CASSCF level and are essentially the result of non-dynamical correlation. The second ones involve double excitations from the reference CASSCF wave function to the virtual orbitals[41,42] and are described reasonably well by second order perturbation theory based methods,[43] although one must also be aware of possible artifacts due to the slow convergence of the perturbation series.[44] In the case of ferromagnetic compounds, the main contribution comes from direct exchange[41,42] and it is necessary to go well beyond double excitation from the reference space to improve the description. It is likely that this is the origin of the difficulties of the present exchange–correlation functionals in describing ferromagnetic interactions.

5. Conclusions

A new series of seven dinuclear Cu(II) compounds with a common triple bridge consisting of hydroxo, aquo and carboxylato ligands has been synthesized, the crystal structures were solved and the magnetic properties studied by EPR and magnetic susceptibility measurements as a function of temperature. The seven compounds thus obtained exhibit ferromagnetic coupling which is a consequence of the topology introduced by the type of bridging ligands as previously shown.[10–12] Nevertheless, the magnetic coupling constant J between the Cu centers spans a rather broad range from 73 to 104 cm^{-1} which is clearly governed by the different external ligands. These affect the Cu$\cdots$Cu distance and the Cu–OH–Cu bonding angle which indeed appear to be reasonable structural parameters defining magnetostructural correlations. Nevertheless, these trends are far from being quantitative.

The magnetic coupling in these triple bridged dinuclear compounds has been examined by a series of density functional methods going from simple hybrids such as B3LYP and BHHLYP to the M06 and M06-2X meta-hybrid and including also the HSE and LC-ωPBE range separated functionals. Interestingly, all these methods consistently predict the compounds to be ferromagnetic but all fail to reproduce the variation from compound to compound. In fact, for a given functional, the calculated J values along the series are almost constant and, in some cases very far away from experiment. The best results are provided by the BHHLYP functional where results obtained at the AE and ECP levels are also close to each other. The M06-2X functional, which contains a similar amount of Fock exchange, also predicts values in the experimental range although here the AE and ECP calculated values differ by a noticeable amount. The popular B3LYP functional largely overestimates J and this is also the behavior of M06 which contains a similar amount of Fock exchange. In addition, M06 calculated values depend on whether the Cu core electrons are treated with AE or with a

small core ECP. This is similar to the behavior described above for the M06-2X and the origin remains unclear. Finally, the HSE and LC-ωPBE range separated functionals which have found to perform the best in previous work dealing with a family of compounds spanning a broad range of values, from moderately ferromagnetic to strong antiferromagnetic, fail to reproduce the order of magnitude of J for the present new compounds. Furthermore, AE and ECP values obtained with the range separated functionals differ, which may be due to the inadequacy of the standard parameter governing range separation.

Therefore, the most important conclusion of the present work is that while the different exchange–correlation functionals explored in this work to investigate the magnetic coupling constant of the new ferromagnetic Cu(II) dinuclear compounds properly predict the qualitative nature of the experimental coupling, none of them is able to reproduce the trend in ferromagnetism along the series, and only BHHLYP predicts values in the experimental range. It is likely that the origin of the difficulties of the present exchange–correlation functionals in describing ferromagnetic interactions is due to the fact that a proper description in terms of wave function based methods requires including higher order terms in the perturbation treatment or, equivalently, to go beyond double excitations out of the CASSCF reference wave function defined by the magnetic orbitals only.[45] Clearly, the current density functional needs to be further improved to be able to properly describe ferromagnetism. The present series of compounds provides an excellent playground to test new and improved functionals.

Acknowledgements

Financial support has been provided by the Spanish MICINN (grant FIS2008-02238), Generalitat de Catalunya (grants 2009SGR1041 and XRQTC), The Thailand Research Fund, The Royal Golden Jubilee PhD Program (Grant No. PHD/0234/2550), the Higher Education Research Promotion and National Research University Project of Thailand, Office of the Higher Education Commission, through the Advanced Functional Materials Cluster of Khon Kaen University and the Center of Excellence for Innovation in Chemistry (PERCH-CIC), Office of the Higher Education Commission, Ministry of Education. Part of the computational time has been provided by the Centre de Supercomputació de Catalunya (CESCA) which is also gratefully acknowledged. F.I. acknowledges additional support through the ICREA Academia award for excellence in research.

References

1 J. R. Friedman, M. P. Sarachik, J. Tejada and R. Ziolo, *Phys. Rev. Lett.*, 1996, **76**, 3830.
2 G. L. J. A. Rikken and E. Raupach, *Nature*, 2000, **405**, 932.
3 S. Tanase and J. Reedijk, *Coord. Chem. Rev.*, 2006, **250**, 2501.
4 O. Kahn, *Molecular Magnetism*, VCH Publishers, New York, 1993.
5 O. Kahn, *Adv. Inorg. Chem.*, 1996, **43**, 179.
6 G. Christou, S. P. Perlepes, E. Libby, K. Folting, J. C. Huffman, R. J. Webb and D. N. Hendrickson, *Inorg. Chem.*, 1990, **29**, 3657.
7 S. Youngme, C. Chailuecha, G. A. van Albada, C. Pakawatchai, N. Chaichit and J. Reedijk, *Inorg. Chim. Acta*, 2004, **357**, 2532.
8 S. Youngme, C. Chailuecha, G. A. van Albada, C. Pakawatchai, N. Chaichit and J. Reedijk, *Inorg. Chim. Acta*, 2005, **358**, 1068.
9 C. Chailuecha, S. Youngme, C. Pakawatchai, N. Chaichit, G. A. van Albada and J. Reedijk, *Inorg. Chim. Acta*, 2006, **359**, 4168.
10 S. Youngme, J. Phatchimkun, N. Wannarit, N. Chaichit, S. Meejoo, G. A. van Albada and J. Reedijk, *Polyhedron*, 2008, **27**, 304.
11 R. Costa, I. de P. R. Moreira, S. Youngme, K. Siriwong, N. Wannarit and F. Illas, *Inorg. Chem.*, 2010, **49**, 285.
12 N. Wannarit, K. Siriwong, N. Chaichit, S. Youngme, R. Costa, I. de P. R. Moreira and F. Illas, *Inorg. Chem.*, 2011, **50**, 10648.
13 A. W. Addison, T. N. Rao, J. Reedijk, J. van Rijn and G. C. Verschoor, *J. Chem. Soc., Dalton Trans.*, 1984, 1349.
14 O. A. Vydrov and G. E. Scuseria, *J. Chem. Phys.*, 2006, **125**, 234109.
15 I. de P. R. Moreira and F. Illas, *Phys. Chem. Chem. Phys.*, 2006, **8**, 1645 and references therein.
16 Siemens SAINT, *Version 4 Software Reference Manual*, Siemens Analytical X-ray Systems, Inc., Madison, WI, USA, 1996.
17 G. M. Sheldrick, *SADABS: Program for Empirical Absorption correction of Area Detector Data*, University of Göttingen, Göttingen, Germany, 1996.
18 Bruker, *XSHELL, Version 6.12 Reference Manual*, Bruker AXS, Inc., Madison, WI, USA, 1999.
19 Basis set parameters have been extracted from the Basis Set Exchange web page at https://bse.pnl.gov/bse/portal.
20 A. D. Becke, *J. Chem. Phys.*, 1993, **98**, 5648.
21 P. J. Stephens, F. J. Devlin, C. F. Chabalowski and M. J. Frisch, *J. Phys. Chem.*, 1994, **98**, 11623.
22 Y. Zhao and D. G. Truhlar, *J. Chem. Phys.*, 2006, **125**, 194101.
23 Y. Zhao and D. G. Truhlar, *J. Phys. Chem. A*, 2006, **110**, 13126.
24 Y. Zhao and D. G. Truhlar, *Theor. Chem. Acc.*, 2008, **120**, 215.
25 J. Heyd, G. E. Scuseria and M. Ernzernhof, *J. Chem. Phys.*, 2003, **518**, 8207 bid. 2006, **124**, 219906(E).
26 F. Illas, I. de P. R. Moreira, J. M. Bofill and M. Filatov, *Phys. Rev. B: Condens. Matter Mater. Phys.*, 2004, **70**, 132414.
27 F. Illas, I. de P. R. Moreira, J. M. Bofill and M. Filatov, *Theor. Chem. Acc.*, 2006, **115**, 587.
28 I. de P. R. Moreira, R. Costa, M. Filatov and F. Illas, *J. Chem. Theory Comput.*, 2007, **3**, 764.
29 R. Caballol, O. Castell, F. Illas, J. P. Malrieu and I. de P. R. Moreira, *J. Phys. Chem. A*, 1997, **101**, 7860.
30 R. Valero, R. Costa, I. de P. R. Moreira, D. G. Truhlar and F. Illas, *J. Chem. Phys.*, 2008, **128**, 114103.
31 P. Rivero, I. de P. R. Moreira, F. Illas and G. E. Scuseria, *J. Chem. Phys.*, 2008, **129**, 184110.

32 J. J. Phillips and J. E. Peralta, *J. Chem. Phys.*, 2011, **134**, 034108.
33 E. Ruiz, P. Alemany, S. Alvarez and J. Cano, *J. Am. Chem. Soc.*, 1997, **119**, 1297.
34 E. Ruiz, *J. Comput. Chem.*, 2011, **32**, 1998.
35 R. Valero, F. Illas and D. G. Truhlar, *J. Chem. Theory Comput.*, 2011, **7**, 3523.
36 M. J. Frisch, *et al.*, *Gaussian 09, Revision A., 1*, Gaussian, Inc., Wallingford CT, 2009.
37 A. Bencini and D. Gatteschi, *Electron Paramagnetic Resonance of Exchange Coupled Systems*, Springer-Verlag, Berlin and Heidelberg, 1990.
38 B. Bleaney and K. D. Bowers, *Proc. R. Soc. London, Ser. A*, 1952, **97**, 451.
39 P. W. Anderson, *Phys. Rev.*, 1950, **79**, 350.
40 P. W. Anderson, in *Theory of the Magnetic Interaction: Exchange in Insulators and Superconductors*, ed. F. Turnbull and F. Seitz, Academic Press, New York, 1963, vol. 14, p. 99.
41 C. J. Calzado, J. Cabrero, J. P. Malrieu and R. Caballol, *J. Chem. Phys.*, 2002, **116**, 2728.
42 C. J. Calzado, J. Cabrero, J. P. Malrieu and R. Caballol, *J. Chem. Phys.*, 2002, **116**, 3985.
43 C. de Graaf, C. Sousa, I. de P.R. Moreira and F. Illas, *J. Phys. Chem. A*, 2001, **105**, 11371.
44 C. J. Calzado, C. Angeli, D. Taratiel, R. Caballol and J. P. Malrieu, *J. Chem. Phys.*, 2009, **131**, 044327.
45 Ph. de Loth, P. Karafiloglou, J. P. Daudey and O. Kahn, *J. Am. Chem. Soc.*, 1988, **110**, 76.

CSIRO PUBLISHING

Aust. J. Chem. **2013**, *66*, 477–484
http://dx.doi.org/10.1071/CH12433

Full Paper

Solvent-Induced Reversible Crystal-to-Amorphous Transformation Properties of Cobalt(II) 4-Aminomethylpyridine-Sulfate with Chromotropism

Achareeya Cheansirisomboon,[A] *Chaveng Pakawatchai,*[B] *and Sujittra Youngme*[A,C]

[A]Materials Chemistry Research Unit, Department of Chemistry and Center of Excellence for Innovation in Chemistry, Faculty of Science, Khon Kaen University, Khon Kaen 40002, Thailand.

[B]Department of Chemistry, Faculty of Science, Prince of Songkla University, Hat Yai, Songkhla 90112, Thailand.

[C]Corresponding author. Email: sujittra@kku.ac.th

The crystalline Co^{II} coordination compound with empirical formula $[Co(Hampy)_2(H_2O)_4](SO_4)_2(H_2O)_3$ (**1**); ampy = 4-aminomethylpyridine was obtained. The structure contains a mononuclear $[Co(Hampy)_2(H_2O)_4]^{4+}$ cation unit, two sulfate ions, and three lattice water molecules. The Co^{2+} cation shows an elongated octahedral geometry comprised of four oxygen atoms from water molecules at equatorial positions and two nitrogen atoms from Hampy ligands which are protonated at NH_2. Each mononuclear cation unit is assembled by intermolecular hydrogen bonding and π–π stacking interactions by the coordinated and lattice water molecules, amino group, and sulfate anions to form a 3D supramolecular network. Investigations of the dynamic structural behaviour demonstrate that the title compound exhibits a solvent-induced reversible crystal-to-amorphous transformation with chromotropism when exposed to water and methanol vapour. This indicates that the dehydrated amorphous form, $[Co(Hampy)_2(SO_4)_2]$ **1A**, may be utilised as an indicator for humidity and methanol vapour.

Manuscript received: 21 September 2012.
Manuscript accepted: 9 December 2012.
Published online: 25 January 2013.

Introduction

Recently, flexible and dynamic coordination compounds, which can change their structures in response to external stimuli, have attracted growing interest since they are important for the development of certain devices and sensors.[1–8] Structural transformations involving coordination polymers and networks have been studied more recently.[9–16] These kinds of solid-state structural transformations not only directly reflect the relationship between the structures involved but can also affect the properties of coordination polymers with small structural changes. Several types of structural transformations are primarily influenced by the following pathways, including expansion of the metal coordination number, thermal dissociation/association, condensation, rearrangement of bonds, or the removal or exchange of solvents.[17] The guest-induced crystalline-to-amorphous transformation and the guest-induced backward transformation are typically found in the dynamic and flexible coordination frameworks supported by weak intermolecular interactions, such as hydrogen bonds, π–π stacking, van der Waals forces, and others. Therefore, the guest molecules may also play a key role by acting as an essential support to the cavity of the host framework.[18–20]

From our previous work, we reported the reversible thermal dehydration and rehydration of the supramolecular frameworks $[M(H_2O)_4(ampyz)_2][M(H_2O)_6](SO_4)_2(H_2O)_2$ (M = Co^{II}, Fe^{II} and mixed Co^{II}/Fe^{II}, ampyz = 2-aminopyrazine)[21] and Co^{II}–3, 5-pyridinedicarboxylate compounds.[22] These compounds exhibit water-induced reversible crystal-to-amorphous transformations with chromotropism. The reversibility is driven by very strong hydrogen bonding between lattice and coordinated water molecules and sulfate anions. In this contribution, it is clearly known that sulfate is found as a framework former which has diverse coordination chemistry to transition metal ions, sometimes displaying more than one coordination mode in a single framework. Sulfate is also a very suitable anion for the construction of hydrogen-bonded networks because it readily forms strong hydrogen bonds.[23] In our study, we sought to synthesise coordination compounds with strong (classical) hydrogen-bonding properties of the sulfate anion to produce solids which featured both coordination polymers and hydrogen-bonding motifs in the extended structures. During achieving this aim, we successfully synthesised a new 3D supramolecular framework $[Co(Hampy)_2(H_2O)_4](SO_4)_2(H_2O)_3$ which contains strong intermolecular hydrogen bonding generated from coordinated and uncoordinated water molecules, amino, and sulfate groups. This compound shows a reversible crystal-to-amorphous transformation upon desorption and resorption processes, which is verified by elemental analysis, thermogravimetric analysis (TGA), X-ray powder diffraction (XRPD), as well as spectroscopic identification.

Experimental

Materials and Measurements

All reagents were commercial grade materials and were used without further purification. The IR spectra were recorded as KBr discs on a Perkin–Elmer Spectrum One FT-IR spectrophotometer in the 4000–450 cm^{-1} spectroscopic range. Solid-state (diffuse reflectance) electronic spectra were measured as polycrystalline samples on a Perkin–Elmer Lambda2S spectrophotometer, within the range 200–1100 nm. Elemental analyses (C, H, and N) were determined using a Perkin–Elmer PE-2400 CHNS/O Analyzer. TGA was perform with a Perkin Elmer Pyris Diamond TG-DTA between 30 and 800°C in a N_2 atmosphere with a heating rate of 10°C min^{-1} by using α-Al_2O_3 as a standard material. The XRPD data were collected on a Bruker D8 ADVANCE diffractometer using monochromatic $Cu_{K\alpha}$ radiation, and the recording speed was 1 s $step^{-1}$ over the 2θ range of 5–50°C at room temperature.

Synthesis of $[Co(Hampy)_2(H_2O)_4](SO_4)_2(H_2O)_3$ (**1**)

An aqueous solution (10 mL) of $Co(SO_4)\cdot 7H_2O$ (0.2810 g, 1.0 mmol) was added to a methanolic solution (5 mL) of 4-aminomethylpyridine (ampy, 0.1081 g, 1.0 mmol). A methanolic solution (5 mL) of NaN_3 (0.0655 g, 1.0 mmol) was then added. After 3 weeks, orange crystals were obtained. Yield ~75 %. Anal. Calcd for $C_{12}H_{32}N_4O_{15}S_2Co$: C 24.20, H 5.42, N 9.41. Found: C 24.13, H 5.37, N 9.27 %. ν_{max} (KBr)/cm^{-1} 3319s ν(O–H), 1625m, 1524m and 1429m ν(C=C), 1176s, 1108vs, 1089vs, and 1022s ν(S–O), 825 δ(N–H), 661m δ(C–C). λ_{max} (diffuse reflectance)/cm^{-1} 20408, slightly less than 9000.

Dehydration was performed by heating single crystals of **1** to 200°C in air and maintaining this temperature for 2 h, resulting in the dehydrated form. The rehydration process was performed by exposing the evacuated sample in air for 24 h. The solvent-induced reversible structural transformation properties were also tested for various solvents (methanol, ethanol, acetone, acetonitrile, dichloromethane, and hexane) by exposing the dehydrated samples to solvent vapour for 1 day at room temperature and heating the solvated samples at 200°C for 20 min. These processes were verified many times to repeat the reversibility of the de- and readsorption processes.

Crystallography

The X-ray single-crystal data was collected at 293 K. Reflection data were collected on a 1K Bruker SMART APEX CCD area-detector diffractometer using rotating mode, graphite-monochromated $Mo_{K\alpha}$ radiation (λ 0.71073 Å) at a detector distance of 4.5 cm and swing angle of −30°. Raw data frame integration was performed with *SAINT*,[24] which also applied correction for Lorentz and polarization effects. An empirical absorption correction was applied using the *SADABS* program,[25] which resulted in transmission coefficients ranging from 1.000 to 0.897. The structures were solved by direct methods and refined by full-matrix least-squares methods on $(F_{obs})^2$ using the *SHELXTL-PC Version 6.12* software package.[26] All hydrogen atoms were located by difference synthesis and refined isotropically. The details of crystal data, selected bond lengths and angles are listed in Tables 1 and 2. For the water lattice molecule, the oxygen atom (O15) was disordered with site occupancies of 0.5.

Table 1. Crystallographic data for compound $[Co(Hampy)_2(H_2O)_4](SO_4)_2(H_2O)_3$ (1)

Parameter	**1**
Formula	$CoC_{12}H_{32}N_4O_{15}S_2$
Formula weight	595.47
T [K]	293(2)
Crystal system	Monoclinic
Space group	$P2(1)/c$
a [Å]	9.4969(5)
b [Å]	18.005(1)
c [Å]	14.7005(8)
α [deg.]	90.00
β [deg.]	108.213(1)
γ [deg.]	90.00
V [Å^3]	2387.8(2)
Z	4
D_c [g cm^{-3}]	1.656
μ [mm^{-1}]	0.971
$F(000)$	1244
Crystal size [mm^3]	0.048 × 0.184 × 0.188
Number of reflection collected	33049
Number of unique reflection [R_{int}]	5923 (0.0487)
Data/restraints/parameter	5923/0/444
GOF	1.131
Final R indices [$I > 2\sigma(I)$]	R_1 0.0714, wR_2 0.1574
$R = \Sigma\|\|F_o\| - \|F_c\|\|/\Sigma\|F_o\|$	
$R_w = [\Sigma w\{\|\|F_o\| - \|F_c\|\}^2/\Sigma w\|F_o\|^2]^{1/2}$	
R indices (all data)	R_1 0.0871, wR_2 0.1665
Max/min electron density [e Å^3]	1.743/−0.653

Table 2. Selected bond lengths [Å] and angles [deg.] for compound 1

Bond distances			
Co–O1	2.101(3)	Co–O4	2.087(3)
Co–O2	2.063(3)	Co–N1	2.156(3)
Co–O3	2.079(3)	Co–N2	2.168(3)
Bond angles			
O1–Co–O2	88.33(15)	O3–Co–N1	93.69(14)
O1–Co–O3	179.16(15)	O4–Co–N1	89.11(13)
O1–Co–O4	91.49(14)	O1–Co–N2	93.00(13)
O2–Co–O3	91.58(16)	O2–Co–N2	92.00(14)
O2–Co–O4	179.33(14)	O3–Co–N2	87.84(14)
O3–Co–O4	88.59(16)	O4–Co–N2	88.66(13)
O1–Co–N1	85.47(13)	N1–Co–N2	177.27(12)
O2–Co–N1	90.23(14)		

Results and Discussion

Spectroscopic Characterisations

The IR spectrum of compound **1** shows a strong band in the region 3400–3000 cm^{-1} which is assigned to the stretching ν(N–H) of the primary amine in the Hampy ligand overlapping with the ν(O–H) of water molecules. The NH_3 scissoring mode[27] shows a medium band at 1625 cm^{-1} and the strongest bands due to SO_4^{2-} stretching vibrations are observed around 1100 cm^{-1}.[28] Those of the dehydrated materials show similar spectra to that of the original crystalline compound **1**, but the broad band of ν(O–H) of water molecules disappeared. The solid-state UV-vis diffuse reflectance spectrum of **1** agrees with

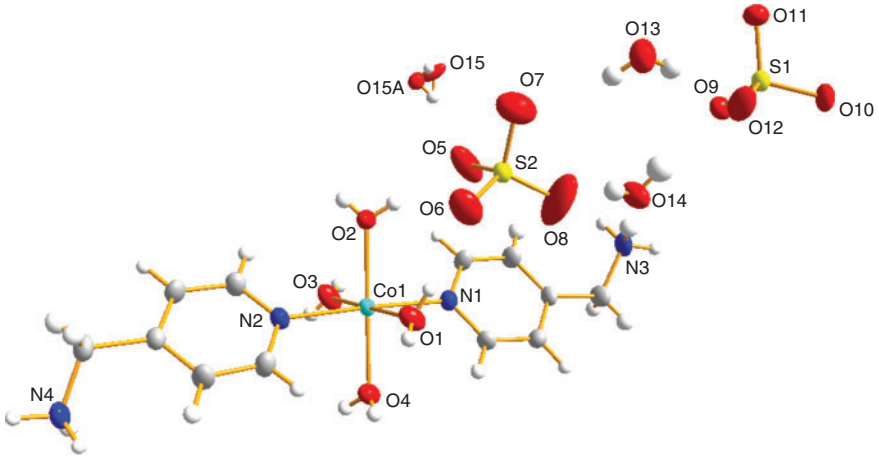

Fig. 1. Crystal structure and atomic labelling scheme of $[Co(Hampy)_2(H_2O)_4](SO_4)_2(H_2O)_3$ (**1**) (ampy = 4-aminomethylpyridine). The ellipsoids are shown at a 50 % probability level.

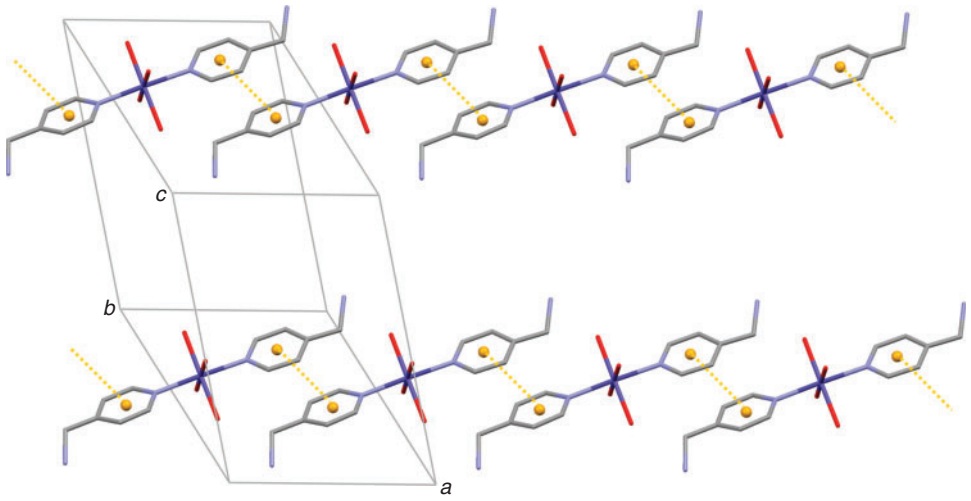

Fig. 2. 1D structure of compound **1** connected by face-to-face π–π interactions between pyridine rings of the Hampy ligand (ampy = 4-aminomethylpyridine). Hydrogen atoms, sulfate anions, and lattice water molecules are omitted for clarity.

the typical d–d transition of high-spin Co^{II} in an octahedral geometry with two observed bands at 20408 cm^{-1} (490 nm) and slightly less than 9000 cm^{-1} (1100 nm), which are assigned to the $^4T_{1g} \rightarrow {}^4T_{1g}(P)$ and $^4T_{1g} \rightarrow {}^4T_{2g}$ transitions, respectively, the $^4T_{1g} \rightarrow {}^4A_{2g}$ transition expected at around 600 nm was not observed. The band around 28571 cm^{-1} (350 nm) appears due to a charge transfer transition and internal transition within Hampy.

*Crystal Structure of $[Co(Hampy)_2(H_2O)_4](SO_4)_2(H_2O)_3$ (**1**)*

Compound **1** crystallizes in the monoclinic crystal system with the $P2_1/c$ space group. The crystal structure of **1** consists of a compound cation, two sulfate anions, and three water molecules as shown in Fig. 1 together with the numbering scheme. Selected distances and angles are listed in Table 2. The Co^{II} ion exhibits a distorted octahedral coordination through four aqua ligands with the average Co–O distance of 2.0825(1) Å composing the basal plane and two *trans*-nitrogen atoms from the monodentate Hampy ligand with Co–N distances of 2.156(3) and 2.168(3) Å occupying the axial sites. Both Hampy ligands are protonated at NH_2, leading to a mononuclear cation unit $[Co(Hampy)_2(H_2O)_4]^{4+}$. The $Co–N_{Hampy}$ lengths in the title compound are in good agreement with the corresponding distances reported for other mononuclear Co^{II} compounds such as $[Co(na)_2(H_2O)_4](sac)_2$ [Co–N: 2.153(1) Å],[29] $[Co(ina)_2(H_2O)_4](sac)_2$ [Co–N: 2.169(1) Å][30] but slightly different from those found in $[Co(dmpy)_2](sac)_2(H_2O)_2$ [Co–N: 2.034(2) Å] (na = nicotinamide, sac = saccharine, ina = isonicotinamide, dmpy = 2,6-dimethanolpyridine).[31] The Co–O_{aqua} distances are in good agreement with those found in $[Co(4\text{-acpy})_2(H_2O)_4](sac)_2$ [Co–O: 2.068(1)–2.099(1) Å][32] and $[Co(mein)_2(H_2O)_4](sac)_2$ [Co–O: 2.085(2)–2.099(1) Å] (4-acpy = 4-acetylpyridine, mein = methylisonicotinate).[33] The basal plane is planar with a slight tetrahedral twist of 1.05° and the Co atom lies 0.136 Å above the basal plane towards the axial site. The bond angles around the octahedron are in the ranges of 85.47(13)°–93.69(14)° and 177.27(12)°–179.33(15)°, which are close to the ideal octahedral geometry. In the extended molecular structure each mononuclear cation unit is linked by π–π stacking by pyridine rings of Hampy moieties to build a 1D chain (Fig. 2). Moreover, these chains are supported by electrostatic forces and the intermolecular hydrogen bonds involving oxygen atoms of sulfate anions, amine moieties on Hampy (N3 and N4), coordination waters in the $[Co(Hampy)_2(H_2O)_4]^{4+}$

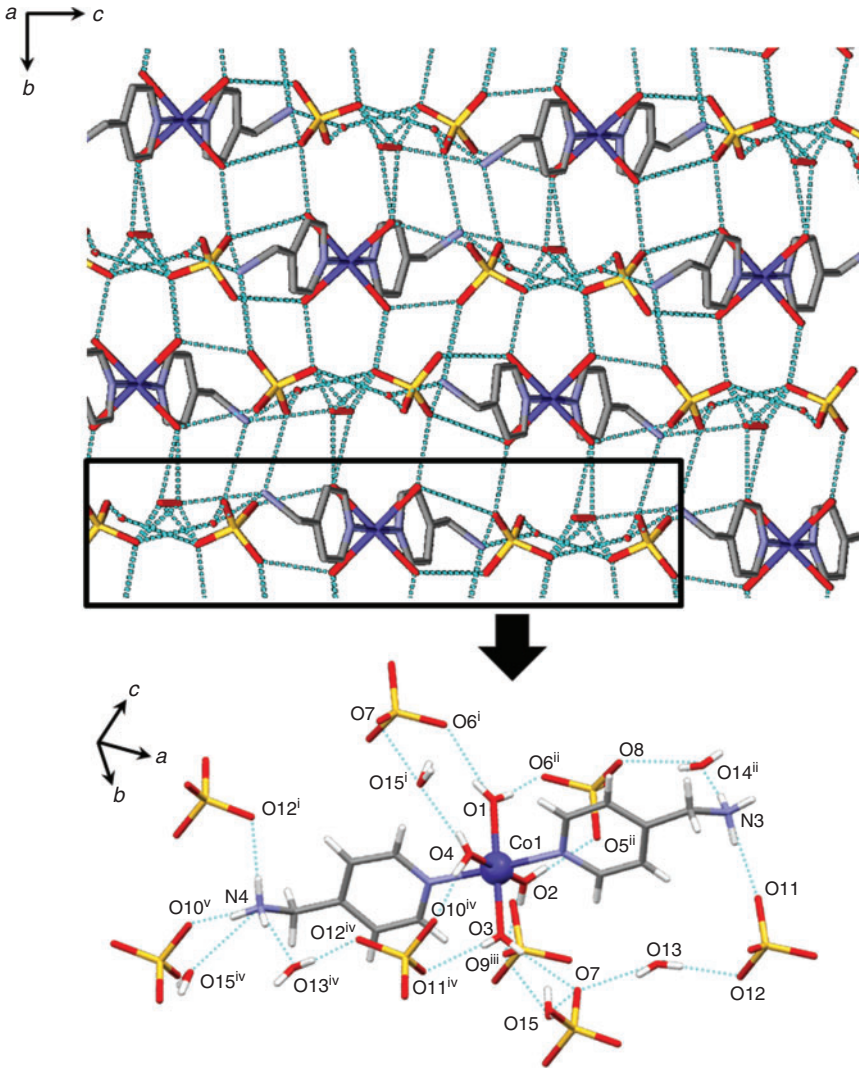

Fig. 3. 3D packing structure of compound **1** in the *bc* plane formed by intermolecular hydrogen bonding (blue dot lines) among layers through Hampy (ampy = 4-aminomethylpyridine), sulfate anions, and lattice and coordinated water molecules.

unit (O1–O4), and lattice water molecules, to provide an entire 3D supramolecular structure of **1** as shown in Fig. 3. Details of hydrogen bonds are summarised in Table 3.

Thermogravimetric Analysis

The TGA was recorded for the crystalline samples in the temperature range 30–800°C. The TGA curve of compound **1** is shown in Fig. 4. The first step of weight loss in the temperature range 30–180°C (found: 22.05 % and calc.: 21.17 %) corresponds to the loss of all seven water molecules per formula unit, resulting in the dehydrated form of $[Co(Hampy)_2(SO_4)_2]$ (**1A**). This dehydrated form of **1A** is stable up to approximately 200°C and then rapidly decomposes to unidentified products.

Solvent-Induced Reversible Crystal-to-Amorphous Transformation Properties

Compound **1** contains both guest water and coordinated water. In order to obtain more insight into the dynamic properties relative to these water molecules, the dehydration and rehydration processes were performed and verified by elemental analyses, TGA, XRPD, and spectroscopic techniques. Interestingly, the water molecules can be readsorbed fully by exposing the evacuated samples to water vapour at room temperature, evidenced by elemental analysis. The heating and exposing procedures were repeated several times to demonstrate the reversibility of the de- and rehydration processes.

The most distinguished feature of the crystals of **1** is that they undergo a water-induced reversible crystal-to-amorphous transformation with chromotropism driven by thermal dehydration and rehydration. When the single crystals of **1** were heated to 200°C in air and maintained at this temperature for 2 h, these crystals suddenly lose crystallinity and the colour changes from orange (**1**) to purple (**1A**). The elemental analysis (Anal. Calc. for $C_{12}H_{18}N_4O_8S_2Co$: C 30.71, H 3.87, N 11.94. Found: C 30.48, H 3.70, N 12.29 %) and XRPD results (Fig. 5c) indicate that the chemical composition of the non-crystalline solid is $[Co(Hampy)_2(SO_4)_2]$ (**1A**) in an amorphous powder which is formed by the collapse of the supramolecular structure of **1** accompanied with the destruction of the hydrogen bonding network when all water molecules are removed. Interestingly, the amorphous form **1A** can be restored to the crystalline form $[Co(Hampy)_2(H_2O)_4](SO_4)_2(H_2O)_3$ (**1′**) in which the colour

Table 3. Hydrogen bonds of compound 1

D–H···A[A]	D–H	H···A [Å]	D···A [Å]	D–H···A [deg.]
O(1)–H(1A)···O(6)^{i}	0.73	1.99	2.6942	163
O(1)–H(1B)···O(6)^{ii}	0.75	2.06	2.8017	169
O(2)–H(2A)···O(5)^{ii}	0.76	1.90	2.6598	174
O(2)–H(2B)···O(9)^{iii}	0.73	2.02	2.7428	175
O(3)–H(3A)···O(7)	0.79	2.03	2.8024	165
O(3)–H(3B)···O(11)^{iv}	0.64	2.10	2.7272	166
O(4)–H(4A)···O(10)^{iv}	0.84	1.88	2.7129	171
O(4)–H(4B)···O(15)^{i}	0.66	1.98	2.6312	168
O(4)–H(4B)···O(15A)^{i}	0.66	1.99	2.6413	167
N(3)–H(5)···O(6)^{vi}	0.90	2.04	2.8962	158
N(3)–H(6)···O(14)^{ii}	0.92	1.85	2.7581	174
N(3)–H(7)···O(11)	0.94	1.87	2.7950	170
N(4)–H(8)···O(12)^{i}	0.90	1.98	2.8758	176
N(4)–H(9)···O(10)^{v}	0.91	1.98	2.8266	156
N(4)–H(9)···O(15A)^{iv}	0.91	2.55	3.0393	115
N(4)–H(10)···O(13)^{iv}	0.85	1.95	2.7606	160
O(13)–H(13A)···O(12)	0.75	2.02	2.7682	177
O(13)–H(13B)···O(7)	0.73	2.13	2.8422	166
O(14)–H(14A)···O(9)	0.85	2.08	2.8644	153
O(14)–H(14B)···O(8)	0.72	2.01	2.7085	163
O(15)–H(15A)···O(7)	0.56	2.21	2.7621	166
O(15)–H(15B)···O(9)^{iii}	0.92	1.95	2.7171	140

[A]Symmetry codes: (i) $-x$, $-1/2+y$, $1/2-z$; (ii) x, $1/2-y$, $1/2+z$; (iii) $-1+x$, y, z; (iv) $-1+x$, $1/2-y$, $-1/2+z$; (vi) $1+x$, $1/2-y$, $1/2+z$; (v) $-2+x$, $1/2-y$, $-1/2+z$.

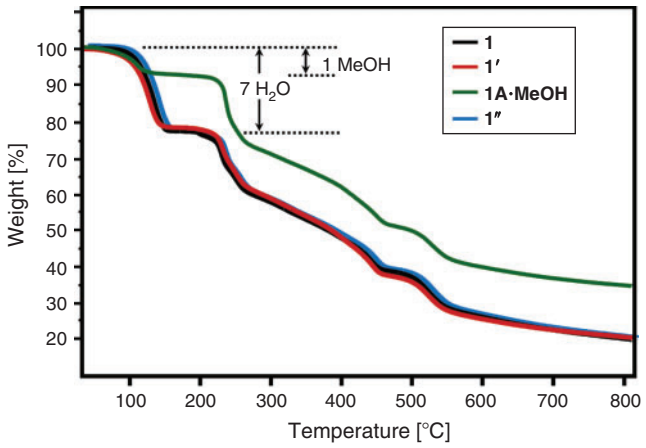

Fig. 4. Thermogravimetric analysis curves of as-synthesised **1**, the rehydrated form **1′**, the methanolic form **1A·MeOH**, and the rehydrated form **1″** after exposed **1A·MeOH** in air for 3 h.

returns to the original crystalline one after being exposed in air for 24 h, as confirmed by the elemental analysis (Anal. Calc. for $C_{12}H_{32}N_4O_{15}S_2Co$: C 24.20, H 5.42, N 9.41. Found: C 24.10, H 5.27, N 9.30 %) and the XRPD measurement results. The restored solid has the same XRPD pattern as the simulated one from the single crystal X-ray diffraction data of **1** (see Fig. 5a, d). These results suggest the crystalline-to-amorphous and reversible amorphous-to-crystalline transformations in the supramolecular framework of **1** induced by the hydration control.

Furthermore, to verify the solvent-induced reversible structural transformation properties, the dehydrated [$Co(Hampy)_2(SO_4)_2$] (**1A**) was further studied with various solvents (methanol,

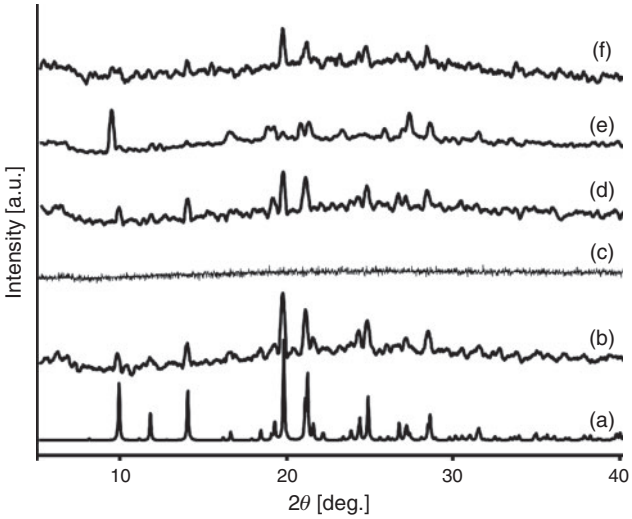

Fig. 5. The X-ray powder diffraction patterns for compound **1**. (a) Simulated pattern based on the single-crystal X-ray raw data of **1**; (b) as-synthesised **1**; (c) dehydrated form **1A** that was prepared by drying at 200°C under vacuum for 2 h; (d) rehydrated form **1′** after exposed in air for 24 h; (e) the methanolic form **1A·MeOH** after exposed to methanol vapour for 1 day at room temperature; and (f) the rehydrated form **1″** after exposing **1A·MeOH** to air for 3 h.

ethanol, acetone, acetonitrile, dichloromethane, and hexane) by exposing **1A** to solvent vapour for 1 day at room temperature. The results show that the purple colour of solid **1A** in all solvent vapours still remains, excluding in methanol vapour when the colour changes from purple (**1A**) to pink (**1A·MeOH**). The pink solid **1A·MeOH** loses a methanol molecule after exposure to air for 3 h and the colour returns from pink to the original orange crystalline sample (**1″**). Moreover, after heating **1A·MeOH** at 200°C for 20 min the colour changes from pink (**1A·MeOH**) to purple (**1A**) which manifests the reversible process with chromotropism. Therefore, the rehydrated form **1A** was heated and cooled many times to repeat the reversibility of the de- and re-adsorption processes. The results exhibit the colour shuttle change from purple to orange (exposed in air) and from purple to pink (exposed in MeOH vapour), suggesting the solvent-induced reversible structural transformation phenomenon.

These dynamic structural behaviours with chromotropism are summarised as a schematic representation in Fig. 6 and these were proved by TGA, XRPD, and spectroscopic techniques. The TGA curve of **1A·MeOH** (see Fig. 4, green line) indicates the release of one methanol molecule from $Co(Hampy)_2(SO_4)_2(MeOH)$ (**1A·MeOH**). The TGA curve of **1″** is found to have identical weight loss to that of **1** and **1′**, indicating the same composition. The XRPD pattern of **1A·MeOH** and **1″** are shown in Fig. 5e, f. When the amorphous phase **1A** is exposed to methanol vapour, the XRPD pattern is readily converted into the second crystalline form of **1A·MeOH** in which the colour changes to pink and then returned to the original orange crystalline form **1″** after evaporation of methanol in air for 3 h.

In addition, the reversibility of the water or methanol adsorption and the change in the coordination environment can be visualised by the change in colour of the compound.[34,35] This change of colour can be attributed to the change of the crystal field splitting of the central Co^{2+} ions during the adsorption and removal of solvent molecules. The change in colour of the Co compound prompted us to study the change in

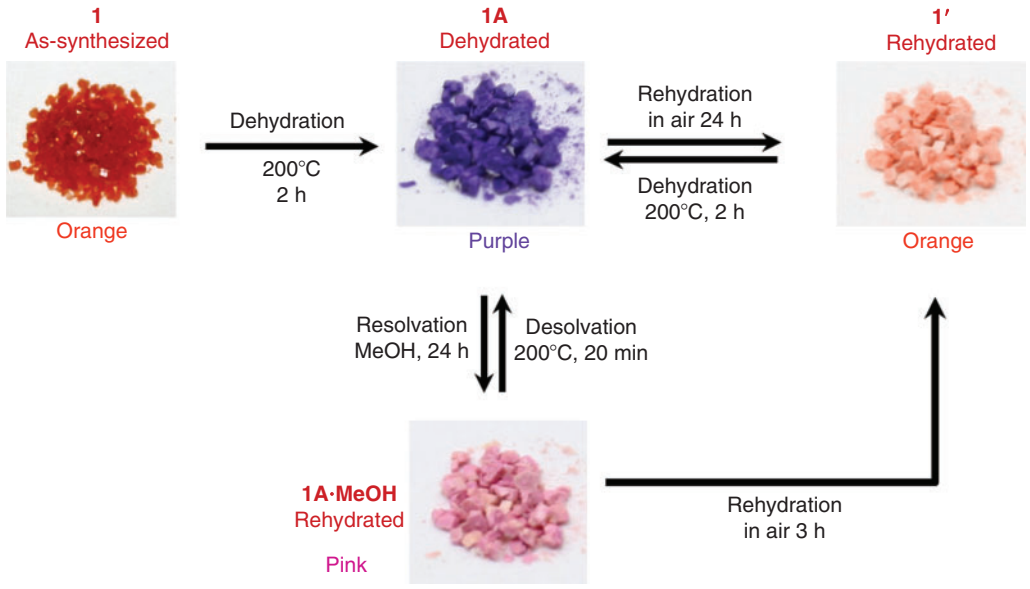

Fig. 6. Changes in colour during de- and re-adsorption of water and methanol molecules in crystalline sample **1**.

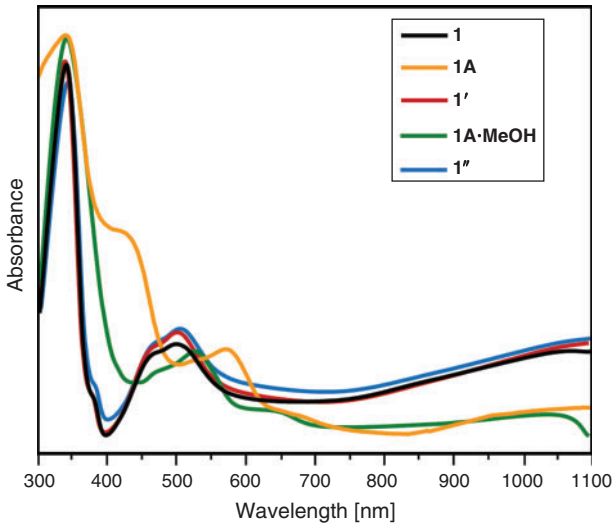

Fig. 7. The UV-vis diffuse reflectance spectra of as-synthesised **1**, the dehydrated form **1A**, the rehydrated form **1′**, the methanolic form **1A·MeOH**, and the rehydrated form **1″**.

electronic transitions in the samples. For this, the solid-state UV-vis diffuse reflectance spectra as shown in Fig. 7 clearly show that the bands observed in **1**, **1′**, and **1″** correspond very well to the identical transitions causing the same colour of products, and evidence that **1**, **1′**, and **1″** have the same Co^{2+} environments. Whereas the amorphous form **1A** shows the different d–d transitions with two broad bands at 575 and around 1100 nm, and two shoulders at around 660 and 417 nm, giving the distinctive purple colour. The higher energy shoulder at 417 nm is due to a charge transfer transition and internal transition within Hampy. That of the crystalline form **1A·MeOH** agrees with the typical d–d transitions of high spin Co^{2+} in distorted octahedral geometry with two broad bands at 540 and 1050 nm, with a shoulder around 640 nm, which are assigned to the $^4T_{1g} \rightarrow {}^4T_{1g}(P)$, $^4T_{1g} \rightarrow {}^4T_{2g}$, and $^4T_{1g} \rightarrow {}^4A_{2g}$ transitions, respectively. The first broad band at 540 nm shows a similar characteristic to that of the original crystalline form but slightly shifted around 50 nm to lower energy, resulting in the distinctive pink colour. The chromotropic behaviour of this compound is principally ascribed to the changes of the d-orbital energy level, induced by the drastic change in the coordination environments around the metal centre during de- and read-sorption processes.[36] As found in nature, cobalt-containing metal–organic frameworks (MOFs) can have a wide range of colours which make it easy, in many cases, to identify different phases. The most common colours are a very light pink for octahedral coordinated ones and an intense blue for tetrahedral coordination. For distorted octahedra, the pink colour can intensify to orange, dark red, purple, and violet depending on the ligand and the type of distortions.[37] All of the results confirm the solvent-induced reversible transformation with chromotropism in the supramolecular network of **1** and are indicative of the high selective recognition of **1A** to water molecules. The selective methanol accommodation with chromotropism in dehydrated **1A** when compared with many solvents excluding water could be attributed to the proper size of methanol molecules and weak host–guest interactions.

Interestingly, the conspicuous dynamic behaviour of **1** is similar to that found in our previously published data of the mononuclear compounds $[M(H_2O)_4(ampyz)_2][M(H_2O)_6](SO_4)_2(H_2O)_2$ ($M = Co^{II}$, Fe^{II}, and mixed Co^{II}/Fe^{II}; ampyz = 2-aminopyrazine) which exhibit crystal-to-amorphous transformations with chromotrophism.[21] Both **1** and those previous compounds contain abundant hydrogen donors and hydrogen acceptors from coordinated and uncoordinated water molecules, amino, and sulfate groups to generate the intermolecular hydrogen-bond interactions as well as π–π stacking. Thus, they have more accessible intermolecular hydrogen bonding that is able to trigger the reversible crystal-to-amorphous transformation after de- and re-adsorption processes. In contrast, the reversible process is not found for the 2D framework of $[Co(pydc)(H_2O)_2]_n$ (pydc = 3,5-pyridinedicarboxylate).[22] This structure was not recovered but changed to another crystalline form of a polymeric chain of $[Co(pydc)(H_2O)_4]_n(H_2O)_n$ after the water re-adsorption process, and the reversibility takes place between this resulting 1D compound and the dehydrated amorphous form after de- and rehydration processes. This may

be due to the fewer intermolecular interactions in the original structure which are not enough to trigger the structural transformation to the original 2D framework as compared with that of the title compound **1**.

The process of reversibility between the amorphous and crystalline materials only take place in the presence of the water and methanol, and this could be a dissolution/recrystallization process rather than a solvent-induced solid-state reaction as this involves structural reorganization of the supramolecular framework or rearrangements of the molecules interacting by intermolecular hydrogen bonds and non-covalent contacts.[38]

Conclusion

In summary, $[Co(Hampy)_2(H_2O)_4](SO_4)_2(H_2O)_3$ with a three-dimensional supramolecular framework has been successfully prepared and structurally characterised. The crystal structure shows a network of mononuclear units which contain intermolecular π–π stacking and hydrogen-bonding interactions stabilising the whole structure. Thermal decomposition, elemental analysis, XRPD, and spectroscopic results indicate that the transformation from the crystal form of $[Co(Hampy)_2(H_2O)_4](SO_4)_2(H_2O)_3$ to the amorphous powder of $[Co(Hampy)_2(SO_4)_2]$ is reversible with the colour changes. The original crystalline form is recovered from the collapsed amorphous sample by the restoration of water molecules. Moreover, the dried amorphous powder also transforms to the second crystalline form $Co(Hampy)_2(SO_4)_2(MeOH)$ after exposure to methanol vapour and then recovered to the original one in air. Thus the desorption/resorption processes involving the weak intermolecular interactions can trigger the reversible crystal-to-amorphous transformation with chromotropism for compounds **1** and the dried amorphous powder of $[Co(Hampy)_2(SO_4)_2]$ may be applied as an indicator for humidity and methanol vapour.

Supplementary Material

CIFs and CheckCIFs for compound **1** are available on the Journal's website. CCDC number 899500 contains the supplementary crystallographic data for the title compound. This data can be obtained free of charge through http://www.ccdc.cam.ac.uk/conts/retrieving.html, or from the Cambridge Crystallographic Data Centre, 12 Union Road, Cambridge CB2 1EZ, UK; fax: (+44) 1223–336–033; or email: deposit@ccdc.cam.ac.uk.

Acknowledgements

Funding for this work is provided by The Thailand Research Fund, The Royal Golden Jubilee Ph.D. Program of The Thailand Research Fund (Grant No. PHD/0328/2551), the Higher Education Research Promotion and National Research University Project of Thailand, Office of the Higher Education Commission, through the Advanced Functional Materials Cluster of Khon Kaen University and the Center of Excellence for Innovation in Chemistry (PERCH-CIC), Office of the Higher Education Commission, Ministry of Education, Thailand.

References

[1] E. Y. Lee, M. P. Suh, *Angew. Chem. Int. Ed.* **2004**, *43*, 2798. doi:10.1002/ANIE.200353494

[2] E. Y. Lee, S. Y. Jang, M. P. Suh, *J. Am. Chem. Soc.* **2005**, *127*, 6374. doi:10.1021/JA043756X

[3] K. Biradha, M. Fujita, *Angew. Chem. Int. Ed.* **2002**, *41*, 3392. doi:10.1002/1521-3773(20020916)41:18<3392::AID-ANIE3392>3.0.CO;2-V

[4] K. Biradha, Y. Hongo, M. Fujita, *Angew. Chem. Int. Ed.* **2002**, *41*, 3395. doi:10.1002/1521-3773(20020916)41:18<3395::AID-ANIE3395>3.0.CO;2-D

[5] C. J. Kepert, M. J. Rosseinsky, *Chem. Commun.* **1999**, 375. doi:10.1039/A809746A

[6] K. Takaoka, M. Kawano, M. Tominaga, M. Fujita, *Angew. Chem. Int. Ed.* **2005**, *44*, 2151. doi:10.1002/ANIE.200462214

[7] C.-D. Wu, W. Lin, *Angew. Chem. Int. Ed.* **2005**, *44*, 1958. doi:10.1002/ANIE.200462711

[8] D. N. Dybtsev, H. Chun, K. Kim, *Angew. Chem. Int. Ed.* **2004**, *43*, 5033. doi:10.1002/ANIE.200460712

[9] N. L. Toh, M. Nagarathinam, J. J. Vittal, *Angew. Chem. Int. Ed.* **2005**, *44*, 2237. doi:10.1002/ANIE.200462673

[10] T. H. Kim, Y. W. Shin, J. S. Kim, J. Kim, *Angew. Chem. Int. Ed.* **2008**, *47*, 685. doi:10.1002/ANIE.200704349

[11] J. Y. Lee, S. Y. Lee, W. Sim, K. M. Park, J. Kim, S. S. Lee, *J. Am. Chem. Soc.* **2008**, *130*, 6902. doi:10.1021/JA8008693

[12] C. Hu, U. Englert, *Angew. Chem. Int. Ed.* **2005**, *44*, 2281. doi:10.1002/ANIE.200462100

[13] B. Rather, B. Moulton, R. D. B. Walsh, M. J. Zaworotko, *Chem. Commun.* **2002**, 694. doi:10.1039/B111280P

[14] S. Oliver, A. Kuperman, A. Lough, G. A. Ozin, *Chem. Mater.* **1996**, *8*, 2391. doi:10.1021/CM960216T

[15] W. Lin, O. R. Evans, R. G. Xiong, Z. Y. Wang, *J. Am. Chem. Soc.* **1998**, *120*, 13272. doi:10.1021/JA983415H

[16] J. H. Kim, S. M. Hubig, S. V. Lindeman, J. K. Kochi, *J. Am. Chem. Soc.* **2001**, *123*, 87. doi:10.1021/JA001939N

[17] J. J. Vittal, *Coord. Chem. Rev.* **2007**, *251*, 1781. doi:10.1016/J.CCR.2007.02.002

[18] H. K. Chae, D. Y. Siberio-Perez, J. Kim, Y. Go, M. Eddaoudi, A. J. Matzger, M. O'Keeffe, O. M. Yaghi, *Nature* **2004**, *427*, 523. doi:10.1038/NATURE02311

[19] P. Sozzani, S. Bracco, A. Comotti, L. Ferretti, R. Simonutti, *Angew. Chem. Int. Ed.* **2005**, *44*, 1816. doi:10.1002/ANIE.200461704

[20] T. K. Prasad, M. V. Rajasekharan, *Cryst. Growth Des.* **2006**, *6*, 488. doi:10.1021/CG050417M

[21] J. Boonmak, M. Nakano, N. Chaichit, C. Pakawatchai, S. Youngme, *Dalton Trans.* **2010**, *39*, 8161. doi:10.1039/C002556A

[22] A. Cheansirisomboon, C. Pakawatchai, S. Youngme, *Dalton Trans.* **2012**, *41*, 10698. doi:10.1039/C2DT31183F

[23] (a) T. J. Prior, B. Yotnoi, A. Rujiwatra, *Polyhedron* **2011**, *30*, 259. doi:10.1016/J.POLY.2010.10.010
(b) S. D. Huang, R. G. Xiong, P. H. Sotero, *J. Solid State Chem.* **1998**, *138*, 361. doi:10.1006/JSSC.1997.7591
(c) G. A. Jeffrey, *An Introduction to Hydrogen Bonding* **1997** (OUP: Oxford).

[24] *SAINT 4.0 Software Reference Manual* **2000** (Siemens Analytical X-Ray Systems, Inc.: Madison, WI).

[25] G. M. Sheldrick, *SADABS: Program for Empirical Absorption Correction of Area Detector Data* **2000** (University of Göttingen: Göttingen).

[26] G. M. Sheldrick, *Acta Crystallogr. A* **2008**, *64*, 112. doi:10.1107/S0108767307043930

[27] J. R. Allan, A. D. Paton, K. Turvey, H. J. Bowley, D. L. Gerrad, *Inorg. Chim. Acta* **1987**, *134*, 259. doi:10.1016/S0020-1693(00)88092-5

[28] K. Nakamoto, *Infrared and Raman Spectra of Inorganic and Coordination Compounds* **1997**, 5th edn (John Wiley & Sons: New York, NY).

[29] E. E. Castellano, O. E. Piro, B. S. Parajon-Costa, E. J. Baran, *Z. Naturforsch.* **2002**, *57*, 657.

[30] B. I. Uçar, H. Karabulut, O. Pasaõglu, A. Büuyükgüngör, A. Bulut, *J. Mol. Struct.* **2006**, *787*, 38.

[31] O. Andac, S. Guney, Y. Topcu, V. T. Yilmaz, W. T. A. Harrison, *Acta Crystallogr. C* **2002**, *58*, m17. doi:10.1107/S0108270101018807

[32] Y. Çelik, E. Bozkurt, I. Uçar, B. Karabulut, *J. Phys. Chem. Solids* **2012**, *73*, 1010. doi:10.1016/J.JPCS.2012.03.005

[33] E. Bozkurt, H. Ayaz, I. Uçar, B. Karabulut, *Inorg. Chim. Acta* **2012**, *390*, 1. doi:10.1016/J.ICA.2012.04.008

[34] K. Takaoka, M. Kawano, T. Hozumi, S. Ohkoshi, M. Fujita, *Inorg. Chem.* **2006**, *45*, 3976. doi:10.1021/IC052138U
[35] M.-L. Sun, L. Zhang, Q.-P. Lin, J. Zhang, Y.-G. Yao, *Cryst. Growth Des.* **2010**, *10*, 1464. doi:10.1021/CG901468D
[36] (a) D. Bradshaw, J. E. Warren, M. J. Rosseinsky, *Science* **2007**, *315*, 977. doi:10.1126/SCIENCE.1135445
(b) S.-J. Fu, C.-Y. Cheng, K.-J. Lin, *Cryst. Growth Des.* **2007**, *7*, 1381. doi:10.1021/CG070361R
(c) C.-L. Chen, A. M. Goforth, M. D. Smith, C.-Y. Su, H.-C. zur Loye, *Angew. Chem. Int. Ed.* **2005**, *44*, 6673. doi:10.1002/ANIE.200502309
(d) L. G. Beauvais, M. P. Shores, J. R. Long, *J. Am. Chem. Soc.* **2000**, *122*, 2763. doi:10.1021/JA994186H
[37] M. Kurmoo, *Chem. Soc. Rev.* **2009**, *38*, 1353. doi:10.1039/B804757J
[38] A. N. Khlobystov, N. R. Champness, C. J. Roberts, S. J. B. Tendler, C. Thompson, M. Schroder, *CrystEngComm* **2002**, *4*, 426. doi:10.1039/B202217F

Inorganic Chemistry Communications 44 (2014) 111–113

Contents lists available at ScienceDirect

Inorganic Chemistry Communications

journal homepage: www.elsevier.com/locate/inoche

Flexible metal supramolecular framework of 2D cobalt(II) coordination polymer with water-induced reversible crystal-to-amorphous transformation

Jureepan Piromchom [a], Nanthawat Wannarit [b], Jaursup Boonmak [a], Kittipong Chainok [c], Chaveng Pakawatchai [d], Sujittra Youngme [a,*]

[a] Materials Chemistry Research Unit, Department of Chemistry and Center of Excellence for Innovation in Chemistry, Faculty of Science, Khon Kaen University, Khon Kaen 40002, Thailand
[b] Department of Chemistry, Faculty of Science and Technology, Thammasat University, Rangsit Campus, Klong Luang, Pathumthani 12121, Thailand
[c] Department of Physics, Faculty of Science and Technology, Thammasat University, Rangsit Campus, Klong Luang, Pathumthani 12121, Thailand
[d] Department of Chemistry, Faculty of Science, Prince of Songkla University, Hat Yai, Songkhla 90112, Thailand

ARTICLE INFO

Article history:
Received 24 December 2013
Accepted 19 March 2014
Available online 26 March 2014

Keywords:
Cobalt(II)
4,4′-Bipyridine
Propionate
2D frameworks
Chromotropism
Structural transformation

ABSTRACT

A new flexible 3D supramolecular framework, $[Co(4,4'\text{-bipy})(pro)_2(H_2O)]$ (**1**) (4,4′-bipy = 4,4′-bipyridine and pro = propionate) has been prepared and structurally characterized. This compound crystallizes in monoclinic, space group $P2_1/c$. Each Co(II) cation shows an octahedral geometry. The Co(II) ions are assembled by the bridging propionate and 4,4′-bipyridine ligands in *c* and *a* axes, generating an infinite 2D layer. These 2D layer networks are further linked to one another by hydrogen bonding interactions, leading to a 3D supramolecular framework. Interestingly, compound **1** exhibits water-induced reversible crystal-to-amorphous transformation with chromotropism confirmed by spectroscopic techniques, elemental analysis, TGA, and XRPD. Thus, dehydrated amorphous form, $Co(4,4'\text{-bipy})(pro)_2$ (**1A**), may be utilized as an indicator for humidity.

The construction of metal-organic frameworks (MOFs) is currently attracting considerable attention because of their intriguing molecular topologies and crystal packing motifs, along with their potential applications such as adsorption, separation, ion exchange, catalysis, magnetism, optics, and electrical conductivity [1,2]. One of the important properties of MOFs is the framework flexibility which exhibits solid-state structural transformations with breaking, making, or rearrangement of bonds driven by chemical stimuli [3–5]. The structural transformations are generally accompanied by removal or exchange of guest, changes in coordination number of metal containing nodes, and conformational changes in flexible parts of organic ligands [3]. The water-induced structural reversible transformation is typically found in the dynamic and flexible coordination frameworks supported by weak intermolecular interactions, such as hydrogen bonds, π–π stacking, van der Waals forces, and others. Therefore, the solvent molecules may also play a key role by acting as an essential support to the structure of the host framework and it is important for expanding the field of crystal engineering by controlling the weak interaction of MOFs [3–5].

From our previous work, the reversible thermal dehydration and rehydration of 1D coordination framework $[Co(3,5\text{-pydc})(H_2O)_4]_n(H_2O)_n$; 3,5-pydc = 3,5-pyridinedicarboxylate have been reported [6]. The reversibility is driven by strong hydrogen bonding between guest water and coordinated water molecules and other components. Without guest water like a 2D coordination network $[Co(3,5\text{-pydc})(H_2O)_2]_n$, the irreversibility is observed. Herein, we report the contradictory case, the highly stable 3D supramolecular framework $[Co(4,4'\text{-bipy})(pro)_2(H_2O)]$ (**1**). Its 2D coordination layers are assembled by hydrogen bonding interactions, leading to a 3D supramolecular framework. This compound shows a reversible crystal-to-amorphous transformation upon desorption and resorption processes.

Single-crystal X-ray structural analysis shows that compound **1** is a 2D coordination network. The asymmetric unit consists of one cobalt atom, one 4,4′-bipy ligand, two pro ligands, and one coordinated water molecule (Fig. 1a, and Fig. S1) [7,8]. Each Co(II) ion exhibits a distorted octahedral geometry; the coordinate environment comprises of two O atoms from two different pro bridges, one O atom from water molecule and one O atom from a monodentate, terminal pro ligand, forming a square base (Fig. 1b, Fig. S1 and Table S1), while two axial positions of octahedron are completed by two N atoms from different 4,4′-bipy ligands (Table S1). These Co(II) ions are linked by the bridging 4,4′-bipy ligand (N(1) and N(2)) in *a* axis and the bridging pro ligand (O(3) and O(4)) along *c* axis, leading to an infinite 2D layer network (Fig. 1c and Fig. S2) leaving a water molecule and a remaining monodentate propionate as the terminal ligands in which both coordinated water and the uncoordinated O(2) of non-bridging propionate

* Corresponding author. Fax: +66 4320 2373.
E-mail address: sujittra@kku.ac.th (S. Youngme).

http://dx.doi.org/10.1016/j.inoche.2014.03.015
1387-7003/

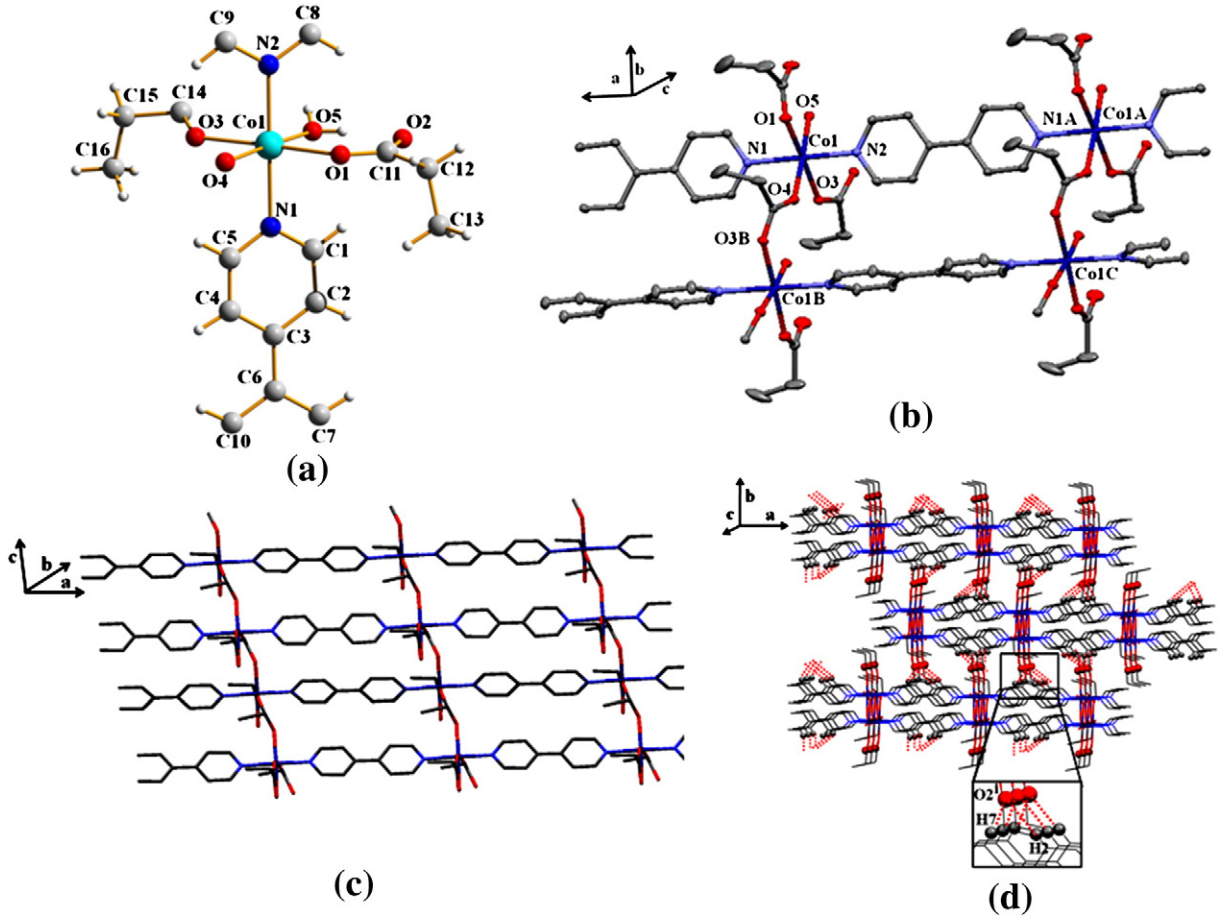

Fig. 1. Perspective view of **1** showing, (a) asymmetric unit and (b) coordination environment of the cobalt atom. (c) Crystal packing diagram of 2D layer structure in *ac* plane. (d) Crystal packing diagram of 3D supramolecular network, assembled by hydrogen bonding interactions. [Symmetry codes: A = −*x*, −*y*, −*z*; B = −*x*, 1/2-+*y*, 1/2-*z*; C = *x*, 1/2-*y*, 1/2 + *z*, i = 2 − *x*, 1 − *y*, 1 − *z*].

ligand are hydrogen-bonded (O(5) – H(6w)···O(2)) to one another (Fig. S3a). These 2D layers of compound **1** are linked to one another by strong interlayer hydrogen bonding among the uncoordinated O atom of the monodentate, terminal propionate ligands and H atoms of 4,4′-bipy ligand (C(2) – H(2)···O(2) and C(9) – H(7)···O(2)) with H···O distances of 2.481(19) and 2.364(19) Å (see Table S2), leading to a 3D supramolecular framework (Fig. S3b).

To assess the thermal stability, TGA was recorded for the single-phase polycrystalline samples in the temperature range of 30–800 °C. During the heating process, the TGA profile of **1** indicates the release of one coordinated water molecule at the first step of weight loss which is in the temperature range of 100–134 °C (found, 3.81%; anal. calcd, 4.21%), resulting to the dehydrated form of Co(4,4′-bipy)(pro)$_2$ (**1A**), which is stable up to ≈215 °C and then the structure rapidly decomposes at higher temperature, as shown in Fig. S4.

The dynamic structural behaviors of **1** relating to their dehydration and rehydration processes are studied by elemental analyses, XRPD, and spectroscopic techniques. When the single crystals of **1** were heated to 150 °C in air for 20 min, these crystals suddenly lose their crystallinity and the color changes from orange (**1**) to pink (**1A**). Then this non-crystalline solid was exposed to water vapor for 12 h and the color of the solid **1A** was returned to that of the original crystals **1′**, as shown

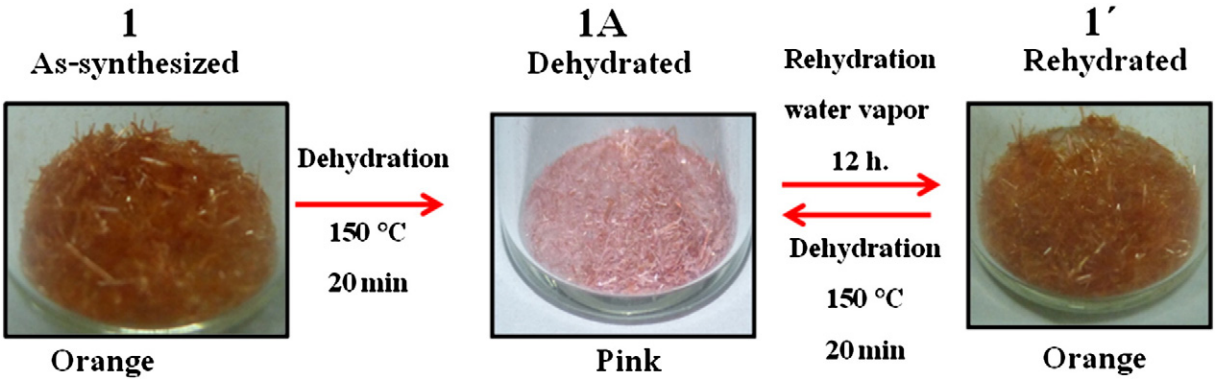

Fig. 2. Change in color during de- and rehydration in crystalline sample.

in Fig. 2 and Fig. S5. For this, the solid-state UV–vis diffuse reflectance spectra as shown in Fig. S6, clearly show that the bands observed in **1** and **1′** correspond very well to the identical transitions causing the same color of products, and evidence that **1** and **1′** have the same Co(II) environments. This spectral feature agrees with the typical d–d transitions of high spin Co(II) in distorted octahedral geometry with two broad bands at 471 and 1180 nm, assigned to the ν_3: $^4T_{1g} \rightarrow {}^4T_{1g}(P)$ and ν_1: $^4T_{1g} \rightarrow {}^4T_{2g}$, transitions, respectively [9]. Whereas the amorphous form **1A** shows different d–d transitions with three broad bands, ν_3: $^4T_{1g} \rightarrow {}^4T_{1g}(P)$ which is splitted into two shoulders at around 484 nm and 518 nm (^4E_g and $^4A_{2g}$), ν_2: $^4T_{1g} \rightarrow {}^4A_{2g}$ at 656 nm and then ν_1: $^4T_{1g} \rightarrow {}^4T_{2g}$ which is splitted into two shoulders at around 934 nm and 1337 nm ($^4B_{2g}$ and ^4E_g), giving the distinctive pink color and corresponding to the tetragonally distorted octahedral geometry [9]. Furthermore, the IR spectra also confirm the structural transformation behavior in **1**, as shown in Fig S7. In **1A**, the broad and strong peaks of O–H stretching around 3300 cm^{-1} and H–O–H bending around 1500–1600 cm^{-1} of coordinated water molecule disappear, resulting to the sharper IR spectrum with different splitting feature and a shift in some peak positions. In contrast, these features are removed in the IR spectrum of the rehydrated form **1′**, which are identical to that of the as-synthesized **1**. The XRPD pattern of the as-synthesized product closely match the simulated one from the single-crystal data (Fig. S8). However, the XRPD pattern of dehydrated **1A** shows peak disappearance, indicating that the dehydrated Co(4,4′-bipy)$(pro)_2$ (**1A**) is in an amorphous phase (anal. calcd: C, 53.19; H, 5.02; N, 7.75%. Found: C, 52.26; H, 5.04; N, 7.61%) which is formed by the collapse of supramolecular structure of **1** accompanied with the destruction of hydrogen bonding networks when all water molecules are removed. Interestingly, this amorphous phase **1A** can be restored to the original crystalline phase of **1′** in which the color returns to that of the original color after being exposed in water vapor for 24 h, as indicated by elemental analysis with the chemical composition of [Co(4,4′-bipy)$(pro)_2(H_2O)$] (**1′**) (anal. calcd: C, 50.67; H, 5.32; N, 7.39%. Found: C, 50.34; H, 5.28; N, 7.42%) and the XRPD measurement results. The restored solid has the same XRPD pattern as the simulated one from the single-crystal X-ray diffraction data of **1**. This behavior was also investigated for other solvents vapor such as methanol, ethanol, acetone, acetonitrile, dichloromethane, DMF and DMSO, but sensitive only with water vapor.

In the present case, although water molecule does not directly involve in the reversible crystal-to-amorphous transformation but induces the strong interlayer hydrogen bonding, after heating, water molecule is removed with the breaking of O(5)–H(6w)···O(2) hydrogen bonds in the layer (Fig. S3). This consequently breaks the strong interlayer hydrogen bonds (C(2)–H(2)···O(2) and C(9)–H(7)···O(2)) as the uncoordinated O(2) atom of terminal propionate group may move toward metal center for weak coordination, thus immediately destroying such hydrogen bonds between layers.

In summary, a new 2D coordination framework **1** has been successfully prepared and structurally characterized. The layer networks are linked to one another by hydrogen bonds, leading to a 3D supramolecular framework. Compound **1** exhibits reversible structural transformation from the crystal form (**1**) to the amorphous powder (**1A**) with the color changes, triggered by the weak intermolecular interactions during the removal and restoration of water molecule. This work may have potential application as adsorbent material for moisture.

Acknowledgments

Financial support has been provided by the Thailand Research Fund (Grant No. BRG5680009), the Higher Education Research Promotion and National Research University Project of Thailand, Office of the Higher Education Commission, through the Advanced Functional Materials Cluster of Khon Kaen University and the Center of Excellence for Innovation in Chemistry (PERCH-CIC), Office of the Higher Education Commission, Ministry of Education, Thailand.

Appendix A. Supplementary data

Supplementary material X-ray crystallographic files in CIF format (for compound **1** (CCDC No. 977060)). Supplementary data to this article can be found online at http://dx.doi.org/10.1016/j.inoche.2014.03.015.

References

[1] Z.-Y. Liu, E.-C. Y, L.-L. Li, X.-J. Z, A reversible SCSC transformation from a blue metamagnetic framework to a pink antiferromagnetic ordering layer exhibiting concomitant solvatochromic and solvatomagnetic effects, Dalton Trans. 41 (2012) 6827–6832.
[2] T.R. Cook, Y.-R. Zheng, P.J. Stang, Metal-organic frameworks and self-assembled supramolecular coordination complexes: comparing and contrasting the design, synthesis, and functionality of metal-organic materials, Chem. Rev. 113 (2013) 734–777.
[3] A. Kondo, H. Kajiro, H. Noguchi, L. Carlucci, D.M. Proserpio, G. Ciani, K. Kato, M. Takata, H. Seki, M. Sakamoto, Y. Hattori, F. Okino, K. Maeda, T. Ohba, K. Kaneko, H. Kanoh, Super flexibility of a 2D Cu-based porous coordination framework on gas adsorption in comparison with a 3D framework of identical composition: framework dimensionality-dependent gas adsorptivities, J. Am. Chem. Soc. 133 (2011) 10512–10522.
[4] J. Boonmak, M. Nakano, N. Chaichit, C. Pakawatchai, S. Youngme, Water-induced reversible structural phase transformation with chromotropism in metal supramolecular frameworks containing aminopyrazine and sulfate anions, Dalton Trans. 39 (2010) 8161–8167.
[5] A. Cheansirisomboon, C. Pakawatchai, S. Youngme, Solvent-induced reversible crystal-to-amorphous transformation properties of cobalt(II) 4-aminomethylpyridine-sulfate with chromotropism, Aust. J. Chem. 66 (2013) 477–484.
[6] A. Cheansirisomboon, C. Pakawatchai, S. Youngme, 2D–1D structural phase transformation of Co(II) 3,5-pyridinedicarboxylate frameworks with chromotropism, Dalton Trans. 41 (2012) 10698–10706.
[7] Crystal data for **1**: formula: $CoC_{16}H_{20}N_2O_5$, $M_r = 379.27$, Monoclinic, space group $P2_1/c$, $a = 11.4322(5)$, $b = 17.8277(7)$, $c = 8.5398(3)$ Å, $\alpha = 90.00°$ $\beta = 103.9910(10)°$ $\lambda = 90.00°$ $V = 1688.86(12)$ $Å^3$, $Z = 4$; $D_c = 1.492$ g cm^{-3}, $F(000) = 788.0$, $T = 150(2)$ K, $R_1 = 0.0318$, $wR_2 = 0.0723$, for 4197(0.0300) unique reflections and 259 parameters, $S = 1.081$. Structural data for **1** was collected on a Bruker Smart Apex CCD with graphite monochromated Mo Kα radiation. The struture was solved by direct methods and refined with the full matrix least-squares technique using the SHELXS-97 and SHELXL-97 programs [8]. CCDC: **1**, 977060.
[8] G.M. Sheldrick, SHELXL-97 Program for X-ray Crystal Structure Refinement, University of Göttingen, Göttingen, Germany, 1997.
[9] S.-J. Fu, C.-Y. Cheng, K.-J. Lin, A reversible octahedral to trigonal–bipyramidal cobalt coordination change in an aquo-accessible coordination network, Cryst. Growth Des. 7 (2007) 1381–1384

Inorganic Chemistry Communications 40 (2014) 59–61

Contents lists available at ScienceDirect

Inorganic Chemistry Communications

journal homepage: www.elsevier.com/locate/inoche

Synthesis, crystal structure and water-induced reversible crystal-to-amorphous transformation property of $[Co_2(2,4\text{-pydc})_2(bpa)(H_2O)_6](H_2O)_2$

Jureepan Piromchom [a], Nanthawat Wannarit [b], Jaursup Boonmak [a], Chaveng Pakawatchai [c], Sujittra Youngme [a,*]

[a] Materials Chemistry Research Unit, Department of Chemistry and Center of Excellence for Innovation in Chemistry, Faculty of Science, Khon Kaen University, Khon Kaen 40002, Thailand
[b] Department of Chemistry, Faculty of Science and Technology, Thammasat University, Rangsit Campus, Klong Luang, Pathumthani 12121, Thailand
[c] Department of Chemistry, Faculty of Science, Prince of Songkla University, Hat Yai, Songkhla 90112, Thailand

ARTICLE INFO

Article history:
Received 19 September 2013
Accepted 23 November 2013
Available online 1 December 2013

Keywords:
Dinuclear cobalt(II)
2,4-Pyridinedicarboxylic acid
1,2-Bis(4-pyridyl)ethane
Hydrogen bonding
Structural transformation

ABSTRACT

The dinuclear Co^{II} coordination compound with empirical formula $[Co_2(2,4\text{-pydc})_2(bpa)(H_2O)_6](H_2O)_2$ (**1**); bpa = 1,2-bis(2,4-pyridyl)ethane, 2,4-pydc = 2,4-pyridinedicarboxylate anion, has been synthesized and õcharacterized by elemental analysis, single crystal X-ray diffraction, IR and UV–vis spectra, TGA and XRPD. Compound **1** is a symmetry-related dinuclear compound consisting of two six coordinated cobalt atoms, one bpa ligand, two 2,4-pydc ligands and two lattice water molecules. Each Co^{II} ion is coordinated by one oxygen atom and one nitrogen atom from 2,4-pydc bidentate chelate ligand, one nitrogen atom of bpa bidentate bridging ligand and three water molecules, giving a distorted octahedral geometry with CoN_2O_4 chromophore. The crystal packing of this compound reveals a novel 3D supramolecular network, formed by hydrogen-bonding and C–H···π interactions. Investigations of the dynamic structural transformation behavior demonstrate that the title compound exhibits a solvent-induced reversible crystal-to-amorphous transformation with chromotropism when exposed to water vapor. This indicates that the dehydrated amorphous form, $Co_2(2,4\text{-pydc})_2(bpa)(H_2O)_2$ (**1A**), may be utilized as an indicator for humidity.

The design and synthesis of extended frameworks via supramolecular interactions represent a new area of considerable interest [1,2]. In particular, hydrogen bonding has been exploited for molecular recognition associated with biological activity, and for engineering of molecular solids [1,2]. Much progress has been made in the construction of organic building blocks into 1D, 2D and 3D hydrogen-bonding architectures, and the use of metal complexes as building blocks to assemble multidimensional frameworks by hydrogen bonding has also attracted much recent attention [3]. Recently, flexible and dynamic coordination compounds, which can change their structures in response to external stimuli, have attracted growing interest since they are important for the development of certain devices and sensors [4–11]. The guest-induced crystalline-to-amorphous transformation and the guest-induced reverse transformation are typically found in the dynamic and flexible coordination frameworks supported by weak intermolecular interactions, such as hydrogen bonds, π–π stacking, van der Waals forces, and others. Therefore, the guest molecules may also play a key role by acting as an essential support to the structure of the host framework [12–14]. From our previous works, we reported the reversible thermal dehydration and rehydration of the supramolecular frameworks, $[M(H_2O)_4(ampyz)_2][M(H_2O)_6](SO_4)_2(H_2O)_2$ (M = Co^{II}, Fe^{II} and mixed Co^{II}/Fe^{II}, ampyz = 2-aminopyrazine) [15] and $[Co(3,5\text{-pydc})(H_2O)_2]_n$, $[Co(3,5\text{-pydc})(H_2O)_4]_n(H_2O)_n$; 3,5-pydc = 3,5-pyridinedicarboxylate [16] and then $[Co(Hampy)_2(H_2O)_4](SO_4)_2(H_2O)_3$; ampy = 4-aminomethylpyridine [17]. The reversibility is driven by strong hydrogen bonding between lattice and coordinated water molecules and other components.

Herein, we report highly stable 3D supramolecular framework $[Co_2(2,4\text{-pydc})_2(bpa)(H_2O)_6](H_2O)_2$ (**1**) which contains strong intermolecular hydrogen bonding generated from coordinated and uncoordinated water molecules (Fig. 1). This compound shows a reversible crystal-to-amorphous transformation upon desorption and resorption processes, which is verified by elemental analysis, thermogravimetric analysis (TGA), X-ray powder diffraction (XRPD), as well as spectroscopic identification.

Single-crystal X-ray structural analysis shows that complex **1** is a 3D supramolecular network structure crystallized in the triclinic *P*-1 space group [18]. The symmetry-related dinuclear compound consisting of two six coordinated cobalt atoms, one bpa ligand, two 2,4-pydc ligands and two lattice water molecules. Each Co^{II} ion is coordinated by one oxygen atom and one nitrogen atom from 2,4-pydc bidentate chelate ligand, one nitrogen atom of bpa ligand and three water molecules, this feature give a distorted octahedral geometry with CoN_2O_4 chromophore

* Corresponding author. Fax: +66 4320 2373.
E-mail address: sujittra@kku.ac.th (S. Youngme).

1387-7003/$ – see front matter © 2013 Elsevier B.V. All rights reserved.
http://dx.doi.org/10.1016/j.inoche.2013.11.035

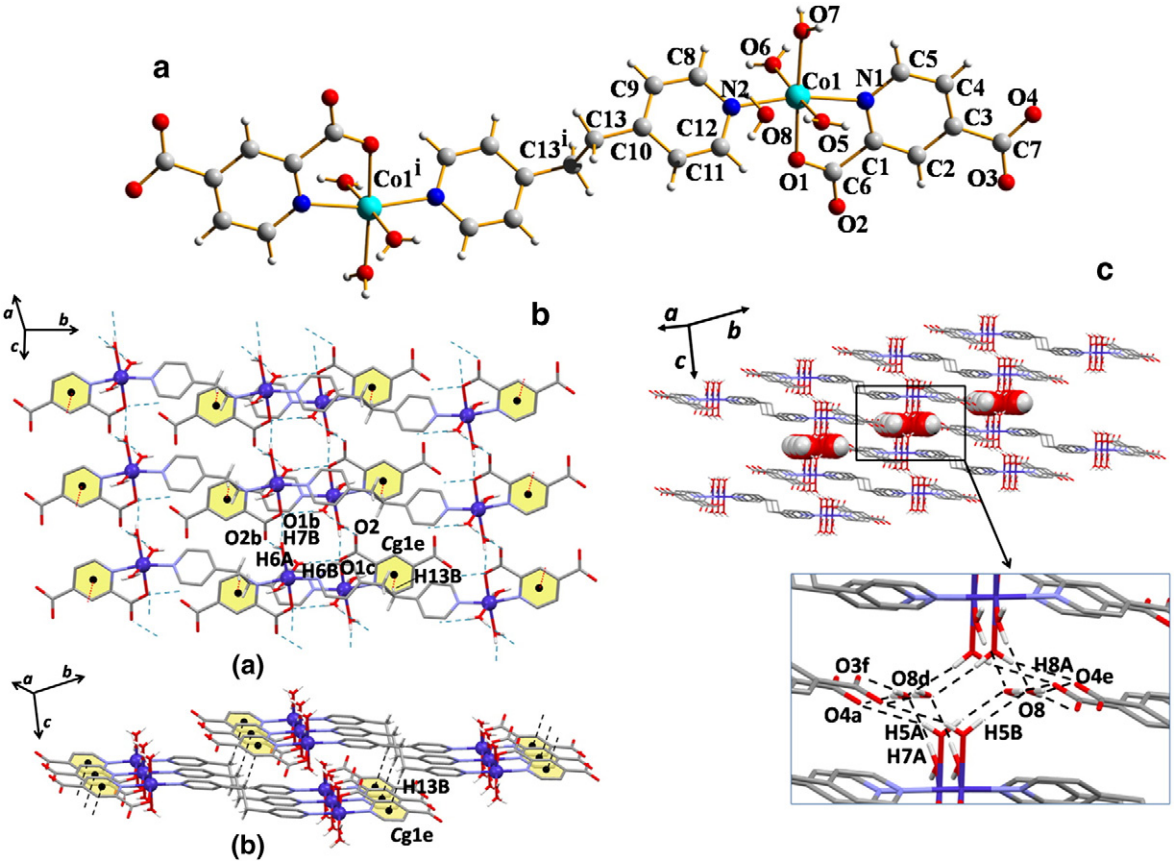

Fig. 1. (a) Perspective view of the coordination environment of the cobalt atom in compound **1**. (b) Crystal packing diagram of two-dimensional supramolecular structure of compound **1**, via hydrogen bonding and C–H···π interactions b(a) top view and b(b) side view. Hydrogen atoms on aromatic rings are omitted for clarity. (c) Crystal packing diagram of 3D supramolecular network of compound **1**, assembled by hydrogen bonding interactions. Hydrogen atoms on carbon atoms are omitted for clarity. [Symmetry codes: (i) = 1-x, -y, -z; (a) = 2-x, 2-y, 1-z; (b) = −1 + x, y, z; (c) = 1-x, 1-y, -z; (d) = 1-x, 1-y, 1-z; (e) = x, -1 + y, z and (f) = 1 + x, 1 + y, z].

(Fig. 1a and Fig. S1). The bpa bidentate bridging ligand links between both chromophores in the axial positions. The Co1–N and Co1–O distances are in the range of 2.1081(14)–2.1466(14) Å and 2.0696(15)–2.1116(16) Å, respectively. The selected bond distances and angles are shown in Supplementary Material. These dimeric units are connected to each other via hydrogen bonds with distances of 2.724(2), 2.974(2) and 2.970 (2) Å for O6–H6A···O2b, O7–H7B···O1b and O6–H6B···O1c, respectively and C–H···π interactions with distances of 2.78 Å for C13–H13B···Cg1e, generating two-dimensional network as shown in Fig. 1b and Fig. S2. Details of the hydrogen bonding are given in Table S1. These 2D layers are assembled into a three-dimensional supramolecular framework as by hydrogen-bonding interactions through lattice water molecules with distances of 2.803(2) Å, 2.682(2), 2.764(3) and 2.680(2) for O5–H5B···O8, O7–H7A···O8d, O8–H8A···O4e and O8–H8B···O3f and between coordinated water and caboxylate group of 2,4-pydc ligand with distance of 2.644(2) Å for O5–H5A···O4a (Fig. 1c and Fig. S3).

Compound **1** contains both guest and coordinated water molecules. The stability and dynamic structural behavior of **1** relating to their dehydration and rehydration processes are studied by TGA, elemental analyses, powder X-ray diffraction UV–vis and IR spectra, and XRPD. TGA (Fig. S4) reveals a weight loss of six water molecules in a range of 100–170 °C (calcd 11.6%, obsd 11.3%). When the single-crystals of **1** were heated at 200 °C in air for 40 min, these crystals suddenly lose their crystallinity and the color changed from orange to purple. Then these non-crystalline solids **1A** were exposed to the laboratory air for 24 h and the color of solids **1A** returned to that of original crystals. Consequently, the bulk sample of **1** was used to study in detail. The dehydrated **1A** was obtained by heating the bulk samples at 200 °C in air for 24 h and the rehydrated **1′** was obtained by exposing the dehydrated sample to water vapor for 24 h at room temperature without condensation (Fig. 2). The XRPD pattern of **1** is shown in Fig. S5. The elemental analysis, TGA and XRPD pattern results indicate that the chemical composition of the powder is $Co_2(2,4\text{-pydc})_2(bpe)(H_2O)_2$ (**1A**) in an amorphous phase (Anal. Calcd: C, 46.58; H, 3.61; N, 8.36%. Found: C, 45.91; H, 3.92; N, 7.95%). Interestingly, this amorphous phase **1A** can be restored to the original crystalline phase of **1′** in which the color returns to that of the original after being exposed in water vapor for 24 h, as indicated by elemental analysis with the chemical composition

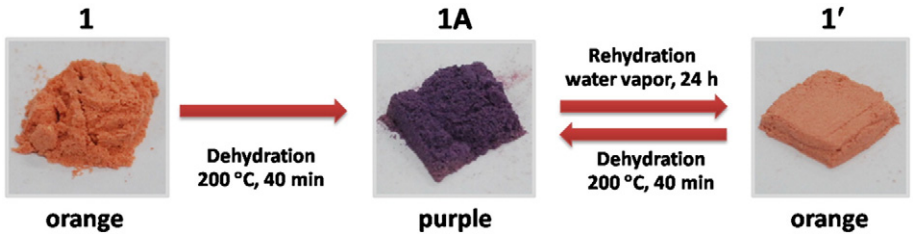

Fig. 2. Change in color during de- and rehydration processes in bulk samples.

of $[Co_2(2,4\text{-pydc})_2(bpe)(H_2O)_6](H_2O)_2$ (**1**) (Anal. Calcd: C, 40.22; H, 4.41; N, 7.22%. Found: C, 39.54; H, 4.43; N, 7.06%) and the XRPD measurement results. The restored solid has the same XRPD pattern as the simulated one from the single-crystal X-ray diffraction data of **1** as shown in Fig. S5, indicating that **1′** and **1** are the same compound. These results suggest the crystalline-to-amorphous and amorphous-to-crystalline transformations in supramolecular network of **1** triggered by the hydration control. The heating and exposing procedures were repeated several times to demonstrate the reversibility of the de- and rehydration processes. Furthermore, this structural change of bulk sample is accompanied with a remarkable color change (Fig. 2) as confirmed by the solid-state UV–vis diffuse reflectance spectra (Fig. S6). The electronic spectra clearly show that the bands observed in **1** and **1′** correspond very well to the identical transitions causing the same color of products, and evidence that **1** and **1′** have the same Co^{II} environments. That of the crystalline form **1** and **1′** agrees with the typical d–d transitions of high spin Co^{II} in distorted octahedral geometry with two broad bands at 498 and 1146 nm, which are assigned to the $^4T_{1g} \rightarrow {}^4T_{1g}(P)$, and $^4T_{1g} \rightarrow {}^4T_{2g}$ transitions, respectively. The amorphous form **1A** also shows the same d–d transitions with two broad bands, but remarkably shifted to 560 (Δ ~62) and 1190 (Δ ~44) nm, resulting in distinctive purple color and corresponding to the high-spin Co^{II} in distorted octahedral geometry with different type of distortion [19]. The chromotropic behavior of this compound is principally ascribed to the changes of the d-orbital energy level, induced by the drastic change in the coordination environments around the metal center during water de- and resorption processes. In addition, these results agree with the reversible change of the vibrational band in IR spectra (Fig. S7) where the broader bands are observed for the amorphous phase. In contrast, this feature is removed for the IR spectra of the rehydrated form, which are identical to those of the as-synthesized **1**.

All of these results confirm the water-induced crystalline-to-amorphous phase transformation in the supramolecular network of **1** with reversible processes. Remarkably, the reversibility of the water adsorption and the change in the coordination environment can be visualized by the change in color of the compound. This behavior takes place in water which could be a dissolution/recrystallization process rather than a solvent-induced solid-state reaction as this involves structural reorganization of the supramolecular framework or rearrangements of the molecules interacting by inter-molecular hydrogen bonds and non-covalent contacts [20].

In summary, a novel 3D supramolecular network formed by hydrogen-bonding and C–H···π interaction, has been synthesized and structurally characterized. The successful synthesis of **1** shows that strong intermolecular interactions (C–H···π and hydrogen-bonding interactions) contribute to the formation of higher-dimensional network. Thermal decomposition, elemental analysis, XRPD, and spectroscopic results indicate that the transformation from the crystal form of $[Co_2(2,4\text{-pydc})_2(bpa)(H_2O)_6](H_2O)_2$ (**1**) to the amorphous powder of $Co_2(2,4\text{-pydc})_2(bpa)(H_2O)_2$ (**1A**) is reversible with the color changes. The original crystalline form is recovered from the collapsed amorphous sample by the restoration of water molecules. Thus, the desorption/resorption processes involving the weak intermolecular interactions can trigger the reversible crystal-to-amorphous transformation.

Acknowledgments

Financial support has been provided by the Thailand Research Fund (Grant No. BRG5680009), the Higher Education Research Promotion and National Research University Project of Thailand, Office of the Higher Education Commission, through the Advanced Functional Materials Cluster of Khon Kaen University and the Center of Excellence for Innovation in Chemistry (PERCH-CIC), Office of the Higher Education Commission, Ministry of Education, Thailand.

Appendix A. Supplementary material

Supplementary data to this article can be found online at http://dx.doi.org/10.1016/j.inoche.2013.11.035.

References

[1] G.A. Hogan, N.P. Rath, A.M. Beatty, A stable hydrogen-bonded coordination network with removable guests, Cryst. Growth Des. 11 (2011) 3740–3743.
[2] T.R. Cook, Y.-R. Zheng, P.J. Stang, Metal–organic frameworks and self-assembled supramolecular coordination complexes: comparing and contrasting the design, synthesis, and functionality of metal–organic materials, Chem. Rev. 113 (2013) 734–777.
[3] S.-S. Yu, H. Zhou, H.-B. Duan, Three-dimensional hydrogen bonding framework in the crystal structure of a zinc(II) complex of imidazole multicarboxylic acid, Synth. React. Inorg. Met. Org. Nano Met. Chem. 43 (2013) 1521–1524.
[4] E.Y. Lee, M.P. Suh, A robust porous material constructed of linear coordination polymer chains: reversible single-crystal to single-crystal transformations upon dehydration and rehydration, Angew. Chem. Int. Ed. 43 (2004) 2798–2801.
[5] E.Y. Lee, S.Y. Jang, M.P. Suh, Multifunctionality and crystal dynamics of a highly stable, porous metal–organic framework $[Zn_4O(NTB)_2]$, J. Am. Chem. Soc. 127 (2005) 6374–6381.
[6] K. Biradha, M. Fujita, A springlike 3D-coordination network that shrinks or swells in a crystal-to-crystal manner upon guest removal or readsorption, Angew. Chem. Int. Ed. 41 (2002) 3392–3395.
[7] K. Biradha, Y. Hongo, M. Fujita, Crystal-to-crystal sliding of 2D coordination layers triggered by guest exchange, Angew. Chem. Int. Ed. 41 (2002) 3395–3398.
[8] D.-X. Xue, W.-X. Zhang, X.-M. Chen, H.-Z. Wang, Single-crystal-to-single-crystal transformation involving release of bridging water molecules and conversion of chain helicity in a chiral three-dimensional metal–organic framework, Chem. Commun. (2008) 1551–1553.
[9] K. Takaoka, M. Kawano, M. Tominaga, M. Fujita, In situ observation of a reversible single-crystal-to-single-crystal apical-ligand-exchange reaction in a hydrogen-bonded 2D coordination network, Angew. Chem. Int. Ed. 44 (2005) 2151–2154.
[10] C.-D. Wu, W. Lin, Highly porous, homochiral metal–organic frameworks: solvent-exchange-induced single-crystal to single-crystal transformations, Angew. Chem. Int. Ed. 44 (2005) 1958–1961.
[11] D.N. Dybtsev, H. Chun, K. Kim, Rigid and flexible: a highly porous metal–organic framework with unusual guest-dependent dynamic behavior, Angew. Chem. Int. Ed. 43 (2004) 5033–5036.
[12] H.K. Chae, D.Y. Siberio-Pérez, J. Kim, Y.B. Go, M. Eddaoudi, A.J. Matzger, M. O'Keeffe, O.M. Yaghi, A route to high surface area, porosity and inclusion of large molecules in crystals, Nature 427 (2004) 523–527.
[13] P. Sozzani, S. Bracco, A. Comotti, L. Ferretti, R. Simonutti, Methane and carbon dioxide storage in a porous van der Waals crystal, Angew. Chem. Int. Ed. 44 (2005) 1816–1820.
[14] T.K. Prasad, M.V. Rajasekharan, A novel water octamer in Ce(dipic)2(H2O)3·4H2O: crystallographic, thermal, and theoretical studies, Cryst. Growth Des. 6 (2006) 488–491.
[15] J. Boonmak, M. Nakano, N. Chaichit, C. Pakawatchai, S. Youngme, Water-induced reversible structural phase transformation with chromotropism in metal supramolecular frameworks containingaminopyrazine and sulfate anions, Dalton Trans. 39 (2010) 8161–8167.
[16] A. Cheansirisomboon, C. Pakawatchai, S. Youngme, 2D–1D structural phase transformation of Co(II) 3,5-pyridinedicarboxylate frameworks with chromotropism, Dalton Trans. 41 (2012) 10698–10706.
[17] A. Cheansirisomboon, C. Pakawatchai, S. Youngme, Solvent-induced reversible crystal-to-amorphous transformation properties of cobalt(II) 4-aminomethylpyridine-sulfate with chromotropism, Aust. J. Chem. 66 (2013) 477–484.
[18] Crystal data for **1**: formula: $C_{26}H_{34}N_4O_{16}Co_2$, $M_r = 776.43$, Triclinic, space group *P*-1, $a = 6.0640(5)$, $b = 11.365(9)$, $c = 11.857(9)$ Å, $\alpha = 98.65(2)^\circ$ $\beta = 101.33(2)^\circ$ $\lambda = 102.75(2)$, $V = 765.31(11)$ Å^3, $Z = 1$; $D_c = 1.685$ g cm^{-3}, $F(000) = 400$, $T = 293(2)$ K, $R_1 = 0.0330$, $wR_2 = 0.0782$, for 3685 unique reflections and 249 parameters, $S = 1.064$. Structural data for **1** was collected on a Bruker Smart Apex CCD with graphite monochromated Mo Kα radiation. Their structures were solved by direct methods and refined with the full matrix least-squares technique using the SHELXS-97 and SHELXL-97 programs [21]. CCDC: **1**, 961055.
[19] M. Kurmoo, Magnetic metal–organic frameworks, Chem. Soc. Rev. 38 (2009) 1353–1379.
[20] A.N. Khlobystov, N.R. Champness, C.J. Roberts, S.J.B. Tendler, C. Thompson, M. Schroder, Anion exchange in co-ordination polymers: a solid-state or a solvent-mediated process? CrystEngComm 4 (2002) 426–431.
[21] G.M. Sheldrick, SHELXL-97 Program for X-ray Crystal Structure Refinement, University of Göttingen, Göttingen, Germany, 1997.

Inorganica Chimica Acta 403 (2013) 35–42

Contents lists available at SciVerse ScienceDirect

Inorganica Chimica Acta

journal homepage: www.elsevier.com/locate/ica

New 3D supramolecular networks built from 1D and 2D frameworks via π–π and H-bonding interactions: Topology and catalytic properties

Pongthipun Phuengphai [a], Sujittra Youngme [b,*], Narongsak Chaichit [c], Jan Reedijk [d,e]

[a] Department of Fundamental Science, Faculty of Science and Technology, Surindra Rajabhat University, Surin 32000, Thailand
[b] Materials Chemistry Research Unit, Department of Chemistry and Center of Excellence for Innovation in Chemistry, Faculty of Science, Khon Kaen University, Khon Kaen 40002, Thailand
[c] Department of Physics, Faculty of Science and Technology, Thammasat University Rangsit, Pathumthani 12121, Thailand
[d] Leiden Institute of Chemistry, Leiden University, P.O. Box 9502, 2300 RA Leiden, The Netherlands
[e] Department of Chemistry, College of Science, King Saud University, P.O. Box 2455, Riyadh 11451, Saudi Arabia

ARTICLE INFO

Article history:
Available online 9 April 2013

Coordination Polymers Special Issue

Keywords:
Metal organic frameworks
Heterogeneous catalysts
Cyanosilylation reaction

ABSTRACT

Two new metal-organic frameworks, $\{[Zn(dpe)(\mu\text{-}OOCCH_3)_2](H_2O)\}_n$ (**1**) and $\{[Zn_3(dpe)_4(\mu\text{-}OOCC_2H_5)_4](dpe)(ClO_4)_2\}_n$ (**2**) (dpe = 1,2-bis(4-pyridyl)ethene), have been prepared and investigated. Their structures were determined by X-ray crystallography. The different structures of both compounds indicate that the different steric constraints for a methyl group (acetato, compound **1**) and an ethyl group (propionato, compound **2**), as well as the counteranion effects (ClO_4^- for **2**), play an important role in the formation and structure of these coordination polymers. Compound **1** exhibits a 1D zig–zag polymeric chain based on mononuclear secondary building units. The replacement of the acetate by propionate ligands, in the presence of additional ClO_4^- during the synthesis procedure, gives rise to a 2D network that is assembled from trinuclear secondary building units (compound **2**). In addition, both compounds are further stabilized by π–π interactions and by hydrogen bonds to form intricate supramolecular frameworks. The 1D (**1**) and 2D (**2**) networks exhibit voids that contain guest water molecules for compound **1** and perchlorate/dpe for compound **2**. Both coordination compounds have been structurally characterized and the thermal stability, potential cation-exchange and selected catalytic properties have been investigated. Interestingly, both Zn(II) compounds act as active heterogeneous catalysts for the high-yield cyanosilylation of acetaldehyde in dichloromethane and show highly size-selective properties for the substrate benzaldehyde. The metal sites in each compound have been studied in some more detail by using doped species with Mn(II) and Cu(II) and the EPR properties.

1. Introduction

The design and construction of coordination polymers, often called metal organic frameworks, have attracted great attention owing to their interesting topologies, their potential applications in catalysis, gas storage, molecular recognition, and their magnetic, electrical, and non-linear optical properties [1–10]. Generally, the preparation of such materials can be influenced by many factors, such as the nature of organic ligands, the coordination preference of central metal ion, the crystallization conditions, the metal/ligand ratio, and the reaction solvent system, etc. [11–16]. Numerous examples of metal organic frameworks were constructed making use of hydrogen bonding, π–π contacts, and/or other weak and non-covalent interactions [17,18]. In the vast amount of the reported work, a variety of 1D, 2D, and 3D metal organic frameworks have been successfully obtained via the use of coordinating functional groups, such as carboxylates, 4,4′-bpy-based ligands, and mixtures of both carboxylate and 4,4′-bpy ligands [19–22]. In coordination networks in general the 4,4′-bpy ligands may act in a bidentate bridging, or monodentate terminal modes, resulting in 1D linear, zigzag, ladder, molecular antenna railroads and chains, 2D bilayer, square and rectangular grid networks, or 3D non-interpenetrated and interpenetrated networks.

Therefore, the diversity and topologies on the molecular architecture have now been further extended by using a more flexible organic linker, i.e. 1,2-bis(4-pyridyl)ethene (dpe) (Scheme 1), during the synthesis of the coordination assembly and related to recent literature [23–27].

In the present study, the semi-flexible ligand dpe (see Scheme 1), the effect of the steric hindrance of different carboxylato ligands (acetato and propionato ligands) and the influence of the nature of the anion used, on the solid-state structure of the corresponding coordination materials have been investigated. Thus, multicomponent polymeric networks have been synthesized from zinc(II) ions,

* Corresponding author. Fax: +66 43 202 373.
E-mail address: sujittra@kku.ac.th (S. Youngme).

0020-1693/$ - see front matter © 2013 Elsevier B.V. All rights reserved.
http://dx.doi.org/10.1016/j.ica.2013.03.041

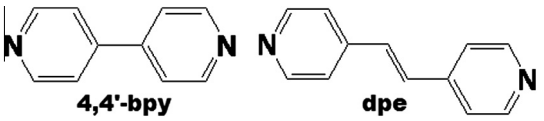

Scheme 1. The conformations of rigid ligand 4,4′-bpy and semi-flexible ligand dpe.

dpe and a carboxylato ligand. It appears that their single-crystal X-ray structures reveal a significant influence of a methyl (acetate) and an ethyl (propionate) group on the assembly of the coordination framework, as well as the effect of counteranion on the observed coordination topology. The compounds $\{[Zn(dpe)(\mu\text{-}OOCCH_3)_2](H_2O)\}_n$ (**1**) and $\{[Zn_3(dpe)_4(\mu\text{-}OOCC_2H_5)_4](dpe)(ClO_4)_2\}_n$ (**2**) have been synthesized and characterized using XRD and EPR of their doped Mn(II) and Cu(II) derivatives. The thermal stability and catalytic properties of both compounds in the cyanosilylation of aldehydes have been investigated. Furthermore, the potential use in cation-exchange for compound **2** has been explored.

2. Experimental

2.1. Materials and physical measurements

All commercially available reagents were used as received. FT-IR spectra were recorded on a Perkin–Elmer Paragon 1000 FT-IR spectrophotometer, equipped with a Golden Gate ATR device, using the reflectance technique (4000–300 cm^{-1}). Elemental analyses for C, H and N were performed with a Perkin–Elmer 2400 analyzer. Thermogravimetric analyses were carried out using a Perkin–Elmer Pyris Diamond analyzer in flowing nitrogen at a heating rate of 10 °C min^{-1}. The X-band powder EPR spectra were obtained on polycrystalline samples at room temperature and 70 K using a Bruker EMX-plus spectrometer with DPPH (g = 2.0036) as a reference.

2.2. Synthesis

2.2.1. Synthesis of $\{[Zn(dpe)(\mu\text{-}OOCCH_3)_2](H_2O)\}_n$ (**1**)

An aqueous solution (15 mL) of $Zn(NO_3)_2{\cdot}6H_2O$ (0.306 g, 1.0 mmol) was added to a solution of dpe (0.182 g, 1.0 mmol) in ethanol (10 mL). Next, an aqueous solution (20 mL) of NaO_2CCH_3 (0.138 g, 2.0 mmol) was added under continuous stirring. This solution was allowed to stand unperturbed for the slow evaporation of the solvent at room temperature, producing colorless needle crystals of 1 after a few days. Yield ca. 69%. Elemental *Anal.* Calc. for $C_{16}H_{18}N_2O_5Zn$ (383.71): C, 50.08; H, 4.73; N, 7.30. Found: C, 50.09; H, 4.84; N, 7.59%. IR (cm^{-1}): ν_{as}(COO) 1575, ν_s(COO) 1416, δ(O–C–O) 644.

2.2.2. Synthesis of $\{[Zn_3(dpe)_4(\mu\text{-}OOCC_2H_5)_4](dpe)(ClO_4)_2\}_n$ (**2**)

An aqueous solution (10 mL) of $Zn(NO_3)_2{\cdot}6H_2O$ (0.313 g, 1.0 mmol) was added to a solution of dpe (0.182 g, 1.0 mmol) in ethanol (10 mL). Subsequently, an aqueous solution (10 mL) of $NaCOOCH_2CH_3$ (0.201 g, 2.0 mmol) was added, followed by $KClO_4$ (0.152 g, 1.0 mmol) under continuous stirring. Next, a few drops of 98% CH_3CH_2COOH were added, yielding a clear colorless solution, which was allowed to stand unperturbed for the slow evaporation of the solvent at room temperature. Colorless crystals of 2 were collected from the solution by filtration after several days. Yield ca. 70%. Elemental *Anal.* Calc. for $C_{72}H_{70}Cl_2N_{10}O_{16}Zn_3$ (1598.46): C, 54.10; H, 4.41; N, 8.76. Found: C, 53.72; H, 4.74; N, 9.07%. IR (cm^{-1}): ν_{as}(COO) 1569, ν_s(COO) 1417, δ(O–C–O) 643, $\nu(ClO_4)$ 1104–1045.

Caution! Although no problems were encountered in this work, perchlorate salts are potentially explosive and should be handled in small quantities.

2.2.3. Synthesis of $\{[Zn_3(dpe)_4(\mu\text{-}OOCC_2H_5)_4](dpe)(ClO_4)_2\}_n$ (**2**) doped with Cu^{2+} (**2a**) and Mn^{2+} (**2b**)

An aqueous solution (10 mL) of $Zn(NO_3)_2{\cdot}6H_2O$ (0.313 g, 1.0 mmol) was added to a solution of dpe (0.184 g, 1.0 mmol) in ethanol (10 mL). Subsequently, an aqueous solution (10 mL) of $NaCOOCH_2CH_3$ (0.201 g, 2.0 mmol) was added, followed by $KClO_4$ (0.152 g, 1.0 mmol) and 0.003 g (0.002 mmol) of $Cu(NO_3)_2{\cdot}3H_2O$ (or 0.003 g $Mn(NO_3)_2{\cdot}4H_2O$ (0.002 mmol)) under continuous stirring. Next, a few drops of CH_3CH_2COOH 98% were added, yielding a clear colorless solution, which was allowed to stand unperturbed for the slow evaporation of the solvent at room temperature. After several days, colorless crystals of **2a** (or **2b**) were obtained. The crystals were filtered, washed with the mother liquor and dried in air. Yield ca. 66% (ca. 58% for **2b**). The IR spectra of **2a** and **2b** are similar to that of **2**.

2.3. Crystal structure determination

The X-ray single-crystal data for compounds **1** and **2** were collected at 293(2) K on a 1 K Bruker SMART CCD area detector diffractometer using graphite monochromated Mo Kα radiation (λ = 0.71073 Å) at a detector distance of 4.5 cm and swing angle of −35°. A hemisphere of the reciprocal space was covered by combination of three sets of exposures; each set had a different ϕ angle (0°, 88°, and 180°) and each exposure of 40 s covered 0.3° in ω. Data reduction and cell refinements were performed using the program SAINT [28]. An empirical absorption correction by using the SADABS [29] program was applied, which resulted in transmission coefficients ranging from 0.642 to 0.823 and 0.600 to 0.680 for compounds **1** and **2**, respectively. The structures were solved by direct methods and refined by full matrix least-squares method on $(F_{obs})^2$ with anisotropic thermal parameters for all non-hydrogen atoms using the SHELXTL-PC V 6.12 software package [30]. The H atoms were introduced at calculated positions and refined with a fixed geometry with respect to their carrier atoms. One water oxygen atom of **1** and the perchlorate groups of **2** were found disordered and were refined with site occupancies of 0.5. The crystal

Table 1
Crystal and refinement data for compounds **1** and **2**.

Compound	**1**	**2**
Empirical formula	$C_{16}H_{18}N_2O_5Zn$	$C_{72}H_{70}Cl_2N_{10}O_{16}Zn_3$
Formula weight	383.71	1598.46
T (K)	293(2)	293(2)
Crystal system	Monoclinic	Triclinic
Space group	$P2/c$	$P\bar{1}$
a (Å)	9.5897(6)	12.3805(9)
b (Å)	5.6970(4)	13.1086(9)
c (Å)	17.5177(9)	13.7188(9)
α (°)	90.00	110.40
β (°)	115.035	96.63
γ (°)	90.00	112.46
V (Å^3)	867.12	1847.39
Z	2	1
D_{calc} (g cm^{-3})	1.470	1.437
μ(mm^{-1})	1.443	1.111
F(000)	396	824
θ range (°)	2.34–27.99	2.21–28.00
Goodness-of-fit	1.089	1.052
Final R indices	R_1 = 0.0371	R_1 = 0.0623
[$I > 2\sigma(I)$]	wR_2 = 0.1049	wR_2 = 0.1578
R indices (all data)	R_1 = 0.0403, wR_2 = 0.1089	R_1 = 0.0754, wR_2 = 0.1709

$R_1 = \sum||F_o| - |F_c||/\Sigma|F_o|$, $wR_2 = [\sum[w(F_o^2 - F_c^2)^2]/\sum[w(F_o^2)^2]]^{1/2}$.

data and refinement details of the both compounds are listed in Table 1; selected bond lengths and angles of **1** and **2** are given in Tables 2 and 3.

2.4. Catalytic reactions

A typical cyanosilylation reaction was performed as follows: 40 mg (0.006 mmol, 0.2 mmol of Zn) of MOF catalyst was suspended in 5 mL of dry dichloromethane (CH_2Cl_2) or tetrahydrofuran (THF), followed by the addition of the aldehyde (1.5 mmol) and trimethylsilyl cyanide (3 mmol). The reaction mixtures were stirred at room temperature under argon. The reaction conversions as a function of time were determined by gas chromatography (GC) analysis.

3. Results and discussion

3.1. Synthesis and structure

Crystalline materials were obtained for both compounds prepared from zinc(II) ions, dpe and carboxylato ligands in ethanol–H_2O solvent mixtures. Other solvent combinations were used, i.e. methanol–H_2O and acetone–H_2O, but the solvent pair ethanol–H_2O gave the best results in terms of yield and quality of crystals. Moreover, other counter anions (i.e. PF_6^-, BF_4^- and $CF_3SO_3^-$) were examined. Unfortunately, the quality of these crystals was not good enough for single-crystal X-ray analysis. Compounds **1** and **2** exhibit different topologies, induced by the different carboxylate ligands used, as well as the counteranion effects (ClO_4^- for **2**), play an important role in the formation and structure of these coordination polymers.

The combination Zn(II)/dpe/acetate generates a 1D zig–zag polymeric chain of **1** resulting from the secondary building units with tetrahedral geometry (Fig. 2(A)). The complete replacement of acetate by propionate for the case of the ClO_4^- ion results in the formation of a 2D network (compound **2**; Fig. 5). This simple framework is built from trinuclear propionato-bridged units that are linked to two adjacent ones, to form a triple-stranded chain.

3.2. Crystal structure of $\{[Zn(dpe)(\mu\text{-}OOCCH_3)_2](H_2O)\}_n$ (*1*)

The 1D molecular structure of compound **1** exhibits only one type of zinc(II) ion, with a tetrahedral N_2O_2 coordination environment (Fig. 1). Each Zn(II) ion lies on an inversion centre and is surrounded by two oxygen atoms belonging to two acetato ligands and two nitrogen atoms occupying by two pyridine N-donors from two different (bridging) dpe moieties. Two acetato ligands [O1 and O1a] act as a monodentate terminal ligands. The Zn–O and Zn–N bond distances can be considered as normal for this type of ZnN_2O_2 coordination environment (Table 2) [31]. The distance Zn–O2 of 2.982(1) Å is too long to be considered as coordination.

The metal organic framework is formed from mononuclear units which are connected through two dpe ligands to the other Zn(II) ions, generating 1D zig–zag infinite chains (Fig. 2A). These chains show π–π interactions along dpe units (with centroid-to-centroid distances ranging from 3.711(1) to 4.704(1) Å) and are connected to each other producing the closely packed 2D layers (Fig. 2B). Each layer is linked to one layer above and to one layer below through hydrogen bonded lattice water molecules forming "ABAB.." layers (Fig. 2C), and the corresponding schematic mode, illustrated top layer and bottom layer by blue and green, respectively (Fig. 2D). The corners of these layers, made up by the $Zn(OOCH_3)_2$ groups, are surrounded by the disordered water molecules and all of these are connected to the acetato ligands in corners via relatively strong O–H···H hydrogen bonding interactions (O5a···O2 = 2.690(1) Å and O5b···O2 = 2.865(1) Å). Through these hydrogen bonds the zig–zag layers are connected with each other via the guest water molecules (O5) to form a 3D supramolecular network with an empty cavity (Fig. 3).

Table 2
Selected bond lengths (Å) and angles (°) for **1**.

Zn1–O1a	1.939(1)	O1a–Zn1–O1	100.5(1)
Zn1–O1	1.939(1)	O1a–Zn1–N1	124.6(1)
Zn1–N1	2.043(1)	O1–Zn1–N1	103.1(1)
Zn1–N1a	2.043(1)	O1a–Zn1–N1a	103.1(1)
		O1–Zn1–N1a	124.6(1)
		N1–Zn1–N1a	103.1(1)

Symmetry operation: (a) $1-x, y, 0.5-z$.

Table 3
Selected bond lengths (Å) and angles (°) for **2.**

Zn1–O2	1.992(6)	Zn2–O1a	2.095(5)
Zn1–N3	2.124(7)	Zn2–O1	2.095(5)
Zn1–O4	2.171(5)	Zn2–N4a	2.146(6)
Zn1–N1	2.183(6)	Zn2–N4	2.146(6)
Zn1–N2	2.202(6)	Zn2–O3	2.185(6)
Zn1–O3	2.220(4)	O1a–Zn2–N4a	89.8(2)
O2–Zn1–N3	99.9(3)	O1–Zn2–N4a	90.2(2)
O2–Zn1–O4	162.0(2)	O1a–Zn2–N4	90.2(2)
N3–Zn1–O4	98.1(3)	O1–Zn2–N4	89.7(2)
O2–Zn1–N1	91.6(3)	O1a–Zn2–O3	88.7(2)
N3–Zn1–N1	89.9(3)	O1–Zn2–O3	91.3(2)
O4–Zn1–N1	89.3(2)	N4a–Zn2–O3	90.7(2)
O2–Zn1–N2	90.6(2)	N4–Zn2–O3	89.3(2)
N3–Zn1–N2	89.1(3)	O1a–Zn2–O3a	91.3(2)
O4–Zn1–N2	88.7(2)	O1–Zn2–O3a	88.7(2)
N1–Zn1–N2	177.6(3)	N4a–Zn2–O3a	89.3(2)
O2–Zn1–O3	102.7(2)	N4–Zn2–O3a	90.7(2)
N3–Zn1–O3	157.3(3)		
O4–Zn1–O3	59.4(2)		

Symmetry operation: (a) $-x, 2-y, 1-z$.

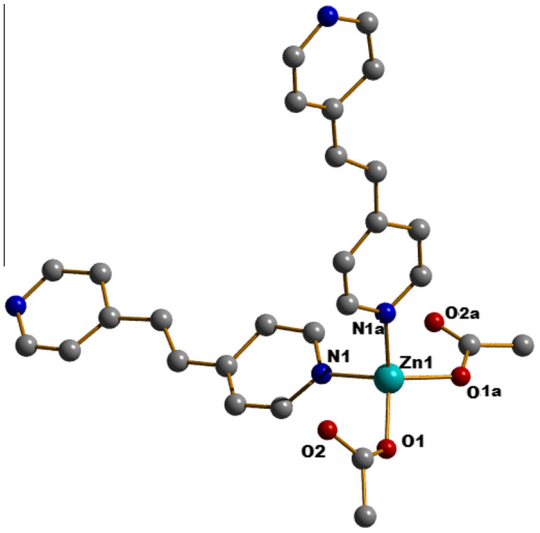

Fig. 1. Representation of part of the molecular structure of **1** showing the atom labeling scheme for the zinc(II) ion. The H atoms are not shown for clarity. Symmetry operations: (a) $1-x, y, 0.5-z$.

3.3. Crystal structure of $\{[Zn_3(dpe)_4(\mu\text{-}OOCC_2H_5)_4](dpe)(ClO_4)_2\}_n$ (*2*)

The influence of counteranion and steric effect on the molecular architecture has been investigated by using a propionato ligand

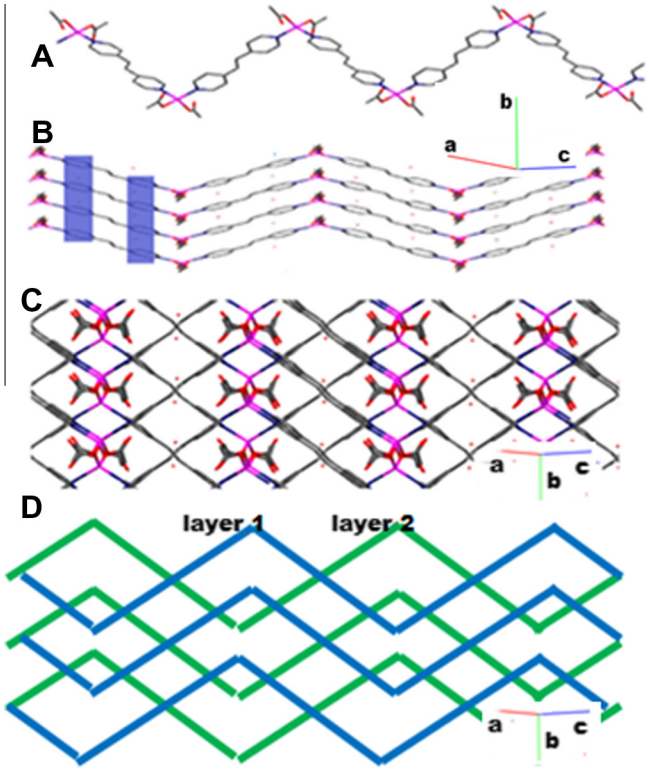

Fig. 2. (A) 1D zig–zag infinite chain of **1**, (B) the π–π interactions along dpe units form 2D layers, (C) and (D) each layer is stacked atop of each other to form a square grid structure in the top view and the corresponding schematic mode.

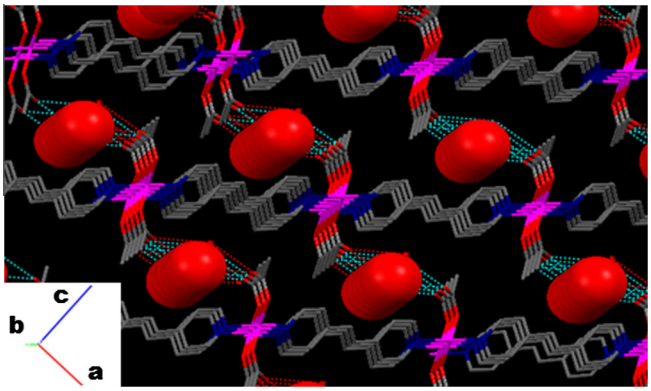

Fig. 3. 3D packing structure of **1** projected on the *bc* plane, and illustrating the intermolecular hydrogen bonding by the dotted lines.

during the synthesis of the coordination assembly from reaction of the $Zn(NO_3)_2{\cdot}6H_2O$, dpe and propionato ligand in an $EtOH/H_2O$ mixture with an incorporated ClO_4^- anion during synthesis procedure. Indeed, the solid-state structure of compound $\{[Zn_3(dpe)_4(\mu\text{-}OOCC_2H_5)_4](dpe)(ClO_4)_2\}_n$ (**2**), bearing ethyl groups, shows significant differences compared to that of **1** (holding methyl groups).

The 2D molecular structure of compound **2** exhibits two different types of zinc(II) ions with octahedral-based N_3O_3 (Zn1) and N_2O_4 (Zn2) geometries (Fig. 4). Zn1 is characterized by a strongly distorted octahedral coordination environment, owing to the small bite angle of the μ-O,O′,O′ bridging mode of one of the two propionato ligands (the angle O3–Zn1–O4 is only 59.4(2) Å; Table 3). The basal plane is constituted of three oxygen atoms belonging to two propionato ligands (O2, O3 and O4) and one dpe ligand (N3). The octahedron is completed by two dpe nitrogen atoms

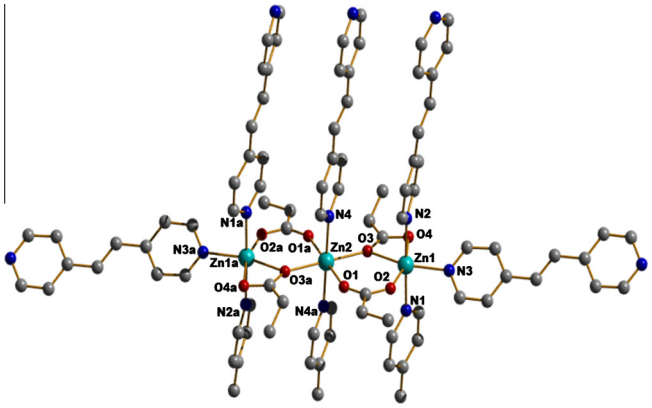

Fig. 4. Representation of the molecular structure of **2** showing the atom labeling scheme for the zinc(II) ions. The perchlorate anions, the lattice dpe molecules and the H atoms are not shown for clarity. Symmetry operations: (a) $-x$, $2-y$, $1-z$.

(N1 and N2), at the axial positions, linking Zn1 to two symmetry-related Zn1a ions, generating a polymeric chain exhibiting the sequence {Zn1, Zn1a, Zn1, Zn1a,...} along *c* axis (Fig. 5). The Zn–O and Zn–N bond distances are in normal ranges for this type of coordination moiety [32].

Zn2 lies on an inversion centre. The coordination environment around the Zn2 ion is an almost undistorted octahedron, since the basal angles, varying from 88.7(2)° to 91.3(2)°, are close to the ideal value of 90°. At the basal plane, Zn2 is coordinated by four oxygen atoms (O1, O3, O1a and O3a) from different propionato ligands. The axial positions are occupied by nitrogen atoms N4 and N4a, belonging to two dpe ligands (located on an inversion centre) at common distances. Zn2 is bridged to two symmetry-related Zn1 ions via two μ-O,O′- and two μ-O,O′,O′-propionato ligands, generating a linear trinuclear [Zn1a, Zn2, Zn1] cluster (Fig. 5).

The trinuclear [Zn1a, Zn2, Zn1] clusters are connected to each other, in a head-to-tail fashion, through the coordination of the zinc(II) ions by dpe ligands, producing a 1D chain exhibiting the sequence {Zn2, Zn2, Zn2,...} for the central metal ion and {Zn1, Zn1a, Zn1, Zn1a,...} for the external zinc(II) ions. This arrangement gives rise to triple-stranded chains, illustrated by the blue, green and yellow dpe ligands in Fig. 5. These coordination polymeric chains are compared to those observed for compound **1** (see Figs. 2 and 5). In contrast to the methyl groups in **1**, the ethyl groups of the propionato ligands in **2** do not allow a close packing of the zig-zag polymeric chains, as the result of steric constraints (Fig. 6). This spatial organization allows the coordination of dpe ligands at the

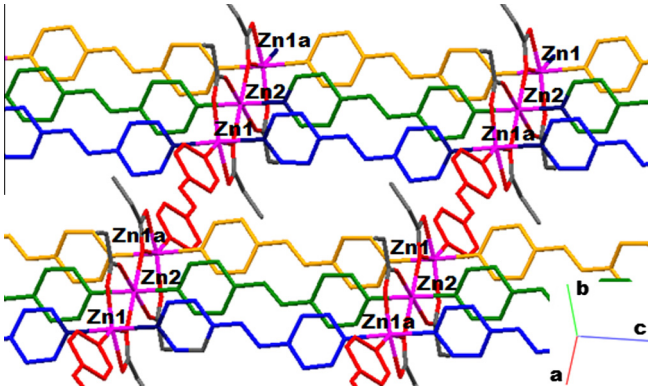

Fig. 5. 2D coordination network in **2**. The dpe ligands involved in the formation of trinuclear zinc(II) units are shown in blue, green and yellow-orange and those connecting the 1D triple-stranded chains are shown in red. (For interpretation of the references to color in this figure legend, the reader is referred to the web version of this article.)

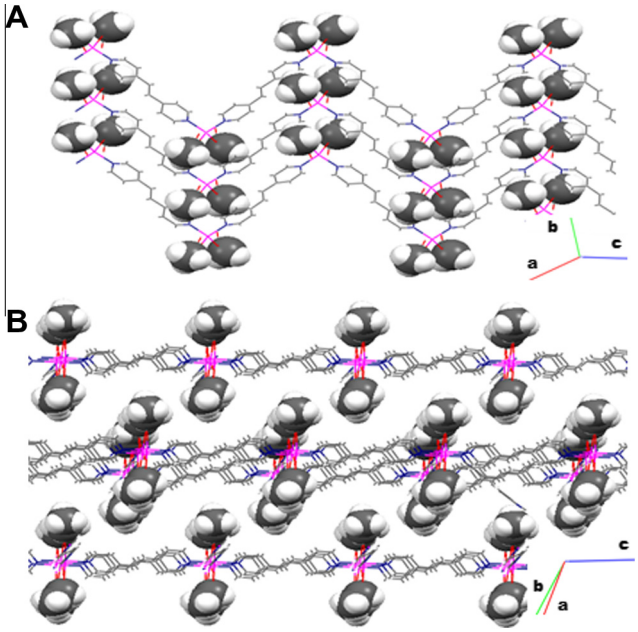

Fig. 6. Illustrations of the steric hindrance due to the acetato methyl groups (shown in the space-filling mode) in **1** (A) and propionato ethyl groups in **2** (B), which prevents close contacts between the 1D zig-zag chains.

two external positions of the trizinc moieties (red-colored dpe ligands coordinated to Zn1 and Zn1a along *a* axis; Fig. 5), connecting the triple-stranded chains to each other to form a 2D network. Consequently, each layer in **2** exhibits two distinct types of channels, narrow channels (3.820×13.719 Å^2) within the triple-stranded chains and larger channels (13.578×13.719 Å^2) between the triple-stranded chains are found (see Fig. 7). Indeed, the shorter interlayer Zn···Zn separation distance is 7.054(3) Å for compound **2**, while that of **1** is 9.401(3) Å.

The herringbone-type architecture exhibits large cavities that can accommodate bulky guest molecules, namely non-coordinated dpe ligands and disordered perchlorate anions (Fig. 7) which are hydrogen-bonded to each other ($O(ClO_4)\cdots H–C = 2.527(6)–2.671(6)$ Å. In addition, these guest molecules do significantly interact with the metal organic framework. The non-coordinated dpe ligands are hydrogen bonded to pyridine rings of dpe ligands to adjacent layer (N5···H–C = 3.471(6)–3.662(6) Å) and the disordered perchlorate anions are also hydrogen bonded to the pyridine rings of the dpe ligands to adjacent layer (O5B···H–C = 2.459(6)–2.527(6) Å, O6A···H–C = 2.362(6)–2.617(6) Å, O6B···H–C = 2.598(6)–2.612(6) Å, and O8B···H–C = 2.558(6)–2.675(6) Å). This intricate network of supramolecular bonds produces a three-dimensional structure.

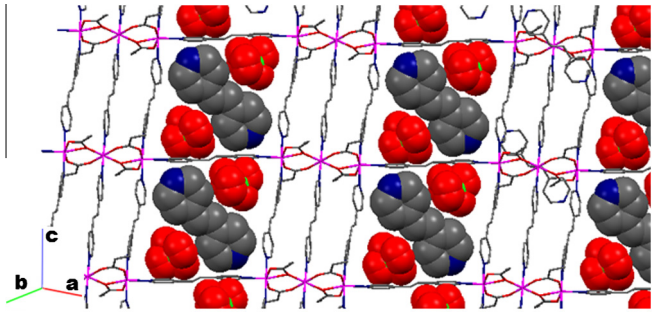

Fig. 7. Representation of the 2D network of compound **2**, illustrating the large cavities which contain non-coordinated dpe ligands and disordered perchlorate anions (space-filling mode).

*3.4. Effect of the couteranion and carboxylato ligand on the topologies of compounds **1** and **2***

Single crystal X-ray analyses revealed that compounds **1** and **2** have different structural topologies. The use of slightly different carboxylato, namely the acetato and propionato moieties as secondary co-ligands of [Zn(II)/dpe] coordination units, applying the similar reaction conditions, but with additional ClO_4^- ions for **2**, indeed leads to the formation of drastically distinct networks (Scheme 2). The combination of Zn(II) ions, dpe ligands and acetato co-ligands in **1** generates a 1D zig–zag polymeric chain (Scheme 2A) resulting from the assembly of mononuclear chain secondary building units with tetrahedral geometry. The sole replacement of acetate by propionate without additional ClO_4^- ion, did not result in a crystalline product. Hence the $KClO_4$ was added to the reaction during synthesis procedure, and these results in the formation of 2D network (Scheme 2B) confirming that ClO_4^- anions influence in the formation of the framework. This simple framework is built from trinuclear propionato-bridged units that are linked to two adjacent ones, to form a triple-stranded chain. These triple-stranded chains are connected to each other via dpe ligands (vertical red lines in Scheme 2B). This indicates that not only the steric hindrance between acetate and propionate ligands but also the nature of the counter ion is one of the factors that can affect the overall structure of coordination networks [33]. Therefore, the combination of effects between steric hindrance of carboxylate ligands and anions play an important role in the construction of metal organic frameworks.

3.5. Thermogravimetric analysis

The thermal analysis of **1** (Fig. 8A) exhibits a two-stage decomposition of the material. A first weight loss of 4.49% is observed in the temperature range 52–95 °C, which corresponds to the release of one lattice water molecule (calculated 4.69%). The structure is stable up to about 230 °C, when it starts to decomposes gradually to produce a white residue of ZnO at ca. 300 °C.

The thermogravimetric analysis of compound **2** (Fig. 8B) shows a first weight loss in the temperature range 100–300 °C, characterizing the loss of guest dpe ligand and two propionate ligands (experimental value, 21.09%; calculated, 20.54%). In the temperature range 300–400 °C, the decomposition of the coordination material is observed. As for compound **1**, a white residue (ZnO) of **2** is obtained when the sample is heated to 400 °C.

3.6. Zn(II) compounds doped with Cu(II) and Mn(II)

To learn more on the details of the coordination site, the influence of the nature of the doping metal ion, namely Cu(II) and Mn(II), has been investigated by EPR. This study illustrates the flexibility of the coordination geometry of Cu(II) compared to Mn(II). Such investigations are of great interest in the context of potential cation-exchange properties of metal organic frameworks with structure retention. All doped compounds have been characterized by IR spectroscopy and EPR at room temperature and 70 K (see Figs. 9 and 10). The IR spectra of the doped compounds are similar to that of the original Zn(II) compound, thus indicating that the structure and therefore the environment around the zinc(II) centers are essentially not altered.

The polycrystalline EPR spectrum of the trinuclear secondary building units of Zn(II) compound **2** doped with Cu(II) shows signals revealing the presence of only one type of Cu(II) species which is characterized by a four-lines hyperfine pattern with $g_{//} = 2.314$; (with $A_{//} = 124$, Fig. 9A) $g_{\perp} = 2.080$; this would be in agreement with a distorted-octahedral geometry [34]. No super-hyperfine splitting is resolved. These EPR data are could be indicative of

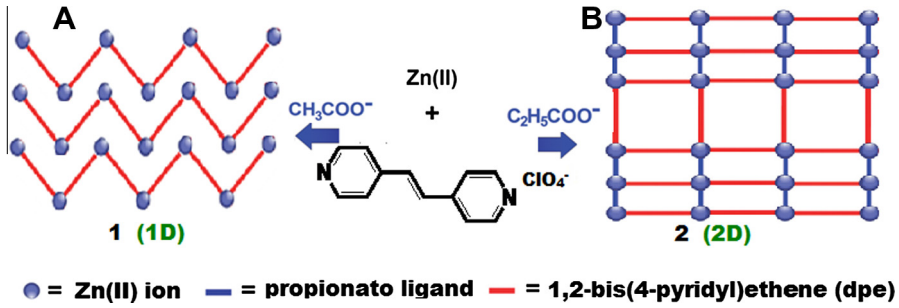

Scheme 2. Coordination networks of mononuclear 1D zig–zag chain of compound **1** and trinuclear 2D layers of compound **2**.

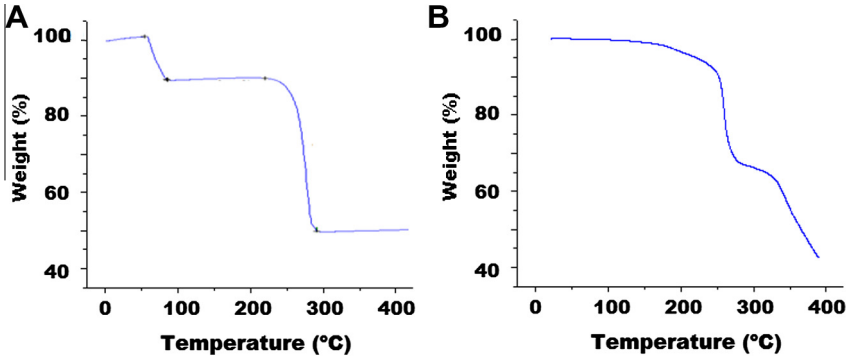

Fig. 8. Thermogravimetric analysis of compounds **1**(A) and **2**(B).

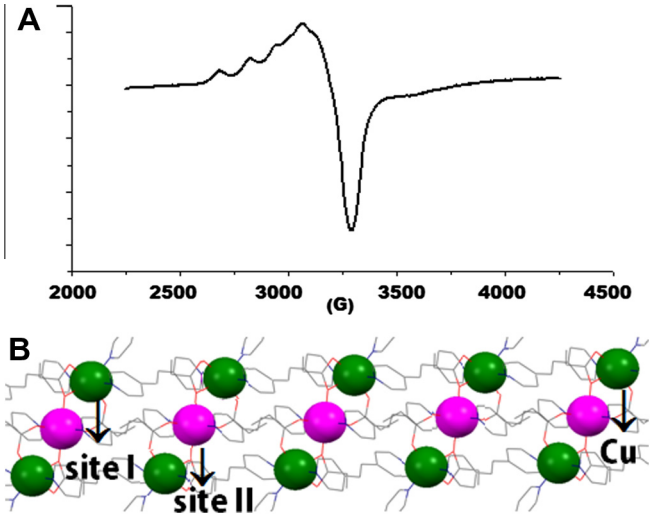

Fig. 9. (A) Polycrystalline EPR spectrum of **2** doped with Cu(II), recorded at 70 K and (B) Trinuclear Zn(II) units of **2** where zinc(II) ions (pink) have been replaced by Cu(II) ions (green) in only one site I. (For interpretation of the references to color in this figure legend, the reader is referred to the web version of this article.)

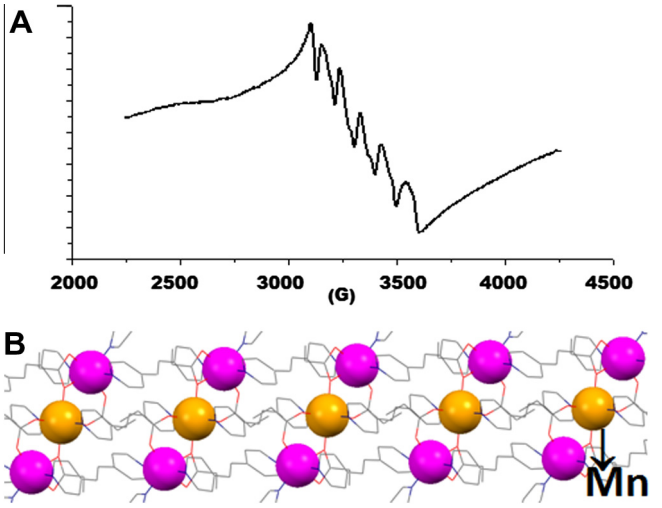

Fig. 10. (A) Polycrystalline EPR spectrum of **2** doped with Mn(II), recorded at 70 K and (B) Trinuclear Zn(II) unit of **2**, where only the central Zn(II) sites have been replaced by Mn(II) ions (orange). (For interpretation of the references to color in this figure legend, the reader is referred to the web version of this article.)

the occurrence of only one predominant site for the Zn(II) ions in **2**, which has been replaced by Cu(II) ions. In fact only a small fraction of Zn ions in site I species are replaced by Cu or Mn, so in a very small amount (by far not every Zn in site I is replaced. In the molecular structure of **2** two distinct coordination geometries for the zinc(II) ions are present, i.e. a highly distorted octahedron (site I) and a rather perfect octahedron (site II in Fig. 9B) [35]. The simple EPR, i.e. one species, could suggest that the EPR spectrum of the Cu(II) ion is due to only one site, and hardly any in the other site. So it could be that the EPR parameters are due to the outer two ions, as a central Cu(II) would have a different EPR (compressed octahedron). However, given the low resolution no firm conclusion about a single species is allowed. Similarly, the doping with Mn(II) ions leads to a heteronuclear compound, whose EPR spectrum shows only a simple spectrum with one set of six lines, characterizing a Mn(II) species (Fig. 10A). These data would suggest that only one from the two potential coordination sites has experienced cation exchange. Probably the Mn(II) ions are occupying only site II (Fig. 10B), since Mn(II) has the tendency to form rather regular octahedral complexes.

3.7. Catalytic properties

Both MOFs **1** and **2** have been tested as heterogeneous catalysts for the cyanosilylation of acetaldehyde and benzaldehyde. Thus, the selectivity and activity of the 1D (**1**) and 2D (**2**) coordination polymers have been examined. Typically, the powdered catalyst is suspended in CH_2Cl_2 or THF. The aldehydic substrate and trimethylsilyl cyanide (1:2 molar ratio) are subsequently added at room temperature and the reaction is carried out for 24 h (Scheme 3) [36]. The course of the reactions has been monitored by gas chromatography.

Blank reactions have been performed by carrying the cyanosilylation of acetaldehyde and benzaldehyde without solid catalyst, at 25 °C. These test reactions give only conversions of 18% for acetaldehyde and 10% for benzaldehyde, after a reaction time of 24 h. When solid **1** is used as catalyst, a conversion of 74% (and even 82% when using **2**) of acetaldehyde is reached after 24 h reaction time in CH_2Cl_2 (Table 4 and Fig. 11). This high conversion suggests first of all that both catalysts act as a efficient catalyst for this reaction, and that both acetaldehyde and trimethylsilyl cyanide can diffuse through the pores to attain the Lewis metallic sites, to generate 2-(methylsiloxy)propionitrile with a yield of 74% (**1**) and 82% (**2**).

When benzaldehyde, a sterically more demanding substrate, is used under similar reaction conditions, a conversion of only 14% is observed (18% for **2**; Table 4). This significantly lower reactivity, hardly better than the blank, suggests that the dimension of the channels of the porous coordination polymer plays an important role and leads to size selectivity.

Next, the influence of another organic solvent, namely THF, on the conversion of acetaldehyde has been examined for each MOF catalyst. For instance, in THF, compound **1** promotes the conversion of only 57% acetaldehyde (59% for **2**; Table 4). So, the reaction is less efficient in THF, which may be explained by a competitive binding of the substrate and the solvent to the metal site. This competitive binding obviously does not occur with CH_2Cl_2 as the solvent.

For instance, the reactions performed of **2** are more efficient than for **1** (Table 4). These disparities regarding the distinct catalytic activities in CH_2Cl_2 and THF may be explained by structural features characterizing both compounds. As mentioned above, the crystal packing of the 2D framework of **2** generates huge cavities filled with perchlorate anions and non-coordinated 1,2-bis(4-pyridyl)ethene (dpe) molecules. Most likely, both solvents are capable of displacing the dpe guest molecules of **2**, therefore increasing the accessibility of the aldehydic substrate to the metal centers, as compared to the close contacts between the 1D zig–zag chains in **1**.

The catalytic activities of compounds **1** and **2** for the cyanosilylation of aldehydes have been compared with those of zinc(II) porous coordination frameworks, as well as with other porous coordination frameworks. As reported earlier by our group [37], $\{[Zn_3(4,4'\text{-bpy})_{3.5}(\mu\text{-}O_2CH)_4(H_2O)_2](ClO_4)_2(H_2O)_2\}_n$ (3D), $\{[Zn_3(4,4'\text{-bpy})_4(\mu\text{-}O_2CCH_2CH_3)_4](ClO_4)_2(4,4'\text{-bpy})_2(H_2O)_4\}_n$ (2D) and $\{[Zn_3(4,4'\text{-bpy})_3(\mu\text{-}O_2CCH_3)_4(H_2O)_2](PF_6)_2(H_2O)_2\}_n$ (1D), have been tested as heterogeneous catalysts for the cyanosilylation of acetaldehyde and benzaldehyde. For example, the conversion of 3D framework (95%) is significantly higher than that of 2D and 1D frameworks (86% and 71%, respectively). This significant reactivity suggests that the dimension of the channels of the MOF plays an important role and leads to size selectivity. When, the catalytic properties of both Zn(II) compounds are compared with those of copper(II) coordination frameworks, i.e. the 2D networks $\{[Cu_3(4,4'\text{-bpy})_3(\mu\text{-OOCH})_4(H_2O)_2](ClO_4)_2(H_2O)_6\}_n$, $\{[Cu(4,4'\text{-bpy})(\mu\text{-OOCH})(NO_3)]\}_n$ and $\{[Cu_2(4,4'\text{-bpy})_2(\mu\text{-OOCCH}_3)_3](PF_6)(H_2O)\}_n$ a much lower activity is observed [38]. The higher catalytic activities of **1** and **2** may suggest that the Lewis acidity of these zinc(II) compounds is higher than that of the tested copper(II) ones.

Scheme 3. Cyanosilylation reaction.

Table 4
Cyanosilylation of aldehydes catalyzed by compounds **1** and **2**.

Catalyst	Types	Substrate	Solvent	Time (h)	Conversion (%)
1	1D	acetaldehyde	CH_2Cl_2	24	74
		acetaldehyde	THF	24	57
		benzaldehyde	CH_2Cl_2	24	14
2	2D	acetaldehyde	CH_2Cl_2	24	82
		acetaldehyde	THF	24	59
		benzaldehyde	CH_2Cl_2	24	18

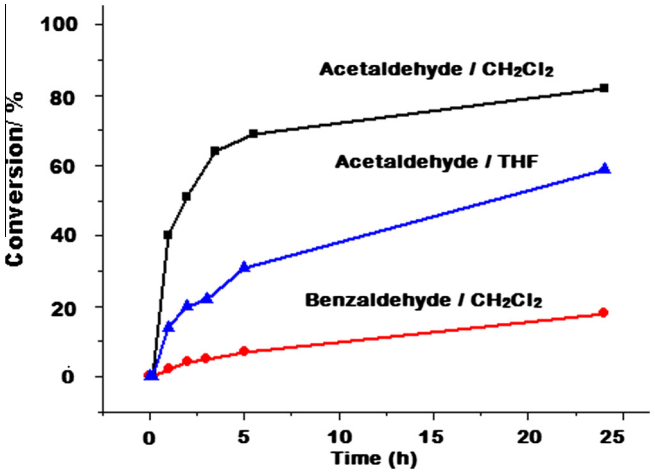

Fig. 11. Cyanosilylation of acetaldehyde and benzaldehyde with MOF **2** as catalyst.

4. Conclusions

In summary, two new metal organic frameworks, [Zn(II)/dpe/carboxylato] crystalline solids based on 1D and 2D coordination networks of different topology have been prepared and characterized crystallographically. The influence of small secondary ligands, namely common monocarboxylato ligands and the nature of the counter ion, on the overall solid state structure of both compounds have been investigated. This study suggests that the steric hindrance of the carboxylato co-ligand (acetato or propionato) and the effect of counteranion may have drastic effects on the resultant coordination networks. These results clearly indicate that *a priori* minor synthetic changes give rise to the formation of drastically distinct frameworks. Such studies are important in crystal engineering, as they contribute to increase knowledge about ligand steric effect on framework topologies.

Furthermore, the catalytic activities of zinc(II)-dpe-carboxylato compounds in the cyanosilylation of aldehydes have been investigated. Both compounds display good heterogeneous catalytic properties and show a high conversion of acetaldehyde in dichloromethane and also showed highly size-selective for the substrate compound with benzaldehyde.

Acknowledgments

This work was supported by The Thailand Research Fund, The Higher Education Research Promotion and National Research

University Project of Thailand, Office of the Higher Education Commission, through the Advanced Functional Materials Cluster of Khon Kaen University and the Center of Excellence for Innovation in Chemistry (PERCH-CIC), Commission on Higher Education, Ministry of Education, Thailand.

Appendix A. Supplementary material

CCDC 894458 and 894459 contain the supplementary crystallographic data for this paper. These data can be obtained free of charge from The Cambridge Crystallographic Data Centre via http://www.ccdc.cam.ac.uk/data_request/cif. Supplementary data associated with this article can be found, in the online version, at doi:10.1016/j.ica.XXXXXXX.

References

[1] S. Keskin, J. Liu, R.B. Rankin, J.K. Johnson, D.S. Sholl, Ind. Eng. Chem. Res. 48 (2009) 2355.
[2] J. Crassous, Chem. Soc. Rev. 38 (2009) 830.
[3] Z. Wang, G. Chen, K.L. Ding, Chem. Rev. 109 (2009) 322.
[4] J.M. Yan, X.B. Zhang, S. Han, H. Shioyama, Q. Xu, Angew. Chem., Int. Ed. 47 (2008) 2287.
[5] H.K. Liu, X.H. Huang, T. Lu, X. Wang, W.Y. Sun, B.S. Kang, Dalton Trans. (2008) 3178.
[6] G. Ferey, C. Mellot-Draznieks, C. Serre, F. Millange, Acc. Chem. Res. 38 (2005) 217.
[7] B.-B. Ding, Y.-Q. Weng, Z.-W. Mao, C.-K. Lam, X.-M. Chen, B.-H. Ye, Inorg. Chem. 44 (2005) 8836.
[8] L. Pan, D.H. Olson, L.R. Ciemnolonski, R. Heddy, J. Li, Angew. Chem., Int. Ed. 45 (2006) 616.
[9] Q. Fang, G. Zhu, M. Xue, J. Sun, F. Sun, S. Qiu, Inorg. Chem. 45 (2006) 3582.
[10] G. Becht, S.-J. Hwu, Chem. Mater. 18 (2006) 4221.
[11] Y.J. Song, H. Kwak, Y.M. Lee, S.H. Kim, S.H. Lee, B.K. Park, J.Y. Jun, S.M. Yu, C.I. Yu, S.-J. Kim, Y. Kim, Polyhedron 28 (2009) 1241.
[12] M. Du, X.-G. Wang, Z.-H. Zhang, L.-F. Tang, X.-J. Zhao, CrystEngComm 8 (2006) 788.
[13] A.-Q. Wu, Y. Li, F.-K. Zheng, G.-C. Guo, J.-S. Huang, Cryst. Growth Des. 6 (2006) 444.
[14] P. Ren, N. Xu, C. Chen, H.-B. Song, W. Shi, P. Cheng, Inorg. Chem. Commun. 11 (2008) 730.
[15] C.Y. Chen, P.Y. Cheng, H.H. Wu, H.M. Lee, Inorg. Chem. 46 (2007) 5691.
[16] P. Phuengphai, S. Youngme, P. Kongsaeree, C. Pakawatchai, N. Chaichit, S.J. Teat, P. Gamez, J. Reedijk, CrystEngComm 11 (2009) 1723.
[17] K. Biradha, CrystEngComm 5 (2003) 374.
[18] D. Braga, Chem. Commun. (2003) 2751.
[19] X.J. Li, C. Rong, D.F. Feng, W.H. Bi, Y. Wang, X. Li, M.C. Hong, Cryst. Growth Des. 4 (2004) 775.
[20] J.C. Dai, X.-T. Wu, S.-M. Hu, Z.-Y. Fu, J.-J. Zhang, W.-X. Du, H.-H. Zhang, R.-Q. Sun, Eur. J. Inorg. Chem. (2004) 2096.
[21] Q.-Y. Liu, L. Xu, CrystEngComm 7 (2005) 87.
[22] Y.-C. Liao, F.-L. Liao, W.-K. Chang, S.-L. Wang, J. Am. Chem. Soc. 126 (2004) 1320.
[23] S.P. Jang, J.I. Poong, S.H. Kim, T.G. Lee, J.Y. Noh, C. Kim, Y. Kim, S.-J. Kim, Polyhedron 33 (2012) 194.
[24] C.R. Maldonado, M. Quiros, J.M. Salas, Inorg. Chim. Acta 365 (2011) 371.
[25] A. Aslani, A. Morsali, V.T. Yilmaz, O. Büyükgüngör, Inorg. Chim. Acta 362 (2009) 1506.
[26] Z.R. Ranjbar, A. Morsali, Inorg. Chim. Acta 360 (2007) 2056.
[27] H.W. Roesky, M. Andruh, Coord. Chem. Rev. 236 (2003) 91.
[28] SAINT, Version 4 Software Reference Manual, Siemens Analytical X-Ray Systems, Inc., Madison, WI, USA, 1996.
[29] G.M. Sheldrick, SADABS, Program for Empirical Absorption correction of Area Dectector, University of Göttingen, Göttingen, Germany, 1996.
[30] SHELXTL, Version 6.12 Reference Manual, Siemens Analytical X-Ray Systems, Inc., Madison, WI, USA, 1997.
[31] B.F. Hoskins, R. Robson, J. Am. Chem. Soc. 112 (1990) 1546.
[32] Y.M. Dai, E. Ma, E. Tang, J. Zhang, Z.J. Li, X.D. Huang, Y.G. Yao, Cryst. Growth Des. 5 (2005) 1313.
[33] L. Carlucci, G. Ciani, D.M. Proserpio, S. Rizzato, CrystEngComm 4 (2002) 121.
[34] B.J. Hathaway, G. Wilkinson, R.D. Gill, J.A. McCleverty (Eds.), Comprehensive Coordination Chemistry, vol. 5, Pergamon Press, Oxford, 1987.
[35] J.M. Thomas, Angew. Chem., Int. Ed. Engl. 27 (1988) 1673.
[36] S. Horike, M. Dinca, K. Tamaki, J.R. Long, J. Am. Chem. Soc. 130 (2008) 5854.
[37] P. Phuengphai, S. Youngme, P. Gamez, J. Reedijk, Dalton Trans. 39 (2010) 7936.
[38] P. Phuengphai, S. Youngme, I. Mutikainen, P. Gamez, J. Reedijk, Polyhedron 42 (2012) 10.

Polyhedron 102 (2015) 593–599

Contents lists available at ScienceDirect

Polyhedron

journal homepage: www.elsevier.com/locate/poly

Water-induced dynamic crystal-to-amorphous transformation of cobalt(II) coordination and supramolecular frameworks containing benzene-1,2,4,5-tetracarboxylic acid and trans-1-(2-pyridyl)-2-(4-pyridyl)ethylene ligands

Jureepan Piromchom [a], Jaursup Boonmak [a], Kittipong Chainok [b], Sujittra Youngme [a,*]

[a] Materials Chemistry Research Center, Department of Chemistry, Center of Excellence for Innovation in Chemistry, Khon Kaen University, Khon Kaen 40002, Thailand
[b] Department of Chemistry, Thammasat University, Rangsit Campus, Klong Luang, Pathumthani 12121, Thailand

ARTICLE INFO

Article history:
Received 30 April 2015
Accepted 6 November 2015
Available online 11 November 2015

Keywords:
Cobalt(II) coordination and supramolecular framework
Trans-1-(2-pyridyl)-2-(4-pyridyl)ethylene
Benzene-1,2,4,5-tetracarboxylic acid
Chromotropism
Dynamic structural transformation

ABSTRACT

Two new Co^{II} coordination and supramolecular frameworks containing carboxylate and N-donor ligands, $\{Co_2(bpe)(btec)(H_2O)_5\}_n$ **(1)** and $[Co_2(bpe)_4(btec)(H_2O)_6]\cdot 8H_2O$ **(2)** (ppe = trans-1-(2-pyridyl)-2-(4-pyridyl)ethylene, btec = benzene-1,2,4,5-tetracarboxylic acid) have been synthesized and structurally characterized by single-crystal X-ray diffraction. The structure of **1** reveals an infinite 3D coordination network while compound **2** forms a molecule. The units in **2** are connected to each other and through lattice water molecules via hydrogen bonding, generating 3D supramolecular network. Interestingly, both compounds exhibit water-induced reversible crystal-to-amorphous transformations with chromotropism confirmed by spectroscopic techniques, elemental analyses, TGA, and XRPD. This phenomena is typically found in the dynamic frameworks triggered by weak intermolecular interactions, especially hydrogen bonds.

1. Introduction

Solid-state reversible structural transformations and functional studies of bistable dynamic coordination polymers (CPs) or metal organic frameworks (MOFs) and supramolecular frameworks have recently attracted great attention to obtain smart functional materials [1,2]. The dynamic frameworks have a blend of both rigidity and flexibility. Rigidity makes material efficient in storage and flexibility in selective sorption. Kitagawa et al. classified these dynamic frameworks as "third generation coordination polymers", also called "soft porous crystals" [3–5]. Dynamic structural transformation based on flexible frameworks is one of the most interesting and presumably characteristic phenomena of coordination polymers [6,7].

The bistable dynamic frameworks exhibit solid-state structural transformations with breaking, making, or rearrangement of bonds driven by external stimuli like heat, light, pressure, etc. [5]. Structural transformations are generally accompanied by removal or exchange of guest, changes in coordination number of metal containing nodes, and conformational changes in flexible parts of organic ligands [6]. However, reports of such bistable dynamic MOFs are limited, especially in the supramolecular frameworks generated from discrete molecules. Generally, such structural changes in response to external stimuli are facilitated by weak bonding interactions like hydrogen-bonding and π–π and C–H···π interactions [6,7]. These structural transformations induced by chemical and/or physical processes are much more complicated than encountered in the rigid frameworks. Thus, investigation of solid-state structural transformations between bistable phases and their correlations with the properties is very crucial to design smart functional materials.

The dynamic structural transformation with chromotropism of cobalt(II) coordination and supramolecular frameworks have been extensively studied [8] including our previous works [9]. These compounds are liable to collapse/deform upon thermal dehydration/rehydration and shows selective adsorption for water over organic solvents. The reversibility is driven by strong hydrogen bonding between lattice and coordinated water molecules and other components.

Herein, we report the synthesis of the 3D coordination and supramolecular frameworks, $\{Co_2(bpe)(btec)(H_2O)_5\}_n$ (**1**) and $[Co_2(bpe)_4(btec)(H_2O)_6]\cdot 8H_2O$ (**2**), respectively and their dynamic behaviors. The reversible solid-state crystal-to-amorphous structural transformations are accompanied with the distinct color change on de/rehydration. The selective sorption properties were observed for adsorbates like H_2O over methanol, ethanol, acetone,

* Corresponding author.

http://dx.doi.org/10.1016/j.poly.2015.11.012
0277-5387/

acetonitrile, dichloromethane, and hexane. The dynamics of the de/rehydrated forms of compounds **1** and **2** were performed to investigate the possible reversible structural transformations with chromotropism.

2. Experimental

2.1. Materials and physical measurements

All reagents are commercial grade materials and were used without further purification. The IR spectra were recorded as KBr discs on a Perkin-Elmer Spectrum One FT-IR spectrophotometer in the 4000–450 cm^{-1} spectral range. Solid-state (diffuse reflectance) electronic spectra were measured as polycrystalline samples on a SHIMADZU Spectrum One spectrophotometer, within the range 200–1500 nm. Elemental analyses (C, H, N) were determined using a Perkin-Elmer PE-2400 CHNS/O Analyzer. Thermogravimetric analyses (TGA) were perform with a Perkin Elmer Pyris Diamond TG-DTA between 30 °C and 800 °C in N_2 atmosphere with a heating rate of 10 °C min^{-1} by using α-Al_2O_3 as a standard material. The X-ray powder diffraction (XRPD) data were collected on a Bruker D8 ADVANCE diffractometer using monochromatic Cu Kα radiation, and the recording speed was 0.5 s per step over the 2θ range of 5–50° at room temperature.

2.2. Preparation of $\{Co_2(bpe)(btec)(H_2O)_5\}_n$ (**1**)

A mixture of $Co(NO_3)_2{\cdot}6H_2O$ (0.2 mmol, 0.0586 g), benzene-1,2,4,5-tetracarboxylic acid (0.1 mmol, 0.0254 g), trans-1-(2-Pyridyl)-2-(4-pyridyl)ethylene (0.1 mmol, 0.0182 g), potassium hydroxide (0.4 mmol, 0.0224 g) in distilled water (8 mL) was stirred for 30 min in air, then transferred and sealed in a 25 mL Teflon reactor, which was heated at 140 °C for 24 h. The solution was then cooled to room temperature for 12 h, to yield purple block crystals; the yield based on Co was about 74%. *Anal.* Calc. for: $Co_2C_{22}H_{16}N_2O_{13}$ C, 41.01; H, 4.07; N, 4.35. Found: C, 41.20; H, 4.13; N, 4.52%. IR spectrum (cm^{-1}): 3348 (br), 1602 (s), 1559 (s), 1385 (s), 1325 (m), 1135 (m), 1021 (w), 814 (m), 765 (w), 536 (m).

2.3. Preparation of $[Co_2(bpe)_4(btec)(H_2O)_6]{\cdot}8H_2O$ (**2**)

Compound **2** was synthesized by the reaction of two aqueous solutions at room temperature, one containing a mixture of Co $(NO_3)_2{\cdot}6H_2O$ (0.2 mmol, 0.0586 g) and trans-1-(2-pyridyl)-2-(4-pyridyl)ethylene (0.1 mmol, 0.0182 g), in distilled water (8 mL), and the other one containing benzene-1,2,4,5-tetracarboxylic acid (0.1 mmol, 0.0254 g) and potassium hydroxide (0.4 mmol, 0.0224 g) in distilled water (7 mL), and was stirred for 30 min in air. This was allowed to stand undisturbed at room temperature. After two days, orange crystals were obtained; the yield based on Co was about 68%. *Anal.* C. for: $Co_2C_{58}H_{50}N_8O_{22}$ C, 52.42; H, 3.79; N, 8.43. Found: C, 52.20; H, 3.71; N, 8.32%. IR spectrum (cm^{-1}): 3313 (br), 1613 (s), 1563 (s), 1423 (m), 1383 (s), 1017 (w), 968 (w), 823 (m), 1343 (s), 773 (m), 738 (w), 548 (w).

2.4. X-ray data collection and structure determination

The X-ray single-crystal data for **1** and **2** compounds were collected on a 1 K Bruker SMART CCD area-detector diffractometer with graphite-monochromated Mo Kα radiation (λ = 0.71073 Å) using the SMART program [10]. Raw data frame integration was performed with SAINT [11], which also applied correction for Lorentz and polarization effects. An empirical absorption correction by using the SADABS [12] program was applied. The structure was solved by direct methods and refined by the full-matrix least-squares method on F^2 with anisotropic thermal parameters for all non-hydrogen atoms using the SHELXTL-PC V 6.1 software package [13]. All carbon hydrogen atoms of **1** and **2** compounds were fixed and included in calculated positions and treated as riding atoms. That of the coordinated water molecules were located and refined isotropically, except that of O11, O12 and O13 in **1** which could not be located. In addition, O13 in **1** were disordered which were divided into O(13A) and O(13B), with site occupancies of 0.5. In case compound **2**, hydrogen atoms of coordinated water (O7) and lattice water molecules (O8–O16) could not be located. In addition, two lattice water molecules (O15 and O13) were located with site occupancies of 0.5.

3. Results and discussion

3.1. Syntheses

3.1.1. Description of $\{Co_2(bpe)(btec)(H_2O)_5\}_n$ (**1**)

Single-crystal X-ray diffraction reveals that **1** crystallizes in the triclinic space group $P\bar{1}$ (Table 1), showing a 3D coordination network. The asymmetric unit contains two independent Co(II) ions, one btec, one bpe and five coordinated H_2O molecules. The Co1 atom is coordinated by three carboxylato oxygen atoms from two btec ligands (Co(1)–O(3) 2.059(4), Co(1)–O(4) 2.430(5) and Co(1)–O(1A) 2.070(4) Å), one nitrogen atom from bpe (Co(1)–N(1) 2.104(5) Å) and two oxygen atoms from water molecules (Co(1)–O(9) 2.060(5) and Co(1)–O(10) 2.090(5) Å), showing a significantly distorted octahedral coordination geometry with $Co(1)O_5N$ chromophore. The Co2 atom also adopts a significantly distorted octahedral coordination geometry with $Co(2)O_5N$ chromophore, which is coordinated by two carboxylato oxygen atoms of two different btec ligands (Co(2)–O(5) 2.082(5) and Co(2)–O(7) 2.063(4) Å), one nitrogen atom from bpe (Co(2)–N(2) 2.111(5) Å) and three oxygen atoms from water molecules ((Co(2)–O(11) 2.115(5), Co(2)–O(12) 2.215(8), Co(2)–O(13A) 2.23(2) and Co(2)–O(13B) 2.21(2) Å) (Fig. 1). The selected bond lengths and angles around both Co(1) and Co(2) as given in Table S1 indicate the significant distortion from the regular octahedral geometry.

Table 1
Crystallographic data for compounds **1**–**2**.

Crystal data	**1**	**2**
Formula	$Co_2C_{22}H_{16}N_2O_{13}$	$Co_2C_{58}H_{50}N_8O_{30}$
Formula weight	634.23	1456.92
T (K)	273(2)	120(2)
Crystal system	triclinic	monoclinic
Space group	$P\bar{1}$	$P21/c$
a (Å)	6.9906(6)	15.1072(5)
b (Å)	11.4556(9)	17.9546(6)
c (Å)	15.8377(13)	13.8683(5)
α (Å)	86.149(2)	90.00
β (Å)	80.046(2)	103.7480(10)
γ (Å)	72.436(2)	90.00
V (Å^3)	1190.83(17)	3653.9(2)
Z	2	2
D_c (g cm^{-3})	1.768	1.324
μ (mm^{-1})	1.469	0.539
$F(000)$	640	1496
Crystal size (mm^3)	0.309 × 0.078 × 0.04	0.08 × 0.11 × 0.48
Number of reflections collected	49928	38685
Number of unique reflections [R_{int}]	5913(0.00036)	7473(0.0278)
Data/restraints/parameter	5913/0/377	7473/0/467
Goodeness-of-fit (GOF) on F^2	1.063	1.113
Final R indices [$I > 2\sigma(I)$]	R_1 = 0.0887	R_1 = 0.0829
	wR_2 = 0.1473	wR_2 = 0.2411
R indices (all data)	R_1 = 0.1842	R_1 = 0.0947
	wR_2 = 0.1767	wR_2 = 0.2496
Max/min electron density (e Å^3)	1.543 and −0.607	1.937 and −0.858

$R = \Sigma||F_o| - |F_c||/\Sigma|F_o||$, $R_w = [\Sigma w\{|F_o| - |F_c|\}^2/\Sigma w|F_o^2|^2]^{1/2}$.

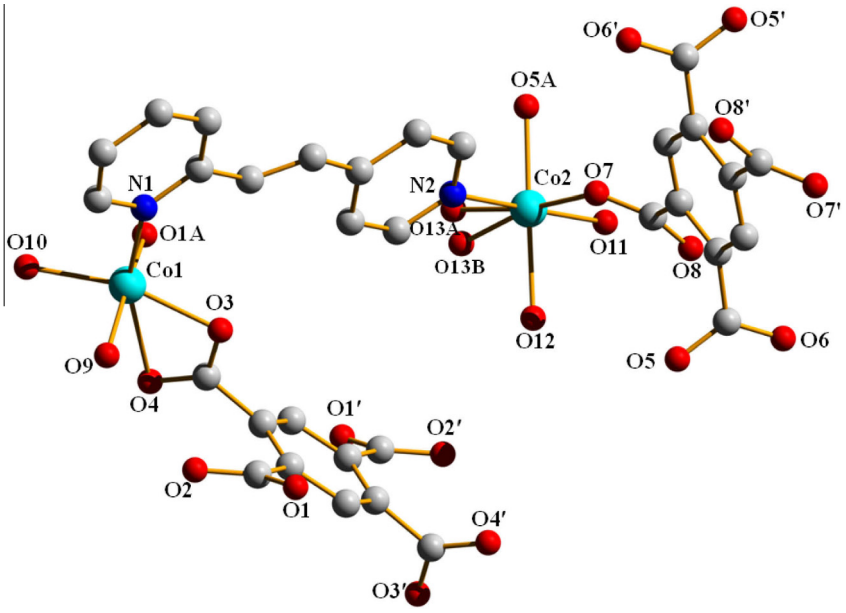

Fig. 1. Perspective view of the coordination environment of cobalt atoms in **1**. H atoms were omitted for clarity.

These Co(II) ions are linked by the bridging bpe ligand (N(1) and N(2)) with the Co1–Co2 distance of 9.1484(14) Å in *c*-axis and the bridging btec ligand in *a*-axis, generating 2D layer network (Fig. 2). The adjacent layers are further twisting along the *b*-axis via btec ligands to give an infinite flexible 3D framework (Fig. 3). In addition, the free carboxylate oxygens of btec and the coordinated waters are involved in an extensive hydrogen bonding (O9–H9A···O8^{i} 2.20(6), O10–H10A···O6^{ii} 1.86(6), O6···O11 2.8079(83) and O12···O2 3.2782(104) Å) (Fig. 4; Table S2).

3.1.2. Description of $[Co_2(bpe)_4(btec)(H_2O)_6]\cdot 4.5H_2O$ (**2**)

Single-crystal X-ray structural analysis shows that **2** is a compound crystallized in the monoclinic $P2_1/c$ space group (Table 1). The symmetry-related unit consists of two Co(II) ions, four bpe ligands, one btec, six coordinated waters and eight lattice water molecules. Each Co(II) ion is coordinated by two nitrogen atoms from two bpe terminal ligands (Co(1)–N(1) 2.159(4) and Co(1)–N(3) 2.128(4) Å), one oxygen atom of the bridging btec ligand (Co(1)–O(1) 2.032(3) Å) and three coordinated water molecules (Co(1)–O(5) 2.196(4), Co(1)–O(6) 2.045(3) and Co(1)–O(7) 2.134(4) Å), this feature gives a slightly distorted octahedral geometry with CoN_2O_4 chromophore as compared to that of 1 (Fig. 5; Table S3). The btec ligand links between both chromophores in monodentate fashion to each Co atom. The selected bond distances and angles are shown in Table S3. These units are connected to each other in ABAB... arrangement via hydrogen bonds with distance of 1.82(5) Å for O6–H6B···O2 and 3.20(5) Å for O5–H5A···O7 (Table S4), generating 2D layer network in *bc* plane as shown in Fig. 6. All lattice water molecules (O8–O16) form a cluster via hydrogen bonds and occupy the channels between

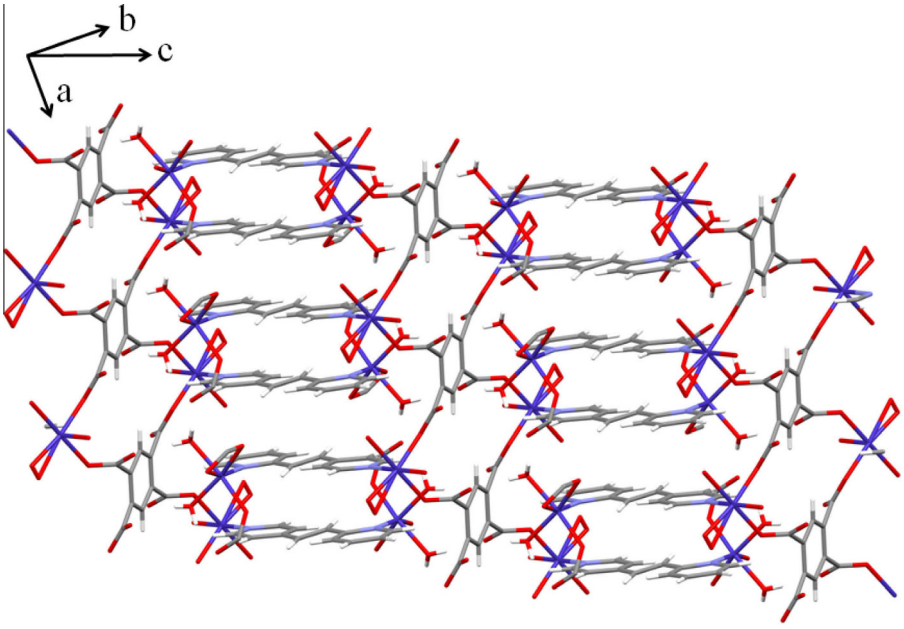

Fig. 2. A partial packing diagram in two-dimensional network of **1** in *ac* plane.

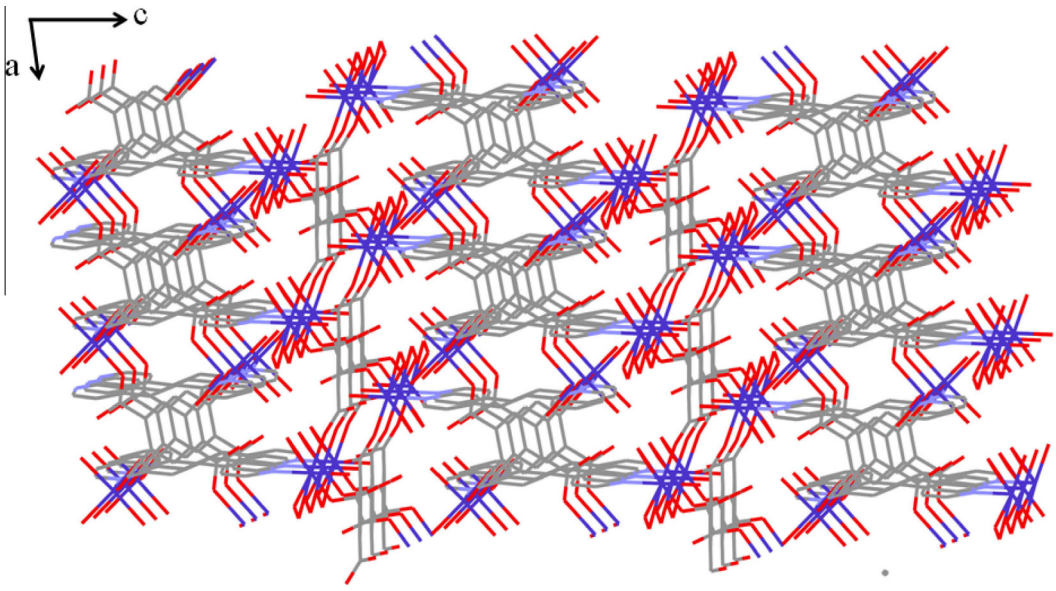

Fig. 3. 3D framework of **1**, showing along the *b*-axis.

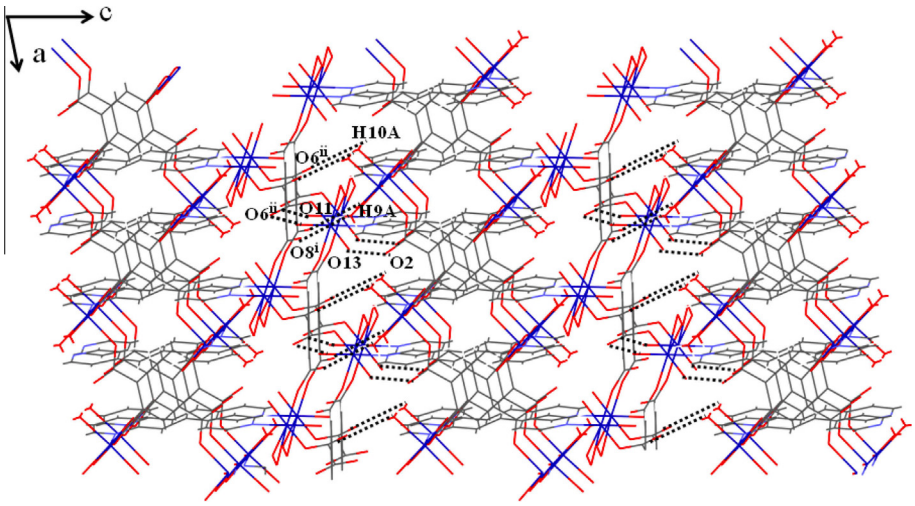

Fig. 4. 3D framework of **1**, showing extensive hydrogen bonding interactions by free carboxylate oxygens of btec and the coordinated waters along the *b*-axis [Symmetry codes: i = 1 + *x*, *y*, −1 + *z*; ii = *x*, *y*, −1 + *z*].

these layers along *c* axis, some of them bonded with free carboxylate oxygens (O4···O10 2.727 Å), nitrogen atom (N4···O9 2.799 Å) and coordinated waters (O6–H6A···O8 2.047 Å) as well as with aromatic carbon atoms (C–H···O 2.663–3.905 Å) on the surface of the tube, generating 3D supramolecular framework (Fig. S1; Tables S4–S5). Interestingly water molecules filling in each nano tube are further extended to 1D water chain via hydrogen bond interactions along *c* axis, the bond distances O···O (D···A) are in the range of 2.362–3.524 Å which are typically expected for hydrogen bonding interaction [14] (Fig. S2; Table S5).

3.1.3. Thermogravimetric analyses

To assess the thermal stability, thermal gravimetric analysis (TGA) was recorded for the single-phase polycrystalline samples in the temperature range 30–700 °C. During the heating process, the TGA profile of **1** (Fig. 7) indicates that the release of five coordinated water molecules occurs at the first step of weight loss in the temperature range 100–250 °C (found, 14.85%; *Anal.* Calc., 14.19%), resulting to the dehydrated form of Co_2(bpe)(btec) (**1A**), which is stable up to ≈300 °C and then the structure rapidly decomposes at higher temperatures. For compound **2** (Fig. 8), the TGA profile indicates that the releases of all fourteen water molecules (coordinated and lattice water molecules) occur at the first step of weight loss in the temperature range 55–100 °C (found, 17.50%; *Anal.* Calc., 17.30%) resulting in the dehydrated form of $Co_2(bpe)_4$(btec) (**2A**). This dehydrated form **2A** is stable up to ≈150 °C and then rapidly decomposes to unidentified products.

3.1.4. Structural phase transformation by thermal de/rehydration processes

The compound **1** contains only coordinated water molecules while **2** contains both lattice and coordinated water molecules. The stable dehydrated forms of **1A** and **2A** were clarified by TGA profiles. The dynamic structural behaviors of **1** and **2** relating to their dehydration and rehydration processes are studied by elemental analyses, XRPD, and spectroscopic techniques. Interestingly, the water molecules can be adsorbed fully by exposing the evacuated samples to water vapor over organic solvents at room

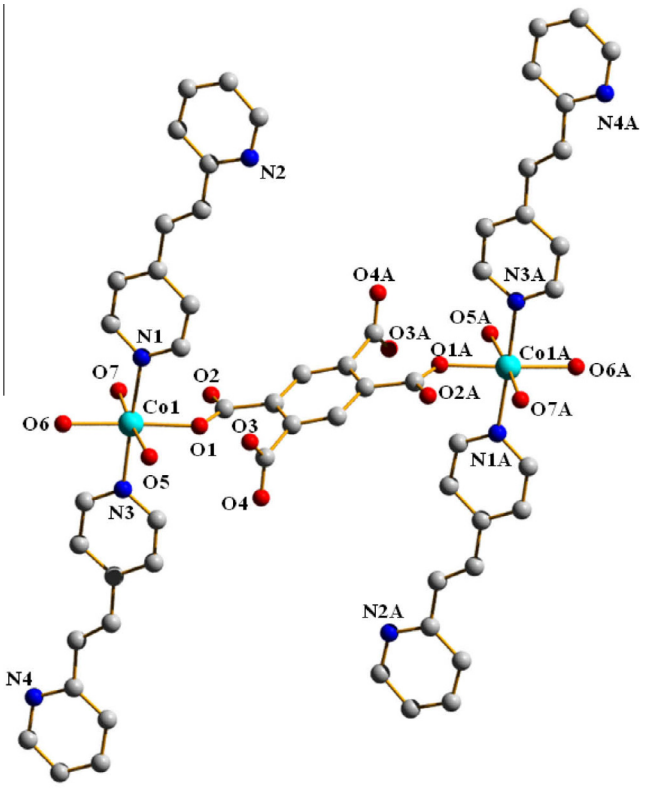

Fig. 5. Perspective view of the coordination environment of cobalt atoms in **2**. H atoms were omitted for clarity.

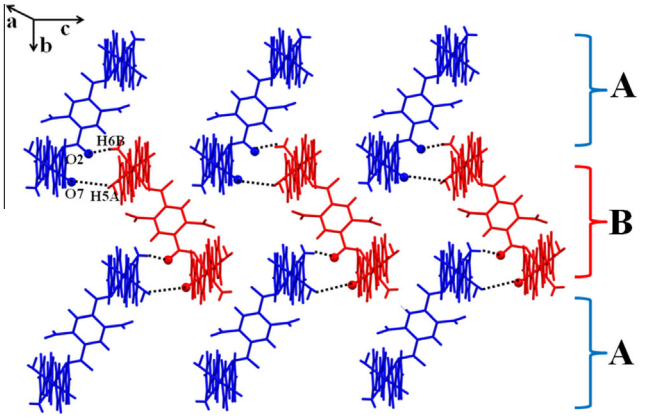

Fig. 6. Crystal packing of dinuclear units in ABAB… arrangement of compound **2** via hydrogen bonding in *bc* plane, generating two-dimensional supramolecular structure.

temperature. The heating and exposing procedures were repeated five times to demonstrate the reversibility of the de- and rehydration processes.

When the crystalline samples were heated to 250 °C for **1** and 100 °C for **2** in air for 10 min, these crystals suddenly lose their crystallinity and the color changes from purple to blue for **1** and orange to purple for **2**. Then these noncrystalline solids were exposed to the laboratory air for 10 min for **1** and 8 h for **2**, and the color of both noncrystalline samples were returned to that of the original samples. Consequently, the bulk samples of **1** and **2** were used to study in detail. The dehydrated form **1A** was obtained by heating the bulk sample at 250 °C in air for 30 min and the rehydrated form **1′** was obtained by exposing the dehydrated sample

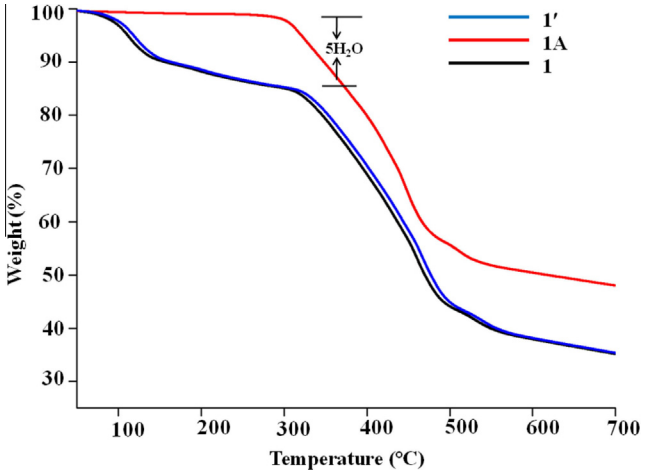

Fig. 7. TGA curves of as-synthesized **1**, dehydrated form **1A**, and rehydrated form **1′**.

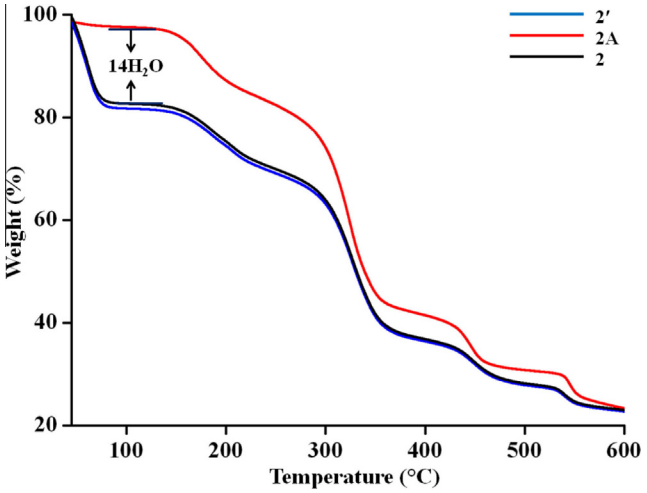

Fig. 8. TGA curves of as-synthesized **2**, dehydrated form **2A**, and rehydrated form **2′**.

to water vapor for 3 min. In case of **2** the dehydrated form **2A** was obtained by heating the bulk sample at 100 °C in air for 30 min and the re-hydrated form **2′** was obtained by exposing the dehydrated sample to water vapor for 12 h at room temperature without condensation, as shown in Fig. 9. For this, the solid-state UV–Vis diffuse reflectance spectra, clearly show that the bands observed in **1** and **1′** and also in **2** and **2′**, correspond very well to the identical transitions causing the same color of products, and evidence that **1** and **1′**, and also **2** and **2′** have the same Co^{II} environments. For **1** this spectral feature agrees with the typical d–d transitions of high spin Co^{II} in distorted octahedral geometry with two broad bands at 520 and 1250 nm, assigned to the ν_3: $^4T_{1g} \rightarrow {}^4T_{1g}(P)$ and ν_1: $^4T_{1g} \rightarrow {}^4T_{2g}$, transitions, respectively and a shoulder at around 650 nm arised from the ν_2: $^4T_{1g} \rightarrow {}^4A_{2g}$ transition [15]. Whereas the amorphous phase **1A** shows the different d–d transition with a lower-energy broad band centered *ca.* 587 nm and a very broad band centered around 1140 nm, giving distinctive blue color which is typical for the four-coordinated tetrahedral geometry in majority of **1A** (Fig. 10). Both broad bands correspond to the ν_3: $^4A_2 \rightarrow {}^4T_1(P)$ and ν_2: $^4A_2 \rightarrow {}^4T_1$ transitions, respectively. In case of **2**, the spectral feature and orange color agree with the typical d–d transitions of high spin Co^{II} in a slightly distorted octahedral geometry with two higher-energy broad bands centred at 512 and 1112 nm, as compared to that of **1**, which are assigned to the ν_3: $^4T_{1g} \rightarrow {}^4T_{1g}(P)$,

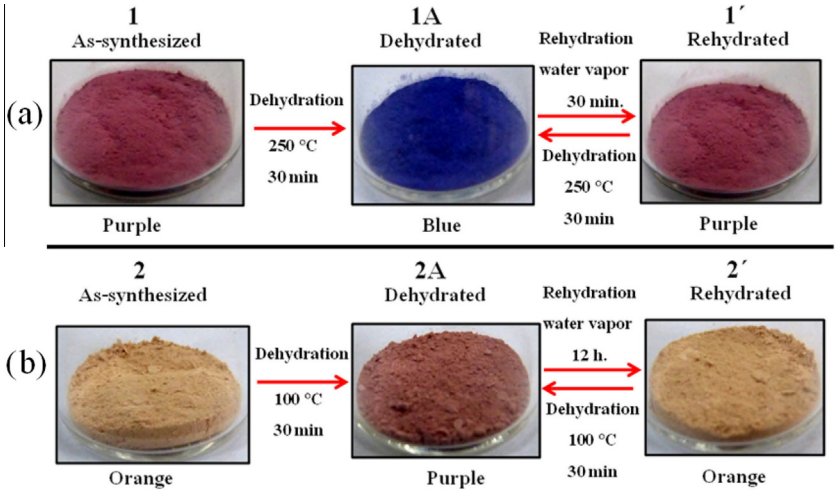

Fig. 9. Changes in color during de- and rehydration processes in bulk samples of (a) **1** and (b) **2**. (Color online.)

and ν_1: $^4T_{1g} \rightarrow {}^4T_{2g}$ transitions, respectively. The amorphous form **2A** also shows the same d–d transitions of two broad bands, but with the substantial shift to lower energy at 540 and 1250 nm, resulting in distinctive purple color and correspond to the majority of high-spin Co^{II} in a significantly distorted octahedral geometry of an amorphous phase [15], similar to that of compound **1** (Fig. 11). The preference of the significantly distorted octahedral geometry rather than tetrahedral one of an amorphous phase **2A** is confirmed from the purple color and a small shift of ν_3 (Δ = 28 nm) as compared to that of **1A** (Δ = 67 nm). The chromotropic behavior of **1** and **2** is principally ascribed to the changes of the d-orbital energy level, induced by the drastic change in the coordination environment around metal center during dehydration and rehydration processes [16]. Furthermore, these results agree with the reversible change of the vibrational bands in IR spectra (Figs. S3 and S4) where the shifted bands are observed for the amorphous phase. In **2A**, the broad and strong peaks of O–H stretching around 3300 cm^{-1} and H–O–H bending around 1500–1600 cm^{-1} of coordinated and lattice water molecules disappear, resulting to the sharper IR spectrum with different splitting feature and a shift in some peak positions. In contrast, these features are disappeared for the IR spectra of the rehydrated forms **1′** and **2′**, which are identical to those of the as-synthesized **1** and **2**. The XRPD patterns of

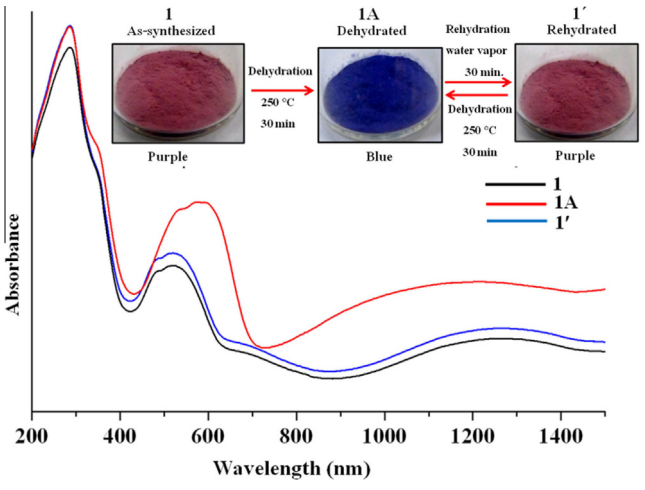

Fig. 10. The UV–Vis diffuse reflectance spectra of as-synthesized **1** (black line), the dehydrated form **1A** (red line), and the rehydrated form **1′** (blue line), representing together with the chromatic changes in bulk samples. (Color online.)

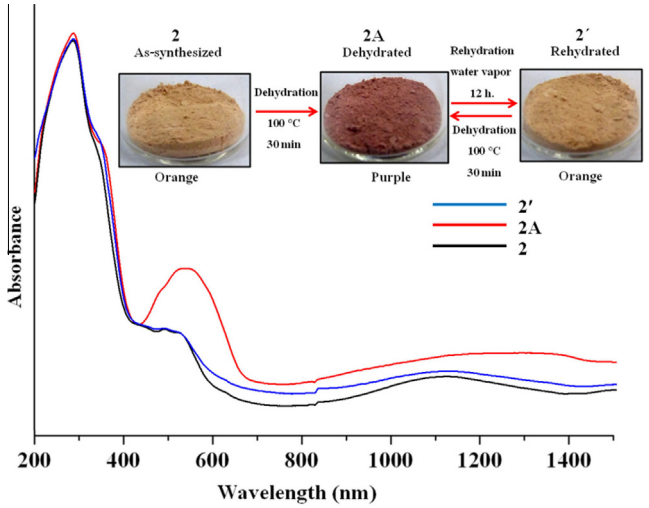

Fig. 11. The UV–Vis diffuse reflectance spectra of as-synthesize **2** (black line), the dehydrated form **2A** (red line), and the rehydrated form **2′** (blue line), representing together with the chromatic changes in bulk samples. (Color online.)

the as-synthesized products **1** and **2** closely match the simulated ones derived from the single-crystal data (Fig. 12). However, the XRPD patterns of dehydrated **1A** and **2A** show peak disappearance, indicating that the dehydrated $Co_2(bpe)(btec)_2$ (**1A**) (*Anal.* Calc.: C, 55.75; H, 3.03; N, 7.65. Found: C, 55.82; H, 3.15; N, 7.93%) and $Co_2(bpe)_4(btec)$ (**2A**) (*Anal.* Calc.: C, 63.28; H, 4.21; N, 10.18. Found: C, 63.32; H, 4.35; N, 10.31%) are in an amorphous phase which are formed by the collapse of the frameworks of **1** and **2** accompanied with the destruction of the frameworks when all water molecules are removed. Interestingly, these amorphous phases, **1A** and **2A** can be restored to the original crystalline phases of **1′** and **2′** in which the color returns to that of the original color after being exposed in water vapor for 30 min for **1′** and 12 h for **2′**, as indicated by elemental analyses with the chemical composition of $[Co_2(bpe)(btec)_2(H_2O)_5]_n$ (**1′**) (*Anal.* Calc.: C, 41.01; H, 4.07; N, 4.35. Found: C, 41.25; H, 4.18; N, 4.59%) and $[Co_2(bpe)_4(btec)(H_2O)_6]\cdot 8H_2O$ (**2′**) (*Anal.* Calc.: C, 52.42; H, 3.79; N, 8.43. Found: C, 52.23; H, 3.78; N, 8.39%), and the XRPD measurement results. The restored solids have the same XRPD patterns as the simulated ones derived from the single-crystal X-ray diffraction data of **1** and **2**.

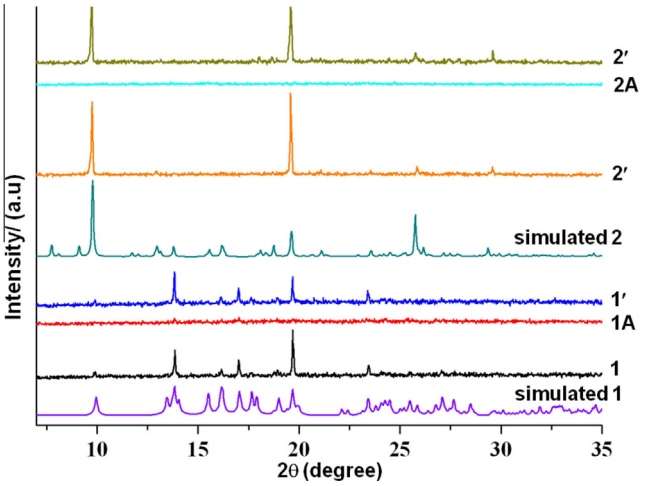

Fig. 12. XRPD patterns for **1** and **2** at different conditions: simulated **1**, as-synthesized **1**, dehydrated form **1A**, rehydrated form **1′**, simulated **2**, as-synthesized **2**, dehydrated form **2A** and rehydrated form **2′**, respectively.

These results of compounds **1** and **2** confirm the water-induced reversible crystalline-to-amorphous phase transformation with chromotropism. This behavior of both compounds was also investigated for other solvents vapor such as methanol, ethanol, acetone, acetonitrile, dichloromethane, DMF and DMSO, but sensitive only with water vapor, indicative of high selective recognition of **1A** and **2A** to water molecules. The selective water accommodation with chromotropism in dehydrated **1A** and **2A** when compared with many solvents could be attributed to the proper size of water molecules and weak host–guest interactions. Remarkably, the reversibility of water adsorption and the change in the coordination environment can be visualized by the change in color of the compounds. This behavior takes place in water which could be a dissolution/recrystallization process rather than a water-induced solid-state reaction as this involves structural reorganization of the coordination and supramolecular frameworks or rearrangements of the molecules interacting by intermolecular hydrogen bonds and non-covalent contacts [17].

4. Conclusions

Two novel 3D Co^{II} coordination and supramolecular frameworks containing carboxylate and N-donor ligands, $[Co_2(bpe)(btec)_2(H_2O)_5]_n$ **(1)** and $[Co_2(btec)(bpe)_4(H_2O)_6]\cdot 8H_2O$ **(2)** have been successfully synthesized by hydrothermal and direct methods, respectively. We have demonstrated that the water molecules in both compounds can be reversibly exchanged along with the change in color of the samples. The dehydrated form **1A** is found to be very sensitive to water in the color change as compared to that of **2A**. The reversibility of the solid transformation has been supported by spectroscopic techniques, elemental analysis, TGA and XRPD and revealed that **1** and **2** exhibit water induced crystal-to-amorphous transformation with high selectivity of water adsorption and the change in the coordination environments can be visualized by the change in color of the compounds. The crystalline-to-amorphous transformations between original crystalline phases (**1**, **2**) → dehydration (amorphous powder (**1A**, **2A**)) → rehydration (crystalline phases (**1′**, **2′**)) involve dynamic motions altering the coordination geometry of Co^{II}. These are triggered by the weak intermolecular interactions during the removal and restoration of water molecules. This work may contribute to potential application as sensing adsorbent material for moisture.

Acknowledgments

Financial support has been provided by The Thailand Research Fund (Grant No. BRG5680009 (for Youngme, S.) and TRG5780003 (for Boonmak, J.), the Higher Education Research Promotion and National Research University Project of Thailand, Office of the Higher Education Commission, through the Advanced Functional Materials Cluster of Khon Kaen University and the Center of Excellence for Innovation in Chemistry (PERCH-CIC), Office of the Higher Education Commission, Ministry of Education, Thailand.

Appendix A. Supplementary data

CCDC 1051014 and 1051015 contains the supplementary crystallographic data for compounds **1** and **2**. These data can be obtained free of charge via http://www.ccdc.cam.ac.uk/conts/retrieving.html, or from the Cambridge Crystallographic Data Centre, 12 Union Road, Cambridge CB2 1EZ, UK; fax: (+44) 1223-336-033; or e-mail: deposit@ccdc.cam.ac.uk. Supplementary data associated with this article can be found, in the online version, at http://dx.doi.org/10.1016/j.poly.2015.11.012.

References

[1] (a) S. Kitagawa, R. Kitaura, S. Noro, Angew. Chem., Int. Ed. 43 (2004) 2334;
(b) S. Horike, S. Shimomura, S. Kitagawa, Nat. Chem. 1 (2009) 695.
[2] (a) M. Dinca, J.R. Long, Angew. Chem., Int. Ed. 47 (2008) 2;
(b) J.J. Vittal, Coord. Chem. Rev. 251 (2007) 1781;
(c) S. Dalai, J. Phys. Sci. 15 (2011) 223;
(d) G.A. Hogan, N.P. Rath, A.M. Beatty, Cryst. Growth Des. 11 (2010) 3740;
(e) T.R. Cook, Y.R. Zheng, P.J. Stang, Chem. Rev. 113 (2013) 734.
[3] (a) K. Uemura, S. Kitagawa, M. Kondo, K. Fukui, R. Kitaura, H.-C. Chang, T. Mizutani, Chem. Eur. J. 8 (2002) 3586;
(b) K.S. Min, M.P. Suh, J. Am. Chem. Soc. 122 (2000) 6834;
(c) B. Gomez-Lor, E. GutiYrrez-Puebla, M. Iglesias, A. Ruiz Valero, Inorg. Chem. 41 (2002) 2429.
[4] (a) S. Kitagawa, M. Kondo, Bull. Chem. Soc. Jpn. 71 (1998) 1739;
(b) C. Janiak, J.K. Vieth, New J. Chem. 34 (2010) 2366;
(c) D.D. MacNicol, J.J. McKendrick, D.R. Wilson, Chem. Soc. Rev. 7 (1978) 65;
(d) R. Kitaura, K. Seki, G. Akiyama, S. Kitagawa, Angew. Chem., Int. Ed. 42 (2003) 428.
[5] (a) T. Pretsch, K.W. Chapman, G.J. Halder, C. Kepert, J. Chem. Commun. (2006) 1857;
(b) M.C. Bernini, F. Gandara, M. Iglesias, N. Snejko, E. Gutierrez-Puebla, E.V. Brusau, G.E. Narda, M.A. Monge, Chem. Eur. J. 15 (2009) 4896.
[6] (a) S.K. Ghosh, S. Bureekaew, S. Kitagawa, Angew. Chem., Int. Ed. 47 (2008) 3403;
(b) X. Bao, P. Guo, J. Liu, J. Leng, M. Tong, Chem. Eur. J. 17 (2011) 2335;
(c) S.S. Xantheas, Chem. Phys. 258 (2000) 225.
[7] (a) P.D. Beer, P.A. Gale, D.K. Smith, Supramolecular Chemistry, Oxford University Press, New York, 1999;
(b) J.-M. Lehn, Pure Appl. 50 (1978) 871.
[8] (a) K. Uemura, R. Matsuda, S. Kitagawa, J. Solid State Chem. 178 (2005) 2420;
(b) R. Sun, Y.-Z. Li, J. Bai, Y. Pan, Cryst. Growth Des. 7 (2007) 890;
(c) L. Bo, R. Chen, W. YaoYu, H. Lei, L. RuiTing, S. QiZhen, Sci. China Chem. 55 (2012) 341.
[9] (a) J. Boonmak, M. Nakano, N. Chaichit, C. Pakawatchai, S. Youngme, Dalton Trans. 39 (2010) 8161;
(b) A. Cheansirisomboon, C. Pakawatchai, S. Youngme, Aust. J. Chem. 66 (2012) 477;
(c) J. Piromchom, W. Nanthawat, B. Jaursup, C. Pakawatchai, S. Youngme, Inorg. Chem. Commun. 40 (2014) 59;
(d) J. Piromchom, W. Nanthawat, B. Jaursup, C. Pakawatchai, K. Chainok, S. Youngme, Inorg. Chem. Commun. 44 (2014) 111.
[10] SMART 5.6, Bruker AXS Inc., Madison, WI, 2000.
[11] SAINT 4.0 Software Reference Manual, Siemens Analytical X-Ray Systems Inc, Madison, WI, 2000.
[12] G.M. Sheldrick, SADABS, Program for Empirical Absorption correction of Area Detector Data, University of Göttingen, Göttingen, Germany, 2000.
[13] G.M. Sheldrick, Acta Crystallogr., Sect. A: Fund. Crystallogr. A64 (2008) 112.
[14] G.A. Jeffery, An Introduction to Hydrogen Bonding, Oxford University Press, Oxford, 1997.
[15] A.B.P. Lever, Inorganic Electronic Spectroscopy, 2 ed., Elsevier, The Netherlands, 1984.
[16] M. Kurmoo, Chem. Soc. Rev. 38 (2009) 1353.
[17] A.N. Khlobystov, N.R. Champness, C.J. Roberts, S.J.B. Tendler, C. Thompson, M. Schroder, CrystEngComm 4 (2002) 426.

EurJIC European Journal of Inorganic Chemistry

ChemPubSoc Europe

FULL PAPER

DOI:10.1002/ejic.201201085

CLUSTER ISSUE

Subtlety of the Spin-Crossover Phenomenon Observed with Dipyridylamino-Substituted Triazine Ligands

Nanthawat Wannarit,[a,b] Olivier Roubeau,*[c] Sujittra Youngme,*[b] and Patrick Gamez*[a,d]

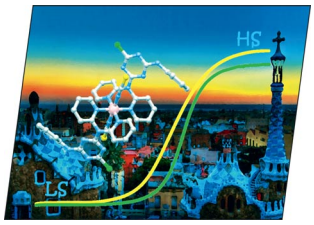

FRONT COVER

Keywords: Iron / LIESST effect / Calorimetry / Supramolecular interactions / Spin crossover

Reactions of the new, closely related ligands 4,6-dichloro-*N*,*N*-di(pyridine-2-yl)-1,3,5-triazine-amine (Cldpat) and 6-chloro-*N*′-phenyl-*N*,*N*-di(pyridin-2-yl)-1,3,5-triazine-2,4-diamine (Cladpat) with iron(II) thiocyanate produced coordination compounds with drastically distinct magnetic properties. The compound *trans*-$[Fe(Cldpat)_2(NCS)_2](H_2O)$ (**1**) is a high-spin complex from room temperature down to 5 K whereas the analogous compound *trans*-$[Fe(Cladpat)_2(NCS)_2]$ (**2**) exhibits spin-crossover (SCO) properties with $T_{1/2}$ = 178 K. Compounds **1** and **2** (both in its low-spin and high-spin states) have been structurally characterized by X-ray diffraction studies, which revealed identical metal coordination spheres. The SCO properties of **2** have been thoroughly investigated by temperature-dependent magnetic susceptibility measurements and differential scanning calorimetry (DSC), and a LIESST process with rapid relaxation of the trapped HS species has been observed. The equivalent coordination compound with selenocyanate anions, namely $[Fe(Cladpat)_2(NCSe)_2]$ (**3**) also displays SCO properties, although more gradual and with a lower $T_{1/2}$ value of 166 K.

Introduction

The phenomenon of spin crossover (SCO) is a particular and very interesting illustration of the ligand-field theory.[1,2] For octahedral coordination complexes of transition-metal ions, the d orbitals split into two sets, i.e. the t_{2g} and e_g sets, whose energy difference is given by the crystal-field splitting parameter Δ_{oct}.[3] The size of Δ_{oct} determines the electronic structure of the d^4–d^7 metal ions. Thus, for iron(II) complexes, a small Δ_{oct} will favour the high-spin state (HS, $e_g^2t_{2g}^4$, $S = 2$) while a large Δ_{oct} will produce a low-spin (LS, t_{2g}^6, $S = 0$) compound. With an appropriate ligand-field strength (namely for an intermediate Δ_{oct} value), the transition-metal compound may exhibit LS ↔ HS bistability through the application of an external stimulus, like temperature, pressure or light.[4–7] Hence, such SCO materials may find potential applications in molecular switches, data storage devices and optical displays, especially in the case of Fe^{II} ions, for which the LS state is diamagnetic.[8–11] Therefore, SCO species have received a great deal of attention from the scientific community for the past decade.[12,13] A great number of SCO Fe^{II} complexes have been synthesized that were principally obtained from ligands based on nitrogen-containing aromatic donor groups (such as pyridine and azole rings).[14–19]

For the past seven years, we have been involved in the design and preparation of SCO iron(II) compounds with polypyridine ligands.[20–22] In particular, the use of a ligand derived from the *s*-triazine ring and 2,2′-dipyridylamine units, namely 2,4,6-tris(dipyridin-2-ylamino)-1,3,5-triazine (dpyatriz),[23] has led to remarkable SCO systems.[22,24,25] Subsequently, Murray and coworkers have developed a variety of dipyridylamino-substituted-triazine ligands,[26–30] which were easily prepared from the highly versatile building block 2,4,6-trichloro-1,3,5-triazine.[31–33] The utilization of these ligands has allowed the preparation of SCO coordination compounds, hence corroborating the great potential of (2,2′dipyridylamine/triazine)-based ligands to generate molecular switches.

In the present study, we have taken advantage of the straightforward and highly selective substitution of the chloride atoms of 2,4,6-trichloro-1,3,5-triazine to synthesize two related dipyridylamino-substituted-triazine ligands, namely 4,6-dichloro-*N*,*N*-di(pyridine-2-yl)-1,3,5-triazine-amine (Cldpat) and 6-chloro-*N*′-phenyl-*N*,*N*-di(pyridin-2-yl)-1,3,5-triazine-2,4-diamine (Cladpat) (Scheme 1), whose sole difference lies in the replacement of one of the two

[a] Departament de Química Inorgànica, QBI,
Universitat de Barcelona,
Martí I Franquès 1–11, 08028 Barcelona, Spain
Fax: +34-93-490-7725
E-mail: patrick.gamez@qi.ub.es
Homepage: www.bio-inorganic-chemistry-icrea-ub.com
[b] Materials Chemistry Research Unit, Department of Chemistry and Center of Excellence for Innovation in Chemistry, Faculty of Science, Khon Kaen University,
Khon Kaen 40002, Thailand
E-mail: sujittra@kku.ac.th
[c] Instituto de Ciencia de Materiales de Aragón (ICMA),
CSIC and Universidad de Zaragoza,
Plaza San Francisco s/n, 50009 Zaragoza, Spain
E-mail: roubeau@unizar.es
[d] Institució Catalana de Recerca i Estudis Avançats (ICREA),
Passeig Lluís Companys 23, 08010 Barcelona, Spain
Supporting information for this article is available on the WWW under http://dx.doi.org/10.1002/ejic.201201085.

chloride atoms of Cldpat by an aniline unit, producing Cladpat. Actually, the use of these similar ligands to bind iron(II) ions leads to the formation of mononuclear coordination compounds with similar molecular structures, but dissimilar magnetic behaviours, thus revealing the drastic effect of tiny structural changes on the physical properties of related molecules.

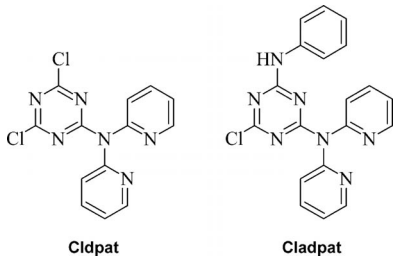

Scheme 1. Triazine-based ligands 4,6-dichloro-*N*,*N*-di(pyridine-2-yl)-1,3,5-triazine-amine (Cldpat) and 6-chloro-*N*′-phenyl-*N*,*N*-di-(pyridin-2-yl)-1,3,5-triazine-2,4-diamine (Cladpat).

Results and Discussion

Synthesis

As evidenced by earlier studies by Murray[26–29] and some of us,[22,24,25] *s*-triazine-based ligands containing at least one 2,2′-dipyridylamine unit allow the preparation of SCO iron(II) compounds. Herein, it was decided to investigate the potential ability of the simplest member of this family of dipyridylamino-substituted-triazine ligands, namely 4,6-dichloro-*N*,*N*-di(pyridine-2-yl)-1,3,5-triazine-amine (Cldpat; Scheme 1), to generate SCO properties upon coordination to an iron(II) ion in the presence of thiocyanates or selenocyanates. Hence, Cldpat was prepared in THF by the reaction of 2,2′-dipyridylamine with 1 equiv. of 2,4,6-trichloro-1,3,5-triazine, in the presence of *N*,*N*-diisopropylethylamine (DIPEA).

Next, one of the chloride atoms of Cldpat was replaced by an aniline group with the aim of examining the influence of this slight modification of the ligand on the magnetic properties of the ensuing iron(II) complex. Thus, the ligand 6-chloro-*N*′-phenyl-*N*,*N*-di(pyridin-2-yl)-1,3,5-triazine-2,4-diamine (Cladpat; Scheme 1) was synthesized from Cldpat through substitution of one of its chloride atoms by aniline, using sodium carbonate as a base in acetone/water. The molecular structure of Cladpat could be determined by single-crystal X-ray diffraction (Figure S1). The solid-state structure of Cladpat shows that the molecules are strongly associated by strong hydrogen-bonding interactions [$N_{aniline}$–H···$N_{triazine}$ = 2.972(3) Å; ∠ $N_{aniline}$–H–$N_{triazine}$ = 176(3)°; Figure S1], giving rise to a 1D supramolecular chain along the crystallographic *c* axis. Such anticipated H bonds, for which the ligand Cladpat was actually designed, may be crucial to favour the occurrence of cooperative SCO, if maintained in complexes of Cladpat.

The coordination compounds **1**–**3** were synthesized by the direct addition of a freshly prepared methanolic solution of $Fe(NCX)_2$ (X = S or Se) to a methanolic solution containing 2 equiv. of the dipyridylamino-substituted-triazine ligand (Cldpat or Cladpat). The solution of $Fe(NCS)_2$ was obtained from iron(II) sulfate and potassium thiocyanate while $Fe(NCSe)_2$ was made from iron(II) perchlorate and potassium selenocyanate.

Description of the Crystal Structure of *trans*-[$Fe(Cldpat)_2(NCS)_2$](H_2O) (1)

Reaction of 1 equiv. of iron(II) thiocyanate with 2 equiv. of Cldpat generates compound **1** with a yield of 73%. Structural information on **1** has been obtained from X-ray diffraction studies at 100 K. The high *R* value found (see Table S2) is most likely due to unresolved crystal twinning. Nevertheless, the data collected are satisfactory for a reasonably accurate determination of the molecular structure of **1**. Actually, the iron(II) centre in **1** exhibits the anticipated octahedral coordination environment [typically observed for iron(II) thiocyanate complexes with this family of ligands[25,34]], which is formed by two Cldpat ligands in the equatorial plane and two *trans* thiocyanate anions (Fig-

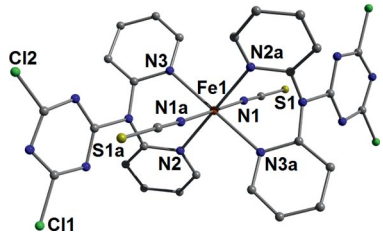

Figure 1. Representation of the molecular structure of compound **1** with partial atom numbering scheme. The thermal ellipsoids are drawn at the 50% probability level. The hydrogen atoms and the lattice water molecule are not shown for clarity. Symmetry operation: a, 1 – *x*, 1 – *y*, –*z*.

Table 1. Coordination bond lengths [Å] and angles [°], and supramolecular interactions for compound **1**.

Distances			
Fe1–N1	2.090(13)	Fe1–N3	2.264(15)
Fe1–N2	2.214(13)	$Fe1\cdots Fe1_{inter}$[a]	8.396(16)
Angles			
N2–Fe1–N3	81.7(5)	N3a–Fe1–N2[b]	98.3(5)
N2a–Fe1–N3	98.3(5)	N2a–Fe1–N3a	81.7(5)
N1–Fe1–N1a[b]	180		
Σ Fe1°[c]	43	Φ°[d]	74
Hydrogen bond			
Cl3···O2So	2.739(5)		
Lone pair–π interactions			
Cg10···S2s[e]	3.242(7)	Cg10···S2	3.337(8)

[a] Closest inter-monomer Fe···Fe distance. [b] Symmetry operation: a 1 – *x*, 1 – *y*, –*z*. [c] Σ° = the sum of |90 – θ| for the 12 N–Fe–N angles in the octahedron.[12,35,36] [d] Φ° = sum of |60 – θ| for the 24 N–Fe–N angles describing the trigonal twist angle as described by Marchivie and coworkers.[12,37] [e] Symmetry operation: o – *x*, 1 – *y*, 1 – *z*; s – *x*, 1/2 + *y*, 1/2 – *z*.

ure 1). Selected bond lengths and angles are listed in Table 1. Surprisingly, The Fe–N_{Py} bond lengths in the range 2.214(13)–2.264(15) Å and the Fe–N_{NCS} distances of 2.090(13) Å characterize a high-spin iron(II) compound. This fact is confirmed by temperature-dependent magnetic-susceptibility measurements revealing that the FeN_6 species in **1**, rather unexpectedly, does not present a SCO process (see below).

The solid-state structure of **1** shows the occurrence of intramolecular lone pair···π interactions [Cg10···S2 = 3.337(8) Å; Table 1]. In addition, the molecules are associated by means of intermolecular lone pair···π interactions [Cg10···S2s = 3.242(7) Å; Table 1], which generate a supramolecular 1D chain. The chains interact with each other through $S_{lonepair}$···$triazine_{\pi}$ contacts, producing a 2D layer in the crystallographic *bc* plane (Figures 2 and S2). These 2D layers are further connected through hydrogen bonds between lattice water molecules and the chloride atoms of the triazine rings that give rise to a 3D network (Figure S3).

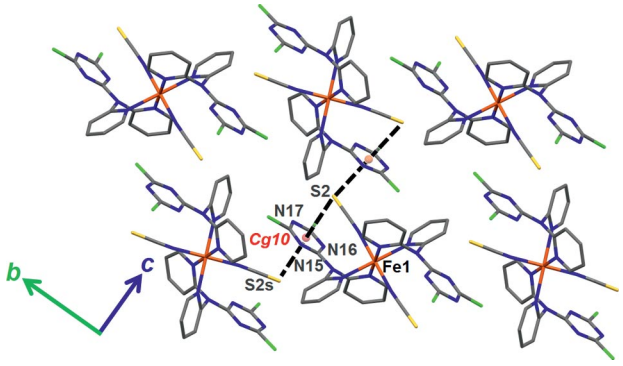

Figure 2. View of the crystal packing of **1** showing the formation of a supramolecular 2D network in the *bc* plane by means of lone pair···π interactions (black dotted lines) between the triazine rings and neighbouring thiocyanate anions [Cg10···S2 = 3.337(8) Å and Cg10···S2s = 3.242(7) Å]. Symmetry operation: s – *x*, 1/2 + *y*, 1/2 – *z*.

Description of the Crystal Structure of *trans*-[Fe(Cladpat)$_2$(NCS)$_2$] (2)

Reaction of 1 equiv. of iron(II) thiocyanate with 2 equiv. of Cladpat produces compound **2** with a yield of 89%. Compound **2**, which shows SCO properties (see magnetic studies), crystallizes in the monoclinic space group $P2_1/c$, both at 100 K and at 270 K (Table S2). The molecular structure of low-spin **2** is depicted in Figure 3, and selected bond lengths and angles are listed in Table 2. Compound **2** consists of an octahedral iron(II) ion coordinated by four pyridine units from two Cladpat ligands and two *trans* N-bonded thiocyanate anions.

Such a FeN_6 coordination environment is known to potentially produce SCO iron(II) species.[35] The Fe–N_{Py} distances ranging from 1.965(3) to 2.000(4) Å are typical of a LS iron(II) entity, as is the case for the Fe–N_{NCS} distances of 1.945(4) and 1.948(4) Å (Table 2). These bond lengths increase by ca. 0.20 Å for Fe–N_{Py} and ca. 0.15 Å for Fe–N_{NCS} when the temperature is raised to 270 K (Table 2), which is indicative of a full spin transition, as also observed during magnetic studies on **2** (see below).

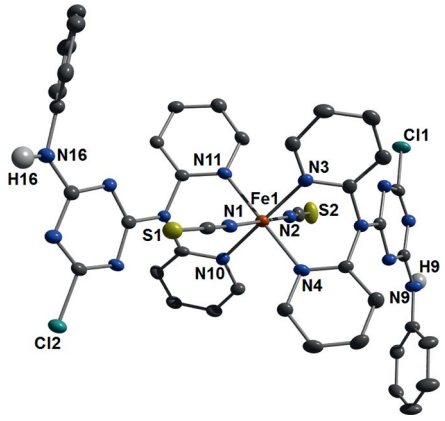

Figure 3. Representation of the molecular structure of compound **2** (LS state, determined at 100 K) with partial atom numbering scheme. The thermal ellipsoids are drawn at the 50% probability level, and only the hydrogen atoms involved in hydrogen-bonding interactions are shown for clarity.

Table 2. Coordination bond lengths [Å] and angles [°], and supramolecular interactions for compound **2** (low-spin and high-spin states).

2	LS[a]	HS[b]
	Distances	
Fe1–N1	1.948(4)	2.090(6)
Fe1–N2	1.945(4)	2.087(6)
Fe1–N3	1.984(3)	2.190(5)
Fe1–N4	1.994(4)	2.201(6)
Fe1–N10	1.965(3)	2.178(5)
Fe1–N11	2.000(4)	2.214(6)
Fe1···$Fe1_{inter}$[c]	8.424(4)	8.584(6)
	Angles	
N3–Fe1–N4	86.27(15)	82.7(2)
N4–Fe1–N10	93.68(15)	97.7(2)
N10–Fe1–N11	86.86(15)	82.3(2)
N11–Fe1–N3	93.19(15)	97.4(2)
N1–Fe1–N2	176.6(2)	176.6(2)
ΣFe1°[d]	32	47
Φ°[e]	43	70
	Hydrogen bonds[f]	
N9–H9···N15a	3.010(5)	3.035(8)
∠ N9–H9–N15a	177(6)	165(6)
N16–H16···N8b	2.995(5)	3.023(8)
∠ N16–H16–N8b	157(5)	157(6)
	Lone pair–π interactions	
Cg5···S2	3.459(2)	3.589(4)
Cg8···S1	3.504(2)	3.564(3)
	π–π interactions	
Cg9···Cg10	3.976(3)	4.236(5)

[a] At 100 K. [b] At 270 K. [c] Closest inter-monomer Fe···Fe distance. [d] Σ° = the sum of $|90 - \theta|$ for the 12 N–Fe–N angles in the octahedron.[12,35,36] [e] Φ° = sum of $|60 - \theta|$ for the 24 N–Fe–N angles describing the trigonal twist angle as described by Marchivie and coworkers.[12,37] [f] Symmetry operations: a 1 – *x*, –1/2 + *y*, 1/2 – *z*; b 1 + *x*, 1/2 – *y*, 1/2 + *z*.

The distortion parameters $\Sigma°$ and $\Phi°$ reflect the deviation from an ideal octahedral geometry.[38] $\Sigma°$ directly measures the distortion from a perfect octahedron while $\Phi°$ defines the deformation of the octahedral coordination geometry towards a trigonal-prismatic environment.[12] For a perfect octahedron, $\Sigma° = \Phi° = 0$. For LS **2**, $\Sigma° = 32$ and $\Phi° = 43$, whereas the respective values for HS **2** are 43 and 70 (Table 2). The lower $\Sigma°$ and $\Phi°$ values for the LS compound are typical since LS complexes are less deformed than HS ones.[35,37] Hence, $\Delta\Sigma°$ ($\Sigma°_{HS} - \Sigma°_{LS}$) and $\Delta\Phi°$ ($\Phi°_{HS} - \Phi°_{LS}$) quantify the magnitude of the structural changes occurring during the SCO. For **2**, $\Delta\Sigma° = 15$ and $\Delta\Phi° = 27$; the high $\Delta\Phi°$ value observed for **2** is indicative of a significant alteration of the octahedral geometry upon the LS → HS transition. Such a large structural variation may be associated with cooperativity between the iron(II) centres, possibly through intermolecular interactions (actually, the magnetic measurements show a relatively cooperative SCO; see below). In fact, the crystal packing reveals that the iron(II) molecules are connected through double $N_{aniline}$–H···$N_{triazine}$ bonds (Table 2), which generate a 1D supramolecular chain (Figure 4). These hydrogen bonds are affected by the spin transition (a variation of about 0.025 Å is observed); in particular, the N9–H9···N15a bond experiences a bending of ca. 7%, the angle varying from 177(6)° to 165(6)° during the LS → HS transition (Table 2). In addition, the molecules of **2** exhibit intramolecular lone pair···π interactions[39,40] (Cg5···S2 and Cg8···S1 contacts; Figure 4), which are also altered by the SCO (Table 2). A closer look at the solid-state structure of **2** reveals that the 1D supramolecular chains are linked into a 2D layer by parallel-displaced π–π interactions,[41,42] involving neighbouring aniline rings [centroid-to-centroid distance Cg9···Cg10 = 3.976(3) Å in LS **2**; Figure S4]. The shortest arene–arene contact distances are C17···C39i = 3.257(7) Å and C18···C40i = 3.335(7) Å (Figure S4B), and rise to 3.283(12) Å and 3.397(11) Å, respectively, upon LS → HS transition [corresponding to an increase of the centroid-to-centroid distance of ca. 7%, from 3.976(3) to 4.236(5) Å; Table 2]. All these supramolecular bonding interactions may favour cooperativity between the transiting iron(II) ions.

It has to be noted that the $\Sigma°$ and $\Phi°$ values for HS **2** are comparable to those of **1** (see Table 1), therefore suggesting analogous octahedral distortions for the two high-spin molecules, and corroborating the metal coordination environment in **1**.

Reaction of the ligand Cladpat with iron(II) selenocyanate [instead of iron(II) thiocyanate] yields the analogous compound [Fe(Cladpat)$_2$(NCSe)$_2$] (**3**), as indicated by elemental analyses, which also exhibits SCO properties (see the section Magnetic Studies). Although the molecular structure of **3** could not be determined by X-ray diffraction studies, it is expected that the coordination environment of the iron(II) centres in **3** is equivalent to those of **1** and **2**, with two *trans* N-bonded selenocyanate ions. Actually, the IR absorption band observed at 2061 cm^{-1} for compound **3** is identical to that reported by Murray and coworkers for an iron(II) SCO complex from a dipyridylamino-substituted-triazine ligand with *trans*-coordinated NCSe ions.[30]

Magnetic Studies

The effect of the substituent (ligands Cldpat and Cladpat) and the replacement of thiocyanate by selenocyanate anions have been investigated by magnetic measurements. Hence, the temperature dependence of the χT product of compounds **1**–**3**, χ being the molar paramagnetic susceptibility, were derived from magnetization measurements on bulk samples in an applied field of 0.5 T for **1** and **3**, and 1 T for **2** (see Experimental Section), and in the temperature range 2–300 K. The data for compounds **1** and **2**, shown in Figure 5, corroborate the structural observations, evidencing the occurrence of a complete thermal SCO for compound **2**, and the – surprising – absence of such a process in the case of compound **1**. Indeed, the χT product of **1** remains practically constant at 3.11–3.09 cm^3 mol^{-1} K from 300 K down to 50 K, the temperature below which a de-

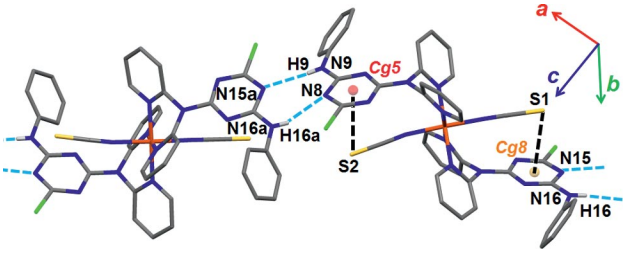

Figure 4. View of the crystal packing of LS **2** showing $N_{aniline}$–H···$N_{triazine}$ bonds [N9–H9···N15a = 3.010(5) Å and N16a–H16a···N8 = 2.995(5) Å; blue dotted lines] connecting the iron(II) molecules to generate a 1D supramolecular chain. Intramolecular lone pair···π interactions (black dotted lines) take place between the thiocyanate sulfur atoms and the triazine rings [Cg5···S2 = 3.459(2) Å and Cg8···S1 = 3.504(2) Å]. Symmetry operations: a 1 – x, –1/2 + y, 1/2 – z.

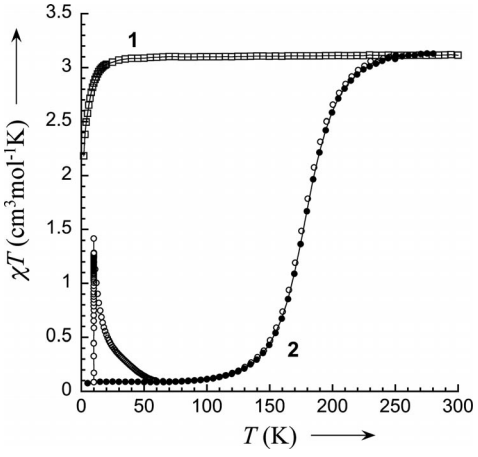

Figure 5. χT vs. T plot for **1** (squares) and **2**, showing the process of SCO (full circles), the partial LS to HS photo-induced trapping at 10 K (LIESST effect) and the relaxation back to the LS ground state and normal behaviour upon warming (empty circles).

crease of χT is observed down to 2.18 $cm^3 mol^{-1} K$. The magnetic properties of **1** are thus in agreement with an S = 2 HS ground state for the Fe^{II} ion, with g close to 2, throughout the whole temperature range considered, the decrease at low temperatures being due to zero-field-splitting effects of the S = 2 spins. Magnetization vs. field measurements at 2 K indeed show saturation at ca. 4.05 $N_A\mu_B$ at 5 T (see Figure S5), in agreement with an S = 2 spin ground state and a g value slightly above 2. On the other hand, the χT product of **2** decreases upon cooling, from similar values to those of **1**, i.e. 3.13 $cm^3 mol^{-1} K$ at 280 K, reaching a plateau at 0.11 $cm^3 mol^{-1} K$ below 100 K, and down to 0.08 $cm^3 mol^{-1} K$ at 5 K. Compound **2** thus undergoes a complete SCO centred at ca. 178 K and with a limited cooperative character, as indicated by a ΔT_{80} of 50 K (80% of the transition occurs within about 50 K). In agreement with the structural observations, the process of SCO is virtually completed at 100 K. These observations are perfectly reproducible upon warming, thus with no detectable hysteresis, and over various cycles.

The possibility of trapping the HS metastable state at low temperature through irradiation, the so-called LIESST effect,[43] was examined on a thin sample of **2**. At 10 K, a fast increase of χT is indeed observed when irradiating with green light, clearly demonstrating the efficiency of the LIESST effect in this compound (Figures 5 and 6 top). Nevertheless, the rate of increase rapidly drops and virtually stable values are reached after ca. 1 h (Figure 6 top). After turning the irradiation OFF and thermalization, the resulting χT value of 1.42 $cm^3 mol^{-1} K$ corresponds to ca. 50% of trapped HS centres, based on the χT value of **1** at the same temperature. An incomplete LIESST effect in thin samples with an apparent steady state similar to that observed herein may be due to an overlap of the $^5T_2 \rightarrow {}^5E$ (HS) and $^1A_1 \rightarrow {}^3T_1$ (LS) bands, resulting in competitive LIESST and reverse-LIESST processes.[44] Another cause of such an incomplete light-induced trapping, even in thin samples, is the competition of the light-induced LS→HS trapping with the relaxation of the trapped HS species back to the LS ground state, at the origin of light-induced bistability in cooperative SCO systems.[45,46] Measurements vs. time at 10 K after 1 h of irradiation for **2** indeed show that χT rapidly drops in an exponential manner, already reaching values of ca. 0.40 $cm^3 mol^{-1} K$ after only 1 h. It is therefore clear that the HS→LS relaxation is fast, even at 10 K (Figure 6 bottom). An estimation of the characteristic relaxation time at 10 K of 765 s is obtained by adjusting the experimental data to a stretched exponential with β = 0.67 (red line in Figure 6 bottom). Confirmation of the relative instability of the trapped HS state is obtained from the measurements upon warming after irradiation (Figure 5). χT rapidly decreases to reach values similar to those of a normal LS state at temperatures as low as 55 K, as could be expected from the thermal activation of a relaxation process that is already fast at 10 K.

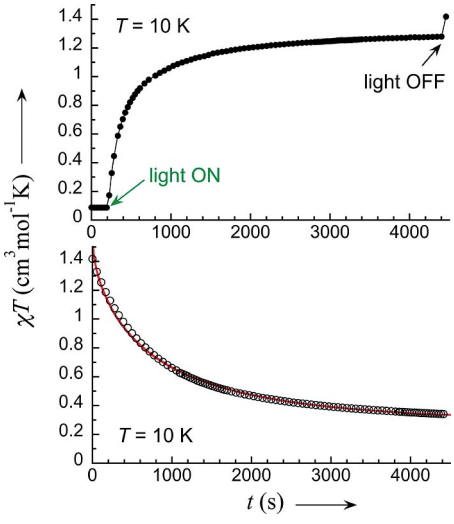

Figure 6. Top: χT vs. time evolution for **2** at 10 K showing the increase due to LIESST during irradiation with a green light. Bottom: χT vs. time evolution for **2** at 10 K in obscurity after the irradiation with a green light, showing an exponential-like behaviour. The full red line is a fit to a stretched exponential with β = 0.67 and critical time of 765 s.

Magnetic properties of compound **3** are shown in Figure 7 as a χT vs. T plot. Similar to **2**, a decrease of χT is observed, from 3.43 $cm^3 mol^{-1} K$ at 280 K, down to a plateau at ca. 0.15–0.11 $cm^3 mol^{-1} K$ below 90 K and down to 0.11 $cm^3 mol^{-1} K$ at 5 K, thus confirming a likely comparable molecular structure to that of **2**. Compound **3** thus also presents a complete SCO, although centred at a lower temperature, e.g. 166 K, and more gradual than that of **2**, with a ΔT_{80} of ca. 80 K. Such a low cooperativity in a selenocyanate compound with respect to its thiocyanate analogue is documented, and is possibly related to the participation of the more diffuse Se atom in intermolecular interactions.[47,48] This is likely the case here since the S atoms in the structure of **2** do participate in the network of intermolecular interactions (see above). The lower SCO temperature in **3** with respect to **2** is more surprising since the replacement of S by Se in NCX^--based SCO compounds usually results in an increase in the SCO temperature.[47–51]

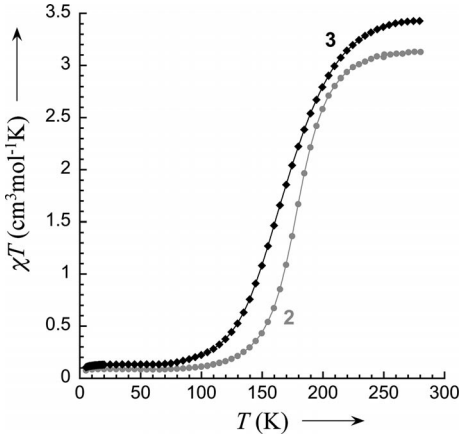

Figure 7. χT vs. T plot for **3** (rhombus), showing a complete SCO centred at around 166 K. The data of compound **2** is recalled as light circles for comparison.

Thermal Properties

The molar heat capacity at constant pressure, C_p, of **2** was derived from differential scanning calorimetry (DSC) measurements over the temperature range 110–290 K (see DSC traces in Figure S6). A strong heat capacity anomaly is detected between 135 and 245 K, culminating at ca. 180 K, which can be associated with the SCO phenomenon in **2**. Indeed, both the temperature range and maxima are in excellent agreement with the magnetic data. A lattice heat capacity was estimated from data below 135 K and above 245 K (dashed line in Figure 8), allowing the determination of the excess heat capacity associated with the SCO phenomenon in **2** (inset in Figure 8). The related excess enthalpy and entropy were derived by integration of the excess heat capacity and amount to 8.08 kJ mol^{-1} and 44.6 J mol^{-1} K^{-1}, respectively (see Figures S7 and S8). Both figures are relatively large, which is usually taken as a consequence of a cooperative character of the SCO. In particular, the excess entropy is well above the purely electronic component, *R*Ln5, thus containing a significant content arising from the coupling of the electronic transition with lattice phonons. The so-called domain model (developed by Sorai and widely used in SCO studies when calorimetric data are available[52]) allows such a cooperative character to be quantified through the number *n* of like-spin SCO centres within an interacting domain; the larger the domains are, the more cooperative the transition is. Values of *n* close to 1 are typical of solution-like gradual SCO,[53–55] while values of ca. 10 to 95[47,56,57] have been derived for cooperative to very cooperative systems. Here, the excess heat capacity of **2** is very nicely reproduced by this model with $n = 3.33$ (red line in the inset of Figure 8), indicative of a relatively weakly cooperative SCO, and in agreement with the magnetic studies.

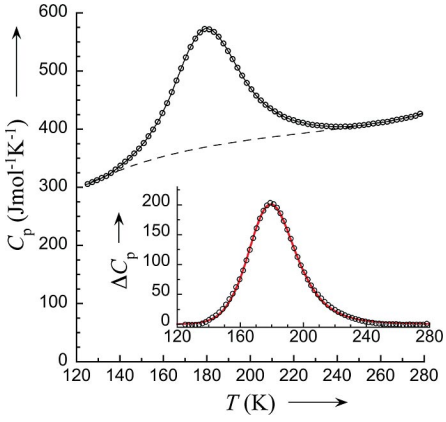

Figure 8. Molar heat capacities of **2** showing a broad hump associated with the SCO. The dashed line is the estimated lattice component. Inset: excess heat capacities associated with the SCO in **2**. The full line is a fit to the domain model of Sorai (see text and SI) with $n = 3.3$.

Conclusions

The present study has shown that an apparent minor modification of a ligand, namely the substitution of one of the chloride atoms of Cldpat by an aniline group (ligand Cladpat) gives rise to a drastic change of the magnetic properties of the corresponding iron(II) complexes. Indeed, the coordination compounds **1** and **2**, which exhibit identical coordination spheres for their metal centre, display distinct magnetic behaviours; **1** is a high-spin species whereas **2** is a SCO complex with a (weakly cooperative) transition. These opposite comportments are obviously due to the different ligands. Since the coordination bond lengths and angles are comparable for **1** and HS **2**, the distinct magnetic properties observed are most likely caused by different ligand-field strengths (i.e. Cldpat has a smaller Δ_{oct} value). Theoretical studies and the preparation of dipyridylamino-substituted triazine ligands bearing electron-withdrawing and/or electron-donating substituents may help to understand these disparities. Therefore, these investigations will be carried out and the results will be reported in a future paper.

Experimental Section

General: All reagents and solvents were used as received from commercial sources. The reactions were typically carried out in air. IR spectra (as KBr pellets) were recorded with a Nicolet 5700 FTIR spectrometer. Elemental analyses were performed by the Servei de Microanalisi, Consejo Superior de Investigaciones Cientificas (CSIC) of Barcelona. MS spectra were recorded with a MALDI-TOF Voyager DE-RP mass spectrometer equipped with a nitrogen laser (337 nm, 3 ns pulse) and an accelerating voltage of 20–25 kV or an LC/MSD-TOF ESI-mass spectrometer from Agilent Technologies, at the Serveis Cientificotècnics of the University of Barcelona. ^{1}H NMR spectra were recorded at room temperature with a Varian Unity 300 MHz spectrometer; chemical shifts are reported in ppm relative to the residual solvent signal of $CDCl_3$ (δ = 7.26 ppm). TLC was performed on Alugram® SIL G/UV/254 silica-gel precoated sheets (Macherey–Nagel, Germany).

Single-Crystal X-ray Diffraction Studies: Data for Cladpat, **1** and **2** (LS and HS states) were collected using Mo-K_α radiation (λ = 0.7107 Å) with a Bruker APEX II QUAZAR diffractometer equipped with a microfocus multilayer monochromator at T = 100(2) K and at T = 270(2) K for HS **2**. The structures were solved by direct methods and refined on F^2 using the SHELX-TL suite.[58] In the case of **1**, although the data collected appeared to be of good quality and the processing took place normally, the refinement could only converge to high final *R* values, and required displacement parameter restraints for most of the organic ligands. This situation is likely due to the presence of twinning; unfortunately, we were not able to settle it. Therefore, even though the molecular structure and the intermolecular interactions are likely accurate, the X-ray structure described herein for **1** should be considered as a preliminary report. Crystal data and refinement parameters are given in Tables S1 (Cladpat) and S2 (**1**, LS **2** and HS **2**). CCDC-901348 (Cladpat), -901349 (**1**), -901350 (**2**, 100 K) and -901351 (**2**, 270 K) contain the supplementary crystallographic data for this paper. These data can be obtained free of charge from The Cambridge Crystallographic Data Centre via www.ccdc.cam.ac.uk/data_request/cif.

Magnetic Measurements: Variable-temperature magnetic-susceptibility data for compound **1**–**3** were obtained on microcrystalline samples with a Quantum Design MPMS-XL SQUID magnetometer housed at the SAI Physical Measurements of the University of

Zaragoza. Variable-temperature measurements were performed in a 0.5 T applied field, still in the linear range of M vs. H. Pascal's constants were used to estimate diamagnetic corrections to the molar paramagnetic susceptibility, and a correction was applied for the sample holder. Warming and cooling rates were of the order of 0.3 K min^{-1}. Irradiation experiments were performed using the Quantum Design fibre optics setup (FOSH). Using this setup, measurements at low fields were noisy, and the applied field was 1 T throughout the whole study. This field was found to be the best compromise to remain close to the linear range of M vs. H curves and obtain good quality data. The light source was a Xenon arc lamp equipped with sets of short-pass and long-pass filters (SPF or LPF). Specifically for the present study, a SPF 650 nm and a LPF at 500 nm were used. Data were corrected for the empty FOSH signal, determined beforehand.

Differential Scanning Calorimetry Measurements: DSC experiments were performed with a differential scanning calorimeter Q1000 with the LNCS accessory from TA Instruments. The temperature and enthalpy scales were calibrated with a standard sample of indium, using its melting transition (156.6 °C, 3296 J mol^{-1}). Measurements were carried out using aluminium pans with a mechanical crimp, with an empty pan as reference. The zero-heat flow procedure described by TA Instruments was followed to derive heat capacities, using synthetic sapphire as the reference compound. An overall accuracy of ca. 0.2 K in temperature and up to 5 to 10% in the heat capacity was estimated over the whole temperature range, by comparison with the synthetic sapphire.

4,6-Dichloro-*N*,*N*-di(pyridine-2-yl)-1,3,5-triazin-2-amine (Cldpat): 2,4,6-Trichloro-1,3,5-triazine (cyanuric chloride) (2.7 g, 14.6 mmol) was dissolved in THF. *N*,*N*-Diisopropylethylamine (DIPEA) (2.55 mL, 1.89 g; 14.6 mmol) was added whilst stirring. The resulting yellow solution was cooled down to 0 °C using an ice bath. Subsequently, a solution of 2,2′-dipyridylamine (5.10 g, 14.6 mmol) in THF (50 mL) was added dropwise, and the reaction mixture was stirred at this temperature for 1 h. The yellow precipitate obtained (i.e. hydrochloride salt of DIPEA) was separated by filtration, and the filtrate was concentrated under reduced pressure using a rotary evaporator at 35 °C. The resulting crude product was purified by column chromatography on silica gel with ethyl acetate as the eluent (R_f = 0.54) to give pure Cldpat as a white powder (4.44 g, 13.9 mmol, 95%). $C_{13}H_8Cl_2N_6$ (319.15): calcd. C 48.92, H 2.53, N 26.33; found C 48.90, H 2.48, N 26.21. ^{1}H NMR (300 MHz, $CDCl_3$, room temp.): δ = 7.24–7.33 (m, 2 H), 7.54 (dt, J = 8.1, J = 0.9 Hz, 2 H), 7.80–7.89 (m, 2 H), 8.50 (ddd, J = 4.9, J = 1.9, J = 0.8 Hz, 2 H) ppm. MS (ESI$^+$): m/z = 320.17 [M + H]$^+$. IR (KBr): $\tilde{\nu}$ = 1585 (s), 1548 (br.), 1491 (s), 1461 (s), 1430 (s), 1324 (m), 1220 (s), 1182 (s), 842 (s), 796 (m), 778 (m), 746 (m), 667 (m) cm^{-1}.

6-Chloro-*N*′-phenyl-*N*,*N*-di(pyridin-2-yl)-1,3,5-triazine-2,4-diamine (Cladpat): Aniline (0.57 mL, (0.58 g, 6.27 mmol) was added to a solution of Cldpat (2.00 g, 6.27 mmol) in acetone (35 mL). Subsequently, a solution of Na_2CO_3 (0.30 g, 3.14 mmol) in water (10 mL) was added dropwise, giving rise to a white precipitate. After a reaction time of 6 h, the content was poured into crushed ice and the resulting mixture was stirred until all of the ice had melted. The white precipitate of pure Cladpat was isolated by filtration, washed with water and dried overnight under vacuum (2.33 g, 6.21 mmol, 99%). $C_{19}H_{14}ClN_7$ (375.82): calcd. C 60.72, H 3.75, N 26.09; found C 60.64, H 3.67, N 25.96. ^{1}H NMR (300 MHz, $CDCl_3$, room temp.): δ = 6.97–7.33 (m, 8 H), 7.60 (t, J = 16.9, J = 1.8 Hz, 2 H), 7.82 (td, J = 7.9, J = 1.8 Hz, 2 H), 8.49 (d, J = 3.8 Hz, 2 H) ppm. MS (ESI$^+$): m/z = 376 [M + H]$^+$. IR (KBr): $\tilde{\nu}$ = 3239 (w), 3079 (w), 1608 (m), 1550 (s), 1464 (s), 1382 (s), 1226 (m), 988 (m), 804 (w), 767 (w), 662 (w) cm^{-1}.

***trans*-[Fe(Cldpat)$_2$(NCS)$_2$](H$_2$O) (1):** A methanolic solution (5 mL) of KNCS (0.019 g; 0.2 mmol) was added to an aqueous solution (2 mL) of $FeSO_4 \cdot 7H_2O$ (0.028 g; 0.1 mmol). After 15 min of stirring, the precipitate of K_2SO_4 was removed by filtration. Ascorbic acid (in a small quantity) was added to the filtrate to prevent oxidation to iron(III). Subsequently, this iron(II) solution was added to a solution of Cldpat (0.064 g; 0.2 mmol) in dichloromethane (15 mL). The resulting yellow reaction mixture was filtered and the filtrate was left unperturbed for the slow evaporation of the solvent. After two days, small yellow crystals of **1** were obtained (0.605 g, 0.730 mmol, 73%). $C_{28}H_{16}Cl_4FeN_{14}S_2$ (**1**–H_2O): calcd. C 41.50, H 1.99, N 24.20; found C 40.94, H 1.78, N 24.23. IR (KBr): $\tilde{\nu}$ = 3239 (w), 3079 (w), 1608 (m), 1550 (s), 1464 (s), 1382 (s), 1226 (m), 988 (m), 804 (w), 767 (w), 662 (w) cm^{-1}.

***trans*-[Fe(Cladpat)$_2$(NCS)$_2$] (2):** A methanolic solution (5 mL) of KNCS (0.019 g; 0.2 mmol) was added to an aqueous solution (2 mL) of $FeSO_4 \cdot 7H_2O$ (0.028 g; 0.1 mmol). After 15 min of stirring, the precipitate of K_2SO_4 was removed by filtration. Ascorbic acid (in a small quantity) was added to the filtrate to prevent oxidation to iron(III). Next, a solution of Cldpat (0.075 g, 0.2 mmol) in dichloromethane (5 mL) was added to the iron(II) solution. The resulting yellow reaction mixture was filtered and the filtrate was left unperturbed for the slow evaporation of the solvent. After 2 d, small yellowish-green single crystals of **2**, suitable for X-ray diffraction studies, were obtained (0.082 g; 0.089 mmol, 89%; based on iron). $C_{40}H_{28}Cl_2FeN_{16}S_2$ (923.64): calcd. C 52.01, H 3.06, N 24.26; found C 52.11, H 3.02, N 24.34. IR (KBr): $\tilde{\nu}$ = 3433 (br.), 3244 (w), 2061 (s), 1603 (m), 1558 (s), 1462 (s), 1417 (s), 1383 (m), 1226 (m), 996 (w), 800 (w) cm^{-1}.

[Fe(Cladpat)$_2$(NCSe)$_2$] (3): A small quantity of ascorbic acid was added to a methanolic solution (2 mL) of $Fe(ClO_4)_2 \cdot 6H_2O$ (0.064 g, 0.25 mmol). A methanolic solution (10 mL) of Cldpat (0.188 g, 0.5 mmol) was subsequently added. Finally, a solution of KNCSe (0.072 g, 0.5 mmol) in methanol (10 mL) was added and the resulting reaction mixture was filtered. The filtrate was left unperturbed for the slow evaporation of the solvent. After 2 d, small yellow single crystals of **3** were obtained (0.207 g, 0.203 mmol, 81%). $C_{40}H_{28}Cl_2FeN_{16}Se_2$ (1017.44): calcd. C 47.22, H 2.77, N 22.03; found C 47.19, H 2.51, N 21.83. IR (KBr): $\tilde{\nu}$ = 3447 (br.), 3245 (w), 2061 (s), 1605 (s), 1560 (s), 1461 (m), 1416 (s), 1383 (m), 1225 (m), 996 (w), 799 (w) cm^{-1}.

Supporting Information (see footnote on the first page of this article): Crystallographic data for the ligand Cladpat (Table S1), compounds **1**, LS **2** and HS **2** (Table S2); representation of the molecular structure of Cladpat (Figure S1); views of the crystal packing of **1** (Figures S2 and S3); view of the crystal packing of **2** (Figure S4); representation of the magnetization vs. applied field at 2 K for compound **1** (Figure S5); DSC traces of compound **2** for warming and cooling modes (Figure S6); Excess enthalpy and entropy involved in the SCO process in compound **2** (Figure S7); Details of modellization of ΔC_p data with the so-called domain model.

Acknowledgments

P. G. acknowledges ICREA (Institució Catalana de Recerca i Estudis Avançats) and the Ministerio de Economía y Competitividad of Spain (Project CTQ2011-27929-C02-01). The Royal Golden Jubilee Ph. D Program (PHD/0234/2550), the Thailand Research Fund and Khon Kaen University, the Higher Education Research Promotion and National Research University Project of Thailand and the Center of Excellence for Innovation in Chemistry (PERCH-CIC), Office of the Higher Education Commission, Min-

istry of Education are also acknowledged. O. R. acknowledges funding from the Ministerio de Economía y Competitividad of Spain (Project MAT2011-24284).

[1] B. N. Figgis, M. A. Hitchman, in *Ligand Field Theory and Its Applications*, Wiley-VCH, New York, **2000**.
[2] A. B. Koudriavtsev, W. Linert, *J. Struct. Chem.* **2010**, *51*, 335–365.
[3] A. B. P. Lever, in *Werner Centennial* (Ed.: G. B. Kauffman), ACS Publications, Washington, USA, **1967**, pp. 430–451.
[4] P. Gütlich, A. Hauser, H. Spiering, *Angew. Chem.* **1994**, *106*, 2109; *Angew. Chem. Int. Ed. Engl.* **1994**, *33*, 2024–2054.
[5] P. Gütlich, H. A. Goodwin, in *Spin Crossover in Transition Metal Compounds I*, Springer-Verlag Berlin, Berlin, **2004**, vol. 233, pp. 1–47.
[6] J. A. Real, A. B. Gaspar, M. C. Muñoz, *Dalton Trans.* **2005**, 2062–2079.
[7] A. Bousseksou, G. Molnar, J. A. Real, K. Tanaka, *Coord. Chem. Rev.* **2007**, *251*, 1822–1833.
[8] A. B. Gaspar, M. Seredyuk, R. Gütlich, *Coord. Chem. Rev.* **2009**, *253*, 2399–2413.
[9] P. Gamez, J. S. Costa, M. Quesada, G. Aromí, *Dalton Trans.* **2009**, 7845–7853.
[10] A. Bousseksou, G. Molnar, L. Salmon, W. Nicolazzi, *Chem. Soc. Rev.* **2011**, *40*, 3313–3335.
[11] P. Gütlich, Y. Garcia, H. A. Goodwin, *Chem. Soc. Rev.* **2000**, *29*, 419–427.
[12] M. A. Halcrow, *Chem. Soc. Rev.* **2011**, *40*, 4119–4142.
[13] J. Tao, R. J. Wei, R. B. Huang, L. S. Zheng, *Chem. Soc. Rev.* **2012**, *41*, 703–737.
[14] G. Aromí, L. A. Barrios, O. Roubeau, P. Gamez, *Coord. Chem. Rev.* **2011**, *255*, 485–546.
[15] J. Olguin, S. Brooker, *Coord. Chem. Rev.* **2011**, *255*, 203–240.
[16] M. Boca, R. F. Jameson, W. Linert, *Coord. Chem. Rev.* **2011**, *255*, 290–317.
[17] M. A. Halcrow, *Coord. Chem. Rev.* **2009**, *253*, 2493–2514.
[18] J. A. Kitchen, S. Brooker, *Coord. Chem. Rev.* **2008**, *252*, 2072–2092.
[19] K. S. Murray, *Eur. J. Inorg. Chem.* **2008**, 3101–3121.
[20] S. Bonnet, M. A. Siegler, J. S. Costa, G. Molnar, A. Bousseksou, A. L. Spek, P. Gamez, J. Reedijk, *Chem. Commun.* **2008**, 5619–5621.
[21] J. S. Costa, K. Lappalainen, G. de Ruiter, M. Quesada, J. K. Tang, I. Mutikainen, U. Turpeinen, C. M. Grunert, P. Gütlich, H. Z. Lazar, J. F. Létard, P. Gamez, J. Reedijk, *Inorg. Chem.* **2007**, *46*, 4079–4089.
[22] M. Quesada, V. A. de la Pena-O'Shea, G. Aromí, S. Geremia, C. Massera, O. Roubeau, P. Gamez, J. Reedijk, *Adv. Mater.* **2007**, *19*, 1397–1402.
[23] P. Gamez, P. de Hoog, M. Lutz, W. L. Driessen, A. L. Spek, J. Reedijk, *Polyhedron* **2003**, *22*, 205–210.
[24] M. Quesada, P. de Hoog, P. Gamez, O. Roubeau, G. Aromí, B. Donnadieu, C. Massera, M. Lutz, A. L. Spek, J. Reedijk, *Eur. J. Inorg. Chem.* **2006**, 1353–1361.
[25] M. Quesada, M. Monrabal, G. Aromí, V. A. de la Pena-O'Shea, M. Gich, E. Molins, O. Roubeau, S. J. Teat, E. J. MacLean, P. Gamez, J. Reedijk, *J. Mater. Chem.* **2006**, *16*, 2669–2676.
[26] T. M. Ross, B. Moubaraki, S. R. Batten, K. S. Murray, *Dalton Trans.* **2012**, *41*, 2571–2581.
[27] T. M. Ross, B. Moubaraki, S. M. Neville, S. R. Batten, K. S. Murray, *Dalton Trans.* **2012**, *41*, 1512–1523.
[28] T. M. Ross, B. Moubaraki, D. R. Turner, G. J. Halder, G. Chastanet, S. M. Neville, J. D. Cashion, J. F. Létard, S. R. Batten, K. S. Murray, *Eur. J. Inorg. Chem.* **2011**, 1395–1417.
[29] T. M. Ross, B. Moubaraki, K. S. Wallwork, S. R. Batten, K. S. Murray, *Dalton Trans.* **2011**, *40*, 10147–10155.
[30] S. M. Neville, B. A. Leita, D. A. Offermann, M. B. Duriska, B. Moubaraki, K. W. Chapman, G. J. Halder, K. S. Murray, *Eur. J. Inorg. Chem.* **2007**, 1073–1085.
[31] T. J. Mooibroek, P. Gamez, *Inorg. Chim. Acta* **2007**, *360*, 381–404.
[32] P. Gamez, J. Reedijk, *Eur. J. Inorg. Chem.* **2006**, 29–42.
[33] P. de Hoog, P. Gamez, W. L. Driessen, J. Reedijk, *Tetrahedron Lett.* **2002**, *43*, 6783–6786.
[34] H. S. Scott, T. M. Ross, S. R. Batten, I. A. Gass, B. Moubaraki, S. M. Neville, K. S. Murray, *Aust. J. Chem.* **2012**, *65*, 874–882.
[35] P. Guionneau, M. Marchivie, G. Bravic, J. F. Létard, D. Chasseau, *Top. Curr. Chem.* **2004**, *234*, 97–128.
[36] M. Quesada, F. Prins, E. Bill, H. Kooijman, P. Gamez, O. Roubeau, A. L. Spek, J. G. Haasnoot, J. Reedijk, *Chem. Eur. J.* **2008**, *14*, 8486–8499.
[37] M. Marchivie, P. Guionneau, J. F. Létard, D. Chasseau, *Acta Crystallogr., Sect. B-Struct. Sci.* **2005**, *61*, 25–28.
[38] J. K. McCusker, A. L. Rheingold, D. N. Hendrickson, *Inorg. Chem.* **1996**, *35*, 2100–2112.
[39] T. J. Mooibroek, P. Gamez, *CrystEngComm* **2012**, *14*, 1027–1030.
[40] T. J. Mooibroek, P. Gamez, *CrystEngComm* **2012**, *14*, 3902–3906.
[41] C. A. Hunter, J. K. M. Sanders, *J. Am. Chem. Soc.* **1990**, *112*, 5525–5534.
[42] S. A. Arnstein, C. D. Sherrill, *Phys. Chem. Chem. Phys.* **2008**, *10*, 2646–2655.
[43] A. Hauser, *Top. Curr. Chem.* **2004**, *234*, 155–198.
[44] A. Hauser, *J. Chem. Phys.* **1991**, *94*, 2741–2748.
[45] A. Desaix, O. Roubeau, J. Jeftic, J. G. Haasnoot, K. Boukheddaden, E. Codjovi, J. Linarès, M. Noguès, F. Varret, *Eur. Phys. J. B* **1998**, *6*, 183–193.
[46] F. Varret, K. Boukheddaden, E. Codjovi, C. Enachescu, J. Linarès, *Top. Curr. Chem.* **2004**, *234*, 199–229.
[47] M. Sorai, S. Seki, *J. Phys. Chem. Solids* **1974**, *35*, 555–570.
[48] L. Capes, J.-F. Létard, O. Kahn, *Chem. Eur. J.* **2000**, *6*, 2246–2255.
[49] T. Buchen, H. Toftlund, P. Gütlich, *Chem. Eur. J.* **1996**, *2*, 1129–1133.
[50] J. A. Real, I. Castro, A. Bousseksou, M. Verdaguer, R. Burriel, M. Castro, J. Linarès, F. Varret, *Inorg. Chem.* **1997**, *36*, 455–464.
[51] N. Moliner, M. C. Muñoz, J.-F. Létard, X. Solans, R. Burriel, M. Castro, O. Kahn, J. A. Real, *Inorg. Chim. Acta* **1999**, *291*, 279–288.
[52] M. Sorai, *Chem. Rev.* **1996**, *106*, 976–1031.
[53] T. Nakamoto, Z. C. Tan, M. Sorai, *Inorg. Chem.* **2001**, *40*, 3805–3809.
[54] O. Roubeau, M. de Vos, A. F. Stassen, R. Burriel, J. G. Haasnoot, J. Reedijk, *J. Phys. Chem. Solids* **2003**, *64*, 1003–1013.
[55] O. Roubeau, M. Evangelisti, E. Natividad, *Chem. Commun.* **2012**, *48*, 7604–7606.
[56] M. Sorai, *Top. Curr. Chem.* **2004**, *235*, 153–170.
[57] Z. Arcis-Castíllo, S. Zheng, M. A. Siegler, O. Roubeau, S. Bedoui, S. Bonnet, *Chem. Eur. J.* **2011**, *17*, 14826–14836.
[58] G. M. Sheldrick, *Acta Crystallogr., Sect. A* **2008**, *64*, 112–122.

Received: September 14, 2012
Published Online: November 27, 2012

EurJIC European Journal of Inorganic Chemistry

ChemPubSoc Europe

FULL PAPER

DOI:10.1002/ejic.201402475

One-Pot Multiple Metal–Organic Framework Formation: Concomitant Generation of Structural Isomers or of Drastically Distinct Materials

Achareeya Cheansirisomboon,[a,b] Jorge Salinas-Uber,[a] Chiara Massera,[c] Olivier Roubeau,[d] Sujittra Youngme,*[b] and Patrick Gamez*[a,e]

Keywords: Metal–organic frameworks / Crystal engineering / Topological diversity / Structural isomers / Structure elucidation

The solvothermal reaction of 2,5-dihydroxyterephthalic acid (H_2dhtp) and magnesium(II) nitrate in *N*,*N*-dimethylformamide (DMF) led to the simultaneous formation of two structural isomers, namely, the **lvt** network Mg(dhtp)$(dmf)_2$ (**1**) and the compound $Mg_3(dhtp)_3(dmf)_6{\cdot}0.75H_2O$ (**2**) with the **pcu** α-Po primitive cubic topology. The same reaction conditions with manganese(II) nitrate and terephthalic acid (H_2tp) resulted in the concomitant generation of two drastically different metal–organic frameworks (MOFs), namely, $Mn_2(tp)_2(dmf)_2$ (**3**) and $[Mn(HCOO)_3][NC_2H_8]$ (**4**), in which the formato ligands and *N*,*N*-dimethylammonium cations arise from DMF degradation.

Introduction

Crystal engineering may be regarded as the rational design and building of crystal structures from well-chosen constituent molecules.[1,2] Although great progress has been achieved through several decades of intense investigation in this area of chemistry, there is still no general approach to predict precisely the arrangement of molecules in crystalline lattices.[3–6] The obvious reason for this situation is the potential involvement of numerous factors during the crystallization process in addition to the specific nature of the molecular building blocks (internal factors). Accordingly, external factors such as solvent, temperature, pH, pressure, supersaturation or the presence of impurities may play a crucial role in crystallization.[5,7,8]

The crystal engineering of metal–organic frameworks (MOFs) has drawn great interest from the scientific community in the last 15 years.[9–11] This enthusiasm for MOFs is due to their high structural versatility, porosity and their broad variety of properties, functions and potential applications,[12–15] such as gas adsorption and storage,[16] magnetism,[17] luminescence,[18] catalysis[19] and ion exchange.[20] The integration of a specific functionality or functionalities can be achieved easily through rational variation of the building blocks (ligands and metal ions)[21] or by postsynthetic modification of MOFs that possess adequate reactive sites.[10]

The great popularity of MOFs undoubtedly arises from their typical porous nature provided by their 2D or 3D network topology. In principle, the topology of the coordination polymer can be adjusted through the choice of the ligand, the metal ion (with its preferred coordination geometry), the counterion, the solvent (or solvent mixture), the pH, the ligand-to-metal ratio and so on.[11,22–24] The influence of temperature on the ultimate topologies of MOFs has been comparatively less investigated.[25–27]

Different types of building blocks are involved in the generation of MOFs, namely, the organic ligand, the metal ion (and the counterion) and the solvent (or mixture of solvents). Clearly, distinct combinations of these components will lead to the formation of various MOF assemblies, and temperature can play a crucial role during this process. For instance, the severe reaction conditions commonly used in MOF synthesis (and particularly the high temperatures usually applied) may even result in ligand (or solvent) degradation, which can yield new organic linkers. Hence, the simultaneous generation of more than one extended coordi-

[a] Departament de Química Inorgànica, Universitat de Barcelona, Martí i Franquès 1–11, 08028 Barcelona, Spain
E-mail: patrick.gamez@qi.ub.es
www.bio-inorganic-chemistry-icrea-ub.com
[b] Materials Chemistry Research Center, Department of Chemistry and Center of Excellence for Innovation in Chemistry, Faculty of Science, Khon Kaen University, Khon Kaen 40002, Thailand
E-mail: sujittra@kku.ac.th
[c] Dipartimento di Chimica, Università degli Studi di Parma, Vialle delle Scienze 17/A, 43124 Parma, Italy
[d] Instituto de Ciencia de Materiales de Aragón (ICMA), CSIC and Universidad de Zaragoza, Plaza San Francisco s/n, 50009 Zaragoza, Spain
[e] Institució Catalana de Recerca i Estudis Avançats (ICREA), Passeig Lluís Companys 23, 08010 Barcelona, Spain
Supporting information for this article is available on the WWW under http://dx.doi.org/10.1002/ejic.201402475.

nation structure in the same reaction batch may clearly be envisaged.

In the present study, two pertinent illustrations of the one-pot, concurrent formation of more than one MOF are described, namely, $Mg(dhtp)(dmf)_2$ (**1**, dmf = *N*,*N*-dimethylformamide, H_2dhtp = 2,5-dihydroxyterephthalic acid) together with $Mg_3(dhtp)_3(dmf)_6{\cdot}0.75H_2O$ (**2**) and $Mn_2(tp)_2(dmf)_2$ (**3**, H_2tp = terephthalic acid) together with $[Mn(HCOO)_3][NC_2H_8]$ (**4**). The consequent implications regarding their potential applications is considered; for instance, the consequences in relation to the previously reported properties of **1** and **3** as a luminescent material and cyanosilylation catalyst, respectively, are discussed.

Results and Discussion

Description of MOF Structures

Compounds **1**–**4** were obtained under solvothermal conditions in DMF (in the temperature range 80–140 °C) from the corresponding ligands and metal salts (see Exp. Sect. for details). Compounds **1** and **2** as well as **3** and **4** were generated simultaneously as two different products of the respective reactions.

Crystal Structure of Mg(dhtp)(dmf)$_2$ (1)

The reaction of 2,5-dihydroxyterephthalic acid (H_2dhtp) with magnesium(II) nitrate hexahydrate in DMF at 120 °C (or above) produces light orange, needle-shaped crystals of $Mg(dhtp)(dmf)_2$ (**1**) in a yield of 68%. Compound **1** is air-stable and insoluble in most organic solvents. Compound **1** crystallizes in the centred monoclinic space group *C*2/*c* (Table S1), as reported earlier by George, Maji and coworkers.[28,29] A representation of the molecular structure of **1**, which highlights the coordination environment around the metal ion, with its atom-numbering scheme is shown in Figure 1.

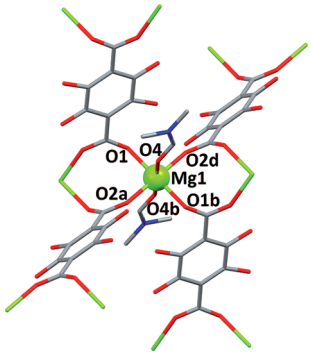

Figure 1. Representation of the molecular structure of **1** showing the coordination environment around the magnesium(II) atom. The hydrogen atoms are omitted for clarity. Symmetry operations, a: 1 – *x*, *y*, 3/2 – *z*; b: 1 – *x*, 1 – *y*, 2 – *z*; d: *x*, 1 – *y*, 1/2 + *z*. The oxygen atoms of the phenolic hydroxy groups are disordered over two positions with occupancy factors of 0.8 and 0.2; hence, the dhtp ligands are shown with four OH groups.

The magnesium(II) centre in **1** is in an octahedral coordination environment. Selected bond lengths and angles are listed in Table S2. The equatorial plane of the octahedron is formed by four oxygen atoms (O1, O2a, O1b and O2d; Figure 1) belonging to four different dhtp ligands. The axial positions are occupied by two DMF molecules (O4 and O4b; Figure 1). The Mg1–O bond lengths and O–Mg1–O coordination angles can be considered as normal for this type of MgO_6 environment.[30] Mg1 is bridged to two symmetry-related magnesium atoms through four $\mu_{1,3}$-dhtp ligands to generate an infinite 1D chain of metal ions along the crystallographic *c* axis (Figure 2, A). This chain is connected to four adjacent, parallel chains in the *ab* plane to produce a 3D framework that exhibits channels occupied by the coordinated DMF molecules (Figure 2, B).

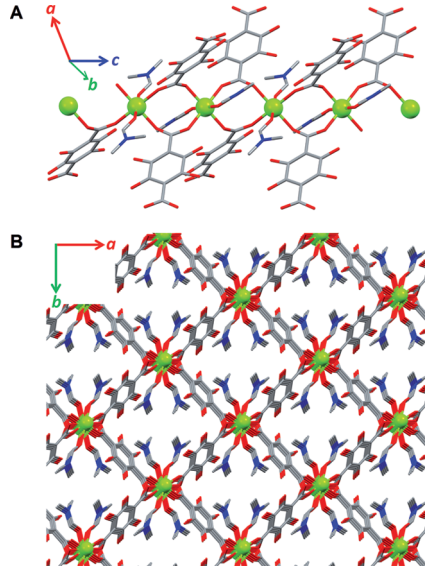

Figure 2. (A) Formation of an infinite 1D magnesium chain along the crystallographic *c* axis in **1**. (B) 3D framework generated through the interlinking of the 1D chains by bis($\mu_{1,3}$-dhtp) ligands. The oxygen atoms of the phenolic hydroxy groups are disordered over two positions with occupancy factors of 0.8 and 0.2; hence, the dhtp ligands are shown with four OH groups.

Crystal Structure of $Mg_3(dhtp)_3(dmf)_6{\cdot}0.75H_2O$ (2)

If the reaction is performed at a temperature between 90 and 120 °C, two types of single crystals are obtained simultaneously (Figure 3), namely, needles (**1**) and blocks, which have been identified as $Mg_3(dhtp)_3(dmf)_6{\cdot}0.75H_2O$ (**2**) by X-ray diffraction. Compound **2**, which is not air-stable (in contrast to **1**) and is insoluble in most organic solvents, can only be obtained as a mixture with **1**; therefore, its yield could not be determined. It has been observed that the relative amount of block crystals of **2** increases when the reaction temperature is decreased (that is, the **2**/**1** ratio appears to increase when the temperature of the reaction decreases). The fact that **1** is always obtained suggests that this coordination polymer is (thermodynamically) favoured. Compound **2** crystallizes in a distinct crystallographic system, namely, the centrosymmetric triclinic space group $P\bar{1}$ (Table S1).

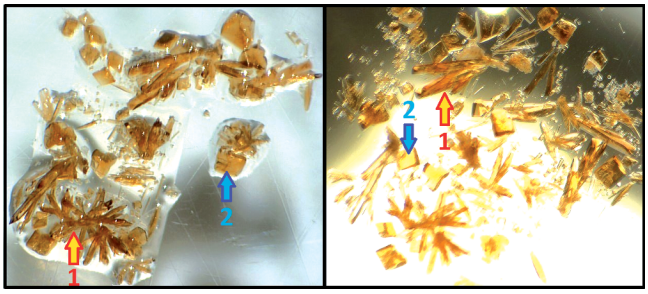

Figure 3. Images of two different reaction samples (obtained at temperatures below 120 °C) illustrating the presence of two types of materials, namely, **1** (needles, yellow and red arrows) and **2** (blocks, blue arrows).

Whereas **1** is formed by infinite 1D chains of metal ions (see above), **2** is built from trimagnesium(II) linear units. A view of this trinuclear building block is shown in Figure 4 (A), and an illustration of the trimetallic core with the corresponding atom-numbering scheme is depicted in Figure 4 (B). The central magnesium(II) ion, Mg2, is in a distorted octahedral environment formed by six carboxylato oxygen atoms (O2, O8, O19, O25, O14a′ and O33d′; Figure 4, B) belonging to different dhtp ligands. The equatorial angles vary from 82.54(9) to 99.32(10)° (Tables S2 and S3) and are illustrative of the strong distortion of the octahedron, which most likely results from steric hindrance induced by the coordination of six dhtp ligands. The Mg2–O bond lengths range from 2.036(3) to 2.053(2) Å (Table S2) and can be considered as normal for such a MgO_6 moiety.[31] The six dhtp ligands triply bridge Mg2 to two related magnesium(II) atoms, namely, Mg1 and Mg3 (Figure 4). The geometry about Mg1 and Mg3 is octahedral with three oxygen atoms from bridging $\mu_{1,3}$-dhtp ligands (connecting Mg1 and Mg3 to Mg2) and three DMF oxygen atoms (Figure 4). The coordinated DMF molecules in **2** act as capping ligands and impede the formation of a 1D metallic chain, as observed for **1** (see parts A in Figures 2 and 4). The Mg–O_{COO} and Mg–O_{DMF} bond lengths in the range 2.017(2)–2.110(3) Å (Table S2) are regular for this type of coordination environment.[32]

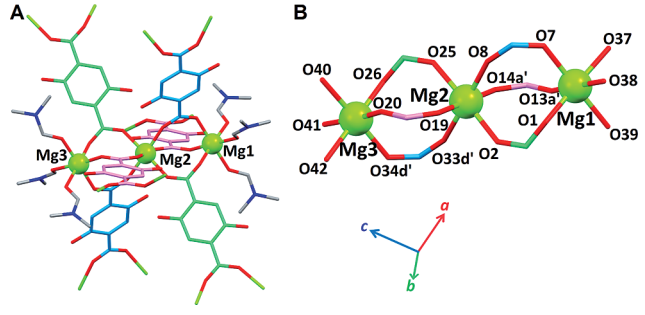

Figure 4. (A) Representation of the molecular structure of **2** showing the trinuclear building block. (B) The trimagnesium(II) core illustrating the coordination environment around each magnesium(II) atom. The hydrogen atoms are omitted for clarity. The three types of dhtp ligands that connect the Mg_3 cluster to adjacent trinuclear units are shown in pink, green and blue. Symmetry operations, a′: –*x*, 1 – *y*, 1 – *z*; d′: 1 – *x*, 1 – *y*, 1 – *z*.

The basal coordination angles vary from 85.92(10) to 97.29(10)° (Table S2) and reflect a strong distortion of the octahedron (for both Mg1 and Mg3), which is probably caused by steric hindrance induced by the coordination of three $\mu_{1,3}$-bridging dhtp ligands [as evidenced by the angles O1–Mg1–O13a′ 97.29(10)° and O20–Mg3–O26 95.29(10)° for Mg1 and Mg3, respectively]. It should be mentioned here that the solid-state structure of **2** includes another trimagnesium(II) moiety (Mg4, Mg5 and Mg6) with slight metric variations compared to those for Mg1, Mg2 and Mg3 (see Table S3). The linear trimagnesium(II) clusters are connected to six adjacent trinuclear units in a shifted manner through three different types of dhtp ligands, which are shown in distinct colours in parts A of Figures 4 and 5 (the three types of dhtp ligands are depicted in pink, green and blue). Hence, the Mg_3 building blocks are connected in three directions (Figure 5, A) to produce an intricate 3D framework (Figure 5, B). Although **1** exhibits diamondoid channels (containing the coordinated DMF molecules; Figure 2, B), **2** displays triangular channels that are occupied by the coordinated DMF molecules (Figure 5, B). Remarkably, these drastically distinct frameworks are formally obtained from the same proportion of constituent molecules, that is, a combination of one magnesium ion, one dhtp ligand and two DMF molecules. Thus, **1** and **2** are not polymorphs, they are structural isomers. The different coordination arrangements observed are achieved by a slight variation of the reaction temperature; indeed, whereas needle crystals of **1** are solely produced above 120 °C, block crystals of **2** are obtained at 110 °C (together with needle crystals of **1**; Figure 3), which illustrates the great importance of the temperature in the formation of MOFs. Finally, the framework of **2** contains some water molecules (oxygen atoms O1w and O2w), which are hydrogen bonded to dhtp hydroxy acceptor groups [O1w···O11 2.817(5) Å and O2w···O36 2.826(5) Å].

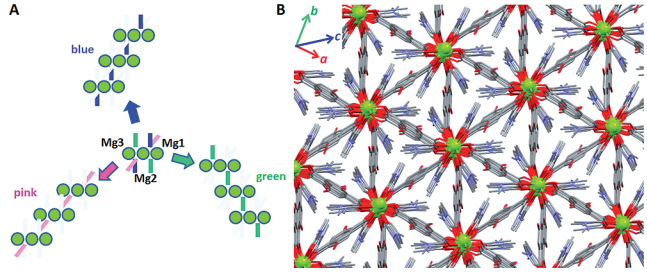

Figure 5. (A) The connectivity of the three different types of dhtp ligands (pink, blue and green; see Figure 4, A) in **2** and (B) the resulting 3D framework built up from Mg_3 clusters in **2**.

Crystal Structures of $Mn_2(tp)_2(dmf)_2$ (3) and $[Mn(HCOO)_3][NC_2H_8]$ (4)

The reaction of terephthalic acid (H_2tp) with manganese(II) nitrate tetrahydrate in DMF at 120 °C yields two different types of crystalline materials, namely, rhombic-shaped crystals of **3** and hexagonal-shaped crystals of **4** (Figure 6). Compounds **3** and **4** have always been obtained as a mixture; therefore, their respective yields could not be

determined. Compound **3** crystallizes in the monoclinic space group $P2_1/c$ (Table S4), as reported previously.[33] The solid-state structure of **3**, which is a 3D MOF that exhibits channels filled with the coordinated DMF molecules (see Figures S1 and S2), has been fully described in previous reports.[33]

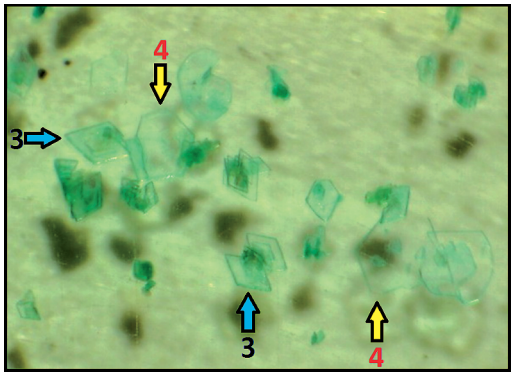

Figure 6. Image illustrating the presence of two types of materials, namely, **3** (rhombic-shaped crystals; blue and black arrows) and **4** (hexagonal-shaped crystals; yellow and black arrows).

Compound **4** crystallizes in the trigonal space group $R\bar{3}c$ (Table S4). A representation of its molecular structure, which highlights the coordination environment around the Mn^{II} ion, with its atom-numbering scheme is shown in Figure 7 (A). The metal centre in **4** is in an almost perfect octahedral environment [the O–Mn–O angles vary from 89.19(3) to 90.81(3)°; see Table S5] formed by six formato ligands with Mn–O bond lengths of 2.188(1) Å (Figure 7, A). Each Mn^{II} atom is linked to six neighbouring metal ions through the bridging μ-*O*,*O*′-formato ligands to produce an octahedral 3D framework (Figure 7, B). This anionic network {formed by $[Mn(HCOO)_3]^-$ units} exhibits channels along the crystallographic *a* axis that are filled

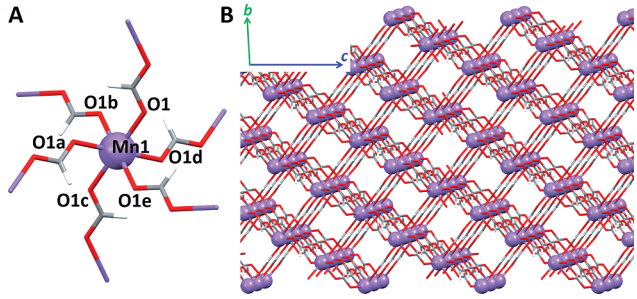

Figure 7. (A) Representation of the molecular structure of **4** showing the coordination environment around the manganese(II) ion. The hydrogen atoms and the dimethylammonium cations are omitted for clarity. (B) Illustration of the 3D framework built up from $[Mn(HCOO)_3]^-$ units in **4**. Symmetry operations, a: $y/3 - x + y$, $-z/3 + y$, $-c/6 + z$; b: $y/3 - x + y$, $-z/3 + y$, $-c/6 + z$; c: $y/3 - x + y$, $-z/3 + y$, $-c/6 + z$; d: $y/3 - x + y$, $-z/3 + y$, $-c/6 + z$; e: $y/3 - x + y$, $-z/3 + y$, $-c/6 + z$.

Table 1. Results of the solvothermal reactions between manganese(II) nitrate and terephthalic acid (H_2tp) (with different metal/ligand ratios) performed at various temperatures (from 80 to 140 °C) in distinct solvent/solvent mixtures for 24 h.[a,b]

Temp. [°C] → / Mn:H_2tp ratio ↓	80	90	100	110	120	130	140	Solvent(s) 15 mL ↓
1:1	-	□	□	■	■	■	□	DMF
	-	-	□	□	□	□	●	DMF/CH_3OH 10/5
	-	-	●	●	●	●	●	DMF/CH_3CN 10/5
	-	-	○	○	○	○	-	DMF/H_2O 10/5
1.33:2	-	□	■	■	■	■	□	DMF
	-	-	□	□	□	□	□	DMF/CH_3OH 10/5
	-	-	●	●	●	●	●	DMF/CH_3CN 10/5
	-	-	○	○	○	○	-	DMF/H_2O 10/5
1:1.5	-	□	□	■	■	■	□	DMF
	-	-	□	□	□	□	□	DMF/CH_3OH 10/5
	-	-	●	●	●	●	●	DMF/CH_3CN 10/5
	-	-	○	○	○	○	-	DMF/H_2O 10/5
1:3	-	-	●	●	●	●	●	DMF
	-	-	○	○	○	○	-	DMF/CH_3OH 10/5
	-	-	●	●	●	●	●	DMF/CH_3CN 10/5
	-	-	○	○	○	○	○	DMF/H_2O 10/5

[a] –: no solid material was obtained; ■: mixture of good-quality single crystals of **3** and **4**; □: mixture of low-quality crystals of **3** and **4**; ●: mixture of tiny (unidentified) crystals with a white microcrystalline powder; ○: mixture of low-quality crystals of various shapes (more than two) with a white microcrystalline powder. [b] The same results were obtained with reaction times of 48 and 72 h.

with dimethylammonium cations. Both the $HCOO^-$ ligands and the $[(CH_3)_2NH_2]^+$ cations result from the degradation of DMF, which is most likely catalyzed by manganese. Indeed, under the same reaction conditions (in DMF at 120 °C), the generation of formate and dimethylammonium ions is not observed in the presence of magnesium (preparation of **1** and **2**; see above and Exp. Sect.).

It can be mentioned here that the same anionic metal formate framework has been previously reported by Gao and co-workers;[34] in one case a structure that is isomorphous to **4** was obtained, but it was described as a different underlying net (i.e., the binodal, 6,6-c **nia**, see below).[34b] However, in contrast to the present case, the 3D network was purposely produced by the reaction of formic acid and an amine (which acts as the reaction template) in methanol.[35,36] For instance, the use of *N*,*N*′-dimethylethylenediamine generates the octahedral network with channels filled with *N*,*N*′-dimethylethylenediammonium $[dmenH_2]^{2+}$ cations {instead of the $[(CH_3)_2NH_2]^+$ cations in **4**}.[34]

As already mentioned above, compound **4** was obtained as a side product (arising from DMF degradation) of the reaction to prepare **3**. Hence, several reaction conditions were subsequently applied to attempt to generate pure **3**. Thus, several Mn-to-ligand ratios were used, and reactions were performed at different temperatures (from 80 to 140 °C), with various solvent mixtures and for distinct reaction times (24, 48 and 72 h). All of the results are listed in Table 1. None of the reaction parameter changes applied allowed the exclusive formation of **3** (Table 1). Nice crystals of **3** are always obtained together with **4** when the reaction is performed in pure DMF at 110–130 °C (and even at 100 °C when the Mn/H_2tp ratio is 1.33:2; see Table 1) with metal-to-ligand ratios from 1:1 to 1:1.5. All other reaction conditions (that yield solid materials) produce mixtures of low-quality crystals or microcrystalline powders, and sometimes more than two compounds seem to have formed (see Table 1).

Consequences Regarding Potential Applications

As mentioned above, although **1** and **2** are built from the same components [i.e., magnesium(II) ions, dhtp ligands and DMF molecules] with the same molar ratio, they exhibit drastically distinct solid-state structures. The comparative analysis of the network topologies of **1** and **2** by using the TOPOS software[37] reveals their structural disparities. In **1**, the underlying net[38] is obtained by considering both the metal centres and the terephthalic ligands as four-connected (4-c) nodes. After this standard simplification, the 3D framework can be considered as a four-connected **lvt** network (Figure 8) with point symbol $(4^2.8^4)$ and vertex symbol $(4.4.8^4.8^4.8^8.8^8)$.[37] An examination of the TTD/TTO (TTD = TOPOS Topological Database, TTO = topological types observed) collection reveals that there are 57 structures with the same underlying net among valence-bonded MOFs described with a standard representation, seven of which contain the terephthalic acid moiety.[28,39] Six of them are isostructural compounds $(C_8H_8MO_6)_n$ with M = Mg, Co, Fe, Mn,[39c] whereas one[39b] is a manganese MOF $(C_{32}H_{32}Mn_2N_8O_8)_n$ with methylpyrazole as an ancillary ligand. In all of the reported cases, the terephthalic acid is connected to four metal centres through all four oxygen donor atoms of the carboxylic groups. The coordination around the metal is completed by monodentate ligands (DMF, water or methylpyrazole), which are not involved in the formation of the network. The topology of **2** can be best described by using the cluster representation,[38] in which the $[Mg_3(COO)_6]$ units are the cluster nodes, and the phenyl rings of the terephthalic acid are the two-connected linkers (see Figure 9, A; the terminal, one-connected OH groups are not considered in the analysis and have been previously removed). The first simplification leads to the 3D net shown in part B of Figure 9, in which the green spheres are the nodes, and the blue bonds represent the 2-c organic linkers. When the linker is further simplified into an edge, the resulting 6-c net is of the **pcu** α-Po primitive cubic topological type (Figure 9, C) with point symbol $(4^{12}.6^3)$ and vertex symbol (4.4.4.4.4.4.4.4.4.4.4.*.*.*). The standard simplification for this structure would give a trinodal net named 3,4,6T2,[38] in which the carboxylate ligands act as four-connected nodes, and two types of nonequivalent magnesium centres behave either as 3-c or 6-c nodes. There are 23 MOF structures (containing terephthalic acid, naphthalene or biphenyl dicarboxylates) with the same underlying net;[40] in the cluster representation, they are all represented as **pcu**. The majority of these compounds possess two nonequivalent metal centres with coordination spheres occupied by monodentate solvent molecules and by the oxygen atoms of the carboxylic groups. In all cases, the biscarboxylic benzene derivatives act as μ_4 ligands; in particular, in **2**, all of the terephthalic acids of the structure display a bridging coordination mode with the four oxygen atoms bonded to four distinct metal ions. In the other MOFs of the series, however, two distinct coordination modes are almost always present simultaneously (bridging, chelating or chelating and bridging with one oxygen atom).

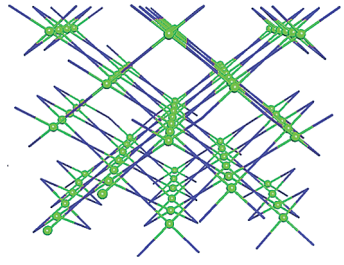

Figure 8. View along the *c* axis of the **lvt** network that describes the topology of **1**. The Mg atoms and the organic ligands that act as 4-c nodes are represented as green spheres and blue rods, respectively.

Clearly, such structural disparities will affect the functional and physical properties of the corresponding MOFs, for instance, their porosity.

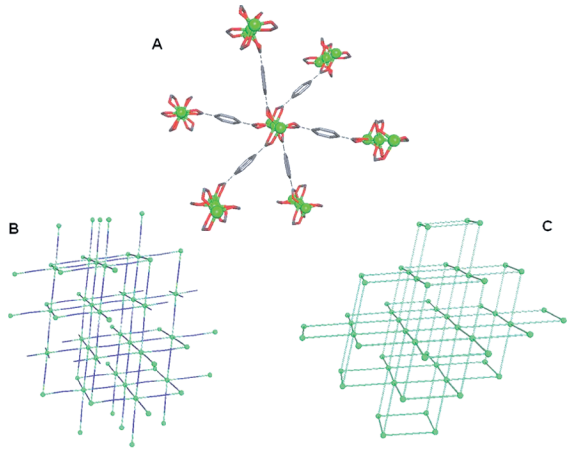

Figure 9. Simplification process used to describe the topology of **2**. (A) The cluster nodes $Mg_3(COO)_6$ (six-connected) and C_6 (two-connected). Mg: green spheres; oxygen: red; carbon: grey. The interactions between the nodes are shown as grey dashed lines. (B) The underlying net derived from the cluster representation (6-c nodes as green spheres, 2-c nodes as blue rods). (C) The **pcu** α-Po primitive cubic net obtained by simplifying the 2-c nodes into edges.

The apparent surface area of MOFs (S in $m^2 g^{-1}$) can be estimated from their crystal structures by using the free volume (V_{free} in %) after removal of the lattice and coordinated solvent molecules, and their density (d_{MOF} in $g cm^{-3}$) can be determined by single-crystal X-ray diffraction by applying the simple Equation (1).[41]

$$S = 28 \times \frac{V_{free}}{d_{MOF}} \quad (1)$$

Accordingly, for **1**, the apparent surface area is $S1 = 28 \times (52/1.452) \approx 1000\ m^2 g^{-1}$. For **2**, $S2 = 28 \times (59/1.402) \approx 1200\ m^2 g^{-1}$. Thus, from **1** to **2**, the surface area increases by 20%.

As already mentioned above, compound **1** has been reported previously and has been used as a porous luminescent material (both in solution and in the solid state) with tuneable emission properties triggered by guest solvent molecules.[28] Hence, **1** (which shows a bright green emission centred at ca. 500 nm) has been dispersed in various solvents, namely, ethanol, dimethyl sulfoxide, water and *N*,*N*-dimethylformamide.[28] It has been observed that **1** is partially soluble in polar solvents and that its fluorescence properties vary depending on the solvent used.

The powder X-ray diffraction (PXRD) patterns of **1** recovered from the different (guest) solvents were recorded (see Figures S9 and S13 in the Supporting Information of ref.[28]), and the authors concluded that **1** does not disintegrate during the dispersion process.[28] However, a re-examination of these PXRD patterns indicates that the PXRD data of as-synthesized **1** (see Figure 10, bottom of this paper and Figures S9 and S13 of ref.[28]) and those of the MOFs retrieved after dispersion in the four different solvents are significantly different (see Figures S9 and S13 of ref.[28]); almost all of the original peaks (of **1**; see Figure 10, bottom) cannot be found in the PXRD patterns of the recovered materials. Indeed, numerous new diffraction peaks are observed, and the consequent new PXRD patterns actually resemble that of **2** (Figure 10, top), obtained in the present study. The PXRD pattern of **1** treated with water (Figure 10, middle)[28] exhibits a number of common peaks with the simulated pattern of **2** (Figure 10, top). Thus, it appears that **1** may be converted to **2** (at least in part)[29] during the solvent-immersion procedure (the solubility of **1** in polar solvents has been noted). Consequently, it is not clear whether the fluorescence behaviour observed is due to the host–guest properties of **1** or to those of **2** (or any other MOF structure).

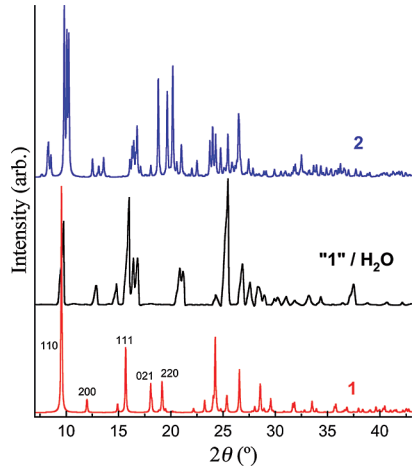

Figure 10. Powder diffraction patterns of **1** (bottom) and **2** (top) calculated from the single-crystal X-ray data and the experimental pattern for **1** after contact with H_2O as reported by Jayaramulu et al.[28] (middle, data taken from ref.[28]). The main reflections of the pattern of **1** are labelled to highlight the differences upon exposure of **1** to H_2O.

As stated above, the structure of **3**[33] and the framework of **4** with different cations (various ammonium ions) have been described previously.[34–36] Compounds **3** and **4** are drastically distinct materials; therefore, their physical and functional properties will clearly be different. From a topological point of view, the standard simplification of **3** results in a 4,4,5,5T7 underlying net, in which the two metal centres and the terephthalic ligands both behave as 4-c and 5-c nodes (see Figure 11) with point symbol $\{4^2.6^2.8^2\}\{4^3.6^3.8^4\}\{4^4.6^2\}\{4^4.6^5.8\}$ (another MOF has been reported with the same underlying net but with Mg ions instead of Mn ions).[40k] The structure of **4** can be described by the **pcu** underlying net, as for **2**. This description is obtained by using a standard representation in which the 2-c formato ligands are simplified into edges and the metal ions are six-connected nodes. An examination of the TTD/TTO collection reveals that there are several structures with the same underlying net among the valence-bonded MOFs based on the same anionic metal–formate framework, 16 of which are isomorphous to **4**.[34a,42]

Compound **3** has been used by some of us as a Lewis catalyst for the cyanosilylation of acetaldehyde, which yields

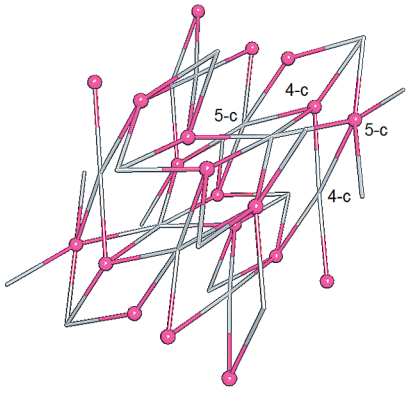

Figure 11. View of the 4,4,5,5T7 network that describes the topology of **3**. The Mn atoms and the organic ligands are represented as pink spheres and gray rods, respectively.

an *O*-silylated cyanohydrin.[33a] Several manganese-containing MOFs have been employed to mediate this reaction, and **3** showed the best catalytic activity.[33a] It can be mentioned here that the MOF **3** previously reported[33a] was prepared by following the same synthetic procedure as that described herein (see Exp. Sect.). As we have not been able to produce pure **3** in the present investigation (the presence of **4** has always been detected under various reactions conditions; see Table 1), it is assumed that **3** was also obtained together with **4** in the previous study without realization of this.

Compounds **3** and **4** are significantly different; first, the organic linkers are considerably distinct, terephthalate for **3** and formate for **4**. Whereas **3** is a neutral network, **4** is an anionic framework in which the cavities are filled with cationic $[(CH_3)_2NH_2]^+$ guests. Finally, **3** contains coordinated DMF molecules, whereas **4** does not (**4** results from DMF degradation). Consequently, **3** and **4** may act as radically distinct catalysts for the cyanosilylation of acetaldehyde; **4** is not expected to catalyze this reaction. Indeed, the channels in the structure of **4** (along the crystallographic *a* axis; see Figure 7, B) are filled with *N*,*N*-dimethylammonium cations, which cannot be replaced or expelled by neutral molecules (contrary to the coordinated DMF molecules in **3**), such as trimethylsilyl cyanide and acetaldehyde (the reactants of the cyanosilylation reaction[33]). Moreover, the cavities in **4** are too small to accommodate molecules such as trimethylsilyl cyanide (the calculated apparent surface area of **4** without $[(CH_3)_2NH_2]^+$ ions, *S*4, amounts to $28 \times (6/1.709) \approx 100\ m^2\,g^{-1}$). In contrast, the channels in **3** (Figure S2), which are significantly wider than those of **4** [for instance, the apparent surface area of **3** after removal of the coordinated DMF molecules is $S3 = 28 \times (18/1.615) \approx 310\ m^2\,g^{-1}$], can host trimethylsilyl cyanide and acetaldehyde and, therefore, the Mn sites in **3** can mediate the cyanosilylation reaction. Consequently, in the previous work,[33] the quantity of catalyst **3** used has been underestimated owing to the probable presence of **4**. This situation thus indicates that **3** is an even better catalyst than initially thought.

Conclusions

As they are solid materials, MOFs may exist in more than one crystal structure or polymorph. Polymorphic and pseudo-polymorphic MOFs have been described in the literature.[25,43–45] Naturally, such polymorphs may have different physical properties;[46] for example, an interpenetrated form of MOF-5 [i.e., $Zn_4O(tp)_3$] has been reported that exhibits significantly lower surface area than the non-interpenetrated one (ca. 700–1000 vs. 3500 $m^2\,g^{-1}$).[47]

Diverse types of isomeric MOFs may also be obtained.[27,48–50] For instance, the temperature-dependent formation of MOF structural isomers was described in 2007.[26] Furthermore, the solvent-induced formation of structural isomers has been reported recently.[27] Compounds **1** and **2** represent a rare case[51,52] of structural isomers concomitantly obtained.

Although the simultaneous formation of distinct MOFs from the same building blocks, namely, the metal ion and organic linker (and sometimes also the solvent molecules) but with different molar ratios has been repeatedly observed,[27,53,54] the one-pot generation of MOFs including at least one different component, such as **3** and **4** with distinct organic ligands (terephthalate for **3** and formate for **4**), appears to be unique.

In summary, the two examples of multi-MOF formation reported herein stress the absolute necessity to carefully inspect the solid material(s) (e.g., crystals) after reaction completion. Indeed, as observed in the present study, the production of more than one compound can occur in the same reaction vessel, and this feature does not seem to be uncommon. As distinct MOFs will exhibit dissimilar physical properties, the failure to observe such an occurrence will cause misinterpretation of results regarding the functional applications of the materials.

Experimental Section

Materials and Measurements: 2,5-Dihydroxyterephthalic acid (H_2dhtp), terephthalic acid (H_2tp), manganese(II) nitrate tetrahydrate and magnesium(II) nitrate hexahydrate were purchased from Sigma–Aldrich and used as received. DMF was obtained from Acros Organics. Infrared spectra (samples as KBr pellets) were recorded with a Nicolet 5700 FTIR spectrometer. Elemental analyses were performed by the Servei de Microanalisi, Consejo Superior de Investigaciones Cientificas (CSIC) of Barcelona.

$Mg(dhtp)(dmf)_2$ (1): A DMF solution (15 mL) of $Mg(NO_3)_2{\cdot}6H_2O$ (46 mg, 0.18 mmol) and 2,5-dihydroxyterephthalic acid (H_2dhtp; 53 mg, 0.27 mmol) corresponding to a metal-to-ligand ratio of 1:1.5 was sealed in a glass tube and heated at 120 °C for 1 d. Subsequently, the reaction mixture was cooled at a rate of 5 °C h^{-1}. Needle-shaped, light orange crystals of **1**, which were not air-sensitive, were obtained in a yield of 68% (44 mg) based upon magnesium. $C_{14}H_{18}MgN_2O_8$ (366.61): calcd. C 45.89, H 4.96, N 7.65; found C 45.66, H 4.89, N 7.43). IR (KBr): $\tilde{\nu}$ = 3421 (m), 2932 (m), 1655 (ws), 1613 (s), 1487 (m), 1452 (s), 1414 (m), 1388 (m), 1368 (m), 1332 (m), 1238 (s), 1107 (m), 917 (w), 864 (w), 821 (m), 784 (m), 685 (m), 617 (w), 538 (w) cm^{-1}.

$Mg_3(dhtp)_3(dmf)_6{\cdot}0.75H_2O$ (2): When the reaction was performed in the temperature range $90 < T < 120$ °C, block-shaped crystals

were obtained in addition to the needle ones (corresponding to **1**). This new compound was identified as $Mg_3(dhtp)_3(dmf)_6{\cdot}0.75H_2O$ (**2**) by single-crystal X-ray analysis. It should be mentioned here that when the reaction was performed below 90 °C, an unidentified brown powder was produced together with a crystalline material. The yield of **2** could not be determined as this compound was always obtained as a mixture with **1** (see Figure 3). It should also be noted that although **1** is air-stable, the crystallinity of **2** is lost upon atmospheric exposure. $C_{42}H_{55.5}Mg_3N_6O_{24.75}$ (1113.34): calcd. C 45.31, H 5.02, N 7.55; found C 45.85, H 4.82, N 7.69). IR (KBr) for **2**: $\tilde{\nu}$ = 3445 (m), 1652 (ws), 1496 (m), 1455 (s), 1385 (m), 1336 (w), 1238 (s), 1110 (m), 911 (w), 867 (w), 817 (m), 785 (m), 670 (m), 611 (w), 546 (w) cm^{-1}.

$Mn_2(tp)_2(dmf)_2$ (3) and $[Mn(HCOO)_3][NC_2H_8]$ (4): A DMF solution (15 mL) of $Mn(NO_3)_2{\cdot}4H_2O$ (334 mg, 1.33 mmol) and terephthalic acid (H_2tp; 332 mg, 2 mmol) corresponding to a metal-to-ligand ratio of 1:1.5 was sealed in a glass tube and heated at 120 °C for 1 d. Subsequently, the reaction mixture was cooled at a rate of 5 °C h^{-1}. Rhombic- and hexagonal-shaped single crystals were obtained (as a mixture; Figure 6) and identified as $Mn_2(tp)_2(dmf)_2$ (**3**) and $[Mn(HCOO)_3][NC_2H_8]$ (**4**), respectively, by X-ray diffraction studies. Pure **3** or **4** could not be obtained (see main text for details); therefore, **3** and **4** were separated manually. $C_{22}H_{22}Mn_2N_2O_{10}$ (**3**, 584.30): calcd. C 45.22, H 3.80, N 4.79; found C 44.48, H 4.04, N 4.50. $C_5H_{11}MnNO_6$ (**4**, 236.08): calcd. C 25.44, H 4.96, N 7.65; found C 27.57, H 3.40, N 8.95, (the elemental analyses suggest that some crystals of **3** were included). IR (KBr) for **3**: $\tilde{\nu}$ = 3401 (m), 1670 (ws), 1659 (ws), 1626 (ws), 1585 (ws), 1500 (m), 1440 (m), 1388 (ws), 1311 (w), 1253 (w), 1105 (m), 1025 (w), 883 (w), 864 (w), 814 (m), 749 (m), 674 (w), 521 (w) cm^{-1}; for **4**: $\tilde{\nu}$ = 3401 (m), 1670 (m), 1659 (m), 1626 (m), 1563 (s), 1503 (ws), 1385 (ws), 1311 (w), 1155 (w), 1102 (m), 1023 (w), 864 (w), 715 (m), 510 (w) cm^{-1}.

Crystal Structure and Refinement: The crystal structures of the reported compounds were determined by X-ray diffraction methods. The intensity data and cell parameters for **1** and **4** were recorded at 190(2) and 293(2) K, respectively, with a Bruker APEX II diffractometer equipped with a CCD area detector and a graphite monochromator (Mo-K_α radiation, λ = 0.71073 Å). The X-ray data for **2** and **3** were collected with Mo-K_α radiation at 100 K with a Bruker APEX II QUAZAR diffractometer equipped with a microfocus multilayer monochromator. In all cases, data reduction and absorption corrections were performed with SAINT[55] and SADABS,[56] respectively. The structures of **1** and **4** were solved by direct method by using SIR97[57] and refined on F_o^2 by full-matrix least-squares procedures by using the SHELXL-97[58] program in the WinGX suite.[59] All non-hydrogen atoms were refined with anisotropic atomic displacements, with the exception of the oxygen atoms of the phenolic hydroxy groups in **1**, which were disordered over two positions with occupancy factors of 0.8 and 0.2. The hydrogen atoms were included in the refinement at idealized geometries and refined as "riding" on the corresponding parent atoms with isotropic displacement parameters [U_{iso}(H) = 1.2U_{eq}C(i), U_{iso}(H) = 1.2U_{eq}O(i) or U_{iso}(H) = 1.5U_{eq}C(i) for methyl groups]. Owing to the disorder in **1**, the two aromatic hydrogen atoms could not be calculated in their expected position and were omitted from the structural model (but they were included in the compound formula and molecular weight). The structure of **2** was solved and refined on F_o^2 by using the SHELXTL suite.[58] The hydrogen atoms bound to the hydroxy oxygen atoms O(i) were found in the difference Fourier map and refined freely with fixed isotropic displacement parameters {U_{iso}(H) = 1.2U_{eq}O(i)}. The remaining hydrogen atoms were placed at calculated positions on their carrier atom C(i) and refined with a riding model with fixed isotropic displacement parameters [U_{iso}(H) = 1.2U_{eq}C(i) or U_{iso}(H) = 1.5U_{eq}C(i) for methyl groups]. The hydrogen atoms bound to the lattice water oxygen atoms could not be found nor fixed and were omitted in the structural model, although they were included in the formula. The structure of **3** was solved and refined on F_o^2 with SHELX[58] through Olex2.[60] The hydrogen atoms were placed at calculated positions on their carrier atom C(i) and refined with a riding model with fixed isotropic displacement parameters [U_{iso}(H) = 1.2U_{eq}C(i) or U_{iso}(H) = 1.5U_{eq}C(i) for methyl groups].

CCDC-989982 (for **1**), -989983 (for **2**), -989984 (for **3**) and -989985 (for **4**) contain the supplementary crystallographic data for this paper. These data can be obtained free of charge from The Cambridge Crystallographic Data Centre via www.ccdc.cam.ac.uk/data_request/cif.

Supporting Information (see footnote on the first page of this article): Solid-state structure of **3**, bond lengths and angles.

Acknowledgments

P. G. acknowledges Institució Catalana de Recerca i Estudis Avançats (ICREA) and the Spanish Ministerio de Economía y Competitividad (MEC) (project number CTQ2011-27929-C02-01). A. C. and S. Y. thank the Royal Golden Jubilee Program (RGJ, grant number PHD/0328/2551) and Khon Kaen University for a research grant. S. Y. acknowledges The Thailand Research Fund (grant number BRG5680009), the National Research University Project of Thailand, Office of the Higher Education Commission, through the Advanced Functional Materials Cluster of Khon Kaen University and the Korean Ministry of Education (Center of Excellence for Innovation in Chemistry, PERCH-CIC, Office of the Higher Education Commission).

[1] G. R. Desiraju, *Chem. Commun.* **1997**, 1475.
[2] D. Braga, F. Grepioni, G. R. Desiraju, *Chem. Rev.* **1998**, *98*, 1375.
[3] M. D. Hollingsworth, *Science* **2002**, *295*, 2410.
[4] D. Braga, L. Brammer, N. R. Champness, *CrystEngComm* **2005**, *7*, 1.
[5] M. A. Neumann, F. J. J. Leusen, J. Kendrick, *Angew. Chem. Int. Ed.* **2008**, *47*, 2427; *Angew. Chem.* **2008**, *120*, 2461.
[6] M. Lusi, L. J. Barbour, *Chem. Commun.* **2013**, *49*, 2634.
[7] N. Rodriguez-Hornedo, D. Murphy, *J. Pharm. Sci.* **1999**, *88*, 651.
[8] J. Swift, *CrystEngComm* **2011**, *13*, 1059.
[9] S. R. Batten, N. R. Champness, X. M. Chen, J. Garcia-Martinez, S. Kitagawa, L. Ohrstrom, M. O'Keeffe, M. P. Suh, J. Reedijk, *CrystEngComm* **2012**, *14*, 3001.
[10] S. M. Cohen, *Chem. Rev.* **2012**, *112*, 970.
[11] T. R. Cook, Y. R. Zheng, P. J. Stang, *Chem. Rev.* **2013**, *113*, 734.
[12] S. Kitagawa, R. Kitaura, S. Noro, *Angew. Chem. Int. Ed.* **2004**, *43*, 2334; *Angew. Chem.* **2004**, *116*, 2388.
[13] K. Sumida, D. L. Rogow, J. A. Mason, T. M. McDonald, E. D. Bloch, Z. R. Herm, T. H. Bae, J. R. Long, *Chem. Rev.* **2012**, *112*, 724.
[14] J. R. Li, J. Sculley, H. C. Zhou, *Chem. Rev.* **2012**, *112*, 869.
[15] D. Y. Hong, Y. K. Hwang, C. Serre, G. Ferey, J. S. Chang, *Adv. Funct. Mater.* **2009**, *19*, 1537.
[16] U. Eberle, M. Felderhoff, F. Schuth, *Angew. Chem. Int. Ed.* **2009**, *48*, 6608; *Angew. Chem.* **2009**, *121*, 6732.
[17] E. Coronado, G. M. Espallargas, *Chem. Soc. Rev.* **2013**, *42*, 1525.
[18] J. Rocha, L. D. Carlos, F. A. A. Paz, D. Ananias, *Chem. Soc. Rev.* **2011**, *40*, 926.

[19] M. Yoon, R. Srirambalaji, K. Kim, *Chem. Rev.* **2012**, *112*, 1196.
[20] P. Phuengphai, C. Massera, J. Reedijk, S. Youngme, P. Gamez, *Eur. J. Inorg. Chem.* **2013**, 4812.
[21] N. L. Rosi, M. Eddaoudi, J. Kim, M. O'Keeffe, O. M. Yaghi, *CrystEngComm* **2002**, 401.
[22] J. G. Lin, Y. Y. Xu, L. Qiu, S. Q. Zang, C. S. Lu, C. Y. Duan, Y. Z. Li, S. Gao, Q. J. Meng, *Chem. Commun.* **2008**, 2659.
[23] N. Stock, S. Biswas, *Chem. Rev.* **2012**, *112*, 933.
[24] C. McKinstry, E. J. Cussen, A. J. Fletcher, S. V. Patwardhan, J. Sefcik, *Cryst. Growth Des.* **2013**, *13*, 5481.
[25] S. Masaoka, D. Tanaka, Y. Nakanishi, S. Kitagawa, *Angew. Chem. Int. Ed.* **2004**, *43*, 2530; *Angew. Chem.* **2004**, *116*, 2584.
[26] Y. B. Dong, Y. Y. Jiang, J. Li, J. P. Ma, F. L. Liu, B. Tang, R. Q. Huang, S. R. Batten, *J. Am. Chem. Soc.* **2007**, *129*, 4520.
[27] X. G. Guo, W. B. Yang, X. Y. Wu, K. Zhang, L. Lin, R. M. Yu, C. Z. Lu, *CrystEngComm* **2013**, *15*, 3654.
[28] K. Jayaramulu, P. Kanoo, S. J. George, T. K. Maji, *Chem. Commun.* **2010**, *46*, 7906.
[29] Compound **1** has been described earlier as light yellow block-shaped crystals.[28] In the present study, **1** was obtained as light yellow needle-shaped crystals, and the block-shaped crystals have been identified as **2**.
[30] K. C. Yang, C. C. Chang, C. S. Yeh, G. H. Lee, S. M. Peng, *Organometallics* **2001**, *20*, 126.
[31] W. Clegg, I. R. Little, B. P. Straughan, *Inorg. Chem.* **1988**, *27*, 1916.
[32] S. Q. Ma, J. A. Fillinger, M. W. Ambrogio, J. L. Zuo, H. C. Zhou, *Inorg. Chem. Commun.* **2007**, *10*, 220.
[33] a) T. Ladrak, S. Smulders, O. Roubeau, S. J. Teat, P. Gamez, J. Reedijk, *Eur. J. Inorg. Chem.* **2010**, 3804; b) G. Xu, X. Zhang, P. Guo, C. Pan, H. Zhang, C. Wang, *J. Am. Chem. Soc.* **2010**, *132*, 3656; c) S.-Y. Yang, H.-B. Yuan, X.-B. Xu, R.-B. Huang, *Inorg. Chim. Acta* **2013**, *403*, 53.
[34] a) X.-Y. Wang, L. Gan, S.-W. Zhang, S. Gao, *Inorg. Chem.* **2004**, *43*, 4615; b) Z. M. Wang, X. Y. Zhang, S. R. Batten, M. Kurmoo, S. Gao, *Inorg. Chem.* **2007**, *46*, 8439.
[35] Z. M. Wang, B. Zhang, T. Otsuka, K. Inoue, H. Kobayashi, M. Kurmoo, *Dalton Trans.* **2004**, 2209.
[36] Z. M. Wang, B. Zhang, Y. J. Zhang, M. Kurmoo, T. Liu, S. Gao, H. Kobayashi, *Polyhedron* **2007**, *26*, 2207.
[37] V. A. Blatov, *Struct. Chem.* **2012**, *23*, 955.
[38] E. V. Alexandrov, V. A. Blatov, A. V. Kochetkov, D. M. Proserpio, *CrystEngComm* **2011**, *13*, 3947.
[39] a) C. S. Hong, Y. Do, *Inorg. Chem.* **1997**, *36*, 5684; b) M. Kurmoo, H. Kumagai, M. A. Green, B. W. Lovett, S. J. Blundell, A. Ardavan, J. Singleton, *J. Solid State Chem.* **2001**, *159*, 343; c) J. A. Kaduk, *Acta Crystallogr., Sect. B: Struct. Sci.* **2002**, *58*, 815.
[40] a) H. Li, C. E. Davis, T. L. Groy, D. G. Kelley, O. M. Yaghi, *J. Am. Chem. Soc.* **1998**, *120*, 2186; b) K. O. Kongshaug, H. Fjellvag, *Solid State Sci.* **2003**, *5*, 303; c) M. Dinca, J. R. Long, *J. Am. Chem. Soc.* **2005**, *127*, 9376; d) B.-H. Ye, B.-B. Ding, Y.-Q. Weng, X.-M. Chen, *Cryst. Growth Des.* **2005**, *5*, 801; e) I. Senkovska, S. Kaskel, *Eur. J. Inorg. Chem.* **2006**, 4564; f) J. A. Rood, B. C. Noll, K. W. Henderson, *Main Group Chem.* **2006**, *5*, 21; g) I. Senkovska, J. Fritsch, S. Kaskel, *Eur. J. Inorg. Chem.* **2007**, 5475; h) S. H. Kim, H. S. Huh, S. W. Lee, *J. Mol. Struct.* **2007**, *841*, 78; i) R. P. Davies, R. J. Less, P. Lickiss, A. J. P. White, *Dalton Trans.* **2007**, 2528; j) X.-F. Wang, Y.-B. Zhang, X.-N. Cheng, X.-M. Chen, *CrystEngComm* **2008**, *10*, 753; k) C. A. Williams, A. J. Blake, C. Wilson, P. Hubberstey, M. Schroder, *Cryst. Growth Des.* **2008**, *8*, 911; l) B. Liu, R.-Q. Zou, R.-Q. Zhong, S. Han, H. Shioyama, T. Yamada, G. Maruta, S. Takeda, Q. Xu, *Microporous Mesoporous Mater.* **2008**, *111*, 470; m) Y. Du, A. L. Thompson, D. O'Hare, *Chem. Commun.* **2008**, 5987; n) Y. Du, A. L. Thompson, D. O'Hare, *Dalton Trans.* **2010**, *39*, 3384; o) R.-Q. Zhong, R.-Q. Zou, M. Du, T. Yamada, G. Maruta, S. Takeda, J. Li, Q. Xu, *CrystEngComm* **2010**, *12*, 677; p) X.-F. Wang, Y.-B. Zhang, W.-X. Zhang, W. Xue, H.-L. Zhou, X.-M. Chen, *CrystEngComm* **2011**, *13*, 4196; q) L.-N. Yang, Y.-X. Zhi, J.-H. Hei, J. Li, F.-X. Zhang, S.-Y. Gao, *J. Coord. Chem.* **2011**, *64*, 2912; r) M. R. V. Jorgensen, H. F. Clausen, M. Christensen, R. D. Poulsen, J. Overgaard, B. B. Iversen, *Eur. J. Inorg. Chem.* **2011**, 549.
[41] O. M. Yaghi, H. Furukawa, J. Kim, N. Ko, S. B. Choi, WO 2011/038208 A2, **2011**.
[42] a) H. F. Clausen, R. D. Poulsen, A. D. Bond, M.-A. S. Chevallier, B. B. Iversen, *J. Solid State Chem.* **2005**, *178*, 3342; b) Y. Wang, R. Cao, W. Bi, X. Li, D. Yuan, D. Sun, *Microporous Mesoporous Mater.* **2006**, *91*, 215; c) C. Zhou, Y. Li, J. Guo, P. Yang, *Zh. Strukt. Khim. Zh. Strukt. Khim.* **2006**, *47*, 780; d) P. Jain, N. S. Dalal, B. H. Toby, H. W. Kroto, A. K. Cheetham, *J. Am. Chem. Soc.* **2008**, *130*, 10450; e) A. Rossin, A. Ienco, F. Costantino, T. Montini, B. Di Credico, M. Caporali, L. Gonsalvi, P. Fornasiero, M. Peruzzini, *Cryst. Growth Des.* **2008**, *8*, 3302; f) A. Plutecka, U. Rychlewska, *Acta Crystallogr., Sect. C: Cryst. Struct. Commun.* **2009**, *65*, m75; g) M. Qin, D.-H. Lee, G. Park, *J. Korean Chem. Soc.* **2009**, *53*, 73; h) S.-Q. Xu, J.-M. Li, *Z. Kristallogr. New Cryst. Struct.* **2009**, *224*, 383; i) K. S. Hagen, S. G. Naik, B. H. Huynh, A. Masello, G. Christou, *J. Am. Chem. Soc.* **2009**, *131*, 7516; j) P. Jain, V. Ramachandran, R. J. Clarke, H. D. Zhou, B. H. Toby, N. S. Dalal, H. W. Kroto, A. K. Cheetham, *J. Am. Chem. Soc.* **2009**, *131*, 13625; k) S. Gao, S. W. Ng, *Acta Crystallogr., Sect. E. Struct. Rep. Online* **2010**, *66*, m1599; l) C. Zou, T. Zhang, M.-H. Xie, L. Yan, G.-Q. Kong, X.-L. Yang, A. Ma, C.-D. Wu, *Inorg. Chem.* **2013**, *52*, 3620; m) V. Paredes-Garcia, I. Rojas, R. Madrid, A. Vega, E. Navarro-Moratalla, W. Canon-Mancisidor, E. Spodine, D. Venegas-Yazigi, *New J. Chem.* **2013**, *37*, 2120.
[43] K. Uemura, S. Kitagawa, M. Kondo, K. Fukui, R. Kitaura, H. C. Chang, T. Mizutani, *Chem. Eur. J.* **2002**, *8*, 3586.
[44] F. Gándara, V. A. de la Peña-O'Shea, F. Illas, N. Snejko, D. M. Proserpio, E. Gutiérrez-Puebla, M. A. Monge, *Inorg. Chem.* **2009**, *48*, 4707.
[45] H. Yim, E. Kang, J. Kim, *Bull. Korean Chem. Soc.* **2010**, *31*, 1041.
[46] W. Schmitt, N. Zhu, M. J. Lennox, T. Duren, *Chem. Commun.* **2014**, *50*, 4207–4210.
[47] J. Hafizovic, M. Bjorgen, U. Olsbye, P. D. C. Dietzel, S. Bordiga, C. Prestipino, C. Lamberti, K. P. Lillerud, *J. Am. Chem. Soc.* **2007**, *129*, 3612.
[48] T. L. Hennigar, D. C. MacQuarrie, P. Losier, R. D. Rogers, M. J. Zaworotko, *Angew. Chem. Int. Ed. Engl.* **1997**, *36*, 972; *Angew. Chem.* **1997**, *109*, 1044.
[49] S. Q. Ma, D. F. Sun, M. Ambrogio, J. A. Fillinger, S. Parkin, H. C. Zhou, *J. Am. Chem. Soc.* **2007**, *129*, 1858.
[50] B. Moulton, M. J. Zaworotko, *Chem. Rev.* **2001**, *101*, 1629.
[51] T. Panda, T. Kundu, R. Banerjee, *Chem. Commun.* **2013**, *49*, 6197.
[52] S. A. Barnett, A. J. Blake, N. R. Champness, C. Wilson, *Chem. Commun.* **2002**, 1640.
[53] D. Moon, J. Song, M. S. Lah, *CrystEngComm* **2009**, *11*, 770.
[54] S. Geranmayeh, A. Abbasi, *J. Inorg. Organomet. Polym. Mater.* **2013**, *23*, 1138.
[55] *SAINT*, version 6.0, Bruker Analytical X-ray Systems, Madison, WI, USA, **1999**.
[56] G. M. Sheldrick, *SADABS*, version 2.03, University of Göttingen, Germany, **1999**.
[57] A. Altomare, M. C. Burla, M. Camalli, G. L. Cascarano, C. Giacovazzo, A. Guagliardi, A. G. G. Moliterni, G. Polidori, R. Spagna, *J. Appl. Crystallogr.* **1999**, *32*, 115.
[58] G. M. Sheldrick, *Acta Crystallogr., Sect. A* **2008**, *64*, 112.
[59] L. J. Farrugia, *J. Appl. Crystallogr.* **1999**, *32*, 837.
[60] O. V. Dolomanov, L. J. Bourhis, R. J. Gildea, J. A. K. Howard, H. Puschmann, *J. Appl. Crystallogr.* **2009**, *42*, 339.

Received: May 28, 2014
Published Online: July 30, 2014

Acta Crystallographica Section E
Structure Reports
Online
ISSN 1600-5368

Di-μ-acetato-κ^4O:O'-bis[(1,10-phenanthroline-κ^2N,N')(trifluoromethanesulfonato-κO)copper(II)]

Nanthawat Wannarit, Chaveng Pakawatchai and Sujittra Youngme

Acta Cryst. (2013). E**69**, m591–m592

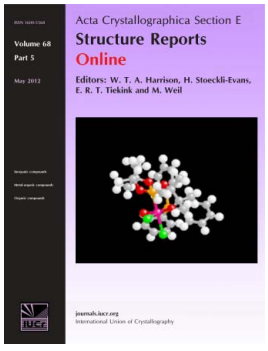

Acta Crystallographica Section E
Structure Reports Online
ISSN 1600-5368

Di-μ-acetato-κ^4O:O'-bis[(1,10-phenanthroline-κ^2N,N')(trifluoromethanesulfonato-κO)copper(II)]

Nanthawat Wannarit,[a] Chaveng Pakawatchai[b] and Sujittra Youngme[a]*

[a]Materials Chemistry Research Unit, Department of Chemistry and Center of Excellence for Innovation in Chemistry, Faculty of Science, Khon Kaen University, Khon Kaen 40002, Thailand, and [b]Department of Chemistry, Faculty of Science, Prince of Songkla University, Hat Yai, Songkhla 90112, Thailand
Correspondence e-mail: sujittra@kku.ac.th

Received 30 August 2013; accepted 4 October 2013

Key indicators: single-crystal X-ray study; T = 293 K; mean σ(C–C) = 0.003 Å; disorder in main residue; R factor = 0.034; wR factor = 0.102; data-to-parameter ratio = 15.4.

The complete molecule of the title compound, $[Cu_2(C_2H_3O_2)_2(CF_3O_3S)_2(C_{12}H_8N_2)_2]$, is completed by the application of a twofold rotation and comprises two Cu^{II} ions, each of which is pentacoordinated by two N atoms from a bidentate 1,10-phenanthroline (phen) ligand, two O atoms from acetate ligands and an O atom from a trifluoromethanesulfonate anion, forming a (4 + 1) distorted square-pyramidal coordination geometry. The Cu^{II} ions are connected by two acetate bridges in a *syn–syn* configuration. The F atoms of the trifluoromethanesulfonate ligands are disordered, with site-occupation factors of 70 and 30. The molecular structure is stabilized by intramolecular face-to-face π–π interactions with centroid–centroid distances in the range 3.5654 (12)–3.8775(12) Å. The crystal structure is stabilized by C—H···O interactions, leading to a three-dimensional lattice structure.

Related literature

For general background to this work, see: Moreira *et al.* (2007); Calvo *et al.* (2011); Reinoso *et al.* (2005, 2007); Ritchie *et al.* (2006); Wang *et al.* (2006). For literature used in the synthetic procedures, see: Youngme *et al.* (2008). For a related crystal structure, see: Tokii *et al.* (1990). For potential applications, see: Hill & Brown (1986); Mansuy *et al.* (1991); Hill & Zhang (1995). For an explanation of the τ parameter, see: Addison *et al.* (1984). For spectroscopic properties, see: Castro *et al.* (1992); Sletten & Julve (1999).

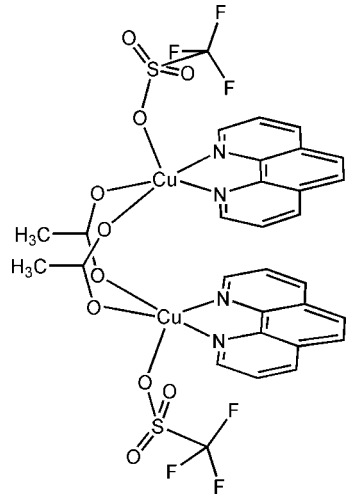

Experimental

Crystal data

$[Cu_2(C_2H_3O_2)_2(CF_3O_3S)_2(C_{12}H_8N_2)_2]$
M_r = 903.72
Monoclinic, $C2/c$
a = 13.1198 (5) Å
b = 16.1282 (6) Å
c = 16.3659 (6) Å
β = 95.507 (1)°
V = 3447.0 (2) Å^3
Z = 4
Mo $K\alpha$ radiation
μ = 1.45 mm^{-1}
T = 293 K
0.24 × 0.21 × 0.18 mm

Data collection

Bruker SMART APEX CCD diffractometer
Absorption correction: multi-scan (*SADABS*; Sheldrick, 2000)
T_{min} = 0.872, T_{max} = 1.000
23313 measured reflections
4178 independent reflections
3491 reflections with $I > 2\sigma(I)$
R_{int} = 0.022

Refinement

$R[F^2 > 2\sigma(F^2)]$ = 0.034
$wR(F^2)$ = 0.102
S = 1.04
4178 reflections
272 parameters
H-atom parameters constrained
$\Delta\rho_{max}$ = 0.37 e Å^{-3}
$\Delta\rho_{min}$ = −0.32 e Å^{-3}

Table 1
Hydrogen-bond geometry (Å, °).

D—H···A	D—H	H···A	D···A	D—H···A
C1—H1···O5^{i}	0.93	2.43	3.229 (3)	144
C3—H3···O4^{ii}	0.93	2.34	3.213 (3)	157
C8—H8···O3^{iii}	0.93	2.56	3.421 (3)	154

Symmetry codes: (i) $-x+1, -y+2, -z+1$; (ii) $x-\frac{1}{2}, y-\frac{1}{2}, z$; (iii) $-x+\frac{3}{2}, y-\frac{1}{2}, -z+\frac{3}{2}$.

Data collection: *SMART* (Bruker, 2000); cell refinement: *SMART*; data reduction: *SAINT* (Bruker, 2000) and *SHELXTL* (Sheldrick, 2008); program(s) used to solve structure: *SHELXTL*; program(s) used to refine structure: *SHELXL97* (Sheldrick, 2008); molecular graphics: *ORTEP-3 for Windows* (Farrugia, 2012) and *Mercury* (Macrae *et al.*, 2006); software used to prepare material for publication: *PLATON* (Spek, 2009) and *pubCIF* (Westrip, 2010).

The authors gratefully acknowledge financial support from the Thailand Research Fund, the Higher Education Research Promotion and National Research University Project of

Thailand, Office of the Higher Education Commission, through the Advanced Functional Materials Cluster of Khon Kaen University and the Center of Excellence for Innovation in Chemistry (PERCH–CIC), Commission on Higher Education, Ministry of Education, Thailand.

Supplementary data and figures for this paper are available from the IUCr electronic archives (Reference: IM2439).

References

Addison, A. W., Rao, T. N., Reedijk, J., van Rijn, J. & Verschoor, G. C. (1984). *J. Chem. Soc. Dalton Trans*. pp. 1349–1356.

Bruker (2000). *SMART* and *SAINT*. Bruker AXS Inc., Madison, Wisconsin, USA.

Calvo, R., Abud, J. E., Sartoris, R. P. & Santana, R. C. (2011). *Phys. Rev. B*, **84**, 104433, 1–13.

Castro, I., Faus, J., Julve, M., Bois, C., Real, J. A. & Lloret, F. (1992). *J. Chem. Soc. Dalton Trans*. pp. 47–52.

Farrugia, L. J. (2012). *J. Appl. Cryst.* **45**, 849–854.

Hill, C. L. & Brown, R. B. (1986). *J. Am. Chem. Soc*. **108**, 536–538.

Hill, C. L. & Zhang, X. (1995). *Nature (London)*, **373**, 324–326.

Macrae, C. F., Edgington, P. R., McCabe, P., Pidcock, E., Shields, G. P., Taylor, R., Towler, M. & van de Streek, J. (2006). *J. Appl. Cryst.* **39**, 453–457.

Mansuy, D., Bartoli, J. F., Battioni, P., Lyon, D. K. & Finke, R. G. (1991). *J. Am. Chem. Soc*. **113**, 7222–7226.

Moreira, I. P. R., Costa, R., Filatov, M. & Illas, F. (2007). *J. Chem. Theory Comput*. **3**, 764–774.

Reinoso, S., Vitoria, P., Felices, L. S., Lezama, L. & Gutiérrez-Zorrilla, J. M. (2005). *Chem. Eur. J*. **11**, 1538–1548.

Reinoso, S., Vitoria, P., Gutiérrez-Zorrilla, J. M., Lezama, L., Madariaga, J. M., Felices, L. S. & Iturrospe, A. (2007). *Inorg. Chem*. **46**, 4010–4021.

Ritchie, C., Burkholder, E., Kögerler, P. & Cronin, L. (2006). *Dalton Trans*. pp. 1712–1714.

Sheldrick, G. M. (2000). *SADABS*. University of Göttingen, Germany.

Sheldrick, G. M. (2008). *Acta Cryst.* A**64**, 112–122.

Sletten, J. & Julve, M. (1999). *Acta Chem. Scand*. **53**, 631–633.

Spek, A. L. (2009). *Acta Cryst.* D**65**, 148–155.

Tokii, T., Watanabe, N., Nakashima, M., Muto, Y., Morooka, M., Ohba, S. & Saito, I. (1990). *Bull. Chem. Soc. Jpn*, **63**, 364–369.

Wang, J.-P., Ren, Q., Zhao, J.-W. & Niu, J.-Y. (2006). *Inorg. Chem. Commun*. **9**, 1281–1285.

Westrip, S. P. (2010). *J. Appl. Cryst.* **43**, 920–925.

Youngme, S., Cheansirisomboon, A., Danvirutai, C., Pakawatchai, C., Chaichit, N., Engkagul, C., van Albada, G. A., Costa, J. S. & Reedijk, J. (2008). *Polyhedron*, **27**, 1875–1882.

supplementary materials

Acta Cryst. (2013). E**69**, m591–m592 [doi:10.1107/S1600536813027323]

Di-μ-acetato-κ^4O:O'-bis[(1,10-phenanthroline-κ^2N,N')(trifluoromethanesulfonato-κO)copper(II)]

Nanthawat Wannarit, Chaveng Pakawatchai and Sujittra Youngme

1. Comment

The synthesis and characterization of polycarboxylato-bridged dinuclear copper(II) compounds namely dinuclear tetracarboxylato-bridged Cu^{II} compounds (paddlewheel-like structure) (*e.g.* Moreira *et al.*, 2007; Youngme *et al.*, 2008) and also dinuclear Cu^{II} compounds containing dicarboxylato-bridges (Tokii *et al.*, 1990; Reinoso *et al.*, 2005; Ritchie *et al.*, 2006) have attacted much attention in several years. These compounds have been prepared with the aim of studying their intramolecular magnetic properties which are determined predominantly by strong antiferromagnetic interactions. In addition, the dicarboxylato-bridged dinuclear Cu^{II} compounds have been frequently used as the models for the basic understanding of their magneto-structural correlations in theoretical studies (Moreira *et al.*, 2007; Calvo *et al.*, 2011). Copper(II) compounds containing doubly acetato-bridged dinuclear units, $[Cu(phen)(\mu\text{-}OOCCH_3)_2Cu(phen)]^{2+}$ (where phen = 1,10-phenanthroline), have also been shown to exhibit antiferromagnetic behavior (Tokii *et al.*, 1990). Furthermore, this type of dinuclear unit was used as the secondary building block in functionalized polyoxometalate (POMs) materials (Wang *et al.*, 2006; Reinoso *et al.*, 2007; Calvo *et al.*, 2011) to extend the dimensionality of structures leading to new hybrid materials and more selective applications, for example catalytic properties in organic oxidations (Hill & Brown, 1986; Mansuy *et al.*, 1991; Hill, & Zhang, 1995).

A new doubly acetato-bridged dinuclear Cu^{II} compound containing additional trifluoromethanesulfonate anions has been synthesized and its structural features are reported here. Compound **I**, bis((μ-acetato)(trifluoromethanesulfonato)(1,10-phenanthroline))dicopper(II) crystallized in the space group *C*2/*c* with an asymmetric unit containing one half of the dinuclear unit (Fig.1). This dinuclear unit has C_2 symmetry around the *b* axis with Cu···Cu distance of 3.0309 (4) Å. Structurally, compound **I** consists of two $[Cu(phen)(OSO_2CF_3)]^+$ cations connected together by two bridging acetato ligands in a *syn-syn* configuration. Both Cu^{II} atoms exhibit five coordination of CuN_2O_2O' chromophore, with the basal plane consisting of two phen N atoms [Cu—N = 2.0153 (18) and 1.9980 (18) Å] and two O atoms from acetate ligands [Cu—O = 1.9387 (17) and 1.9377 (18)]. Due to symmetry both square planes are parallel to one another. The apical position at Cu^{II} is occupied by an O atom from trifluoromethanesulfonate anion [Cu—O = 2.261 (2)], leading to the (4 + 1) square-pyramidal geometry. The square base of Cu^{II} chromophore is not perfectly planar, with the tetrahedral twist of 16.52 (7)° and Cu^{II} is situated above the basal plane by 0.14 (1) Å pointing towards the O atom of the trifluoromethanesulfonate anion. The distortion of a square pyramid can be best described by the structural parameter τ (τ = 0 for a square pyramid and τ =1 for a trigonal bipyramid (Addison *et al.*, 1984)), with τ = 0.23 for the title compound. The molecular structure of **I** reveals intramolecular face-to-face π-π interaction between aromatic rings of phen ligands (Fig. 1). Phenanthroline molecules are parallel with an average contact and angle of phen planes of 3.63 (3) Å and 5.96 (3)°, respectively. In general, the ligands are featureless: neither of phen group departs significantly from planarity [maximum deviations: 0.082 Å for C11 and 0.099 Å for C10 of *Cg*3 ring(N2, C6, C9, C10, C11, C12)] and the C—O bonds in the

acetato bridging ligands display an almost perfect resonance [C13⋯O1 = 1.257 (3) Å and C13⋯O2 = 1.250 (3) Å]. The crystal structure of compound **I** is determined by intermolecular hydrogen bonding interactions between methyl groups of acetato ligands (H14A) or phen ligands (H7 as hydrogen bond donor sites and H10) and oxygen/fluoride accepetors at trifluoromethanesulfonate anions (O3, O5 and F3) (see Table 1), generating two-dimensional layers parallel to the *ab* plane (Fig. 2). Moreover, these two-dimensional sheets are interconnected by hydrogen bond interactions between C—H of phen ligands and oxygen atoms of trifluoromethanesulfonate anions [C1—H1···O5^{i}; symetry code (i) = -*x*+1, -*y*+2, -*z*+1] (see Table 2) in direction of crystallographic *c* axis, leading to three-dimensional lattice structure (Fig. 3). Although containing the same [(phen)Cu(μ-OOCCH$_3$)$_2$Cu(phen)]$^{2+}$ unit, the structural topology of **I** is distinct from that of the related compound [Cu(phen)(μ-O$_2$CCH$_3$)(H$_2$O)]$_2$(NO$_3$)$_2$.4H$_2$O (Tokii *et al.*, 1990) in which the apical position is occupied by water molecule. The dinuclear unit of this related compound also crystallized in *C*2/*c* space group and has C_2 symmetry around the *b* axis with Cu···Cu distance of 3.063 Å, but its crystal lattice is mainly stabilized by intra- and intermolecular π-π interactions, generating a one-dimensional chain-like sructure. It is clear that the difference of the structural topology between compound **I** and the related compound caused by the effect of coordinated trifluoromethanesulfonate anions whereas nitrate anions are not coordinated to Cu in the other structure.

The diffuse reflectance spectrum of **I** displays a broad band at 15400 cm^{-1} and a lower energy shoulder at 14300 cm^{-1}. This feature corresponds to a dominantly distorted square pyramidal geometry of Cu^{II} ions and is consistent with the observed structural parameters. The transitions may be assigned as d_{xy}, d_{yz}, $d_{xz}\rightarrow d_{x2-y2}$ and $d_{z2}\rightarrow d_{x2-y2}$. The IR spectrum of **I**, in addition to the phen vibrations shows the broad and intense bands of the stretching of the ionic $CF_3SO_3^-$ at 1276 ν_{as}(S–O), 1158 ν_{as}(C–F) and 1031 ν_s(S–O) cm^{-1} (Castro *et al.*, 1992). The IR spectrum also shows two broad and intense bands at 1567 and 1385 cm^{-1}, corresponding to the $\nu_{as}(COO^-)$ and $\nu_s(COO^-)$ vibrations of acetate bridging ligands. The latter spectral properties completely disappear for related mononuclear compounds as [Cu(phen)$_3$](CF$_3$SO$_3$)$_2$.H$_2$O (Sletten & Julve, 1999).

2. Experimental

A warm ethanolic solution (25 ml) of phen (0.198 g, 1.0 mmol) was added to a warm aqueous solution (15 ml) of Cu(CF$_3$SO$_3$)$_2$ (0.370 g, 1.0 mmol). Then NaO$_2$CCH$_3$ solid (0.124 g, 1.0 mmol) was added to the mixture, yielding a clear dark blue solution. After a week, the blue rectangle-shaped crystals of compound **I** were obtained. The crystals were filtered off, washed with mother liquor and air-dried. Yield: *ca* 45%. Anal. Calc. for Cu$_2$C$_{30}$H$_{24}$N$_4$O$_{10}$F$_6$S$_2$: C, 39.78; H, 2.67; N, 6.19%. Found: C, 39.12; H, 2.51; N, 6.36%.

3. Refinement

All H atoms were constrained to ideal positions, with C—H = 0.93 Å and U_{iso}(H) =1.2U$_{eq}$(C) for H atoms at phen and C—H = 0.96 Å and U_{iso}(H) =1.2U$_{eq}$(C) for H atoms of acetate groups. Fluorine atoms of the trifluoromethanesulfonato ligands are disordered with site occupation factors of 70:30%.

Computing details

Data collection: *SMART* (Bruker, 2000); cell refinement: *SMART* (Bruker, 2000); data reduction: *SAINT* (Bruker, 2000) and *SHELXTL* (Sheldrick, 2008); program(s) used to solve structure: *SHELXTL* (Sheldrick, 2008); program(s) used to refine structure: *SHELXL97* (Sheldrick, 2008); molecular graphics: *ORTEP-3 for Windows* (Farrugia, 2012) and *Mercury* (Macrae *et al.*, 2006); software used to prepare material for publication: *PLATON* (Spek, 2009) and pubCIF (Westrip, 2010).

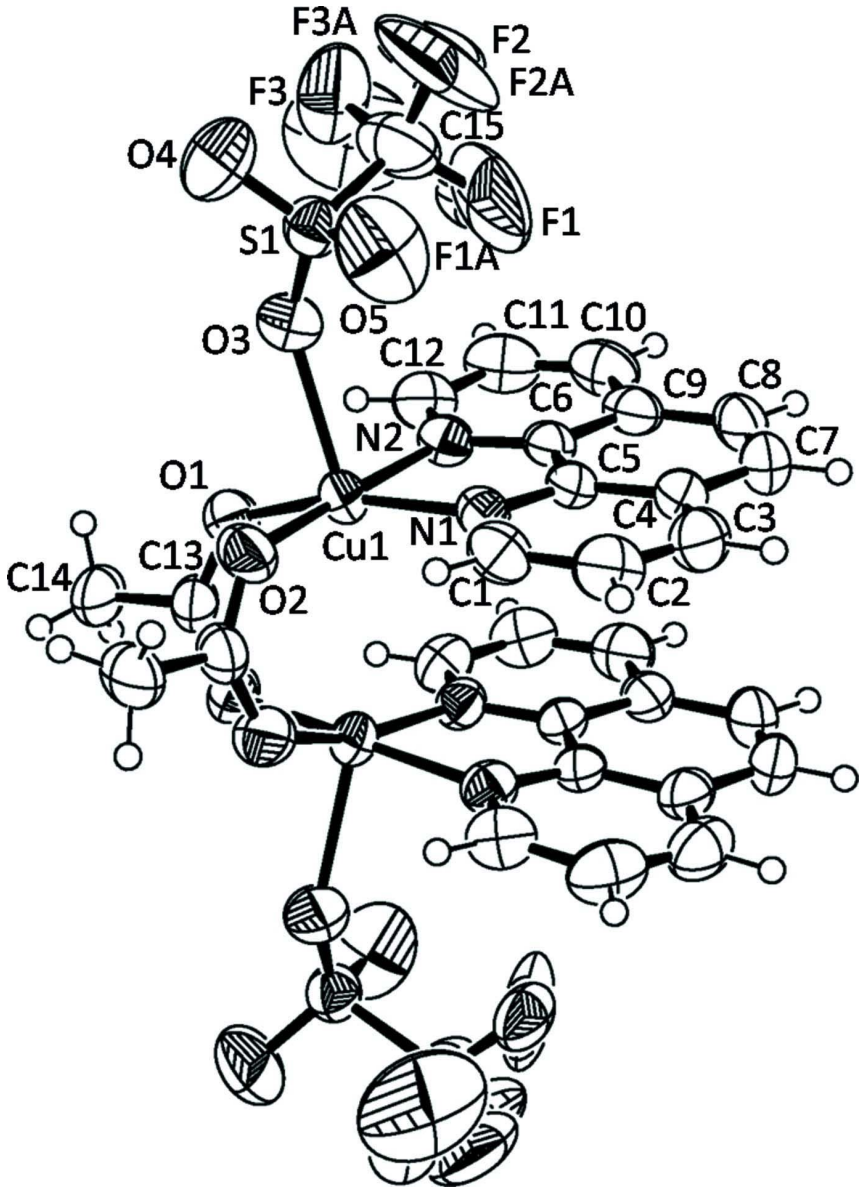

Figure 1

Molecular structure and atomic numbering scheme with thermal ellipsoids shown at 50% probability level.

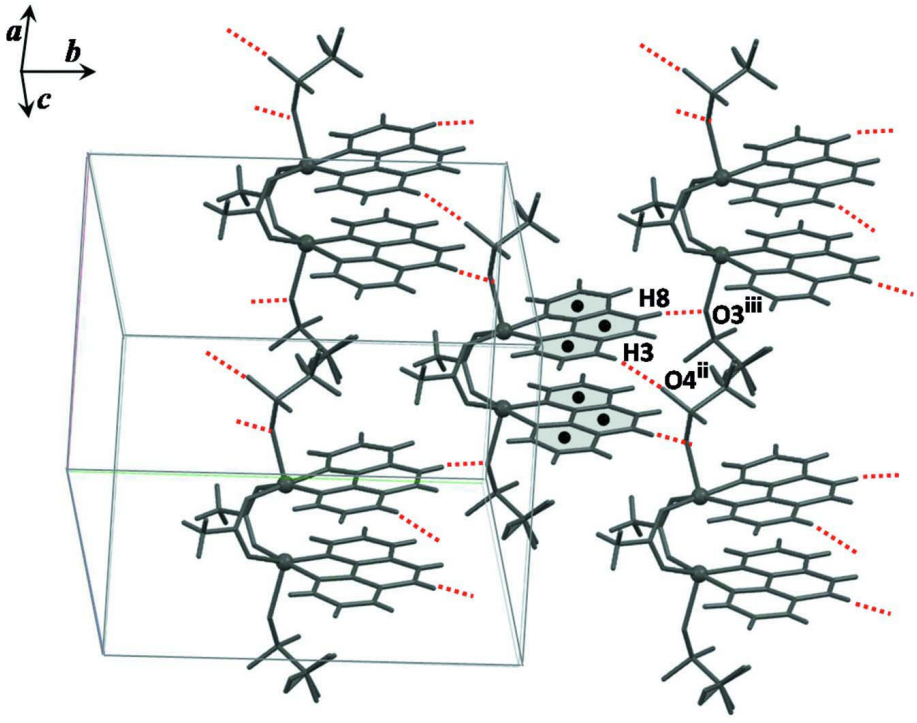

Figure 2

The crystal packing. View of two-dimensional layer constructed by intermolecular hydrogen bonding and view of the intramolecular face-to-face π-π interactions between aromatic rings of phen ligands.

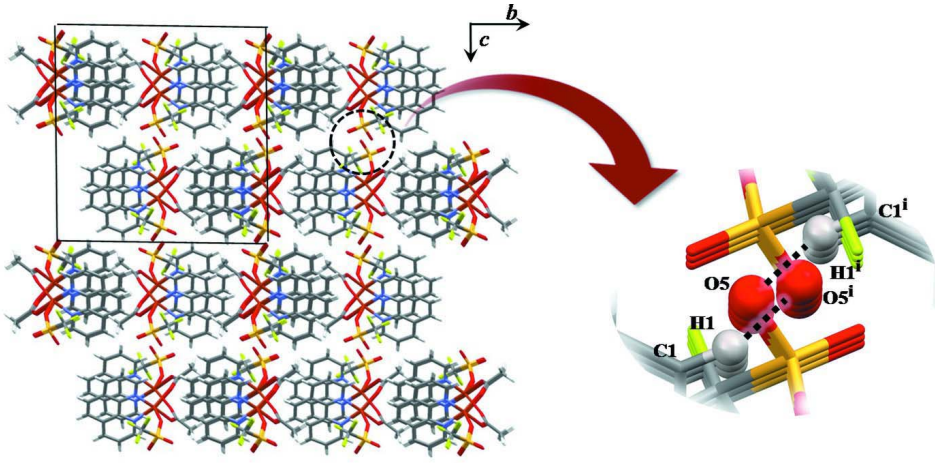

Figure 3

The crystal packing. View of three-dimensional framework (side view) constructued by intermolecular hydrogen bonding interactions between two-dimensional layers (C1—H1···O5^{i}, symmetry code: (i) = -*x*+*1*, -*y*+*2*, -*z*+*1*).

Di-μ-acetato-κ^4O:O'-bis[(1,10-phenanthroline-κ^2N,N')(trifluoromethanesulfonato-κO)copper(II)]

Crystal data

$[Cu_2(C_2H_3O_2)_2(CF_3O_3S)_2(C_{12}H_8N_2)_2]$
$M_r = 903.72$
Monoclinic, $C2/c$
Hall symbol: -C 2yc
$a = 13.1198$ (5) Å
$b = 16.1282$ (6) Å
$c = 16.3659$ (6) Å
$\beta = 95.507$ (1)°
$V = 3447.0$ (2) Å^3
$Z = 4$
$F(000) = 1816$
$D_x = 1.741$ Mg m^{-3}
Mo $K\alpha$ radiation, $\lambda = 0.71073$ Å
Cell parameters from 8485 reflections
$\theta = 2.3$–$26.4°$
$\mu = 1.45$ mm^{-1}
$T = 293$ K
Block, blue
0.24 × 0.21 × 0.18 mm

Data collection

Bruker SMART APEX CCD diffractometer
Radiation source: fine-focus sealed tube
Graphite monochromator
phi and ω scans
Absorption correction: multi-scan (*SADABS*; Sheldrick, 2000)
$T_{min} = 0.872$, $T_{max} = 1.000$
23313 measured reflections
4178 independent reflections
3491 reflections with $I > 2\sigma(I)$
$R_{int} = 0.022$
$\theta_{max} = 28.1°$, $\theta_{min} = 2.0°$
$h = -17\rightarrow17$
$k = -21\rightarrow21$
$l = -21\rightarrow21$

Refinement

Refinement on F^2
Least-squares matrix: full
$R[F^2 > 2\sigma(F^2)] = 0.034$
$wR(F^2) = 0.102$
$S = 1.04$
4178 reflections
272 parameters
0 restraints
Primary atom site location: structure-invariant direct methods
Secondary atom site location: difference Fourier map
Hydrogen site location: inferred from neighbouring sites
H-atom parameters constrained
$w = 1/[\sigma^2(F_o^2) + (0.0624P)^2 + 1.5014P]$ where $P = (F_o^2 + 2F_c^2)/3$
$(\Delta/\sigma)_{max} = 0.001$
$\Delta\rho_{max} = 0.37$ e Å^{-3}
$\Delta\rho_{min} = -0.32$ e Å^{-3}

Special details

Geometry. Bond distances, angles *etc*. have been calculated using the rounded fractional coordinates. All e.s.d.'s are estimated from the variances of the (full) variance-covariance matrix. The cell e.s.d.'s are taken into account in the estimation of distances, angles and torsion angles

Fractional atomic coordinates and isotropic or equivalent isotropic displacement parameters (Å^2)

	x	*y*	*z*	U_{iso}*/U_{eq}	Occ. (<1)
Cu1	0.59608 (2)	0.99743 (1)	0.70547 (2)	0.0458 (1)	
S1	0.78035 (4)	1.01647 (3)	0.56674 (3)	0.0539 (2)	
F1	0.8335 (6)	0.8733 (4)	0.6161 (4)	0.176 (4)	0.700
F2	0.9340 (5)	0.9174 (4)	0.5429 (4)	0.137 (2)	0.700
F3	0.9359 (6)	0.9687 (6)	0.6618 (6)	0.199 (4)	0.700
O1	0.63242 (11)	1.07473 (9)	0.79413 (10)	0.0626 (5)	
O2	0.51246 (12)	1.08054 (9)	0.64547 (10)	0.0608 (5)	
O3	0.73435 (13)	1.03226 (11)	0.64052 (11)	0.0712 (6)	
O4	0.8331 (2)	1.08491 (14)	0.53822 (17)	0.1123 (10)	

O5	0.7149 (2)	0.97542 (18)	0.50650 (17)	0.1224 (11)	
N1	0.53445 (12)	0.90229 (9)	0.63975 (10)	0.0449 (5)	
N2	0.68014 (12)	0.90588 (10)	0.76211 (9)	0.0472 (5)	
C1	0.46043 (16)	0.90316 (14)	0.57797 (12)	0.0556 (7)	
C2	0.41990 (18)	0.83081 (17)	0.54255 (14)	0.0640 (8)	
C3	0.45639 (18)	0.75590 (15)	0.56951 (15)	0.0633 (8)	
C4	0.53672 (15)	0.75244 (12)	0.63350 (13)	0.0509 (6)	
C5	0.57234 (13)	0.82808 (11)	0.66659 (11)	0.0423 (5)	
C6	0.65295 (13)	0.82997 (11)	0.73215 (11)	0.0430 (5)	
C7	0.58190 (18)	0.67773 (13)	0.66651 (17)	0.0649 (8)	
C8	0.65946 (18)	0.67936 (13)	0.72685 (16)	0.0642 (8)	
C9	0.69878 (15)	0.75606 (13)	0.76071 (13)	0.0526 (6)	
C10	0.78116 (18)	0.76280 (16)	0.82166 (15)	0.0664 (8)	
C11	0.81020 (18)	0.83952 (18)	0.85040 (15)	0.0701 (8)	
C12	0.75733 (17)	0.91011 (15)	0.82085 (13)	0.0605 (7)	
C13	0.57629 (16)	1.10508 (11)	0.84421 (13)	0.0514 (6)	
C14	0.6188 (2)	1.17618 (14)	0.89565 (17)	0.0706 (8)	
C15	0.8783 (3)	0.9414 (2)	0.5977 (2)	0.0953 (14)	
F3A	0.9596 (9)	0.9817 (7)	0.6337 (13)	0.153 (7)	0.300
F1A	0.8515 (8)	0.8809 (8)	0.6463 (7)	0.083 (3)	0.300
F2A	0.9048 (15)	0.9173 (13)	0.5189 (12)	0.193 (8)	0.300
H1	0.43520	0.95390	0.55800	0.0670*	
H2	0.36750	0.83360	0.50010	0.0770*	
H3	0.42880	0.70730	0.54610	0.0760*	
H7	0.55740	0.62700	0.64600	0.0780*	
H12	0.77660	0.96160	0.84290	0.0730*	
H14A	0.68970	1.18380	0.88760	0.1060*	
H14B	0.61240	1.16460	0.95250	0.1060*	
H14C	0.58140	1.22570	0.87990	0.1060*	
H8	0.68800	0.62970	0.74680	0.0770*	
H10	0.81550	0.71570	0.84220	0.0800*	
H11	0.86560	0.84480	0.89000	0.0840*	

Atomic displacement parameters (Å²)

	U^{11}	U^{22}	U^{33}	U^{12}	U^{13}	U^{23}
Cu1	0.0501 (2)	0.0364 (1)	0.0522 (2)	0.0032 (1)	0.0111 (1)	−0.0044 (1)
S1	0.0583 (3)	0.0503 (3)	0.0537 (3)	0.0031 (2)	0.0083 (2)	0.0036 (2)
F1	0.280 (8)	0.069 (3)	0.194 (7)	0.081 (4)	0.099 (6)	0.051 (4)
F2	0.115 (3)	0.157 (5)	0.152 (4)	0.072 (3)	0.077 (4)	0.039 (4)
F3	0.128 (6)	0.280 (9)	0.172 (5)	0.051 (5)	−0.073 (5)	0.031 (5)
O1	0.0620 (9)	0.0553 (8)	0.0732 (10)	−0.0075 (7)	0.0200 (7)	−0.0240 (7)
O2	0.0659 (9)	0.0482 (7)	0.0716 (9)	0.0163 (7)	0.0235 (7)	0.0118 (7)
O3	0.0704 (10)	0.0658 (10)	0.0820 (11)	0.0007 (8)	0.0305 (9)	−0.0070 (9)
O4	0.135 (2)	0.0787 (14)	0.1311 (19)	−0.0137 (13)	0.0530 (16)	0.0345 (13)
O5	0.127 (2)	0.131 (2)	0.0992 (18)	0.0116 (17)	−0.0404 (16)	−0.0369 (16)
N1	0.0464 (8)	0.0425 (8)	0.0464 (8)	0.0047 (6)	0.0076 (6)	−0.0021 (6)
N2	0.0475 (8)	0.0505 (9)	0.0444 (8)	0.0024 (7)	0.0084 (6)	−0.0017 (6)
C1	0.0570 (11)	0.0594 (12)	0.0500 (11)	0.0093 (9)	0.0027 (9)	−0.0019 (9)
C2	0.0589 (12)	0.0782 (16)	0.0539 (12)	−0.0017 (10)	−0.0005 (9)	−0.0116 (10)

C3	0.0647 (13)	0.0629 (13)	0.0634 (13)	−0.0117 (10)	0.0125 (10)	−0.0195 (10)
C4	0.0527 (10)	0.0442 (9)	0.0586 (11)	−0.0023 (8)	0.0194 (9)	−0.0061 (8)
C5	0.0433 (8)	0.0400 (8)	0.0458 (9)	0.0023 (7)	0.0154 (7)	−0.0022 (7)
C6	0.0423 (8)	0.0433 (9)	0.0456 (9)	0.0042 (7)	0.0154 (7)	0.0017 (7)
C7	0.0725 (14)	0.0384 (10)	0.0869 (16)	−0.0017 (9)	0.0240 (13)	−0.0038 (10)
C8	0.0719 (14)	0.0399 (10)	0.0845 (16)	0.0131 (9)	0.0271 (12)	0.0100 (10)
C9	0.0505 (10)	0.0547 (11)	0.0554 (11)	0.0112 (8)	0.0189 (9)	0.0101 (9)
C10	0.0628 (13)	0.0766 (15)	0.0608 (13)	0.0211 (11)	0.0104 (10)	0.0149 (11)
C11	0.0553 (12)	0.1009 (19)	0.0528 (12)	0.0110 (12)	−0.0016 (10)	0.0062 (12)
C12	0.0567 (11)	0.0728 (14)	0.0515 (11)	−0.0018 (10)	0.0028 (9)	−0.0072 (10)
C13	0.0623 (11)	0.0364 (8)	0.0575 (11)	−0.0067 (8)	0.0154 (9)	−0.0053 (8)
C14	0.0791 (15)	0.0531 (12)	0.0838 (16)	−0.0205 (11)	0.0291 (13)	−0.0256 (11)
C15	0.083 (2)	0.098 (2)	0.109 (3)	0.0357 (18)	0.0305 (19)	0.0181 (19)
F3A	0.046 (3)	0.082 (5)	0.32 (2)	0.000 (3)	−0.039 (7)	0.004 (8)
F1A	0.093 (4)	0.075 (5)	0.087 (5)	0.038 (3)	0.042 (3)	0.038 (4)
F2A	0.165 (14)	0.234 (16)	0.185 (14)	0.086 (10)	0.037 (10)	−0.120 (12)

Geometric parameters (Å, º)

Cu1—O1	1.9376 (16)	C3—C4	1.414 (3)
Cu1—O2	1.9385 (16)	C4—C5	1.397 (3)
Cu1—O3	2.2597 (18)	C4—C7	1.426 (3)
Cu1—N1	1.9995 (15)	C5—C6	1.433 (2)
Cu1—N2	2.0148 (16)	C6—C9	1.395 (3)
S1—O3	1.4237 (18)	C7—C8	1.349 (4)
S1—O4	1.406 (2)	C8—C9	1.431 (3)
S1—O5	1.409 (3)	C9—C10	1.403 (3)
S1—C15	1.803 (4)	C10—C11	1.365 (4)
F1—C15	1.295 (8)	C11—C12	1.395 (4)
F1A—C15	1.327 (13)	C13—C14	1.498 (3)
F2—C15	1.270 (7)	C1—H1	0.9302
F2A—C15	1.42 (2)	C2—H2	0.9304
F3—C15	1.309 (10)	C3—H3	0.9304
F3A—C15	1.337 (15)	C7—H7	0.9299
O1—C13	1.253 (3)	C8—H8	0.9300
O2—C13^{i}	1.256 (3)	C10—H10	0.9295
N1—C1	1.333 (3)	C11—H11	0.9301
N1—C5	1.353 (2)	C12—H12	0.9307
N2—C12	1.329 (3)	C14—H14A	0.9598
N2—C6	1.354 (2)	C14—H14B	0.9605
C1—C2	1.386 (3)	C14—H14C	0.9596
C2—C3	1.358 (4)		
Cu1···O5	3.760 (3)	O4···H3^{iv}	2.3363
Cu1···O1^{i}	3.2474 (15)	O4···H11^{v}	2.7477
Cu1···O2^{i}	3.2315 (16)	O5···H14B^{v}	2.7315
Cu1···N1^{i}	3.5407 (16)	O5···H1^{vi}	2.4275
Cu1···N2^{i}	3.9955 (16)	N1···Cu1^{i}	3.5407 (16)
Cu1···C1^{i}	3.991 (2)	N2···F1A	3.103 (11)
Cu1···C5^{i}	4.1970 (18)	N2···Cu1^{i}	3.9955 (16)

Cu1···H8^{ii}	3.5723	N2···C1^{i}	3.344 (3)
F1···O3	2.920 (7)	C1···C12^{i}	3.439 (3)
F1···O5	2.796 (7)	C1···O5^{vi}	3.229 (3)
F1···C6	3.251 (8)	C1···N2^{i}	3.344 (3)
F1···C14^{iii}	3.249 (7)	C1···C13^{i}	3.546 (3)
F1A···N2	3.103 (11)	C1···Cu1^{i}	3.991 (2)
F1A···C6	3.184 (11)	C3···O4^{vii}	3.213 (3)
F1A···C12	3.254 (11)	C3···C9^{i}	3.599 (3)
F1A···O5	3.160 (12)	C5···C6^{i}	3.525 (2)
F1A···O3	2.881 (12)	C5···Cu1^{i}	4.1970 (18)
F2···O5	3.027 (7)	C5···C5^{i}	3.472 (2)
F2···O4	3.006 (7)	C6···C5^{i}	3.525 (2)
F2A···O4	2.89 (2)	C6···F1A	3.184 (11)
F2A···O5	2.65 (2)	C6···F1	3.251 (8)
F3···O4	2.983 (10)	C8···O1^{iii}	3.256 (3)
F3···O3	2.826 (8)	C9···C3^{i}	3.599 (3)
F3A···O4	2.733 (16)	C11···O4^{viii}	3.293 (4)
F3A···O3	3.078 (12)	C12···C1^{i}	3.439 (3)
F1···H14C^{iii}	2.6275	C12···F1A	3.254 (11)
F1A···H14C^{iii}	2.7013	C13···C13^{i}	3.512 (3)
F3A···H7^{iv}	2.6700	C13···C1^{i}	3.546 (3)
O1···C8^{ii}	3.256 (3)	C13···O5^{viii}	3.335 (3)
O1···Cu1^{i}	3.2474 (15)	C14···O5^{viii}	3.228 (4)
O2···Cu1^{i}	3.2315 (16)	C14···F1^{ii}	3.249 (7)
O3···F3	2.826 (8)	C2···H14B^{v}	3.0447
O3···F1	2.920 (7)	C8···H14A^{iii}	2.8533
O3···F3A	3.078 (12)	C13···H1^{i}	2.9284
O3···F1A	2.881 (12)	H1···C13^{i}	2.9284
O4···F3	2.983 (10)	H1···O5^{vi}	2.4275
O4···C3^{iv}	3.213 (3)	H1···O2	2.6401
O4···F2	3.006 (7)	H3···H7	2.5822
O4···C11^{v}	3.293 (4)	H3···O4^{vii}	2.3363
O4···F2A	2.89 (2)	H7···F3A^{vii}	2.6700
O4···F3A	2.733 (16)	H7···H3	2.5822
O5···Cu1	3.760 (3)	H8···H10	2.5804
O5···F2A	2.65 (2)	H8···Cu1^{iii}	3.5723
O5···C13^{v}	3.335 (3)	H8···O1^{iii}	2.6624
O5···C14^{v}	3.228 (4)	H8···O3^{iii}	2.5589
O5···F2	3.027 (7)	H10···H8	2.5804
O5···F1A	3.160 (12)	H11···O4^{viii}	2.7477
O5···F1	2.796 (7)	H12···O1	2.6934
O5···C1^{vi}	3.229 (3)	H14A···C8^{ii}	2.8533
O1···H12	2.6934	H14B···C2^{viii}	3.0447
O1···H8^{ii}	2.6624	H14B···O5^{viii}	2.7315
O2···H1	2.6401	H14C···F1^{ii}	2.6275
O3···H8^{ii}	2.5589	H14C···F1A^{ii}	2.7013

O1—Cu1—O2	91.21 (6)	C8—C9—C10	124.5 (2)
O1—Cu1—O3	92.37 (6)	C9—C10—C11	119.1 (2)

O1—Cu1—N1	162.62 (7)	C10—C11—C12	120.5 (2)
O1—Cu1—N2	92.44 (6)	N2—C12—C11	121.8 (2)
O2—Cu1—O3	91.76 (7)	O1—C13—C14	117.14 (19)
O2—Cu1—N1	94.48 (6)	O1—C13—O2^{i}	125.13 (18)
O2—Cu1—N2	176.35 (6)	O2^{i}—C13—C14	117.73 (19)
O3—Cu1—N1	103.84 (7)	S1—C15—F1	107.9 (4)
O3—Cu1—N2	88.28 (6)	S1—C15—F2	116.7 (4)
N1—Cu1—N2	81.97 (6)	S1—C15—F3	109.9 (5)
O3—S1—O4	113.79 (13)	S1—C15—F1A	116.1 (5)
O3—S1—O5	113.45 (13)	S1—C15—F2A	99.1 (8)
O3—S1—C15	103.33 (13)	S1—C15—F3A	108.3 (5)
O4—S1—O5	115.02 (16)	F1—C15—F2	102.1 (5)
O4—S1—C15	105.09 (16)	F1—C15—F3	109.8 (6)
O5—S1—C15	104.55 (16)	F2—C15—F3	110.0 (6)
Cu1—O1—C13	128.57 (14)	F1A—C15—F2A	116.4 (10)
Cu1—O2—C13^{i}	129.53 (14)	F1A—C15—F3A	109.8 (9)
Cu1—O3—S1	141.19 (11)	F2A—C15—F3A	106.2 (12)
Cu1—N1—C1	128.86 (14)	N1—C1—H1	118.98
Cu1—N1—C5	112.78 (12)	C2—C1—H1	118.97
C1—N1—C5	118.28 (16)	C1—C2—H2	119.86
Cu1—N2—C6	112.49 (12)	C3—C2—H2	119.87
Cu1—N2—C12	129.82 (15)	C2—C3—H3	120.32
C6—N2—C12	117.66 (17)	C4—C3—H3	120.31
N1—C1—C2	122.0 (2)	C4—C7—H7	119.34
C1—C2—C3	120.3 (2)	C8—C7—H7	119.47
C2—C3—C4	119.4 (2)	C7—C8—H8	119.37
C3—C4—C5	116.78 (18)	C9—C8—H8	119.37
C3—C4—C7	124.6 (2)	C9—C10—H10	120.49
C5—C4—C7	118.66 (19)	C11—C10—H10	120.44
N1—C5—C4	123.22 (17)	C10—C11—H11	119.78
N1—C5—C6	116.49 (16)	C12—C11—H11	119.74
C4—C5—C6	120.29 (17)	N2—C12—H12	119.07
N2—C6—C5	116.13 (16)	C11—C12—H12	119.09
N2—C6—C9	124.13 (17)	C13—C14—H14A	109.53
C5—C6—C9	119.74 (17)	C13—C14—H14B	109.45
C4—C7—C8	121.2 (2)	C13—C14—H14C	109.45
C7—C8—C9	121.3 (2)	H14A—C14—H14B	109.50
C6—C9—C8	118.75 (19)	H14A—C14—H14C	109.50
C6—C9—C10	116.73 (19)	H14B—C14—H14C	109.39

O2—Cu1—O1—C13	68.10 (18)	Cu1—N1—C1—C2	−174.67 (16)
O3—Cu1—O1—C13	159.91 (17)	C5—N1—C1—C2	1.8 (3)
N2—Cu1—O1—C13	−111.71 (17)	Cu1—N1—C5—C4	176.12 (15)
O1—Cu1—O2—C13^{i}	−78.62 (18)	Cu1—N1—C5—C6	−4.0 (2)
O3—Cu1—O2—C13^{i}	−171.03 (18)	C1—N1—C5—C4	−0.9 (3)
N1—Cu1—O2—C13^{i}	84.94 (18)	C1—N1—C5—C6	178.99 (17)
O1—Cu1—O3—S1	−175.37 (18)	Cu1—N2—C6—C5	0.7 (2)
O2—Cu1—O3—S1	−84.09 (18)	Cu1—N2—C6—C9	−179.80 (15)
N1—Cu1—O3—S1	10.96 (19)	C12—N2—C6—C5	−177.49 (17)

N2—Cu1—O3—S1	92.26 (18)	C12—N2—C6—C9	2.0 (3)
O2—Cu1—N1—C1	−0.85 (18)	Cu1—N2—C12—C11	−176.94 (16)
O2—Cu1—N1—C5	−177.49 (13)	C6—N2—C12—C11	0.9 (3)
O3—Cu1—N1—C1	−93.78 (17)	N1—C1—C2—C3	−1.1 (3)
O3—Cu1—N1—C5	89.58 (13)	C1—C2—C3—C4	−0.6 (3)
N2—Cu1—N1—C1	−180.00 (18)	C2—C3—C4—C5	1.4 (3)
N2—Cu1—N1—C5	3.37 (13)	C2—C3—C4—C7	−179.5 (2)
O1—Cu1—N2—C6	161.25 (13)	C3—C4—C7—C8	179.0 (2)
O1—Cu1—N2—C12	−20.80 (18)	C5—C4—C7—C8	−1.9 (3)
O3—Cu1—N2—C6	−106.45 (13)	C7—C4—C5—C6	0.2 (3)
O3—Cu1—N2—C12	71.50 (18)	C3—C4—C5—N1	−0.7 (3)
N1—Cu1—N2—C6	−2.21 (12)	C3—C4—C5—C6	179.43 (18)
N1—Cu1—N2—C12	175.74 (18)	C7—C4—C5—N1	−179.86 (19)
O4—S1—O3—Cu1	146.81 (18)	C4—C5—C6—C9	2.6 (3)
O5—S1—O3—Cu1	12.8 (2)	N1—C5—C6—N2	2.2 (2)
C15—S1—O3—Cu1	−99.8 (2)	N1—C5—C6—C9	−177.30 (17)
O3—S1—C15—F1	67.4 (4)	C4—C5—C6—N2	−177.90 (17)
O3—S1—C15—F2	−178.4 (4)	N2—C6—C9—C10	−3.1 (3)
O3—S1—C15—F3	−52.3 (5)	C5—C6—C9—C8	−3.8 (3)
O4—S1—C15—F1	−173.0 (4)	C5—C6—C9—C10	176.37 (18)
O4—S1—C15—F2	−58.8 (4)	N2—C6—C9—C8	176.76 (19)
O4—S1—C15—F3	67.2 (5)	C4—C7—C8—C9	0.6 (4)
O5—S1—C15—F1	−51.5 (4)	C7—C8—C9—C6	2.2 (3)
O5—S1—C15—F2	62.7 (4)	C7—C8—C9—C10	−178.0 (2)
O5—S1—C15—F3	−171.3 (5)	C8—C9—C10—C11	−178.5 (2)
Cu1—O1—C13—C14	−167.96 (15)	C6—C9—C10—C11	1.3 (3)
Cu1—O1—C13—O2^{i}	12.1 (3)	C9—C10—C11—C12	1.4 (4)
Cu1—O2—C13^{i}—O1^{i}	−5.3 (3)	C10—C11—C12—N2	−2.6 (4)
Cu1—O2—C13^{i}—C14^{i}	174.68 (15)		

Symmetry codes: (i) −*x*+1, *y*, −*z*+3/2; (ii) −*x*+3/2, *y*+1/2, −*z*+3/2; (iii) −*x*+3/2, *y*−1/2, −*z*+3/2; (iv) *x*+1/2, *y*+1/2, *z*; (v) *x*, −*y*+2, *z*−1/2; (vi) −*x*+1, −*y*+2, −*z*+1; (vii) *x*−1/2, *y*−1/2, *z*; (viii) *x*, −*y*+2, *z*+1/2.

Hydrogen-bond geometry (Å, º)

D—H···*A*	*D*—H	H···*A*	*D*···*A*	*D*—H···*A*
C1—H1···O5^{vi}	0.93	2.43	3.229 (3)	144
C3—H3···O4^{vii}	0.93	2.34	3.213 (3)	157
C8—H8···O3^{iii}	0.93	2.56	3.421 (3)	154

Symmetry codes: (iii) −*x*+3/2, *y*−1/2, −*z*+3/2; (vi) −*x*+1, −*y*+2, −*z*+1; (vii) *x*−1/2, *y*−1/2, *z*.

Acta Crystallographica Section C
Crystal Structure Communications
ISSN 0108-2701

The heterometallic cadmium–silver complex *cis*-bis[dicyanidoargentato(I)-κN]bis(5,5′-dimethyl-2,2′-bipyridyl-$\kappa^2 N,N'$)cadmium(II) monohydrate

Jureepan Piromchom, Nanthawat Wannarit, Chaveng Pakawatchai and Sujittra Youngme

Acta Cryst. (2013). C**69**, 1136–1139

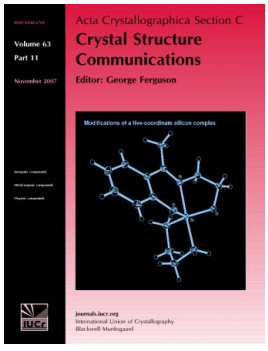

Acta Crystallographica Section C: Crystal Structure Communications specializes in the rapid dissemination of high-quality studies of crystal and molecular structures of interest in fields such as chemistry, biochemistry, mineralogy, pharmacology, physics and materials science. The numerical and text descriptions of each structure are submitted to the journal electronically as a Crystallographic Information File (CIF) and are checked and typeset automatically prior to peer review. The journal is well known for its high standards of structural reliability and presentation. *Section C* publishes approximately 1000 structures per year; readers have access to an archive that includes high-quality structural data for over 10000 compounds.

Acta Crystallographica Section C
Crystal Structure Communications
ISSN 0108-2701

The heterometallic cadmium–silver complex *cis*-bis[dicyanidoargentato(I)-κN]bis(5,5′-dimethyl-2,2′-bipyridyl-κ^2N,N')cadmium(II) monohydrate

Jureepan Piromchom,[a] Nanthawat Wannarit,[a] Chaveng Pakawatchai[b] and Sujittra Youngme[a]*

[a]Materials Chemistry Research Unit, Department of Chemistry and Center of Excellence for Innovation in Chemistry, Faculty of Science, Khon Kaen University, Khon Kaen 40002, Thailand, and [b]Department of Chemistry, Faculty of Science, Prince of Songkla University, Hat Yai, Songkhla 90112, Thailand
Correspondence e-mail: sujittra@kku.ac.th

Received 1 August 2013
Accepted 11 September 2013

In the title complex, $[Ag_2Cd(CN)_4(C_{12}H_{12}N_2)_2]\cdot H_2O$ or *cis*-$[Cd\{Ag(CN)_2\}_2(5,5'\text{-dmbpy})_2]\cdot H_2O$, where 5,5′-dmbpy is 5,5′-dimethyl-2,2′-bipyridyl, the asymmetric unit consists of a discrete neutral $[Cd\{Ag(CN)_2\}_2(5,5'\text{-dmbpy})_2]$ unit and a solvent water molecule. The Cd^{II} cation is coordinated by two bidentate chelate 5,5′-dmbpy ligands and two monodentate $[Ag^I(CN)_2]^-$ anions, which are in a *cis* arrangement around the Cd^{II} cation, leading to an octahedral CdN_6 geometry. The overall structure is stabilized by a combination of intermolecular hydrogen bonding, and $Ag^I\cdots Ag^I$ and π–π interactions, forming a three-dimensional supramolecular network.

Keywords: crystal structure; supramolecular architectures; dicyanidoargentate ligands; cadmium–silver compounds.

1. Introduction

The design and synthesis of supramolecular architectures currently attract a great deal of attention, due to the various network topologies and the potential uses of these materials in microelectronics, nonlinear optics, porous materials and other applications (Dong *et al.*, 2003). Various intermolecular interactions such as hydrogen bonding, π–π stacking and van der Waals interactions can greatly influence the resulting crystal structure and its dimensionality (Blake *et al.*, 1999). The bridging dicyanidoargentate(I) ligand, $[Ag^I(CN)_2]^-$, has frequently been employed to construct multidimensional (one-, two- and three-dimensional) coordinated and non-coordinated supramolecular network architectures and can further stabilize the coordination framework *via* silver–silver attractions (argentophilic interactions; Jansen, 1987; Pyykkö, 1997). In the present work, a new three-dimensional supramolecular framework of the title heterometallic Cd^{II}–Ag^I coordination compound, *cis*-$[Cd^{II}\{Ag^I(CN)_2\}_2(5,5'\text{-dmbpy})_2]\cdot H_2O$, (I) (5,5′-dmbpy is 5,5′-dimethyl-2,2′-bipyridyl), was successfully synthesized and structurally characterized.

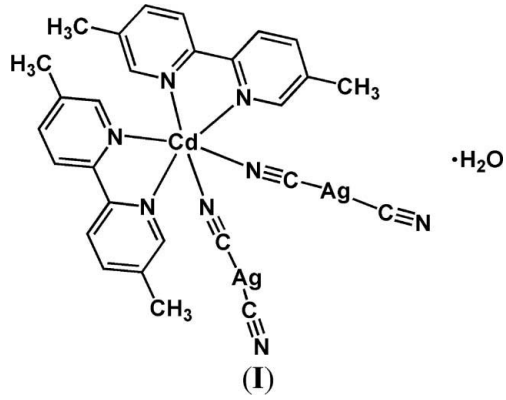

(I)

2. Experimental

2.1. Synthesis and crystallization

Compound (I) was synthesized by the reaction of two aqueous solutions at room temperature, one containing a mixture of $Cd(NO_3)_2\cdot 4H_2O$ (0.25 mmol, 77 mg) and 5,5′-dmbpy (0.5 mmol, 92 mg) in water (10 ml), and the other containing $K[Ag^I(CN)_2]$ (0.5 mmol, 10.6 mg) in water (5 ml). After 4 d, colourless crystals were obtained; the yield based on Cd was about 76%.

2.2. Refinement

Crystal data, data collection and structure refinement details are summarized in Table 1. C-bound H atoms were positioned geometrically, with C—H = 0.93 (aromatic) or 0.96 Å (methyl), and included as riding atoms, with $U_{iso}(H) = 1.5U_{eq}(C)$ for methyl groups and $1.2U_{eq}(C)$ otherwise. Water H atoms were located in difference Fourier maps and refined isotropically.

3. Results and discussion

Compound (I) crystallizes in the triclinic space group $P\overline{1}$. The asymmetric unit consists of a discrete neutral *cis*-$[Cd^{II}\{Ag^I(CN)_2\}_2(5,5'\text{-dmbpy})_2]$ unit and a solvent water molecule, as shown in Fig. 1. The Cd^{II} cation adopts an octahedral CdN_6 geometry, surrounded by four N atoms from two bidentate chelate 5,5′-dmbpy ligands and two N atoms from two monodentate $[Ag^I(CN)_2]^-$ anions, which are in a *cis* arrangement around the Cd^{II} cation; selected bond distances and angles are given in Table 2.

The molecular structure of (I) is self-assembled to form a centrosymmetric dimeric unit (Fig. 2) *via* hydrogen-bonding interactions between the solvent water molecule and the terminal cyanide group of one of the dicyanidoargentate ligands in each of two adjacent complex molecules, as shown in Table 3. These dimeric units are connected *via* $Ag^I\cdots Ag^I$ interactions across another centre of inversion, with an

  doi:10.1107/S0108270113025201

Table 1
Experimental details.

Crystal data	
Chemical formula	$[Ag_2Cd(CN)_4(C_{12}H_{12}N_2)_2]\cdot H_2O$
M_r	818.72
Crystal system, space group	Triclinic, $P\overline{1}$
Temperature (K)	293
a, b, c (Å)	9.6964 (4), 11.2487 (5), 15.7456 (7)
α, β, γ (°)	109.525 (1), 100.572 (1), 98.324 (1)
V (Å^3)	1551.30 (12)
Z	2
Radiation type	Mo $K\alpha$
μ (mm^{-1})	1.96
Crystal size (mm)	0.39 × 0.16 × 0.09
Data collection	
Diffractometer	Bruker SMART CCD area-detector diffractometer
Absorption correction	Multi-scan (*SADABS*; Sheldrick, 2000)
T_{min}, T_{max}	0.799, 1.000
No. of measured, independent and observed [$I > 2\sigma(I)$] reflections	21735, 7667, 6749
R_{int}	0.017
(sin $\theta/\lambda)_{max}$ (Å^{-1})	0.667
Refinement	
$R[F^2 > 2\sigma(F^2)]$, $wR(F^2)$, S	0.026, 0.065, 1.03
No. of reflections	7667
No. of parameters	373
H-atom treatment	H atoms treated by a mixture of independent and constrained refinement
$\Delta\rho_{max}$, $\Delta\rho_{min}$ (e Å^{-3})	0.60, −0.31

Computer programs: *SMART* (Bruker, 2000), *SAINT* (Bruker, 2000), *SHELXTL* (Sheldrick, 2008), *SHELXL97* (Sheldrick, 2008), *ORTEPIII* for Windows (Farrugia, 2012), *Mercury* (Macrae *et al.*, 2008), *PLATON* (Spek, 2009) and *publCIF* (Westrip, 2010).

Ag1···Ag2^{ii} distance of 3.2575 (3) Å (symmetry code as in Table 2), and by face-to-face π–π interactions between the aromatic rings of 5,5′-dmbpy ligands from adjacent dimeric

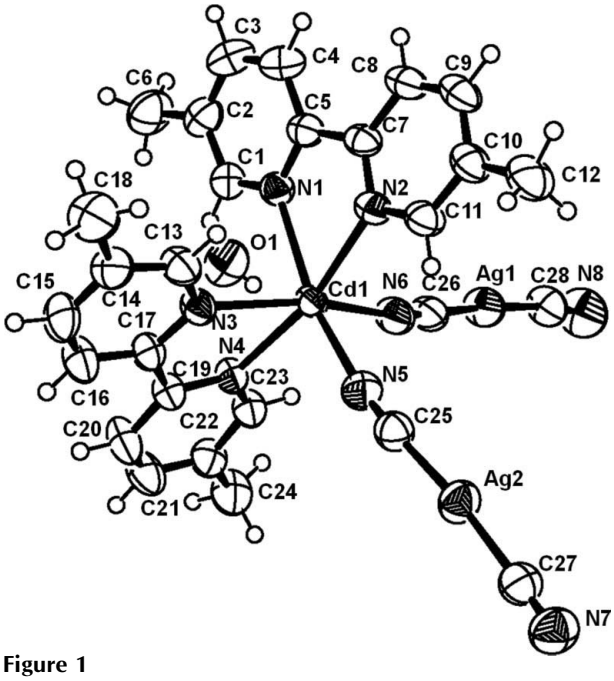

Figure 1
A view of the asymmetric unit and the local coordination of the Cd^{II} cation in (I), showing the atom-numbering scheme. Displacement ellipsoids are drawn at the 50% probability level.

Table 2
Selected geometric parameters (Å, °).

Cd1—N1	2.3654 (19)	Cd1—N4	2.3924 (19)
Cd1—N2	2.375 (2)	Cd1—N5	2.291 (2)
Cd1—N3	2.3609 (18)	Cd1—N6	2.299 (2)
Ag1···Ag1^{i}	3.7997 (4)	Ag1···Ag2^{ii}	3.2575 (3)
N1—Cd1—N2	70.48 (7)	N2—Cd1—N6	97.23 (7)
N1—Cd1—N3	87.77 (6)	N3—Cd1—N4	69.78 (7)
N1—Cd1—N4	100.04 (7)	N3—Cd1—N5	92.99 (7)
N1—Cd1—N5	161.90 (7)	N3—Cd1—N6	159.69 (8)
N1—Cd1—N6	92.37 (7)	N4—Cd1—N5	97.18 (7)
N2—Cd1—N3	101.93 (7)	N4—Cd1—N6	90.24 (7)
N2—Cd1—N4	168.07 (7)	N5—Cd1—N6	93.10 (8)
N2—Cd1—N5	91.71 (7)		

Symmetry codes: (i) $-x+1, -y+2, -z+1$; (ii) $-x+1, -y+1, -z+1$.

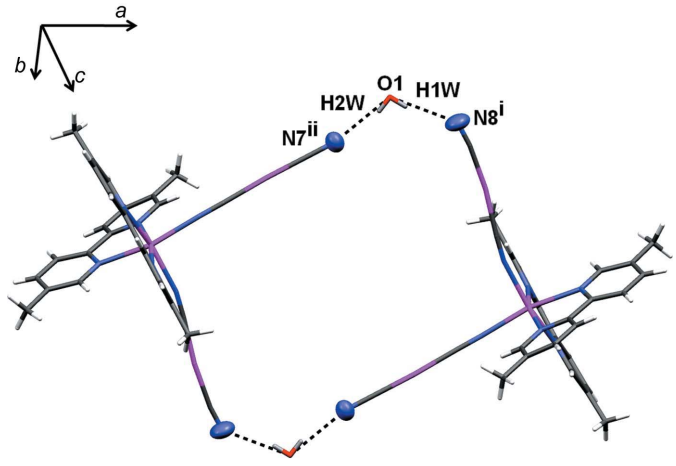

Figure 2
A partial packing diagram for (I), showing intermolecular hydrogen-bonding interactions between two molecules *via* O—H···N interactions (dashed lines), generating the dimeric unit. [Symmetry codes: (i) $-x+1, -y+2, -z+1$; (ii) $x-1, y+1, z$.]

units ($Cg4\cdots Cg3^{v}$; Table 4), giving a one-dimensional chain-like structure running parallel to the [$\overline{1}$10] direction, as represented in Fig. 3. The Ag^{I}···Ag^{I} distances are significantly

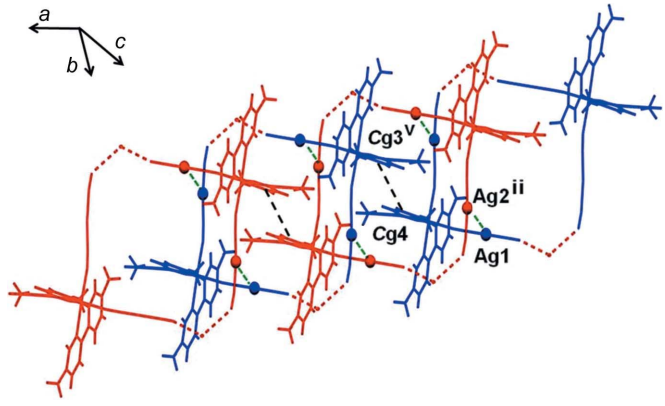

Figure 3
A partial packing diagram for (I), showing the one-dimensional chain-like structure *via* π–π interactions and Ag^{I}···Ag^{I} interactions (dashed lines). [Symmetry codes: (ii) $-x+1, -y+1, -z+1$; (v) $-x, 1-y, 1-z$.]

Table 3
Hydrogen-bond geometry (Å, °).

D—H···A	D—H	H···A	D···A	D—H···A
O1—H1W···N8^{i}	0.73 (5)	2.26 (5)	2.975 (5)	166 (6)
O1—H2W···N7^{iii}	0.72 (5)	2.23 (4)	2.920 (5)	162 (5)
C16—H16···O1^{iv}	0.93	2.53	3.453 (4)	174
C20—H20···O1^{iv}	0.93	2.57	3.502 (4)	178
C24—H24B···N8^{i}	0.96	2.51	3.431 (4)	161

Symmetry codes: (i) $-x+1, -y+2, -z+1$; (iii) $x-1, y+1, z$; (iv) $-x, -y+1, -z$.

shorter than the sum of the van der Waals radii for two Ag^{I} cations (3.44 Å; Bondi, 1964).

The one-dimensional chains are linked together *via* weak nonclassical intermolecular hydrogen-bonding interactions between a methyl group (C24—H24B) of the 5,5′-dmbpy ligand and an NC group (N8) of the dicyanidoargentate ligand, and by weaker $Ag^{I}\cdots Ag^{I}$ interactions with an Ag1···Ag1^{i} distance of 3.7997 (4) Å (see Tables 2 and 3), generating a two-dimensional network, as shown in Fig. 4. These two-dimensional layers are assembled along the *a* axis *via* additional π–π interactions ($Cg5\cdots Cg5^{vi}$; Table 4), and by hydrogen-bonding interactions *via* the solvent water molecule, the C—H groups of the 5,5′-dmbpy ligand and the NC groups of the dicyanidoargentate ligands (Table 3), leading to a three-dimensional supramolecular framework, as shown in Fig. 5.

Among the successful synthetic strategies for the formation of Ag^{I} coordination polymers, the $[Ag^{I}(CN)_2]^-$ anion is particularly effective because it can form additional coordinate bonds through the N atoms of the cyanide groups, leading it to play a variety of roles in the stabilization of crystal structures (Černák *et al.*, 1998). The $[Ag(CN)_2]^-$ anion behaves: (i) as a discrete anion simply playing the role of counter-ion and space filler (Range *et al.*, 1989; Omary *et al.*, 1998); (ii) as a rod ligand building up multidimensional structures by bridging between two coordination centres (Dasna *et al.*, 2001; Soma & Iwamoto, 1994); (iii) as a monodentate ligand blocking some coordination sites of the central atom (Soma & Iwamoto, 1996). Examples of these different roles of the dicyanidoargentate anion have been demonstrated in the following structures. In $[Ni(bpy)_3]_2[Ag^{I}(CN)_2]_3Cl\cdot 9H_2O$ (bpy is 2,2′-bipyridine; Černák *et al.*, 1994) and $\{[SnMe_3(bpe)][Ag^{I}(CN)_2]\cdot 2H_2O\}$ [bpe is 1,2-bis(pyridin-4-yl)ethane; Etaiw *et al.*, 2011], it acts as an isolated counterion in structures with ionic character. In $[N(PPh_3)_2][ClPh_3Sn(\mu\text{-}NC)Ag^{I}(CN)]$ (Ph is phenyl), it acts as a ligand when bonded *via* one bridging cyanide group (Carcelli *et al.*, 1992). In $\{Mn^{II}(ampyz)(H_2O)[Ag^{I}_2(CN)_3][Ag^{I}(CN)_2]\cdot ampyz\}_n$ and $\{[Mn^{II}(benzim)_2\{Ag^{I}(CN)_2\}_2][(benzim)Ag^{I}(CN)]\cdot H_2O\}_n$ (ampyz is 2-aminopyrazine and benzim is benzimidazole), it acts as a bridging spacer between two central atoms, giving rise to polymeric two-dimensional structures (Wannarit *et al.*, 2012), while in $[KMn\{Ag^{I}(CN)_2\}_3(H_2O)]_n$ and $[Mn\{Ag^{I}(CN)_2\}_2(bpy)_2]_n$, the three-dimensional networks are constructed entirely by coordinative linkages with all the cyanide groups of $[Ag^{I}(CN)_2]^-$ (Dong *et al.*, 2003). In the case of the complex $[Mn^{III}(salen)Ag^{I}(CN)_2]$ [H_2salen is *N*,*N*′-bis(salicylidene)-1,2-diaminoethane], a one-dimensional network is constructed in which the $[Ag^{I}(CN)_2]^-$ anion acts as an NC–Ag^{I}–CN bridging ligand (Panja *et al.*, 2002). Finally, in $[Cu(pn)_2\{Ag^{I}(CN)_2\}_2]$ (pn is 1,2-diaminopropane; Triščíková *et al.*, 2004) and $[Cu(imidazole)_4\{Ag^{I}(CN)_2\}_2]$ (Ahmad *et al.*, 2012), it acts as a monodentate dicyanidoargentate ligand, with a similar coordination mode to that found in (I) but being coordinated in the axial positions of an elongated octahedron.

Table 4
π–π contacts for (I).

CCD is the centre-to-centre distance (distance between ring centroids), IPD is the interplanar distance (perpendicular distance from one plane to the neighbouring ring centroid) and SA is the slippage angle (angle subtended by the intercentroid vector to the plane normal); for details, see Janiak (2000). *Cg*3 is the centroid of the N1/C1–C5 ring, *Cg*4 is the centroid of the N2/C7–C11 ring and *Cg*5 is the centroid of the N3/C13–C17 ring.

Group1/group2	CCD (Å)	SA (°)	IPD (Å)
$Cg4\cdots Cg3^{v}$	3.7582 (14)	16.5/29.5	3.2708 (11)/3.5978 (10)
$Cg5\cdots Cg5^{vi}$	3.8263 (16)	21.5	3.5590 (11)

Symmetry codes: (v) $-x, -y+1, -z+1$; (vi) $-x, -y, -z$.

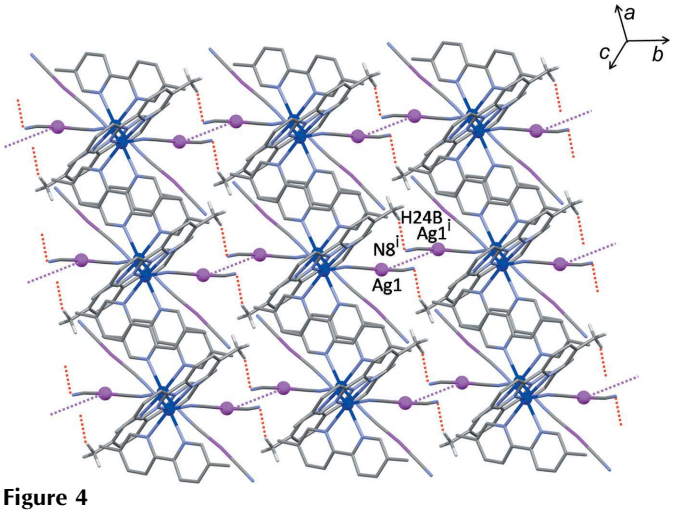

Figure 4
A partial packing diagram for (I), stabilized *via* hydrogen bonding and $Ag^{I}\cdots Ag^{I}$ interactions (dashed lines) in the *ab* plane, giving a two-dimensional layer-like structure. [Symmetry code: (i) $-x+1, -y+2, -z+1$.]

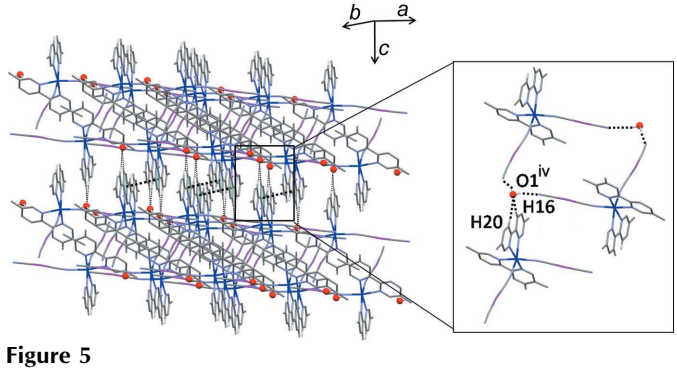

Figure 5
A view of (I), showing the intermolecular hydrogen bonding and π–π interactions (dashed lines) between layers, generating a three-dimensional supramolecular framework. [Symmetry code: (iv) $-x, -y+1, -z$.]

In summary, the monodentate dicyanidoargentate(I) ligand in the structure of the title compound has been demonstrated, with an extended three-dimensional supramolecular structure built up *via* hydrogen bonds and silver–silver and π–π interactions, thus stabilizing the overall crystal structure.

The authors gratefully acknowledge the Thailand Research Fund (BRG5680009), the Higher Education Research Promotion and National Research University Project of Thailand, through the Advanced Functional Materials Cluster of Khon Kaen University, and the Center of Excellence for Innovation in Chemistry (PERCH–CIC), Office of the Higher Education Commission, Ministry of Education, Thailand, for financial support.

Supplementary data for this paper are available from the IUCr electronic archives (Reference: WQ3049). Services for accessing these data are described at the back of the journal.

References

Ahmad, S., Tahir, M. N., Javaid, H. M., Monim-ul-Mehboob, M., Shaheen, M. A. & Mahmood, R. (2012). *J. Chem. Crystallogr.* **42**, 401–404.
Blake, A. J., Champness, N. R., Hubberstey, P., Li, W.-S., Withersby, M. A. & Schröder, M. (1999). *Coord. Chem. Rev.* **183**, 117–138.
Bondi, A. (1964). *J. Phys. Chem.* **68**, 441–451.
Bruker (2000). *SMART* and *SAINT*. Bruker AXS Inc., Madison, Wisconsin, USA.
Carcelli, M., Ferrari, C., Pelizzi, C., Pelizzi, G., Predieri, G. & Solinas, C. (1992). *J. Chem. Soc. Dalton Trans.* pp. 2127–2128.
Černák, J., Chomič, J., Gravereau, P., Orendáčová, A., Orendáč, M., Kováč, J., Feher, A. & Kappenstein, C. (1998). *Inorg. Chim. Acta*, **281**, 134–140.
Černák, J., Kaňuchová, M., Chomič, J., Potočňák, I., Kameníček, J. & Žák, Z. (1994). *Acta Cryst.* C**50**, 1563–1566.
Dasna, I., Golhen, S., Ouahab, L., Daro, N. & Sutter, J.-P. (2001). *Polyhedron*, **20**, 1371–1374.
Dong, W., Wang, Q.-L., Si, S.-F., Liao, D.-Z., Jiang, Z.-H., Yan, S.-P. & Cheng, P. (2003). *Inorg. Chem. Commun.* **6**, 873–876.
Etaiw, S.-d'H., Sultan, A. S. & Badr El-din, A. S. (2011). *Eur. J. Med. Chem.* **46**, 5370–5378.
Farrugia, L. J. (2012). *J. Appl. Cryst.* **45**, 849–854.
Janiak, C. (2000). *J. Chem. Soc. Dalton Trans.* pp. 3885–3896.
Jansen, M. (1987). *Angew. Chem. Int. Ed. Engl.* **26**, 1098–1110.
Macrae, C. F., Bruno, I. J., Chisholm, J. A., Edgington, P. R., McCabe, P., Pidcock, E., Rodriguez-Monge, L., Taylor, R., van de Streek, J. & Wood, P. A. (2008). *J. Appl. Cryst.* **41**, 466–470.
Omary, M. A., Webb, T. R., Assefa, Z., Shankle, G. E. & Patterson, H. H. (1998). *Inorg. Chem.* **37**, 1380–1386.
Panja, A., Shaikh, N., Vojtíšek, P., Gao, S. & Banerjee, P. (2002). *New J. Chem.* **26**, 1025–1028.
Pyykkö, P. (1997). *Chem. Rev.* **97**, 597–636.
Range, K.-J., Kühnel, S. & Zabel, M. (1989). *Acta Cryst.* C**45**, 1419–1420.
Sheldrick, G. M. (2000). *SADABS*. University of Göttingen, Germany.
Sheldrick, G. M. (2008). *Acta Cryst.* A**64**, 112–122.
Soma, T. & Iwamoto, T. (1994). *Chem. Lett.* pp. 821–824.
Soma, T. & Iwamoto, T. (1996). *Inorg. Chem.* **35**, 1849–1856.
Spek, A. L. (2009). *Acta Cryst.* D**65**, 148–155.
Triščíková, L., Chomič, J., Abboud, K. A., Park, J.-H., Meisel, M. W. & Černák, J. (2004). *Inorg. Chim. Acta*, **357**, 2763–2768.
Wannarit, N., Hahnvajanawong, V., Pakawatchai, C. & Youngme, S. (2012). *Transition Met. Chem.* **37**, 79–84.
Westrip, S. P. (2010). *J. Appl. Cryst.* **43**, 920–925.

supplementary materials

Acta Cryst. (2013). C**69**, 1136-1139 [doi:10.1107/S0108270113025201]

The heterometallic cadmium–silver complex *cis*-bis[dicyanidoargentato(I)-κN]bis(5,5′-dimethyl-2,2′-bipyridyl-κ^2N,N')cadmium(II) monohydrate

Jureepan Piromchom, Nanthawat Wannarit, Chaveng Pakawatchai and Sujittra Youngme

Computing details

Data collection: *SMART* (Bruker, 2000); cell refinement: *SMART* (Bruker, 2000); data reduction: *SAINT* (Bruker, 2000); program(s) used to solve structure: *SHELXTL* (Sheldrick, 2008); program(s) used to refine structure: *SHELXL97* (Sheldrick, 2008); molecular graphics: *ORTEPIII* for Windows (Farrugia, 2012) and *Mercury* (Macrae *et al.*, 2008); software used to prepare material for publication: *PLATON* (Spek, 2009) and *publCIF* (Westrip, 2010).

Di-μ-cyanido-1:3κ^2C:N;2:3κ^2C:N-\ dicyanido-1κC,2κC-bis(5,5′-dimethyl-2,2′-bipyridyl-\ 3κ^2N,N')cadmium(II)disilver(I) monohydrate

Crystal data

$[Ag_2Cd(CN)_4(C_{12}H_{12}N_2)_2]\cdot H_2O$
$M_r = 818.72$
Triclinic, $P\overline{1}$
Hall symbol: -P 1
$a = 9.6964$ (4) Å
$b = 11.2487$ (5) Å
$c = 15.7456$ (7) Å
$\alpha = 109.525$ (1)°
$\beta = 100.572$ (1)°
$\gamma = 98.324$ (1)°
$V = 1551.30$ (12) Å^3
$Z = 2$
$F(000) = 800$
$D_x = 1.753$ Mg m^{-3}
Mo $K\alpha$ radiation, $\lambda = 0.71073$ Å
Cell parameters from 9313 reflections
$\theta = 2.2$–28.2°
$\mu = 1.96$ mm^{-1}
$T = 293$ K
Block, colourless
0.39 × 0.16 × 0.09 mm

Data collection

Bruker SMART CCD area-detector diffractometer
Radiation source: sealed tube
Graphite monochromator
φ and ω scans
Absorption correction: multi-scan (*SADABS*; Sheldrick, 2000)
$T_{min} = 0.799$, $T_{max} = 1.000$
21735 measured reflections
7667 independent reflections
6749 reflections with $I > 2\sigma(I)$
$R_{int} = 0.017$
$\theta_{max} = 28.3°$, $\theta_{min} = 2.0°$
$h = -12\rightarrow12$
$k = -14\rightarrow14$
$l = -20\rightarrow20$

Refinement

Refinement on F^2
Least-squares matrix: full
$R[F^2 > 2\sigma(F^2)] = 0.026$
$wR(F^2) = 0.065$
$S = 1.03$
7667 reflections
373 parameters
0 restraints
Primary atom site location: structure-invariant direct methods
Secondary atom site location: difference Fourier map
Hydrogen site location: inferred from neighbouring sites

H atoms treated by a mixture of independent and constrained refinement
$w = 1/[\sigma^2(F_o^2) + (0.0329P)^2 + 0.3861P]$ where $P = (F_o^2 + 2F_c^2)/3$

$(\Delta/\sigma)_{max} = 0.001$
$\Delta\rho_{max} = 0.60$ e Å^{-3}
$\Delta\rho_{min} = -0.31$ e Å^{-3}

Special details

Geometry. Bond distances, angles *etc*. have been calculated using the rounded fractional coordinates. All e.s.d.'s are estimated from the variances of the (full) variance-covariance matrix. The cell e.s.d.'s are taken into account in the estimation of distances, angles and torsion angles

Fractional atomic coordinates and isotropic or equivalent isotropic displacement parameters (Å^2)

	x	*y*	*z*	U_{iso}*/U_{eq}
Cd1	0.15538 (2)	0.37614 (1)	0.26425 (1)	0.0382 (1)
Ag1	0.45743 (2)	0.84462 (2)	0.52250 (1)	0.0632 (1)
Ag2	0.58525 (2)	0.11057 (2)	0.26944 (1)	0.0597 (1)
N1	−0.04988 (19)	0.45002 (17)	0.30232 (12)	0.0429 (5)
N2	0.0790 (2)	0.28808 (18)	0.36992 (13)	0.0437 (6)
N3	0.0035 (2)	0.23139 (18)	0.12025 (12)	0.0453 (6)
N4	0.1799 (2)	0.45737 (17)	0.14417 (12)	0.0427 (5)
N5	0.3336 (2)	0.2628 (2)	0.25121 (15)	0.0557 (7)
N6	0.3095 (2)	0.5613 (2)	0.37332 (15)	0.0570 (7)
N7	0.8463 (3)	−0.0316 (3)	0.2747 (2)	0.0726 (10)
N8	0.6444 (3)	1.1098 (3)	0.6773 (2)	0.0906 (10)
C1	−0.1172 (3)	0.5219 (2)	0.26298 (16)	0.0495 (7)
C2	−0.2455 (3)	0.5529 (3)	0.27778 (19)	0.0570 (8)
C3	−0.3055 (3)	0.5064 (3)	0.3363 (2)	0.0653 (10)
C4	−0.2369 (3)	0.4349 (3)	0.3788 (2)	0.0589 (9)
C5	−0.1076 (2)	0.4079 (2)	0.36096 (15)	0.0437 (6)
C6	−0.3162 (4)	0.6334 (3)	0.2315 (3)	0.0783 (11)
C7	−0.0290 (2)	0.3310 (2)	0.40449 (15)	0.0431 (6)
C8	−0.0638 (3)	0.3044 (2)	0.47878 (17)	0.0529 (8)
C9	0.0090 (3)	0.2305 (2)	0.51591 (17)	0.0552 (8)
C10	0.1166 (3)	0.1825 (2)	0.47934 (17)	0.0535 (8)
C11	0.1478 (3)	0.2151 (2)	0.40653 (17)	0.0510 (8)
C12	0.1971 (4)	0.0985 (3)	0.5169 (2)	0.0754 (11)
C13	−0.0901 (3)	0.1260 (2)	0.11166 (17)	0.0544 (8)
C14	−0.1800 (3)	0.0397 (2)	0.02833 (19)	0.0562 (8)
C15	−0.1664 (3)	0.0652 (3)	−0.04963 (19)	0.0630 (8)
C16	−0.0705 (3)	0.1732 (3)	−0.04249 (17)	0.0607 (9)
C17	0.0125 (2)	0.2565 (2)	0.04402 (15)	0.0437 (7)
C18	−0.2863 (4)	−0.0753 (3)	0.0243 (2)	0.0811 (11)
C19	0.1134 (3)	0.3778 (2)	0.05683 (15)	0.0445 (7)
C20	0.1370 (3)	0.4096 (3)	−0.01767 (17)	0.0641 (9)
C21	0.2304 (3)	0.5235 (3)	−0.00145 (19)	0.0662 (10)
C22	0.3007 (3)	0.6058 (2)	0.08750 (17)	0.0512 (8)
C23	0.2694 (3)	0.5686 (2)	0.15831 (16)	0.0472 (7)
C24	0.4050 (3)	0.7307 (3)	0.1068 (2)	0.0681 (10)
C25	0.4237 (3)	0.2099 (3)	0.25489 (18)	0.0538 (8)
C26	0.3655 (3)	0.6603 (3)	0.42730 (18)	0.0548 (8)

C27	0.7536 (3)	0.0190 (3)	0.2737 (2)	0.0578 (9)
C28	0.5693 (3)	1.0190 (3)	0.6243 (2)	0.0626 (9)
O1	0.0393 (4)	0.7899 (3)	0.2477 (2)	0.0808 (10)
H1	−0.07490	0.55250	0.22360	0.0590*
H3	−0.39300	0.52350	0.34720	0.0780*
H4	−0.27690	0.40490	0.41930	0.0710*
H6A	−0.40290	0.58070	0.18610	0.1180*
H6B	−0.25180	0.66760	0.20150	0.1180*
H6C	−0.33910	0.70350	0.27740	0.1180*
H8	−0.13670	0.33680	0.50340	0.0640*
H9	−0.01440	0.21280	0.56580	0.0660*
H11	0.22130	0.18430	0.38160	0.0610*
H12A	0.29590	0.14310	0.54480	0.1130*
H12B	0.19200	0.01910	0.46710	0.1130*
H12C	0.15460	0.07990	0.56290	0.1130*
H13	−0.09500	0.10960	0.16530	0.0650*
H15	−0.22260	0.00900	−0.10780	0.0760*
H16	−0.06170	0.18980	−0.09550	0.0730*
H18A	−0.37440	−0.05040	0.03410	0.1210*
H18B	−0.24710	−0.10540	0.07180	0.1210*
H18C	−0.30500	−0.14320	−0.03560	0.1210*
H20	0.09000	0.35440	−0.07820	0.0770*
H21	0.24620	0.54520	−0.05150	0.0790*
H23	0.31310	0.62400	0.21940	0.0570*
H24A	0.49940	0.71460	0.10580	0.1020*
H24B	0.40750	0.79200	0.16690	0.1020*
H24C	0.37460	0.76510	0.06010	0.1020*
H1W	0.114 (5)	0.826 (5)	0.270 (3)	0.114 (19)*
H2W	0.007 (4)	0.844 (4)	0.263 (3)	0.081 (14)*

Atomic displacement parameters (Å²)

	U^{11}	U^{22}	U^{33}	U^{12}	U^{13}	U^{23}
Cd1	0.0405 (1)	0.0403 (1)	0.0319 (1)	0.0044 (1)	0.0107 (1)	0.0121 (1)
Ag1	0.0617 (1)	0.0520 (1)	0.0560 (1)	−0.0052 (1)	0.0135 (1)	0.0029 (1)
Ag2	0.0566 (1)	0.0598 (1)	0.0620 (1)	0.0197 (1)	0.0125 (1)	0.0200 (1)
N1	0.0425 (10)	0.0429 (9)	0.0398 (9)	0.0068 (8)	0.0114 (8)	0.0116 (8)
N2	0.0466 (10)	0.0461 (10)	0.0421 (10)	0.0080 (8)	0.0171 (8)	0.0187 (8)
N3	0.0483 (10)	0.0421 (10)	0.0380 (9)	0.0001 (8)	0.0095 (8)	0.0103 (8)
N4	0.0474 (10)	0.0416 (9)	0.0359 (9)	0.0055 (8)	0.0078 (8)	0.0137 (7)
N5	0.0536 (12)	0.0586 (12)	0.0559 (12)	0.0179 (10)	0.0163 (10)	0.0189 (10)
N6	0.0559 (12)	0.0567 (12)	0.0464 (11)	−0.0035 (10)	0.0146 (9)	0.0097 (10)
N7	0.0700 (16)	0.0769 (16)	0.0861 (18)	0.0267 (14)	0.0258 (14)	0.0416 (15)
N8	0.100 (2)	0.0572 (15)	0.0827 (19)	−0.0109 (15)	0.0157 (16)	0.0014 (14)
C1	0.0470 (12)	0.0545 (13)	0.0453 (12)	0.0115 (10)	0.0097 (10)	0.0174 (11)
C2	0.0486 (13)	0.0540 (14)	0.0632 (16)	0.0137 (11)	0.0099 (12)	0.0162 (12)
C3	0.0459 (14)	0.0631 (16)	0.090 (2)	0.0161 (12)	0.0260 (14)	0.0257 (15)
C4	0.0518 (14)	0.0571 (15)	0.0726 (17)	0.0093 (12)	0.0290 (13)	0.0243 (13)
C5	0.0429 (11)	0.0391 (11)	0.0419 (11)	0.0005 (9)	0.0136 (9)	0.0079 (9)
C6	0.0664 (19)	0.086 (2)	0.094 (2)	0.0363 (17)	0.0206 (17)	0.0396 (19)

C7	0.0437 (11)	0.0391 (11)	0.0422 (11)	−0.0003 (9)	0.0156 (9)	0.0110 (9)
C8	0.0567 (14)	0.0544 (13)	0.0469 (13)	0.0040 (11)	0.0252 (11)	0.0147 (11)
C9	0.0672 (16)	0.0546 (14)	0.0434 (12)	−0.0001 (12)	0.0218 (11)	0.0189 (11)
C10	0.0625 (15)	0.0545 (14)	0.0473 (13)	0.0050 (11)	0.0171 (11)	0.0251 (11)
C11	0.0541 (13)	0.0571 (14)	0.0509 (13)	0.0125 (11)	0.0214 (11)	0.0271 (11)
C12	0.088 (2)	0.092 (2)	0.0743 (19)	0.0295 (18)	0.0332 (17)	0.0555 (18)
C13	0.0598 (15)	0.0508 (13)	0.0455 (13)	−0.0013 (11)	0.0155 (11)	0.0134 (11)
C14	0.0539 (14)	0.0432 (12)	0.0565 (14)	−0.0016 (10)	0.0110 (11)	0.0064 (11)
C15	0.0649 (16)	0.0536 (14)	0.0471 (14)	−0.0036 (12)	−0.0040 (12)	0.0057 (11)
C16	0.0751 (18)	0.0551 (14)	0.0399 (12)	−0.0002 (13)	0.0030 (12)	0.0147 (11)
C17	0.0494 (12)	0.0401 (11)	0.0372 (11)	0.0071 (9)	0.0076 (9)	0.0115 (9)
C18	0.076 (2)	0.0612 (18)	0.079 (2)	−0.0203 (15)	0.0156 (16)	0.0086 (15)
C19	0.0516 (13)	0.0433 (11)	0.0368 (11)	0.0079 (10)	0.0084 (9)	0.0152 (9)
C20	0.085 (2)	0.0606 (15)	0.0377 (12)	−0.0013 (14)	0.0049 (12)	0.0196 (11)
C21	0.086 (2)	0.0667 (17)	0.0494 (14)	0.0029 (15)	0.0166 (13)	0.0319 (13)
C22	0.0547 (14)	0.0504 (13)	0.0533 (13)	0.0072 (11)	0.0109 (11)	0.0283 (11)
C23	0.0521 (13)	0.0440 (12)	0.0419 (12)	0.0034 (10)	0.0067 (10)	0.0169 (10)
C24	0.0747 (18)	0.0619 (16)	0.0696 (18)	−0.0022 (14)	0.0112 (14)	0.0376 (14)
C25	0.0552 (14)	0.0526 (14)	0.0496 (13)	0.0095 (12)	0.0131 (11)	0.0151 (11)
C26	0.0505 (13)	0.0563 (14)	0.0466 (13)	−0.0048 (11)	0.0147 (11)	0.0108 (11)
C27	0.0599 (16)	0.0593 (15)	0.0626 (16)	0.0138 (13)	0.0188 (12)	0.0310 (13)
C28	0.0722 (18)	0.0495 (14)	0.0569 (15)	0.0020 (13)	0.0160 (13)	0.0130 (12)
O1	0.0730 (17)	0.0722 (16)	0.0863 (17)	0.0184 (14)	0.0120 (14)	0.0190 (13)

Geometric parameters (Å, º)

Cd1—N1	2.3654 (19)	C13—C14	1.381 (4)
Cd1—N2	2.375 (2)	C14—C15	1.375 (4)
Cd1—N3	2.3609 (18)	C14—C18	1.508 (5)
Cd1—N4	2.3924 (19)	C15—C16	1.377 (5)
Cd1—N5	2.291 (2)	C16—C17	1.381 (3)
Cd1—N6	2.299 (2)	C17—C19	1.489 (3)
Ag1—C26	2.059 (3)	C19—C20	1.383 (4)
Ag1—C28	2.059 (3)	C20—C21	1.374 (5)
Ag2—C25	2.074 (3)	C21—C22	1.372 (4)
Ag2—C27	2.055 (3)	C22—C23	1.382 (3)
O1—H2W	0.72 (5)	C22—C24	1.510 (4)
O1—H1W	0.73 (5)	C1—H1	0.9308
N1—C5	1.340 (3)	C3—H3	0.9300
N1—C1	1.343 (3)	C4—H4	0.9315
N2—C7	1.344 (3)	C6—H6B	0.9598
N2—C11	1.336 (3)	C6—H6C	0.9602
N3—C13	1.336 (3)	C6—H6A	0.9597
N3—C17	1.336 (3)	C8—H8	0.9292
N4—C23	1.340 (3)	C9—H9	0.9301
N4—C19	1.339 (3)	C11—H11	0.9302
N5—C25	1.129 (4)	C12—H12C	0.9613
N6—C26	1.131 (4)	C12—H12B	0.9591
N7—C27	1.132 (4)	C12—H12A	0.9600
N8—C28	1.123 (4)	C13—H13	0.9306

C1—C2	1.379 (4)	C15—H15	0.9304
C2—C3	1.375 (4)	C16—H16	0.9298
C2—C6	1.503 (5)	C18—H18B	0.9595
C3—C4	1.374 (5)	C18—H18A	0.9596
C4—C5	1.388 (4)	C18—H18C	0.9599
C5—C7	1.481 (3)	C20—H20	0.9299
C7—C8	1.386 (3)	C21—H21	0.9307
C8—C9	1.369 (4)	C23—H23	0.9308
C9—C10	1.374 (4)	C24—H24C	0.9597
C10—C12	1.507 (4)	C24—H24A	0.9604
C10—C11	1.384 (4)	C24—H24B	0.9603

Ag1···C12^{i}	4.088 (4)	C24···C6^{v}	3.565 (5)
Ag1···C12^{ii}	3.525 (4)	C24···Ag2^{i}	4.093 (3)
Ag1···Ag1^{iii}	3.7997 (4)	C24···N8^{iii}	3.431 (4)
Ag1···Ag2^{ii}	3.2575 (3)	C25···Ag1^{ii}	3.762 (3)
Ag1···N8^{iii}	3.350 (3)	C26···C8^{iv}	3.526 (4)
Ag1···C8^{iv}	3.934 (3)	C27···C7^{v}	3.526 (4)
Ag1···C10^{ii}	4.190 (3)	C27···Ag1^{ii}	4.107 (3)
Ag1···C11^{ii}	4.004 (3)	C28···Ag1^{iii}	3.167 (3)
Ag1···C28^{iii}	3.167 (3)	C28···Ag2^{ii}	3.014 (3)
Ag1···C25^{ii}	3.762 (3)	C28···C12^{ii}	3.546 (5)
Ag1···C27^{ii}	4.107 (3)	C4···H8	2.6587
Ag2···C28^{ii}	3.014 (3)	C6···H24A^{xii}	2.8864
Ag2···C5^{v}	3.802 (2)	C8···H4	2.6643
Ag2···Ag1^{ii}	3.2576 (3)	C15···H24C^{ix}	2.9918
Ag2···N8^{ii}	3.505 (3)	C16···H20	2.6573
Ag2···C18^{v}	4.236 (3)	C20···H16	2.6563
Ag2···C24^{vi}	4.093 (3)	C24···H6A^{v}	3.0562
Ag2···C3^{v}	4.141 (4)	C25···H11	3.0939
Ag2···C4^{v}	3.484 (3)	C25···H15^{vii}	2.8931
Ag2···C7^{v}	3.941 (2)	C26···H23	3.0947
Ag2···C8^{v}	4.016 (3)	C26···H8^{iv}	2.6456
Ag1···H4^{iv}	3.5591	C26···H4^{iv}	2.9788
Ag1···H12B^{i}	3.6084	C27···H18B^{v}	3.0133
Ag1···H12B^{ii}	3.4715	C27···H13^{v}	2.7850
Ag1···H12A^{ii}	2.7920	C28···H12B^{ii}	2.9511
Ag1···H8^{iv}	3.3382	H1···O1	2.6103
Ag1···H11^{ii}	3.3145	H1···H6B	2.3377
Ag2···H4^{v}	3.2643	H1W···N8^{iii}	2.26 (5)
Ag2···H13^{v}	3.7636	H2W···N7^{viii}	2.23 (4)
Ag2···H18A^{v}	3.6627	H4···H8	2.1231
Ag2···H24B^{vi}	3.4267	H4···Ag1^{iv}	3.5591
Ag2···H15^{vii}	3.7027	H4···C26^{iv}	2.9788
O1···C1	3.278 (4)	H4···C8	2.6643
O1···N7^{viii}	2.920 (5)	H4···Ag2^{xii}	3.2643
O1···N8^{iii}	2.975 (5)	H6A···C24^{xii}	3.0562
O1···H16^{ix}	2.5268	H6A···H24A^{xii}	2.4518
O1···H20^{ix}	2.5723	H6B···O1	2.8004

O1···H6B	2.8004	H6B···H1	2.3377
O1···H1	2.6103	H8···H4	2.1231
N7···O1^{x}	2.920 (5)	H8···Ag1^{iv}	3.3382
N8···Ag1^{iii}	3.350 (3)	H8···C4	2.6587
N8···Ag2^{ii}	3.505 (3)	H8···C26^{iv}	2.6456
N8···C24^{iii}	3.431 (4)	H8···N6^{iv}	2.8551
N8···O1^{iii}	2.975 (5)	H9···H12C	2.3693
N5···H11	2.8168	H11···Ag1^{ii}	3.3145
N6···H8^{iv}	2.8551	H11···C25	3.0939
N6···H23	2.7457	H11···N5	2.8168
N7···H12C^{xi}	2.7874	H12A···Ag1^{ii}	2.7919
N7···H18B^{v}	2.9434	H12B···Ag1^{vi}	3.6083
N7···H13^{v}	2.7822	H12B···Ag1^{ii}	3.4715
N7···H2W^{x}	2.23 (4)	H12B···C28^{ii}	2.9511
N8···H1W^{iii}	2.26 (5)	H12C···H9	2.3693
N8···H23^{iii}	2.8148	H12C···N7^{xi}	2.7874
N8···H24B^{iii}	2.5088	H13···Ag2^{xii}	3.7636
C1···O1	3.278 (4)	H13···N7^{xii}	2.7822
C1···C9^{iv}	3.509 (3)	H13···C27^{xii}	2.7850
C2···C9^{iv}	3.479 (4)	H13···H18B	2.4458
C3···Ag2^{xii}	4.141 (4)	H15···H18C	2.4698
C3···C9^{iv}	3.594 (4)	H15···Ag2^{vii}	3.7027
C4···C8^{iv}	3.586 (4)	H15···C25^{vii}	2.8931
C4···Ag2^{xii}	3.484 (3)	H16···O1^{ix}	2.5268
C5···Ag2^{xii}	3.802 (2)	H16···C20	2.6563
C5···C8^{iv}	3.324 (3)	H16···H20	2.0960
C6···C24^{xii}	3.565 (5)	H18A···Ag2^{xii}	3.6627
C7···C27^{xii}	3.526 (4)	H18B···N7^{xii}	2.9434
C7···Ag2^{xii}	3.941 (2)	H18B···C27^{xii}	3.0133
C8···Ag1^{iv}	3.934 (3)	H18B···H13	2.4458
C8···Ag2^{xii}	4.016 (3)	H18C···H15	2.4698
C8···C26^{iv}	3.526 (4)	H20···H16	2.0960
C8···C4^{iv}	3.586 (4)	H20···O1^{ix}	2.5723
C8···C5^{iv}	3.324 (3)	H20···C16	2.6573
C9···C1^{iv}	3.509 (3)	H21···H24C	2.4812
C9···C3^{iv}	3.594 (4)	H23···C26	3.0947
C9···C2^{iv}	3.479 (4)	H23···H24B	2.4318
C10···Ag1^{ii}	4.190 (3)	H23···N6	2.7457
C11···Ag1^{ii}	4.004 (3)	H23···N8^{iii}	2.8148
C12···Ag1^{ii}	3.525 (4)	H24A···C6^{v}	2.8864
C12···Ag1^{vi}	4.088 (4)	H24A···H6A^{v}	2.4518
C12···C28^{ii}	3.546 (5)	H24B···H23	2.4318
C13···C15^{vii}	3.578 (4)	H24B···Ag2^{i}	3.4267
C15···C13^{vii}	3.578 (4)	H24B···N8^{iii}	2.5088
C18···Ag2^{xii}	4.236 (3)	H24C···C15^{ix}	2.9918
C20···C20^{ix}	3.585 (4)	H24C···H21	2.4812

N1—Cd1—N2	70.48 (7)	C17—C19—C20	122.1 (2)
N1—Cd1—N3	87.77 (6)	N4—C19—C17	117.4 (2)

N1—Cd1—N4	100.04 (7)	C19—C20—C21	119.4 (2)
N1—Cd1—N5	161.90 (7)	C20—C21—C22	121.0 (3)
N1—Cd1—N6	92.37 (7)	C21—C22—C24	121.8 (2)
N2—Cd1—N3	101.93 (7)	C23—C22—C24	121.9 (2)
N2—Cd1—N4	168.07 (7)	C21—C22—C23	116.2 (3)
N2—Cd1—N5	91.71 (7)	N4—C23—C22	123.8 (2)
N2—Cd1—N6	97.23 (7)	Ag2—C25—N5	176.0 (3)
N3—Cd1—N4	69.78 (7)	Ag1—C26—N6	176.6 (3)
N3—Cd1—N5	92.99 (7)	Ag2—C27—N7	179.0 (3)
N3—Cd1—N6	159.69 (8)	Ag1—C28—N8	171.9 (3)
N4—Cd1—N5	97.18 (7)	N1—C1—H1	118.19
N4—Cd1—N6	90.24 (7)	C2—C1—H1	118.23
N5—Cd1—N6	93.10 (8)	C4—C3—H3	119.80
C26—Ag1—C28	172.77 (12)	C2—C3—H3	119.79
C25—Ag2—C27	173.82 (12)	C5—C4—H4	120.31
H1W—O1—H2W	96 (5)	C3—C4—H4	120.21
Cd1—N1—C1	123.81 (16)	C2—C6—H6A	109.50
C1—N1—C5	118.9 (2)	C2—C6—H6C	109.49
Cd1—N1—C5	117.05 (15)	H6A—C6—H6B	109.51
Cd1—N2—C7	116.22 (16)	C2—C6—H6B	109.50
Cd1—N2—C11	124.74 (17)	H6B—C6—H6C	109.40
C7—N2—C11	118.3 (2)	H6A—C6—H6C	109.43
Cd1—N3—C13	123.07 (15)	C7—C8—H8	119.90
Cd1—N3—C17	118.12 (15)	C9—C8—H8	119.97
C13—N3—C17	118.81 (19)	C10—C9—H9	120.06
Cd1—N4—C23	123.82 (14)	C8—C9—H9	120.04
C19—N4—C23	119.0 (2)	N2—C11—H11	118.00
Cd1—N4—C19	116.63 (16)	C10—C11—H11	117.92
Cd1—N5—C25	172.5 (2)	C10—C12—H12B	109.50
Cd1—N6—C26	168.7 (2)	C10—C12—H12C	109.47
N1—C1—C2	123.6 (2)	H12A—C12—H12B	109.55
C1—C2—C3	117.0 (3)	H12A—C12—H12C	109.46
C1—C2—C6	121.2 (3)	H12B—C12—H12C	109.44
C3—C2—C6	121.8 (3)	C10—C12—H12A	109.41
C2—C3—C4	120.4 (3)	N3—C13—H13	117.87
C3—C4—C5	119.5 (3)	C14—C13—H13	117.87
N1—C5—C4	120.6 (2)	C16—C15—H15	119.64
C4—C5—C7	121.9 (2)	C14—C15—H15	119.70
N1—C5—C7	117.45 (18)	C15—C16—H16	120.23
N2—C7—C5	117.68 (19)	C17—C16—H16	120.32
C5—C7—C8	121.7 (2)	C14—C18—H18B	109.43
N2—C7—C8	120.6 (2)	C14—C18—H18C	109.46
C7—C8—C9	120.1 (3)	C14—C18—H18A	109.46
C8—C9—C10	119.9 (2)	H18A—C18—H18C	109.45
C9—C10—C11	116.9 (2)	H18B—C18—H18C	109.52
C11—C10—C12	121.6 (3)	H18A—C18—H18B	109.51
C9—C10—C12	121.5 (2)	C19—C20—H20	120.28
N2—C11—C10	124.1 (3)	C21—C20—H20	120.32
N3—C13—C14	124.3 (2)	C22—C21—H21	119.51

C13—C14—C18	121.3 (2)	C20—C21—H21	119.53
C15—C14—C18	122.6 (3)	N4—C23—H23	118.09
C13—C14—C15	116.1 (3)	C22—C23—H23	118.07
C14—C15—C16	120.7 (3)	C22—C24—H24B	109.49
C15—C16—C17	119.4 (2)	C22—C24—H24C	109.52
N3—C17—C16	120.7 (2)	C22—C24—H24A	109.52
C16—C17—C19	122.0 (2)	H24A—C24—H24C	109.47
N3—C17—C19	117.28 (19)	H24B—C24—H24C	109.43
N4—C19—C20	120.5 (2)	H24A—C24—H24B	109.40

N2—Cd1—N1—C1	−175.0 (2)	C17—N3—C13—C14	−0.1 (4)
N2—Cd1—N1—C5	−0.62 (15)	Cd1—N3—C17—C16	178.02 (19)
N3—Cd1—N1—C1	−71.48 (18)	Cd1—N3—C17—C19	−2.8 (3)
N3—Cd1—N1—C5	102.86 (16)	C13—N3—C17—C16	−1.8 (4)
N4—Cd1—N1—C1	−2.46 (19)	C13—N3—C17—C19	177.4 (2)
N4—Cd1—N1—C5	171.88 (15)	Cd1—N4—C19—C17	9.6 (3)
N6—Cd1—N1—C1	88.20 (19)	Cd1—N4—C19—C20	−171.4 (2)
N6—Cd1—N1—C5	−97.46 (16)	C23—N4—C19—C17	−178.8 (2)
N1—Cd1—N2—C7	−5.87 (15)	C23—N4—C19—C20	0.2 (4)
N1—Cd1—N2—C11	−175.9 (2)	Cd1—N4—C23—C22	169.4 (2)
N3—Cd1—N2—C7	−89.15 (16)	C19—N4—C23—C22	−1.6 (4)
N3—Cd1—N2—C11	100.78 (19)	N1—C1—C2—C3	0.0 (4)
N5—Cd1—N2—C7	177.42 (16)	N1—C1—C2—C6	−179.8 (3)
N5—Cd1—N2—C11	7.4 (2)	C6—C2—C3—C4	−178.9 (3)
N6—Cd1—N2—C7	84.09 (17)	C1—C2—C3—C4	1.4 (4)
N6—Cd1—N2—C11	−86.0 (2)	C2—C3—C4—C5	−1.1 (5)
N1—Cd1—N3—C13	−73.2 (2)	C3—C4—C5—N1	−0.5 (4)
N1—Cd1—N3—C17	107.04 (17)	C3—C4—C5—C7	−179.8 (3)
N2—Cd1—N3—C13	−3.7 (2)	N1—C5—C7—N2	−12.2 (3)
N2—Cd1—N3—C17	176.55 (16)	C4—C5—C7—C8	−13.3 (4)
N4—Cd1—N3—C13	−174.7 (2)	N1—C5—C7—C8	167.4 (2)
N4—Cd1—N3—C17	5.49 (16)	C4—C5—C7—N2	167.2 (2)
N5—Cd1—N3—C13	88.7 (2)	C5—C7—C8—C9	178.5 (2)
N5—Cd1—N3—C17	−91.07 (17)	N2—C7—C8—C9	−2.0 (4)
N6—Cd1—N3—C13	−164.0 (2)	C7—C8—C9—C10	−0.1 (4)
N6—Cd1—N3—C17	16.2 (3)	C8—C9—C10—C12	−178.7 (3)
N1—Cd1—N4—C19	−91.80 (19)	C8—C9—C10—C11	1.4 (4)
N1—Cd1—N4—C23	97.0 (2)	C9—C10—C11—N2	−0.8 (4)
N3—Cd1—N4—C19	−7.96 (18)	C12—C10—C11—N2	179.3 (3)
N3—Cd1—N4—C23	−179.1 (2)	N3—C13—C14—C18	−178.1 (3)
N5—Cd1—N4—C19	82.60 (19)	N3—C13—C14—C15	1.8 (4)
N5—Cd1—N4—C23	−88.6 (2)	C13—C14—C15—C16	−1.7 (4)
N6—Cd1—N4—C19	175.75 (19)	C18—C14—C15—C16	178.3 (3)
N6—Cd1—N4—C23	4.6 (2)	C14—C15—C16—C17	−0.1 (5)
Cd1—N1—C1—C2	172.7 (2)	C15—C16—C17—N3	1.9 (4)
C5—N1—C1—C2	−1.6 (4)	C15—C16—C17—C19	−177.3 (3)
Cd1—N1—C5—C4	−172.8 (2)	N3—C17—C19—N4	−4.7 (3)
Cd1—N1—C5—C7	6.5 (3)	N3—C17—C19—C20	176.4 (3)
C1—N1—C5—C4	1.8 (3)	C16—C17—C19—N4	174.5 (2)

C1—N1—C5—C7	−178.8 (2)	C16—C17—C19—C20	−4.5 (4)
Cd1—N2—C7—C5	11.4 (3)	C17—C19—C20—C21	179.4 (3)
Cd1—N2—C7—C8	−168.13 (18)	N4—C19—C20—C21	0.5 (4)
C11—N2—C7—C5	−177.9 (2)	C19—C20—C21—C22	0.2 (5)
C11—N2—C7—C8	2.6 (3)	C20—C21—C22—C23	−1.4 (4)
Cd1—N2—C11—C10	168.66 (19)	C20—C21—C22—C24	179.3 (3)
C7—N2—C11—C10	−1.2 (4)	C21—C22—C23—N4	2.2 (4)
Cd1—N3—C13—C14	−179.9 (2)	C24—C22—C23—N4	−178.5 (3)

Symmetry codes: (i) *x*, *y*+1, *z*; (ii) −*x*+1, −*y*+1, −*z*+1; (iii) −*x*+1, −*y*+2, −*z*+1; (iv) −*x*, −*y*+1, −*z*+1; (v) *x*+1, *y*, *z*; (vi) *x*, *y*−1, *z*; (vii) −*x*, −*y*, −*z*; (viii) *x*−1, *y*+1, *z*; (ix) −*x*, −*y*+1, −*z*; (x) *x*+1, *y*−1, *z*; (xi) −*x*+1, −*y*, −*z*+1; (xii) *x*−1, *y*, *z*.

Hydrogen-bond geometry (Å, º)

D—H···*A*	*D*—H	H···*A*	*D*···*A*	*D*—H···*A*
O1—H1*W*···N8^{iii}	0.73 (5)	2.26 (5)	2.975 (5)	166 (6)
O1—H2*W*···N7^{viii}	0.72 (5)	2.23 (4)	2.920 (5)	162 (5)
C16—H16···O1^{ix}	0.93	2.53	3.453 (4)	174
C20—H20···O1^{ix}	0.93	2.57	3.502 (4)	178
C24—H24*B*···N8^{iii}	0.96	2.51	3.431 (4)	161

Symmetry codes: (iii) −*x*+1, −*y*+2, −*z*+1; (viii) *x*−1, *y*+1, *z*; (ix) −*x*, −*y*+1, −*z*.

π–π contacts (Å, °) for (I)

CCD is the centre-to-centre distance (distance between ring centroids), IPD is the mean interplanar distance (perpendicular distance from one plane to the neighbouring ring centroid) and SA is the mean slippage angle (angle subtended by the intercentroid vector to the plane normal); for details, see Janiak (2000). *Cg*3 is the centroid of the N1/C1–C5 ring, *Cg*4 is the centroid of the N2/C7–C11 ring and *Cg*5 is the centroid of the N3/C13–C17 ring.

Group1/group2	CCD (Å)	SA (°)	IPD (Å)
*Cg*4–*Cg*3^{iv}	3.7582 (14)	4.674	3.271
*Cg*5–*Cg*5^{v}	3.8263 (16)	1.405	3.559

Symmetry codes: (iv) -x, -y + 1, -z + 1; (v) -x, -y, -z.

Acta Crystallographica Section E
Structure Reports Online
ISSN 1600-5368

Poly[tris(μ-4,4′-bipyridine-κ²N:N′)bis(dimethyl sulfoxide-κO)tetrakis(thiocyanato-κN)dicobalt(II)]

Surasak Kaenket,[a] Pongthipun Phuengphai,[b] Chaveng Pakawatchai[c] and Sujittra Youngme[a]*

[a]Materials Chemistry Research Unit, Department of Chemistry and Center of Excellence for Innovation in Chemistry, Faculty of Science, Khon Kaen University, Khon Kaen 40002, Thailand, [b]Department of Fundamental Science, Faculty of Science and Technology, Surindra Rajabhat University, Surin 32000, Thailand, and [c]Department of Chemistry, Faculty of Science, Prince of Songkla University, Hat Yai, Songkhla 90112, Thailand
Correspondence e-mail: sujittra@kku.ac.th

Received 27 May 2014; accepted 11 June 2014

Key indicators: single-crystal X-ray study; T = 273 K; mean σ(C–C) = 0.003 Å; R factor = 0.043; wR factor = 0.109; data-to-parameter ratio = 21.2.

The asymmetric unit of the title compound, $[Co_2(NCS)_4(C_{10}H_8N_2)_3(C_2H_6OS)_2]_n$, consists of one Co^{II} atom, two thiocyanate anions, one dimethyl sulfoxide molecule and one and a half 4,4′-bipyridine molecules. The half-molecule is completed by inversion symmetry. The Co^{II} atom is coordinated in a distorted octahedral geometry by two N atoms from two thiocyanate anions, one O atom from dimethyl sulfoxide as a terminal ligand and three N atoms from three 4,4′-bipyridine molecules as bridging ligands linking the cations, with a Co···Co separation of 11.5964 (5) Å. This generates a two-dimensional structure parallel to ($\bar{1}$03). A C—H···S hydrogen bond links the layers into a three-dimensional supramolecular framework. The layers are stacked in an *ABC* fashion preventing the occurrence of interlayer void space and hence leading to the absence of lattice solvent and/or organic guest molecules in the structure.

Related literature

For related coordination polymers with ligands such as pyrazine, pyrimidine, 4,4′-bipyridine and SCN^-, see: Wriedt & Näther (2009, 2010); Wriedt *et al.* (2009); Yao & Wang (2009).

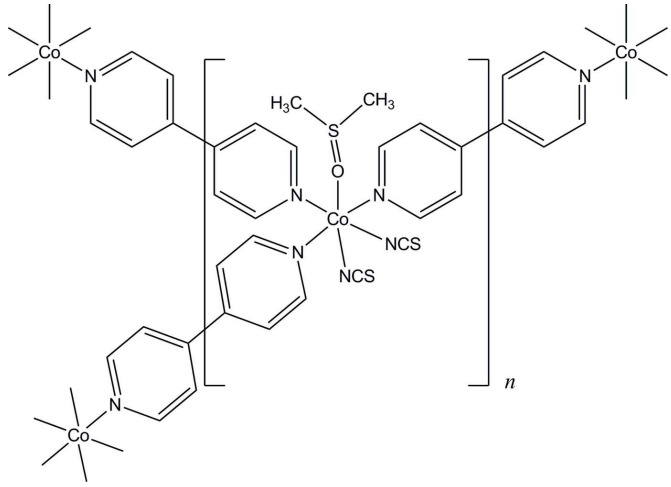

Experimental

Crystal data

$[Co_2(NCS)_4(C_{10}H_8N_2)_3(C_2H_6OS)_2]$
M_r = 974.98
Monoclinic, $P2_1/n$
a = 11.0772 (3) Å
b = 16.9999 (2) Å
c = 11.6843 (3) Å
β = 103.628 (1)°
V = 2138.34 (8) Å³
Z = 2
Mo $K\alpha$ radiation
μ = 1.12 mm^{-1}
T = 273 K
0.40 × 0.16 × 0.10 mm

Data collection

Bruker SMART APEX CCD diffractometer
Absorption correction: multi-scan (*SADABS*; Bruker, 2000)
T_{min} = 0.591, T_{max} = 0.894
14262 measured reflections
5584 independent reflections
3936 reflections with $I > 2\sigma(I)$
R_{int} = 0.032

Refinement

$R[F^2 > 2\sigma(F^2)]$ = 0.043
$wR(F^2)$ = 0.109
S = 1.01
5584 reflections
264 parameters
H-atom parameters constrained
$\Delta\rho_{max}$ = 1.02 e Å^{-3}
$\Delta\rho_{min}$ = −0.58 e Å^{-3}

Table 1
Selected bond lengths (Å).

Co1—N7	2.080 (2)	Co1—N3	2.2187 (19)
Co1—N6	2.102 (2)	Co1—N2	2.244 (2)
Co1—O1	2.1234 (19)	Co1—N1	2.2551 (19)

Table 2
Hydrogen-bond geometry (Å, °).

D—H···A	D—H	H···A	D···A	D—H···A
C1—H1···S1^{i}	0.93	2.82	3.596 (3)	141

Symmetry code: (i) $-x+\frac{3}{2}, y-\frac{1}{2}, -z+\frac{1}{2}$.

Data collection: *SMART* (Bruker, 2000); cell refinement: *SAINT* (Bruker, 2000); data reduction: *SAINT*; program(s) used to solve structure: *SHELXS97* (Sheldrick, 2008); program(s) used to refine structure: *SHELXL97* (Sheldrick, 2008); molecular graphics: *Mercury* (Macrae *et al.*, 2008); software used to prepare material for publication: *publCIF* (Westrip, 2010).

The authors gratefully acknowledge The Thailand Research Fund (BRG5680009), the Higher Education Research Promotion and National Research University Project of Thailand, through the Advanced Functional Materials Cluster of Khon Kaen University, and the Center of Excellence for Innovation in Chemistry (PERCH–CIC), Office of the Higher Education Commission, Ministry of Education, Thailand, for financial support.

Supporting information for this paper is available from the IUCr electronic archives (Reference: IS5365).

References

Bruker (2000). *SMART*, *SAINT* and *SADABS*. Bruker AXS Inc., Madison, Wisconsin, USA.
Macrae, C. F., Bruno, I. J., Chisholm, J. A., Edgington, P. R., McCabe, P., Pidcock, E., Rodriguez-Monge, L., Taylor, R., van de Streek, J. & Wood, P. A. (2008). *J. Appl. Cryst.* **41**, 466–470.
Sheldrick, G. M. (2008). *Acta Cryst.* A**64**, 112–122.
Westrip, S. P. (2010). *J. Appl. Cryst.* **43**, 920–925.
Wriedt, M., Jess, I. & Näther, C. (2009). *Eur. J. Inorg. Chem.* pp. 1406–1413.
Wriedt, M. & Näther, C. (2009). *Dalton Trans.* pp. 10192–10198.
Wriedt, M. & Näther, C. (2010). *Z. Anorg. Allg. Chem.* **636**, 1061–1068.
Yao, R. & Wang, D. E. (2009). *Acta Cryst.* E**65**, m813.

supporting information

Acta Cryst. (2014). E**70**, m265–m266 [doi:10.1107/S1600536814013555]

Poly[tris(μ-4,4′-bipyridine-κ^2N:N')bis(dimethyl sulfoxide-κO)tetrakis(thiocyanato-κN)dicobalt(II)]

Surasak Kaenket, Pongthipun Phuengphai, Chaveng Pakawatchai and Sujittra Youngme

1. Comment

Metal organic frameworks can be prepared in variety methods and there are many effects influencing their structures. The solvent used in preparing is one of the most important effects on the structures. The influence of the solvent on the structure has been widely studied, for example in the study of iron(II) thiocyanato coordination polymers based on 4,4′-bipyridine using methanol as a solvent (Wriedt & Näther, 2010). This finding suggested that if more solvent and higher concentration of N-donor ligand were applied the structure is likely to involve with solvent coordination and the different metal to organic ligand ratio. The solvent has the influence on both metal to organic ligand ratio and the arrangement of the organic linker leading to the variation of the dimension and topology of the network (Yao & Wang, 2009). In addition, the type of N-donor organic linkers also affect the structure (Wriedt & Näther, 2009; Wriedt *et al.*, 2009).

Of interest to us was this effect. A new structure with the different metal to N-donor organic ligand ratio might also be possible by alteration of the solvent, type of N-donor organic ligand, and the metal to N-donor ligand ratio in the preparation. In this contribution, we present synthesis and structural characterization of a two-dimensional framework of poly[μ-tris(4,4′-bipyridine)di(dimethyl sulfoxide)tetrathiocyanato-*N*-dicobalt(II)] (**I**)

The asymmetric unit of the title compound consists of one Co^{II} centre, two SCN^- anions, one and a half 4,4′-bpy molecules and one DMSO molecule (Fig. 1). The Co^{II} is surrounded by two N atoms from terminal SCN^- groups, one O atom from DMSO and three N atoms from three 4,4′-bpy (Table 1). The 4,4′-bpy acts as a bridge linking metal centres and generates a two-dimensional structure with rectangular spaces (11.60 x 23.25 Å) within layer (Fig. 2). Due to the arrangement of the linker and metal to N-donor organic ligand ratio of 1:1.5, the space within the layer is twice as compared to the related two-dimensional compound $\{[Fe(4,4'\text{-bpy})_2(SCN)_2](MeOH)_2\}_n$ (Wriedt & Näther, 2010). The layers are stacked in an ABC fashion (Fig. 3). The plane parallel to the layer is $(\bar{1}03)$. The metal atoms in one layer sit above or below the rectangular spaces. As a result, the terminal SCN^- and DMSO ligands arrange approximately perpendicular to the layer plane and fill up the spaces between adjacent layers. This arrangement of the layers is in the ABC fashion preventing the occurrence of the interlayer spaces along the crystallographic c axis and hence leading to the absence of lattice solvent and/or organic guest molecules in the interlayer spaces (Fig. 3). In addition, the extended structure of **I** has been illustrated (Fig. 4). The hydrogen bonds between H1 and S1 link the layers with the distance of 2.82 Å (Table 2). As a result, these layers are assembled into a three-dimensional supramolecular framework.

2. Experimental

Compound **I** was synthesized by direct method in a molar ratio of 1:3:1 of $Co(NO_3)_2{\cdot}6H_2O$, 4,4′-bpy and KSCN, respectively. To prepare the reaction mixture, $Co(NO_3)_2{\cdot}6H_2O$ (0.5 mmol, 0.15 g) and KSCN (0.5 mmol, 0.05 g) were dissolved in water (10 mL). Then 10 ml of ethanoic solution of 4,4′-bpy (1.5 mmol, 0.23 g) was added. The mixture was stirred, then 10 mL of DMSO and 0.5 mL of 6 M HNO_3 was slowly added to assist dissolution.The mixture was then

heated at 60 °C for 15 mins. It was set at room temperature for a slow evaporation. After 15 days, pink crystals were obtained.

3. Refinement

C-bound H atoms were positioned geometrically, with C—H = 0.93 (aromatic) or 0.96 Å (methyl), and included as riding atoms, with U_{iso}(H) = 1.5U_{eq} (C) for methyl groups and 1.2U_{eq}(C) otherwise.

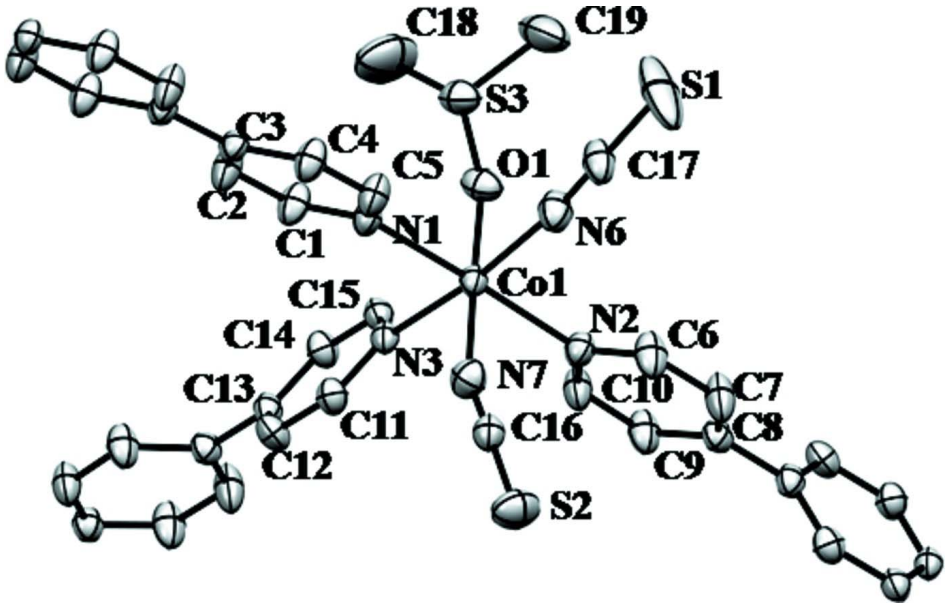

Figure 1

A view of the local coordination of the Co^{II} in the title compound, showing the atom-numbering scheme. Displacement ellipsoids are drawn at the 50% probability level. Hydrogen atoms are omitted for clarity.

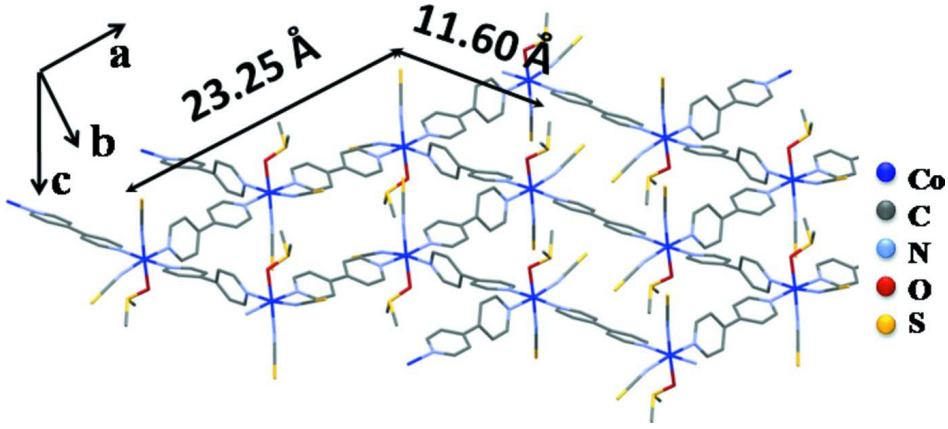

Figure 2

A partial packing diagram of the title compound, showing the two-dimensional structure *via* 4,4′-bpy bridges generating rectangular spaces.

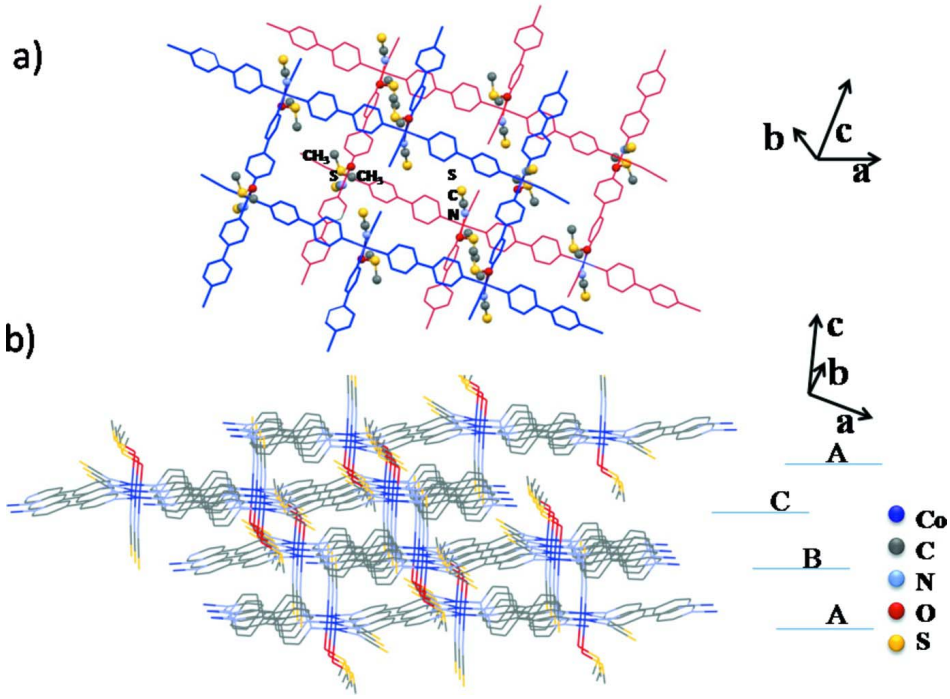

Figure 3

A partial packing diagram of the title compound, showing that terminal ligands, DMSO and SCN^- fill up the rectangular space of adjacent layer (*a*) and ABC arrangement structure layers prevent the occurrence of the channel along C axis (*b*).

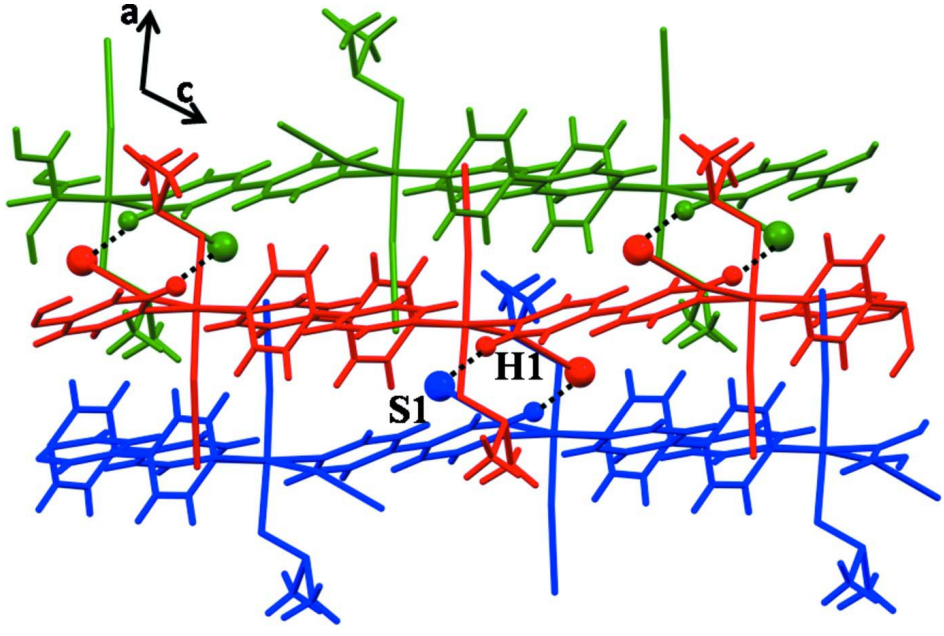

Figure 4

The extended structure of the title compound illustrates the hydrogen bonds (dotted lines) between H1 and S1 (-*x* + 3/2, *y* - 1/2, -*z* + 1/2) linking two-dimensional layers leading to a three-dimensional supramolecular framework. The adjacent layers are shown in different colours.

Poly[tris(μ-4,4′-bipyridine-κ²*N*:*N*′)bis(dimethyl sulfoxide-κ*O*)tetrakis(thiocyanato-κ*N*)dicobalt(II)]

Crystal data

$[Co_2(NCS)_4(C_{10}H_8N_2)_3(C_2H_6OS)_2]$
M_r = 974.98
Monoclinic, $P2_1/n$
Hall symbol: -P 2yn
a = 11.0772 (3) Å
b = 16.9999 (2) Å
c = 11.6843 (3) Å
β = 103.628 (1)°
V = 2138.34 (8) Å^3
Z = 2
$F(000)$ = 1000
D_x = 1.514 Mg m^{-3}
Mo $K\alpha$ radiation, λ = 0.71073 Å
μ = 1.12 mm^{-1}
T = 273 K
Block, pink
0.40 × 0.16 × 0.10 mm

Data collection

Bruker SMART APEX CCD diffractometer
Radiation source: fine-focus sealed tube
Graphite monochromator
phi and ω scans
Absorption correction: multi-scan (*SADABS*; Bruker, 2000)
T_{min} = 0.591, T_{max} = 0.894
14262 measured reflections
5584 independent reflections
3936 reflections with $I > 2\sigma(I)$
R_{int} = 0.032
θ_{max} = 29.8°, θ_{min} = 2.2°
h = −14→14
k = −16→22
l = −12→15

Refinement

Refinement on F^2
Least-squares matrix: full
$R[F^2 > 2\sigma(F^2)]$ = 0.043
$wR(F^2)$ = 0.109
S = 1.01
5584 reflections
264 parameters
0 restraints
Primary atom site location: structure-invariant direct methods
Secondary atom site location: difference Fourier map
Hydrogen site location: inferred from neighbouring sites
H-atom parameters constrained
$w = 1/[\sigma^2(F_o^2) + (0.0522P)^2 + 1.1491P]$ where $P = (F_o^2 + 2F_c^2)/3$
$(\Delta/\sigma)_{max} < 0.001$
$\Delta\rho_{max}$ = 1.02 e Å^{-3}
$\Delta\rho_{min}$ = −0.58 e Å^{-3}

Special details

Geometry. All e.s.d.'s (except the e.s.d. in the dihedral angle between two l.s. planes) are estimated using the full covariance matrix. The cell e.s.d.'s are taken into account individually in the estimation of e.s.d.'s in distances, angles and torsion angles; correlations between e.s.d.'s in cell parameters are only used when they are defined by crystal symmetry. An approximate (isotropic) treatment of cell e.s.d.'s is used for estimating e.s.d.'s involving l.s. planes.

Refinement. Refinement of F^2 against ALL reflections. The weighted R-factor wR and goodness of fit S are based on F^2, conventional R-factors R are based on F, with F set to zero for negative F^2. The threshold expression of $F^2 > \sigma(F^2)$ is used only for calculating R-factors(gt) *etc*. and is not relevant to the choice of reflections for refinement. R-factors based on F^2 are statistically about twice as large as those based on F, and R- factors based on ALL data will be even larger.

Fractional atomic coordinates and isotropic or equivalent isotropic displacement parameters (Å²)

	x	*y*	*z*	U_{iso}*/U_{eq}
Co1	0.61610 (3)	0.238576 (18)	0.34507 (3)	0.02619 (10)
S3	0.74846 (7)	0.21001 (5)	0.14197 (7)	0.04276 (18)
S2	0.57089 (8)	0.31500 (5)	0.72918 (8)	0.0535 (2)
S1	0.93773 (9)	0.42788 (7)	0.32672 (16)	0.1102 (6)
N3	0.47394 (17)	0.14430 (11)	0.30393 (18)	0.0268 (4)

N2	0.47009 (19)	0.33263 (12)	0.30583 (19)	0.0309 (5)
N1	0.76429 (18)	0.14581 (12)	0.39797 (18)	0.0303 (4)
O1	0.62030 (17)	0.22923 (12)	0.16482 (17)	0.0396 (4)
N7	0.6038 (2)	0.25004 (14)	0.5192 (2)	0.0394 (5)
C15	0.4133 (2)	0.12562 (14)	0.1932 (2)	0.0297 (5)
H15	0.4315	0.1541	0.1314	0.036*
N6	0.7569 (2)	0.32360 (14)	0.3613 (2)	0.0435 (6)
C8	0.2944 (2)	0.45622 (14)	0.2665 (2)	0.0299 (5)
C3	0.9512 (2)	0.03082 (14)	0.4782 (2)	0.0279 (5)
C16	0.5904 (2)	0.27781 (15)	0.6063 (2)	0.0324 (6)
C5	0.8725 (2)	0.16319 (15)	0.4734 (2)	0.0366 (6)
H5	0.8856	0.2149	0.4992	0.044*
C9	0.2624 (2)	0.38055 (16)	0.2287 (3)	0.0404 (7)
H9	0.1813	0.3692	0.1888	0.048*
C2	0.8399 (2)	0.01292 (15)	0.3977 (3)	0.0398 (7)
H2	0.8257	−0.0379	0.3681	0.048*
C11	0.4472 (2)	0.10091 (15)	0.3912 (2)	0.0321 (5)
H11	0.4874	0.1128	0.4685	0.039*
C10	0.3514 (2)	0.32131 (15)	0.2502 (3)	0.0395 (6)
H10	0.3268	0.2708	0.2242	0.047*
C4	0.9657 (2)	0.10903 (15)	0.5153 (2)	0.0376 (6)
H4	1.0382	0.1248	0.5682	0.045*
C1	0.7503 (2)	0.07089 (15)	0.3616 (3)	0.0373 (6)
H1	0.6765	0.0568	0.3092	0.045*
C6	0.5003 (3)	0.40610 (16)	0.3448 (3)	0.0447 (7)
H6	0.5817	0.4157	0.3855	0.054*
C17	0.8323 (3)	0.36663 (17)	0.3468 (3)	0.0437 (7)
C14	0.3251 (2)	0.06625 (15)	0.1664 (2)	0.0319 (5)
H14	0.2842	0.0567	0.0886	0.038*
C7	0.4169 (3)	0.46839 (16)	0.3280 (3)	0.0469 (8)
H7	0.4427	0.5180	0.3576	0.056*
C19	0.7763 (4)	0.2828 (3)	0.0436 (4)	0.0746 (12)
H19A	0.7051	0.2873	−0.0214	0.112*
H19B	0.8476	0.2684	0.0148	0.112*
H19C	0.7914	0.3324	0.0838	0.112*
C18	0.7228 (5)	0.1284 (3)	0.0458 (5)	0.0992 (17)
H18A	0.6943	0.0846	0.0842	0.149*
H18B	0.7989	0.1146	0.0250	0.149*
H18C	0.6611	0.1416	−0.0241	0.149*
C12	0.3626 (2)	0.03931 (15)	0.3716 (2)	0.0344 (6)
H12	0.3487	0.0102	0.4347	0.041*
C13	0.2983 (2)	0.02117 (14)	0.2567 (2)	0.0298 (5)

Atomic displacement parameters (Å²)

	U^{11}	U^{22}	U^{33}	U^{12}	U^{13}	U^{23}
Co1	0.02248 (16)	0.02112 (16)	0.03429 (18)	0.00099 (12)	0.00529 (12)	0.00138 (13)
S3	0.0366 (4)	0.0522 (4)	0.0425 (4)	0.0033 (3)	0.0155 (3)	0.0038 (3)

S2	0.0528 (5)	0.0601 (5)	0.0505 (5)	−0.0048 (4)	0.0179 (4)	−0.0164 (4)
S1	0.0445 (5)	0.0713 (7)	0.1993 (16)	−0.0200 (5)	−0.0023 (7)	0.0688 (9)
N3	0.0229 (9)	0.0205 (10)	0.0362 (11)	0.0000 (7)	0.0053 (8)	0.0014 (8)
N2	0.0276 (10)	0.0266 (11)	0.0374 (12)	0.0033 (8)	0.0055 (9)	−0.0002 (9)
N1	0.0289 (10)	0.0263 (10)	0.0344 (11)	0.0059 (8)	0.0049 (8)	0.0017 (9)
O1	0.0297 (9)	0.0504 (12)	0.0399 (10)	−0.0013 (8)	0.0105 (8)	0.0048 (9)
N7	0.0391 (12)	0.0393 (13)	0.0380 (12)	0.0040 (10)	0.0054 (10)	0.0015 (10)
C15	0.0293 (12)	0.0246 (12)	0.0353 (13)	−0.0024 (9)	0.0075 (10)	0.0040 (10)
N6	0.0340 (12)	0.0319 (12)	0.0631 (16)	−0.0024 (10)	0.0083 (11)	−0.0004 (11)
C8	0.0277 (12)	0.0257 (12)	0.0364 (13)	0.0050 (9)	0.0079 (10)	0.0004 (10)
C3	0.0249 (11)	0.0260 (12)	0.0325 (12)	0.0051 (9)	0.0061 (9)	0.0009 (10)
C16	0.0292 (12)	0.0264 (13)	0.0394 (14)	−0.0001 (9)	0.0035 (10)	0.0015 (10)
C5	0.0342 (13)	0.0252 (12)	0.0450 (15)	0.0050 (10)	−0.0017 (11)	−0.0053 (11)
C9	0.0274 (13)	0.0291 (13)	0.0589 (18)	0.0036 (10)	−0.0012 (12)	−0.0063 (12)
C2	0.0325 (13)	0.0233 (12)	0.0560 (17)	0.0040 (10)	−0.0048 (12)	−0.0074 (12)
C11	0.0326 (13)	0.0286 (13)	0.0339 (13)	−0.0028 (10)	0.0053 (10)	0.0004 (10)
C10	0.0334 (13)	0.0227 (12)	0.0579 (18)	0.0029 (10)	0.0018 (12)	−0.0071 (12)
C4	0.0316 (13)	0.0296 (14)	0.0452 (15)	0.0038 (10)	−0.0037 (11)	−0.0054 (11)
C1	0.0263 (12)	0.0303 (13)	0.0491 (16)	0.0044 (10)	−0.0032 (11)	−0.0042 (12)
C6	0.0273 (13)	0.0306 (14)	0.069 (2)	0.0041 (10)	−0.0027 (13)	−0.0075 (13)
C17	0.0301 (13)	0.0312 (14)	0.0650 (19)	0.0001 (11)	0.0015 (13)	0.0108 (13)
C14	0.0309 (12)	0.0299 (13)	0.0326 (13)	−0.0054 (10)	0.0029 (10)	0.0001 (10)
C7	0.0348 (14)	0.0253 (13)	0.073 (2)	0.0028 (11)	−0.0029 (14)	−0.0119 (13)
C19	0.063 (2)	0.088 (3)	0.086 (3)	0.014 (2)	0.044 (2)	0.039 (2)
C18	0.111 (4)	0.095 (4)	0.109 (4)	−0.019 (3)	0.059 (3)	−0.054 (3)
C12	0.0374 (14)	0.0312 (13)	0.0352 (14)	−0.0073 (11)	0.0097 (11)	0.0056 (11)
C13	0.0259 (12)	0.0223 (12)	0.0411 (14)	−0.0025 (9)	0.0076 (10)	0.0002 (10)

Geometric parameters (Å, º)

Co1—N7	2.080 (2)	C3—C3^{ii}	1.506 (4)
Co1—N6	2.102 (2)	C5—C4	1.384 (3)
Co1—O1	2.1234 (19)	C5—H5	0.9300
Co1—N3	2.2187 (19)	C9—C10	1.390 (4)
Co1—N2	2.244 (2)	C9—H9	0.9300
Co1—N1	2.2551 (19)	C2—C1	1.392 (3)
S3—O1	1.5401 (19)	C2—H2	0.9300
S3—C19	1.765 (4)	C11—C12	1.388 (3)
S3—C18	1.766 (4)	C11—H11	0.9300
S2—C16	1.629 (3)	C10—H10	0.9300
S1—C17	1.623 (3)	C4—H4	0.9300
N3—C11	1.347 (3)	C1—H1	0.9300
N3—C15	1.348 (3)	C6—C7	1.388 (4)
N2—C10	1.336 (3)	C6—H6	0.9300
N2—C6	1.344 (3)	C14—C13	1.391 (4)
N1—C1	1.340 (3)	C14—H14	0.9300
N1—C5	1.343 (3)	C7—H7	0.9300
N7—C16	1.163 (4)	C19—H19A	0.9600

C15—C14	1.388 (3)	C19—H19B	0.9600
C15—H15	0.9300	C19—H19C	0.9600
N6—C17	1.152 (4)	C18—H18A	0.9600
C8—C9	1.379 (4)	C18—H18B	0.9600
C8—C7	1.393 (4)	C18—H18C	0.9600
C8—C13^{i}	1.489 (3)	C12—C13	1.398 (4)
C3—C4	1.396 (3)	C12—H12	0.9300
C3—C2	1.396 (3)	C13—C8^{iii}	1.489 (3)
N7—Co1—N6	93.76 (10)	C10—C9—H9	120.0
N7—Co1—O1	177.34 (8)	C1—C2—C3	120.2 (2)
N6—Co1—O1	87.22 (9)	C1—C2—H2	119.9
N7—Co1—N3	94.19 (9)	C3—C2—H2	119.9
N6—Co1—N3	171.85 (9)	N3—C11—C12	123.3 (2)
O1—Co1—N3	84.91 (7)	N3—C11—H11	118.4
N7—Co1—N2	85.58 (8)	C12—C11—H11	118.4
N6—Co1—N2	90.69 (8)	N2—C10—C9	123.9 (2)
O1—Co1—N2	91.94 (8)	N2—C10—H10	118.0
N3—Co1—N2	91.71 (7)	C9—C10—H10	118.0
N7—Co1—N1	90.49 (8)	C5—C4—C3	120.1 (2)
N6—Co1—N1	88.83 (8)	C5—C4—H4	119.9
O1—Co1—N1	92.00 (8)	C3—C4—H4	119.9
N3—Co1—N1	89.30 (7)	N1—C1—C2	123.8 (2)
N2—Co1—N1	176.00 (8)	N1—C1—H1	118.1
O1—S3—C19	105.89 (15)	C2—C1—H1	118.1
O1—S3—C18	105.07 (18)	N2—C6—C7	123.8 (2)
C19—S3—C18	99.4 (3)	N2—C6—H6	118.1
C11—N3—C15	116.7 (2)	C7—C6—H6	118.1
C11—N3—Co1	120.20 (16)	N6—C17—S1	179.5 (3)
C15—N3—Co1	123.09 (16)	C15—C14—C13	119.6 (2)
C10—N2—C6	115.9 (2)	C15—C14—H14	120.2
C10—N2—Co1	125.18 (17)	C13—C14—H14	120.2
C6—N2—Co1	118.89 (17)	C6—C7—C8	119.6 (2)
C1—N1—C5	115.8 (2)	C6—C7—H7	120.2
C1—N1—Co1	123.75 (16)	C8—C7—H7	120.2
C5—N1—Co1	120.37 (16)	S3—C19—H19A	109.5
S3—O1—Co1	115.11 (11)	S3—C19—H19B	109.5
C16—N7—Co1	161.0 (2)	H19A—C19—H19B	109.5
N3—C15—C14	123.6 (2)	S3—C19—H19C	109.5
N3—C15—H15	118.2	H19A—C19—H19C	109.5
C14—C15—H15	118.2	H19B—C19—H19C	109.5
C17—N6—Co1	166.3 (3)	S3—C18—H18A	109.5
C9—C8—C7	116.7 (2)	S3—C18—H18B	109.5
C9—C8—C13^{i}	121.3 (2)	H18A—C18—H18B	109.5
C7—C8—C13^{i}	122.0 (2)	S3—C18—H18C	109.5
C4—C3—C2	115.8 (2)	H18A—C18—H18C	109.5
C4—C3—C3^{ii}	122.5 (3)	H18B—C18—H18C	109.5
C2—C3—C3^{ii}	121.7 (3)	C11—C12—C13	119.8 (2)

N7—C16—S2	178.9 (3)	C11—C12—H12	120.1
N1—C5—C4	124.2 (2)	C13—C12—H12	120.1
N1—C5—H5	117.9	C14—C13—C12	117.1 (2)
C4—C5—H5	117.9	C14—C13—C8^{iii}	122.2 (2)
C8—C9—C10	120.0 (2)	C12—C13—C8^{iii}	120.8 (2)
C8—C9—H9	120.0		

N7—Co1—N3—C11	−21.36 (19)	N3—Co1—N7—C16	−124.4 (7)
N6—Co1—N3—C11	145.8 (5)	N2—Co1—N7—C16	−33.0 (7)
O1—Co1—N3—C11	161.15 (19)	N1—Co1—N7—C16	146.2 (7)
N2—Co1—N3—C11	−107.05 (18)	C11—N3—C15—C14	1.3 (4)
N1—Co1—N3—C11	69.08 (18)	Co1—N3—C15—C14	179.32 (19)
N7—Co1—N3—C15	160.68 (19)	N7—Co1—N6—C17	180.0 (10)
N6—Co1—N3—C15	−32.1 (7)	O1—Co1—N6—C17	−2.5 (10)
O1—Co1—N3—C15	−16.81 (19)	N3—Co1—N6—C17	12.8 (14)
N2—Co1—N3—C15	74.99 (19)	N2—Co1—N6—C17	−94.4 (10)
N1—Co1—N3—C15	−108.88 (19)	N1—Co1—N6—C17	89.5 (10)
N7—Co1—N2—C10	−107.9 (2)	C1—N1—C5—C4	−1.1 (4)
N6—Co1—N2—C10	158.4 (2)	Co1—N1—C5—C4	176.5 (2)
O1—Co1—N2—C10	71.1 (2)	C7—C8—C9—C10	−1.5 (4)
N3—Co1—N2—C10	−13.8 (2)	C13^{i}—C8—C9—C10	179.1 (3)
N1—Co1—N2—C10	−118.5 (11)	C4—C3—C2—C1	−1.7 (4)
N7—Co1—N2—C6	69.0 (2)	C3^{ii}—C3—C2—C1	178.4 (3)
N6—Co1—N2—C6	−24.8 (2)	C15—N3—C11—C12	0.4 (4)
O1—Co1—N2—C6	−112.0 (2)	Co1—N3—C11—C12	−177.7 (2)
N3—Co1—N2—C6	163.0 (2)	C6—N2—C10—C9	2.0 (4)
N1—Co1—N2—C6	58.4 (12)	Co1—N2—C10—C9	178.9 (2)
N7—Co1—N1—C1	116.1 (2)	C8—C9—C10—N2	−0.6 (5)
N6—Co1—N1—C1	−150.2 (2)	N1—C5—C4—C3	0.7 (5)
O1—Co1—N1—C1	−63.0 (2)	C2—C3—C4—C5	0.7 (4)
N3—Co1—N1—C1	21.9 (2)	C3^{ii}—C3—C4—C5	−179.4 (3)
N2—Co1—N1—C1	126.6 (11)	C5—N1—C1—C2	0.1 (4)
N7—Co1—N1—C5	−61.4 (2)	Co1—N1—C1—C2	−177.5 (2)
N6—Co1—N1—C5	32.4 (2)	C3—C2—C1—N1	1.4 (5)
O1—Co1—N1—C5	119.5 (2)	C10—N2—C6—C7	−1.4 (5)
N3—Co1—N1—C5	−155.6 (2)	Co1—N2—C6—C7	−178.5 (3)
N2—Co1—N1—C5	−50.8 (12)	N3—C15—C14—C13	−1.8 (4)
C19—S3—O1—Co1	−127.1 (2)	N2—C6—C7—C8	−0.6 (5)
C18—S3—O1—Co1	128.3 (2)	C9—C8—C7—C6	2.0 (5)
N7—Co1—O1—S3	167.2 (18)	C13^{i}—C8—C7—C6	−178.6 (3)
N6—Co1—O1—S3	55.48 (13)	N3—C11—C12—C13	−1.6 (4)
N3—Co1—O1—S3	−122.38 (13)	C15—C14—C13—C12	0.5 (4)
N2—Co1—O1—S3	146.08 (13)	C15—C14—C13—C8^{iii}	−179.4 (2)
N1—Co1—O1—S3	−33.25 (13)	C11—C12—C13—C14	1.1 (4)
N6—Co1—N7—C16	57.4 (7)	C11—C12—C13—C8^{iii}	−179.0 (2)
O1—Co1—N7—C16	−54 (2)		

Symmetry codes: (i) −*x*+1/2, *y*+1/2, −*z*+1/2; (ii) −*x*+2, −*y*, −*z*+1; (iii) −*x*+1/2, *y*−1/2, −*z*+1/2.

Hydrogen-bond geometry (Å, º)

D—H···*A*	*D*—H	H···*A*	*D*···*A*	*D*—H···*A*
C1—H1···S1^{iv}	0.93	2.82	3.596 (3)	141

Symmetry code: (iv) −*x*+3/2, *y*−1/2, −*z*+1/2.

Acta Cryst E STRUCTURE REPORTS

ISSN 1600-5368

Received 1 July 2014
Accepted 13 July 2014

Edited by A. Van der Lee, Université de Montpellier II, France

Keywords: metal–organic framework; dicyanoargentate(I); 1,2-bis(pyridin-2-yl)ethylene; crystal structure

Supporting information: this article has supporting information at journals.iucr.org/e

Crystal structure of a two-dimensional grid-type iron(II) coordination polymer: poly[[diaquatetra-μ-cyanido-diargentate(I)iron(II)] *trans*-1,2-bis(pyridin-2-yl)ethylene disolvate]

Jintana Othong,[a] Nanthawat Wannarit,[b] Chaveng Pakawatchai[c] and Sujittra Youngme[a]*

[a]Materials Chemistry Research Center, Department of Chemistry and Center of Excellence for Innovation in Chemistry, Faculty of Science, Khon Kaen University, Khon Kean 40002, Thailand, [b]Department of Chemistry, Faculty of Science and Technology, Thammasat University, Rangsit Campus, Klong Luang, Pathumthani 12121, Thailand, and [c]Department of Chemistry, Faculty of Science, Prince of Songkla University, Hat Yai, Songkhla 90112, Thailand. *Correspondence e-mail: sujittra@kku.ac.th

In the title compound, $\{[Ag_2Fe(CN)_4(H_2O)_2]\cdot 2C_{12}H_{10}N_2\}_n$, the asymmetric unit contains one Fe^{II} cation, two water molecules, two dicyanidoargentate(I) anions and two uncoordinating 1,2-bis(pyridin-2-yl)ethylene (2,2′-bpe) molecules. Each Fe^{II} atom is six-coordinated in a nearly regular octahedral geometry by four N atoms from dicyanidoargentate(I) bridges and two coordinating water molecules. The Fe^{II} atoms are bridged by dicyanidoargentate(I) units to give a two-dimensional layer with square-grid spaces. The intergrid spaces with interlayer distance of 6.550 (2) Å are occupied by 2,2′-bpe guest molecules which form O—H···N hydrogen bonds to the host layers. This leads to an extended three-dimensional supramolecular architecture. The structure of the title compound is compared with some related compounds containing dicyanidoargentate(I) ligands and N-donor organic co-ligands.

1. Chemical context

Metal–organic frameworks (MOFs) have attracted much attention because of their versatile topologies and dimensions. These structural properties lead to potential interesting applications in the filed of magnetism, sensing, porous materials and catalysis (Biswas *et al.*, 2014; Horike *et al.*, 2008; Sanda *et al.*, 2013). Structural diversity in MOFs can occur as a result of various preparation methods. However, supramolecular chemistry and topologies of MOFs are rather controlled by the nature of the metal ions and the structure of the organic ligands (Yang *et al.*, 2008).

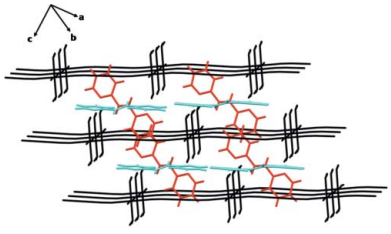

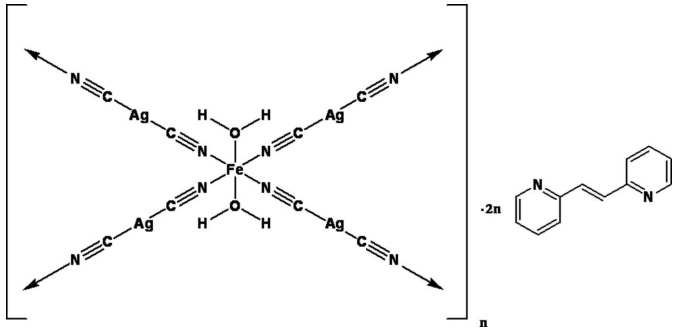

One-, two- and three-dimensional frameworks containing dicyanidoargentate(I) and N-donor linkers such as pyrazine, 4,4′-bpy and 4,4′-bpe [bpy is bipyridineand bpe is 1,2-bis(4-pyridyl)ethylene] ligands have been studied (Soma &

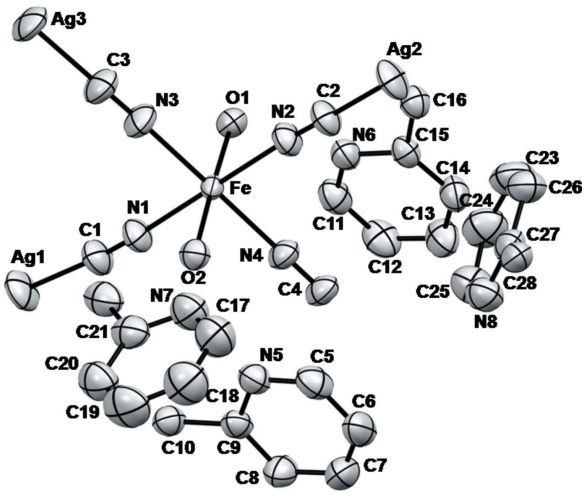

Figure 1
A view of the asymmetric unit in (I), showing displacement ellipsoids at the 50% probability level and the atom-numbering scheme. H atoms have been omitted for clarity.

Iwamoto, 1996; Munoz *et al.*, 2007; Dong *et al.*, 2003). Whereas 4,4′-bpe appears to be somewhat ubiquitous in cyanido compounds, its cousin 2,2′-bpe is not very often used, which led us to prepare a dicyanidoargentate(I) compound with a 2,2′-bpe ligand. In this communication, we report the synthesis and crystal structure of a three-dimensional supramolecular framework of $\{[Ag_2Fe(CN)_4(H_2O)_2]\cdot 2C_{12}H_{10}N_2\}_n$, (I).

2. Structural commentary

The asymmetric unit consists of one Fe^{II} atom, two dicyanidoargentate(I) ligands, two water molecules and two uncoordinating 2,2′-bpe molecules (Fig. 1). Ag1 and Ag2 are situated on inversion centres. The dicyanidoargentate(I) ligands link Fe^{II} atoms into an infinite two-dimensional layer network with a nearly square-grid geometry of 10.66 × 10.64 $Å^2$ (Fig. 2). The Fe^{II} ion is six-cooordinated (Table 1) in a nearly regular octahedral geometry by four N atoms from four dicyanidoargentate(I) ligands and two water molecules.

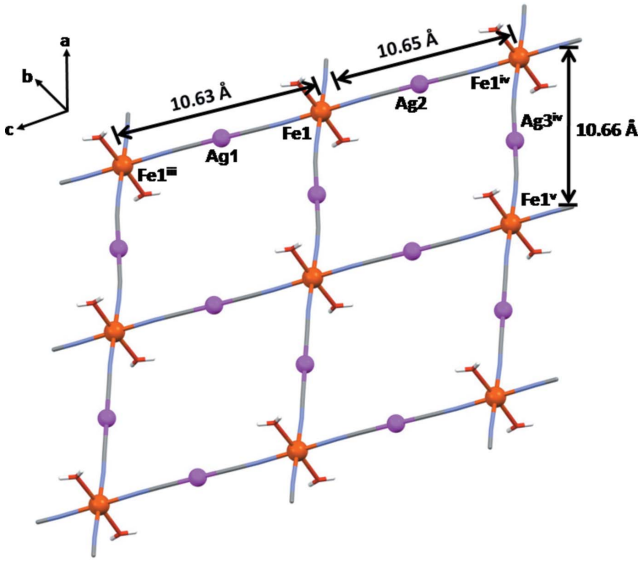

Figure 2
A view of the square grid of (I) in the *ac* plane; the 2,2′-bpe molecules have been omitted. [Symmetry codes: (iii) $-x+1, -y+2, z$; (iv) $-x, -y+1, -z+1$; (v) $-x+1, -y, -z+1$.]

Table 1
Selected bond lengths (Å).

Fe—O1	2.1365 (15)	Fe—N4	2.1489 (16)
Fe—O2	2.1392 (16)	Fe—N2	2.1522 (16)
Fe—N1	2.1440 (17)	Fe—N3	2.1539 (17)

Table 2
Hydrogen-bond geometry (Å, °).

D—H···A	D—H	H···A	D···A	D—H···A
O1—H2*W*···N5	0.76 (3)	2.07 (3)	2.829 (2)	174 (2)
O2—H4*W*···N6	0.73 (3)	2.09 (3)	2.823 (3)	174 (3)
O1—H1*W*···N7^{i}	0.75 (3)	2.14 (3)	2.870 (3)	164
O2—H3*W*···N8^{ii}	0.74 (3)	2.15 (3)	2.868 (3)	162

Symmetry codes: (i) $x-1, y, z$; (ii) $x, y+1, z$.

3. Supramolecular features

Four independent 2,2′-bpe molecules are located between adjacent grid layers of which two are parallel (blue) to the grid layers and two non-parallel (red) (Fig. 3). The interlayer distance is 6.550 (2) Å. The two parallel 2,2′-bpe ligands form hydrogen bonds (Table 2) to the host layer (O1—H2*W*···N5 = 2.07 Å and O2–H4*W*···N6 = 2.09 Å) (Fig. 4*a*), while the other two arrange themselves across the host layer to form also hydrogen bonds (O1—H1*W*···N7 = 2.14 Å and O2—H3*W*···N8 = 2.15 Å) (Fig. 4*b*) to the host layers. These hydrogen bonds generate an extended three-dimensional supramolecular framework.

4. Database survey

The two-dimensional structure of (I) was found to be different from other closely related compounds. In the structure of $[Cd(imH)_4[Ag(CN)_2]_2]_n$ (imH = imidazole), a one-dimen-

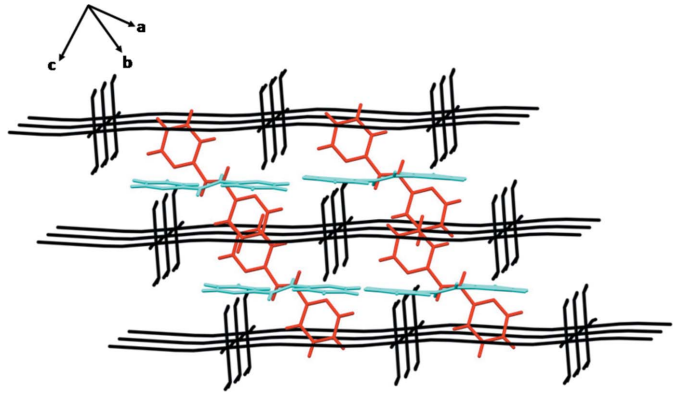

Figure 3
2,2′-Bpe in parallel (blue) and non-parallel (red) fashion between adjacent layers.

Table 3
Experimental details.

Crystal data	
Chemical formula	$[Ag_2Fe(CN)_4(H_2O)_2]\cdot 2C_{12}H_{10}N_2$
M_r	776.14
Crystal system, space group	Triclinic, $P\overline{1}$
Temperature (K)	293
a, b, c (Å)	9.2078 (4), 9.8558 (5), 18.9029 (9)
α, β, γ (°)	77.667 (1), 77.507 (1), 67.900 (1)
V (Å^3)	1535.11 (13)
Z	2
Radiation type	Mo $K\alpha$
μ (mm^{-1})	1.77
Crystal size (mm)	0.43 × 0.11 × 0.09
Data collection	
Diffractometer	Bruker SMART CCD area detector
Absorption correction	Multi-scan (*SADABS*; Bruker, 2007)
T_{min}, T_{max}	0.684, 1.000
No. of measured, independent and observed [$I > 2\sigma(I)$] reflections	21143, 7389, 5865
R_{int}	0.024
(sin $\theta/\lambda)_{max}$ (Å^{-1})	0.661
Refinement	
$R[F^2 > 2\sigma(F^2)]$, $wR(F^2)$, S	0.029, 0.073, 1.03
No. of reflections	7389
No. of parameters	389
H-atom treatment	H atoms treated by a mixture of independent and constrained refinement
$\Delta\rho_{max}$, $\Delta\rho_{min}$ (e Å^{-3})	0.32, −0.37

Computer programs: *SMART* and *SAINT* (Bruker, 2007), *SHELXS97* and *SHELXL97* (Sheldrick, 2008), *Mercury* (Macrae *et al.*, 2008) and *publCIF* (Westrip, 2010).

sional chain *via* bridging dicyanidoargentate(I) is found, while all imidazole molecules act as a terminal ligand (Takayoshi & Toschitake, 1996). In addition, the two-dimensional framework of $[Fe(3\text{-Fpy})_2[Ag(CN)_2]_2]_n$ (3-Fpy = 3-fluoropyridine) consists of four cyanide moieties occupying the equatorial positions generating a square grid-type structure similar to that of the title compound, while the axial positions are occupied by two terminal 3-Fpy ligands instead of two water molecules in (I) (Munoz *et al.*, 2007). When the terminal ligands such as imH and 3-Fpy are replaced by N-donor linkers such as pyrazine, 4,4′-bpy and 4,4′-bpe, three-dimensional interpenetrating frameworks are obtained, as in $\{[Fe(pz)[Ag(CN)_2]_2].pz\}_n$ (pz = pyrazine), $[Mn(4,4'\text{-bpy})_2[Ag(CN)_2]_2]_n$, $[Fe(4,4'\text{-bpy})_2[Ag(CN)_2]_2]_n$ and $[Fe(bpe)_2[Ag(CN)_2]_2]_n$ (Niel *et al.*, 2002; Dong *et al.*, 2003). The last compound contains bpe bridges, while in the title compound 2,2′-bpe behaves as the organic guest molecules in the lattice. This could be the result of the difference in the N-donor position.

5. Synthesis and crystallization

An aqueous solution (5 ml) of $K[Ag(CN)_2]$ (0.0995 g, 0.5 mmol) was added dropwise to an MeOH–H_2O mixed solution (1:1 *v*/*v*, 10 ml) of $(NH_4)_2[Fe(SO_4)_2]\cdot 6H_2O$ (0.0980 g, 0.25 mmol) and 2,2′-bpe (0.0911 g, 0.5 mmol) at room temperature. After filtration and slow evaporation for 1 d, yellow crystals were obtained.

6. Refinement details

Crystal data, data collection and structure refinement details are summarized in Table 3. C-bound H atoms were positioned geometrically and included as riding atoms, with aromatic C—H = 0.93 Å and U_{iso}(H) = 1.2U_{eq}(C). Water H atoms were located in difference Fourier maps and refined isotropically.

Acknowledgements

The authors gratefully acknowledge The Thailand Research Fund (BRG5680009), the Higher Education Research Promotion and National Research University Project of Thailand, through the Advanced Functional Materials Cluster of Khon Kaen University, and the center of Excellence for Innovation in Chemistry (PERCH–CIC), Office of the Higher Education Commission, Ministry of Education, Thailand, for financial support.

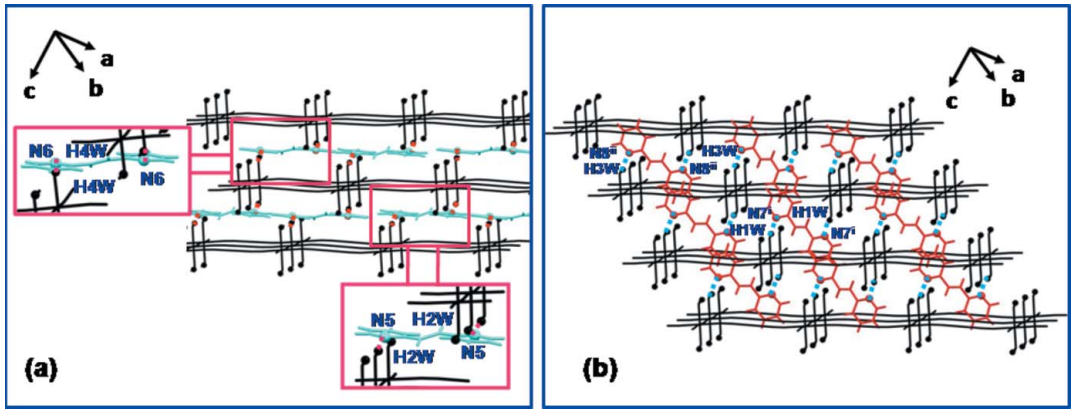

Figure 4
A fragment of the three-dimensional supramolecular framework *via* N···H—O hydrogen-bonding interactions between (*a*) parallel 2,2′-bpe and coordinating water molecules (dashed lines), and (*b*) non-parallel 2,2′-bpe and coordinating water molecules (dashed lines). [Symmetry codes: (i) $x-1$, y, z; (ii) x, $y+1$, z.]

References

Biswas, A., Jana, S. S., Sparkes, H. A., Howard, J. A., Alcalde, N. A. & Mohanta, S. (2014). *Polyhedron*, **74**, 57–66.

Bruker (2007). *SMART*, *SAINT*, and *SADABS*. Bruker AXS Inc., Madison, Wisconsin, USA.

Dong, W., Wang, Q. L., Si, S. F., Liao, D. Z., Jiang, Z. H., Yan, S. P. & Cheng, P. (2003). *Inorg. Chem. Commun.* **6**, 873–876.

Horike, S., Dinca, M., Tamaki, K. & Long, J. R. (2008). *J. Am. Chem. Soc.*, **130**, 5854–5855.

Macrae, C. F., Bruno, I. J., Chisholm, J. A., Edgington, P. R., McCabe, P., Pidcock, E., Rodriguez-Monge, L., Taylor, R., van de Streek, J. & Wood, P. A. (2008). *J. Appl. Cryst.* **41**, 466–470.

Munoz, M. C., Gasper, A. B., Galet, A. & Real, J. A. (2007). *Inorg. Chem.* **46**, 8182–8192.

Niel, V., Munoz, M. C., Gasper, A. B., Galet, A., Levchenko, G. & Real, J. A. (2002). *Chem. Eur. J.* **11**, 2446–2453.

Sanda, S., Parshamoni, S. & Konar, S. (2013). *Cryst. Growth Des.* **13**, 5442–5449.

Sheldrick, G. M. (2008). *Acta Cryst.* A**64**, 112–122.

Soma, T. & Iwamoto, T. (1996). *Inorg. Chem.* **35**, 1849–1856.

Westrip, S. P. (2010). *J. Appl. Cryst.* **43**, 920–925.

Yang, J., Chen, Y. B., Li, Z. J., Qin, Y. Y. & Yao, Y. G. (2008). *Chem. Commun.* **19**, 2233–2235.

supporting information

Acta Cryst. (2014). E**70**, 107-110 [doi:10.1107/S1600536814016250]

Crystal structure of a two-dimensional grid-type iron(II) coordination polymer: poly[[diaquatetra-μ-cyanido-diargentate(I)iron(II)] *trans*-1,2-bis(pyridin-2-yl)ethylene disolvate]

Jintana Othong, Nanthawat Wannarit, Chaveng Pakawatchai and Sujittra Youngme

Computing details

Data collection: *SMART* (Bruker, 2007); cell refinement: *SMART* (Bruker, 2007); data reduction: *SAINT* (Bruker, 2007); program(s) used to solve structure: *SHELXS97* (Sheldrick, 2008); program(s) used to refine structure: *SHELXL97* (Sheldrick, 2008); molecular graphics: *Mercury* (Macrae *et al.*, 2008); software used to prepare material for publication: *publCIF* (Westrip, 2010).

Poly[[diaquatetra-μ-cyanido-diargentate(I)iron(II)] bis[*trans*-1,2-bis(pyridin-2-yl)ethylene]]

Crystal data

$[Ag_2Fe(CN)_4(H_2O)_2]\cdot 2C_{12}H_{10}N_2$
M_r = 776.14
Triclinic, $P\overline{1}$
Hall symbol: -P 1
a = 9.2078 (4) Å
b = 9.8558 (5) Å
c = 18.9029 (9) Å
α = 77.667 (1)°
β = 77.507 (1)°
γ = 67.900 (1)°
V = 1535.11 (13) Å^3
Z = 2
F(000) = 768
776.14
D_x = 1.679 Mg m^{-3}
Mo $K\alpha$ radiation, λ = 0.71073 Å
μ = 1.77 mm^{-1}
T = 293 K
Block, yellow
0.43 × 0.11 × 0.09 mm

Data collection

Bruker SMART CCD area-detector diffractometer
Radiation source: fine-focus sealed tube
Graphite monochromator
phi and ω scans
Absorption correction: multi-scan (*SADABS*; Bruker, 2007)
T_{min} = 0.684, T_{max} = 1.000
21143 measured reflections
7389 independent reflections
5865 reflections with $I > 2\sigma(I)$
R_{int} = 0.024
θ_{max} = 28.0°, θ_{min} = 1.1°
h = −12→12
k = −13→13
l = −24→24

Refinement

Refinement on F^2
Least-squares matrix: full
$R[F^2 > 2\sigma(F^2)]$ = 0.029
$wR(F^2)$ = 0.073
S = 1.03
7389 reflections
389 parameters
0 restraints
Primary atom site location: structure-invariant direct methods
Secondary atom site location: difference Fourier map
Hydrogen site location: inferred from neighbouring sites

H atoms treated by a mixture of independent and constrained refinement
$w = 1/[\sigma^2(F_o^2) + (0.0324P)^2 + 0.1941P]$ where $P = (F_o^2 + 2F_c^2)/3$

$(\Delta/\sigma)_{max} = 0.001$
$\Delta\rho_{max} = 0.32$ e Å^{-3}
$\Delta\rho_{min} = -0.37$ e Å^{-3}

Special details

Geometry. All e.s.d.'s (except the e.s.d. in the dihedral angle between two l.s. planes) are estimated using the full covariance matrix. The cell e.s.d.'s are taken into account individually in the estimation of e.s.d.'s in distances, angles and torsion angles; correlations between e.s.d.'s in cell parameters are only used when they are defined by crystal symmetry. An approximate (isotropic) treatment of cell e.s.d.'s is used for estimating e.s.d.'s involving l.s. planes.

Refinement. Refinement of F^2 against ALL reflections. The weighted *R*-factor *wR* and goodness of fit *S* are based on F^2, conventional *R*-factors *R* are based on *F*, with *F* set to zero for negative F^2. The threshold expression of $F^2 > \sigma(F^2)$ is used only for calculating *R*-factors(gt) *etc*. and is not relevant to the choice of reflections for refinement. *R*-factors based on F^2 are statistically about twice as large as those based on *F*, and *R*- factors based on ALL data will be even larger.

Fractional atomic coordinates and isotropic or equivalent isotropic displacement parameters (Å^2)

	x	*y*	*z*	U_{iso}*/U_{eq}
Ag3	−0.235709 (19)	1.239825 (17)	0.249406 (10)	0.06308 (7)
Ag2	0.0000	0.5000	0.5000	0.05956 (8)
Ag1	0.5000	1.0000	0.0000	0.06538 (9)
Fe	0.26653 (3)	0.74083 (2)	0.251508 (12)	0.02989 (7)
O1	0.15978 (19)	0.64325 (19)	0.19630 (8)	0.0437 (3)
O2	0.3821 (2)	0.83190 (18)	0.30581 (9)	0.0440 (3)
N3	0.0604 (2)	0.9394 (2)	0.25270 (11)	0.0562 (5)
N2	0.1689 (2)	0.64872 (19)	0.35630 (9)	0.0476 (4)
N1	0.3633 (2)	0.83204 (19)	0.14683 (9)	0.0497 (4)
N4	0.4711 (2)	0.54179 (18)	0.24955 (10)	0.0453 (4)
N5	0.3585 (2)	0.37522 (19)	0.14391 (9)	0.0472 (4)
N6	0.6565 (2)	0.62355 (18)	0.36001 (9)	0.0446 (4)
N7	0.9350 (3)	0.7412 (3)	0.09581 (12)	0.0717 (6)
C26	0.2054 (3)	0.1175 (3)	0.52221 (14)	0.0675 (7)
H26	0.1402	0.1178	0.5673	0.081*
C3	−0.0459 (3)	1.0458 (3)	0.25155 (14)	0.0618 (6)
C2	0.1135 (3)	0.5943 (2)	0.40815 (11)	0.0508 (5)
C1	0.4140 (3)	0.8860 (3)	0.09364 (11)	0.0541 (5)
C4	0.5760 (2)	0.4344 (2)	0.24875 (12)	0.0494 (5)
C5	0.3629 (3)	0.2536 (3)	0.19190 (12)	0.0577 (6)
H5	0.2794	0.2601	0.2304	0.069*
C6	0.4827 (3)	0.1197 (3)	0.18812 (13)	0.0653 (7)
H6	0.4789	0.0369	0.2220	0.078*
C7	0.6076 (3)	0.1114 (3)	0.13335 (13)	0.0676 (7)
H7	0.6930	0.0232	0.1303	0.081*
C8	0.6063 (3)	0.2340 (2)	0.08276 (12)	0.0569 (6)
H8	0.6908	0.2295	0.0450	0.068*
C9	0.4787 (2)	0.3644 (2)	0.08807 (10)	0.0422 (4)
C10	0.4628 (2)	0.4983 (2)	0.03421 (11)	0.0458 (5)
H10	0.3953	0.5880	0.0492	0.055*
C11	0.7884 (3)	0.6068 (2)	0.31163 (11)	0.0534 (5)

H11	0.7929	0.6865	0.2756	0.064*
C12	0.9174 (3)	0.4796 (3)	0.31178 (13)	0.0596 (6)
H12	1.0074	0.4736	0.2771	0.072*
C13	0.9117 (3)	0.3612 (3)	0.36401 (13)	0.0610 (6)
H13	0.9963	0.2719	0.3646	0.073*
C14	0.7776 (3)	0.3769 (2)	0.41567 (12)	0.0516 (5)
H14	0.7718	0.2984	0.4521	0.062*
C15	0.6523 (2)	0.5092 (2)	0.41323 (10)	0.0405 (4)
C16	0.5075 (2)	0.5375 (2)	0.46672 (11)	0.0442 (5)
H16	0.4180	0.6149	0.4528	0.053*
C17	0.8716 (4)	0.6370 (3)	0.10434 (16)	0.0836 (8)
H17	0.8639	0.5809	0.1504	0.100*
C18	0.8173 (4)	0.6069 (4)	0.05021 (19)	0.0864 (9)
H18	0.7721	0.5338	0.0590	0.104*
C19	0.8315 (4)	0.6881 (4)	−0.01761 (19)	0.0913 (10)
H19	0.7987	0.6689	−0.0564	0.110*
C20	0.8947 (3)	0.7982 (3)	−0.02814 (15)	0.0754 (7)
H20	0.9050	0.8541	−0.0741	0.091*
C21	0.9428 (3)	0.8251 (3)	0.03048 (14)	0.0603 (6)
C22	1.0045 (3)	0.9443 (3)	0.02706 (13)	0.0649 (7)
H22	1.0535	0.9411	0.0658	0.078*
C23	0.3203 (4)	0.1815 (3)	0.50884 (18)	0.0817 (9)
H23	0.3330	0.2257	0.5448	0.098*
C24	0.4143 (4)	0.1796 (3)	0.44306 (17)	0.0782 (8)
H24	0.4900	0.2252	0.4321	0.094*
C25	0.3943 (3)	0.1080 (3)	0.39311 (15)	0.0762 (7)
H25	0.4617	0.1032	0.3486	0.091*
N8	0.2859 (2)	0.0455 (2)	0.40410 (11)	0.0627 (5)
C27	0.1880 (3)	0.0527 (2)	0.46773 (12)	0.0534 (5)
C28	0.0623 (3)	−0.0088 (2)	0.47413 (12)	0.0574 (6)
H28	0.0714	−0.0651	0.4386	0.069*
H1W	0.096 (3)	0.684 (2)	0.1727 (12)	0.044 (7)*
H2W	0.211 (3)	0.574 (3)	0.1795 (13)	0.062 (8)*
H3W	0.339 (3)	0.887 (3)	0.3313 (13)	0.053 (8)*
H4W	0.450 (3)	0.779 (3)	0.3230 (14)	0.062 (9)*

Atomic displacement parameters (Å²)

	U^{11}	U^{22}	U^{33}	U^{12}	U^{13}	U^{23}
Ag3	0.04673 (11)	0.03995 (10)	0.08458 (15)	0.01369 (7)	−0.01787 (10)	−0.01697 (9)
Ag2	0.06824 (17)	0.07681 (18)	0.03192 (12)	−0.03820 (14)	0.00292 (11)	0.00933 (11)
Ag1	0.08051 (19)	0.07607 (18)	0.03474 (13)	−0.03990 (15)	0.00655 (12)	0.01030 (12)
Fe	0.02927 (13)	0.02553 (12)	0.02578 (13)	−0.00351 (10)	0.00002 (10)	−0.00020 (9)
O1	0.0401 (8)	0.0444 (8)	0.0442 (8)	−0.0085 (7)	−0.0104 (7)	−0.0089 (7)
O2	0.0484 (9)	0.0357 (8)	0.0442 (9)	−0.0082 (7)	−0.0085 (7)	−0.0083 (7)
N3	0.0452 (10)	0.0412 (10)	0.0621 (12)	0.0063 (8)	−0.0073 (9)	−0.0065 (9)
N2	0.0514 (10)	0.0524 (10)	0.0336 (9)	−0.0206 (8)	0.0007 (8)	0.0023 (7)
N1	0.0570 (11)	0.0512 (10)	0.0345 (9)	−0.0208 (8)	0.0017 (8)	0.0025 (8)

N4	0.0391 (9)	0.0361 (8)	0.0541 (10)	0.0004 (7)	−0.0125 (8)	−0.0127 (7)
N5	0.0513 (10)	0.0511 (10)	0.0395 (9)	−0.0182 (8)	−0.0043 (8)	−0.0090 (8)
N6	0.0517 (10)	0.0450 (9)	0.0375 (9)	−0.0177 (8)	−0.0080 (8)	−0.0038 (7)
N7	0.0780 (15)	0.0757 (15)	0.0653 (14)	−0.0183 (12)	−0.0273 (12)	−0.0168 (12)
C26	0.0747 (17)	0.0638 (15)	0.0627 (16)	−0.0141 (13)	−0.0104 (13)	−0.0247 (12)
C3	0.0515 (13)	0.0444 (12)	0.0731 (16)	0.0079 (10)	−0.0148 (12)	−0.0148 (11)
C2	0.0566 (13)	0.0598 (13)	0.0332 (11)	−0.0254 (11)	0.0003 (9)	0.0016 (9)
C1	0.0663 (14)	0.0579 (13)	0.0349 (11)	−0.0274 (11)	0.0017 (10)	0.0015 (10)
C4	0.0424 (11)	0.0383 (10)	0.0636 (14)	0.0011 (9)	−0.0189 (10)	−0.0162 (10)
C5	0.0677 (15)	0.0672 (15)	0.0414 (12)	−0.0327 (13)	0.0031 (11)	−0.0089 (11)
C6	0.103 (2)	0.0478 (13)	0.0464 (13)	−0.0329 (14)	−0.0056 (13)	−0.0022 (10)
C7	0.090 (2)	0.0433 (13)	0.0573 (15)	−0.0114 (13)	−0.0043 (14)	−0.0107 (11)
C8	0.0627 (14)	0.0482 (12)	0.0491 (13)	−0.0138 (11)	0.0050 (11)	−0.0087 (10)
C9	0.0516 (12)	0.0421 (10)	0.0383 (11)	−0.0199 (9)	−0.0060 (9)	−0.0105 (8)
C10	0.0500 (12)	0.0423 (11)	0.0462 (11)	−0.0165 (9)	−0.0036 (9)	−0.0108 (9)
C11	0.0642 (14)	0.0580 (13)	0.0425 (12)	−0.0310 (12)	−0.0055 (10)	−0.0008 (10)
C12	0.0448 (12)	0.0818 (17)	0.0503 (13)	−0.0248 (12)	−0.0002 (10)	−0.0073 (12)
C13	0.0452 (12)	0.0687 (16)	0.0562 (14)	−0.0060 (11)	−0.0112 (11)	−0.0042 (12)
C14	0.0489 (12)	0.0544 (12)	0.0428 (12)	−0.0122 (10)	−0.0103 (10)	0.0036 (10)
C15	0.0431 (10)	0.0472 (11)	0.0352 (10)	−0.0190 (9)	−0.0102 (8)	−0.0040 (8)
C16	0.0423 (11)	0.0463 (11)	0.0430 (11)	−0.0141 (9)	−0.0099 (9)	−0.0034 (9)
C17	0.095 (2)	0.084 (2)	0.0752 (19)	−0.0251 (17)	−0.0280 (17)	−0.0129 (16)
C18	0.084 (2)	0.092 (2)	0.096 (2)	−0.0307 (17)	−0.0325 (18)	−0.0203 (19)
C19	0.086 (2)	0.109 (3)	0.092 (2)	−0.0224 (19)	−0.0425 (19)	−0.034 (2)
C20	0.0716 (17)	0.089 (2)	0.0643 (17)	−0.0151 (15)	−0.0242 (14)	−0.0176 (15)
C21	0.0434 (12)	0.0682 (15)	0.0641 (15)	−0.0006 (11)	−0.0167 (11)	−0.0247 (13)
C22	0.0491 (13)	0.0804 (18)	0.0590 (16)	−0.0037 (13)	−0.0168 (12)	−0.0234 (12)
C23	0.094 (2)	0.0747 (19)	0.088 (2)	−0.0216 (17)	−0.0221 (18)	−0.0403 (17)
C24	0.083 (2)	0.0746 (18)	0.090 (2)	−0.0330 (16)	−0.0194 (17)	−0.0229 (16)
C25	0.0807 (19)	0.089 (2)	0.0634 (17)	−0.0311 (16)	−0.0094 (14)	−0.0180 (14)
N8	0.0666 (13)	0.0675 (13)	0.0563 (12)	−0.0171 (11)	−0.0154 (10)	−0.0189 (10)
C27	0.0594 (13)	0.0383 (11)	0.0583 (14)	−0.0029 (10)	−0.0216 (11)	−0.0111 (10)
C28	0.0711 (16)	0.0411 (11)	0.0533 (14)	−0.0038 (11)	−0.0189 (11)	−0.0124 (10)

Geometric parameters (Å, º)

Ag3—C4^{i}	2.0449 (19)	C8—H8	0.9300
Ag3—C3	2.048 (2)	C9—C10	1.465 (3)
Ag2—C2^{ii}	2.056 (2)	C10—C10^{v}	1.326 (4)
Ag2—C2	2.056 (2)	C10—H10	0.9300
Ag1—C1	2.058 (2)	C11—C12	1.364 (3)
Ag1—C1^{iii}	2.058 (2)	C11—H11	0.9300
Fe—O1	2.1365 (15)	C12—C13	1.368 (3)
Fe—O2	2.1392 (16)	C12—H12	0.9300
Fe—N1	2.1440 (17)	C13—C14	1.378 (3)
Fe—N4	2.1489 (16)	C13—H13	0.9300
Fe—N2	2.1522 (16)	C14—C15	1.377 (3)
Fe—N3	2.1539 (17)	C14—H14	0.9300

O1—H1W	0.75 (2)	C15—C16	1.462 (3)
O1—H2W	0.76 (2)	C16—C16^{vi}	1.324 (4)
O2—H3W	0.74 (2)	C16—H16	0.9300
O2—H4W	0.73 (3)	C17—C18	1.360 (4)
N3—C3	1.133 (3)	C17—H17	0.9300
N2—C2	1.129 (3)	C18—C19	1.367 (4)
N1—C1	1.126 (3)	C18—H18	0.9300
N4—C4	1.133 (2)	C19—C20	1.374 (4)
N5—C5	1.333 (3)	C19—H19	0.9300
N5—C9	1.343 (2)	C20—C21	1.386 (3)
N6—C11	1.332 (3)	C20—H20	0.9300
N6—C15	1.347 (2)	C21—C22	1.471 (4)
N7—C17	1.327 (3)	C22—C22^{vii}	1.322 (5)
N7—C21	1.336 (3)	C22—H22	0.9300
C26—C23	1.378 (4)	C23—C24	1.352 (4)
C26—C27	1.387 (3)	C23—H23	0.9300
C26—H26	0.9300	C24—C25	1.371 (3)
C4—Ag3^{iv}	2.0449 (19)	C24—H24	0.9300
C5—C6	1.369 (3)	C25—N8	1.318 (3)
C5—H5	0.9300	C25—H25	0.9300
C6—C7	1.360 (3)	N8—C27	1.335 (3)
C6—H6	0.9300	C27—C28	1.469 (3)
C7—C8	1.369 (3)	C28—C28^{viii}	1.320 (5)
C7—H7	0.9300	C28—H28	0.9300
C8—C9	1.382 (3)		

C4^{i}—Ag3—C3	179.00 (8)	C10^{v}—C10—H10	117.5
C2^{ii}—Ag2—C2	180.000 (1)	C9—C10—H10	117.5
C1—Ag1—C1^{iii}	180.00 (16)	N6—C11—C12	123.8 (2)
O1—Fe—O2	177.77 (6)	N6—C11—H11	118.1
O1—Fe—N1	88.80 (6)	C12—C11—H11	118.1
O2—Fe—N1	90.70 (7)	C11—C12—C13	118.7 (2)
O1—Fe—N4	88.18 (7)	C11—C12—H12	120.7
O2—Fe—N4	89.65 (7)	C13—C12—H12	120.7
N1—Fe—N4	90.30 (7)	C12—C13—C14	118.5 (2)
O1—Fe—N2	90.90 (6)	C12—C13—H13	120.7
O2—Fe—N2	89.60 (6)	C14—C13—H13	120.7
N1—Fe—N2	179.69 (6)	C15—C14—C13	119.9 (2)
N4—Fe—N2	89.68 (7)	C15—C14—H14	120.0
O1—Fe—N3	91.17 (7)	C13—C14—H14	120.0
O2—Fe—N3	91.00 (7)	N6—C15—C14	121.16 (19)
N1—Fe—N3	89.61 (7)	N6—C15—C16	115.02 (17)
N4—Fe—N3	179.35 (6)	C14—C15—C16	123.81 (18)
N2—Fe—N3	90.41 (7)	C16^{vi}—C16—C15	125.7 (2)
Fe—O1—H1W	126.2 (17)	C16^{vi}—C16—H16	117.2
Fe—O1—H2W	119.1 (19)	C15—C16—H16	117.2
H1W—O1—H2W	106 (2)	N7—C17—C18	124.3 (3)
Fe—O2—H3W	123.3 (19)	N7—C17—H17	117.9

Fe—O2—H4W	116 (2)	C18—C17—H17	117.9
H3W—O2—H4W	106 (3)	C17—C18—C19	117.6 (3)
C3—N3—Fe	178.0 (2)	C17—C18—H18	121.2
C2—N2—Fe	174.23 (18)	C19—C18—H18	121.2
C1—N1—Fe	176.22 (19)	C18—C19—C20	119.7 (3)
C4—N4—Fe	177.91 (19)	C18—C19—H19	120.2
C5—N5—C9	117.53 (19)	C20—C19—H19	120.2
C11—N6—C15	117.80 (18)	C19—C20—C21	119.2 (3)
C17—N7—C21	118.4 (2)	C19—C20—H20	120.4
C23—C26—C27	119.3 (3)	C21—C20—H20	120.4
C23—C26—H26	120.4	N7—C21—C20	120.8 (3)
C27—C26—H26	120.4	N7—C21—C22	114.9 (2)
N3—C3—Ag3	179.1 (2)	C20—C21—C22	124.3 (3)
N2—C2—Ag2	176.6 (2)	C22^{vii}—C22—C21	124.8 (3)
N1—C1—Ag1	175.4 (2)	C22^{vii}—C22—H22	117.6
N4—C4—Ag3^{iv}	178.9 (2)	C21—C22—H22	117.6
N5—C5—C6	124.1 (2)	C24—C23—C26	119.5 (3)
N5—C5—H5	118.0	C24—C23—H23	120.2
C6—C5—H5	118.0	C26—C23—H23	120.2
C7—C6—C5	118.0 (2)	C23—C24—C25	117.7 (3)
C7—C6—H6	121.0	C23—C24—H24	121.1
C5—C6—H6	121.0	C25—C24—H24	121.1
C6—C7—C8	119.4 (2)	N8—C25—C24	124.3 (3)
C6—C7—H7	120.3	N8—C25—H25	117.9
C8—C7—H7	120.3	C24—C25—H25	117.9
C7—C8—C9	119.7 (2)	C25—N8—C27	118.2 (2)
C7—C8—H8	120.2	N8—C27—C26	120.8 (2)
C9—C8—H8	120.2	N8—C27—C28	115.41 (19)
N5—C9—C8	121.18 (19)	C26—C27—C28	123.8 (2)
N5—C9—C10	115.36 (18)	C28^{viii}—C28—C27	125.7 (3)
C8—C9—C10	123.46 (19)	C28^{viii}—C28—H28	117.2
C10^{v}—C10—C9	125.1 (2)	C27—C28—H28	117.2

O1—Fe—N3—C3	−98 (7)	C7—C8—C9—C10	−176.4 (2)
O2—Fe—N3—C3	82 (7)	N5—C9—C10—C10^{v}	−158.2 (3)
N1—Fe—N3—C3	−9 (7)	C8—C9—C10—C10^{v}	21.1 (4)
N4—Fe—N3—C3	−91 (9)	C15—N6—C11—C12	1.8 (3)
N2—Fe—N3—C3	172 (7)	N6—C11—C12—C13	0.6 (4)
O1—Fe—N2—C2	6.4 (19)	C11—C12—C13—C14	−2.0 (4)
O2—Fe—N2—C2	−171.4 (19)	C12—C13—C14—C15	1.0 (4)
N1—Fe—N2—C2	5 (14)	C11—N6—C15—C14	−2.8 (3)
N4—Fe—N2—C2	−81.7 (19)	C11—N6—C15—C16	176.90 (17)
N3—Fe—N2—C2	97.6 (19)	C13—C14—C15—N6	1.5 (3)
O1—Fe—N1—C1	153 (3)	C13—C14—C15—C16	−178.2 (2)
O2—Fe—N1—C1	−29 (3)	N6—C15—C16—C16^{vi}	−159.6 (3)
N4—Fe—N1—C1	−119 (3)	C14—C15—C16—C16^{vi}	20.1 (4)
N2—Fe—N1—C1	155 (12)	C21—N7—C17—C18	1.7 (4)
N3—Fe—N1—C1	62 (3)	N7—C17—C18—C19	1.1 (5)

O1—Fe—N4—C4	−34 (5)	C17—C18—C19—C20	−1.9 (5)
O2—Fe—N4—C4	146 (5)	C18—C19—C20—C21	0.0 (5)
N1—Fe—N4—C4	−123 (5)	C17—N7—C21—C20	−3.8 (4)
N2—Fe—N4—C4	57 (5)	C17—N7—C21—C22	176.0 (2)
N3—Fe—N4—C4	−41 (9)	C19—C20—C21—N7	3.0 (4)
Fe—N3—C3—Ag3	−52 (20)	C19—C20—C21—C22	−176.8 (3)
C4^{i}—Ag3—C3—N3	−52 (18)	N7—C21—C22—C22^{vii}	−167.0 (3)
Fe—N2—C2—Ag2	−54 (5)	C20—C21—C22—C22^{vii}	12.9 (5)
C2^{ii}—Ag2—C2—N2	95 (100)	C27—C26—C23—C24	−0.2 (4)
Fe—N1—C1—Ag1	−20 (6)	C26—C23—C24—C25	−2.4 (5)
C1^{iii}—Ag1—C1—N1	−164 (100)	C23—C24—C25—N8	2.5 (5)
Fe—N4—C4—Ag3^{iv}	−78 (13)	C24—C25—N8—C27	0.4 (4)
C9—N5—C5—C6	0.7 (3)	C25—N8—C27—C26	−3.2 (3)
N5—C5—C6—C7	2.2 (4)	C25—N8—C27—C28	175.4 (2)
C5—C6—C7—C8	−2.6 (4)	C23—C26—C27—N8	3.2 (4)
C6—C7—C8—C9	0.2 (4)	C23—C26—C27—C28	−175.4 (2)
C5—N5—C9—C8	−3.3 (3)	N8—C27—C28—C28^{viii}	−167.6 (3)
C5—N5—C9—C10	176.02 (18)	C26—C27—C28—C28^{viii}	11.0 (4)
C7—C8—C9—N5	2.9 (3)		

Symmetry codes: (i) *x*−1, *y*+1, *z*; (ii) −*x*, −*y*+1, −*z*+1; (iii) −*x*+1, −*y*+2, −*z*; (iv) *x*+1, *y*−1, *z*; (v) −*x*+1, −*y*+1, −*z*; (vi) −*x*+1, −*y*+1, −*z*+1; (vii) −*x*+2, −*y*+2, −*z*; (viii) −*x*, −*y*, −*z*+1.

Hydrogen-bond geometry (Å, º)

D—H···*A*	*D*—H	H···*A*	*D*···*A*	*D*—H···*A*
O1—H2*W*···N5	0.76 (3)	2.07 (3)	2.829 (2)	174 (2)
O2—H4*W*···N6	0.73 (3)	2.09 (3)	2.823 (3)	174 (3)
O1—H1*W*···N7^{ix}	0.75 (3)	2.14 (3)	2.870 (3)	164
O2—H3*W*···N8^{x}	0.74 (3)	2.15 (3)	2.868 (3)	162

Symmetry codes: (ix) *x*−1, *y*, *z*; (x) *x*, *y*+1, *z*.

STRUCTURAL CHEMISTRY

ISSN: 2053-2296
journals.iucr.org/c

A novel one-dimensional metal–organic framework with a μ-cyanido-argentate group: *catena*-poly[[(5,5′-dimethyl-2,2′-bipyridyl-κ^2N,N')silver(I)]-μ-cyanido-κ^2N:*C*]

Jureepan Piromchom, Jintana Othong, Jaursup Boonmak, Ilpo Mutikainen and Sujittra Youngme

Acta Cryst. (2015). C**71**, 1057–1061

Acta Cryst C STRUCTURAL CHEMISTRY
ISSN 2053-2296

A novel one-dimensional metal–organic framework with a μ-cyanido-argentate group: *catena*-poly-[[(5,5′-dimethyl-2,2′-bipyridyl-κ^2N,N')silver(I)]-μ-cyanido-κ^2N:*C*]

Jureepan Piromchom,[a] Jintana Othong,[a] Jaursup Boonmak,[a] Ilpo Mutikainen[b] and Sujittra Youngme[a]*

[a]Materials Chemistry Research Center, Department of Chemistry and Center of Excellence for Innovation in Chemistry, Faculty of Science, Khon Kaen University, Khon Kaen 40002, Thailand, and [b]Department of Inorganic Chemistry, Faculty of Science, University of Helsinki, Helsinki, Finland. *Correspondence e-mail: sujittra@kku.ac.th

Received 19 February 2015
Accepted 27 October 2015

Edited by C. S. Frampton, Brunel University, England

Keywords: metal–organic framework; one-dimensional chain; supramolecular architecture; cyanide ligand; crystal structure; silver(I) complex; spectroscopic analysis; thermal stability; powder XRD.

CCDC reference: 1433351

Supporting information: this article has supporting information at journals.iucr.org/c

The design and synthesis of metal coordination and supramolecular frameworks containing *N*-donor ligands and dicyanidoargentate units is of interest due to their potential applications in the fields of molecular magnetism, catalysis, nonlinear optics and luminescence. In the design and synthesis of extended frameworks, supramolecular interactions, such as hydrogen bonding, π–π stacking and van der Waals interactions, have been exploited for molecular recognition associated with biological activity and for the engineering of molecular solids.The title compound, $[Ag(CN)(C_{12}H_{12}N_2)]_n$, crystallizes with the Ag^I cation on a twofold axis, half a cyanide ligand disordered about a centre of inversion and half a twofold-symmetric 5,5′-dimethyl-2,2′-bipyridine (5,5′-dmbpy) ligand in the asymmetric unit. Each Ag^I cation exhibits a distorted tetrahedral geometry; the coordination environment comprises one C(N) atom and one N(C) atom from substitutionally disordered cyanide bridging ligands, and two N atoms from a bidentate chelating 5,5′-dmbpy ligand. The cyanide ligand links adjacent Ag^I cations to generate a one-dimensional zigzag chain. These chains are linked together *via* weak nonclassical intermolecular interactions, generating a two-dimensional supramolecular network.

1. Introduction

The design and synthesis of metal coordination and supramolecular frameworks containing *N*-donor ligands and dicyanidoargentate units is currently an active area of research

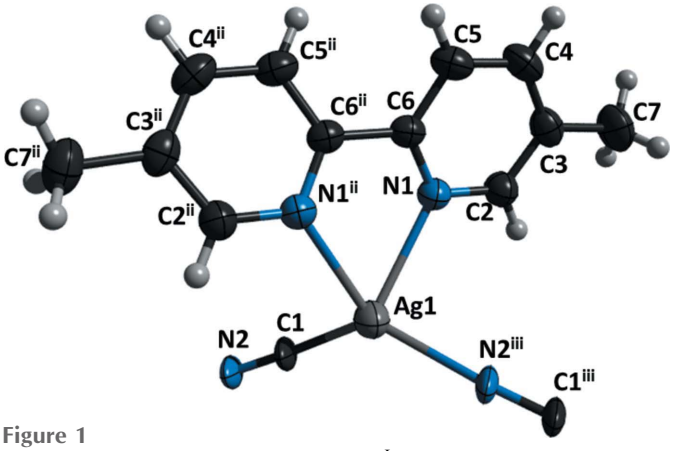

Figure 1
A view of the local coordination of the Ag^I atom in (I), showing the atom-numbering scheme. Displacement ellipsoids are drawn at the 50% probability level. [Symmetry codes: (ii) $-x, y, -z+\frac{1}{2}$; (iii) $x, -y+1, z+\frac{1}{2}$.]

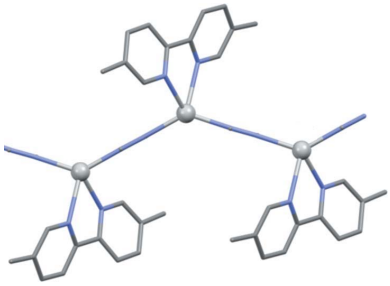

due to their potential applications in the fields of molecular magnetism (Xie *et al.*, 2010), catalysis (Ma *et al.*, 2009), nonlinear optics (Zang *et al.*, 2006) and luminescence (Mao *et al.*, 2014). The design and synthesis of extended frameworks *via* supramolecular interactions represent areas of considerable interest (Hogan *et al.*, 2011; Cook *et al.*, 2013). In particular, hydrogen bonding, π–π stacking and van der Waals interactions have been exploited for molecular recognition associated with biological activity and for the engineering of molecular solids (Hogan *et al.*, 2011; Cook *et al.*, 2013). In the present work, a new two-dimensional supramolecular framework of the one-dimensional chain compound $[Ag(CN)(5,5'\text{-dmbpy})]_n$ (5,5′-dmbpy is 5,5′-dimethyl-2,2′-bipyridine), (I), was synthesized successfully, structurally characterized and compared with the structures of other relevant compounds.

2. Experimental

2.1. Synthesis and crystallization

Compound (I) was synthesized by the reaction of two aqueous solutions at room temperature, one containing a mixture of $(NH_4)_2Fe(SO_4)_2\cdot H_2O$ (0.10 mmol, 98 mg) and 5,5′-dmbpy (0.2 mmol, 92 mg) in water (10 ml), and the other containing $K[Ag(CN)_2]$ (0.5 mmol, 10.6 mg) in water (5 ml). After 3 d, brown crystals of (I) were obtained; the yield based on Ag was about 71%.

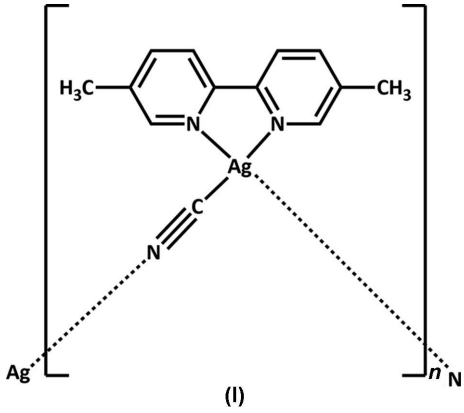

(I)

2.2. Refinement

Crystal data, data collection and structure refinement details are summarized in Table 1. C-bound H atoms were positioned geometrically, with C—H = 0.93 (aromatic) or 0.96 Å (methyl), and included as riding atoms, with $U_{iso}(H) = 1.5U_{eq}(C)$ for methyl groups and $1.2U_{eq}(C)$ otherwise. The C and N atoms of the cyanide group are substitutionally disordered (N1 and C1), with site occupancies of 0.5. The C and N atoms of the cyanide group (N1 and C1) are disordered across a centre of inversion. The model treats C—N as an overlapping reversed disordered conformation. The refinement included site occupancies of 0.5 and a C—N distance restraint of 1.12 (1) Å (Bowmaker *et al.*, 2004), while the atomic displacement ellipsoids of these two atoms were constrained to be identical and restrained to be pseudo-isotropic.

Table 1
Experimental details.

Crystal data	
Chemical formula	$[Ag(CN)(C_{12}H_{12}N_2)]$
M_r	318.13
Crystal system, space group	Monoclinic, *C*2/*c*
Temperature (K)	293
a, *b*, *c* (Å)	15.464 (2), 8.663 (1), 9.912 (2)
β (°)	112.832 (2)
V (Å^3)	1223.8 (3)
Z	4
Radiation type	Mo $K\alpha$
μ (mm^{-1})	1.63
Crystal size (mm)	0.25 × 0.15 × 0.09
Data collection	
Diffractometer	Bruker APEX CCD area-detector diffractometer
Absorption correction	Multi-scan (*SADABS*; Sheldrick, 2000)
T_{min}, T_{max}	0.748, 0.865
No. of measured, independent and observed [$I > 2\sigma(I)$] reflections	8245, 1525, 1395
R_{int}	0.017
(sin $\theta/\lambda)_{max}$ (Å^{-1})	0.667
Refinement	
$R[F^2 > 2\sigma(F^2)]$, $wR(F^2)$, *S*	0.029, 0.071, 1.14
No. of reflections	1525
No. of parameters	82
No. of restraints	7
H-atom treatment	H-atom parameters constrained
$\Delta\rho_{max}$, $\Delta\rho_{min}$ (e Å^{-3})	0.89, −0.70

Computer programs: *SMART* (Bruker, 2000), *SAINT* (Bruker, 2003), *SHELXS97* (Sheldrick, 2008), *SHELXL2014* (Sheldrick, 2015) and *SHELXTL* (Sheldrick, 2008).

3. Results and discussion

In the IR spectrum of (I), a sharp ν(CN) band of medium intensity is observed at 2134 cm^{-1} and compares favourably with that at 2140 cm^{-1} found for $K[Ag(CN)_2]$ (Ahmad *et al.*, 2007; Zhang *et al.*, 2006), thus confirming the presence of the cyanide group in the structure of (I). The ν(C═C) vibration of 5,5′-dmbpy is observed at 1481 cm^{-1}. Weak signals in the region of 3123–2921 cm^{-1} due to C—H stretching of 5,5′-dmbpy are also observed. Two sharp bands of medium intensity are observed at 2038 and 833 cm^{-1} due to the pyridine ring of 5,5′-dmbpy.

The results of the single-crystal X-ray analysis are consistent with the formulation of (I) as $[(AgCN)(5,5'\text{-dmbpy})]_n$ with an Ag–CN–5,5′-dmbpy stoichiometric ratio of 1:1:1. It crystallizes with the Ag^{I} cation on a twofold axis, half a cyanide ligand disordered about a centre of inversion and half a twofold symmetric molecule of 5,5′-dmbpy in the asymmetric unit.

Each Ag^{I} cation exhibits a distorted tetrahedral geometry (Table 2); the coordination environment comprises one C(N) atom and one N(C) atom from two disordered cyanide groups, and two N atoms from a bidentate chelating 5,5′-dmbpy ligand (Fig. 1), with the twist angle between the two bpy rings being 26.62 (9)° and the N1—Ag1—N1^{ii} bite angle being 68.13 (10)° [symmetry code: (ii) $-x, y, -z+\frac{1}{2}$]. The cyanide group exhibits substitutional disorder with site occupancies of 0.5 for the C and N atoms, and links adjacent Ag^{I} cations, generating a one-

Table 2
Selected geometric parameters (Å, °).

Ag1—C1	2.12 (3)	Ag1—N1^{ii}	2.459 (2)
Ag1—N2^{i}	2.19 (2)	Ag1···Ag1^{i}	5.4161 (11)
N2^{iii}—Ag1—N1	96.4 (6)	N1^{ii}—Ag1—N1	68.13 (10)
N2^{i}—Ag1—N1^{ii}	96.5 (6)	C1^{ii}—Ag1—N2^{i}	131.1
C1^{ii}—Ag1—N1	92.0 (7)	Ag1^{i}···Ag1···Ag1^{iv}	132.43 (2)

Symmetry codes: (i) $-x, -y+1, -z$; (ii) $-x, y, -z+\frac{1}{2}$; (iii) $x, -y+1, z+\frac{1}{2}$; (iv) $-x, -y+1, -z+1$.

Table 3
Hydrogen-bond geometry (Å, °).

*Cg*4 is the centroid of the N1/C2–C6 ring.

D—H···*A*	*D*—H	H···*A*	*D*···*A*	*D*—H···*A*
C7—H7*C*···*Cg*4^{iv}	0.96	2.89	3.734 (4)	146

Symmetry code: (iv) $x, -y, z+\frac{1}{2}$.

dimensional zigzag chain (Fig. 2), with an Ag1^{i}···Ag1···Ag1^{iii} angle of 132.3 (1)° and an Ag···Ag^{i} separation of 5.4161 (11) Å [symmetry codes: (i) $-x, -y+1, -z$; (iii) $x, -y+1, z+\frac{1}{2}$].

These chains are linked together *via* a weak nonclassical intermolecular C—H···π interaction between the methyl group (C7—H7*C*) and the centroid of the N1/C2–C6 aromatic ring of an adjacent 5,5′-dmbpy ligand (*Cg*4^{iv}) (Table 3) and a strong interchain face-to-face π–π interaction between adjacent aromatic rings of 5,5′-dmbpy ligands (*Cg*4) (Table 4), generating a two-dimensional supramolecular network, as shown in Fig. 3.

Cyanidometallates, such as $[Fe(CN)_6]^{3-}$ (Nayak *et al.*, 2006), $[Ni(CN)_4]^{2-}$ (Akitsu *et al.*, 2008), $[Pd(CN)_4]^{2-}$ (Manna *et al.*, 2007), $[Au(CN)_2]^{-}$ (Katz *et al.*, 2008) and $[Ag(CN)_2]^{-}$ (Ahmad *et al.*, 2007; Zhang *et al.*, 2006), have been used extensively as the design elements in supramolecular coordination systems, where they can act as multidentate ligands linking numerous metal centres together to form stable and high-dimensional coordination polymers with transition metal cations. Following this approach, the combination of metal(II) ions, $[Ag(CN)_2]^{-}$ groups and *N*-donor ligands has produced metal–organic frameworks (MOFs) with different topologies and interesting properties (Agustí *et al.*, 2008). Listed here are

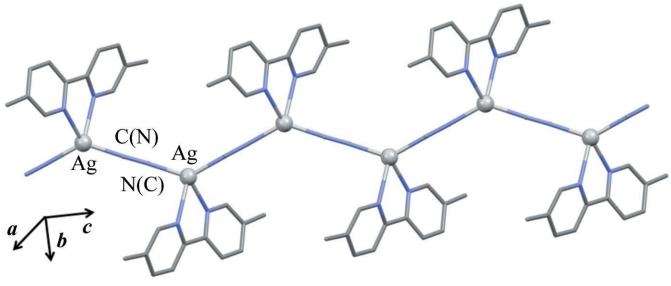

Figure 2
A view of the one-dimensional coordination polymer chain in the structure of (I), which extends in the [001] direction.

Table 4
π–π contacts (Å, °) for (I).

CCD is the centre-to-centre distance (distance between ring centroids), IPD is the mean interplanar distance (perpendicular distance from one plane to the neighbouring centroid) and SA is the mean slippage angle (angle subtended by the intercentroid vector to the plane normal); for details, see Janiak (2000). *Cg*4 is the centroid of the N1/C2–C6 ring.

Group1/group2	CCD (Å)	SA (°)	IPD (Å)
*Cg*4···*Cg*4^{v}	3.7222 (17)	20.0	3.4981 (11)

Symmetry codes: (v) $-x, -y, -z+1$.

important studies related to the present compound system: the spin-crossover three-dimensional coordination framework of $[Fe(pmd)_2\{Ag(CN)_2\}_2]_n$ (pmd is pyrimidine; Rodríguez-Velamazán *et al.*, 2014), the novel silver complex $[Ag_5(CN)_5(bipy)_2]_n$, with a one-dimensional architecture constructed through a ligand-unsupported argentophilic interaction (Liu *et al.*, 2006), the one-dimensional chain structure of $[Cu(en)_2Ag_2(CN)_4]$ (Černák *et al.*, 1998), exhibiting magnetic properties, the quasi-linear chain of $\{[Zn(en)_2NCAgCN][Ag(CN)_2]\}_n$ (en is 1,2-diaminoethane; Kappenstein *et al.*, 1988), and some adducts of silver(I) cyanide and (oligo-)pyridine bases with a one-dimensional polymeric zigzag chain, *viz.* $\{[LAg_2(CN)_2][Ag_2(CN)_2]_2[L(py)Ag_2(CN)_2]\}_n$ and $[(bpy)Ag(CN)]_n$ (*L* is 2,2′:6′,2″-terpyridine, bpy is 2,2′-bipyridine and py is pyridine; Bowmaker *et al.*, 2004). In addition, two multiple-layer heterometallic Mn^{II}–Ag^{I} coordination polymers, namely $[Mn(ampyz)(H_2O)\{Ag_2(CN)_3\}\{Ag(CN)_2\}(ampyz)]_n$ (ampyz is 2-aminopyrazine) and $\{[Mn(benzim)_2\{Ag(CN)_2\}_2][(benzim)$-

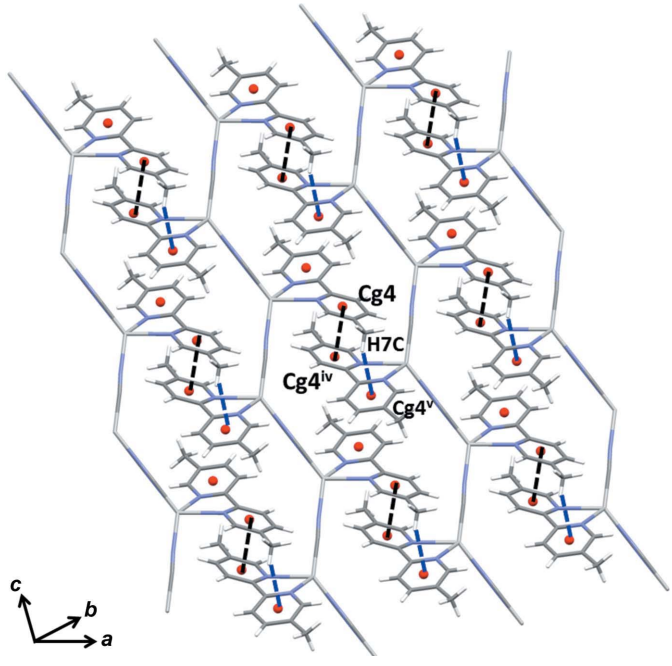

Figure 3
A crystal packing diagram of the two-dimensional supramolecular network of (I), assembled by C—H···π and π–π interactions (dashed lines). [Symmetry codes: (iv) $-x, -y, -z+1$; (v) $x, -y, z+\frac{1}{2}$.]

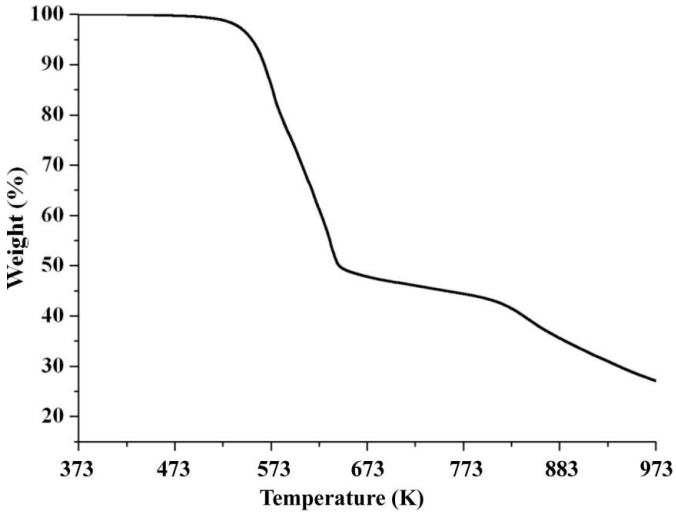

Figure 4
The TGA curve measured for (I).

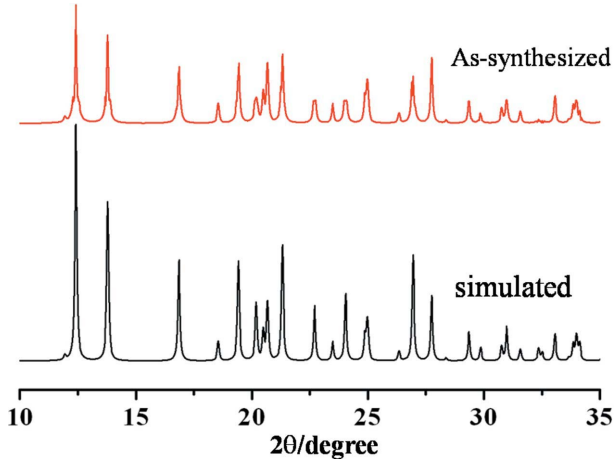

Figure 5
The powder X-ray diffraction pattern for (I).

$Ag(CN)]\cdot H_2O\}_n$ (benzim is benzimidazole) were observed (Wannarit *et al.*, 2012), with an additional tricyanidodiargentate group in the former and an additional monocyanidoargentate group in the latter. However, mononuclear compounds have also been observed, *viz.* $[Cd\{Ag(CN)_2\}_2(5,5'\text{-dmbpy})_2]$ (Piromchom *et al.*, 2013) and $[Cu(imidazole)_4\{Ag(CN)_2\}_2]$ (Ahmad *et al.*, 2012), and these molecular units are self-assembled *via* supramolecular interactions (hydrogen bonding, π–π and Ag···Ag interactions), generating three-dimensional supramolecular networks. With the iron(II) salt in the synthesis of (I), a novel one-dimensional chain structure containing only a monocyanidoargentate group and an *N*-donor bidentate chelating ligand was observed.

To investigate the thermal stability of (I), thermogravimetric analysis (TGA) was carried out under a nitrogen atmosphere (Fig. 4). The TGA curve shows a weight loss of 57.03% in the temperature range 553–803 K, corresponding to the loss of the 5,5′-dmbpy ligand (calculated 57.87%). The framework collapses on further heating. The phase purity of the bulk as-synthesized sample of (I) was examined by powder X-ray diffraction (PXRD). All peaks from the experimental PXRD trace match well with those from the simulated PXRD pattern, indicating reasonable crystalline phase purity (Fig. 5).

Acknowledgements

The authors gratefully acknowledge the Thailand Research Fund (grant No. BRG5680009 for SY and No. TRG5780003 for JB), the National Research University Project of Thailand, Office of the Higher Education Commission, and the Center of Excellence for Innovation in Chemistry (PERCH–CIC), Office of the Higher Education Commission, Ministry of Education, Thailand, for financial support.

References

Agustí, G., Thompson, A. L., Gaspar, A. B., Muñoz, M. C., Goeta, A. E., Rodríguez-Velamazán, J. A., Castro, M., Burriel, R. & Real, J. A. (2008). *Dalton Trans.* pp. 642–649.
Ahmad, S., Monim-ul-Mehboob, M., Altaf, M., Stoeckli Evans, H. & Mehmood, R. (2007). *J. Chem. Crystallogr.* **37**, 685–689.
Ahmad, S., Tahir, M. N., Javaid, H. M., Monim-ul-Mehboob, M., Shaheen, M. A. & Mahmood, R. (2012). *J. Chem. Crystallogr.* **42**, 401–404.
Akitsu, T. & Einaga, Y. (2008). *Inorg. Chim. Acta*, **361**, 36–42.
Bowmaker, G. A., Effendy Junk, P. C., Skelton, B. W. & White, A. H. (2004). *Z. Naturforsch. Teil B*, **59**, 1277–1292.
Bruker (2000). *SMART*. Bruker AXS Inc., Madison, Wisconsin, USA.
Bruker (2003). *SAINT*. Bruker AXS Inc., Madison, Wisconsin, USA.
Černák, J., Chomič, J., Gravereau, P., Orendáčová, A., Orendáč, M., Kováč, J., Feher, A. & Kappenstein, C. (1998). *Inorg. Chim. Acta*, **281**, 134–140.
Cook, T. R., Zheng, Y.-R. & Stang, P. J. (2013). *Chem. Rev.* **113**, 734–777.
Hogan, G. A., Rath, N. P. & Beatty, A. M. (2011). *Cryst. Growth Des.* **11**, 3740–3743.
Janiak, C. (2000). *J. Chem. Soc. Dalton Trans.* pp. 3885–3896.
Kappenstein, C., Ouali, A., Guerin, M., Černák, J. & Chomič, J. (1988). *Inorg. Chim. Acta*, **147**, 189–197.
Katz, M. J., Michaelis, V. K., Aguiar, P. M., Yson, R., Lu, H., Kaluarachchi, H., Batchelor, R. J., Schreckenbach, G., Kroeker, S., Patterson, H. H. & Leznoff, D. B. (2008). *Inorg. Chem.* **47**, 6353–6363.
Liu, X., Guo, G.-C., Fu, M.-L., Liu, X. H., Wang, M. S. & Huang, J. S. (2006). *Inorg. Chem.* **45**, 3679–3685.
Ma, L., Abney, C. & Lin, W. (2009). *Chem. Soc. Rev.* **38**, 1248–1256.
Manna, S. C., Ribas, J., Zangrando, E. & Ray Chaudhuri, N. (2007). *Polyhedron*, **26**, 3189–3198.
Mao, L.-L., Liu, W., Li, Q.-W., Jia, J.-H. & Tong, M.-L. (2014). *Cryst. Growth Des.* **14**, 4674–4680.
Nayak, M., Kundu, P., Lemoine, P., Koner, R., Wei, H. H. & Mohanta, S. (2006). *Polyhedron*, **25**, 2007–2014.
Piromchom, J., Wannarit, N., Pakawatchai, C. & Youngme, S. (2013). *Acta Cryst.* C**69**, 1136–1139.
Rodríguez-Velamazán, J. A., Cañadillas-Delgado, L., Castro, M., McIntyre, G. J. & Real, J. A. (2014). *Acta Cryst.* B**70**, 436–443.
Sheldrick, G. M. (2000). *SADABS*. University of Göttingen, Germany.
Sheldrick, G. M. (2008). *Acta Cryst.* A**64**, 112–122.
Sheldrick, G. M. (2015). *Acta Cryst.* C**71**, 3–8.

Wannarit, N., Hahnvajanawong, V., Pakawatchai, C. & Youngme, S. (2012). *Transition Met. Chem.* **37**, 79–84.
Xie, C.-Z., Li, R.-F., Wang, L.-Y. & Zhang, Q.-Q. (2010). *Z. Anorg. Allg. Chem.* **636**, 657–661.
Zang, S. Q., Su, Y., Li, Y. Z., Ni, Z. P. & Meng, Q. J. (2006). *Inorg. Chem.* **45**, 174–180.
Zhang, H., Zhang, Y., Wang, C., Cai, L., Xie, Y. & Xue, G. (2006). *Inorg. Chem. Commun.* **9**, 555–558.

supporting information

Acta Cryst. (2015). C**71**, 1057-1061 [doi:10.1107/S2053229615020288]

A novel one-dimensional metal–organic framework with a μ-cyanido-argentate group: *catena*-poly[[(5,5′-dimethyl-2,2′-bipyridyl-κ^2N,N')silver(I)]-μ-cyanido-κ^2N:*C*]

Jureepan Piromchom, Jintana Othong, Jaursup Boonmak, Ilpo Mutikainen and Sujittra Youngme

Computing details

Data collection: *SMART* (Bruker, 2000); cell refinement: *SAINT* (Bruker, 2003); data reduction: *SAINT* (Bruker, 2003); program(s) used to solve structure: *SHELXS97* (Sheldrick, 2008); program(s) used to refine structure: *SHELXL2014* (Sheldrick, 2015); molecular graphics: *SHELXTL* (Sheldrick, 2008); software used to prepare material for publication: *SHELXTL* (Sheldrick, 2008).

catena-Poly[[(5,5′-dimethyl-2,2′-bipyridyl-κ^2N,N')silver(I)]-μ-cyanido-κ^2N:*C*]

Crystal data

$[Ag(CN)(C_{12}H_{12}N_2)]$
$M_r = 318.13$
Monoclinic, *C*2/*c*
$a = 15.464$ (2) Å
$b = 8.663$ (1) Å
$c = 9.912$ (2) Å
$\beta = 112.832$ (2)°
$V = 1223.8$ (3) Å^3
$Z = 4$
$F(000) = 632$
$D_x = 1.727$ Mg m^{-3}
Mo $K\alpha$ radiation, $\lambda = 0.71073$ Å
Cell parameters from 8541 reflections
$\theta = 2.8$–28.3°
$\mu = 1.63$ mm^{-1}
$T = 293$ K
Block, colourless
0.25 × 0.15 × 0.09 mm

Data collection

Bruker APEX CCD area-detector diffractometer
Radiation source: fine-focus sealed tube
Graphite monochromator
φ and ω scans
Absorption correction: multi-scan (*SADABS*; Sheldrick, 2000)
$T_{min} = 0.748$, $T_{max} = 0.865$
8245 measured reflections
1525 independent reflections
1395 reflections with $I > 2\sigma(I)$
$R_{int} = 0.017$
$\theta_{max} = 28.3°$, $\theta_{min} = 2.8°$
$h = -20\rightarrow20$
$k = -11\rightarrow11$
$l = -13\rightarrow13$

Refinement

Refinement on F^2
Least-squares matrix: full
$R[F^2 > 2\sigma(F^2)] = 0.029$
$wR(F^2) = 0.071$
$S = 1.14$
1525 reflections
82 parameters
7 restraints
Hydrogen site location: inferred from neighbouring sites
H-atom parameters constrained
$w = 1/[\sigma^2(F_o^2) + (0.0262P)^2 + 2.5229P]$ where $P = (F_o^2 + 2F_c^2)/3$
$(\Delta/\sigma)_{max} < 0.001$
$\Delta\rho_{max} = 0.89$ e Å^{-3}
$\Delta\rho_{min} = -0.70$ e Å^{-3}

Special details

Geometry. All e.s.d.'s (except the e.s.d. in the dihedral angle between two l.s. planes) are estimated using the full covariance matrix. The cell e.s.d.'s are taken into account individually in the estimation of e.s.d.'s in distances, angles and torsion angles; correlations between e.s.d.'s in cell parameters are only used when they are defined by crystal symmetry. An approximate (isotropic) treatment of cell e.s.d.'s is used for estimating e.s.d.'s involving l.s. planes.

Fractional atomic coordinates and isotropic or equivalent isotropic displacement parameters (Å²)

	x	*y*	*z*	U_{iso}*/U_{eq}	Occ. (<1)
Ag1	0.0000	0.37392 (4)	0.2500	0.04983 (12)	
N2	0.0135 (9)	0.523 (3)	−0.041 (2)	0.041 (2)	0.5
C1	0.0105 (12)	0.473 (3)	0.061 (3)	0.041 (2)	0.5
N1	−0.08214 (15)	0.1388 (2)	0.2735 (2)	0.0385 (4)	
C2	−0.15096 (19)	0.1412 (3)	0.3238 (3)	0.0434 (6)	
H2A	−0.1811	0.2347	0.3212	0.052*	
C3	−0.18042 (18)	0.0141 (3)	0.3794 (3)	0.0442 (6)	
C4	−0.1333 (2)	−0.1224 (3)	0.3851 (3)	0.0485 (6)	
H4A	−0.1497	−0.2107	0.4230	0.058*	
C5	−0.0618 (2)	−0.1278 (3)	0.3343 (3)	0.0449 (6)	
H5A	−0.0298	−0.2196	0.3380	0.054*	
C6	−0.03821 (16)	0.0043 (3)	0.2780 (3)	0.0350 (5)	
C7	−0.2595 (2)	0.0266 (5)	0.4316 (4)	0.0627 (8)	
H7A	−0.2893	−0.0722	0.4233	0.094*	
H7B	−0.3045	0.1007	0.3728	0.094*	
H7C	−0.2351	0.0592	0.5321	0.094*	

Atomic displacement parameters (Å²)

	U^{11}	U^{22}	U^{33}	U^{12}	U^{13}	U^{23}
Ag1	0.05559 (19)	0.04347 (17)	0.0614 (2)	0.000	0.03473 (15)	0.000
N2	0.043 (6)	0.0368 (16)	0.044 (5)	0.003 (5)	0.017 (5)	−0.001 (3)
C1	0.043 (6)	0.0368 (16)	0.044 (5)	0.003 (5)	0.017 (5)	−0.001 (3)
N1	0.0439 (11)	0.0333 (10)	0.0424 (10)	0.0019 (8)	0.0211 (9)	0.0025 (8)
C2	0.0437 (13)	0.0420 (14)	0.0487 (14)	0.0023 (11)	0.0226 (11)	0.0027 (11)
C3	0.0384 (12)	0.0547 (16)	0.0388 (12)	−0.0075 (11)	0.0143 (10)	0.0026 (11)
C4	0.0486 (14)	0.0456 (14)	0.0495 (14)	−0.0099 (12)	0.0172 (12)	0.0099 (12)
C5	0.0468 (14)	0.0341 (12)	0.0513 (14)	−0.0024 (11)	0.0163 (11)	0.0048 (11)
C6	0.0363 (11)	0.0312 (11)	0.0350 (11)	−0.0009 (9)	0.0111 (9)	0.0007 (9)
C7	0.0503 (16)	0.080 (2)	0.0669 (19)	−0.0075 (16)	0.0333 (15)	0.0062 (17)

Geometric parameters (Å, º)

Ag1—C1^{i}	2.12 (3)	C2—H2A	0.9300
Ag1—C1	2.12 (3)	C3—C4	1.378 (4)
Ag1—N2^{ii}	2.19 (2)	C3—C7	1.505 (4)
Ag1—N2^{iii}	2.19 (2)	C4—C5	1.382 (4)
Ag1—N1^{i}	2.459 (2)	C4—H4A	0.9300
Ag1—N1	2.459 (2)	C5—C6	1.383 (3)

N2—C1	1.123 (6)	C5—H5A	0.9300
N2—N2^{iii}	1.13 (4)	C6—C6^{i}	1.488 (5)
N2—Ag1^{iii}	2.19 (2)	C7—H7A	0.9600
C1—C1^{iii}	1.22 (5)	C7—H7B	0.9600
N1—C2	1.339 (3)	C7—H7C	0.9600
N1—C6	1.341 (3)	Ag1—Ag1^{iii}	5.4161 (11)
C2—C3	1.385 (4)		

C1^{i}—Ag1—C1	132.1 (16)	C4—C3—C2	116.6 (2)
N2^{ii}—Ag1—N2^{iii}	131.6 (13)	C4—C3—C7	122.3 (3)
C1^{i}—Ag1—N1^{i}	129.7 (7)	C2—C3—C7	121.1 (3)
C1—Ag1—N1^{i}	92.0 (7)	C3—C4—C5	120.0 (2)
N2^{ii}—Ag1—N1	96.4 (6)	C3—C4—H4A	120.0
N2^{iii}—Ag1—N1^{i}	96.5 (6)	C5—C4—H4A	120.0
C1^{i}—Ag1—N1	92.0 (7)	C4—C5—C6	119.5 (3)
C1—Ag1—N1	129.7 (7)	C4—C5—H5A	120.3
N2^{ii}—Ag1—N1	96.5 (6)	C6—C5—H5A	120.3
N2^{iii}—Ag1—N1	124.4 (5)	N1—C6—C5	121.5 (2)
N1^{i}—Ag1—N1	68.13 (10)	N1—C6—C6^{i}	116.94 (14)
C1—N2—Ag1^{iii}	172.5 (4)	C5—C6—C6^{i}	121.52 (16)
N2^{iii}—N2—Ag1^{iii}	154.9 (15)	C3—C7—H7A	109.5
N2—C1—Ag1	177.5 (10)	C3—C7—H7B	109.5
C1^{iii}—C1—Ag1	162 (2)	H7A—C7—H7B	109.5
C2—N1—C6	117.8 (2)	C3—C7—H7C	109.5
C2—N1—Ag1	122.45 (17)	H7A—C7—H7C	109.5
C6—N1—Ag1	116.70 (16)	H7B—C7—H7C	109.5
N1—C2—C3	124.6 (3)	C1^{i}—Ag1—N2^{iii}	131.1
N1—C2—H2A	117.7	Ag1^{iii}—Ag1—Ag1^{iv}	132.43 (2)
C3—C2—H2A	117.7		

Symmetry codes: (i) −*x*, *y*, −*z*+1/2; (ii) *x*, −*y*+1, *z*+1/2; (iii) −*x*, −*y*+1, −*z*; (iv) −*x*, −*y*+1, −*z*+1.

Hydrogen-bond geometry (Å, º)

*Cg*4 is the centroid of the N1/C2–C6 ring.

D—H···*A*	*D*—H	H···*A*	*D*···*A*	*D*—H···*A*
C7—H7*C*···*Cg*4^{v}	0.96	2.89	3.734 (2)	146

Symmetry code: (v) *x*, −*y*, *z*+1/2.

CRYSTAL GROWTH & DESIGN

Article

pubs.acs.org/crystal

A Series of Cyanoacetato Copper(II) Coordination Polymers with Various *N,N′*-Ditopic Spacers: Structural Diversity, Supramolecular Robustness, and Magnetic Properties

Porntiva Suvanvapee,[†] Jaursup Boonmak,*[,†] Fatima Klongdee,[†] Chaveng Pakawatchai,[‡] Boujemaa Moubaraki,[§] Keith S. Murray,[§] and Sujittra Youngme[†]

[†]Materials Chemistry Research Center, Department of Chemistry and Center of Excellence for Innovation in Chemistry, Faculty of Science, Khon Kaen University, Khon Kaen 40002, Thailand

[‡]Department of Chemistry, Faculty of Science, Prince of Songkla University, Hat Yai, Songkla 90112, Thailand

[§]School of Chemistry, Monash University, Building 23, 17 Rainforest Walk, Melbourne, Victoria 3800, Australia

Supporting Information

ABSTRACT: Five novel copper(II) coordination polymers containing cyanoacetate (cna) anion with various *N,N′*-ditopic spacers $[Cu(cna)_2(pyz)]_n$ (**1**), $[Cu(cna)_2(bpy)(H_2O)_2]_n$ (**2**), $[Cu(cna)_2(dpe)]_n$ (**3**), $[Cu(cna)_2(dpe)]_n(H_2O)_n$ (**4**), and $[Cu(cna)_2(bpa)]_n$ (**5**) (when pyz = pyrazine, bpy = 4,4′-bipyridyl, dpe = 1,2-di(4-pyridyl)ethylene, and bpa = 1,2-di(4-pyridyl)ethane) were structurally and spectroscopically characterized. Compound **1** shows a two-dimensional (2D) sheet structure constructed from μ_2-1,3(*syn,anti*) coordinative mode of cyanoacetate and μ_2-pyz linking adjacent Cu(II) centers. Compound **2** exhibits a one-dimensional (1D) polymeric chain which is formed by μ_2-bpy bridging between $[Cu(cna)_2(H_2O)_2]$ units, whereas compounds **3**−**5** reveal 1D ladder-like structures which are built from double-μ_2-dpe/bpa spacers connecting neighboring Cu(II) cyanoacetate dimers. Weak interactions such as hydrogen bonding and N···π and/or C−H···π interactions join the adjacent layers of **1** or polymeric chains of **2**−**5** to stabilize overall supramolecular networks. The thermal stabilities of **1**−**5** were investigated. Interestingly, compound **2** reveals a robust supramolecular framework constructed by 1D polymeric chains during thermal dehydration and rehydration processes, which has been further verified by spectroscopic techniques, elemental analyses, thermogravimetric analysis, and X-ray powder diffraction. Moreover, this behavior is not observed in the isomorphous series containing Co(II) and Ni(II) ions. The magnetic properties of **1** and **3** exhibit very weak antiferromagnetic interactions between Cu(II) centers.

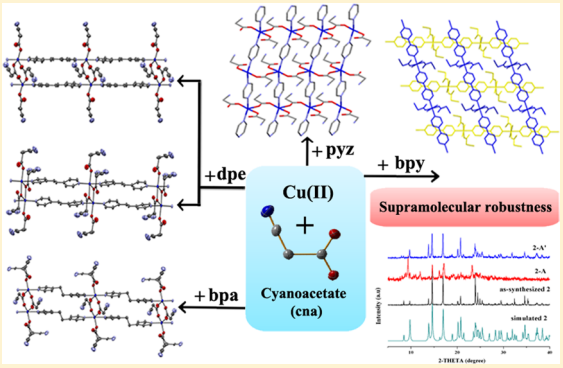

INTRODUCTION

The design and construction of coordination polymers have received much attention and have become an interesting research area of chemistry in recent decades due to their potential applications in gas storage, catalysis, luminescence, ion exchange, and magnetism.[1−9] Generally, the structural diversity and the construction of such promising materials strongly depend on the chemical nature of the main or ancillary ligands and the coordination geometries of metal ions. It is well-known that the coordination polymers containing carboxylates show various dimensional networks with interesting properties.[10−18] This diversity results from the fact that the carboxylate groups can bind metal centers in various ways and may account for the possible intermolecular hydrogen bonds spreading low dimensional materials to higher dimensional supramolecular frameworks.[1,6,13−19] Besides the structural aspect, the carboxylate bridges provide an efficient pathway for transmitting magnetic information between paramagnetic centers. Different coordination modes contribute different forms of cooperative coupling which can be principally used to modulate the overall magnetic behavior in a coordination network.[17,18,20,21] In the present studies, the cyanoacetate anion (cna) is used as a ligand for binding more than one metal ion through carboxylate bridge. The cyanoacetate ($NC_2H_2CO_2^-$) is a monocarboxylate with many interaction sites. It contains both nitrile (−C≡N) and carboxylic groups which not only provides coordination sites but also effectively serves as a hydrogen acceptor site at the cyano group as well as fabricating the intermolecular N···π interaction toward neighboring electron-deficient aromatic moieties.[22−29] In general, the intermolecular noncovalent interactions are useful tools for the construction of a soft supramolecular framework[3,5,30,31] with low dimensional molecular building blocks that can show a variety of structural dynamic behaviors, such as reversible single-crystal-to-single-crystal, reversible single crystal

Received: April 2, 2015
Revised: June 28, 2015
Published: July 2, 2015

DOI: 10.1021/acs.cgd.5b00453
Cryst. Growth Des. 2015, 15, 3804−3812

Scheme 1. A Series of Cu(II) Coordination Polymers 1−5

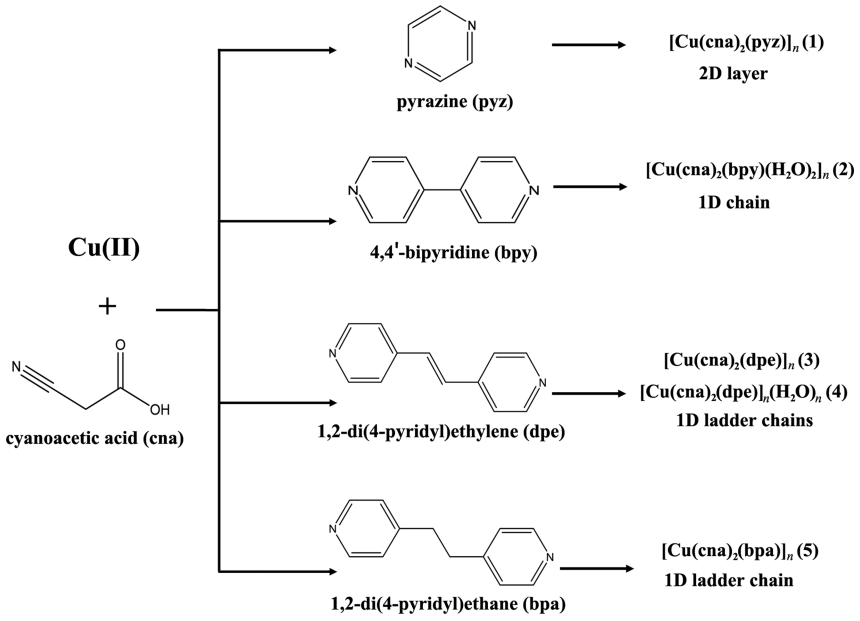

to amorphous, and also nonreversible transformations.[3,5,31−40] Therefore, these versatile connection sites allow the cyanoacetate to be a promising candidate for constructing flexible but robust coordination frameworks. However, the chemistry of coordination complexes containing cyanoacetate has been rarely explored to date.[22−29] Apart from carboxylate linkers, the *N,N′*-ditopic spacers are frequently used as ancillary ligands for dimensional extension. Their length, rigidity, and functional groups have consequential effects on the final structures of coordination networks. Therefore, the development of synthetic routes to novel coordination polymers by mixed bridging ligands remains to be much explored.[10,41−50]

Consequently, in our efforts toward rational design and systematic synthesis of coordination polymers, the use of *N,N′*-ditopic spacers acting as coligands, i.e., pyrazine (pyz), 4,4′-bipyridyl (bpy), 1,2-di(4-pyridyl)ethylene (dpe), and 1,2-di(4-pyridyl)ethane (bpa), in combination with cyanoacetate in the Cu(II) system have been used to construct a variety of new coordination polymers. We found that cyanoacetate can bind Cu(II) ions through diverse coordination modes of carboxylate to generate Cu(II) dinuclear unit and one-dimensional (1D) coordination polymeric chain. To connect these segments, an ancillary *N,N′*-ditopic spacer has been fulfilled. Herein, we report the syntheses and characterizations of a novel series of Cu(II) coordination polymers, namely, $[Cu(cna)_2(pyz)]_n$ (**1**), $[Cu(cna)_2(bpy)(H_2O)_2]_n$ (**2**), $[Cu(cna)_2(dpe)]_n$ (**3**), $[Cu(cna)_2(dpe)]_n(H_2O)_n$ (**4**) and $[Cu(cna)_2(bpa)]_n$ (**5**) (see Scheme 1). The resulting coordination networks exhibit a variation of architectures from 1D polymeric chain, 1D-ladder chain, to 2D layer depending upon the length and rigidity of the spacers and diverse coordination modes of carboxylates. The nitrile functional group in cyanoacetate plays a key role in 3D packing motifs via intermolecular hydrogen bonding and N···π interactions. Furthermore, we found that compound **2** reveals a robust supramolecular framework during dehydration and rehydration processes which is not observed in the Co(II) and Ni(II) analogues. This behavior is not common for low dimensional coordination polymers because the noncovalent supramolecular motif easily collapses upon removal of the coordination water molecules.[36,38] The result demonstrates the significant role of various weak intermolecular interactions among interlaced covalently bonded chain in **2** and the influence of Jahn−Teller distortion in octahedral Cu(II) system to preserve the crystalline phase of anhydrous frameworks of **2**. The magnetic properties of **1** and **3** have also been investigated.

EXPERIMENTAL SECTION

General. All chemicals were obtained from commercial sources and were used without further purification. Elemental analyses (C, H, N) were carried out with a PerkinElmer PE 2400CHNS analyzer. FT-IR spectra were obtained in KBr disks on a PerkinElmer Spectrum One FT-IR spectrophotometer in 4000−450 cm^{-1} spectral range. Solid-state (diffuse reflectance) electronic spectra were measured as polycrystalline samples on a PerkinElmer Lambda2S spectrophotometer, within the range 400−1100 nm. The X-ray powder diffraction (XRPD) data were collected on a Bruker D8 ADVANCE diffractometer using monochromatic Cu$K\alpha$ radiation, and the recording speed was 0.5 s/step over the 2θ range of 5−40° at room temperature. Thermogravimetric analyses (TGA) were performed using a TG-DTA 2010S MAC apparatus between 30 and 500 °C in N_2 atmosphere with heating rate of 10 °C min^{-1}. Magnetic susceptibility measurements (2−300 K) were carried out using a Quantum design MPMS-5S SQUID magnetometer. Measurements carried out using a 1 kOe dc field. Accurately weighed samples of ∼25 mg were contained in a gel capsule that was held in the center of a soda straw that was attached to the end of the sample rod. Data were corrected for magnetization of the sample holder and for diamagnetic contributions, which were estimated from Pascal constants.

Syntheses. $[Cu(cna)_2(pyz)]_n$ (1). The aqueous solution (4 mL) of $Cu(NO_3)_2{\cdot}3H_2O$ (120 mg, 0.5 mmol) and cyanoacetic acid (85 mg, 1 mmol) was mixed with pyrazine (40 mg, 0.5 mmol) in dimethylformamide (2 mL). This mixture solution was allowed to stand undisturbed at room temperature, yielding blue crystals of **1** after 2 days. Yield: 97 mg (62%) based on copper salt. Anal. Calcd for $CuC_{10}H_8N_4O_4$: C, 38.53; H, 2.59; N, 17.93%. Found: C, 37.65; H, 2.62; N, 18.03%. IR (KBr, cm^{-1}): 3096(w), 3045(w), 2255(w), 1645(s), 1600(s), 1440(m), 1365(s), 1253(m), 1160(m), 1126(m), 1075(m), 923(m), 838(m), 718(w), 574(w), 506(m). UV−vis (diffuse reflectance, cm^{-1}): 15450.

$[Cu(cna)_2(bpy)(H_2O)_2]_n$ (2). The mixture solution of $Cu(NO_3)_2{\cdot}3H_2O$ (120 mg, 0.5 mmol) and 4,4′-bipyridyl (78 mg, 0.5 mmol) in aqueous media (4 mL) was carefully layered on cyanoacetic acid (85 mg, 1 mmol) in dimethylformamide (2 mL) in 15 mL of glass vial. The vial was sealed and allowed to stand undisturbed at room temperature. After

DOI: 10.1021/acs.cgd.5b00453
Cryst. Growth Des. 2015, 15, 3804−3812

Table 1. Crystallographic Data for Compounds 1−5

compound	1	2	3	4	5
formula	$CuC_{10}H_8N_4O_4$	$CuC_{16}H_{16}N_4O_6$	$CuC_{18}H_{14}N_4O_4$	$CuC_{18}H_{16}N_4O_5$	$CuC_{18}H_{16}N_4O_4$
molecular weight	311.74	423.87	413.87	431.87	415.90
T (K)	293(2)	293(2)	293(2)	293(2)	293(2)
crystal system	monoclinic	orthorhombic	triclinic	monoclinic	triclinic
space group	$P2_1/c$	$Pccn$	$P\bar{1}$	$C2/c$	$P\bar{1}$
a (Å)	4.8966(1)	12.7963(12)	9.6394(7)	23.9507(12)	8.1148(3)
b (Å)	13.3780(4)	18.0945(17)	10.0132(7)	11.7986(6)	10.2084(3)
c (Å)	17.6679(5)	7.4363(7)	10.2337(7)	14.5996(8)	12.3390(4)
α (deg)	90.00	90.00	97.073(2)	90.00	105.745(1)
β (deg)	101.794(1)	90.00	91.002(2)	110.044(1)	95.226(1)
γ (deg)	90.00	90.00	117.107(1)	90.00	110.908(1)
V (Å^3)	1132.93(5)	1721.8(3)	869.54(11)	3875.7(3)	898.72(5)
Z	4	4	2	8	2
ρ_{calcd} (g cm^{-3})	1.828	1.635	1.581	1.473	1.537
μ (Mo Kα) (mm^{-1})	1.945	1.312	1.289	1.163	1.247
data collected	3028	2075	4324	3988	3670
unique data (Rint)	2239(0.0320)	1796(0.0192)	3493(0.0463)	3451(0.0219)	3177(0.0182)
$R_1{}^a/wR_2{}^b$ [$I > 2\sigma(I)$]	0.0567/0.1378	0.0347/0.0921	0.0467/0.1001	0.0322/0.0820	0.0331/0.0837
$R_1{}^a/wR_2{}^b$ [all data]	0.0731/0.1488	0.0395/0.0958	0.0625/0.1064	0.0405/0.0864	0.0420/0.0882
GOF	0.996	1.091	1.072	1.055	1.056
max/min electron density (e Å^{-3})	0.469/−0.775	0.332/−1.238	0.584/−0.250	0.354/−0.264	0.542/−0.217

$^aR = \sum||F_o| - |F_c||/\sum|F_o|$. $^bR_w = \{\sum[w(|F_o| - |F_c|)]^2/\sum[w|F_o|^2]\}^{1/2}$.

2 days, blue crystals of **2** were obtained. Yield: 100 mg (47%) based on copper salt. Anal. Calcd for $CuC_{16}H_{16}N_4O_6$: C, 45.34; H, 3.80; N, 13.22%. Found: C, 44.55; H, 3.53; N, 12.40%. IR (KBr, cm^{-1}): 3544(br), 3199(w), 3007(w), 2923(w), 2259(w), 1610(s), 1373(s), 1276(m), 1218(m), 1075(m), 942(w), 818(m), 714(m), 645(w), 596(w), 491(w). UV−vis (diffuse reflectance, cm^{-1}): 15470.

[Cu(cna)$_2$(dpe)]$_n$ (3) and [Cu(cna)$_2$(dpe)]$_n$(H$_2$O)$_n$ (4). A mixture solution of ethanol and water (4 mL, 1:1 v/v) was carefully layered on an aqueous solution (4 mL) containing $Cu(BF_4)_2{\cdot}nH_2O$ (118 mg, 0.5 mmol) and cyanoacetic acid (85 mg, 1 mmol) in 15 mL of glass vial. Then an ethanolic solution (2 mL) of 1,2-di(4-pyridyl)ethylene (90 mg, 0.5 mmol) was layered over the mixture layer. Then, the vial was sealed and allowed to stand undisturbed at room temperature. After 2 days, greenish-blue block-shaped crystals of **3** and blue polygonal crystals of **4** were obtained. These crystals were manually separated, washed with water and dried in air. Yield for **3**: 49 mg (24%) based on copper salt. Anal. Calcd for $CuC_{18}H_{14}N_4O_4$: C, 52.24; H, 3.41; N, 13.54%. Found: C, 51.82; H, 3.41; N, 13.27%. IR (KBr, cm^{-1}): 3088(w), 2258(w), 1633(s), 1613(s), 1496(m), 1385(s), 1266(m), 1207(m), 1073(m), 816(m), 720(w), 643(w). UV−vis (diffuse reflectance, cm^{-1}): 13770. Yield for **4**: 11 mg (5%) based on copper salt. Anal. Calcd for $CuC_{18}H_{16}N_4O_5$: C, 50.06; H, 3.73; N, 12.97%. Found: C, 50.92; H, 3.40; N, 13.07%. IR (KBr,cm^{-1}): 3419(br), 3060(w), 2933(w), 2258(w), 1626(s), 1463(s), 1372(s), 1286(s), 1080(m), 1030(m), 903(w), 844(s), 727(m), 549(m). UV−vis (diffuse reflectance, cm^{-1}): 16860. The single-crystals of **4** were synthesized in a similar manner but using dimethylformamide instead of ethanol. After 1 week, suitable single-crystals of **4** for X-ray diffraction study were obtained. The low yields of **3** and **4** are owing to the tiny crystals of the mixed products which are difficult to separate manually.

[Cu(cna)$_2$(bpa)]$_n$ (5). The solution containing $Cu(BF_4)_2{\cdot}nH_2O$ (118 mg, 0.5 mmol) and cyanoacetic acid (85 mg, 1 mmol) in water and ethanol (4 mL, 1:1 v/v) was mixed with 1,2-di(4-pyridyl)ethane (90 mg, 0.5 mmol) in dimethylformamide (2 mL). This mixture solution was allowed to stand undisturbed at room temperature. After 2 days, greenish-blue crystals of **5** were obtained. Yield: 86 mg (41%) based on copper salt. Anal. Calcd for $CuC_{18}H_{16}N_4O_4$: C, 51.98; H, 3.88; N, 13.47%. Found: C, 51.73; H, 3.78; N, 13.36%. IR (KBr, cm^{-1}): 3432(br), 2258(w), 1627(s), 1367(s), 1255(m), 1073(w), 1030(w), 901(w), 849(m), 719(w), 555(w). UV−vis (diffuse reflectance, cm^{-1}): 13770.

X-ray Crystallography. The reflection data of **1**−**4** and **2-Co** were collected on a 1 K Bruker SMART CCD area-detector diffractometer with graphite-monochromated MoKα radiation (λ = 0.71073 Å) using the SMART program.[51] The reflection data of **5** was collected on a Bruker D8 Quest PHOTON100 CMOS detector with graphite-monochromated MoKα radiation using the APEX2 program.[52] Raw data frame integration was performed with SAINT,[53] which also applied correction for Lorentz and polarization effects. An empirical absorption correction by using the SADABS program[54] was applied. The structure was solved by direct methods and refined by full-matrix least-squares method on F^2 with anisotropic thermal parameters for all non-hydrogen atoms using the SHELXTL software package.[55] All hydrogen atoms were placed in calculated positions and refined isotropically, with the exception of the hydrogen atoms of all coordination water molecules in **2** were found via difference Fourier maps, then restrained at fixed positions and refined isotropically whereas hydrogen atoms on the disordered lattice water molecule in **4** could not be located. The nitrile groups of μ-cna for **4** and those of terminal cna for **5** are disordered, so the occupancies of conformations A and B refined to 0.8 and 0.2 (for **4**) and 0.7 and 0.3 (for **5**), respectively. Therefore, there are hydrogen bonding networks and N$\cdots\pi$ interactions present via the disordered nitrile N3 atom for **4**, and both are symmetry related in which changing one interaction has a knock-on effect. The details of crystal data, selected bond lengths and angles for compounds **1**−**5** are listed in Tables 1 and S1.

RESULTS AND DISCUSSION

Description of the Structures. [Cu(cna)$_2$(pyz)]$_n$ (1). Single-crystal structure analysis reveals that **1** crystallizes in the monoclinic system $P2_1/c$ space group. The coordination environment of the Cu(II) center is shown in Figure 1a. Each Cu(II) ion is five-coordinated showing a distorted square pyramidal CuN_2O_3 chromophore with a τ value of 0.24 (Addison's parameter τ[56] = 0 for square pyramid and τ = 1 for trigonal bipyramid). The equatorial plane around the copper atom is composed of two carboxylic oxygen atoms (O1 and O2) from two different cyanoacetate groups and two nitrogen atoms from μ_2-pyz with average Cu−O and Cu−N distances of 1.959(2) and 2.030(2) Å, respectively. The apical position is

DOI: 10.1021/acs.cgd.5b00453
Cryst. Growth Des. 2015, 15, 3804−3812

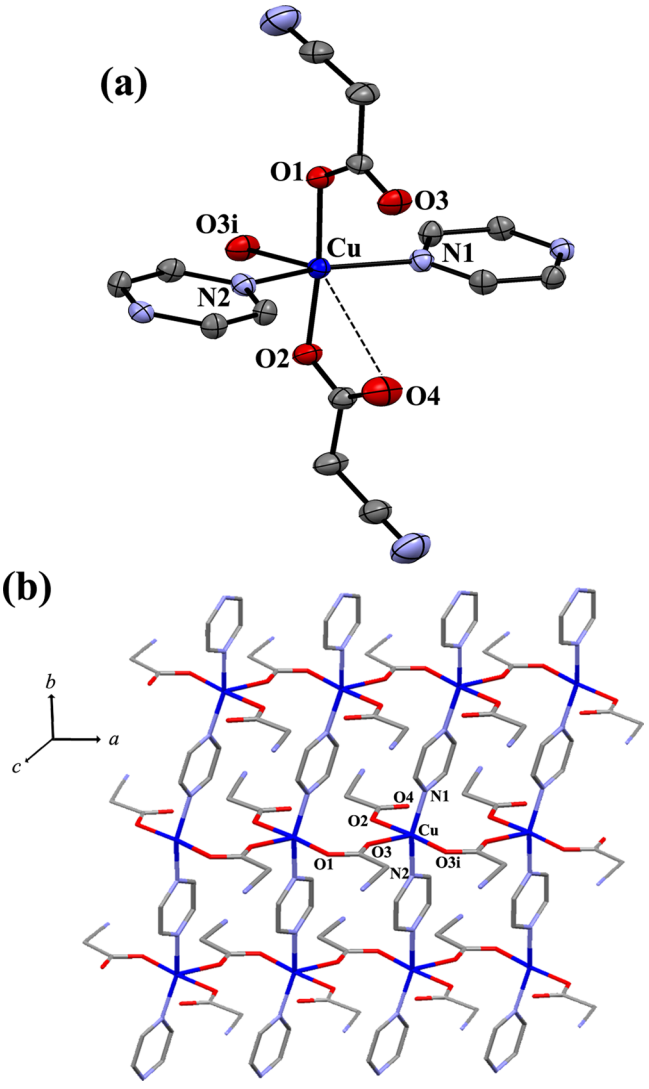

Figure 1. (a) Asymmetric unit and atom labeling scheme of **1**. The ellipsoids are shown at 50% probability level. All hydrogen atoms are omitted for clarity. The dashed line represents weak interaction in the off-the-axis position. (i) = 1 + *x*, *y*, *z*. (b) Two-dimensional sheet structure of **1**.

occupied by oxygen (O3) atom from μ_2-cyanoacetate with the Cu−O3 distance of 2.283(2) Å. The CuN_2O_2 square base is not perfectly planar with tetrahedral twists between the N2−Cu−O2 and N1−Cu−O1 planes of 24.53°. The copper atom is slightly shifted by 0.087 Å from the mean basal plane toward the apical position, which is attributed to semicoordinated O4 atom from the terminal cyanoacetate weakly interacting to copper center in off-the-axis position of an elongated octahedral geometry with the longest Cu···O4 distance of 2.970 Å.[18,57] The cyanoacetate acts as bridging and terminal ligands. The μ_2-cyanoacetate exhibits a *syn,anti*-η^1:η^3:μ_2 coordinative mode of carboxylate bridging between adjacent Cu(II) centers along the *a* axis with Cu···Cu separation of 4.896(5) Å, resulting a zigzag polymeric chain structure of **1**. Moreover, each cyanoacetato Cu(II) wavy chain is connected by μ_2-pyz along *b* axis giving rise to 2D sheet structure of **1** with Cu···Cu separation of 6.832 Å via pyz (Figure 1b). The packing motif of **1** is stabilized by weak hydrogen bonding and N···π interactions between the layers (Figure 2). The interlayer weak hydrogen bonding are constructed from the C−H on pyrazine ring and the nitrogen atom of nitrile group

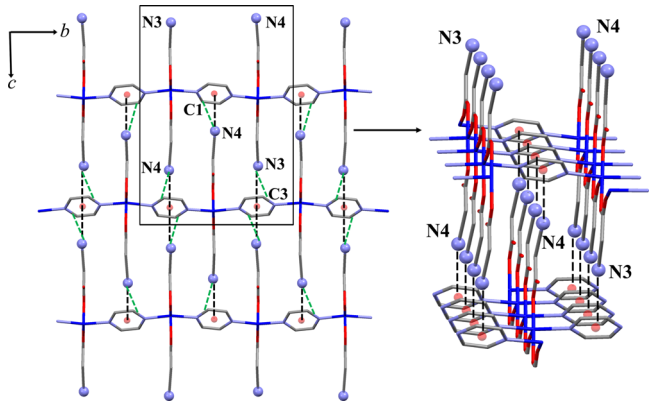

Figure 2. Packing motif of **1** in the *bc* plane; the inset presents the interlayered N···π(pyz) interactions. The green broken lines present weak hydrogen bonding between layers of **1**.

from the terminal and bridging cyanoacetates [C3H···$N3^i$ = 2.61 Å (147°), C3···$N3^i$ = 3.4290(6) Å, (i) = 3 − *x*, 1 − *y*, 1 − *z*; C1H···$N4^{ii}$ = 2.49 Å (147°), C1···$N4^{ii}$ = 3.3091(4) Å, (ii) = 1 + *x*, 1/2 − *y*, 1/2 + *z*]. Moreover, the nitrile N atoms from the terminal and μ_2-cyanoacetate can interact with the electron-deficient μ_2-pyz ring with N···centroid(pyz) distance of 3.420 Å for N3···π and 3.169 Å for N4···π, stabilizing 3D supramolecular framework of **1**, as shown in Figure 2. The distance between a R≡N donor and a centroid of six-membered heteroaromatic rings is found to be in the usual range of 3.00−3.40 Å.[58]

$[Cu(cna)_2(bpy)(H_2O)_2]_n$ (2). Single-crystal structure determination of **2** reveals 1D chain structure that crystallizes in orthorhombic *Pccn* space group. The crystal structure of **2** consists of neutral $[Cu(cna)_2(H_2O)_2]$ unit bridged *via* μ_2-bpy with the Cu···Cu separation of 11.018(8) Å. The cyanoacetate behaves as a monodentate ligand. Each Cu(II) ion is six-coordinated showing a distorted octahedral CuN_2O_4 chromophore (Figure 3a). The two nitrogen atoms from two μ_2-bpy spacers and two oxygen atoms from two terminal cyanoacetates reside in equatorial plane with Cu−N1 and Cu−O2 distances of 2.023(1) and 1.990(1) Å, respectively. Two oxygen atoms from two coordination water molecules are located in the axial positions with Cu−O1 distances of 2.500(1) Å. The adjacent Cu(II) centers are connected by μ_2-bpy forming a 1D chain coordination polymers, as shown in Figure 3b. The two pyridine rings of bipyridyl moieties are not coplanar with the dihedral angle between the two planar pyridine rings of 24.15°. The structure of **2** is isomorphous with previously reported Mn^{II} complex, $[Mn(cna)_2(bpy)(H_2O)_2]_n$.[23] However, the overall packing motif has not been entirely investigated. Each 1D chain of **2** is interlaced by 1D interchain weak hydrogen bonding array between terminal cyanoacetate ligands along *c* axis (C7H···N2) (Figure 4) and the intermolecular hydrogen bonding between unbound O atom from cyanoacetate and H atom from coordination water molecules (O1H···O3), additionally, weak hydrogen bonding between the pyridyl H atom from μ_2-bpy and coordination water molecules (C2H···O3). Moreover, the C2−H···π interaction is observed among the adjacent μ_2-bpy moieties along *c* axis with the separation of 3.372 Å (Figure 4). These weak interactions complete the overall 3D supramolecular motif of **2** with the closest interchain Cu···Cu separation of 7.4363(7) Å. [C2H···$O3^i$ = 2.59 Å (145°), C2···$O3^i$ = 3.391(2) Å, (i) = 1/2 + *x*, 1 − *y*, 1/2 − *z*; C7H···$N2^{ii}$ = 2.59 Å (122°), C7···$N2^{ii}$ = 3.213(3) Å, (ii) = *x*, 1/2 − *y*, 1/2 + *z*; O1H···$O3^{iii}$ = 2.26 Å (147°), O1···$O3^{iii}$ = 3.097(2) Å, (iii) = 1 − *x*, 1 − *y*, 1 − *z*].

DOI: 10.1021/acs.cgd.5b00453
Cryst. Growth Des. 2015, 15, 3804−3812

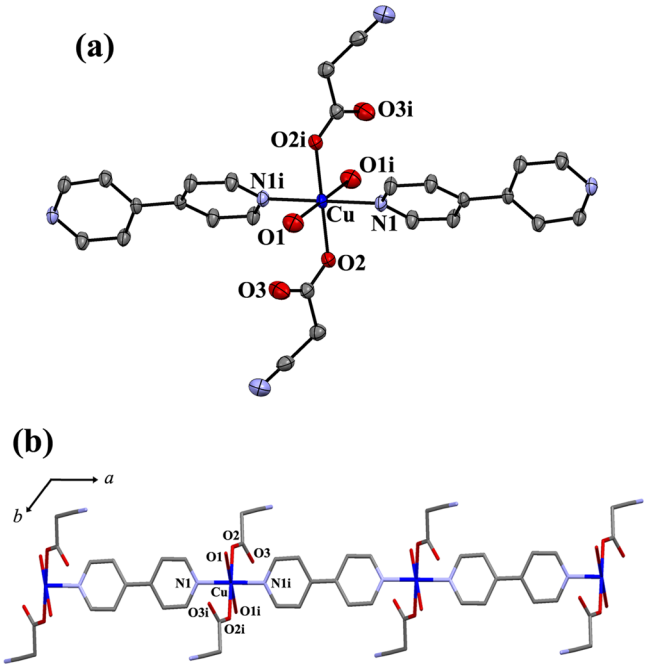

Figure 3. (a) Asymmetric unit and atom labeling scheme of **2**. The ellipsoids are shown at 50% probability level. All hydrogen atoms are omitted for clarity (i) = 1 − *x*, 1 − *y*, −*z*. (b) 1D chain structure of **2** along the *a* axis.

$[Cu(cna)_2(dpe)]_n$ (3), $[Cu(cna)_2(dpe)]_n(H_2O)_n$ (4) and $[Cu(cna)_2(bpa)]_n$ (5). Compounds **3**−**5** exhibit 1D ladder chain structures as shown in Figure 5. Single-crystal structure analysis reveals that **3** and **5** are isostructures crystallizing in the triclinic system $P\bar{1}$ space group whereas compound **4** crystallizes in the monoclinic *C*2/*c* space group. All Cu(II) ions are five-coordination showing distorted square pyramidal geometry CuN_2O_3 chromophore with τ values of 0.42, 0.04, and 0.46 for **3**−**5**, respectively. Each Cu(II) center is surrounded by two carboxylate oxygen atoms from two different cyanoacetates and two nitrogen atoms from two μ_2-dpe (for **3** and **4**) or μ_2-bpa (for **5**) living in an equatorial site with average Cu−O distances of 2.000(2), 1.968(1), and 1.990(2) Å and Cu−N distances of 2.016(2), 2.010(1), and 2.014(2) Å for **3**−**5**, respectively. The leaving one apical position is occupied by carboxylate oxygen atom from bridging cyanoacetate with the distances of Cu−O4 = 2.282(2), Cu−O1 = 2.446(1), and Cu−O2 = 2.264(2) Å for **3**−**5**, respectively. The CuN_2O_2 square base is not completely planar with tetrahedral twists between the planes of 26.61°, 14.45°, and 29.06° for **3**−**5**, respectively. The copper atoms are shifted by 0.303, 0.056, and 0.270 Å from the mean basal planes toward the apical positions for **3**−**5**, respectively. Those of slightly shifted value of **4** results from semicoordinated O4 atom from terminal cyanoacetate weakly interacting to copper center in off-the-axis position of an elongated octahedral geometry with the longest Cu···O4 distance of 2.828(2) Å. The carboxylic bridges for μ_2-cyanoacetate of **3** and **5** exhibit a double-*syn*,*anti*-η^1:η^3:μ_2 coordinative mode connecting between Cu(II) ions, generating the dinuclear Cu(II) units with Cu···Cu separation of 4.278(3) Å for **3** and 4.352(4) Å for **5**, whereas those of **4** exhibit a double-μ_2-1,1-monoatomic bridging mode with the shorter Cu···Cu separation of 3.433(4) Å. The carboxyl-bridged dinuclear Cu(II) units are extended along the particular direction by paired μ_2-dpe (for **3** and **4**) or μ_2-bpa spacers (for **5**) to create the infinite 1D ladder-like structures. The Cu···Cu separations across μ_2-dpe

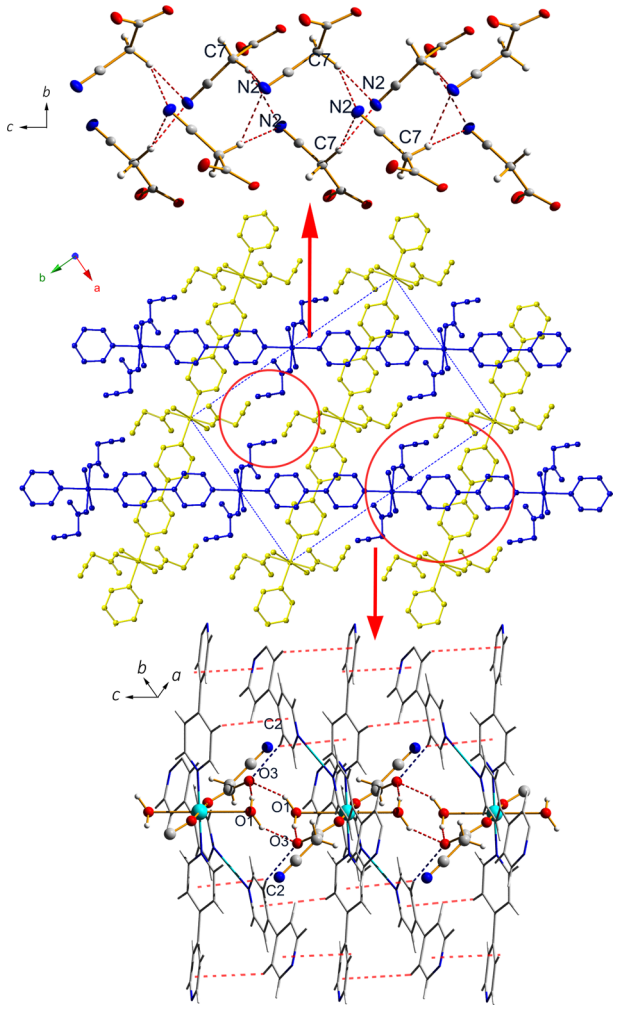

Figure 4. Interlaced chain structure of **2** in *ab* plane formed by 1D intermolecular weak hydrogen bonding array between terminal cyanoacetates along the *c* axis (top). The hydrogen bonding between unbound O3-cyanoacetate and coordination water represents in red dotted lines (bottom). The blue dotted lines represent the C2H···O3 weak hydrogen bonding and the red broken lines represent C−H···π interaction.

(for **3** and **4**) are 13.407(8), 13.349(6) Å and μ_2-bpa (for **5**) 13.288(5) Å, respectively. The two pyridine rings of bipyridyl moieties are not coplanar with the dihedral angles between the two planar pyridine rings of 9.24°, 11.59°, and 18.64° for **3**−**5**, respectively. The conformations of μ_2-dpe and μ_2-bpa ligands are *anti* with C−CH═CH−C torsion angles of 177.30° (for **3**) and 179.03° (for **4**), and C−CH_2−CH_2−C torsion angle of 179.91° (for **5**).

The supramolecular structures of **3** and **5** (Figure S1) are stabilized by weak interchain hydrogen bonding with the closest Cu···Cu distances of 6.7787(7) Å for **3** and 6.5672(5) Å for **5**. [for **3**, C15H···O2^{i}= 2.46 Å (126°), C15···O2^{i} = 3.099(4) Å, (i) = −*x*, 2 − *y*, 1 − *z*; C16H···O2^{i}= 2.60 Å (121°), C16···O2^{i} = 3.147(4) Å; for **5**, C2H···O4^{i}= 2.52 Å (152°), C2···O4^{i} = 3.373(4) Å, (i) = −*x*, −*y*, −*z*; C17H···N4^{ii} = 2.54 Å (161°), C17···N4^{ii} = 3.170(1) Å, (ii) = −*x*, 1 − *y*, 1 − *z*]. Moreover, the nitrile N atoms from the terminal and bridging cyanoacetates interact with the adjacent electron-deficient μ_2-dpe rings with N···centroid distances of 3.665 Å (for N3···π) and 3.274 Å (for N4···π), stabilizing the overall packing structure of **3**. The

DOI: 10.1021/acs.cgd.5b00453
Cryst. Growth Des. 2015, 15, 3804−3812

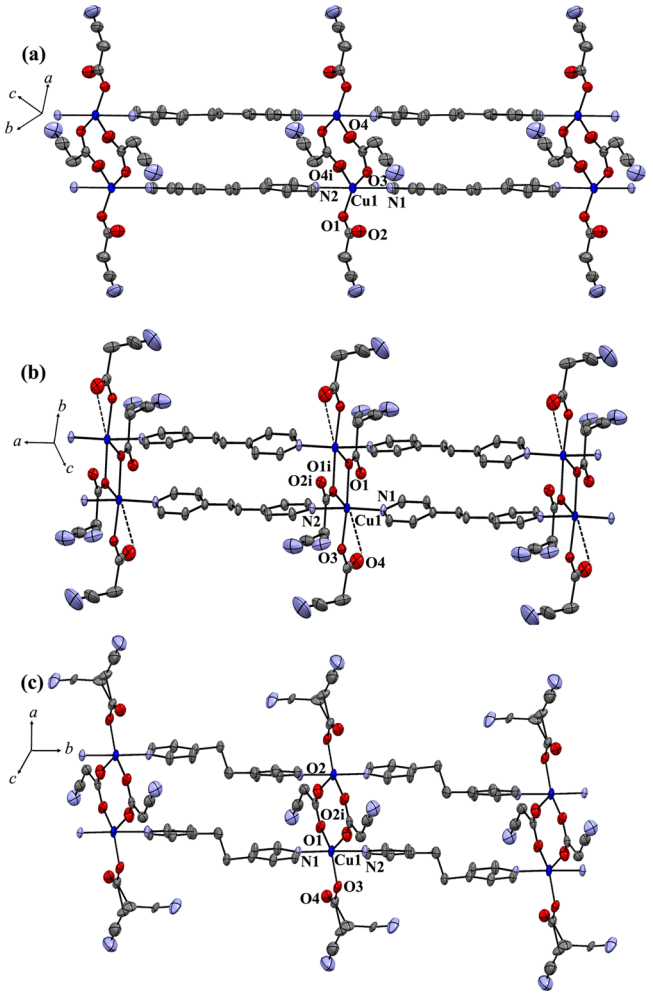

Figure 5. Part of 1D ladder chain structures of **3**(a), **4**(b), and **5**(c) with used atom labeling. The ellipsoids are shown at 35% probability level. The lattice water molecules for **4** and all hydrogen atoms are omitted for clarity. Both disordered nitrile groups of μ_2-cna for **4** and those of terminal cna for **5** are shown.

N···π(bpa) interactions in **5** is not observed because two bipyridyl moieties in a flexible μ_2-bpa spacer are notably twisted with the highest dihedral angle compared with those of **3** and **4**.

In contrast, the ladder chains of **4** are crossed by the hydrogen bonding between the nitrile N atoms from the terminal and bridging cyanoacetates and oxygen atoms from lattice water molecules with N4···O5 = 2.819 Å and N3···O5 = 3.194 Å, as well as, the hydrogen bonding between lattice water molecules with O5···O5i separation of 2.762 Å. In addition, the N3··· centroid(pyridyl) is observed with the distance of 3.328 Å and the weak hydrogen bonding among the carboxylate oxygen of cyanoacetate and pyridyl hydrogen of μ_2-dpe cooperatively stabilizes the entire 3D packing motif of **4** with the closest Cu··· Cu interchain distance of 7.2746(5) Å [C5H···N3^{i} = 2.51 Å (170°), C5···N3^{i} = 3.433(5) Å, (i) = 1/2 − x, 5/2 − y, −z; C7H··· O4^{ii} = 2.56 Å (127°), C7···O4^{ii} = 3.212(3) Å, (ii) = 1/2 − x, −1/ 2 + y, 1/2 − z; C14H···O4^{iii} = 2.50 Å (156°), C14···O4^{iii} = 3.289(4) Å, (iii) = x, 2 − y, 1/2 − z; C17H···O2^{ii} = 2.30 Å (153°), C17···O2^{ii} = 3.191(4) Å] (Figure S2).

IR and UV−visible Spectroscopy. The solid-state IR spectra of **1**−**5** in the region 4000−450 cm^{-1} are displayed in Figure S3. The IR spectra of all compounds exhibit the vibrations of the pyridyl rings for *N,N′*-ditopic spacers in the region 1650−1600 cm^{-1} overlapping the ν_{as}(OCO) bands around ∼1630−1570 cm^{-1}. The strong bands in the region 1430−1360 cm^{-1} are attributed to the ν_s(OCO). The splitting of ν(OCO) reflects that the carboxylate groups of cyanoacetate adopt a variety of coordination modes. The $\Delta\nu_{asym-sym}$ values are in range of 200−260 cm^{-1} which are consistent with monodentate and bridging coordination by the carboxylato group.[10,26,41,59] The medium sharp band at 2258 cm^{-1} can be assigned to the ν(C≡N) from cyanoacetate.[22,26,29] Compounds **2** and **4** show broad bands in the region 3200−3460 cm^{-1} due to the ν(O−H) of water molecules.

The electronic spectra of **1**−**5** were studied in solid state at room temperature (Figure S4). Compounds **1**, **2**, and **4** show a broad absorption band at higher energy around 16860−15450 cm^{-1}, corresponding to the ^2E_g to $^2T_{2g}$ (parent) transition in the distorted octahedral geometry of **2**, and this feature is also consistent with the elongated octahedral geometry with the sixth off-the-axis weakly interacting to Cu center for **1** and **4**,[18,60] while compounds **3** and **5** exhibit the single broad band in much lower transition energy around 13770 cm^{-1}, which is in agreement with the distorted square pyramidal geometry with high τ values.[61−63]

Thermal Analyses. To examine the thermal stabilities of compounds **1**−**5**, thermogravimetric analyses (TGA) were performed in the temperature range 30−500 °C in N_2 atmosphere (Figure 6). Compounds **1**, **3**, **4**, and **5** show no

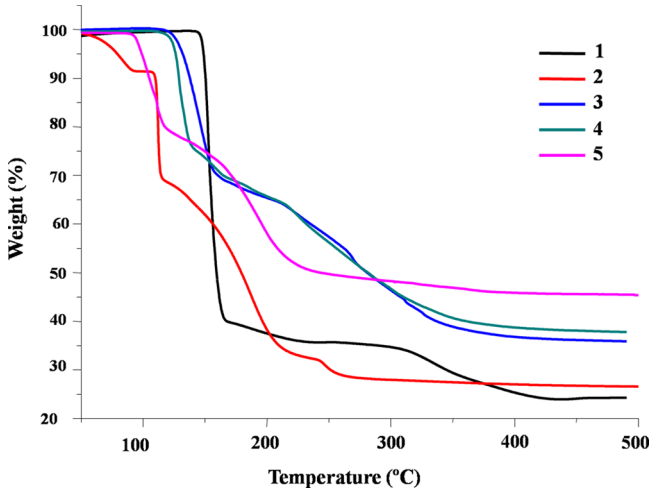

Figure 6. TGA curves of compounds **1**−**5**.

weight loss and are stable up to ∼140, 120, 110, 100 °C, respectively. Then the structures gradually decompose corresponding to the removal of lattice water molecule, cyanoacetate and organic coligands, finally giving a mixture of the CuO and Cu_2O as main products.[64] The TGA curve of **2** reveals the release of two coordination water molecules at the first step of weight loss in the temperature range 50−92 °C (found, 8.33%; Calcd, 8.50%) resulting to the dehydrated form of $[Cu(cna)_2(bpy)]_n$ (**2-A**), which is stable up to ∼107 °C and then the structure gradually collapses.

Supramolecular Robustness in 2. Aforementioned compound **2** contains two coordination water molecules and its anhydrous phase remaining stable up to 107 °C, as evidenced by the TGA profile. This inspired us to examine the dynamic structures of **2** during the dehydration and rehydration processes by elemental analyses, XRPD, and spectroscopic techniques. Consequently, the dehydrated form, $[Cu(cna)_2(bpy)]_n$ (**2-A**)

DOI: 10.1021/acs.cgd.5b00453
Cryst. Growth Des. 2015, 15, 3804−3812

was obtained by heating the polycrystalline samples of **2** at 105 °C for 20 min and the color changed from blue to deep blue. Furthermore, the rehydrated form of **2-A′** was obtained by immersing the dehydrated sample to water for 1 day at room temperature. The XRPD patterns of **2**, **2-A** and **2-A′** are shown in Figure 7. The elemental analysis of **2-A** (Anal. Calcd for

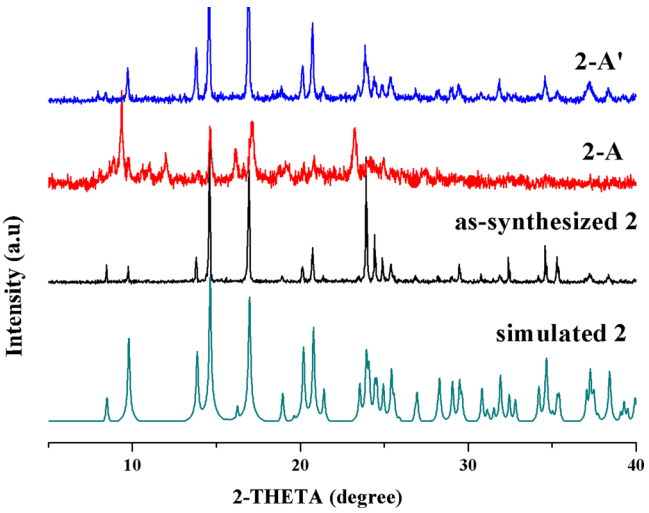

Figure 7. XRPD patterns: simulated from single-crystal X-ray data of **2**; as-synthesized **2**, the dehydrated form **2-A**; the rehydrated form **2-A′**.

$CuC_{16}H_{12}N_4O_4$: C, 49.55; H, 3.12; N, 14.45%. Found: C, 49.30; H, 3.16; N, 14.30%.) and XRPD results indicate that the anhydrous $[Cu(cna)_2(bpy)]_n$ (**2-A**) reveals no significant change of crystalline phase which the main peaks are duplicate to those of XRPD pattern of as-synthesized **2**. The new peaks appear at 9.37° and 23.26° are ascribed to the drastic change in the coordination environments around Cu(II) center during dehydration process. Moreover, the original crystalline phase $[Cu(cna)_2(bpy)(H_2O)_2]_n$ (**2-A′**) can be restored from **2-A** after rehydration process, confirmed by the coincidence in XRPD patterns and elemental analysis (Anal. Calcd $CuC_{16}H_{16}N_4O_6$: C, 45.34; H, 3.80; N, 13.22%. Found: C, 45.26; H, 3.69; N, 13.00%.). This result confirms the rigid supramolecular framework of **2** during thermal dehydration and rehydration processes. Furthermore, this behavior has been further verified by TGA, IR, and solid-state UV−vis diffuse reflectance spectra. The TGA profiles of **2** and **2-A′** (Figure 8) are identical showing the release of two coordination water molecules at the first step of weight loss (Anal. Calcd: 8.50% Found: 8.33% for **2-A′**), whereas the TGA profile of anhydrous form **2-A** shows no weight loss, remaining stable up to ∼107 °C, and then the structure gradually collapses. The UV−vis spectra clearly show that the parallel bands observed in **2** and **2-A′** implying the same Cu(II) environments (Figure S5), whereas the anhydrous **2-A** shows the blue-shifted absorption broadband with λ_{max} around ∼590 nm, giving the deep blue color. In fact these values of the transition energy are in the usual range for the pseudo-octahedral geometry of Cu(II) center.[60] In addition, these results agree with the reversible change in IR spectra for ν(O−H) of coordination water molecules around 3544−3200 cm^{-1} and the ν_s(OCO) of cyanoacetate at ∼1600 cm^{-1} and the fingerprint region below 818 cm^{-1} (Figure S6). All of the results prove the supramolecular robustness of **2**.

Interestingly, this phenomenon is not observed in the isomorphous analogues containing Co(II) (**2-Co**) and Ni(II)

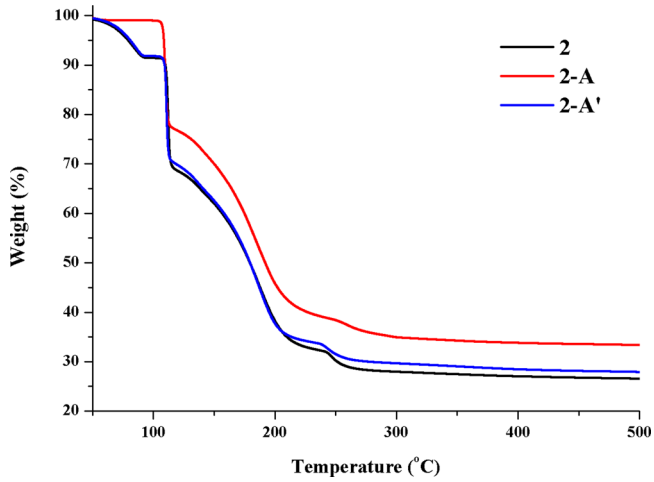

Figure 8. TGA curves of **2**, the dehydrated form **2-A**, and rehydrated form **2-A′**.

(**2-Ni**) centers. The crystal structures of **2-Co** and **2-Ni** are confirmed by XRD, IR spectra, TGA, and elemental analysis (see Figure S7−S9). The coincidence in XRPD patterns and IR spectra of **2**, **2-Co**, and **2-Ni** imply the identical crystalline structures, whereas the TGA profiles of **2-Co** and **2-Ni** reveal the releases of two coordination water molecules at the higher temperature range 85−120 °C for **2-Co** and 95−140 °C for **2-Ni**. Then, the structures continuously decompose with no observed stable anhydrous phases in TGA profiles. The dehydrated forms of **2-Co-A** and **2-Ni-A** were examined and obtained by heating the polycrystalline sample at 115 °C, 135 °C for 20 min for **2-Co** and **2-Ni**, respectively, and the colors changed from orange to brown for **2-Co-A**, blue to green for **2-Ni-A** (Figure S10). The XRPD results indicate that **2-Co-A** and **2-Ni-A** are amorphous forming by the collapse of supramolecular structure. Moreover, these anhydrous amorphous phases cannot be regenerated to the original crystal structure after immersion into water for 1 day (Figure S11 and S12).

The observation of the robust framework of **2** may be attributed to the cooperative effects between the diverse intermolecular interactions stabilizing noncovalent supramolecular motifs together with the Jahn−Teller distortion in Cu(II) d^9 system. The X-ray analysis of **2** revealed that two coordination water molecules in the role of H-donors display the individual intermolecular hydrogen bonds only through unbound oxygen atoms from terminal cyanoacetate as H-acceptors (Figure 4). Thus, upon eliminating the coordination water in **2**, these unbound carboxylic oxygen atoms possibly weakly interact with the vacant Cu(II) sites leading to the elongated octahedral geometry, as evidenced by electronic spectra of **2-A** (Figure S5). In addition, the coordination bridge via rigid bpy backbone plays a role for supporting the structural skeleton, as well as, the other noncovalent interactions especially the 1D hydrogen bonding array involving terminal cyano groups and C−H···π interactions together efficiently support the stabilization of overall supramolecular framework of **2-A** (Figure S13). Furthermore, the structural collapses of the anhydrous analogues **2-Co-A** and **2-Ni-A** point out that besides noncovalent interactions and coordination bridges, the Jahn−Teller effect in the Cu(II), d^9 system plays a significant role in stabilizing the distorted octahedral coordination sphere,[65−67] giving rise to the structural flexibility that is not found in **2-Co-A** and **2-Ni-A** analogues. Remarkably, the dehydration process in **2-A** can be reversed after

DOI: 10.1021/acs.cgd.5b00453
Cryst. Growth Des. 2015, 15, 3804−3812

immersing the dehydrated sample in water, regenerating the original crystalline phase, which is an indication of the robust but flexible supramolecular framework constructed by 1D polymeric chains in **2**.

Magnetic Measurements. The magnetic susceptibilities of powdered sample of **1** and **3** were measured between 2 and 300 K under a constant *dc* magnetic field of 0.1 T (Figures S14 and S15). At 300 K the $\chi_M T$ values are 0.45 and 0.41 cm^3 K mol^{-1} for **1** and **3**, respectively, which are typical of Cu(II) and above that expected for uncoupled Cu(II) centers (0.375 cm^3 K mol^{-1} for $g = 2$) because of spin−orbit coupling, i.e., $g > 2$. The $\chi_M T$ values of **1** slowly decrease, in a linear fashion, down to ∼15 K and then, more rapidly, reaching 0.33 cm^3 K mol^{-1} at 2 K. In contrast, the $\chi_M T$ values for **3** are practically constant until ∼10 K, and then the $\chi_M T$ values abruptly decrease to reach 0.19 cm^3 K mol^{-1} at 2 K. The corresponding plots of χ_M vs T for **1** and **3** show Curie-like behavior with a hint of a maximum in χ_M beginning below 2 K in **3**. The data are generally indicative of very weak antiferromagnetic coupling, this being responsible for the rapid decreases in $\chi_M T$ at very low temperatures,[18,49,68] although Zeeman level thermal depopulation effects may play a part in this region. There is no evidence in the temperature range studied for any long-range magnetic ordering.

In attempting to quantify the magnetic data, the 2D sheet motif of **1** ideally requires a two J model one for the *syn,anti*-$\eta^1{:}\eta^3{:}\mu_2$-cyanoacetate bridged chains, the other for the pyrazine bridged chains. Landee and Turnbull have recently reviewed low-dimensional Cu(II) molecular magnets[69] including related 2D rectangular sheets such as $[Cu(HCO_2)(pyz)(NO_3)]_n$ that showed a mixed antiferromagnetic (pyrazine bridge)/ferromagnetic (formate bridge) behavior and was fitted by Monte Carlo methods.[70] $[Cu(HCO_2)(pyz)(NO_3)]_n$ showed a broad maximum in $\chi_M T$ at 25.3 K, due to ferromagnetic exchange, and a maximum in χ_M at 6.5 K due to antiferromagnetic exchange. Clearly were do not observe such χ_M or $\chi_M T$ maxima in **1** so we conclude that antiferromagnetic exchange occurs along the cyanoacetate- and pyz-bridged chains, and is smaller in magnitude than in $[Cu(HCO_2)(pyz)(NO_3)]_n$. As in the case of 2D β-$[Cu(dca)_2(pyz)]_n$ where dca = $\mu_{1,5}$-NC(N)CN[71] we have used a model by Lines[72] for 2D systems with $S = 1/2$, based on that of Rushbrooke and Wood.[73] A good fit of the data was obtained (Figure S16) using a single J of −0.24 cm^{-1}, but the g value of 1.89 is lower than expected for Cu(II) and the $N\alpha$ (temperature independent susceptibility) of 400 × 10^{-6} cm^3 mol^{-1} is much higher than the normal 60 × 10^{-6} cm^3 mol^{-1}. The size of J is at the lower end of values found for *syn,anti*-$\eta^1{:}\eta^3{:}\mu_2$-carboxylate and pyrazine bridges. It is possible that there are traces of impurity in the sample of **1** that affect the $\chi_M T$ behavior and the fitting thereof.[69]

The $\chi_M T$ plot for **3** is indicative of very weak to zero exchange coupling, and this is not surprising in view of the large Cu···Cu separations and the poor superexchange pathways provided by the 1,2-di(4-pyridyl)ethylene linkers, along the ladder chains.

CONCLUSIONS

Five new coordination polymers constructed by self-assembly of the auxiliary *N,N′*-ditopic spacers and copper(II) cyanoacetates have been structurally characterized. Compounds **2**−**5** exhibit a polymeric chain structure, while **1** shows a 2D layer. This result demonstrated that the length of auxiliary spacers effectively influences the structural dimensionalities. The shortest pyrazine with Cu(II) cyanoacetate well provides the construction of 2D coordination polymer in **1**. Likewise, the structural diversity greatly results from the carboxylate groups in cyanoacetate that can coordinate with the Cu(II) center in various ways. The μ_2-1,3(*syn,anti*) bridging mode for **1**, **3**, and **5**, and μ_2-1,1 monatomic bridge in **4** are found, whereas cyanoacetate in **2** behaves as a terminal monodentate ligand. Besides the various coordination modes of carboxylates, the nitrile group in cyanoacetate has an influence on the established supramolecular interactions via either hydrogen bonding or N···π interactions, which mainly contributes to the stabilization of the overall supramolecular architecture. Particularly, compound **2** exhibits a robust supramolecular framework constructed by 1D polymeric chains during the thermal dehydration and rehydration processes that is not observed in the isomorphous series containing Co(II) and Ni(II) ions. This result demonstrates the significant role of Jahn−Teller distortions in the octahedral Cu(II) center accompanied by various intermolecular noncovalent interactions among interlaced polymeric chains for encouraging the design of a "soft" supramolecular framework with low dimensional building blocks.

ASSOCIATED CONTENT

Supporting Information

Figures of IR and UV−visible spectra, magnetic susceptibilities, XPRD patterns, and X-ray crystallographic information files (CIF) for **1**−**5**. The Supporting Information is available free of charge on the ACS Publications website at DOI: 10.1021/acs.cgd.5b00453. Crystallographic data were deposited with the following Cambridge Crystallographic Data Centre codes: CCDC 1053369−1053373 for **1**−**5** and CCDC 1408728 for **2-Co**.

AUTHOR INFORMATION

Corresponding Author

*E-mail: Jaursup@kku.ac.th; fax: +6643-202-373.

Notes

The authors declare no competing financial interest.

ACKNOWLEDGMENTS

Funding for this work is provided by The Thailand Research Fund: Grant No. TRG5780003 (for J.B.) and BRG5680009 (for S.Y.), the Higher Education Research Promotion and National Research University Project of Thailand, through the Advanced Functional Materials Cluster of Khon Kaen University, and the center of Excellence for Innovation in Chemistry (PERCH-CIC), Office of the Higher Education Commission, Ministry of Education, Thailand. K.S.M. thanks the Australian Research Council for a Discovery grant.

REFERENCES

(1) Cheetham, A. K.; Rao, C. N. R.; Feller, R. K. *Chem. Commun.* **2006**, 4780.
(2) Janiak, C. *Dalton Trans.* **2003**, 2781.
(3) Kitagawa, S.; Kitaura, R.; Noro, S.-i. *Angew. Chem., Int. Ed.* **2004**, *43*, 2334.
(4) Kuppler, R. J.; Timmons, D. J.; Fang, Q.-R.; Li, J.-R.; Makal, T. A.; Young, M. D.; Yuan, D.; Zhao, D.; Zhuang, W.; Zhou, H.-C. *Coord. Chem. Rev.* **2009**, *253*, 3042.
(5) Schneemann, A.; Bon, V.; Schwedler, I.; Senkovska, I.; Kaskel, S.; Fischer, R. A. *Chem. Soc. Rev.* **2014**, *43*, 6062.
(6) Stock, N.; Biswas, S. *Chem. Rev.* **2012**, *112*, 933.
(7) O'Keeffe, M.; Yaghi, O. M. *Chem. Rev.* **2012**, *112*, 675.
(8) Suh, M. P.; Park, H. J.; Prasad, T. K.; Lim, D.-W. *Chem. Rev.* **2012**, *112*, 782.
(9) Yoon, M.; Srirambalaji, R.; Kim, K. *Chem. Rev.* **2012**, *112*, 1196.

DOI: 10.1021/acs.cgd.5b00453
Cryst. Growth Des. 2015, 15, 3804−3812

(10) Carballo, R.; Castineiras, A.; Covelo, B.; Vazquez-Lopez, E. M. *Polyhedron* **2001**, *20*, 899.
(11) Hu, H.-L.; Suen, M.-C.; Yeh, C.-W.; Chen, J.-D. *Polyhedron* **2005**, *24*, 1497.
(12) Jassal, A. K.; Sharma, S.; Hundal, G.; Hundal, M. S. *Cryst. Growth Des.* **2015**, *15*, 79.
(13) Liu, Q.-Y.; Yuan, D.-Q.; Xu, L. *Cryst. Growth Des.* **2007**, *7*, 1832.
(14) Wang, H.; Zhang, D.; Sun, D.; Chen, Y.; Zhang, L.-F.; Tian, L.; Jiang, J.; Ni, Z.-H. *Cryst. Growth Des.* **2009**, *9*, 5273.
(15) Wang, X.-F.; Zhang, Y.-B.; Huang, H.; Zhang, J.-P.; Chen, X.-M. *Cryst. Growth Des.* **2008**, *8*, 4559.
(16) Zhu, H.-F.; Zhang, Z.-H.; Sun, W.-Y.; Okamura, T.-a.; Ueyama, N. *Cryst. Growth Des.* **2005**, *5*, 177.
(17) Mikuriya, M.; Yoshioka, D.; Handab, M. *Coord. Chem. Rev.* **2006**, *250*, 2194.
(18) Boonmak, J.; Youngme, S.; Chaichit, N.; Albada, G. A. v.; Reedijk, J. *Cryst. Growth Des.* **2009**, *9*, 3318.
(19) Boonmak, J.; Youngme, S.; Chotkhun, T.; Engkagul, C.; Chaichit, N.; Albada, G. A. v.; Reedijk, J. *Inorg. Chem. Commun.* **2008**, *11*, 1231.
(20) Kurmoo, M. *Chem. Soc. Rev.* **2009**, *38*, 1353.
(21) Wang, X.-Y.; Wang, Z.-M.; Gao, S. *Chem. Commun.* **2008**, 281.
(22) Sokolova, M. N.; Budantseva, N. A.; Fedoseev, A. M. *Russ. J. Coord. Chem.* **2011**, *37*, 478.
(23) Feng, X.; Shi, X.-G.; Ruan, F. *Z. Kristallogr. - New Cryst. Struct.* **2009**, *224*, 193.
(24) Feng, X.; Feng, T.-C.; Zhao, J.-S.; Shi, X.-G.; Ruan, F. *Z. Kristallogr. New Cryst. Struct.* **2009**, *224*, 541.
(25) Shova, S. G.; Simonov, Y. A.; Gdaniec, M.; Novitchi, G. V.; Lazarescu, A.; Turta, K. I. *Russ. J. Inorg. Chem.* **2002**, *47*, 847.
(26) Novitskii, G.; Shova, S.; Voronkova, V. K.; Korobchenko, L.; Gdanec, M.; Simonov, Y. A.; Turte, K. *Russ. J. Coord. Chem.* **2001**, *27*, 791.
(27) Nakamoto, T.; Hanaya, M.; Katada, M.; Endo, K.; Kitagawa, S.; Sano, H. *Inorg. Chem.* **1997**, *36*, 4347.
(28) Darensbourg, D. J.; Holtcamp, M. W.; Longridge, E. M.; Khandelwal, B.; Klausmeyer, K. K.; Reibenspies, J. H. *J. Am. Chem. Soc.* **1995**, *117*, 318.
(29) Wasson, J. R.; Shyr, C.-I.; Trapp, C. *Inorg. Chem.* **1968**, *7*, 469.
(30) Leong, W. L.; Vittal, J. J. *Chem. Rev.* **2011**, *111*, 688.
(31) Vittal, J. J. *Coord. Chem. Rev.* **2007**, *251*, 1781.
(32) Hu, S.; He, K.-H.; Zeng, M.-H.; Zou, H.-H.; Jiang, Y.-M. *Inorg. Chem.* **2008**, *47*, 5218.
(33) Yu, F.; Li, D.-D.; Cheng, L.; Yin, Z.; Zeng, M.-H.; Kurmoo, M. *Inorg. Chem.* **2015**, *54*, 1655.
(34) Lee, E. Y.; Suh, M. P. *Angew. Chem., Int. Ed.* **2004**, *43*, 2798.
(35) Cingolani, A.; Galli, S.; Masciocchi, N.; Pandolfo, L.; Pettinari, C.; Sironi, A. *J. Am. Chem. Soc.* **2005**, *127*, 6144.
(36) Piromchom, J.; Wannarit, N.; Boonmak, J.; Pakawatchai, C.; Youngme, S. *Inorg. Chem. Commun.* **2014**, *40*, 59−61.
(37) Kitagawa, S.; Uemura, K. *Chem. Soc. Rev.* **2005**, *34*, 109.
(38) Boonmak, J.; Nakano, M.; Chaichit, N.; Pakawatchai, C.; Youngme, S. *Dalton Trans.* **2010**, *39*, 8161.
(39) Hogan, G. A.; Rath, N. P.; Beatty, A. M. *Cryst. Growth Des.* **2011**, *11*, 3740.
(40) Kawano, M.; Fujita, M. *Coord. Chem. Rev.* **2007**, *251*, 2592.
(41) Parshamoni, S.; Sanda, S.; Jena, H. S.; Tomar, K.; Konar, S. *Cryst. Growth Des.* **2014**, *14*, 2022.
(42) Fan, L.; Zhang, X.; Sun, Z.; Zhang, W.; Ding, Y.; Fan, W.; Sun, L.; Zhao, X.; Lei, H. *Cryst. Growth Des.* **2013**, *13*, 2462.
(43) Niu, D.; Yang, J.; Guo, J.; Kan, W.-Q.; Song, S.-Y.; Du, P.; Ma, J.-F. *Cryst. Growth Des.* **2012**, *12*, 2397.
(44) Chang, Z.; Zhang, D.-S.; Chen, Q.; Li, R.-F.; Hu, T.-L.; Bu, X.-H. *Inorg. Chem.* **2011**, *50*, 7555.
(45) Drabent, K.; Ciunik, Z. *Cryst. Growth Des.* **2009**, *9*, 3367.
(46) Tian, A.-x.; Ying, J.; Peng, J.; Sha, J.-q.; Pang, H.-j.; Zhang, P.-p.; Chen, Y.; Zhu, M.; Su, Z.-m. *Cryst. Growth Des.* **2008**, *8*, 3717.
(47) Liu, G.-X.; Huang, Y.-Q.; Chu, Q.; Okamura, T.-a.; Sun, W.-Y.; Liang, H.; Ueyama, N. *Cryst. Growth Des.* **2008**, *8*, 3233.
(48) Brown, S.; Cao, J.; Musfeldt, J. L.; Conner, M. M.; McConnell, A. C.; Southerland, H. I.; Manson, J. L.; Schlueter, J. A.; Phillips, M. D.; Turnbull, M. M.; Landeel, C. P. *Inorg. Chem.* **2007**, *46*, 8577.
(49) Carballo, R.; Covelo, B.; Fallah, M. S. E.; Ribas, J.; Vazquez-Lopez, E. M. *Cryst. Growth Des.* **2007**, *7*, 1069.
(50) Phuengphai, P.; Youngme, S.; Mutikainen, I.; Gamez, P.; Reedijk, J. *Polyhedron* **2012**, *42*, 10.
(51) *SMART 5.6*; Bruker AXS Inc.: Madison, WI, 2000.
(52) *APEX2*; Bruker AXS Inc.: Madison, WI, 2014.
(53) *SAINT 4.0 Software Reference Manual*; Siemens Analytical X-Ray Systems Inc.: Madison, WI, 2000.
(54) Sheldrick, G. M. *SADABS, Program for Empirical Absorption correction of Area Detector Data*; University of Göttingen: Göttingen, Germany, 2000.
(55) Sheldrick, G. M. *Acta Crystallogr., Sect. A: Found. Crystallogr.* **2008**, *A64*, 112.
(56) Addison, A. W.; Rao, T. N.; Reedijk, J.; Van Rijn, J.; Verschoor, G. C. *J. Chem. Soc., Dalton Trans.* **1984**, 1349.
(57) Jasiewicz, B.; Warzajtis, B.; Rychlewska, U. *Polyhedron* **2011**, *30*, 1703.
(58) Mooibroek, T. J.; Gamez, P.; Reedijk, J. *CrystEngComm* **2008**, *10*, 1501.
(59) Chai, X.-C.; Sun, Y.-Q.; Lei, R.; Chen, Y.-P.; Zhang, S.; Cao, Y.-N.; Zhang, H.-H. *Cryst. Growth Des.* **2010**, *10*, 658.
(60) Tabbì, G.; Giuffrida, A.; Bonomo, R. P. *J. Inorg. Biochem.* **2013**, *128*, 137.
(61) Youngme, S.; Wannarit, N.; Remsungnen, T.; Chaichit, N.; Albada, G. A. v.; Reedijk, J. *Inorg. Chem. Commun.* **2008**, *11*, 179.
(62) Youngme, S.; Cheansirisomboon, A.; Danvirutai, C.; Pakawatchai, C.; Chaichit, N. *Inorg. Chem. Commun.* **2008**, *11*, 57.
(63) Youngme, S.; Chotkhun, T.; Leelasubcharoen, S.; Chaichit, N.; Pakawatchai, C.; Albada, G. A. v.; Reedijk, J. *Polyhedron* **2007**, *26*, 725.
(64) Lin, Z.; Han, D.; Li, S. *J. Therm. Anal. Calorim.* **2012**, *107*, 471.
(65) Kozlevcar, B.; Golobic, A.; Strauch, P. *Polyhedron* **2006**, *25*, 2824.
(66) Zabierowski, P.; Szklarzewicz, J.; Kurpiewska, K.; ski, K. L.; Nitek, W. *Polyhedron* **2013**, *49*, 74.
(67) Youngme, S.; Wannarit, N.; Pakawatchai, C.; Chaichit, N.; Somsook, E.; Turpeinen, U.; Mutikainen, I. *Polyhedron* **2007**, *26*, 1459.
(68) Phuengphai, P.; Youngme, S.; Pakawatchai, C.; Albada, G. A. v.; Quesada, M.; Reedijk, J. *Inorg. Chem. Commun.* **2006**, *9*, 147.
(69) Landee, C. P.; Turnbull, M. M. *Eur. J. Inorg. Chem.* **2013**, *2013*, 2266.
(70) Keith, B. C.; Landee, C. P.; Valleau, T.; Turnbull, M. M.; Harrison, N. *Phys. Rev. B: Condens. Matter Mater. Phys.* **2011**, *84*, 104442.
(71) Jensen, P.; Batten, S. R.; Fallon, G. D.; Hockless, D. C. R.; Moubaraki, B.; Murray, K. S.; Robson, R. *J. Solid State Chem.* **1999**, *145*, 387.
(72) Lines, M. E. *J. Phys. Chem. Solids* **1970**, *31*, 101.
(73) Rushbrooke, G. S.; Wood, P. J. *Mol. Phys.* **1958**, *1*, 257.

DOI: 10.1021/acs.cgd.5b00453
Cryst. Growth Des. 2015, 15, 3804−3812

Polyhedron 102 (2015) 693–698

Contents lists available at ScienceDirect

Polyhedron

journal homepage: www.elsevier.com/locate/poly

Structural diversity and luminescent properties of cyanoacetato zinc/cadmium coordination polymers with *N*,*N*′-ditopic auxiliary ligands

Porntiva Suvanvapee, Jaursup Boonmak*, Sujittra Youngme

Materials Chemistry Research Center, Department of Chemistry and Center of Excellence for Innovation in Chemistry, Faculty of Science, Khon Kaen University, Khon Kaen 40002, Thailand

ARTICLE INFO

Article history:
Received 5 August 2015
Accepted 25 October 2015
Available online 31 October 2015

Keywords:
Coordination polymer
Cyanoacetate
4,4′-Bipyridyl
1,2-Di(4-pyridyl)ethane
Luminescence properties

ABSTRACT

By using the carboxylate ligand cyanoacetate (cna) and *N*,*N*′-ditopic organic neutral spacers, four new Zn(II)/Cd(II) coordination polymers, formulated as $[Zn(cna)_2(bpy)(H_2O)_2]_n$ (**1**), $[Cd_3(cna)_6(bpy)_3]_n$ (**2**), $[Zn(cna)_2(bpa)]_n$ (**3**) and $[Cd(cna)_2(bpa)]_n$ (**4**) (bpy = 4,4′-bipyridyl and bpa = 1,2-di(4-pyridyl)ethane) have been obtained. All compounds exhibit one-dimensional (1D) chain coordination polymers with diverse topologies. Compound **1** reveals a linear chain structure which is formed by μ_2-bpy bridging between $[Zn(cna)_2(H_2O)_2]_n$ units. Compound **2** shows a triple-stranded chain consisting of six- and seven-coordinated Cd(II) centers. Compound **3** exhibits a zigzag chain coordination polymer containing μ_2-bpa spacers bridging between tetrahedral Zn(II) ions. Whereas **4** shows a ladder-like structure which is built from double μ_2-bpa spacers connecting between Cd(II) cyanoacetate dimeric units. All compounds are further extended into a 3D supramolecular architectures through non-covalent weak hydrogen bonds and N···π and/or C–H···π interactions. The free bpa ligand exhibits very weak photoluminescence in the solid state, while this property is significantly enhanced in **3** and **4**.

1. Introduction

The construction of coordination polymers (CPs) has attracted attention due to their diverse structural topologies and potential applications such as gas storage, magnetism, catalysis, and luminescence [1–9]. The rational design of CPs is an important goal for synthetic chemistry as it provides an opportunity to modify their functional properties at the molecular level. To date, many CPs have been prepared on the basis of the connector and linker approach [4,6,10]. Connectors are often transition metal ions that can yield different coordination geometries. Linkers are typically organic molecules such as functionalized carboxylates and pyridine-based linkers. Coordination polymers constructed from divalent zinc and cadmium ions have been an active research area because the absence of crystal field stabilization energy in the d^{10} electronic configuration allows these metal ions to have no significant coordination preferences [11–14]. Thus, they can form a variety of structures depending on the organic linker. In the present studies, the cyanoacetate ($NC_2H_2CO_2$, cna) is used for binding metal ions through carboxylate bridge. It contains both nitrile (–C≡N) and carboxylic groups which not only provides many coordination sites but also effectively serves as hydrogen bonding sites and the intermolecular $N_{nitrile}\cdots\pi$ interaction toward neighboring electron-deficient aromatic moieties. These versatile connection sites allow cyanoacetate to be a good candidate for constructing the CPs [15–23]. Meanwhile, the mixed-ligands strategy, including *N*,*N*′-ditopic organic neutral coligands with different lengths and flexibility, has successfully demonstrated various novel CPs [10,24,25]. Recently, we reported a series of cyanoacetato coordination polymers in the Cu(II) system [23]. In consequence, to extend the study of the self-assembly process in d^{10} metal CPs, we have herein taken cyanoacetate and different pyridine-based neutral coligands in the Zn(II)/Cd(II) system (see Scheme 1). The four new 1D coordination polymers, $[Zn(cna)_2(bpy)(H_2O)_2]_n$ (**1**), $[Cd_3(cna)_6(bpy)_3]_n$ (**2**), $[Zn(cna)_2(bpa)]_n$ (**3**) and $[Cd(cna)_2(bpa)]_n$ (**4**) (bpy = 4,4′-bipyridyl and bpa = 1,2-di(4-pyridyl)ethane) have been synthesized. The characterizations have been done through X-ray crystallography, IR spectroscopy, and elemental analysis. The solid-state photoluminescent properties at room temperature have also been studied and this property is significantly enhanced in **3** and **4**.

* Corresponding author. Fax: +66 43 202 373.
E-mail address: Jaursup@kku.ac.th (J. Boonmak).

http://dx.doi.org/10.1016/j.poly.2015.10.043
0277-5387/

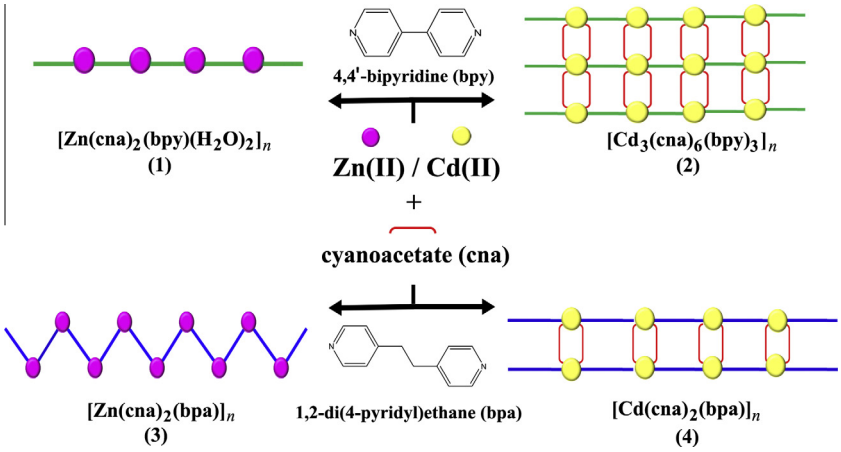

Scheme 1. The coordination polymers **1**–**4**.

2. Experimental

2.1. General remarks

All chemical were obtained from commercial sources and were used without further purification. Elemental analyses (C, H, N) were carried out with a PerkinElmer PE 2400CHNS analyzer. FT-IR spectra were obtained in KBr disks on a PerkinElmer Spectrum One FT-IR spectrophotometer in 4000–450 cm^{-1} spectral range. The X-ray powder diffraction (XRPD) data were collected on a Bruker D8 ADVANCE diffractometer using monochromatic Cu Kα radiation, and the recording speed was 0.5 s/step over the 2θ range of 5–40° at room temperature to determine the phase purity. Photoluminescent spectra of the sample powders were performed on a Shimadzu RF-5301PC spectrofluorophotometer in the wavelength range of 300–550 nm with the spectral band widths at 3 nm for excitation and emission.

2.2. Preparation of $[Zn(cna)_2(bpy)(H_2O)_2]_n$ (**1**)

The solution containing $Zn(NO_3)_2{\cdot}6H_2O$ (148 mg, 0.5 mmol) and cyanoacetic acid (85 mg, 1 mmol) in water and dimethylformamide (4 mL, 1:1 v/v) was mixed with the methanolic solution (2 mL) of 4,4′-bipyridyl (78 mg, 0.5 mmol). This mixture solution was allowed to stand undisturbed at room temperature, yielding colorless block-shaped crystals of **1** after 2 weeks. Yield: 52 mg (24%) based on zinc salt. *Anal.* Calc. for $ZnC_{16}H_{16}N_4O_6$: C, 45.14; H, 3.79; N, 13.16. Found: C, 45.73; H, 3.52; N, 12.98%. IR (KBr, cm^{-1}): 3413br (ν(OH)), 2258w (ν(C≡N)), 1612s (ν_{as}(OCO)), 1436w, 1367s (ν_s(OCO)), 1270w, 1220w, 1083w, 1015m, 907w, 829m, 720w, 551w, 488m.

2.3. Preparation of $[Cd_3(cna)_6(bpy)_3]_n$ (**2**)

An ethanolic solution (4 mL) of cyanoacetic acid (85 mg, 1 mmol) and 4,4′-bipyridyl (78 mg, 0.5 mmol) was carefully layered on an aqueous solution (2 mL) of $Cd(NO_3)_2{\cdot}4H_2O$ (154 mg, 0.5 mmol). After 3 weeks, colorless needle-shaped crystals of **2** were obtained. Yield for **2**: 225 mg (34%) based on cadmium salt. *Anal.* Calc. for $Cd_3C_{48}H_{36}N_{12}O_{12}$: C, 44.01; H, 2.77; N, 12.83. Found: C, 43.76; H, 2.51; N, 12.73%. IR (KBr, cm^{-1}): 2263w (ν(C≡N)), 1635s (ν_{as}(OCO)), 1396s (ν_s(OCO)), 1217w, 1078m, 1007m, 899w, 807m, 635m.

2.4. Preparation of $[Zn(cna)_2(bpa)]_n$ (**3**)

The solution containing $Zn(OAc)_2{\cdot}2H_2O$ (109 mg, 0.5 mmol) and cyanoacetic acid (85 mg, 1 mmol) in water and dimethylformamide (4 mL, 1:1 v/v) was mixed with 1,2-di(4-pyridyl)ethane (92 mg, 0.5 mmol) in methanol (2 mL). This mixture solution was allowed to stand undisturbed at room temperature, yielding colorless rod-shaped crystals of **3** after 3 days. Yield: 134 mg (64%) based on zinc salt. *Anal.* Calc. for $ZnC_{18}H_{16}N_4O_4$: C, 51.75; H, 3.86; N, 13.41. Found: C, 51.43; H, 3.62; N, 13.21%. IR (KBr, cm^{-1}): 2258w (ν(C≡N)), 1610s (ν_{as}(OCO)), 1433w, 1368s (ν_s(OCO)), 1270w, 1221w, 1083m, 1023w, 986w, 835m, 550m.

2.5. Preparation of $[Cd(cna)_2(bpa)]_n$ (**4**)

Compound **4** was synthesized in a similar manner to **3** using $Cd(NO_3)_2{\cdot}4H_2O$ (154 mg, 0.5 mmol) instead of $Zn(OAc)_2{\cdot}2H_2O$. After 3 days, colorless rod-shaped crystals of **4** were obtained. Yield: 106 mg (45%) based on cadmium salt. *Anal.* Calc. for $CdC_{18}H_{16}N_4O_4$: C, 46.52; H, 3.47; N, 12.06. Found: C, 46.13; H, 3.31; N, 11.95%. IR (KBr, cm^{-1}): 2258w (ν(C≡N)), 1619s (ν_{as}(OCO)), 1419w, 1366s (ν_s(OCO)), 1273w, 1216w, 1072w, 1048w, 1010w, 942w, 809m, 724w, 638m.

2.6. X-ray crystallography

The reflection data of **1**–**4** were collected on a Bruker D8 Quest PHOTON100 CMOS detector with graphite-monochromated Mo Kα radiation using the APEX2 program [26]. Raw data frame integration was performed with SAINT [26]. An empirical absorption correction by using the SADABS program [26] was applied. The structure was solved by direct methods and refined by full-matrix least-squares method on F^2 with anisotropic thermal parameters for all non-hydrogen atoms using the SHELXTL software package [27]. All hydrogen atoms were placed in calculated positions and refined isotropically, with the exception of the hydrogen atoms of coordination water molecules in **1** which were found *via* difference Fourier maps, and then restrained at fixed positions. The unbound and coordination oxygen atoms (O4 and O3) of a terminal cyanoacetate for **3** are disordered. The occupancies of two conformations were refined to 0.4 and 0.6. The details of crystal data, selected bond lengths and angles for **1**–**4** are listed in Tables 1 and S1.

Table 1
Crystallographic data for compounds **1**–**4**.

Compound	**1**	**2**	**3**	**4**
Formula	$ZnC_{16}H_{16}N_4O_6$	$Cd_3C_{48}H_{36}N_{12}O_{12}$	$ZnC_{18}H_{16}N_4O_4$	$CdC_{18}H_{14}N_4O_4$
Molecular weight	425.72	1310.09	417.72	464.75
T (K)	293(2)	293(2)	293(2)	293(2)
Crystal system	orthorhombic	monoclinic	triclinic	triclinic
Space group	*Pccn*	*C*2/*c*	$P\bar{1}$	$P\bar{1}$
a (Å)	12.9041(5)	24.9894(19)	9.5264(3)	8.3470(3)
b (Å)	18.5888(7)	11.6868(9)	9.7703(4)	10.7131(5)
c (Å)	7.2082(2)	20.7170(15)	10.9211(4)	11.5269(4)
α (°)	90.00	90.00	112.2500(10)	70.459(2)
β (°)	90.00	123.260(2)	96.906(10)	81.386(10)
γ (°)	90.00	90.00	98.6510(10)	67.1380(10)
V (Å^3)	1729.04(11)	5059.16(7)	912.49(6)	894.85(6)
Z	4	4	2	2
ρ_{calcd} (g cm^{-3})	1.635	1.720	1.520	1.725
μ (Mo Kα) (mm^{-1})	1.464	1.324	1.378	1.253
Data collected	4890	5195	4473	4230
Unique data (R_{int})	3136(0.0307)	5195(0.1666)	3821(0.0173)	3519(0.0340)
R_1[a]/wR_2[b] [$I > 2\sigma(I)$]	0.0404/0.0925	0.0711/0.1096	0.0420/0.1086	0.0338/0.0657
R_1[a]/wR_2[b] [all data]	0.0776/0.1060	0.1890/0.1394	0.0527/0.1159	0.0497/0.0715
Goodness-of-fit (GOF)	1.067	1.007	1.036	1.099
Maximum/minimum electron density (e Å^{-3})	0.395/−0.738	1.164/−0.841	0.946/−0.467	0.693/−0.726

[a] $R = \Sigma||F_o|-|F_c||/\Sigma|F_o|$.
[b] $R_w = \{\Sigma[w(|F_o|-|F_c|)]^2/\Sigma[w|F_o|^2]\}^{1/2}$.

3. Results and discussion

3.1. Crystal structure of $[Zn(cna)_2(bpy)(H_2O)_2]_n$ (**1**)

Compound **1** crystallizes in the orthorhombic system with *Pccn* space group, exhibiting a 1D chain structure, as shown in Fig. 1a. The structure of **1** is isomorphous with previously reported complexes, $[M(cna)_2(bpy)(H_2O)_2]_n$ (M = Cu(II) [23], Mn(II) [16]). Each Zn(II) ion is coordinated by two nitrogen atoms from two μ_2-bpy spacers, two oxygen atoms from two terminal cyanoacetates and two oxygen atoms from two coordination water molecules, adopting a distorted octahedral geometry. The ZnN_2O_4 moiety shows coordination distances in the range of 2.118(9)–2.172(6) Å. The adjacent zinc(II) ions are bridged *via* μ_2-bpy spacers generating 1D linear chain of **1** with the Zn···Zn separation of 11.314(3) Å. The two pyridine rings of bipyridyl moieties are not coplanar with the dihedral angle between the two planar pyridine rings of 15.78°. Each 1D chain of **1** is assembled by various interchain hydrogen bonding among terminal cyanoacetates (C7H···N2$_{nitrile}$) (Fig. 1b, Table S2), and between unbound O atom from cyanoacetate and H atom from coordination water molecule (O3H···O2), as well as, the pyridyl H atom from μ_2-bpy and O atom from coordination water molecule (C4H···O2). Moreover, the C4H···π interaction is observed among the adjacent μ_2-bpy moieties along the *c* axis with the separation of 3.394 Å (Fig. 1b). These weak interactions complete the 3D supramolecular motif of **1** with the closest interchain Zn···Zn separation of 7.208(2) Å. A comparison was made with the previous mixed bridging cna-bpy Zn(II) complex, $[Zn_2(cna)_4(bpy)_2]_n(H_2O)_n$ [17], which was reported to exhibit a 1D zigzag chain constructed from terminal cyanoacetate and μ_2-bpy spacer linking between the distorted tetrahedral ZnN_2O_2 chromophores. The different structural topologies are attributed to the diverse coordination geometries of Zn(II) centers.

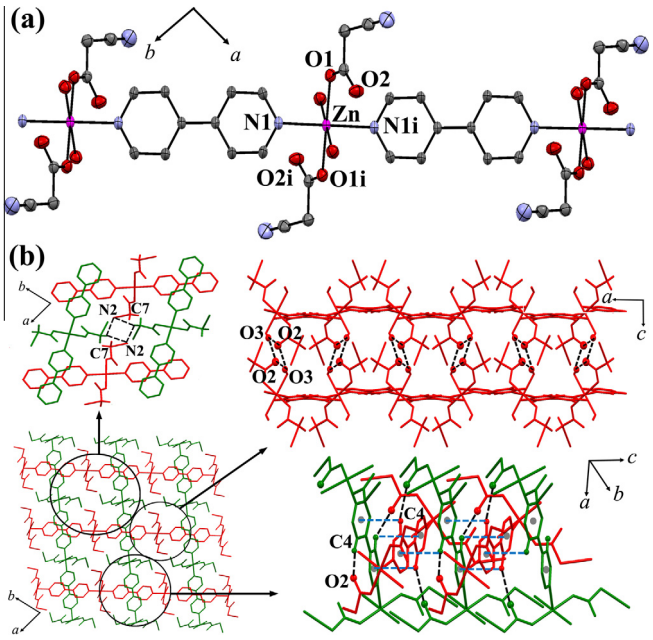

Fig. 1. (a) 1D linear chain structure of **1** with used atom labeling. The ellipsoids are shown at 35% probability level. The hydrogen atoms are omitted for clarity (i) = $-x$, $1-y$, $1-z$. (b) The packing diagram of **1** formed by the interchain hydrogen bonding (black broken lines) and C–H···π interactions (blue broken lines). (Color online.)

3.2. Crystal structure of $[Cd_3(cna)_6(bpy)_3]_n$ (**2**)

Compound **2** crystallizes in the monoclinic *C*2/*c* space group, exhibiting a 1D triple-stranded chain structure, as shown in Fig. 2a. The 1D triple-stranded chain of **2** contains two crystallographic independent Cd(II) centers of different geometries, i.e., two distorted pentagonal bipyramidal $Cd1N_2O_5$ and one distorted octahedral $Cd2N_2O_4$ chromophores. In the $Cd1N_2O_5$ moiety, each Cd1 center is surrounded by five carboxylate O atoms from three different cyanoacetate ligands (Cd1–O = 2.275(7)–2.475(6) Å) and two N atoms from two μ_2-bpy ligands (Cd1–N = 2.311(6) and 2.334(7) Å), while, each Cd2 center is six-coordination, surrounded by four carboxylate O atoms from four different μ_2-cyanoacetates (Cd2–O = 2.328(6)–2.393(6) Å) and two N atoms from two μ_2-bpy molecules (Cd2–N = 2.284(9) and 2.302(9) Å). The Cd–O and Cd–N bond distances are in normal ranges for Cd(II) complexes [28,29]. The Cd2 is bridged to two symmetry-related Cd1 ions *via* double-*syn*,*anti*-η^1:η^3:μ_2-cyanoacetates and double-chelating

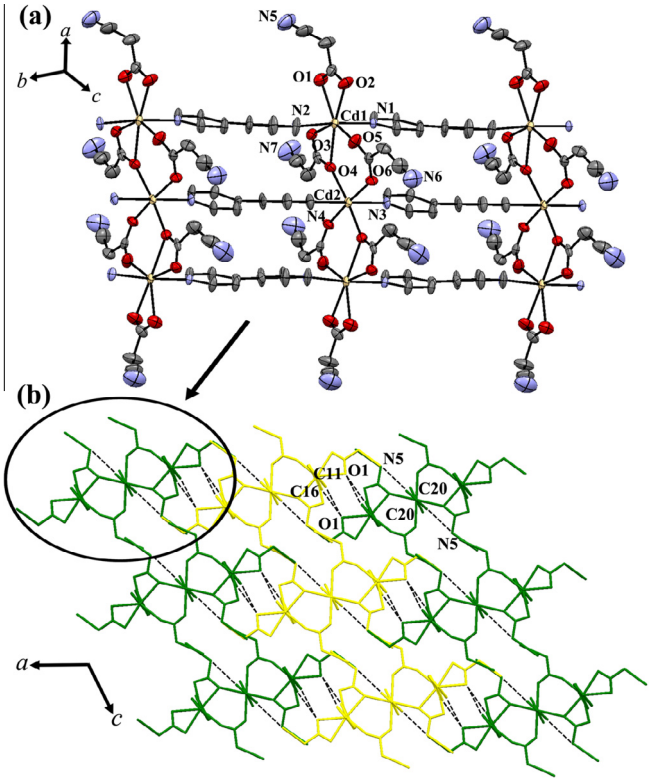

Fig. 2. 1D triple-stranded chain structure of **2** with used atom labeling. The ellipsoids are shown at 35% probability level. All hydrogen atoms are omitted for clarity. (b) The packing diagram of triple-stranded chains in **2** formed by various weak hydrogen bonding in *ac* plane.

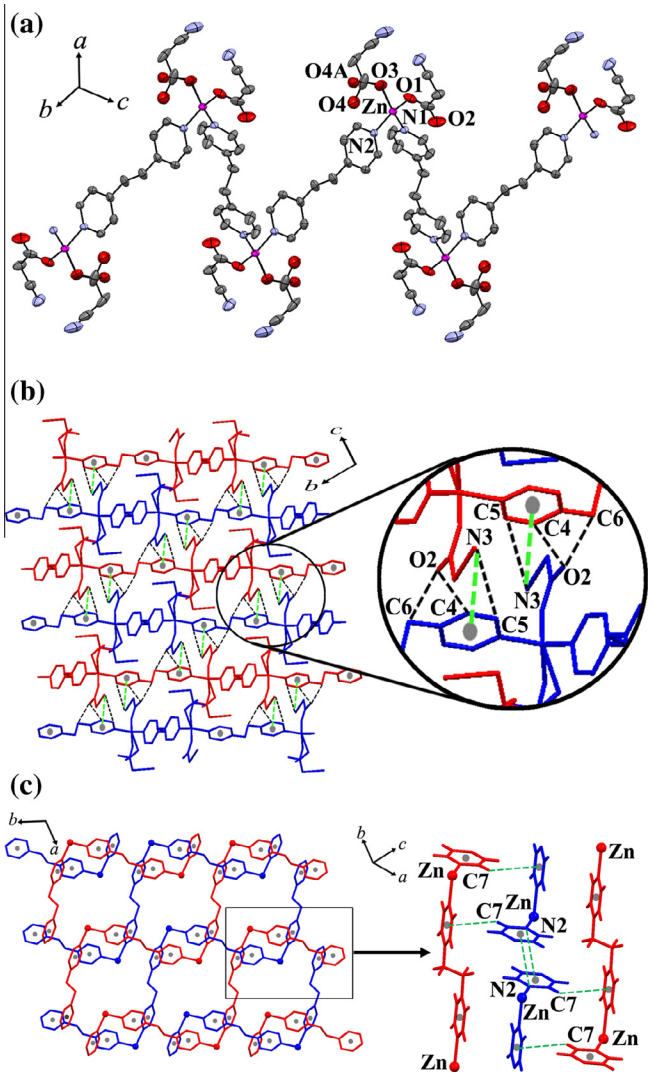

Fig. 3. (a) 1D zigzag chain structure of **3** with used atom labeling. The ellipsoids are shown at 50% probability level. All hydrogen atoms are omitted for clarity. (b) 2D sheet structure of **3** built from weak hydrogen bonding (black broken lines) and $N_{nitrile}\cdots\pi$ interaction (green broken lines) in *bc* plane. (c) Another view in *ab* plane showing 2D sheet structure formed by C–H···π and $N_{pyridyl}\cdots\pi$ interactions. The cyanoacetates are omitted for clarity. (Color online.)

bridging bidentate modes of cyanoacetates, generating a linear trinuclear (Cd1, Cd2, Cd1a) unit with the Cd···Cd separation of 4.184(2) Å. Moreover, each trinuclear unit is linked by μ_2-bpy spacers, giving rise to a 1D triple-stranded chains of **2** with the Cd···Cd separation across μ_2-bpy of 11.687(2) Å. The two pyridine rings of bpy moieties are not coplanar with the dihedral angle between the two planar pyridine rings of 12.66° (Cd1) and 21.13° (Cd2). For the packing motif (Fig. 2b), each chain of **2** is assembled by the intermolecular weak hydrogen bonding among nitrile–N atoms from terminal cyanoacetates, coordination oxygen atoms from cyanoacetates, and pyridyl–H atoms from μ_2-bpy (C20H···N5, C16H···O1, and C11H···O1,) (Fig. 2b, Table S2). All interactions complete the overall 3D packing structure motif of **2** with the closest interchain Cd···Cd separation of 6.672(2) Å.

3.3. Crystal structure of $[Zn(cna)_2(bpa)]_n$ (**3**)

Compound **3** crystallizes in the triclinic $P\bar{1}$ space group, exhibiting a 1D zigzag chain structure, as shown in Fig. 3a. Each Zn(II) ion is coordinated by two oxygen atoms from two different monodentate cyanoacetates and two nitrogen atoms from two bpa spacers, adopting a distorted tetrahedral ZnN_2O_2 chromophore. The coordination distances and angles are in ranges of 1.869(4)–2.094(6) Å and 92.08(16)–126.03(12)°, respectively. The adjacent zinc(II) ions are bridged by μ_2-bpa spacers generating 1D zigzag chains of **3** with the Zn···Zn separation of 13.253(6) and 13.239(5) Å. The *anti* conformation of μ_2-bpa molecule is observed with the C–CH_2–CH_2 angle of 112.17°. The two pyridine rings of bipyridyl moieties are perfectly coplanars, being located on a crystallographic center of symmetry. For the packing motif, each 1D zigzag chain of **3** is assembled by various intermolecular weak hydrogen bonding among terminal nitrile–N atoms and unbound oxygen atoms from cyanoacetates acting as H-acceptor and pyridyl–H, ethyl–H atoms from μ_2-bpa acting as H-donors (C5H···N3, C4H···O2, and C6H···O2) (Fig. 3b, Table S2). In addition, the nitrile N atoms from the terminal cyanoacetates can interact with the adjacent electron deficient μ_2-bpa ring with $N3_{nitrile}\cdots\pi$ distance of 3.482 Å (Fig. 3b). Moreover, the C7–H···π interaction is observed between the interchain μ_2-bpa moieties with the separation of 3.551 Å, and the pyridyl–N atom from μ_2-bpa also interacts with the adjacent bpa rings with $N_{pyridyl}\cdots\pi$ distance of 3.767 Å (Fig. 3c). All interactions complete the overall 3D supramolecular motif of **3** with the closest interchain Zn···Zn separation of 6.324(5) Å.

3.4. Crystal structure of $[Cd(cna)_2(bpa)]_n$ (**4**)

Compound **4** crystallizes in the triclinic $P\bar{1}$ space group, exhibiting a 1D ladder-like chain structure, as shown in Fig. 4. Each Cd(II) ion is six-coordinated, surrounded by four carboxylate oxygen atoms from three different cyanoacetates and two nitrogen atoms from two μ_2-bpa molecules, generating a distorted octahedral

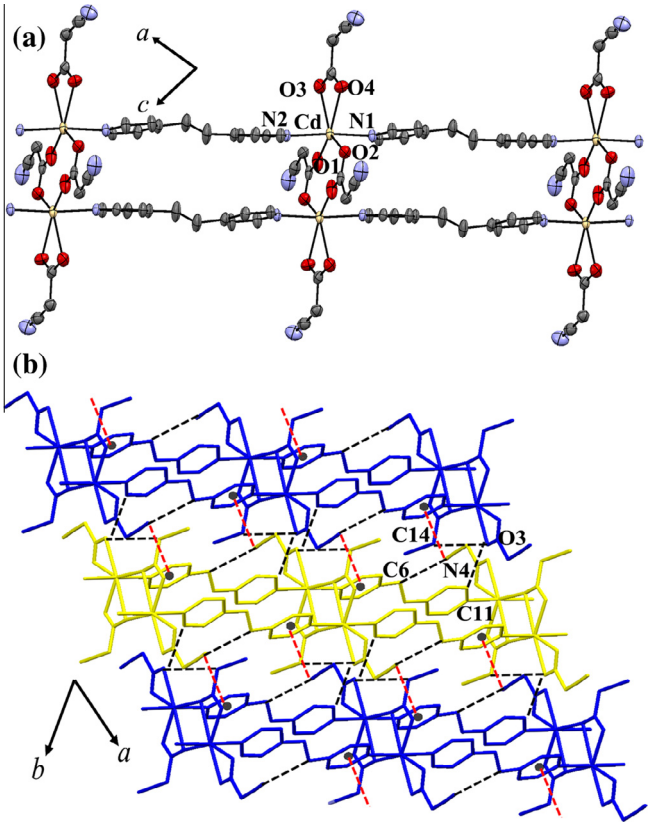

Fig. 4. (a) 1D ladder chain structure of **4** with used atom labeling. The ellipsoids are shown at 50% probability level. All hydrogen atoms are omitted for clarity. (b) The packing diagram of **4** formed by weak interchain hydrogen bonding (black broken lines) and $N_{nitrile}\cdots\pi$ interaction (red broken lines) in *ab* plane. (Color online.)

CdN_2O_4 chromophore. The CdN_2O_4 moiety shows coordination distances and angles in ranges of 2.294(2)–2.420(2) Å and 83.97(8)–149.17(10)°, respectively. The carboxylate bridges from two cyanoacetates exhibit a double-*syn*,*anti*-η^1:η^3:μ_2 coordinative modes connecting between Cd(II) centers, adopting a dinuclear Cd(II) unit with Cd···Cd separation of 3.961(6) Å. An additional cyanoacetate acts as terminal chelating ligand. Moreover, the carboxyl-bridged dinuclear units are assembled by paired μ_2-bpa spacers to create the infinite 1D ladder-like structures (Fig. 4a). The Cd···Cd separation across μ_2-bpa is 6.877(5) Å. The two pyridine rings of bipyridyl moieties are not coplanar with the dihedral angle between the two planar pyridine rings of 9.88°. The *anti* conformation of bpa molecules is observed with C–CH_2–CH_2 angles of 115.98° and 117.22°, and the C–CH_2–CH_2–C torsion angle of 171.69°. For the packing diagram (Fig. 4b, Table S2), each 1D ladder chain of **4** is assembled by the intermolecular weak hydrogen bonding between terminal nitrile–N from cyanoacetate and ethyl–H from μ_2-bpa (C6H···N4), coordination oxygen atoms and alkyl–H from cyanoacetates (C14H···O3) and ethyl–H from μ_2-bpa (C11H···O3). In addition, the nitrile–N atoms from the terminal cyanoacetates effectively interact with the adjacent μ_2-bpa moieties with N···π distance of 3.412 Å, as shown in Fig. 4b.

3.5. Photoluminescent properties

Photoluminescence studies of d^{10} metal-organic CPs with luminescent organic ligands containing aromatic rings have been a subject of immense current research interest because their emissions can be adjusted by involving the coordination environment, the rigidity and the arrangement of organic linkers within CPs [9,30–33]. Recently, the luminescent properties of d^{10} complexes

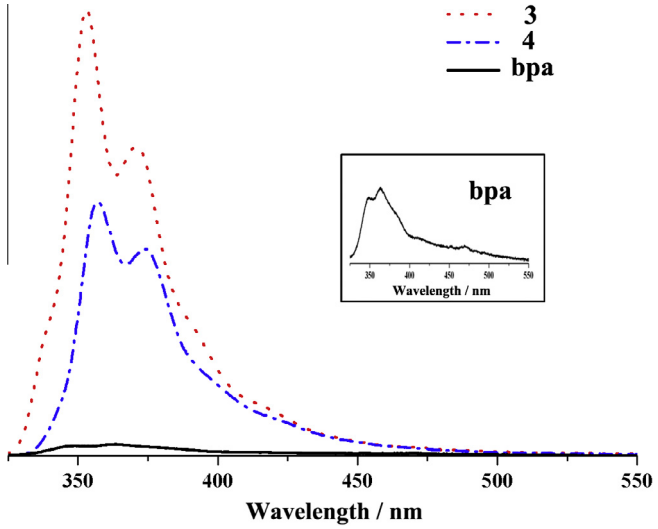

Fig. 5. The solid-state photoluminescent spectra of compounds **3**, **4**, and free bpa ligand. The inset shows the enlarged emission of free bpa.

containing bpa/dpe spacers have been reported [34–37]. Therefore, the solid-state luminescent properties of **3** and **4** were investigated at room temperature. The phase purities of **3** and **4** were confirmed by X-ray powder diffraction (XRPD) (Figs. S1 and S2), in which the experimental diffraction peaks are in good agreement with the patterns simulated from single-crystal data, implying the good phase purities of **3** and **4**. It should be mentioned that both compounds **1** and **2** contain mixed crystals with similar shapes and color and they are difficult to be manually separated to obtain pure bulk products in sufficient amount for the XRPD and photoluminescent measurements. To compare the luminescent intensities, all emission spectra were determined with the same excitation wavelength (λ_{ex} = 285 nm) and the same spectral pass widths. Excitation of the samples at 285 nm leads to the generation of similar emissions in the compounds **3**, **4** and free bpa ligand with the peak maxima occurring at 352 nm for **3**, 357 nm for **4**, and 370 nm for free bpa (Fig. 5). These emissions may be assigned to the intraligand π–π* transition since the Zn(II) and Cd(II) ions are difficult to be oxidized or reduced due to the d^{10} configuration. The spectra of **3** and **4** exhibit more intense and the emission peaks are blue-shifted by about 15 nm compared to free bpa ligand, which may be attributed to the arrangement and the increased rigidity in the bpa ligand resulting from complexation to the Zn(II) and Cd (II) ions. [30–37] A similar emission band around 350 nm has been observed previously for other related mixed-ligands coordination polymers, such as $[Cd_2(cta)(bpa)(H_2O)_3]_n(H_2O)_{5n}$ (H_4cta = cyclohexane-1,2,4,5-tetracarboxylic acid) [37], $[Zn_2(tbip)_2(bpa)(H_2O)]_n$ (H_2tbip = 5-tert-butylisophthalic acid) [38], $[Zn(cna)_2(dpe)]_n$ and $[Cd(cna)_2(dpe)]_n$ [39].

4. Conclusion

In summary, a series of four d^{10} metal coordination polymers based on cyanoacetate and *N*,*N*′-ditopic coligands has been successfully synthesized and characterized. All compounds exhibit polymeric chain structures. In comparison with mixed rigid bridging bpy and cyanoacetate in the Cu(II) system [23], the linear chain structure of **1** is isomorphous to that of Cu(II) complex, whereas **2** shows a triple-stranded chain. This structure is attributed to a larger accessible space of Cd(II) ion which can organize the bridging cyanoacetates and bpy small spacers, leading to a linear trinuclear subunit. Contrary to the flexible extended spacer bpa, compound **3**

shows a zigzag chain structure caused by the tetrahedral Zn(II) connectors, while the ladder-like chain structure of **4** is isomorphous to the Cu(II) analog. These diverse structural topologies significantly depend on the different coordination sites of Zn(II) and Cd(II) centers. Weak interactions such as hydrogen bonding and N···π and/or CH···π interactions join the polymeric chains to stabilize overall supramolecular networks. Moreover, the strong photoluminescence properties of **3** and **4** may make them as the candidates for potential photoactive materials.

Acknowledgments

Funding for this work is provided by The Thailand Research Fund: Grant No. TRG5780003 (for J.B.) and BRG5680009 (for S.Y.), the Higher Education Research Promotion and National Research University Project of Thailand, through the Advanced Functional Materials Cluster of Khon Kaen University, and the Center of Excellence for Innovation in Chemistry (PERCH–CIC), Office of the Higher Education Commission, Ministry of Education, Thailand.

Appendix A. Supplementary data

Supplementary data contains XRPD patterns of **3** and **4**. CCDC 1414051–1414054 contain the supplementary crystallographic data for compounds **1**–**4**. These data can be obtained free of charge via http://www.ccdc.cam.ac.uk/conts/retrieving.html, or from the Cambridge Crystallographic Data Centre, 12 Union Road, Cambridge CB2 1EZ, UK; fax: (+44) 1223-336-033; or e-mail: deposit@ccdc.cam.ac.uk. Supplementary data associated with this article can be found, in the online version, at http://dx.doi.org/10.1016/j.poly.2015.10.043.

References

[1] A. Schneemann, V. Bon, I. Schwedler, I. Senkovska, S. Kaskel, R.A. Fischer, Chem. Soc. Rev. 43 (2014) 6062.
[2] N. Stock, S. Biswas, Chem. Rev. 112 (2012) 933.
[3] R.J. Kuppler, D.J. Timmons, Q.-R. Fang, J.-R. Li, T.A. Makal, M.D. Young, D. Yuan, D. Zhao, W. Zhuang, H.-C. Zhou, Coord. Chem. Rev. 253 (2009) 3042.
[4] A.K. Cheetham, C.N.R. Rao, R.K. Feller, Chem. Commun. (2006) 4780.
[5] S. Kitagawa, R. Kitaura, S.-I. Noro, Angew. Chem. Int. Ed. 43 (2004) 2334.
[6] C. Janiak, Dalton Trans. (2003) 2781.
[7] Y.-W. Li, J.-R. Li, L.-F. Wang, B.-Y. Zhou, Q. Chena, X.-H. Bu, J. Mater. Chem. 1 (2014) 495.
[8] S.-I. Noro, S. Kitagawa, T. Akutagawa, T. Nakamura, Prog. Polym. Sci. 34 (2009) 240.
[9] Y. Cui, Y. Yue, G. Qian, B. Chen, Chem. Rev. 112 (2012) 1126.
[10] D. Tian, Q. Chen, Y. Li, Y.-H. Zhang, Z. Chang, X.-H. Bu, Angew. Chem. Int. Ed. 53 (2014) 837.
[11] X.-Q. Liang, X.-H. Zhou, C. Chen, H.-P. Xiao, Y.-Z. Li, J.-L. Zuo, X.-Z. You, Cryst. Growth Des. 9 (2009) 1041.
[12] L.-F. Ma, X.-Q. Li, Q.-L. Meng, L.-Y. Wang, M. Du, H.-W. Hou, Cryst. Growth Des. 11 (2011) 175.
[13] Q. Zhang, F. Hu, Y. Zhang, W. Bi, D. Wang, D. Sun, Inorg. Chem. Commun. 24 (2012) 195.
[14] Y.-R. Liu, X. Zhang, G.-R. Liang, Inorg. Chem. Commun. 37 (2013) 1.
[15] M.N. Sokolova, N.A. Budantseva, A.M. Fedoseev, Russ. J. Coord. Chem. 37 (2011) 478.
[16] X. Feng, X.-G. Shi, F. Ruan, Z. Kristallogr. NCS 224 (2009) 193.
[17] X. Feng, T.-C. Feng, J.-S. Zhao, X.-G. Shi, F. Ruan, Z. Kristallogr. NCS 224 (2009) 541.
[18] S.G. Shova, Y.A. Simonov, M. Gdaniec, G.V. Novitchi, A. Lazarescu, K.I. Turta, Russ. J. Inorg. Chem. 47 (2002) 946.
[19] G. Novitskii, S. Shova, V.K. Voronkova, L. Korobchenko, M. Gdanec, Y.A. Simonov, K. Turte, Russ. J. Coord. Chem. 27 (2001) 791.
[20] T. Nakamoto, M. Hanaya, M. Katada, K. Endo, S. Kitagawa, H. Sano, Inorg. Chem. 36 (1997) 4347.
[21] P. Startnowicz, Acta Crystallogr., Sect. C. 49 (1993) 1621.
[22] J.R. Wasson, C.-I. Shyr, C. Trapp, Inorg. Chem. 7 (1968) 469.
[23] P. Suvanvapee, J. Boonmak, F. Klongdee, C. Pakawatchai, B. Moubaraki, K.S. Murray, S. Youngme, Cryst. Growth Des. 15 (2015) 3804.
[24] P. Phuengphai, S. Youngme, N. Chaichit, J. Reedijk, Inorg. Chim. Acta 403 (2013) 35.
[25] Z. Chang, D.-S. Zhang, Q. Chen, R.-F. Li, T.-L. Hu, X.-H. Bu, Inorg. Chem. 50 (2011) 7555.
[26] APEX2, SAINT and SADABS, Bruker AXS Inc., Madison, WI, 2014.
[27] G.M. Sheldrick, Acta Crystallogr., Sect. A 64 (2008) 112.
[28] B. Xu, J. Xie, H.-M. Hu, X.-L. Yang, F.-X. Dong, M.-L. Yang, G.-L. Xue, Cryst. Growth Des. 14 (2014) 1629.
[29] P.-P. Cen, X.-Y. Jin, Inorg. Chim. Acta 421 (2014) 38.
[30] M.B. Bushuev, K.A. Vinogradova, V.P. Krivopalov, E.B. Nikolaenkova, N.V. Pervukhina, D.Y. Naumov, M.I. Rakhmanova, E.M. Uskov, L.A. Sheludyakova, A. V. Alekseev, S.V. Larionov, Inorg. Chim. Acta 371 (2011) 88.
[31] F. Guo, Inorg. Chim. Acta 399 (2013) 79.
[32] Y. Zhang, W. Luo, D. Liu, Y. Xu, S.-L. Li, J. Li, Y. Wu, Y. Zhou, M. Fang, H.-K. Liu, Inorg. Chim. Acta 409 (2014) 512.
[33] Z.-G. Kong, X.-R. Sun, L. Li, H.-X. Wang, X.-Y. Wang, S.W. Ng, Transit. Metal Chem. 38 (2013) 449.
[34] W. Zhu, R. Zheng, X. Fu, H. Fu, Q. Shi, Y. Zhen, H. Dong, W. Hu, Angew. Chem. Int. Ed. 54 (2015) 6785.
[35] J.-G. Kang, J.-S. Shin, D.-H. Cho, Y.-K. Jeong, C. Park, S.F. Soh, C.S. Lai, E.R.T. Tiekink, Cryst. Growth Des. 10 (2010) 1247.
[36] L.-F. Ma, C.-P. Li, L.-Y. Wang, M. Du, Cryst. Growth Des. 10 (2010) 2641.
[37] G.-G. Luo, H.-B. Xiong, D. Sun, D.-L. Wu, R.-B. Huang, J.-C. Dai, Cryst. Growth Des. 11 (2011) 1948.
[38] L.-F. Ma, L.-Y. Wang, J.-L. Hu, Y.-Y. Wang, G.-P. Yang, Cryst. Growth Des. 9 (2009) 5334.
[39] P. Suvanvapee, J. Boonmak, S. Youngme, Inorg. Chim. Acta 437 (2015) 11.

Inorganica Chimica Acta 437 (2015) 11–15

Contents lists available at ScienceDirect

Inorganica Chimica Acta

journal homepage: www.elsevier.com/locate/ica

Synthesis, crystal structure and luminescent properties of three new zinc/cadmium coordination polymers containing cyanoacetate and 1,2-di(4-pyridyl)ethylene

Porntiva Suvanvapee, Jaursup Boonmak *, Sujittra Youngme

Materials Chemistry Research Center, Department of Chemistry and Center of Excellence for Innovation in Chemistry, Faculty of Science, Khon Kaen University, Khon Kaen 40002, Thailand

ARTICLE INFO

Article history:
Received 3 May 2015
Received in revised form 8 July 2015
Accepted 27 July 2015
Available online 17 August 2015

Keywords:
Coordination polymer
Crystal structure
Cyanoacetate
1,2-Di(4-pyridyl)ethylene
Luminescence

ABSTRACT

Three mixed-ligand coordination polymers based on cyanoacetate (cna) and 1,2-di(4-pyridyl)ethylene (dpe), namely $[M(cna)_2(dpe)]_n$ ($M = Zn^{II}$ (**1**), (**2**), and Cd^{II} (**3**)) were synthesised and structurally characterized. Compound **1** exhibits a 1D zigzag polymeric chain, while compounds **2** and **3** are isostructural exhibiting 1D-ladder chain structures built from double-μ_2-dpe connecting between $[M_2(\mu_{1,3}\text{-cna})_2(cna)_2]$ secondary building units. The adjacent polymeric chains of **1**–**3** are linked by various intermolecular weak hydrogen bonds and N···π and/or C–H···π interactions through cyanoacetate and dpe ligands, stabilizing overall 3D supramolecular networks. Furthermore, the divergence of structural motifs between **1** and isostructures **2** and **3** strongly influences on their solid-state photoluminescent properties at room temperature. Compound **1** exhibits intense photoluminescence, whereas this is quenched in compounds **2** and **3**.

1. Introduction

The synthesis and design of coordination polymers (CPs) have attracted great attention owing to their interesting topologies and their potential applications in catalysis, gas storage, magnetism and non-linear optical properties and so on [1–10]. However, from a crystal engineering viewpoint, how to construct the predictable networks with desired properties still remains a great challenge owing to the large number of intermolecular forces which are affected by many variable factors such as reaction stoichiometry, temperature, solvent, counterions and so on [1,6,11]. It is well-known that the most common synthetic method for the construction of novel CPs is the mixed-ligands strategy [2,12–15]. The combination of different ligands can effectively contribute a variety of structural frameworks with fascinating properties [2,12–14,16–19]. One of the most powerful ligand used for such strategy is carboxylate anions that can bind toward metal centers in various ways, such as terminal monodentate, chelating to one metal center, bridging bidentate in a *syn–syn*, *syn–anti*, and *anti–anti* configurations and multiple bridges, resulting in the formation of various new structural types of metal carboxylates [20–25]. On the other hand, many rod-like *N*,*N*′-ditopic organic co-ligands have been widely used as additional building blocks for the construction of several multidimensional CPs [2,26–28].

Coordination polymers constructed from d^{10} transition metal ions, particularly, abundant zinc(II) and cadmium(II) ions, together with luminescent organic ligands containing conjugated π systems and aromatic rings have been a growing interest because of their potential applications in chemical sensors and electroluminescent display [2,4,9,29–33]. In addition, the coordination environment and the arrangement of organic linkers within CPs can strongly affect the luminescent properties. Therefore, controlling molecular interactions is crucial to tuning the luminescent properties of CPs [9,16,17,29,32,34–39]. In this work, we choose a cyanoacetate anion (cna) and semi-flexible 1,2-di(4-pyridyl)ethylene (dpe) luminescent spacer incorporating zinc(II) and cadmium(II) ions to develop new luminescent coordination networks. The cyanoacetate ($NC_2H_2CO_2^-$) anion contains both nitrile (—C≡N) and carboxylic groups which not only well provides rich coordination sites but also effectively serves as intermolecular hydrogen-accepter sites, as well as fabricating the N···π interaction toward neighboring aromatic moieties [40–43]. These versatile connection sites allow cyanoacetate to be a good candidate for constructing 3D

* Corresponding author. Fax: +66 43 202 373.
E-mail address: Jaursup@kku.ac.th (J. Boonmak).

http://dx.doi.org/10.1016/j.ica.2015.07.045
0020-1693/

supramolecular structures. However, the mixed-ligands complexes containing cyanoacetate have been rarely reported [40–50]. Herein, three novel mixed-ligands coordination polymers, formulated as $[M(cna)_2(dpe)]_n$ (M = Zn^{II} (**1**), Zn^{II} (**2**), and Cd^{II} (**3**)) were successfully obtained. The syntheses, crystal structures and luminescent properties for **1**–**3** have been studied in this context.

2. Experimental

2.1. Materials and physical measurements

All chemical were obtained from commercial sources and were used without further purification. Elemental analyses (C, H, N) were carried out with a Perkin-Elmer PE 2400CHNS analyzer. FT-IR spectra were obtained in KBr disks on a Perkin-Elmer Spectrum One FT-IR spectrophotometer in 4000–450 cm^{-1} spectral range. The X-ray powder diffraction (XRPD) data were collected on a Bruker D8 ADVANCE diffractometer using monochromatic Cu Kα radiation, and the recording speed was 0.5 s/step over the 2θ range of 5–40° at room temperature. Photoluminescent spectra of the sample powders were performed on a Shimadzu RF-5301PC spectrofluorometer with the excitation at 285 nm in the wavelength range of 300–560 nm. The excitation and emission pass widths are 1.5 and 3.0 nm, respectively.

2.2. Synthesis

2.2.1. $[Zn(cna)_2(dpe)]_n$ (**1**) and (**2**)

The solution containing $Zn(O_2CCH_3)_2{\cdot}2H_2O$ (109 mg, 0.5 mmol) and cyanoacetic acid (85 mg, 1 mmol) in water and methanol (4 mL, 1:1 v/v) was mixed with 1,2-di(4-pyridyl)ethylene (90 mg, 0.5 mmol) in dimethylformamide (2 mL). This mixture solution was allowed to stand undisturbed at room temperature. After five days, deep yellow rhomboid-shaped crystals of **1** and small pale yellow crystals of **2** were obtained. These crystals were manually separated, washed with water and dried in air. Yield for **1**: 75 mg (36%) based on zinc salt. *Anal.* Calc. for $ZnC_{18}H_{14}N_4O_4$: C, 52.00; H, 3.39; N, 13.48. Found: C, 51.79; H, 3.21; N, 13.30%. IR (KBr, cm^{-1}): 3060w, 2918w, 2261m (ν(C≡N)), 1664s, 1623s (ν_{as}(OCO)), 1512w, 1401m, 1371m (ν_s(OCO)), 1269m, 1077w, 1027m, 844m, 733w, 612w, 561m. Yield for **2**: 125 mg (60%) based on zinc salt. *Anal.* Calc. for $ZnC_{18}H_{14}N_4O_4$: C, 52.00; H, 3.39; N, 13.48. Found: C, 51.23; H, 3.33; N, 13.23%. IR (KBr, cm^{-1}): 3066w, 2261m (ν(C≡N)), 1642s, 1612s (ν_{as}(OCO)), 1513m, 1423s, 1383s (ν_s(OCO)), 1263m, 1204m, 1074m, 1015m, 994m, 915m, 836m, 716w, 557s.

2.2.2. $[Cd(cna)_2(dpe)]_n$ (**3**)

The solution containing $Cd(NO_3)_2{\cdot}4H_2O$ (154 mg, 0.5 mmol) and cyanoacetic acid (85 mg, 1 mmol) in water (4 mL) was mixed with 1,2-di(4-pyridyl)ethylene (90 mg, 0.5 mmol) in dimethylformamide (2 mL). This mixture solution was allowed to stand undisturbed at room temperature, yielding pale yellow crystals of **3** after four days. Yield: 145 mg (63%) based on cadmium salt. *Anal.* Calc. for $CdC_{18}H_{14}N_4O_4$: C, 46.72; H, 3.05; N, 12.11. Found: C, 46.15; H, 2.92; N, 11.70%. IR (KBr, cm^{-1}): 2261m (ν(C≡N)), 1609s (ν_{as}(OCO)), 1502w, 1370s (ν_s(OCO)), 1270w, 1201w, 1081w, 1021m, 981m, 892w, 831m, 713w, 544(m).

2.3. X-ray crystallography

All reflection data **1**–**3** were collected on a Bruker D8 Quest PHOTON100 CMOS detector with graphite-monochromated Mo Kα radiation using the APEX2 program [51]. Raw data frame integration was performed with SAINT [51], which also applied correction for Lorentz and polarization effects. An empirical absorption correction by using the SADABS program [51] was applied. The structure was solved by direct methods and refined by full-matrix least-squares method on F^2 with anisotropic thermal parameters for all non-hydrogen atoms using the SHELXTL software package [52]. All hydrogen atoms were placed in calculated positions and refined isotropically. The details of crystal data, selected bond length and angles for compounds **1**–**3** are listed in Tables 1 and 2. The weak intermolecular hydrogen bonding for **1**–**3** are shown in Table 3.

Table 1
Crystallographic data for compounds **1**–**3**.

	1	**2**	**3**
Formula	$C_{18}H_{14}N_4O_4Zn$	$C_{18}H_{14}N_4O_4Zn$	$C_{18}H_{14}N_4O_4Cd$
Molecular weight	415.72	415.72	462.74
T (K)	293(2)	293(2)	293(2)
Crystal system	triclinic	triclinic	triclinic
Space group	$P\bar{1}$	$P\bar{1}$	$P\bar{1}$
a (Å)	9.1501(4)	7.7072(3)	8.0430(3)
b (Å)	10.7211(5)	10.5091(4)	10.7219(4)
c (Å)	11.3426(5)	11.7022(5)	11.5496(4)
α (°)	106.610(1)	70.292(1)	70.838(1)
β (°)	107.798(1)	86.023(1)	82.340(1)
γ (°)	109.208(1)	72.587(1)	69.025(1)
V (Å^3)	903.36(7)	850.89(6)	878.33(6)
Z	2	2	2
ρ_{calcd} (g cm^{-3})	1.528	1.623	1.750
μ (Mo Kα) (mm^{-1})	1.391	1.477	1.276
Data collected	3697	3249	4727
Unique data (R_{int})	3463(0.0150)	2771(0.0261)	4339(0.0169)
R_1[a]/wR_2[b] [$I > 2\sigma(I)$]	0.0253/ 0.0667	0.0424/ 0.1029	0.0248/ 0.0578
R_1[a]/wR_2[b] [all data]	0.0276/ 0.0680	0.0545/ 0.1081	0.0288/ 0.0594
Goodness-of-fit (GOF)	1.060	1.059	1.094
Maximum/minimum electron density (e Å^{-3})	0.320/−0.253	1.195/−0.504	0.562/−0.323

[a] $R = \sum||F_o| - |F_c||/\sum|F_o|$.
[b] $R_w = \{\sum[w(|F_o| - |F_c|)]^2/\sum[w|F_o|^2]\}^{1/2}$.

Table 2
Selected bond lengths/Å and angles/° for **1**–**3**.

1			
Zn–O1	1.9373(13)	Zn–O3	1.9899(13)
Zn–N2	2.0268(13)	Zn–N1	2.0381(13)
O1–Zn–O3	109.03(6)	O1–Zn–N2	111.99(6)
O3–Zn–N2	108.39(6)	O1–Zn–N1	97.13(6)
O3–Zn–N1	109.85(6)	N2–Zn–N1	119.76(5)
2			
Zn–O1	2.035(3)	Zn–O4	2.048(3)
Zn–O3	2.061(3)	Zn–N1	2.146(3)
Zn–N2	2.180(3)	O1–Zn–O4	97.28(13)
O1–Zn–O3	134.17(12)	O4–Zn–O3	128.53(13)
O1–Zn–N1	93.83(10)	O4–Zn–N1	88.77(11)
O3–Zn–N1	89.09(10)	O1–Zn–N2	89.45(10)
O4–Zn–N2	91.58(11)	O3–Zn–N2	88.07(10)
N1–Zn–N2	176.63(10)		
3			
Cd–N2	2.2938(15)	Cd–O3	2.3043(17)
Cd–O4	2.3059(15)	Cd–N1	2.3105(15)
Cd–O2	2.3595(16)	Cd–O1	2.4836(16)
N2–Cd–O3	87.00(6)	N2–Cd–O4	89.66(6)
O3–Cd–O4	127.54(8)	N2–Cd–N1	173.11(5)
O3–Cd–N1	87.76(6)	O4–Cd–N1	89.98(6)
N2–Cd–O2	96.81(6)	O3–Cd–O2	96.88(8)
O4–Cd–O2	135.45(6)	N1–Cd–O2	88.26(6)
N2–Cd–O1	86.75(6)	O3–Cd–O1	148.79(8)
O4–Cd–O1	82.97(6)	N1–Cd–O1	100.04(6)
O2–Cd–O1	53.68(5)		

Table 3
Intermolecular weak hydrogen bond lengths/Å angles/° in studied structures of **1**–**3**.

D–H···*A*	d(*D*–H)	d(H···*A*)	d(*D*···*A*)	<(DHA)
1[a]				
C4–H4···O4^{i}	0.93	2.40	3.313(2)	168
C6–H6···O4^{ii}	0.93	2.54	3.458(3)	170
C11–H11···N3^{iii}	0.93	2.54	3.194(4)	128
C17–H17A···O2^{iv}	0.97	2.35	3.256(3)	155
2[b]				
C6–H6···N3^{i}	0.93	2.61	3.490(7)	158
C7–H7···O2^{ii}	0.93	2.46	3.379(6)	170
C10–H10···O1^{iii}	0.93	2.54	3.239(5)	132
C17–H17B···O1^{iii}	0.97	2.70	3.539(3)	145
C17–H17A···N4^{iv}	0.97	2.49	3.310(9)	142
3[c]				
C6–H6···N3i	0.93	2.51	3.403(4)	160
C7–H7···O2^{ii}	0.93	2.67	3.579(6)	163
C11–H11···O1^{ii}	0.93	2.51	3.355(3)	146
C17–H17B···O1^{iii}	0.97	2.51	3.197(3)	136
C17–H17A···N4	0.97	2.65	3.346(9)	128

[a] Symmetry code for **1**: (i) = 1 − *x*, 2 − *y*, 1 − *z*; (ii) = −1 + *x*, *y*, *z*; (iii) = 1 + *x*, 1 + *y*, 1 + *z*; (iv) = 1 − *x*, 1 − *y*, −*z*.
[b] For **2**: (i) = −1 + *x*, 1 + *y*, *z*; (ii) = −*x*, 1 − *y*, −*z*; (iii) = 1 − *x*, 1 − *y*, −*z*; (iv) = −*x*, −*y*, 1 − *z*.
[c] For **3**: (i) = 1 − *x*, 1 − *y*, −*z*; (ii) = −1 + *x*, 1 + *y*, *z*; (iii) = −1 + *x*, *y*, *z*.

3. Results and discussion

3.1. Crystal structure

3.1.1. $[Zn(cna)_2(dpe)]_n$ (*1*)

Single-crystal structure analysis reveals that all compounds crystallize in the triclinic system, $P\bar{1}$ space group (Table 1). The asymmetric unit of $[Zn(cna)_2(dpe)]_n$ (**1**) is shown in Fig. 1a. Each Zn(II) ion is coordinated by two oxygen atoms from two different monodentate cyanoacetate anions and two nitrogen atoms from two 1,2-di(4-pyridyl)ethylene molecules, showing a distorted tetrahedral ZnN_2O_2 choromophore. The ZnN_2O_2 moiety shows coordination distances and angles in ranges of 1.937(1)–2.038 (1) Å and 109.03(6)–119.76(5)°, respectively (Table 2). The adjacent zinc ions are bridged *via* μ_2-dpe spacers along *a* axis generating 1D zigzag chain of **1** with the Zn···Zn separations of 13.233(6) and 13.452(5) Å (Fig. 1b). The two pyridine rings of bipyridyl moieties are not coplanar with the dihedral angle between the two planar pyridine rings of 13.59°. The conformation of μ_2-dpe molecule is *anti* with C—CH=CH—C torsion angle of 125.59°. In the packing motif, each zigzag polymeric chain of **1** is assembled by the intermolecular weak H-bonding interactions (Fig. 1c) relating terminal nitrile-N from cyanoacetate and pyridyl–H from μ_2-dpe spacer (C11H···N3), unbound oxygen atoms from cyanoacetate acting as H-acceptor and pyridyl–H (C4H···O4), as well as ethylene–H from μ_2-dpe acting as H-donors (C6H···O4) (Table 3). In addition, the interchain C2–H···π interaction is observed between the neighboring μ_2-dpe moieties in *ac* plane with the separation of 3.435 Å. Moreover, the pyridyl–N atom from μ_2-dpe can also interact with the adjacent dpe rings with $N_{pyridyl}$···centroid(dpe) distance of 3.595 Å (Fig. 1c). All interactions complete the overall 3D supramolecular motif of **1** with the closest interchain Zn···Zn separation of 5.509(5) Å.

3.1.2. $[Zn(cna)_2(dpe)]_n$ (*2*) and $[Cd(cna)_2(dpe)]_n$ (*3*)

Compounds **2** and **3** are isostructural exhibiting 1D ladder-like structures. For **2**, each Zn(II) ion is five-coordination showing a distorted trigonal bipyamidal ZnN_2O_3 chromophore with a $\tau = 0.71$ (Addison's parameter [53] $\tau = 0$ for square pyramid and $\tau = 1$ for trigonal bipyramid) (Fig. 2a). The equatorial trigonal plane around the zinc atom is composed of three oxygen atoms from three different cyanoacetates, indicated by the angles of O1–Zn1–O3, O1–Zn1–O4 and O4–Zn1–O3 being 134.17(12)°, 97.28(13)° and 128.53(13)°, respectively. The axial position is occupied by two nitrogen atoms from two different μ_2-dpe spacers with N1–Zn–N2 angle of 176.63(10)°. The average Zn–O and Zn–N distances

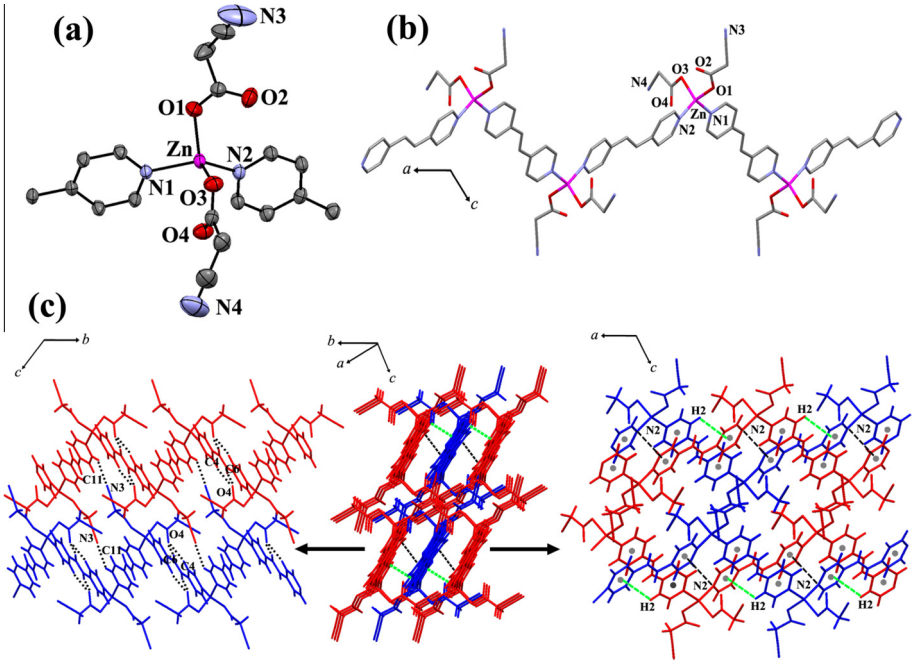

Fig. 1. (a) Asymmetric unit and atom labeling scheme of **1**. The ellipsoids are shown at 50% probability level. All hydrogen atoms are omitted for clarity. (b) 1D zigzag chain along *a* axis. (c) 3D packing diagram of **1** showing the assemblage of six polymeric chains *via* C–H···π (green broken lines) and N···π interactions (black broken lines). 2D sheet structure of **1** built from weak hydrogen bonding (black dotted lines) extending parallel to the *bc* plane (left). Another view in *ac* plane, 2D sheet structure formed by C–H···π (green broken lines) and $N_{pyridyl}$···π (black broken lines) interactions (right). (For interpretation of the references to color in this figure legend, the reader is referred to the web version of this article.)

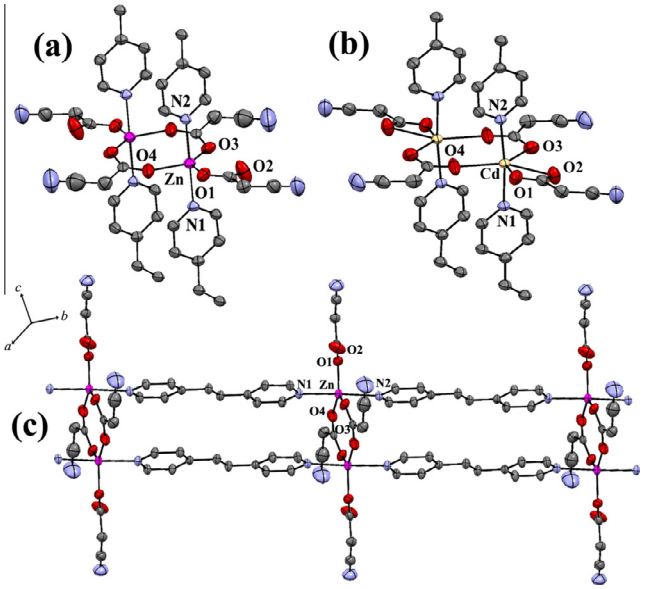

Fig. 2. Part of 1D ladder chain structures of **2**(a) and **3**(b) with used atom labeling. The ellipsoids are shown at 50% probability level. All hydrogen atoms are omitted for clarity. (c) 1D ladder-like structure of **2**.

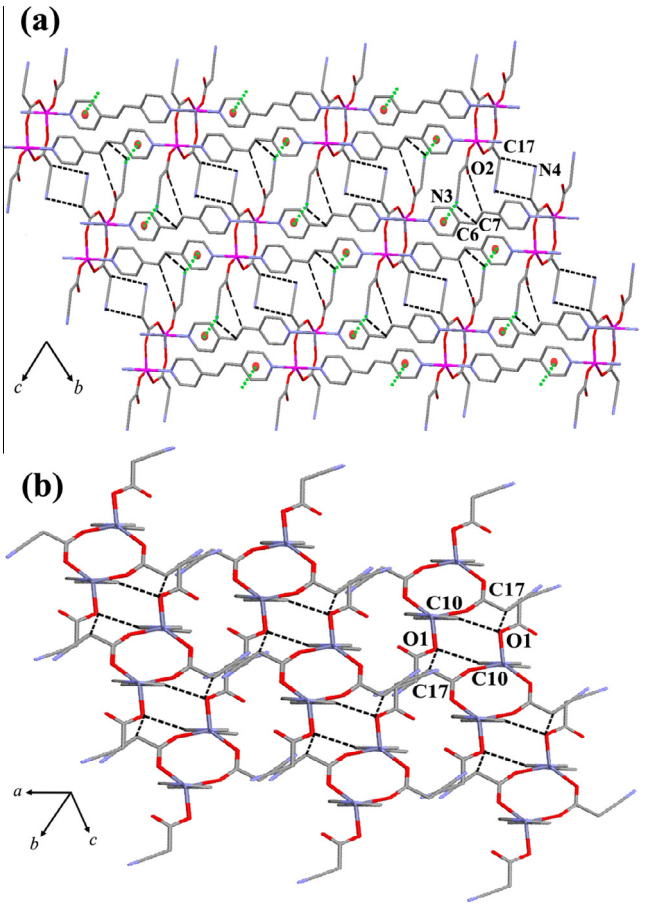

Fig. 3. (a) The packing diagram of ladder chains of **2** in *bc* plane showing weak hydrogen bonding (black broken lines) and $N_{nitrile}\cdots\pi$ interaction (green dotted lines). (b) Another view of 3D packing diagram showing weak hydrogen bonding through carboxylate oxygen from cyanoacetates. (For interpretation of the references to color in this figure legend, the reader is referred to the web version of this article.)

are 2.048(3) and 2.163(3) Å, respectively (Table 2). For compound **3**, each Cd(II) ion shows six-coordination formed by four carboxylate oxygen atoms from three different cyanoacetates and two nitrogen atoms from two μ_2-dpe molecules, generating a distorted octahedral CdN_2O_4 chromophore (Fig. 2b). The coordination distances around Cd(II) center are in the range of 2.294(2)–2.484 (2) Å (Table 2). The carboxylate bridges for μ_2-cna of **2** and **3** exhibit a double-*syn,anti*-η^1:η^3:μ_2 coordinative mode connecting between metal ions, giving rise to the dinuclear units with M···M separations of 3.397(5) and 4.013(2) Å for **2** and **3**, respectively. Additional cyanoacetate acts as terminal monodentate ligand for **2** and terminal chelating ligand for **3**. Moreover, the carboxyl-bridged dinuclear units are extended along the particular direction by paired μ_2-dpe spacers to create the infinite 1D ladder-like structures, as shown in Fig. 2c. The M···M separations across μ_2-dpe are 13.706(6) Å for **2** and 13.956(4) Å for **3**. The two pyridine rings of bipyridyl moieties are not coplanar with the dihedral angles between the two planar pyridine ring of 4.39° and 5.26° for **2** and **3**, respectively. The conformations of dpe molecules is *anti* with C—CH=CH—C torsion angles of 179.81° for **2** and 178.45° for **3**. The 3D packing structures of **2** and **3** are stabilized by various weak interchain H-bonding interactions (Fig. 3) involving terminal nitrile–N and oxygen atoms from cyanoacetates as H-acceptors and pyridyl, ethylene–H atoms from μ_2-dpe and alkyl–H atom from cyanoacetate as H-donors (Table 3). Furthermore, the nitrile–N from the terminal cyanoacetate can interact with the adjacent electron-deficient μ_2-dpe rings with N3···π distances of 3.382 and 3.388 Å for **2** and **3**, respectively, stabilizing the overall packing structures of **2** and **3**. The closest interchain M···M separations are 6.201(7) and 6.602(5) Å for **2** and **3**, respectively.

3.2. Photoluminescent properties

The phase purities of all compounds were confirmed by X-ray powder diffraction (Fig. S1), in which the experimental diffraction peaks are in good agreement with the pattern simulated from single-crystal data, implying the good phase purities of **1**–**3**.

The solid-state photoluminescent properties of **1**–**3** were investigated at ambient temperature. To compare the luminescent intensities, all emission spectra were determined with the same excitation wavelength (λ_{ex} = 285 nm) and the same spectral pass widths. As depicted in Fig. 4, compound **1** shows the intense emission band with maximum at 362 nm and shoulder bands near 380 and 450 nm, upon excitation at 285 nm. In contrast, the isostructures **2** and **3** show much weaker emission intensity with broad band with maxima around 470 nm. To understand the nature of emission bands, the luminescent spectrum of the free dpe ligand was also examined. The emission peaks of free dpe display the maximum in the 340–420 nm region and a broadband around 530 nm (λ_{ex} = 285 nm) [39,54], which may be assigned to intraligand π–π* and n–π* transitions [16,17,37,39]. Typically, in the compounds containing Zn(II)/Cd(II) ion with d^{10} configuration, there is no emission originates from the metal-to-ligand (MLCT) or ligand-to-metal charge transfer (LMCT), since the d^{10} metal ions are normally difficult to be oxidized or reduced [9,30,35,37]. Thus, the emission of **1**–**3** may be attributed to intraligand charge transition. Compared with the free dpe ligand, the emission patterns of **1**–**3** are quite similar to that of free dpe, implying the ligand-centered nature of the emission and display the blue-shifts which were attributed to coordination effects of dpe ligand to the metal centers [9,32,35,37]. The divergences of the emission spectra between **1** and isostructures **2** and **3** are attributed to the differences in coordination environments and the arrangement of π-conjugation between dpe moieties within supramolecular motifs [9,32].

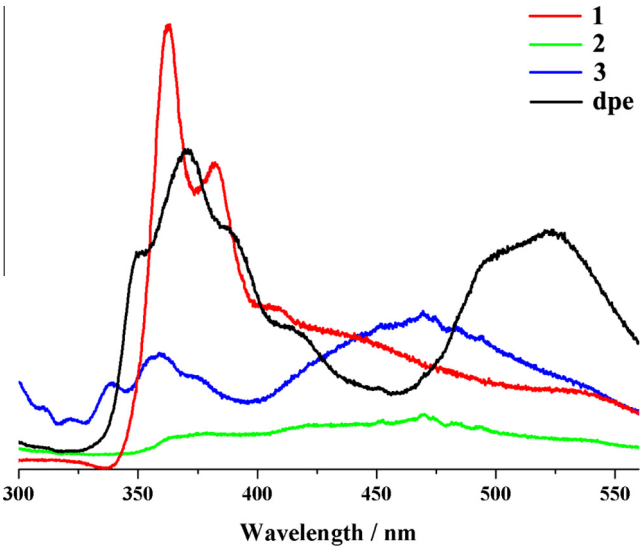

Fig. 4. The solid-state emission spectra of the free dpe and compounds **1**–**3** at room temperature.

4. Conclusion

In summary, three new 1D coordination polymers have been synthesised by self-assemblies of cyanoacetate with Zn(II)/Cd(II) ions and the 1,2-di(4-pyridyl)ethylene. Cyanoacetate well provides coordination site through carboxylate oxygen atoms, as well as, presents either various interchain H-bonding or N···π interactions through nitrile functional group, stabilizing whole 3D supramolecular frameworks. The result of photoluminescence for **1**–**3** in the solid state demonstrated that the orientation and the coordination environment of organic spacer within supramolecular frameworks powerfully affect the luminescent properties, and supports the idea that non-covalent supramolecular assemblies have great potential for utility in the chemistry of luminescent materials.

Acknowledgments

Funding for this work is provided by The Thailand Research Fund: Grant No. TRG5780003 (for Boonmak, J.) and BRG5680009 (for Youngme, S.), the Higher Education Research Promotion and National Research University Project of Thailand, through the Advanced Functional Materials Cluster of Khon Kaen University, and the center of Excellence for Innovation in Chemistry (PERCH–CIC), Office of the Higher Education Commission, Ministry of Education, Thailand.

Appendix A. Supplementary material

CCDC 1060710–1060712 contain the supplementary crystallographic data for **1**–**3**. These data can be obtained free of charge from The Cambridge Crystallographic Data Centre via http://www.ccdc.cam.ac.uk/data_request/cif. Supplementary data associated with this article can be found, in the online version, at http://dx.doi.org/10.1016/j.ica.2015.07.045.

References

[1] A.K. Cheetham, C.N.R. Rao, R.K. Feller, Chem. Commun. (2006) 4780.
[2] C. Janiak, Dalton Trans. (2003) 2781.
[3] S. Kitagawa, R. Kitaura, S.-I. Noro, Angew. Chem., Int. Ed. 43 (2004) 2334.
[4] R.J. Kuppler, D.J. Timmons, Q.-R. Fang, J.-R. Li, T.A. Makal, M.D. Young, D. Yuan, D. Zhao, W. Zhuang, H.-C. Zhou, Coord. Chem. Rev. 253 (2009) 3042.
[5] M. O'Keeffe, O.M. Yaghi, Chem. Rev. 112 (2012) 675.
[6] N. Stock, S. Biswas, Chem. Rev. 112 (2012) 933.
[7] M.P. Suh, H.J. Park, T.K. Prasad, D.-W. Lim, Chem. Rev. 112 (2012) 782.
[8] M. Yoon, R. Srirambalaji, K. Kim, Chem. Rev. 112 (2012) 1196.
[9] Y. Cui, Y. Yue, G. Qian, B. Chen, Chem. Rev. 112 (2012) 1126.
[10] Y.-W. Li, J.-R. Li, L.-F. Wang, B.-Y. Zhou, Q. Chena, X.-H. Bu, J. Mater. Chem. 1 (2014) 495.
[11] S.-I. Noro, S. Kitagawa, T. Akutagawa, T. Nakamura, Prog. Polym. Sci. 34 (2009) 240.
[12] G. Jiang, T. Wu, S.-T. Zheng, X. Zhao, Q. Lin, X. Bu, P. Feng, Cryst. Growth Des. 11 (2011) 3713.
[13] M. Du, X.-J. Jiang, X.-J. Zhao, Inorg. Chem. 46 (2011) 3984.
[14] H. Mao, C. Zhang, G. Li, H. Zhang, H. Hou, L. Li, Q. Wu, Y. Zhub, E. Wanga, Dalton Trans. (2004) 3918.
[15] D. Tian, Q. Chen, Y. Li, Y.-H. Zhang, Z. Chang, X.-H. Bu, Angew. Chem., Int. Ed. 53 (2014) 837.
[16] Y. Zhao, L.-L. He, H. Xu, X.-Y. Li, S.-Q. Zang, Inorg. Chim. Acta 404 (2013) 201.
[17] C.-C. Wang, C.-C. Yang, W.-C. Chung, G.-H. Lee, M.-L. Ho, Y.-C. Yu, M.-W. Chung, H.-S. Sheu, C.-H. Shih, K.-Y. Cheng, P.-J. Chang, P.-T. Chou, Chem. Eur. J. 17 (2011) 9232.
[18] R. Carballo, A. Castineiras, B. Covelo, E.M. Vazquez-Lopez, Polyhedron 20 (2001) 899.
[19] X.-Q. Liang, X.-H. Zhou, C. Chen, H.-P. Xiao, Y.-Z. Li, J.-L. Zuo, X.-Z. You, Cryst. Growth Des. 9 (2009) 1041.
[20] J. Boonmak, S. Youngme, T. Chotkhun, C. Engkagul, N. Chaichit, G.A.V. Albada, J. Reedijk Inorg. Chem. Commun. 11 (2008) 1231.
[21] H. Wang, D. Zhang, D. Sun, Y. Chen, L.-F. Zhang, L. Tian, J. Jiang, Z.-H. Ni, Cryst. Growth Des. 9 (2009) 5273.
[22] X.-F. Wang, Y.-B. Zhang, H. Huang, J.-P. Zhang, X.-M. Chen, Cryst. Growth Des. 8 (2008) 4559.
[23] J. Boonmak, S. Youngme, N. Chaichit, J. Reedijk Cryst. Growth Des. 9 (2009) 3318.
[24] P. Phuengphai, S. Youngme, N. Chaichit, J. Reedijk, Inorg. Chim. Acta 403 (2013) 35.
[25] Y. Kima, D.-Y. Jung, CrystEngComm 14 (2012) 4567.
[26] Z. Chang, D.-S. Zhang, Q. Chen, R.-F. Li, T.-L. Hu, X.-H. Bu, Inorg. Chem. 50 (2011) 7555.
[27] L. Fan, X. Zhang, Z. Sun, W. Zhang, Y. Ding, W. Fan, L. Sun, X. Zhao, H. Lei, Cryst. Growth Des. 13 (2013) 2462.
[28] G.-X. Liu, Y.-Q. Huang, Q. Chu, T.-A. Okamura, W.-Y. Sun, H. Liang, N. Ueyama, Cryst. Growth Des. 8 (2008) 3233.
[29] D. Bruhwiler, G. Calzaferri, T. Torres, J.H. Ramm, N. Gartmann, L.-Q. Dieu, I. Lopez-Duartec, M.V. Martinez-Dıaz, J. Mater. Chem. 19 (2009) 8040.
[30] Q. Zhang, F. Hu, Y. Zhang, W. Bi, D. Wang, D. Sun, Inorg. Chem. Commun. 24 (2012) 195.
[31] S. Jin, D. Wang, W. Chen, Inorg. Chem. Commun. 10 (2007) 685.
[32] X. Zhang, L. Hou, B. Liu, L. Cui, Y.-Y. Wang, B. Wu, Cryst. Growth Des. 13 (2013) 3177.
[33] B. Xu, J. Xie, H.-M. Hu, X.-L. Yang, F.-X. Dong, M.-L. Yang, G.-L. Xue, Cryst. Growth Des. 14 (2014) 1629.
[34] X.-L. Chen, Y.-L. Qiao, L.-J. Gao, H.-L. Cui, M.-L. Zhang, J.-F. Lv, X.-Y. Hou, Z. Anorg. Allg. Chem. 639 (2013) 403.
[35] G.-B. Yang, Z.-H. Sun, Inorg. Chem. Commun. 29 (2013) 94.
[36] X. Wang, C. Qin, E. Wang, Y. Li, N. Hao, C. Hu, L. Xu, Inorg. Chem. 43 (2004) 1850.
[37] R. Sen, D. Mal, P. Branda, R.A.S. Ferreira, Z. Lin, Cryst. Growth Des. 13 (2013) 5272.
[38] J. Ye, L. Zhao, R.F. Bogale, Y. Gao, X. Wang, X. Qian, S. Guo, J. Zhao, G. Ning, Chem. Eur. J. 21 (2015) 2029.
[39] J.-G. Kang, J.-S. Shin, D.-H. Cho, Y.-K. Jeong, C. Park, S.F. Soh, C.S. Lai, E.R.T. Tiekink, Cryst. Growth Des. 10 (2010) 1247.
[40] D.J. Darensbourg, E.V. Atnip, J.H. Reibenspies, Inorg. Chem. 31 (1992) 4475.
[41] T. Nakamoto, M. Hanaya, M. Katada, K. Endo, S. Kitagawa, H. Sano, Inorg. Chem. 36 (1997) 4347.
[42] G. Novitskii, S. Shova, V.K. Voronkova, L. Korobchenko, M. Gdanec, Y.A. Simonov, K. Turte, Russ. J. Coord. Chem. 27 (2001) 791.
[43] M.N. Sokolova, N.A. Budantseva, A.M. Fedoseev, Russ. J. Coord. Chem. 37 (2011) 478.
[44] D.J. Darensbourg, Inorg. Chem. 30 (1991) 358.
[45] D.J. Darensbourg, M.W. Holtcamp, E.M. Longridge, B. Khandelwal, K.K. Klausmeyer, J.H. Reibenspies, J. Am. Chem. Soc. 117 (1995) 318.
[46] D.J. Darensbourg, J.A. Joyce, C.J. Bischoff, J.H. Reibenspies, Inorg. Chem. 30 (1991) 1137.
[47] X. Feng, T.-C. FengII, J.-S. ZhaoIII, X.-G. ShiI, F. RuanI, Z. KristallogrI, NCS 224 (2009) 541.
[48] X. Feng, X.-G. Shi, F. Ruan, Z. Kristallogr, NCS 224 (2009) 193.
[49] S.G. Shova, Y.A. Simonov, M. Gdaniec, G.V. Novitchi, A. Lazarescu, K.I. Turta, Russ. J. Inorg. Chem. 47 (2002) 847.
[50] P. Startnowicz, Acta Crystallogr., Sect. C 49 (1993) 1621.
[51] APEX2 SAINT and SADABS, Bruker AXS Inc., Madison, WI, 2014.
[52] G.M. Sheldrick, Acta Crystallogr., Sect. A 64 (2008) 112.
[53] A.W. Addison, T.N. Rao, J. Reedijk, J. Van Rijn, G.C. Verschoor, J. Chem. Soc., Dalton Trans. (1984) 1349.
[54] W. Zhu, R. Zheng, X. Fu, H. Fu, Q. Shi, Y. Zhen, H. Dong, W. Hu, Angew. Chem., Int. Ed. 54 (2015) 6785.